

ISSN en trámite

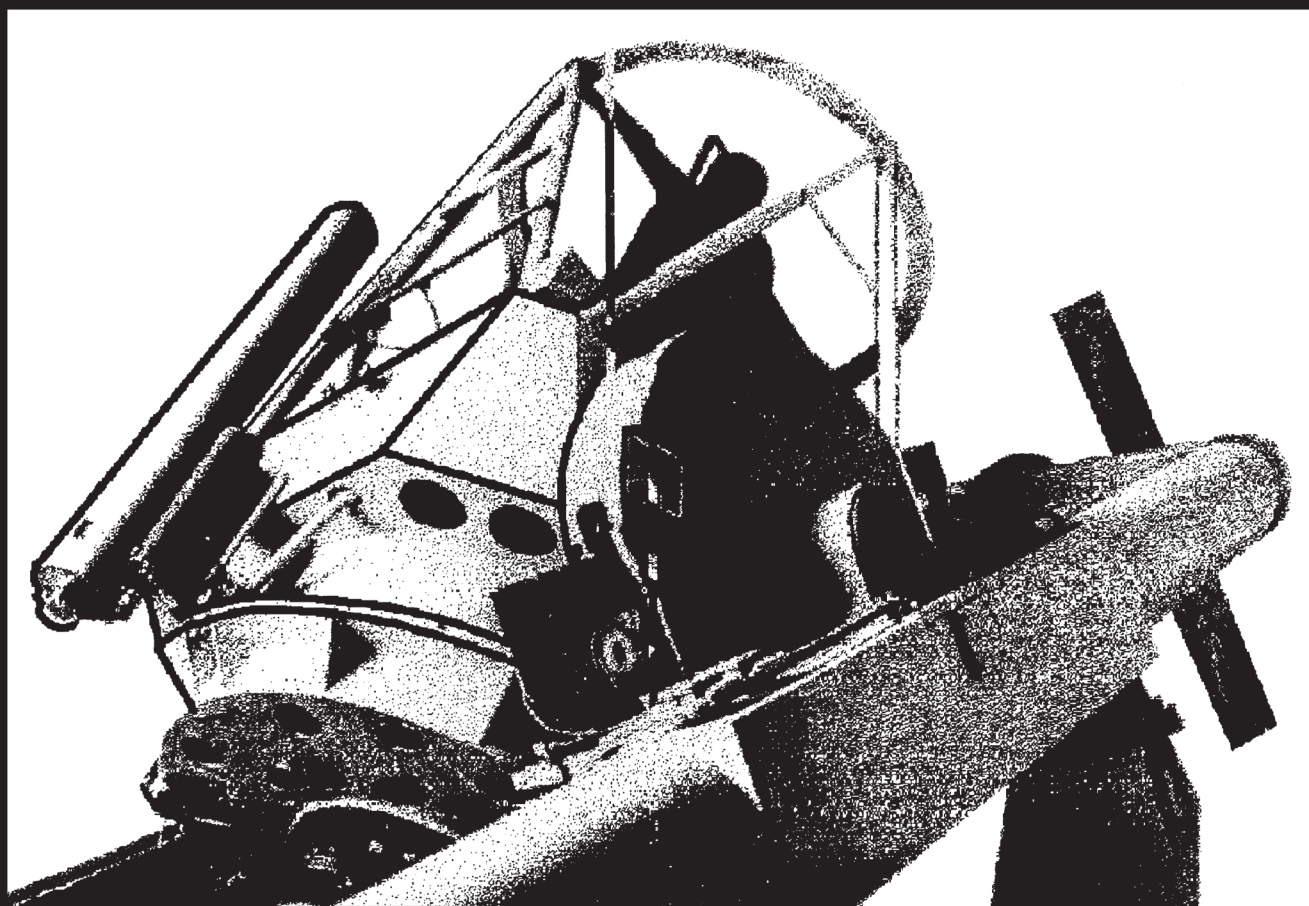
volumen 58, número 2, octubre 2022



instituto de astronomía

unam

revista mexicana de astronomía y astrofísica



revista mexicana de astronomía y astrofísica

volumen 58
número 2
octubre 2022

Instituto de Astronomía
Universidad Nacional Autónoma de México

revista mexicana de astronomía y astrofísica

Editores fundadores

Eugenio E. Mendoza V., Paris Pişmiş y Silvia Torres-Peimbert

Revista Mexicana de Astronomía y Astrofísica

Editora: Christine Allen

Revista Mexicana de Astronomía y Astrofísica. Serie de Conferencias

Editora: Silvia Torres-Peimbert

Editores asociados

William Henney

Comité editorial

Horacio A. Dottori (Universidade Federal Rio Grande do Sul, Brasil)

Guido Garay (Universidad de Chile, Santiago, Chile)

Gloria Koenigsberger (Universidad Nacional Autónoma de México)

Hugo Levato (Complejo Astronómico El Leoncito, Argentina)

Luis F. Rodríguez (Universidad Nacional Autónoma de México)

José-María Torrelles (Institut d'Estudis Espacials de Catalunya, Barcelona, España)

Alan M. Watson (Universidad Nacional Autónoma de México)

Asistentes editoriales

Héctor Miguel Cejudo Camacho

Tulio Lugo Córdova

Asesoría en cómputo

Alfredo Díaz Azuara, Carmelo Guzmán Cerón, Liliana Hernández Cervantes
y Francisco Ruíz Sala

D.R. © 2022, Universidad Nacional Autónoma de México

Av. Universidad 3000

Col. Universidad Nacional Autónoma de México, C. U.

Alcaldía Coyoacán

04510 Ciudad de México

ISSN en trámite

URL de DOI: <https://doi.org/10.22201/ia.01851101p.2022.58.02>

rmaa@astro.unam.mx

<http://www.astrocu.unam.mx/RMxAA/>

La *RMxAA* aparece indexada en Current Contents, Science Citation Index, Astronomy and Astrophysics Abstracts, Physics Briefs, Publicaciones Científicas en América Latina, Astronomy and Astrophysics Monthly Index, PERIODICA, RedALyC, Latindex y SciELO.

Revista Mexicana de Astronomía y Astrofísica, volumen 58, número 2, octubre 2022, es una publicación semestral, editada y distribuida por el Instituto de Astronomía, UNAM, Circuito Exterior, Ciudad Universitaria, 04510, Alcaldía Coyoacán, Ciudad de México, Teléfono: 5556223906, Correo Electrónico: rmaa@astro.unam.mx, ISSN en trámite. Editora responsable: Christine Patricia Allen Armiño. Distribución: Bienes y Servicios del Instituto de Astronomía, UNAM. Impresa por Grupo Edición, S.A. de C.V., Xochicalco 619, Colonia Letrán Valle, 03650, Alcaldía Benito Juárez, Ciudad de México. Fecha de impresión: 27 de septiembre de 2022. Número de ejemplares impresos: 500 en papel Couché de 100 gramos los interiores y en cartulina Couché de 250 gramos los forros. Precio de la publicación: gratuito.

THE DIFFERENTIAL REDSHIFT OF TITANIUM LINES IN K STARS <i>B. Oostra & P. Vargas</i>	173
C, T_1, T_2 : A COMPLEMENTARY METHOD TO DETECT MULTIPLE POPULATIONS WITH THE WASHINGTON FILTER SYSTEM <i>H. Frel̃ijj, D. Geisler, S. Villanova, & C. Munoz</i>	181
ASSESSING THE HIERARCHICAL HAMILTONIAN SPLITTING INTEGRATOR FOR COLLISIONLESS N -BODY SIMULATIONS <i>G. Aguilar-Argüello, O. Valenzuela, H. Velázquez, J. C. Clemente, & J. A. Trelles</i>	197
THE BONDI-HOYLE ACCRETION TAIL OF POINT SOURCES TRAVELING HYPERSONICALLY THROUGH A DENSE ENVIRONMENT <i>A. C. Raga, J. Cantó, A. Castellanos-Ramírez, A. Rodríguez-González, & P. R. Rivera-Ortiz</i>	215
THE OVERCONTACT BINARY V563 LYRAE <i>R. H. Nelson</i>	223
PHOTOMETRIC ANALYSIS OF TWO K SPECTRAL TYPE CONTACT BINARY SYSTEMS <i>C. Barani, M. Martignoni, F. Acerbi, R. Michel, H. Aceves & V. Popov</i>	237
A NON-SINGULAR CLOSED BOUNCING UNIVERSE WITHOUT VIOLATION OF NULL ENERGY CONDITION <i>Nasr Ahmed, Tarek M. Kamel, & Mohamed I. Nouh</i>	245
A VINDICATION OF THE RR LYRAE FOURIER LIGHT CURVE DECOMPOSITION FOR THE CALCULATION OF METALLICITY AND DISTANCE IN GLOBULAR CLUSTERS <i>A. Arellano Ferro</i>	257
SIMULATIONS OF UNEQUAL BINARY COLLISIONS EMBEDDED IN A TURBULENT GAS CLOUD FAR FROM A MASSIVE GRAVITATIONAL CENTER <i>G. Arreaga-García</i>	273
MILDLY RELATIVISTIC, BALLISTIC CORKSCREW JETS AS ROTATED SPIRALS <i>A. C. Raga, J. Cantó, A. Castellanos-Ramírez, A. Rodríguez-González, & P. R. Rivera-Ortiz</i>	301
A NEW ORBIT FOR COMET C/1830 F1 (GREAT MARCH COMET) <i>Richard L. Branham Jr.</i>	309
THE HIPPARCOS PLEIADES PARALLAX ERROR IS ALSO A PROPER MOTION ERROR <i>Valeri V. Makarov</i>	315

CONTENTS

ANN AND ANALYTICAL SOLUTIONS TO RELATIVISTIC ISOTHERMAL GAS SPHERES	321
<i>Mohamed I. Nouh, Yosry A. Azzam, Emad A-B Abdel-Salam, Farag I. Elnagahy, & Tarek M. Kamel</i>	
A STUDY OF THE NGC 1193 AND NGC 1798 OPEN CLUSTERS USING CCD UBV PHOTOMETRIC AND GAIA EDR3 DATA	333
<i>Talar Yontan, Hikmet Çakmak, Selçuk Bilir, Timothy Banks, Michel Raúl, Remziye Canbay, Seliz Koç, Seval Taşdemir, Hülya Erçay, Burçin Tanık Öztürk, & Deniz Cennet Dursun</i>	
CEN X-3 AS SEEN BY MAXI DURING SIX YEARS	355
<i>Á. Torregrosa, J. J. Rodes-Roca, J. M. Torrejón, G. Sanjurjo-Ferrín, & G. Bernabéu</i>	
AN ASTROPHYSICAL PERSPECTIVE OF LIFE. THE GROWTH OF COMPLEXITY	375
<i>F. Sánchez & E. Battaner</i>	
THE PRINCIPAL ASTROPHYSICAL PARAMETERS OF THE OPEN CLUSTERS <i>GULLIVER</i> 18 AND <i>GULLIVER</i> 58 DETERMINED USING GAIA EDR3 DATA	387
<i>A. L. Tadross & E. G. Elhosseiny</i>	
THE HII REGIONS AND BOW SHOCKS AROUND RUNAWAY O STARS	395
<i>A. C. Raga, J. Cantó, & A. Noriega-Crespo</i>	
OBSERVATIONAL CONSTRAINTS ON THE HD 5980 WIND-WIND COLLISION	403
<i>G. Koenigsberger, N. Morrell, D. J. Hillier, W. Schmutz, R. Gamen, J. I. Arias, R. Barbá, & G. Ferrero</i>	
OBITUARY – ARCADIO POVEDA	443
<i>Manuel Peimbert</i>	
OBITUARY – MARÍA ESTELA DE LARA ANDRADE	447
<i>Marco Arturo Moreno Corral</i>	
AUTHOR INDEX	449

THE DIFFERENTIAL REDSHIFT OF TITANIUM LINES IN K STARS

Benjamin Oostra and Paula Catalina Vargas Muñoz

Departamento de Física, Universidad de los Andes, Bogotá, Colombia.

Received November 19 2021; accepted March 2 2022

ABSTRACT

We present measurements of line core positions in UVES spectra of a sample of K-type stars, using the technique of bisector tracing. In all but two of these stars we detect an excess redshift of Ti I lines with respect to Fe I lines. We explain this invoking the temperature-dependence of the line depths. We conclude that the granulation curve is not unique but depends on the chemical species.

RESUMEN

Presentamos posiciones de líneas espectrales en los espectros de una muestra de estrellas tipo K obtenidos por el espectrógrafo UVES. Dichas posiciones fueron medidas empleando la técnica del trazado de bisectrices. En todas estas estrellas, exceptuando dos, encontramos un corrimiento de las líneas de titanio con respecto a las de hierro hacia longitudes de onda mayores. Explicamos esto en términos de la termodependencia de las profundidades de las líneas. Concluimos que la curva de granulación no es única, sino depende del elemento químico.

Key Words: convection — stars: general — Sun: granulation — techniques: spectroscopic

1. INTRODUCTION

Precise determination of stellar radial velocities is always affected by the superposition of convective blue- and redshifts in the upper stellar photosphere. Several authors (Dravins et al. 1981; Dravins 1990; Gray 2009) have addressed this issue, suggesting a method which, in principle, makes it possible to separate the contributions from convective velocities and the overall motion of the star. The key parameter is line depth: shallow or weak absorption lines originate in deeper layers where convective upwelling is fast, being more blueshifted than stronger lines which come from near the surface, where buoyancy disappears and gravity decelerates the convection. The result is a diagonal distribution of the line cores, which for the sun is quite narrow (Gray & Oostra 2018) with a velocity scatter between 50 and 100 m/s. If the granulation diagram of a star features a similar narrow diagonal, the standard solar curve, or a theoretical model curve (Ramírez et al. 2010), may be superposed on it, giving a trustworthy value for the stellar velocity and, as a bonus, an estimate of the strength of convection currents in the star.

Typically, such diagrams have a velocity scatter of about 200 m/s (Allende Prieto et al. 2002;

Ramírez et al. 2010) which is shown by these authors to be of the same order of magnitude as the calibration plus reduction errors.

In cool giants, however, this explanation may not be sufficient, as can be seen, for example, in Gray & Pugh (2012). Sometimes the granulation diagrams show a broad distribution of line cores, with no consistent shape or slope (like the star HD34055 in Figure 6).

Besides measurement errors, several causes have been hinted at, correlating with line strength, excitation potential and wavelength region (Dravins et al. 1981). Here we explore another reason: observed wavelength shift may depend on the chemical species. This effect can be seen in Gray & Pugh (2012). We show that, in some stars, Ti I lines are systematically redshifted with respect to Fe I lines, and discuss the probable reason.

2. DATA

2.1. Data Sources

We use spectra acquired with the UVES spectrograph (Dekker et al. 2000) and published under the Paranal Observatory Project POP (Bagnulo et al.

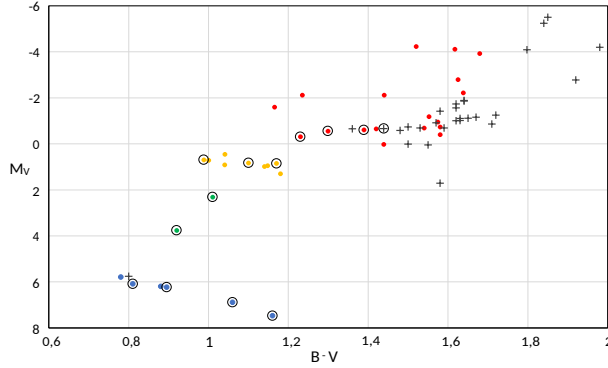


Fig. 1. Shown are all K stars (dots) and M stars (crosses) included in the POP survey. The stars used in the present work are circled. We classify the K stars according to their location. Blue: main sequence. Green: subgiants. Yellow: red clump. Red: red giant branch. The color figure can be viewed online.

2003); this library offers a large sample of stellar spectra, distributed over a major part of the HR diagram, each covering the visible and near infrared at a resolution of 8×10^4 and a sampling frequency of 49 data points per \AA in our chosen wavelength range from 7400 \AA to 7500 \AA . For comparison with higher resolution data, we also use the Hinkle & Wallace spectral atlas of Arcturus (Hinkle et al. 2000), which features a resolution of 150000 and a sampling rate of 112 pixels per \AA .

For line identification and rest wavelengths we use the VALD-3 database (Ryabchikova et al. 2015) from which we also extracted synthetic line depths for several stellar recipes.

2.2. Selection of Stars

The stars were selected from the Paranal Observatory Project (POP) database seeking to cover uniformly several photometric groups. As this source offers only the observed V magnitude, we checked SIMBAD (Wenger, M. et al. 2000) for parallax and multiband magnitudes, to locate the stars on the HR diagram (Figure 1). Three parallaxes reported in SIMBAD are from the revised Hipparcos data (Van Leeuwen 2007); the other ten are from Gaia EDR3 (Vallenari et al. 2021). We divided our sample into several groups according to the location on the HR diagram without any allusion to evolutionary status; in particular, the stars labeled “Red Clump” are not necessarily helium-burning stars.

We chose four main sequence dwarfs, two subgiants, three red clump giants, and four stars on the red giant branch, three of which are classified as

TABLE 1

LIST OF STUDIED LINES. THE “THERMO” NUMBERING IS EXPLAINED IN § 5

Species	λ air (VALD)	χ (eV)	log gf	Thermo
Fe I	7401,6849	4,1864	-1,599	
Fe I	7411,1544	4,2833	-0,299	
Fe I	7418,6674	4,1426	-1,376	
Fe I	7440,911	4,913	-0,573	
Fe I	7443,0224	4,1864	-1,82	
Fe I	7445,7508	4,2562	-0,102	
Fe I	7461,5206	2,5592	-3,58	
Fe I	7473,5539	4,607	-1,87	
Fe I	7476,3747	4,7955	-1,68	
Fe I	7491,6468	4,3013	-0,9	
Fe I	7495,0674	4,2204	0,052	
Ti I	7424,5858	0,8259	-3,48	6
Ti I	7432,6704	1,4601	-2,87	9
Ti I	7440,5765	2,2556	-0,86	1
Ti I	7456,5841	0,8181	-3,46	5
Ti I	7469,938	0,836	-3,26	4
Ti I	7471,2131	0,8129	-3,76	8
Ti I	7474,8944	1,7489	-2,18	7
Ti I	7489,578	2,2492	-0,91	2
Ti I	7496,102	2,2363	-1,06	3

spectral class K and one as type M. For the RGB star Arcturus we use both the UVES and Hinkle spectra, to assess the effect of spectral resolution.

2.3. Choice of Line Sample

We chose our wavelength range to avoid TiO and telluric bands. In the present study we pursue the relation between iron and titanium lines, so we exclude other elements. Only on the diagrams we left the core positions of two Cr lines, which are the deepest lines in this range and provide a visual reference.

Our 9 Ti lines were taken from the VALD database and selected for absence of blends. For Fe we chose the 16 Fe lines marked by Nave et al. (1994) as A-quality, but took the wavelength data from VALD for consistency. Five of these had to be discarded due to blends, leaving us with 11 Fe lines (Table 1).

3. TECHNIQUES

We flux-normalize the spectra with a third-grade polynomial. For the positions of the line cores we draw bisectors, which, additionally, give information on the line formation in deeper layers of the photosphere, and also serve as a quality test of the line, signaling eventual blends (Gray 2009).

3.1. Bisector Extraction

The most straightforward way of drawing bisectors is to interpolate between the data points, using linear segments or some type of spline, and to compute the bisector of this interpolated curve. Applying this method, the bisectors we obtain from the Arcturus-Hinkle spectrum are quite wavy (Figure 2a) and much more so in the Arcturus-UVES spectrum (Figure 2b); this renders the core positions ambiguous. We attribute this to the resolution and/or sampling: UVES resolution is 8×10^4 , while 3×10^5 is recommended for line asymmetry analysis, and 1×10^5 is considered a minimum (Dravins 1990; Landstreet 2017).

However, line asymmetry is measurable in UVES spectra (Dravins 2008) so we still use bisector tracing, but with a different technique. We fit a sixth-grade polynomial to each line profile, including as many data points as possible without impairing the quality of the fit (typically some 15 points), and draw the bisector from this polynomial. This method gives smooth bisectors (Figure 2c), which allow unequivocal positioning of the cores.

The number of data points to be included must be optimized for every line (Figure 3b); the correlation coefficient R^2 has a (slight) local maximum. If many more points are included, the polynomial is clearly incapable of modelling the line profile (Figure 3a); and if many fewer points are used, the point-to-point noise becomes noticeable (Figure 3c). Of course, when including $n+1$ data for a grade- n polynomial, the fit is “perfect” but does not filter out the random flux errors, and noise deformations are evident.

To estimate the uncertainty of the measured velocities, we varied the order of the polynomial and the number of data points included in the fit. Additionally, we compared for our 22 lines the velocities obtained from Arcturus-UVES with those from Arcturus-Hinkle. The differences have a standard deviation of 120 m/s. But this scatter is not random; it is the sum of a random error and a systematic error due to the difference in resolution of the two instruments. Plotting the difference in velocity against the slope of the bisectors, we find that the former has a spread of 65 m/s and the latter, spanning about 100 m/s, may be modeled and corrected.

3.2. Quantification of the Observed Redshift

To quantify the differential redshift of the Ti lines, we define the Mean Differential Redshift (MDR) for each star as the average velocity of the Ti lines minus the average of the Fe lines, divided by

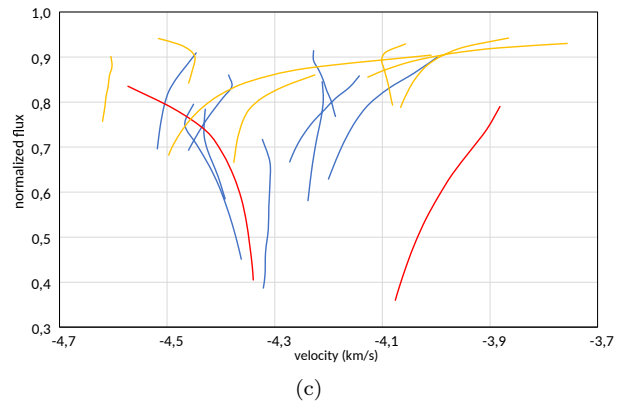
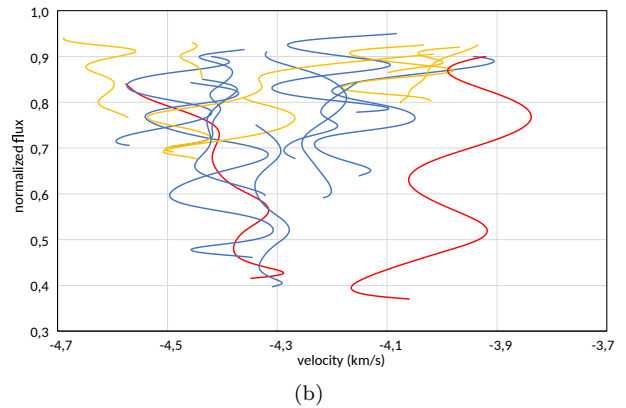
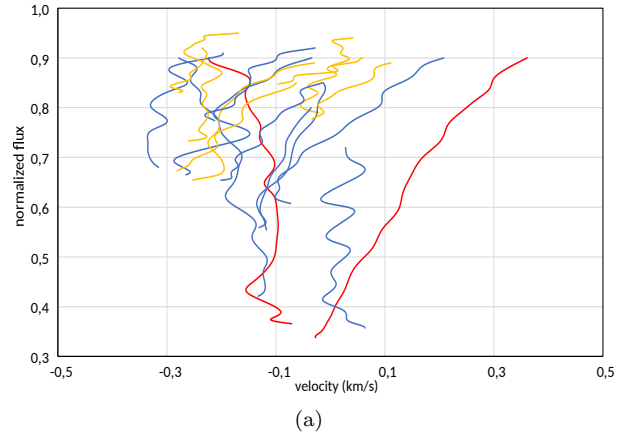


Fig. 2. (a) Bisectors from Arcturus-Hinkle in the range $7400 \text{ \AA} - 7500 \text{ \AA}$, using the usual method of interpolating cubic splines between data points. Blue = iron, green = titanium, red = chromium. (b) Bisectors from Arcturus-UVES, with the same details as in Figure 2a. (c) Bisectors from Arcturus-UVES, with the method of adjusting a single polynomial to each spectral line. The color figure can be viewed online.

the standard deviation of the Ti velocities:

$$MDR = \frac{\langle V_{Ti} \rangle - \langle V_{Fe} \rangle}{\sigma \langle V_{Ti} \rangle}. \quad (1)$$

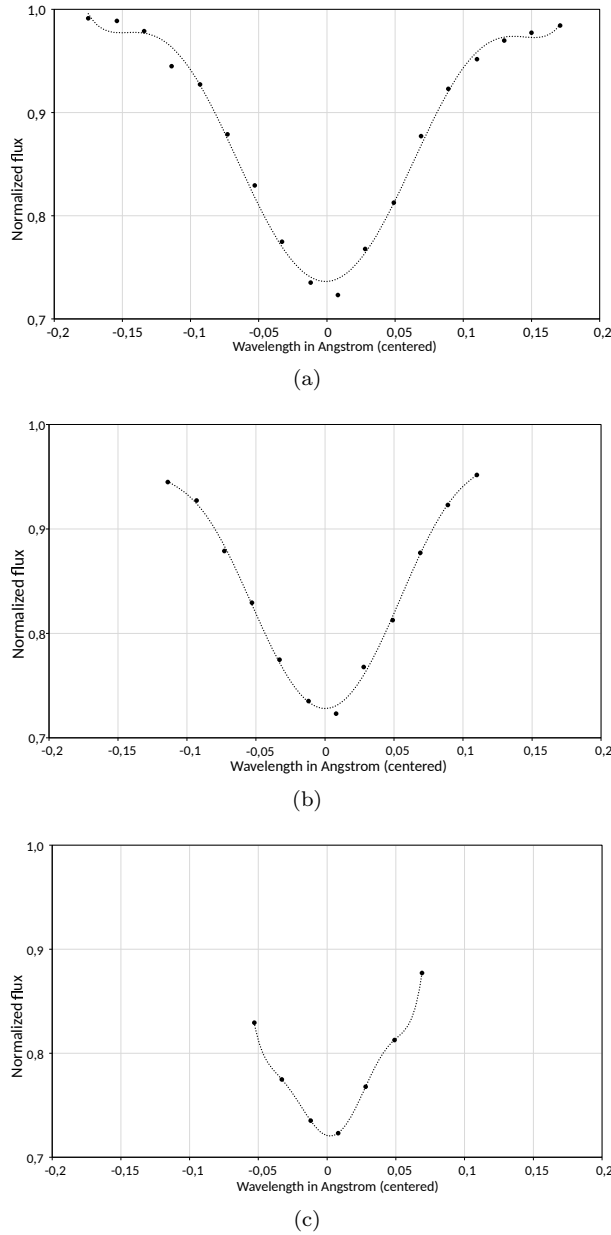


Fig. 3. (a) Profile of the 7489 Å Ti line in the UVES spectrum of HD209100, including 18 data points. The horizontal axis shows a relative wavelength scale in Å, and the dotted line is a 6th grade polynomial. The fit is inadequate because the number of points is too large. (b) The same as Figure 3a but including only 12 data points; this is the optimal number in this case. (c) The same as before but including only 7 data points; the fit is exact but the deformations are evident.

The reason for the “normalization” is that, when the Ti lines are more disperse, any shift of their average position is less significant statistically. For the mean velocities we use the simple average.

We compute the uncertainty of the MDR as the combination of the random uncertainties for the individual lines, which amount to 65 m/s. For N_{Fe} iron lines and N_{Ti} titanium lines, we get

$$\Delta MDR = \sqrt{\frac{1}{N_{Fe}} + \frac{1}{N_{Ti}}} \frac{65 \text{ m/s}}{\sigma(V_{Ti})}. \quad (2)$$

Our line sample includes 9 Ti lines and 11 Fe lines; however, for computing MDR we exclude two high-redshift Ti lines (7432 Å and 7471 Å) which are illegible in some stars and blended in others; omitting them in all stars allows a more balanced comparison. Basically, then, $N_{Fe} = 11$ and $N_{Ti} = 7$; but these values may vary in some stars due to illegible lines. On the plots (Figures 4 to 7), all legible Ti lines are included, joined by line segments in a specific order as explained in § 5.

4. RESULTS

Due to our definition of MDR, the values may give the impression that the effect is smaller than it really is, for two reasons: We eliminated the two Ti lines with the largest redshift, thus reducing $\langle V_{Ti} \rangle$; and the deepest Fe lines are redshifted by granulation (particularly in Arcturus-Hinkle), increasing $\langle V_{Fe} \rangle$. For this reason, we show all the granulation diagrams.

4.1. Main Sequence

The clearest example of Ti redshift is the K5 dwarf HD 156026. From there, climbing the main sequence, the effect weakens gradually. The line with the largest shift in HD 209100 is at 7471 Å; this is due to a blend in some stars; it is excluded from the MDR computation in all stars. The granulation diagrams are shown in Figure 4. All results are summarized in Table 2.

4.2. Red Giant Branch

The three K-type RGB stars are HD124897 (Arcturus), HD138688, and HD198357; for Arcturus we have two redshift data. The granulation diagrams are shown in Figure 5.

Our only M-type RGB star is HD 34055; its granulation diagram is presented in Figure 6. Here we clearly see the change of spectral class: Ti lines are deeper than Fe lines.

4.3. Red Clump and Subgiants

Finally, Figure 7 shows the granulation diagrams of our three red clump stars and two subgiants.

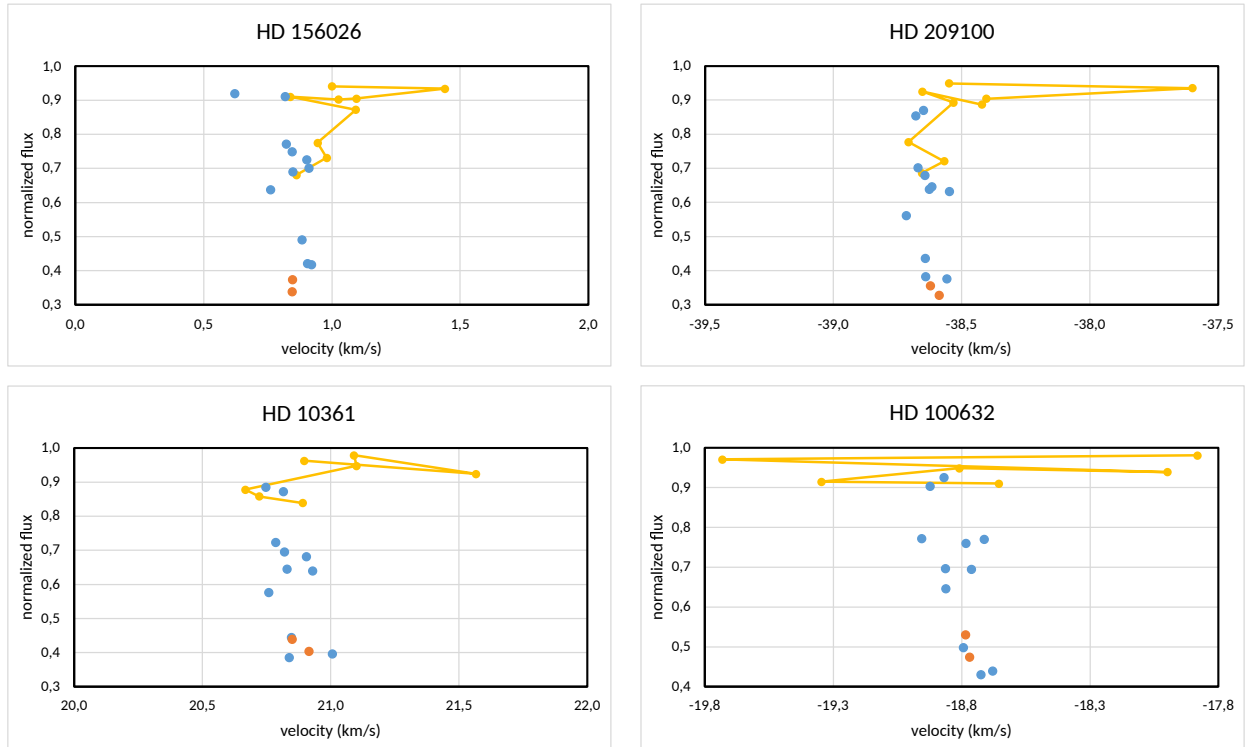


Fig. 4. Granulation diagrams of four MS stars. Ti lines are plotted in yellow, Fe lines in blue, and Cr lines in red. The excess redshift of titanium is evident, as is its gradual decrease. All our granulation diagrams cover a velocity range of 2 km/s. The large dispersion of Ti lines in HD 100623 may be caused by measurement errors due to their small depth. The color figure can be viewed online.

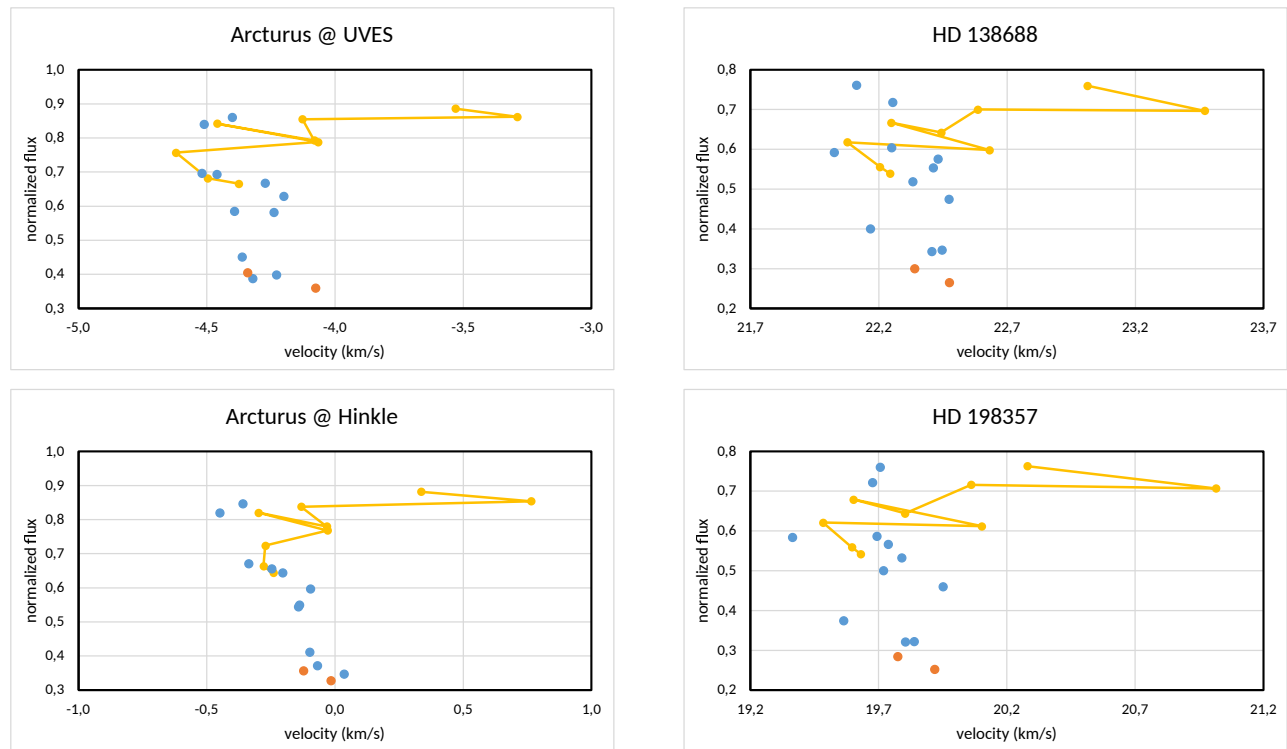


Fig. 5. Granulation diagrams for four RGB stars, including two from Arcturus. The smaller dispersion of the Fe lines in the Hinkle spectrum might be attributed to its higher resolution; but it is similar to the Fe distributions in the UVES spectra of the dwarf stars. The color figure can be viewed online.

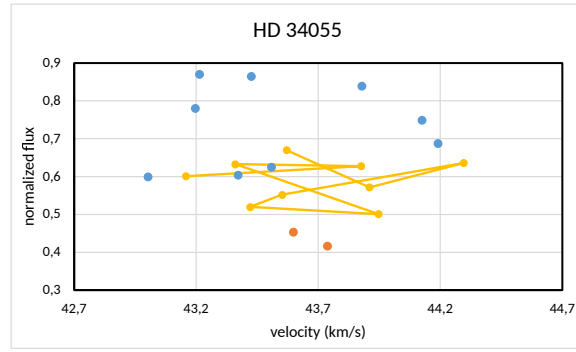


Fig. 6. Granulation diagram of an RGB type M star. The color figure can be viewed online.

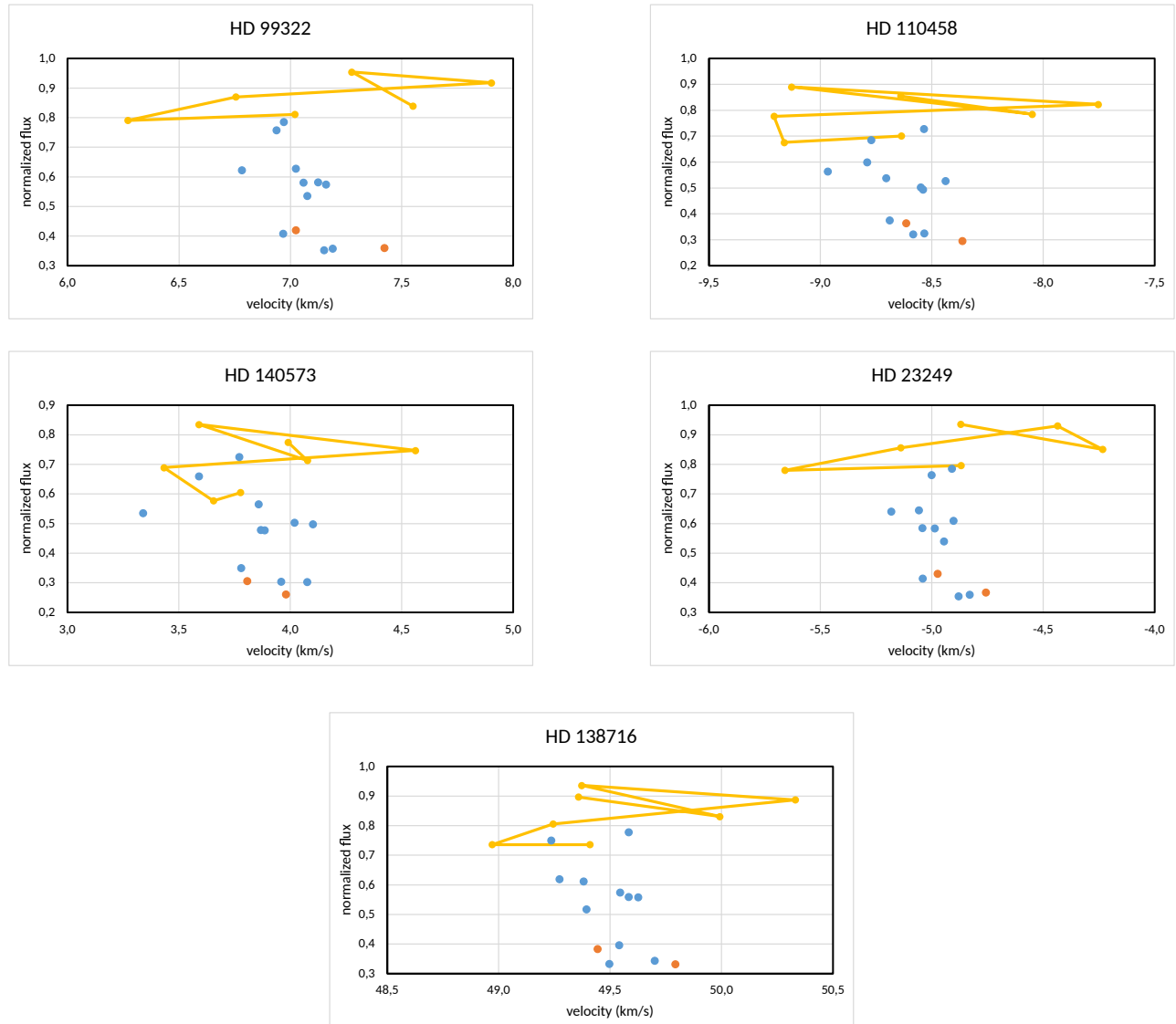


Fig. 7. Granulation diagrams for three red clump stars and two subgiants. There are less Ti lines than in previous examples; several lines are too small to be measured. The color figure can be viewed online.

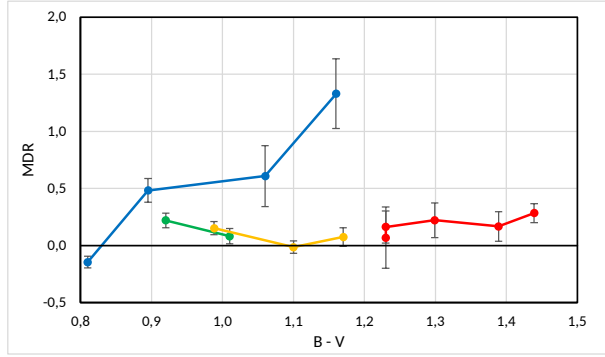


Fig. 8. Color dependence of Ti redshift. The colors indicate the groups as in Figure 1. Blue: main sequence; green: subgiants; yellow: red clump; and red: red giant branch. The color figure can be viewed online.

TABLE 2

MEASURED REDSHIFT OF TI LINES*

	HD	Spectrum	$B-V$	M_V	MDR	Δ MDR
Dwarfs	100623	K0 V	0,81	6,081	-0,146	0,052
	10361	K2 V	0,89	6,231	0,483	0,104
	209100	K5 V	1,06	6,885	0,608	0,267
	156026	K5 V	1,16	7,467	1,329	0,306
SG	23249	K0 IV	0,92	3,759	0,220	0,065
	138716	K1 IV	1,01	2,313	0,081	0,067
RC	99322	K0 III	0,99	0,693	0,152	0,056
	110458	K0 III	1,10	0,826	-0,016	0,054
RGB	140573	K2 IIIb	1,17	0,852	0,074	0,082
	124897-H	K1,5 III	1,23	-0,307	0,068	0,269
	124897-U	K1,5 III	1,23	-0,307	0,162	0,141
	138688	K2/4 III	1,30	-0,556	0,221	0,152
	198357	K3 III	1,39	-0,608	0,166	0,130
	34055	M4 III	1,44	-0,663	0,283	0,082

*Two MDR values are reported for HD 124897 (Arcturus): The first is from the Hinkle spectrum, the second from UVES.

4.4. Color Dependence

It would be natural to inquire how MDR depends on basic stellar parameters such as color index or absolute magnitude. Within each class, the variation of absolute magnitude is rather small; therefore we show the relation between observed redshift and color (Figure 8).

5. DISCUSSION

In search of an explanation for the differential redshift, we studied the temperature-dependence of these spectral lines, extracting synthetic spectra

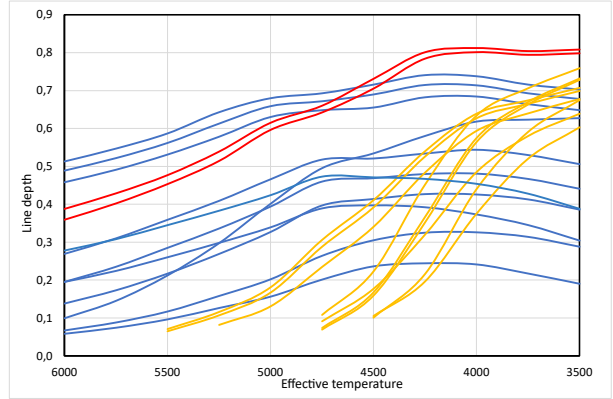


Fig. 9. VALD Line depth versus stellar temperature for Fe (blue), Cr (red) and Ti lines (yellow). The color figure can be viewed online.

from VALD for eleven stellar temperatures between 3500 K and 6000 K and plotting these theoretical depths (Figure 9).

It is evident that Ti lines weaken towards hotter stars much faster than Fe lines. This is due to ionization of Ti in hotter stars. We suggest that this thermosensitivity is also responsible for the redshift of Ti lines as compared to Fe lines. As a further evidence for the relation between these two phenomena, we discriminate between the Ti lines: the lines which disappear faster as the effective temperature increases, i.e. the most thermosensitive lines, are also the lines with a greater differential redshift. To make this more apparent we number the Ti lines in Figure 9 from top left to bottom right, roughly between 4000 K and 4500 K. These numbers are given in Table 1 in the column labeled “Thermo”. In all the granulation diagrams we linked the Ti points by line segments in this order. Lines 1, 2 and 3 are the strongest or deepest; in most diagrams, these lower numbers cluster toward the left while higher numbers are more to the right. In other words, the differential redshift of individual Ti lines correlates roughly with the thermodependence shown in Figure 9.

We propose an explanation of the differential redshift based on granulation. On the star’s photosphere are bright spots of hot, rising gas separated by darker lanes of cool, sinking material. The most thermosensitive lines, which disappear faster as stellar effective temperature increases, originate mainly in the cool intergranular lanes, rather than in the hot granules where line formation is impaired by Ti ionization. The latter regions are blueshifted by upwelling convection currents, while the former are redshifted as the cool material sinks back into the star.

This phenomenon affects Ti lines more than Fe lines, and some Ti lines more than others.

We conclude that the differential redshift is basically a sign of granulation. Three spectroscopic signatures of stellar granulation have been published earlier (Gray 2009): overall line broadening, line profile asymmetry (bisector shape), and a core blueshift which correlates inversely with line depth. The differential redshift of the Ti lines is another such signature.

We are aware that our sample is very small and cannot allow general conclusions.

The spectral region of 7400 Å - 7500 Å which we chose mainly to avoid TiO bands, turned out to include a CN band which is prominent in several of our stars. The Ti lines 7432 Å and 7471 Å are notably affected in some stars. We checked if the differential redshift is not an artifact of CN blends. On the contrary, we found a strong inverse correlation between the CN strength and Ti redshift. We conclude that the CN band partially masks the differential Ti redshift.

The differential redshift of a certain chemical species will broaden some granulation diagrams. A detailed characterization of this effect may help to reduce uncertainties in granulation studies and radial velocity measurements. Another possible strategy is to use only Fe lines.

The greater redshift of the weaker Ti lines constitutes the upper part of the “C” shape of the granulation diagram for cool stars. The same effect is expected for iron lines, but for shallower lines, or deeper layers in the photosphere. This means that the granulation diagram is not a unique curve, but rather one curve is needed for each element.

Considering this, it is to be expected that the differential redshift disappears at the granulation boundary (Gray & Nagel 1989), at the blue side of which the granulation plots resemble the symbol “O” or inverse “C”. The effect is expected to increase from the boundary toward cooler stars, particularly giants where intergranular lanes occupy a relatively larger area.

We appreciate the valuable suggestions and corrections of the referee.

REFERENCES

- Allende Prieto, C., Asplund, M., García López, R. J., & Lambert, D. L. 2002, *ApJ*, 567, 544, <https://doi.org/10.1086/338248>
- Bagnulo, S., Jehin, E., Ledoux, C., et al. 2003, *Msngr*, 114, 10
- Dekker, H., D’Odorico, S., Kaufer, A., Delabre, B., & Kotzlowski, H. 2000, *SPIE*, 4008, 534, <https://doi.org/10.1117/12.395512>
- Dravins, D. 2008, *A&A*, 492, 199, <https://doi.org/10.1051/0004-6361/200810481>
- _____. 1990, *MmSAI*, 61, 513
- Dravins, D., Lindegren, L., & Nordlund, A. 1981, *A&A*, 96, 345
- Gaia Collaboration, Brown, A. G. A., Vallenari, A., et al. 2021, *A&A*, 649, 1, <https://doi.org/10.1051/0004-6361/202039657>
- Gray, D. F. 2009, *ApJ*, 697, 1032, <https://doi.org/10.1088/0004-637x/697/2/1032>
- Gray, D. F. & Nagel, T. 1989, *ApJ*, 341, 421, <https://doi.org/10.1086/167505>
- Gray, D. F. & Oostra, B. 2018, *ApJ*, 852, 42, <https://doi.org/10.3847/1538-4357/aa9c82>
- Gray, D. F. & Pugh, T. 2012, *AJ*, 143, 92, <https://doi.org/10.1088/0004-6256/143/4/92>
- Hinkle, K., Wallace, L., Valenti, J., & Harmer, D. 2000, *Visible and Near Infrared Atlas of the Arcturus Spectrum 3727-9300 Å*, ed. K. Hinkle, L. Wallace, J. Valenti, & D. Harmer (San Francisco, CA:ASP)
- Landstreet, J. D. 2017, *IAUS 239, Convection in Astrophysics*, ed. F. Kupka, I. Roxburgh, & K. Chan, 103
- Nave, G., Johansson, S., Learner, R. C. M., Thorne, A. P., & Brault, J. W. 1994, *ApJS*, 94, 221, <https://doi.org/10.1086/192079>
- Ramírez, I., Collet, R., Lambert, D. L., Allende Prieto, C., & Asplund, M. 2010, *ApJ*, 725, 223, <https://doi.org/10.1088/2041-8205/725/2/L223>
- Ryabchikova, T., Piskunov, N., Kurucz, R. L., et al. 2015, *PhyS*, 90, 054005, <https://doi.org/10.1088/0031-8949/90/5/054005>
- Van Leeuwen, F. 2007, *A&A*, 474, 653, <https://doi.org/10.1051/0004-6361/20078357>
- Wenger, M., Ochsenbein, F., Egret, D., et al. 2000, *A&AS*, 143, 9, <https://doi.org/10.1051/aas:2000332>

C, T_1, T_2 : A COMPLEMENTARY METHOD TO DETECT MULTIPLE POPULATIONS WITH THE WASHINGTON FILTER SYSTEM

Heinz Frelíj¹, Douglas Geisler^{1,2,3}, Sandro Villanova¹, and Cesar Munoz^{3,2,1}

Received January 7 2022; accepted March 18 2022

ABSTRACT

In this research we test the ability of a three Washington filter combination, $(C - T_1) - (T_1 - T_2)$, compared with that of the traditional $C - T_1$ color to find multiple populations on two globular clusters: NGC 7099 and NGC 1851, types I and II Globular clusters, respectively. Our improved photometry and membership selection, now using Gaia proper motions, finds that second population stars are more centrally concentrated than first population stars, as expected and contrary to our previous findings for NGC 7099. We find that multiple populations are more easily detected in both clusters using the new $(C - T_1) - (T_1 - T_2)$ color, although $C - T_1$ conserves the best width/error ratio. We also search for differences of both colors while splitting the red-RGB and the blue-RGB in NGC 1851, but find no significant improvement.

RESUMEN

En este trabajo comparamos la capacidad de una combinación de tres filtros Washington $(C - T_1) - (T_1 - T_2)$ con la del color tradicional $C - T_1$ para encontrar poblaciones múltiples en dos cúmulos globulares, NGC 7099 y NGC 1851, de tipo I y II respectivamente. Con nuestra fotometría mejorada y con la selección de miembros mediante movimientos propios de Gaia encontramos que las estrellas de segunda población están más concentradas al centro que las de primera población, como se espera, pero en contradicción con nuestros resultados previos para NGC 7099. Encontramos que en ambos cúmulos es más fácil detectar poblaciones múltiples usando el color $(C - T_1) - (T_1 - T_2)$, pero que $C - T_1$ conserva la mejor proporción anchura/error. Buscamos también diferencias en ambos colores al separar la RGB roja de la RGB azul en NGC 1851, sin encontrar una mejora significativa.

Key Words: globular clusters: individual: NGC 7099 — globular clusters: individual: NGC 1851 — Hertzsprung–Russell and colour–magnitude diagrams — stars: imaging — techniques: photometric

1. INTRODUCTION

Multiple Populations (MPs) are now recognized as an essential characteristic of almost all globular clusters (GCs). Historically, Cannon & Stobie (1973) almost 50 years ago found an exceptionally large scatter in the red giant branch (RGB) of Omega Cen. Thirty years later Bedin et al. (2004)

found two primary sequences not only in the color of the RGB of Omega Cen, but also in the sub-giant branch (SGB) and main sequence (MS), giving the first detailed photometric glimpse of what would become known as MPs. But it was not until Carretta et al. (2009) realized a heroic high resolution spectroscopic study of thousands of stars in a total of 19 GCs, finding chemical inhomogeneities in all of them, that MPs began to be considered as an intrinsic characteristic of GCs. Subsequently, Carretta et al. (2010) in fact suggested a new definition of a GC: stellar systems showing anti-correlations among the abundances of light-elements, whose main and most widespread example is the Na-O anticorrela-

¹Departamento de Astronomía, Casilla 160-C, Universidad de Concepción, Concepción, Chile.

²Instituto de Investigación Multidisciplinario en Ciencia y Tecnología, Universidad de La Serena. Avenida Raúl Bitran S/N, La Serena, Chile.

³Departamento de Astronomía, Facultad de Ciencias, Universidad de La Serena. Av. Juan Cisternas 1200, La Serena, Chile.

tion. This major study would be complemented 6 years later with that of Piotto et al. (2015), who conducted the HST GC UV Legacy survey using an improved photometric method employing the UV/blue WFC3/UVIS filters F275W, F336W, and F438W, best known as the “magic trio”, to characterize MPs in 57 GCs, showing that they all possess MPs and proving that photometry with appropriate filters is an excellent method to detect MPs. The advantages of photometry over spectroscopy, of course, are the ability to investigate MPs in a much larger sample in a given GC with a much smaller telescope than typically possible with high resolution spectra. Two years later, Milone et al. (2017) divided these 57 GCs into type I(GCs whose stars separate in two distinct groups, identified as first(1P) and second(2P) populations) and type II clusters (those GCs where the 1P and/or the 2P sequences appear to be split and include an additional group of redder stars in the chromosome map. Type II GCs also exhibit multiple SGBs in purely optical CMDs).

The most important conclusion is that virtually all the GC show MPs. But some clusters seemed to be the exception: IC4499 (Walker et al. 2011), E3 (Salinas, & Strader 2015), Terzan 7 (Tautvaišienė et al. 2004) and especially Ruprecht 106 (Villanova et al. 2013; Frelíj et al. 2021) are the best examples (although certain HST studies put in doubt some of them (Dotter et al. 2018; Dalessandro et al. 2018). Thus, every cluster has to be carefully studied to determine whether it has MPs or not, and to study its characteristics, as the UV Legacy survey has demonstrated that every GC is unique in its MP behavior.

Various scenarios for the origin of MPs have been proposed: asymptotic giant branch scenarios like D’Ercole et al. (2008), fast rotating massive stars scenarios like Decressin et al. (2007) and even a scenario that did not invoke multiple epochs of star-formation (Bastian et al. 2013). But currently none of them satisfies all the observational evidence (Renzini et al. 2015; Bastian & Lardo 2018), although newer models, like Elmegreen (2017); Gieles et al. (2018) and Parmentier & Pasquali (2022) are getting closer.

The studies mentioned above have proven photometry to be a very good way to search for MPs, because, while it cannot provide the detailed abundances of spectroscopy, it allows the measurement of a much larger sample of stars simultaneously and to much fainter absolute magnitudes. Sbordone et al. (2011) produced synthetic spectra of two otherwise identical GC giants, one being a 1P star with normal chemical abundances of the light elements

and the other being a 2P star with enhanced He, N and Na and depleted C and O, as observed in many spectroscopic studies. The study shows that significant differences in flux between the two spectra exist and are related to the various CN, CH, NH and OH bands, particularly in the *UB*/blue part of the spectrum.

Some photometric bands, concentrated in the blue-*uv* portion of the spectrum, are specially sensitive to these bands. The best known are the already mentioned “magic trio” of filters used in Piotto et al. (2015), consisting of three HST UVIS/WFC3 filters: F275W, F336W and F438W. The combination of these sensitive filters led to colors maximizing the separation of the different populations of stars. Actually, most blue/*UV* filters are capable of uncovering MPs. However, although most such filters, such as $U_{Johnson-Cousins}$ and u'_{SDSS} , detect MPs quite well, they require long exposure times due to their relatively narrow band and/or low efficiency.

The Washington filter system was designed by Canterna (1976) originally to derive a photometric temperature (from the T_1 and T_2 filters, very similar to $(RI)_{KC}$), as well as a metallicity index (from the M filter) for G and K giants. However, at the time, CN and CH variations were being discovered in GCs and it was felt prudent to include another filter that would be sensitive to such variations independent from metallicity effects, and thus the C (“Carbon”) filter was added. The Washington C filter is a blue-*UV* filter, with $\lambda_{eff} = 3982\text{\AA}$ and $\Delta\lambda = 1070\text{\AA}$ (Bessell 2005). This broadband allows it to encompass 3 CN-Bands and one NH-Band, as well as the CH band. Because of its efficiency, it should be sensitive to MPs in considerably less exposure time than other, more narrow-band, filters. These 2 characteristics make the Washington C filter a good option for detection of MPs. Indeed, the HST WFC3/UVIS instrument includes a C -like filter: F390W.

Initial efforts investigating the possibility of uncovering MPs from the ground with the Washington system used the $C - T_1$ color, obtaining good results (Cummings et al. 2014; Frelíj et al. 2017). These results, although not as accurate as HST data, present an attractive alternative, based on small ground-based telescopes. Our aim here is to investigate if there might be an even better Washington color for detecting MPs, involving the addition of the T_2 filter, which maintains some MP sensitivity (see Figure 2).

This paper is organized as follows:

In § 2 we present the data used, how they were obtained and reduced.

TABLE 1
NGC 1851 & NGC 7099: IMAGES

NGC 7099					
	Swope		SOAR		
<i>C</i>	1(30s)	2(300s)	4(1200s)	4(10s)	2(300s)
<i>R</i>	1(10s)	1(100s)	3(400s)	-	-
<i>I</i>	1(10s)	1(300s)	3(1200s)	-	-
NGC 1851					
	Swope		SOAR		
<i>C</i>	1(30s)	1(300s)	7(1200s)	2(10s)	2(300s)
<i>R</i>	1(10s)	1(100s)	3(400s)	-	-
<i>I</i>	1(10s)	1(300s)	3(1200s)	-	-

§ 3 describes the results using the the new method and compares these with results from the initial technique. We also analyze the results. § 4 contains a summary of the paper.

2. DATA

2.1. Observations

The data consist of 46 images, 23 of NGC 7099 and 23 of NGC 1851. They were obtained from 2 telescopes, the 1-meter Swope telescope from Las Campanas Observatory, Chile; and the 4m SOAR telescope on Cerro Pachon, Chile. The filters selected for this work were the Washington *C* filter (Canterna 1976), and the filters R_{KC} and I_{KC} in replacement of the Washington filters T_1 and T_2 since Geisler (1996) demonstrated that the R_{KC} filter is a more efficient substitute for T_1 and the T_2 filter is almost identical to I_{KC} (Canterna 1976; Geisler 1996). For NGC 7099 we used the same images from Freljij et al. (2017, hereafter F17), only dropping 1 medium and 2 long *C* exposures from the Swope Telescope in order to decrease the average seeing. The air masses vary between 1.0-1.4 while the FWHM is 0.9"-1.7" for the Swope images and 0.39"-0.54" for SOAR images. For NGC 1851 we took the images used in Cummings et al. (2014, hereafter C14) but discarded 3 long, poor-seeing *C* exposures from the Swope telescope, added 1 short exposure from Swope for *C*, *R* & *I*, and added 2 short and 2 long exposures from SOAR in *C*. The air masses vary between 1.0-1.5 while the FWHM is 0.9"-1.58" for the Swope images and 0.49"-0.52" for the SOAR images. All nights appeared photometric visually.

Table 1 gives the details of the exposures.

The Swope images were observed with a CCD (SiTe3) of 2048×3150 pixels at $0.435''/\text{pix}$ and a

field of view of 14.9×22.8 arc minutes. The SOAR detector (SOI) consists of a total of 4096×4096 pixels at $0.1534''/\text{pix}$ ($0.0767''/\text{pix}$ binned 2x2) and a field of view of 5.26×5.26 arc minutes, divided into two CCDs with two amplifiers each, resulting in 4 columns of 1024×4096 pixels.

2.2. Processing and Reduction

IRAF⁴ and its standard tasks were used to process all the photometric data. A linearity correction (Hamuy et al. 2006) was applied to all the Swope (SiTe3) images in order to increase the range of unsaturated stars. DAOPHOT (Stetson 1987) and its suite of tasks were used to perform the photometry in both clusters since it was specially developed to work on crowded fields. A first PSF was determined in each single image by taking the ≈ 200 brightest unsaturated and more isolated stars. These stars were refined subtracting all their detected neighbours to determine a second and more precise PSF that was refined a third time by eye, thus removing all PSF-stars with bad subtracted neighbours. This refined PSF determined in each image was applied to carry out a PSF photometry three successive times through the tasks FIND, PHOT and ALLSTAR. Due to the large pixel scale of the SiTe3 detector ($0.435''/\text{pix}$), we decided to repeat the technique used in C14, setting in DAOPHOT and ALLFRAME a fitting radius 0.4px smaller than the FWHM measured, for all the Swope images with a FWHM smaller than 3 px in order to avoid photometric errors due to "square stars". We experimented with different ALLFRAME (Stetson 1994) methods based on the procedures from C14 and F17, and found that the best photometry is obtained in the following way:

First, applying the cuts used in C14, that consists in removing all the stars with errors larger than 0.15, chi-squared greater than 2.5, absolute sharpness value greater than 1 (1.5 for C filter) and magnitudes above the point (determined for each image by looking in the plot magnitude vs error) where the stars begin to be affected by the nonlinearity of the detector.

Second, using DAOMATCH and DAOMASTER to match all the images to create a single starlist that will be given to ALLFRAME to perform PSF-photometry in all the images simultaneously.

⁴IRAF is distributed by the National Optical Astronomy Observatory, which is operated by the Association of Universities for Research in Astronomy (AURA) under a cooperative agreement with the National Science Foundation.

TABLE 2
NGC 1851 & NGC 7099: CATALOG EXAMPLE

ID	RA(J2000)	DEC(J2000)	X	Y	Rad	C	eC	dC	mC	nC
324	78.684240068	-40.042003974	161.219	1827.654	999.03	20.3654	0.0082	0.0033	0.0082	3
334	78.683674458	-40.043001613	164.868	1835.867	995.23	20.7216	0.0101	0.0016	0.0101	3
347	78.683039621	-40.047603550	169.203	1873.867	991.08	20.8262	0.0113	0.0010	0.0113	3

^aThe columns are: ID, RA and DEC coordinates (in degrees), X and Y coordinates (in px), radial distance of the star to the centre (in px), magnitude, PSF-fitting error (internal error), dispersion (external error), higher value between internal and external error, and the number of frames where the star was detected. (All of this for C, T_1 and T_2 but due to the lack of space this table shows only C).

Third, using DAOMATCH and DAOMASTER to match the catalogs given by ALLFRAME, first combining the images with the same time exposure and filter, and then all the resulting catalogs of each filter to get a robust intensity-weighted mean instrumental magnitude, using the medium exposure as a reference image since it maximizes the number of stars in common with both short and long exposures, facilitating the match.

Finally, use DAOMATCH and DAOMASTER again to generate a full catalog with all the stars found in at least 2 of the 3 filters. The R filter was used as reference filter since its wavelength response lies between the C and I filters, and because it produces the deepest images.

Aperture corrections were determined taking the brightest and unsaturated stars from the entire field comparing their PSF photometry to their aperture photometry. No spatial dependence was found in any filter for both clusters.

The instrumental magnitudes of NGC 7099 were transformed to the standard Washington system using the standard coefficients obtained in F17. The RMS for each filter is $0.038(C)$, $0.022(R)$ and $0.027(I)$. However, for NGC 1851, the standard coefficients from C14 caused an offset of ≈ 0.15 to the red in the RGB with respect to the CMD from C14, probably due to the addition of the new images, so we decided to calibrate calculating the difference between our instrumental magnitudes and the standard magnitudes of the CMD from C14 for each star using the following formulae:

$$C = (c - r) * m_1 + n_1 + c,$$

$$T1 = (c - r) * m_2 + n_2 + r,$$

$$T2 = (r - i) * m_3 + n_3 + i,$$

where C , $T1$ and $T2$ are our calibrated magnitudes, m is the slope, n is the y -intercept of the line and c , r and i our instrumental magnitudes. The resulting

calibrated magnitudes are very similar to those from C14.

According to Bonatto, Campos, & Kepler (2013) NGC 1851 has a mean differential reddening of $\langle \delta E(B - V) \rangle = 0.025 \pm 0.01$, while NGC 7099 has a mean differential reddening of $\langle \delta E(B - V) \rangle = 0.03 \pm 0.01$. Taking into account the relation from Geisler, Claria, & Minniti (1991) $E(C - T1) = 1.966(B - V)$ we obtain a reddening of $E(C - T1) = 0.049$ for NGC 1851 and 0.059 for NGC 7099⁵. We consider these numbers small enough to be negligible, so reddening corrections are not needed. In particular, in this work we are only interested in differential effects between possible different MPs and not absolute effects.

Finally, a World Coordinate System (WCS) was calculated in both NGC 1851 and NGC 7099 catalogues using 12 stars well distributed along the field to transform the x/y coordinates to RA/Dec(J2000) using the xy2sky task from WCSTools.

2.3. Final Sample Selection

As mentioned in previous works, DAOMASTER gives two types of errors: the combined photometric measurement error output by ALLFRAME (internal error) and the σ based directly on the observational scatter across multiple images (external error). We already proved in F17 through an ADDSTAR experiment that external errors are better estimates of the real photometric error than internal errors, but for each star we take the largest of these two errors to avoid the fact that some stars detected in one single frame have error "0". These final errors appear in Table 2 as mC (We use C as an example for T_1 and T_2 too). We removed all the stars with errors greater than 0.1 in each filter, and colors were created from the remaining stars. The errors in colors

⁵Bonatto, Campos, & Kepler (2013) say that differential reddening values lower than 0.04 may be related to zero-point variations.

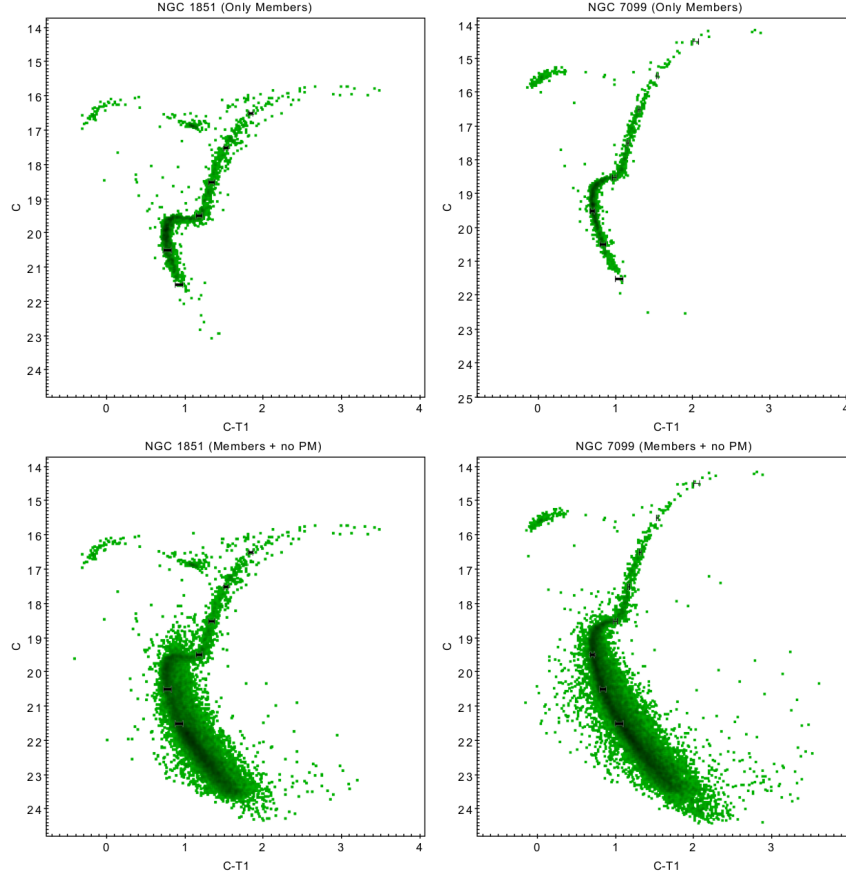


Fig. 1. Definitive CMDs in $C - T_1$ vs C . Top left: NGC 1851 using only member stars according to PMs provided by GAIA. Bottom left: NGC 1851 using member stars according to PMs provided by GAIA plus stars with no PMs detected. Top right: NGC 7099 using only member stars according to PMs provided by GAIA. Bottom right: NGC 7099 using member stars according to PMs provided by GAIA plus stars with no PMs detected. The color figure can be viewed online.

are the square root of the quadratic sum of the final errors from each input magnitude. Radial cuts were applied to both clusters following the previous studies from C14 and F17. For NGC 7099 we removed all the stars from the center up to 80 px(34.8") radius while for NGC 1851 we cut up to 50 px(21.75") due to crowding and we left for both clusters a ring with an outer radius of 1000 px(7.25').

Proper motions (PM) provided by the *Gaia* DR2 mission (Gaia Collaboration et al. 2016, 2018) allowed to select (in a PM-RA vs PM-DEC plot) all the stars with PM similar to our cluster reproducing by hand the selection shown in the Baumgardt Globular Cluster database (3rd version)⁶ removing non-member stars and cleaning the CMD. From now on we work with two kinds of catalog in each clus-

ter, one catalog containing only member stars to ease the detection of different sequences or broadening in the clusters (Figures 1, Top), and a second catalog containing the same member stars plus all the stars that do not have a PM, aiming to have a deeper main sequence (Figures 1, Bottom).

Both catalogs show improvements with respect to their original papers: NGC 1851 is ≈ 1.5 mag deeper in C , and we can see better the double sub-giant branch (SGB) mentioned in C14 and Han et al. (2009), and that Milone et al. (2017) classified as a characteristic of type II GCs. For NGC 7099, since we discarded some bad seeing images, we have a CMD ≈ 1 mag deeper in C and T_2 and a narrower SGB.

⁶<https://people.smp.uq.edu.au/HolgerBaumgardt/globular/>.

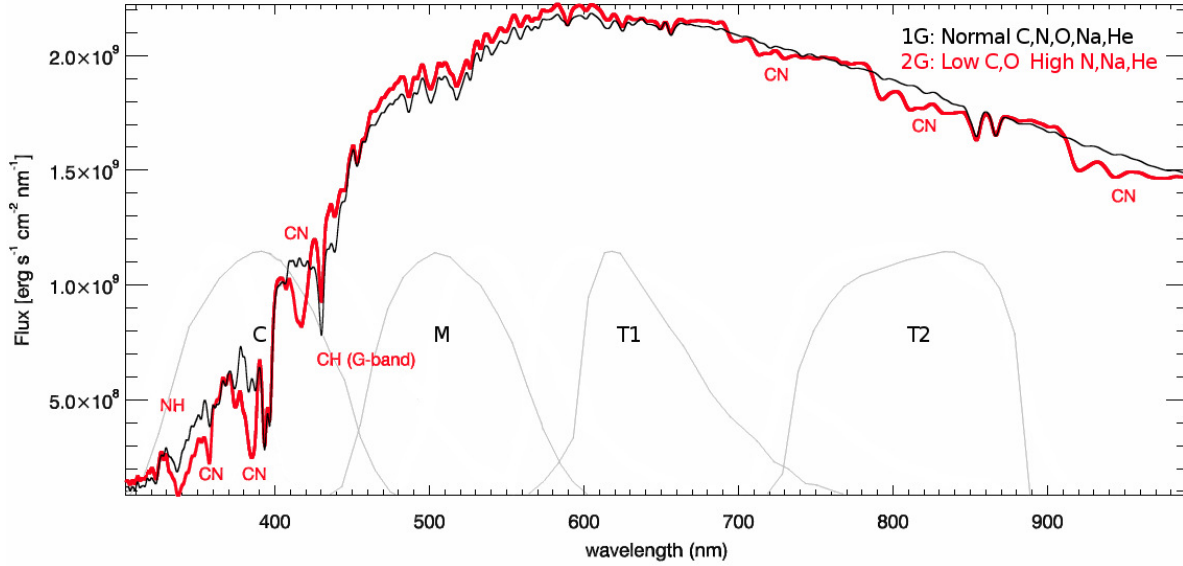


Fig. 2. Comparison of the synthetic spectra from 1P(black) and 2P(red) stars. Illustrative Washington filter response curves are included. The color figure can be viewed online.

3. THE EFFICACY OF THE NEW COLOR IN DETECTING MPS

As mentioned before, C14 and F17 proved the efficacy and efficiency of the Washington C filter to uncover MPs. This filter goes from the atmospheric cutoff at around 3300 Å to beyond the G-band, thus covering 3 CN-bands, a NH-band and a CH-band. This can be seen in Figure 2, that shows the comparison between the synthetic spectra of otherwise identical 1P and 2P stars made by Sbordone et al. (2011) with the Washington filter response curves included. Until now, our best weapon in the Washington System to find MPs was to use the $C - T_1$ color and plot vs C in a CMD, leaving other C filter combinations to show partially defined MPs ($C - T_2$), or how the absence of the C filter fails to separate MPs ($T_1 - T_2$). But careful analysis of Figure 2 shows that the T_2 filter is roughly centered on multiple CN bands which have a fairly significant flux difference between 1P and 2P stars, allowing (in theory) to further separate the populations of the cluster, although our previous studies demonstrated that the spread in $T_1 - T_2$ is almost completely due to the errors. Our hypothesis is that T_2 retains some capability to distinguish MPs due to the CN-bands that it includes (as seen in Figure 2), but the separation of the different sequences is difficult to detect. So based on the technique from Piotto et al. (2015), we created a new combination of colors: $(C - T_1) - (T_1 - T_2)$ (or $C + T_2 - 2T_1$). The idea is that we can potentially

further separate the sequences in a CMD combining the potential of $C - T_1$ with a small additional difference generated in $T_1 - T_2$. We also note that the C filter includes both CN bands as well as the CH band. The former are stronger in 2P vs. 1P stars due to the fact that the CN-band strength is controlled by the N abundance, which is enhanced in 2P over 1P stars. However, the CH band is weaker in 2P vs. 1P stars since C is depleted. Hence, these 2 effects work against each other to some extent, although it is also clear that the strongest effect is due to the various CN bands, so that the flux in the C filter will be less in a 2P star compared to that of an otherwise identical 1P star. Similarly, it should also be less in the T_2 filter for a 2P vs 1P star. Figure 3 shows the new $(C - T_1) - (T_1 - T_2)$ (hereafter C, T_1, T_2) vs C CMDs.

A detailed analysis is shown in the next subsections.

3.1. NGC 7099

For NGC 7099, in both CMDs (PM members and members + stars with no PM), we can see a very broad RGB compared to $C - T_1$, similar to the CMD shown in Piotto et al. (2015) for the same cluster. Based on the C, T_1, T_2 CMDs of NGC 7099 from Figure 3 we included the mean color error in 1 magnitude bins along the principal sequence, but attached to the left border of the RGB. We consider these stars inside the error bars as those associated with

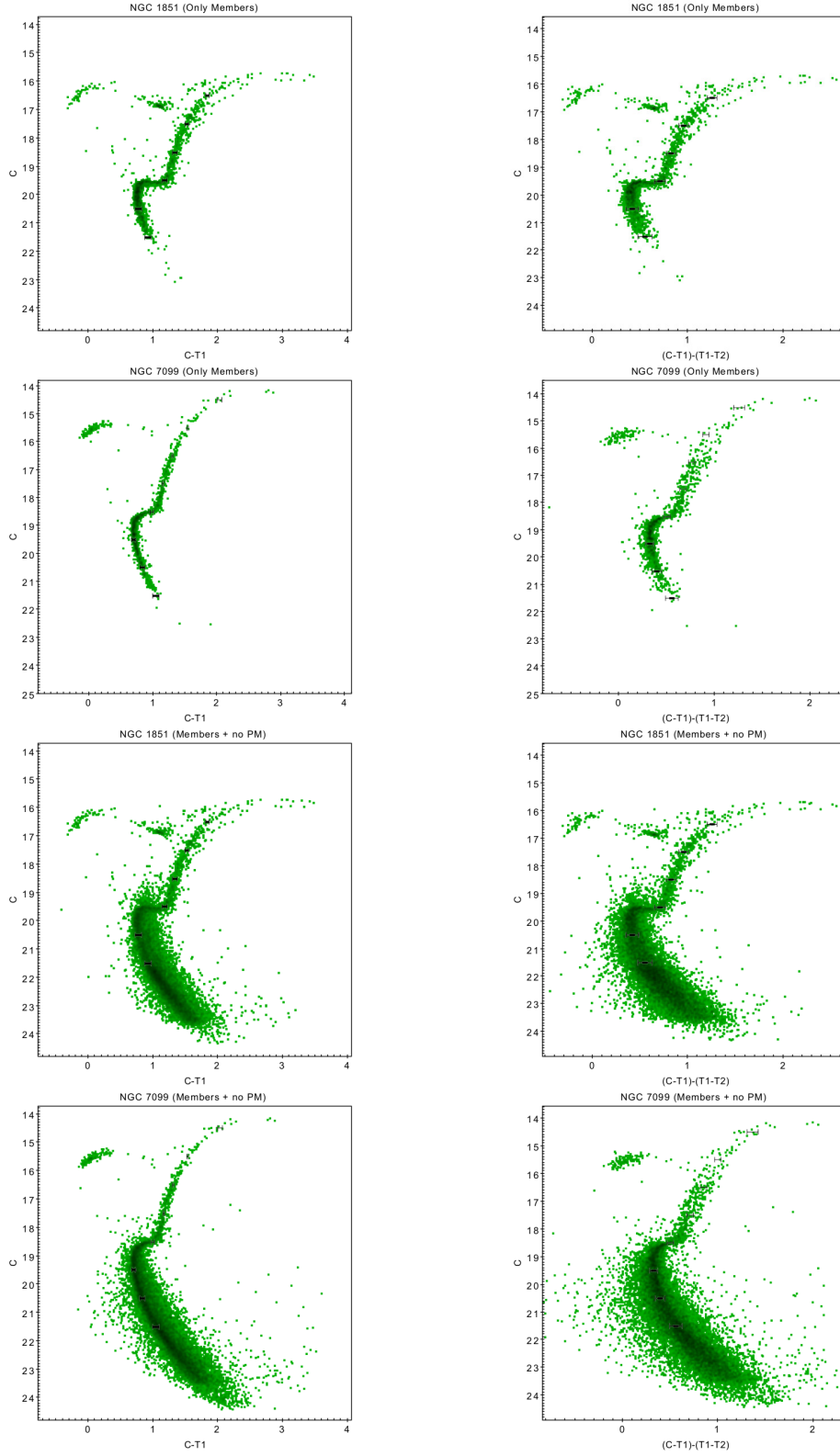


Fig. 3. Left: The $(C - T_1)$ CMDs from Figure 1. Right: The new color $(C - T_1) - (T_1 - T_2)$ vs C . Mean color and magnitude error bars in 1 magnitude bins along the principal sequence are displayed as black crosses. The color figure can be viewed online.

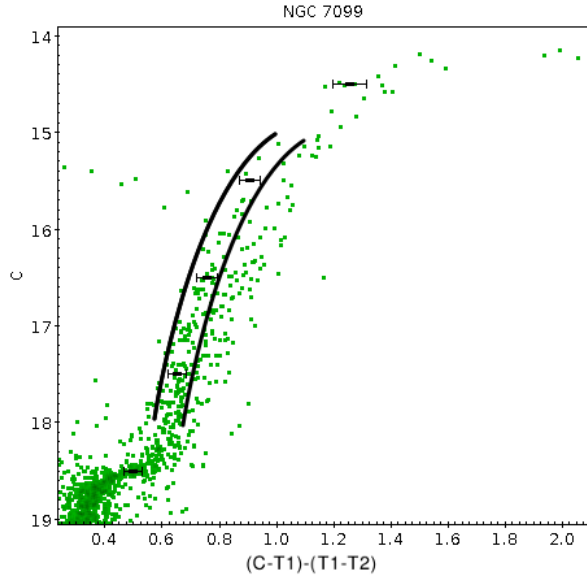


Fig. 4. Criteria to divide the 1P from the 2P. The black lines represent the limits established for being the 1P. The color figure can be viewed online.

the 1P, while those at the right of the limits of the error bars are considered as 2P stars. So, taking this as a guide, we established our 1P/2P division in the catalog containing members + stars with no PM by drawing two lines, each connecting with the limits of the error bars, at both sides, as seen in Figure 4. The samples of each population of stars are taken between the 15-18 magnitude range in C and 13-17 in T_2 since the MPs begin to merge in the brighter bins, and the AGB complicates the separation as well.

In this part we made a correction in F17. There, we took a group of stars at the left of the RGB deemed as the 1P. Comparing the radial distributions of both 1P and 2P stars of NGC 7099 we got the most impressive but unexpected conclusion of the publication: The first population of NGC 7099 was more centrally concentrated than the second, opposite to most of the actual observations, as well as MP formation models. However, our new research proves that conclusion to be wrong, since the 1P subset of F17 does not appear in our new CMD, meaning that probably it was composed of field stars that could not be removed then, given the absence of Gaia PMs at the time. This would also explain why we got a p -value of 0 in our Kolmogorov-Smirnov test,⁷

⁷If $P < 0.05$, one must reject the null hypothesis of no difference between two data sets, more information about this test is found in <http://www.physics.csbsju.edu/stats/KS-test.html>.

indicating that the 1P and 2P subsets were different distributions.

We now take a new subset in $C - T_1$, trying to replicate the one from C, T_1, T_2 assumed to be our 2P and leaving the rest of the RGB as the 1P. These subsets were compared in the other colors and their radial distributions were tested to analyze which pair of subsets was more effective in distinguishing the MPs. What we should expect in this part is to have the 1P at the blue side and the 2P at the red side in both $C - T_1$ and C, T_1, T_2 colors with, hopefully, better defined subsets in the latter, but with totally the opposite occurring in $T_1 - T_2$, since in this color the filter that covers the CN-band appear as the subtrahend (and this explains why subtracting this color from $C - T_1$ should help to increase the spread on the RGB).

The results are shown in Figure 5. As expected, the subsets made based on the color C, T_1, T_2 (upper panels) are a bit less defined in the CMD with $C - T_1$, since the separation in the latter color should be less than that in the former. In $T_1 - T_2$ both populations seem to be well separated but mirrored.

The subsets made from $C - T_1$ (middle panels) show a less effective separation in C, T_1, T_2 and a very similar one in $T_1 - T_2$. Both groups of CMDs look very similar. With $C - T_1$ the percentage of 2P stars is $23.2\% \pm 25\%$ of the RGB while for C, T_1, T_2 the percentage of 2P is $44.9\% \pm 16.7\%$. This big difference in percentages is due to the smaller spread in $C - T_1$, causing that any small error in selecting a subset includes/excludes lots of stars. This is seen in the high percentage of error in $C - T_1$ (higher even than the percentage of the population itself) obtained putting the error bars in the middle of our 1P/2P division and enclosing all the stars inside their limits to see those stars that could be being included/excluded in our 1P/2P selection with respect to the total number of stars in the RGB.

Comparing the radial distributions of both pairs of 1P/2P stars (lower panels) we can see that both of them show a 2P more centrally concentrated, in agreement with most of the MP formation scenarios. In fact, both pairs of subsets give a P -value = 0 in a K-S test. While the subset from $C - T_1$ grows faster with radius than C, T_1, T_2 , the latter color includes all stars after reaching ≈ 780 px from the center (≈ 200 px less than $C - T_1$). The lowest right panel compares both 2P groups of stars. A K-S test between these give a P -value of 0.026, indicating that we should reject the null hypothesis of no difference between both distributions, so there are significant differences while selecting a subset from

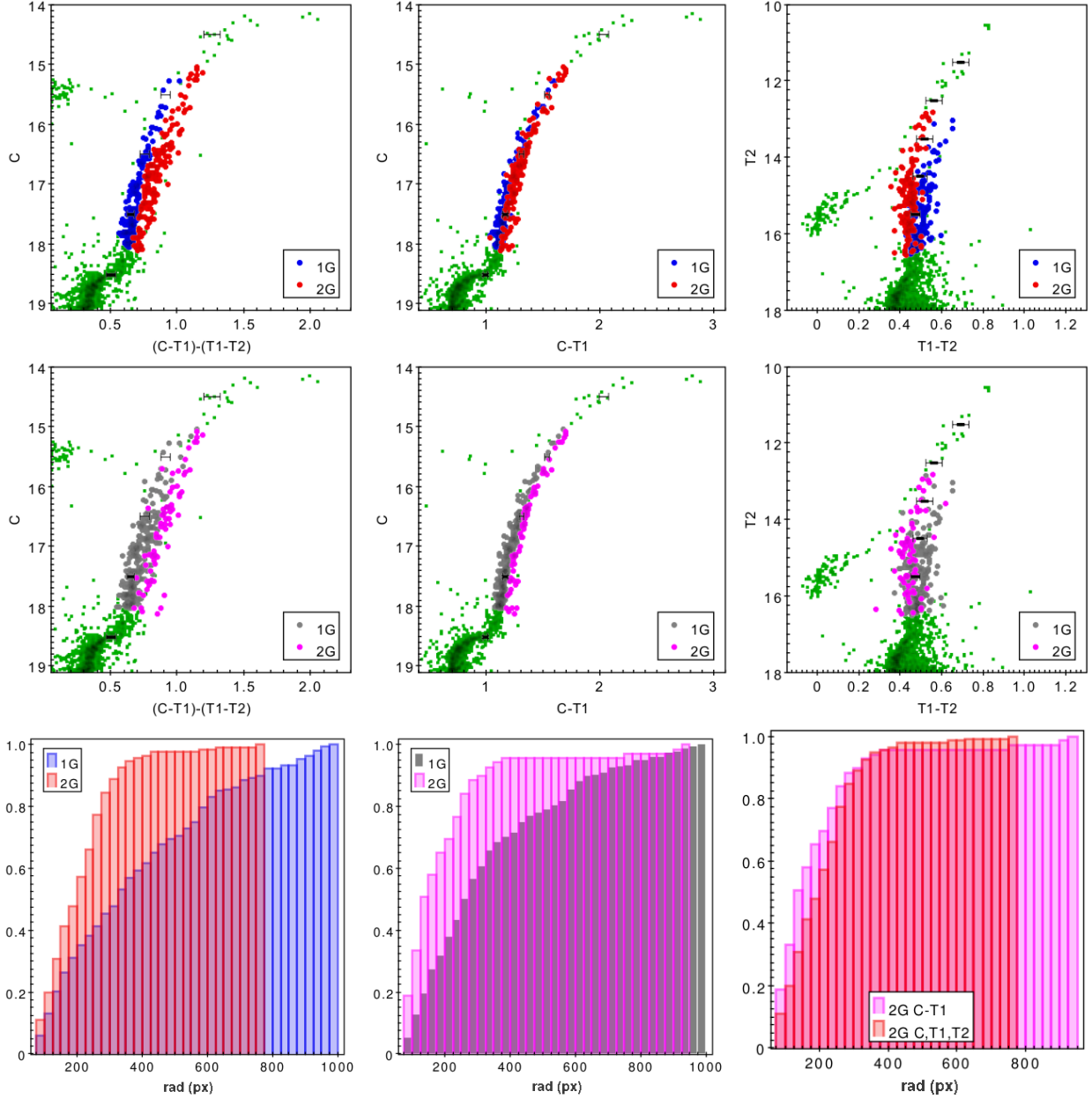


Fig. 5. NGC 7099: Upper panels: A 1P/2P subset chosen from the color C, T_1, T_2 shown in $C - T_1$ and $T_1 - T_2$. Mid panels: A 1P/2P subset chosen from the color $C - T_1$ shown in C, T_1, T_2 and $T_1 - T_2$. Bottom panels: Left: Radial distributions of 1P and 2P of the subset from C, T_1, T_2 . Middle: Radial distributions of 1P and 2P of the subset from $C - T_1$. Right: Comparison of the 2P from the C, T_1, T_2 and the 2P from $C - T_1$. The color figure can be viewed online.

$C - T_1$ or C, T_1, T_2 . And in fact, since $C - T_1$ shows the strongest central concentration in the inner parts, its behavior is preferred in this regard.

Table 3 shows the standard deviation (read as the width) of the RGB and the mean error in bins of 1 magnitude (with the exception of the last bins), for each of the 3 colors, while the last column shows the ratio width/error, which is a robust measurement of

the effectiveness of the colors for separating MPs. As expected, $T_1 - T_2$ shows a mean ratio of 1.68, in agreement with previous studies that indicates that, although this color shows a spread slightly bigger than the errors, it is not very sensitive to the presence of MPs. The small observed difference could in fact come from an undetected source of error. For $C - T_1$, the mean ratio is 2.33, significantly larger,

TABLE 3

COMPARISON OF ERROR VS WIDTH IN NGC 7099

Mag Range	Mean width	Mean error	Ratio
$C - T_1$ vs C			
15-16	0.043	0.021	2.05
16-17	0.038	0.016	2.38
17-17.9	0.041	0.016	2.56
$T_1 - T_2$ vs T_2			
13-14	0.061	0.039	1.56
14-15	0.052	0.033	1.58
15-16.4	0.042	0.022	1.91
C, T_1, T_2 vs C			
15-16	0.073	0.043	1.70
16-17	0.070	0.035	2.00
17-17.9	0.063	0.027	2.33

and enough to assure the detection of MPs. Unfortunately, C, T_1, T_2 only has a mean ratio of 2.01, significantly less than that of $C - T_1$. However, we note that this is not unexpected since it is not a combination of new filters but only a combination of the width and error of the first 2 colors.

3.2. NGC 1851

3.2.1. The Blue and Red RGBs

As shown in Figure 6, NGC 1851 presents a double RGB: The left RGB, hereafter the blue-RGB; and the right RGB, hereafter the red-RGB. Both sequences are already well divided in $C - T_1$, so there are no clear differences in the subsets made from $C - T_1$ or C, T_1, T_2 . Indeed, the amount of red-RGB stars is 11.4% and 9.3% in $C - T_1$ and C, T_1, T_2 , respectively. A K-S test done to the Red-RGB of both subsets give a P -value of 0.995, meaning that there is no significant difference between them. Anyway, a K-S test in both blue-RGB and red-RGB populations of C, T_1, T_2 give a P -value of 0.423 while for $C - T_1$ is 0.313; again neither comparison shows a significant difference. Both subsets also show very similar radial distributions, but as explained in C14, this behavior could be due to the small amount of red-RGB stars in both subsets. Also, opposed to what we expected, the red-RGB does not appear at the right of the blue-RGB in $T_1 - T_2$ but dispersed along the entire blue-RGB.

The ratio width/error in NGC 1851 (Table 4) shows that, although $C - T_1$ give ratios even better than in NGC 7099, the ratios in $T_1 - T_2$ are very

TABLE 4

COMPARISON OF ERROR VS WIDTH IN NGC 1851

Mag Range	Mean width	Mean error	Ratio
$C - T_1$ vs C			
15.7-17	0.078	0.031	2.52
17-18	0.069	0.025	2.76
18-19.2	0.054	0.025	2.16
$T_1 - T_2$ vs T_2			
11.4-13	0.068	0.051	1.33
13-14	0.038	0.051	0.75
14-15	0.032	0.046	0.70
15-16	0.030	0.045	0.67
16-17	0.025	0.032	0.78
17-17.5	0.022	0.032	0.69
C, T_1, T_2 vs C			
15.7-17	0.074	0.056	1.32
17-18	0.068	0.049	1.39
18-19.2	0.060	0.041	1.46

low, indicating a spread completely due to the errors. Naturally, the ratios of C, T_1, T_2 should be between the values of $C - T_1$ and $T_1 - T_2$, as they are. And again, opposite to our original hope, C, T_1, T_2 does not show an improvement in the ratio with respect to $C - T_1$ and, in fact, is substantially worse, indicating that $T_1 - T_2$ is not collaborating to help split the sequences.

Figure 7 shows a comparison of the lower RGB and SGBs of NGC 1851 between C, T_1, T_2 vs C (top) and $C - T_1$ vs C (bottom). Subsets were taken from both colors trying to cover all the SGB. The fainter SGB is somewhat more visible in the former.

Radial distributions between the bright-SGB and faint-SGB were compared in both subsets. The K-S test in $C - T_1$ gives a p -value of 0.729 while in C, T_1, T_2 gives 0.590. Both subsets show no significant differences in radial distributions between bright-SGB and faint-SGB stars. This is in agreement with Milone et al. (2009) who also did not find differences in the radial distributions of the SGBs of NGC 1851.

The combined samples of the SGB and RGB from each bright-SGB/blue-RGB and faint-SGB/red-RGB were analyzed to discard the possibility that the lack of differences in the radial distributions is due to the low amount of stars. $C - T_1$ gives a p -value of 0.095 while C, T_1, T_2 gives 0.128. Both of these are considered values too high to assure that

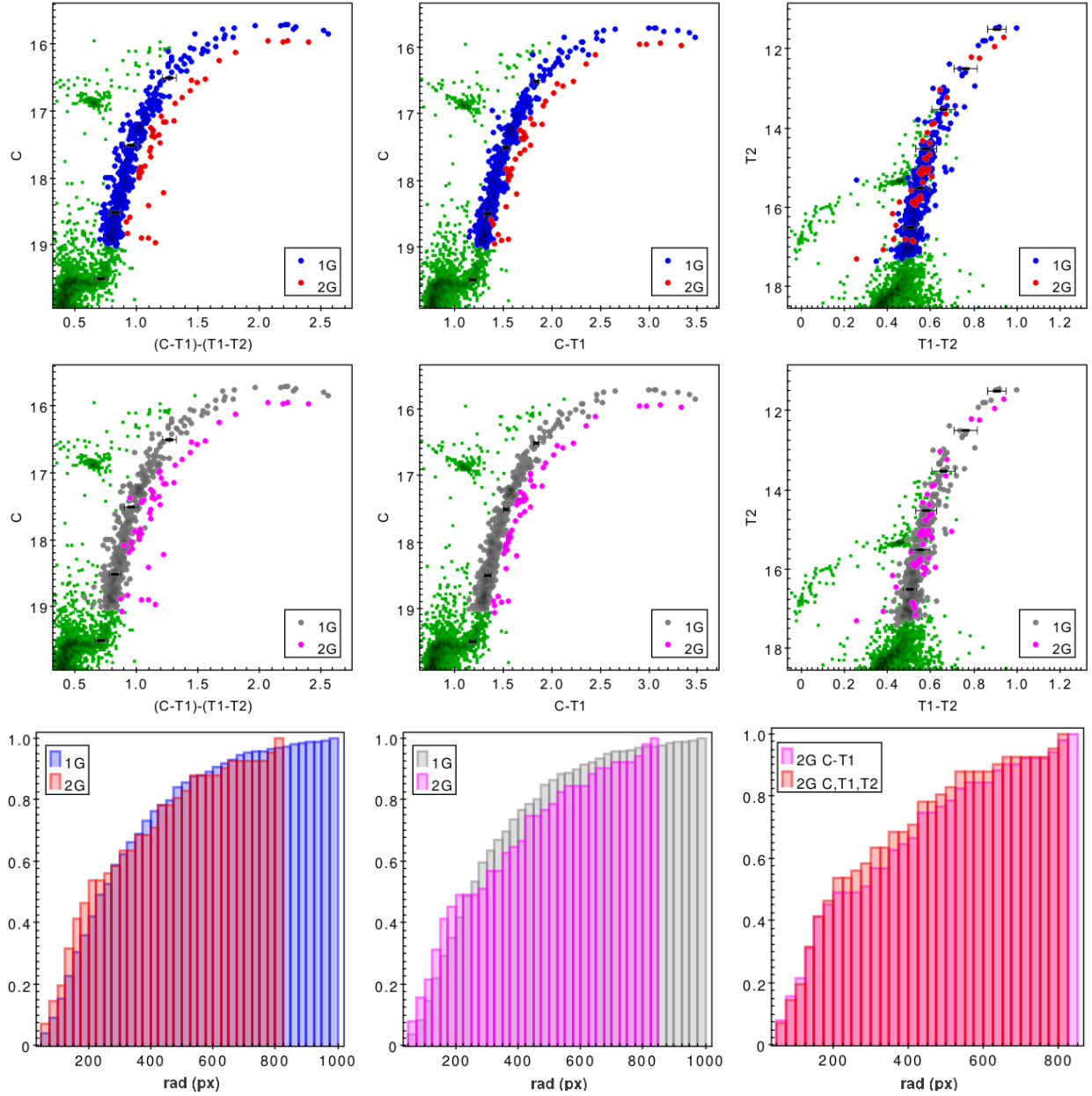


Fig. 6. NGC 1851: Upper panels: A 1P/2P subset chosen from the color C, T_1, T_2 shown in $C - T_1$ and $T_1 - T_2$. Mid panels: A 1P/2P subset chosen from the color $C - T_1$ shown in C, T_1, T_2 and $T_1 - T_2$. Bottom panels: Left: Radial distributions of 1P and 2P of the subset from C, T_1, T_2 . Middle: Radial distributions of 1P and 2P of the subset from $C - T_1$. Right: Comparison of the 2P from the C, T_1, T_2 and the 2P from $C - T_1$. The color figure can be viewed online.

there are differences in radial distributions. Recall that indeed C14 found differences in the radial distributions of the MS but none in the RGB and HB, even after combining them. Also, the percentage of red-*RGB*/faint-*SGB* stars is $14.5\% \pm 2.5\%$ in $C - T_1$ and $14.1\% \pm 3.3\%$ in C, T_1, T_2 , confirming that there is no significant improvement with C, T_1, T_2 with respect to $C - T_1$ for this case. For this case we can

also see that the percentage of error in C, T_1, T_2 is higher than in $C - T_1$ due to, again, the fact that C, T_1, T_2 does not help to split the sequences.

3.2.2. -First and Second Populations in the Blue-*RGB*

According to Campbell et al. (2012), both blue-*RGB* and red-*RGB* could possess a first and second population of stars. This idea is also supported by

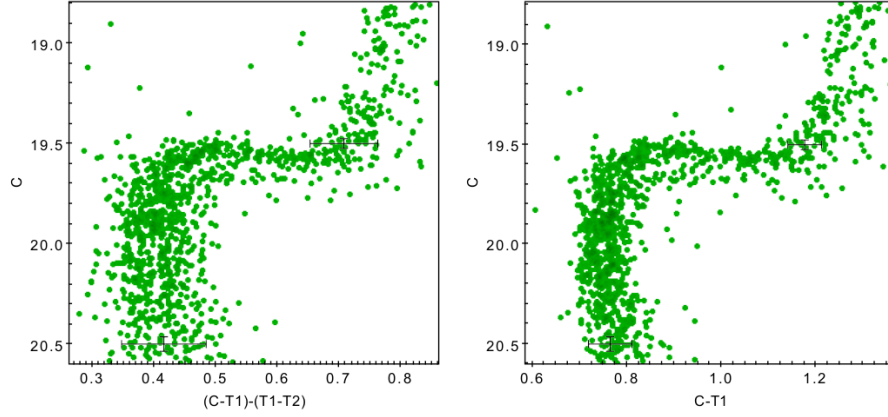


Fig. 7. Comparison of the lower RGB and SGBs of NGC1851 seen in C, T_1, T_2 vs C (top) and $C - T_1$ vs C (bottom). The color figure can be viewed online.

Milone et al. (2017), who found two 2P sequences in the chromosome map of NGC 1851, with a hint of a second 1P as well.

For our case, the number of stars in the red-RGB is too small to analyze it in search of a 1P/2P division, so we will only analyze the blue-RGB.

Following the same procedure used in NGC 7099, we used the error bars from each color to separate the 1P from the 2P. We found a small fraction of stars lying at the left side of the blue-RGB in $C - T_1$ and C, T_1, T_2 , deemed as 1P stars. Figure 8 shows the comparison of the 1P subset chosen from C, T_1, T_2 (upper panels) and $C - T_1$ (central panels). This time the chosen subset from C, T_1, T_2 follows the expected behavior for a different population: well defined at one side of the RGB in C, T_1, T_2 , partially less defined at the same side of the RGB in $C - T_1$, and even less defined and at the opposite side of the RGB in $T_1 - T_2$, although the last point is not as clear in $C - T_1$. With C, T_1, T_2 the blue-RGB has $10.3\% \pm 19.5\%$ of 1P stars while with $C - T_1$ the amount of 1P stars is $40.3\% \pm 19.8\%$.

The radial distributions in $C - T_1$ gives a P -value of 0.014 while C, T_1, T_2 show a P -value of 0.870, although the last result is not as reliable since the 1P are only 21 stars.

A width to error ratio analysis indicates that $C - T_1$ has a mean ratio of 1.79 while C, T_1, T_2 vs C has a mean ratio of 0.97. $C - T_1$ ratio is too small to confirm or reject the presence of MPs while the width of C, T_1, T_2 is completely due to errors ($T_1 - T_2$ was not considered in this table since the Red-RGB is inside the blue-RGB; hence, the values of the last are the same of those in Table 4).

A further analysis was realized using data from the HST UV Globular Cluster Survey described in

TABLE 5
COMPARISON ERROR VS WIDTH IN THE
BLUE-RGB OF NGC 1851

Mag Range	Mean width	Mean error	Ratio
$C - T_1$ vs C			
17.2-18	0.042	0.023	1.83
18-18.8	0.042	0.024	1.75
C, T_1, T_2 vs C			
17.2-18	0.044	0.047	0.93
18-18.8	0.039	0.039	1.00

Piotto et al. (2015), in an attempt to verify if our subset chosen as 1P in the blue-RGB of NGC 1851 was correct or not. Taking as 1P the subset chosen in Milone et al. (2017) using the “Magic Trio” in NGC1851 we recreated our Washington Trio using the Filters F336W, F606W and F814W in replacement of C, T_1 and T_2 respectively. We obtained a very similar CMD, as shown in Figure 9a, where the blue stars are the 1P, the green RGB are the 2P stars and the red stars are the red-RGB stars. The reason for the small amount of 1P stars is because most of them lie less than 22 arc seconds from the center, and we cut those stars (up to 21.75 arc seconds of radius) due to the crowding, as seen in Figure 9b. This would explain the small width to error ratios and the high percentage of error with respect to the amount of 1P stars. Despite this, we were able to detect a small amount of 1P stars thanks to the C, T_1, T_2 color, confirming it as a complementary method to detect MPs.

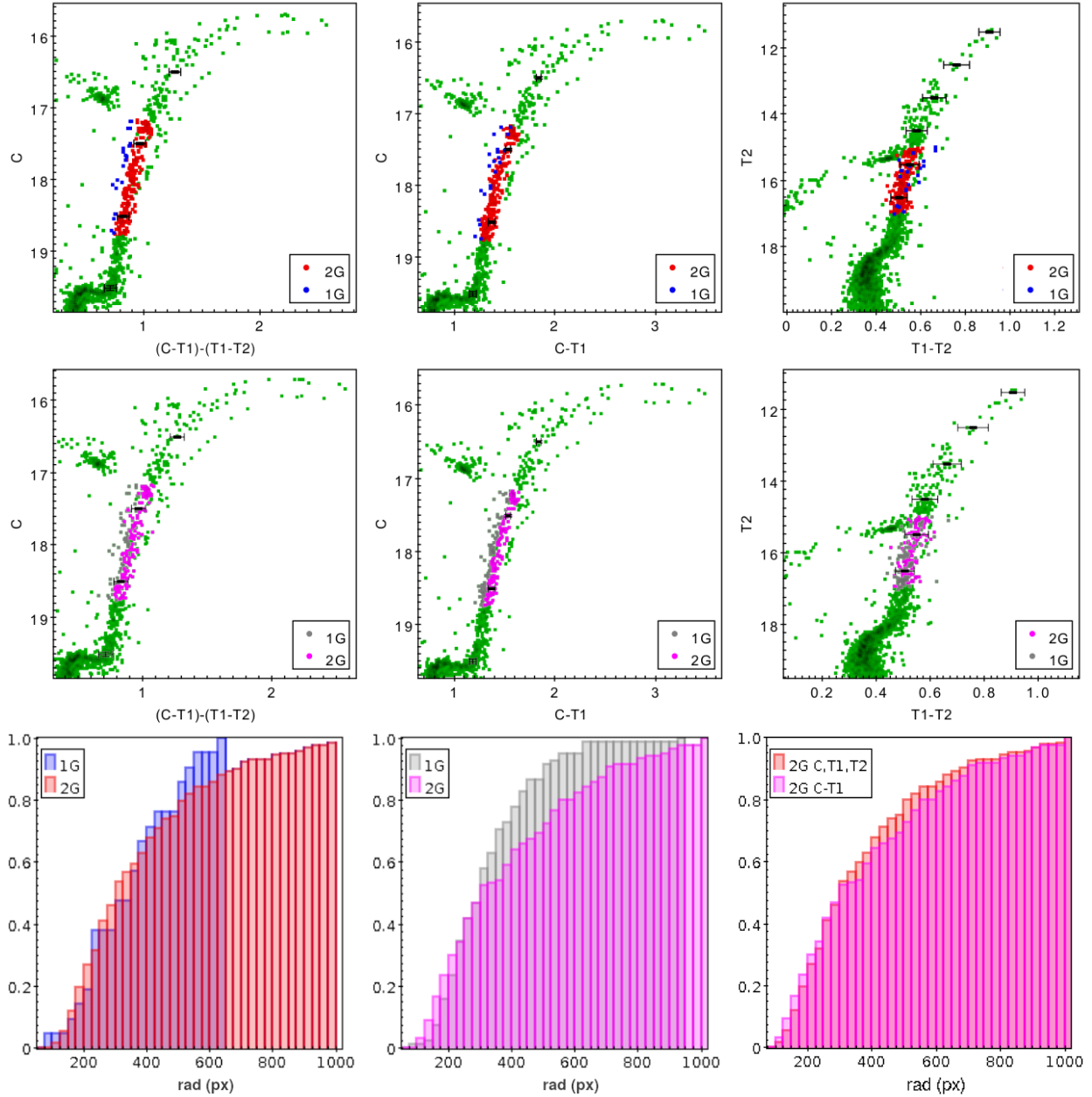


Fig. 8. NGC 1851 Blue-RGB: Upper panels: A 1P/2P subset chosen from the color C, T_1, T_2 shown in $C - T_1$ and $T_1 - T_2$. Mid panels: A 1P/2P subset chosen from the color $C - T_1$ shown in C, T_1, T_2 and $T_1 - T_2$. Bottom panels: Left: Radial distributions of 1P and 2P of the subset from C, T_1, T_2 . Middle: Radial distributions of 1P and 2P of the subset from $C - T_1$. Right: Comparison of the 2P from the C, T_1, T_2 and the 2P from $C - T_1$. The color figure can be viewed online.

4. CONCLUSIONS

In this work we have improved the Washington photometry of the clusters NGC 7099 and NGC 1851 done in Freljij et al. (2017, F17) and Cummings et al. (2014, C14), respectively. We have determined the optimum way to reduce the data, thus obtaining the highest number of stars with the minimum possible

errors. We also added PM information from Gaia to help select members. Finally, we created a new color combination $(C - T_1) - (T_1 - T_2)$ and we tested it in two clusters.

We conclude that:

- (1) An expected behaviour for a 1P/2P subset is to be at one side of the RGB in C, T_1, T_2 ; at the

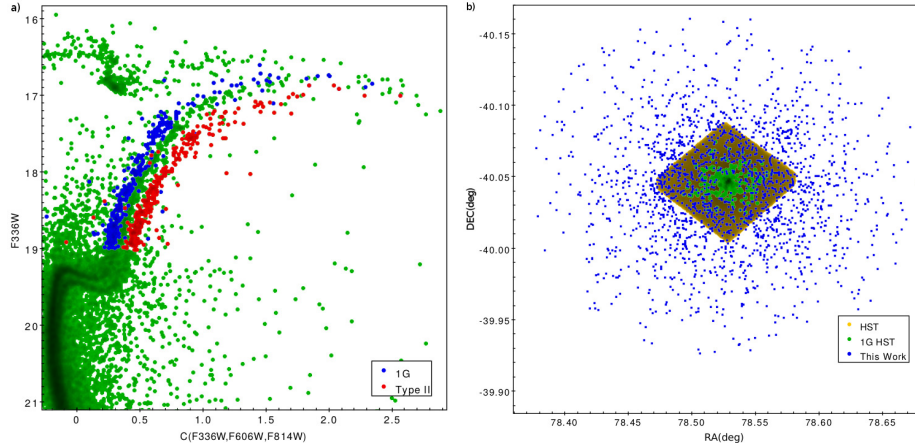


Fig. 9. NGC 1851: (a) CMD using F336W, F606W and F814W from HST in replacement of C , T_1 and T_2 . The blue and red dots are the 1P and Red-RGB stars respectively, identified by Milone et al. (2017). (b) Spatial distributions of the stars of our work and HST. Most of the 1P stars (green dots) were removed in our work due to crowding. The color figure can be viewed online.

same side but less defined in $C - T_1$; and even less defined, at the opposite side, in $T_1 - T_2$.

(2) The subsets chosen as 1P and 2P in F17 for NGC 7099 are incorrect, since the stars belonging to the 1P are actually field stars, removed now thanks to the PM provided by the Gaia mission. This explains why we got a p -value of 0.0 and the 1P stars having radial distributions more concentrated to the center than the 2P.

(3) The new color combination widens the RGB of NGC 7099 better than $(C - T_1)$, allowing to properly select the population subsets. However, $(C - T_1)$ still has the best width/error ratio. Depending on the criteria used, C, T_1, T_2 would have a stronger central concentration than $(C - T_1)$ or weaker. While the 2P subset chosen from $C - T_1$ has the highest fraction of stars within ≈ 300 px from the center, the subset extends until ≈ 980 px, while the 2P subset from C, T_1, T_2 has no stars beyond ≈ 780 px from the center.

(4) We find a very small number of 1P stars at the left side of the blue-RGB of NGC 1851 using both C, T_1, T_2 and $C - T_1$. Despite the subset of C, T_1, T_2 being slightly more accurate, the small number of stars complicates any study. A comparison with analogous HST filters (F336W, F606W and F814W) shows a very similar CMD with a larger amount of 1P stars at the same side of our small subset, confirming our findings. But a spatial analysis of those stars shows that most of them were removed in our catalog due to the crowding of stars at the center.

(5) The red-RGB in NGC 1851 does not follow the expected behavior for a common 2P group of stars. Instead, it appears at the same side, with-

out any improvement, in both C, T_1, T_2 and $C - T_1$ colors, while in $T_1 - T_2$ they are completely merged with the stars from the blue-RGB. Also, little or no difference is seen in the radial distributions between the stars of the blue-RGB and red-RGB using the old and new color combinations, even when combining the samples with the bright-SGB and faint-SGB, respectively.

(6)- The 2P percentage in the RGB of NGC 7099 is $23.2\% \pm 25\%$ for $C - T_1$ and $44.9\% \pm 16.7\%$ for C, T_1, T_2 .

- The percentage of faint-SGB/red-RGB stars respect to the total number of stars in the SGBs and RGBs in NGC 1851 is $14.5\% \pm 2.5\%$ for $C - T_1$ and $14.1\% \pm 3.3\%$ for C, T_1, T_2 .

- The percentage of 1P stars in the blue-RGB of NGC 1851 is $40.3\% \pm 19.8\%$ for $C - T_1$ and $10.3\% \pm 19.5\%$ for C, T_1, T_2 .

Comparing these percentages with those of Milone et al.(2017)($\approx 62\%$ of 2P stars in NGC 7099, $\approx 3\%$ of red-RGB stars in NGC 1851 and $\approx 26.4\%$ of 1P stars in NGC 1851) we find little relation. This difference might occur not only due to our high percentages of error in the populations, but also because we removed the center of our cluster (a radius of $21.75''$ in NGC 1851 and $34.8''$ in NGC 7099) in order to avoid issues due to the crowding. In addition, the HST photometry used here covers the field up to a radius of only $\approx 2.47'$ while our photometry covers up to a radius of $\approx 7.25'$.

This means that our C, T_1, T_2 color combination is a reliable method to detect MPs since it improves the detection of MPs and decreases the uncertainties of the defined 1P and 2P. But looking at the width

that it produces compared to the increase of errors that this implies, it is not as effective as $C - T_1$. It is also less efficient, as the latter requires only observations in 2 filters. So we recommend its use to detect MPs, but as a complementary method together with $C - T_1$ and $T_1 - T_2$ separately.

We thank the anonymous referee for his/her suggestions and comments that have improved the quality of the paper. H. F. acknowledges financial support from Agencia Nacional de Investigación y Desarrollo (ANID) grant 21181653. D. G. and S. V. gratefully acknowledge support from the Chilean Centro de Excelencia en Astrofísica y Tecnologías Afines (CATA) BASAL grant AFB-170002. D. G. also acknowledges financial support from the Dirección de Investigación y Desarrollo de la Universidad de La Serena through the Programa de Incentivo a la Investigación de Académicos (PIA-DIDULS). C. M. thanks the support provided by FONDECYT Postdoctorado No.3210144. S.V. gratefully acknowledges support by the ANID BASAL project ACE210002. S. V. gratefully acknowledges support by the ANID BASAL projects ACE210002 and FB210003. S. V. gratefully acknowledges the support provided by Fondecyt reg. n. 1220264.

Data Availability

This work has made use of data from the European Space Agency (ESA) mission *Gaia* (<https://www.cosmos.esa.int/gaia>), processed by the *Gaia* Data Processing and Analysis Consortium (DPAC, <https://www.cosmos.esa.int/web/gaia/dpac/consortium>). Funding for the DPAC has been provided by national institutions, in particular the institutions participating in the *Gaia* Multilateral Agreement.

This work has made use of data from the HST UV Globular cluster Survey <http://groups.dfa.unipd.it/ESPG/treasury.php>.

The photometric raw data from SOAR and Swope telescopes analysed in this article will be shared on reasonable request to the corresponding author (HF).

REFERENCES

- Bastian, N., Lamers, H. J. G. L. M., de Mink, S. E., et al. 2013, MNRAS, 436, 2398, <https://doi.org/10.1093/mnras/stt1745>
- Bastian, N. & Lardo, C. 2018, ARA&A, 56, 83, <https://doi.org/10.1146/annurev-astro-081817-051839>
- Bedin, L. R., Piotto, G., Anderson, J., et al. 2004, MSAIS, 5, 105
- Bessell, M. S. 2005, ARA&A, 43, 293, <https://doi.org/10.1146/annurev.astro.41.082801.100251>
- Bonatto, C., Campos, F., & Kepler, S. O. 2013, MNRAS, 435, 263, <https://doi.org/10.1093/mnras/stt1304>
- Campbell, S. W., Yong, D., Wylie-de Boer, E. C., et al., 2012, ApJL, 761, 2, <https://doi.org/10.1088/2041-8205/761/1/L2>
- Cannon, R. D. & Stobie, R. S. 1973, MNRAS, 162, 207, <https://doi.org/10.1093/mnras/162.3.207>
- Canterna, R. 1976, AJ, 81, 228, <https://doi.org/10.1086/111878>
- Carretta, E., Bragaglia, A., Gratton, R. G., et al. 2009, A&A, 505, 117, <https://doi.org/10.1051/0004-6361/200912096>
- Carretta, E., Bragaglia, A., Gratton, R. G., et al. 2010, A&A, 516, 55, <https://doi.org/10.1051/0004-6361/200913451>
- Cummings, J. D., Geisler, D., Villanova, S., & Carraro, G. 2014, AJ, 148, 27, <https://doi.org/10.1088/0004-6256/148/2/27>
- Dalessandro, E., Lardo, C., Cadelano, M., et al. 2018, A&A, 618, 131, <https://doi.org/10.1051/0004-6361/201833650>
- D’Ercole, A., Vesperini, E., D’Antona, F., McMillan, S. L. W., & Recchi, S. 2008, MNRAS, 391, 825, <https://doi.org/10.1111/j.1365-2966.2008.13915.x>
- Decressin, T., Charbonnel, C., & Meynet, G. 2007, A&A, 475, 859, <https://doi.org/10.1051/0004-6361:20078425>
- Dotter, A., Milone, A. P., Conroy, Ch., Marino, A. F., & Sarajedini, A. 2018, ApJ, 865, 10, <https://doi.org/10.3847/2041-8213/aae08f>
- Elmegreen B. G. 2017, ApJ, 836, 80, <https://doi.org/10.3847/1538-4357/836/1/80>
- Freljij, H., Geisler, D., Cummings, J., et al. 2017, MNRAS, 472, 4532, <https://doi.org/10.1093/mnras/stx2280>
- Freljij, H., Villanova, S., Muñoz, C., & Fernández-Trincado, J. G. 2021, MNRAS, 503, 867, <https://doi.org/10.1093/mnras/stab443>
- Gaia Collaboration, Prusti, T., de Bruijne, J. H. J., et al. 2016, A&A, 595, 1, <https://doi.org/10.1051/0004-6361/201629272>
- Gaia Collaboration, Brown, A. G. A., Vallenari, A., et al. 2018, A&A, 616, 1, <https://doi.org/10.1051/0004-6361/201833051>
- Gaia Collaboration, Brown, A. G. A., Vallenari, A., et al. 2020, arXiv: 2012.01533v2, <https://doi.org/10.48550/arXiv.2012.01533>
- Geisler, D., Claria, J. J., & Minniti, D. 1991, AJ, 102, 1836, <https://doi.org/10.1086/116008>
- Geisler, D. 1996, AJ, 111, 480, <https://doi.org/10.1086/117799>

- Gieles, M., Charbonnel, C., Krause, M. G. H., et al. 2018, *MNRAS*, 478, 2461, <https://doi.org/10.1093/mnras/sty1059>
- Hamuy, M., Folatelli, G., Morrell, N. I., et al. 2006, *PASP*, 118, 2, <https://doi.org/10.1086/500228>
- Han, S.-I., Lee, Y.-W., Joo, S.-J., et al. 2009, *ApJL*, 707, L190, <https://doi.org/10.1088/0004-637X/707/2/L190>
- Harris, W. E., 1996, *AJ*, 112, 1487, <https://doi.org/10.1086/118116>
- Milone, A. P., Stetson, P. B., Piotto, G., et al. 2009, *A&A*, 503, 755, <https://doi.org/10.1051/0004-6361/200912256>
- Milone, A. P., Piotto, G., Renzini, et al., 2017, *MNRAS*, 464, 3636, <https://doi.org/10.1093/mnras/stw2531>
- Parmentier, G. & Pasquali, A. 2022, *ApJ*, 924, 81, <https://doi.org/10.3847/1538-4357/ac32d8>
- Piotto, G., Milone, A. P., Bedin, L. R., et al. 2015, *AJ*, 149, 91, <https://doi.org/10.1088/0004-6256/149/3/91>
- Renzini, A., D'Antona, F., Cassisi, S., et al. 2015, *MNRAS*, 454, 4197, <https://doi.org/10.1093/mnras/stv2268>
- Salinas, R. & Strader, J. 2015, *ApJ*, 809, 169, <https://doi.org/10.1088/0004-637x/809/2/169>
- Sbordone, L., Salaris, M., Weiss, A., & Cassisi, S. 2011, *A&A*, 534, 9, <https://doi.org/10.1051/0004-6361/201116714>
- Stetson, P. B. 1987, *PASP*, 99, 191, <https://doi.org/10.1086/131977>
- _____. 1994, *PASP*, 106, 250, <https://doi.org/10.1086/133378>
- Tautvaišienė, G., Wallerstein, G., Geisler, D., Gonzalez, G., & Charbonnel, C. 2004, *AJ*, 127, 373, <https://doi.org/10.1086/379561>
- Villanova, S., Geisler, D., Carraro, G., Moni Bidin, C., & Muñoz, C. 2013, *ApJ*, 778, 186, <https://doi.org/10.1088/0004-637x/778/2/186>
- Walker, A. R., Kunder, A. M., Andreuzzi, G., et al. 2011, *MNRAS*, 415, 643, <https://doi.org/10.1111/j.1365-2966.2011.18736.x>

Heinz Frelijj: Departamento de Astronomía, Casilla 160-C, Universidad de Concepción, Chile (heinzfrelijj@gmail.com).

Douglas Geisler: Departamento de Astronomía, Casilla 160-C, Universidad de Concepción, Chile; Instituto de Investigación Multidisciplinario en Ciencia y Tecnología, Universidad de La Serena. Avenida Raúl Bitran S/N, La Serena, Chile; Departamento de Astronomía, Facultad de Ciencias, Universidad de La Serena. Av. Juan Cisternas 1200, La Serena, Chile.

Sandro Villanova: Departamento de Astronomía, Casilla 160-C, Universidad de Concepción, Chile.

Cesar Muñoz: Departamento de Astronomía, Facultad de Ciencias, Universidad de La Serena. Av. Juan Cisternas 1200, La Serena, Chile; Instituto de Investigación Multidisciplinario en Ciencia y Tecnología, Universidad de La Serena. Avenida Raúl Bitran S/N, La Serena, Chile; Departamento de Astronomía, Casilla 160-C, Universidad de Concepción, Chile (cesar.alejandro.munoz.g@gmail.com).

ASSESSING THE HIERARCHICAL HAMILTONIAN SPLITTING INTEGRATOR FOR COLLISIONLESS N -BODY SIMULATIONS

G. Aguilar-Argüello, O. Valenzuela, H. Velázquez, J. C. Clemente, and J. A. Trelles

Instituto de Astronomía, Universidad Nacional Autónoma de México, México, CDMX, México.

Received September 2 2021; accepted March 18 2022

ABSTRACT

The large dynamic range in some astrophysical N -body problems led to the use of adaptive multi-time-steps; however, the search for optimal strategies is still challenging. We numerically quantify the performance of the hierarchical Hamiltonian Splitting (HHS) integrator for collisionless simulations using a direct summation code. We compare HHS with the constant global time-step leapfrog integrator, and with the adaptive one (AKDK). We find that HHS is approximately reversible, whereas AKDK is not. Therefore, it is possible to find a combination of parameters such that the energy drift is considerably milder for HHS, resulting in a better performance. We conclude that HHS is an attractive alternative to AKDK, and it is certainly advantageous for direct summation and P3M codes. Also, we find advantages with GADGET4 (Tree/FMM) HHS implementation that are worth exploring further.

RESUMEN

El gran intervalo dinámico en algunos problemas astrofísicos de N -cuerpos ha llevado al uso de pasos de tiempo múltiples adaptivos, sin embargo, la búsqueda de estrategias óptimas es aún un reto. Estudiamos numéricamente el integrador Hierarchical Hamiltonian Splitting (HHS) utilizando un código de suma directa y lo comparamos con el rendimiento de leapfrog con paso global constante y su versión multi-paso adaptivo (AKDK). Encontramos que HHS es aproximadamente reversible, mientras que AKDK no. Por lo que es posible encontrar una combinación de parámetros tales que el cambio de energía es considerablemente menor para HHS, resultando en una mayor eficiencia. Concluimos que HHS es una alternativa competitiva con ventaja para códigos de suma directa y P3M. También, hallamos ventajas para la implementación de HHS en GADGET4 (Árbol/FMM) que merecen ser investigadas más.

Key Words: celestial mechanics — galaxies: kinematics and dynamics — gravitation — large-scale structure of Universe — methods: numerical — software: simulations

1. INTRODUCTION

Historically, fully self-consistent realistic astrophysical N -body simulations are a challenging problem (Aarseth 1971; Efstathiou et al. 1985; Stadel 2001; Springel et al. 2001; Dehnen & Read 2011; Klypin 2018). On the purely gravitational case, direct summation N -body codes suffer from a bottleneck due to the computational cost of force calculation on a particle-by-particle basis, which scales as the square of particle number (N_p^2). For this reason, they are primarily used for simulating dense stellar

environments or planetary systems. Such limitations triggered the development of sophisticated approximate hybrid collisionless methods, like the TreePM (Tree-Particle Mesh)/P3M (Particle Particle- Particle Mesh)/P3T (Particle Particle- Particle Tree) codes (Xu 1995; Bode et al. 2000; Bagla 2002; Bode & Ostriker 2003) where the short-range component of the force is carried out either by expensive/accurate direct summation or tree force solvers (Couchman 1991; Oshino et al. 2011; Habib et al. 2013). Alternatively, AMR (Adaptive Mesh refine-

ment) methods are used to compute the large dynamical range of the gravitational force (Villumsen 1989; Jessop et al. 1994; Kravtsov et al. 1997; Teyssier 2002), seeking a balance between accuracy and computational efficiency. N -body simulations require both a fast way to calculate the accelerations and an accurate and efficient integration method to evolve particles in time. The second-order leapfrog symplectic integrator (Verlet 1967) is the most widely used in collisionless N -body simulations (e.g. Klypin 2018; Angulo & Hahn 2021). It is strictly symplectic when a global-constant time-step is adopted; however, this is not suitable for addressing problems with a large dynamical range that are currently studied with modern codes. In the quest to improve efficiency, it is necessary to adopt multiple or adaptive time-steps. The general problem of geometric/symplectic (preserving phase space volume), time-symmetric (recover initial conditions after changing dt for $-dt$) and reversible integrators (recover initial conditions after changing the sign of velocities) has been addressed in the field of differential equations for dynamical systems (Hairer et al. 2002). In such work, they point out the differences between adaptive global time-steps or multi-time-steps (several rates of evolution for different parts of the system) and discuss the constraints required for the integration method and the time-step selection function to preserve the mapping properties. In astronomy, the influential study of Quinn et al. (1997) discusses different operator-based leapfrog implementations using time step blocks plus a time-step selection function in the KDK/DKD leapfrog integrator for massive N -body simulations. They point out that particle migration across time-step blocks may break up the symmetry and sometimes involves backward integration, which can be difficult to reconcile with a dissipative component like gas. Current collisionless simulations codes commonly use the KDK leapfrog implementation with adaptive time-steps (e.g. Quinn et al. 1997; Springel 2005; Dehnen & Read 2011; Klypin 2018), which we call hereafter AKDK. Recently, Dehnen (2017) discusses conditions where the Hairer et al. (2002) analysis for time-symmetric integrators can be extended to discrete time-stepping. They conclude that there is no general solution. Many of the proposed integrators truly preserve the symmetries; however, the specific time-step selection function should also respect symmetrization. In several cases, the computational overhead makes the proposal impractical.

In this paper, we explore and quantify the Hierarchical Hamiltonian Splitting (HHS) strategy pro-

posed by Pelupessy et al. (2012), which is, as leapfrog, a second-order scheme. This integrator was tested for small number of bodies or collisional simulations, delivering good energy conservation and momentum conservation at machine accuracy. However, no analysis of time-symmetry or reversibility was presented. Some modern N -body codes like AREPO (Weinberger et al. 2020) and GADGET4 (Springel et al. 2021) have implemented versions of HHS with some differences with respect to the original proposal, although they do not give details of the performance or other properties that allow the comparison with the commonly used integrators. In this work, we extend the discussion of HHS in the context of collisionless N -body simulations, by numerically investigating the time-symmetry and velocity reversibility. We also test some time-step selection functions to explore the potential advantages. In all cases we compare with the global constant time-step leapfrog integrator and the adaptive one (AKDK) in order to assess the conditions under which HHS is a competitive alternative. As we discussed above, in some modern P3M codes running in hybrid architectures, the most expensive calculation is the short-range direct summation force integration, in some cases processed inside GPUs (Habib et al. 2016). Motivated by that, we implemented HHS in a direct summation code running in GPUs and complement that with additional tests with the Tree/FMM code GADGET4.

The rest of the paper has been organized as follows: § 2 summarizes the main properties of the integrators used here to carry out their comparison while § 3 introduces the time-step selection functions. § 4 shows accuracy tests performed with emphasis on the cases on an isolated halo and a minor merger. § 5, § 6 and § 7 contain the results of these tests taking into account the effect of time-step functions, performance and long-term stability, respectively. In § 8, we quantify reversibility and time-symmetry for the different codes. Finally, a discussion and the main conclusions are given in § 9.

2. INTEGRATORS

We implemented three different integrators in a direct summation code dubbed as $\text{NP}_{\text{splitt}}$ (Aguilar-Argüello et al. in prep.), the leapfrog, Adaptive-KDK (AKDK) and the Hierarchical Hamiltonian Splitting integrators (HHS). Below, we describe each integrator. It is common to express integrators as a composition of operators using the Hamiltonian splitting technique in potential (*Kick*) and kinetic energy (*Drift*), although there are other possibilities (Oshino et al. 2011).

2.1. *Leapfrog*

The leapfrog integrator is a second-order widely used integrator. As mentioned previously, this integrator is strictly symplectic only when a global-constant time-step is adopted. Symplectic integrators are designed to numerically preserve the integrals of motion and the phase-space volume of the simulated system.

In the leapfrog method, the evolution of the gravitational system can be written as a sequence of *Kick* (advance of velocities) and *Drift* (advance of positions) operators (e.g. Channell 1993; Quinn et al. 1997), defined by:

$$\begin{aligned} K(dt) : \mathbf{v}(t_n + dt) &= \mathbf{v}(t_n) + dt \mathbf{a}(t_n), \\ D(dt) : \mathbf{x}(t_n + dt) &= \mathbf{x}(t_n) + dt \mathbf{v}(t_n), \end{aligned} \quad (1)$$

where \mathbf{x} , \mathbf{v} and \mathbf{a} are the position, velocity and acceleration of a particle, respectively, and dt is the time step. In this paper, we use the operator sequence called KDK leapfrog (also known as *velocity Verlet*, Swope et al. 1982):

$$KDK : K(dt/2) D(dt) K(dt/2), \quad (2)$$

where we consider that the evolution is for one time step, i.e. from t_n to $t_n + dt$. Through this paper, we will refer to KDK leapfrog with a global-constant time-step as the Leapfrog integrator.

2.2. *AKDK*

Contemporary codes have extensively used KDK (equation 2) combined with a block time-step scheme (Hayli 1967; Sellwood 1985; Hut & McMillan 1986; Hernquist & Katz 1989; Makino 1991), frequently using rungs which are power of two: $dt_r = dt_0 2^{(-r)}$ and different assigning time-step functions, most frequently an acceleration based one (Springel 2005). We will use it as a reference integration scheme, but it should be noted that it is not symplectic (Hairer et al. 2002) and that the block-step is a multi time-step scheme.

2.3. *Hierarchical Hamiltonian Splitting*

The hierarchical Hamiltonian Splitting (HHS) method is a second-order integrator that uses individual time steps of the particles (Pelupessy et al. 2012) through recursively splitting the Hamiltonian. It accurately preserves linear and angular momentum and has a good energy conservation.

This integrator consists of adaptively and recursively splitting the Hamiltonian as a function of the current time step, dt , so that the so called *Slow* system (hereinafter S) contains all the particles with a

time step larger than dt , and the so called *Fast* system (hereinafter F) contains all the particles with a time step smaller than dt . Thus, the splitting is as follows:

$$\begin{aligned} H_S &= T_S + V_{SS} + V_{SF}, \\ H_F &= T_F + V_{FF}, \end{aligned} \quad (3)$$

where:

$$\begin{aligned} T_X &\equiv \sum_{i \in X} \frac{p_i^2}{2m_i}, \\ V_{XX} &\equiv -G \sum_{i \in X} \sum_{j \in X, j > i} \frac{m_i m_j}{|r_i - r_j|}, \\ V_{XY} &\equiv -G \sum_{i \in X} \sum_{j \in Y} \frac{m_i m_j}{|r_i - r_j|}, \end{aligned} \quad (4)$$

are, respectively, the kinetic and potential energies, and V_{SF} is the potential energy of the interactions between S and F particles. The previous splitting scheme is known as HOLD (since it “holds” V_{SF} for evaluation at the slow time-step, Pelupessy et al. 2012).

The S system is solved using the DKD scheme (also known as *position Verlet*, Tuckerman et al. 1990), which consists of *drifts* of the particles in this system (due to T_S) and *kicks* on the particles of both systems (due to $V_{SS} + V_{SF}$). For the F system, the same procedure as for the original system is applied but using a halved time-step. Hence, the splitting is applied recursively to the F system with time-step $dt/2^r$. The recursion ends when the system F (of the rung r) has no particles. At the end of the current integration step, the new time-step of a particle is calculated. In this scheme, a particle can change its time step to higher (lower) value if its current integration time is synchronized with the higher (lower) rung.

It is well known that the *Kick* and *Drift* operators are symplectic. However, using multiple or adaptive time-steps may not preserve such properties in a general way (Hairer et al. 2002). Therefore we need to investigate the behaviour of HHS.

3. TIME-STEP SELECTION FUNCTION

Besides the formulation of integrators with individual time steps based on symmetric operators, the choice for each particle time step is made through the so called time-step selection function. There is no unique choice; arguably the most commonly used time-step function in contemporary collisionless N -body codes (e.g. GADGET, Springel 2005) is based on the acceleration as:

$$\tau_i = \eta_{\text{accel}} \sqrt{\frac{\epsilon}{a_i}}, \quad (5)$$

where a_i is the acceleration acting on the particle i , giving the code the possibility of adapting to high/low accelerations, and ϵ is the force Plummer softening¹. Improvements have been recently discussed by using a dynamical time proxy (Zemp et al. 2007) and a tidal force time scale (Dehnen & Read 2011; Grudić & Hopkins 2020), establishing a balance between short and long time steps, which may translate into higher efficiency. Extensive comparisons of AKDK with both choices have been discussed in Zemp et al. (2007) and Grudić & Hopkins (2020).

In our study, in an attempt to preserve the energy stability of the HHS integrator while allowing adaptive multi time-steps, and following Pelupessy et al. (2012), we use an approximated time-symmetrized time-step extrapolation criterion for each particle. To obtain such a time-step criterion, we start from the implicit criterion (Hut et al. 1995):

$$\tau_{\text{sym}} = \frac{1}{2} [\tau(t) + \tau(t + \tau_{\text{sym}})], \quad (6)$$

where τ is a time-step function (non-symmetrized), and τ_{sym} is the symmetrized time-step function of τ . To a first-order perturbative expansion:

$$\tau(t + \tau_{\text{sym}}) \approx \tau(t) + \frac{d\tau}{dt} \tau_{\text{sym}}; \quad (7)$$

hence, from equation 6:

$$\tau_{\text{sym}} \approx \tau(t) + \frac{1}{2} \frac{d\tau}{dt} \tau_{\text{sym}}, \quad (8)$$

so that the time-step we will use is given by (Pelupessy et al. 2012)

$$\tau_i = \min_j \left[\frac{\tau_{ij}}{\left(1 - \frac{1}{2} \frac{d\tau_{ij}}{dt}\right)} \right]. \quad (9)$$

It is important to state that the minimization indicated above is across the so called *Slow* particles. For a time-step proportional to the inter-particle free-fall time:

$$\tau_{ij} = \eta_{\text{FF}} \sqrt{\frac{r_{ij}^3}{G(m_i + m_j)}}, \quad (10)$$

$$\frac{d\tau_{ij}}{dt} = \frac{3\mathbf{v}_{ij} \cdot \mathbf{r}_{ij}}{2r_{ij}^2} \tau_{ij}.$$

¹We will adopt the softening as twice the average inter-particle distance at the minimum radius where the density profile is not dominated by Poisson fluctuations, as it is usually adopted in collisionless simulations.

The former option is a two-body-based proxy for the dynamical-time-motivated step function suggested by Zemp et al. (2007).

For completeness with Pelupessy et al. (2012), for a time-step proportional to the inter-particle fly-by time (typically used in collisional problems):

$$\tau_{ij} = \eta_{\text{FB}} \frac{r_{ij}}{v_{ij}},$$

$$\frac{d\tau_{ij}}{dt} = \frac{\mathbf{v}_{ij} \cdot \mathbf{r}_{ij}}{r_{ij}^2} \tau_{ij} \left(1 + \frac{G(m_i + m_j)}{v_{ij}^2 r_{ij}} \right). \quad (11)$$

We will quantify the efficiency of such time-step functions. However, the high acceleration derivatives in the case of collisional problems may require going beyond the first order in the perturbative expansion.

Along the paper, we will mostly use the approximated symmetric free-fall time-step for HHS (defined by equations 9 and 10), and only in a few tests we will use the minimum of this and the approximated symmetric fly-by time-step (equations 9 and 11). In § 5, we will present a comparison with the GAD-GET4 implementation of HHS (Springel et al. 2021); this code uses a time-step function similar to equation 5 but the accuracy parameter, η_{accel} , is included inside the square root. For AKDK, we will use the standard time-step function given by equation 5.

Table 1 summarizes the combinations of integrators and time-step selection functions used through this work.

4. ACCURACY TESTS

In this section, we present the test results of the HHS algorithm in terms of accuracy by simulating an isolated halo and sinking satellites, and compare them with the global-constant time-step leapfrog and the adaptive one, AKDK. To proceed with the comparison we implemented the different integrators in a direct summation N -body code (Aguilar-Argüello et al. in prep.). All the experiments were run in a single GPU. As a sanity check, we performed binary system tests (not reported here) and the results are consistent with those reported in other works (e.g. Dehnen & Read 2011; Pelupessy et al. 2012; Springel 2005).

4.1. Isolated Cuspy Halo

We adopted as a reference model an equal particle mass, isolated halo following the NFW cuspy density profile predicted by collisionless dark matter cosmological simulations (Navarro et al. 1997). The large density range and the corresponding different dynamical times make it a suitable system for an

TABLE 1
COMBINATIONS OF INTEGRATORS AND TIME-STEP FUNCTIONS USED ALONG THIS PAPER

Integrator name	Integration scheme	Time-step scheme	Time-step selection function	Reference
Leapfrog	KDK	Global-constant		Verlet (1967)
AKDK	KDK	BLOCK	eq. 5	e.g. Quinn et al. (1997); Springel (2005) Dehnen & Read (2011); Klypin (2018)
HHS	HHS	HOLD	eqs. 9, 10	Pelupessy et al. (2012)
nsHHS	HHS	HOLD	eqs. 9, 10 (without $d\tau_{ij}/dt$)	This work
sAKDK	KDK	BLOCK	eqs. 9, 10	This work

adaptive time-step code. Such tests depend on resolution to actually capture the benefit of individual time-steps as compared with a global-constant time-step scheme. We will use as a reference time scale the dynamical time² at the NFW characteristic radius (r_s), since it has been used to study the stability of the halo in other works (e.g. Klypin et al. 2015).

For the integration of our fiducial model, we adopted $G = 1$ (gravitational constant), $M_{\text{vir}} = 1$ (virial mass) and $r_s = 1$ (scale length, also called characteristic radius), as model units. We will use these model units through the paper.

To investigate and quantify differences in accuracy and performance between the integrators first, we followed a fiducial halo sampled with 10^5 particles for 40 dynamical times at r_s, t_{dyn} .

Because our implementations of AKDK and HHS have different time-step function, a meaningful comparison is to assume an energy conservation threshold, which implies using distinct accuracy parameters for both integrators. For the first test, we considered a 10^{-7} threshold and accuracy parameters $\eta_{\text{FF}} = 0.003$ and $\eta_{\text{accel}} = 0.01$ for HHS and AKDK, respectively, both constrained to 6 time-step rungs. Figure 1 shows the result of these tests. The upper left panel shows the energy error. HHS (black) stays very close to Leapfrog (red) during the first $20 t_{\text{dyn}}$, afterwards it shows a small drift. AKDK (blue) drifts almost linearly and after $20 t_{\text{dyn}}$ it slightly flattens. Because the main computational overhead of HHS over AKDK comes from building and updating the time-step hierarchy in HHS, we decided to explore experiments where we delayed such an update, and denoted them as HHS-sTSS. We observed that such an action results in important savings in com-

putational time (yellow line). The energy accuracy test is lower but acceptable for a collisionless simulation, and it is faster; in addition linear and angular momentum are preserved to machine precision.

Regarding the conservation of other dynamical quantities like linear and angular momentum or the system barycenter the situation is different (see Figure 1). Leapfrog and HHS preserve almost at machine precision the linear and angular momentum (see bottom panels), whereas AKDK presents a smaller accuracy, although it has a slope until $10 t_{\text{dyn}}$, afterwards it flattens. Interestingly, HHS with a delay in updating the time-step hierarchy (HHS-sTSS, yellow) is almost indistinguishable from HHS and leapfrog. The upper right panel shows the accuracy in preserving the halo centroid. Once again, leapfrog and both HHS versions accurately keep the centroid, while the AKDK accuracy is degraded two orders of magnitude. The wall-clock time for leapfrog, HHS and HSS-sTSS experiments was, respectively, 1.7, 0.8 and 0.6 times the corresponding for AKDK. As a complement, we performed tests using larger time steps reaching lower energy accuracy, the general results are the same. Finally, we emphasize that all integrators accurately preserve the density profile, as we can see in Figure 2; with obvious dependence on the number of particles, we decided to show the test with two million particles in order to minimize discreteness effects.

4.2. Minor Merger: Sinking Satellites

Satellite accretion onto larger galaxies is an astrophysical problem commonly simulated by both isolated and cosmological N -body simulations (Miller et al. 2020; Arca-Sedda & Capuzzo-Dolcetta 2016). We simulated a satellite, represented by a softened and massive particle, falling into a spherical system, represented by collisionless softened particles, for seven dynamical times. The spherical system

²A dynamical time, also called crossing time, is the time taken for a typical particle to cross the system. In this paper, a dynamical time is defined as $t_{\text{dyn}}(r) = [r^3/GM(r)]^{1/2}$, where r and $M(r)$ are the radius and mass, respectively.

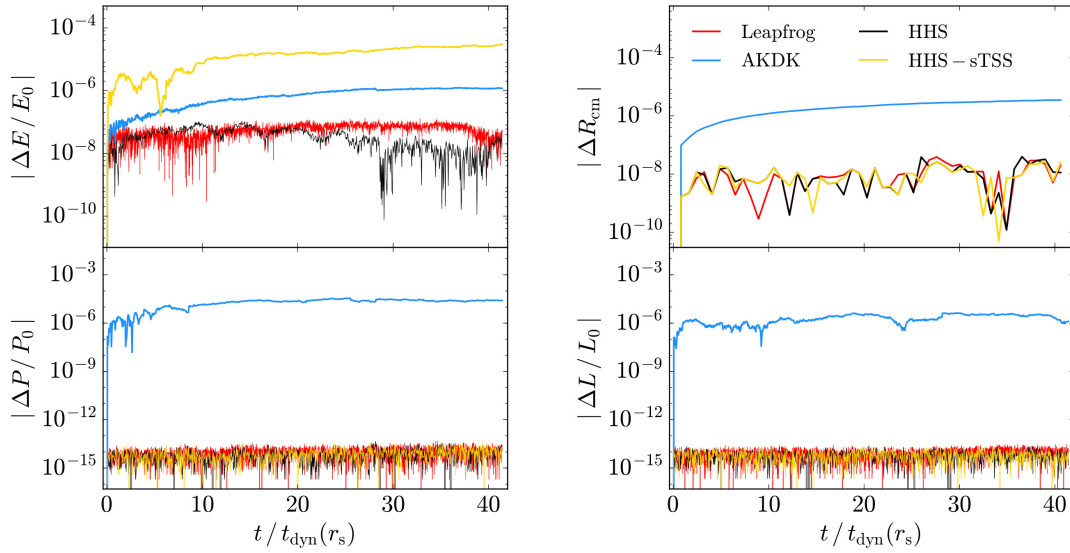


Fig. 1. Error in conserved quantities for an isolated NFW halo with $N = 10^5$ particles, simulated up to 40 dynamical times (at scale radius, r_s). Shown is the energy error (upper left panel), change in center of mass position (upper right panel), error in linear (lower left panel) and angular momentum (lower right panel) for the three integrators: Leapfrog (red), AKDK (blue) and HHS (black). Also, it is shown the HHS with a delay in the time-step hierarchy update (HHS-sTSS, yellow) version. The color figure can be viewed online.

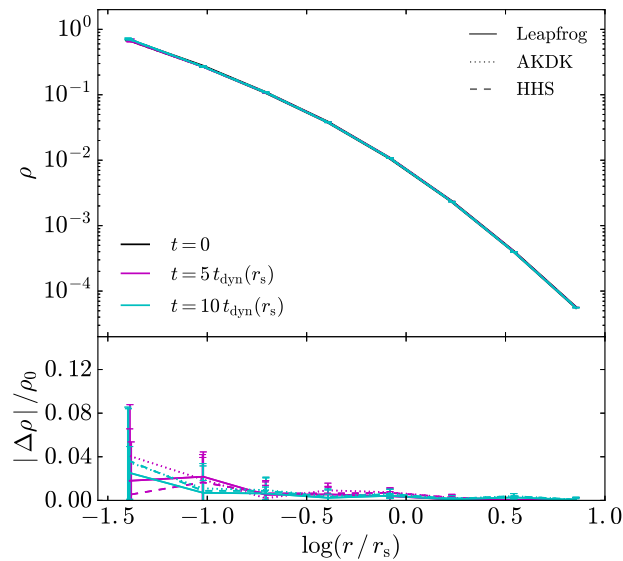


Fig. 2. Density profile, at different times, of the isolated NFW halo with 2×10^6 particles simulated up to 10 dynamical times for the three integrators: Leapfrog (solid lines), AKDK (dotted lines) and HHS (dashed lines). The three integrators accurately preserve the density profile. The color figure can be viewed online.

consists of $N = 10^5$ equal mass particles spatially distributed according to the NFW density profile (Navarro et al. 1997). We adopted the same units

as the previous fiducial isolated halo case. We used Plummer softening and we chose a softening parameter $\epsilon = 0.026$ (in model units). The satellite's initial separation from the center of the spherical system is $R_{\text{sat}} = 2.6$, and its mass is $m_{\text{sat}} = 0.01$, which is ≈ 1300 times bigger than the mass of one collisionless particle.

This test is particularly useful because the sinking process involves orbital angular momentum and energy transfer into the host system. We tracked energy, linear and angular momentum conservation as well as the host center of mass behavior (see Figure 3). Leapfrog (red) stays flat. HHS (black) starts to jump at one dynamical time, afterwards it stays flat. AKDK (blue) shows a lower accuracy in energy conservation and presents a systematic energy growth. As in the case of the isolated halo, the HHS energy drift slope is considerably flatter than the corresponding to AKDK. Linear and angular momentum are less accurate for AKDK by several orders of magnitude, while system barycenter behaves essentially the same for all three integrators. These results indicate that HHS is an excellent alternative for dynamical friction studies.

The evolution of the satellite radial position shows differences below the one percent level (see Figure 4). We conclude that, for a reduced number of dynamical times, the three integrators can provide an accurate description of the sinking process.

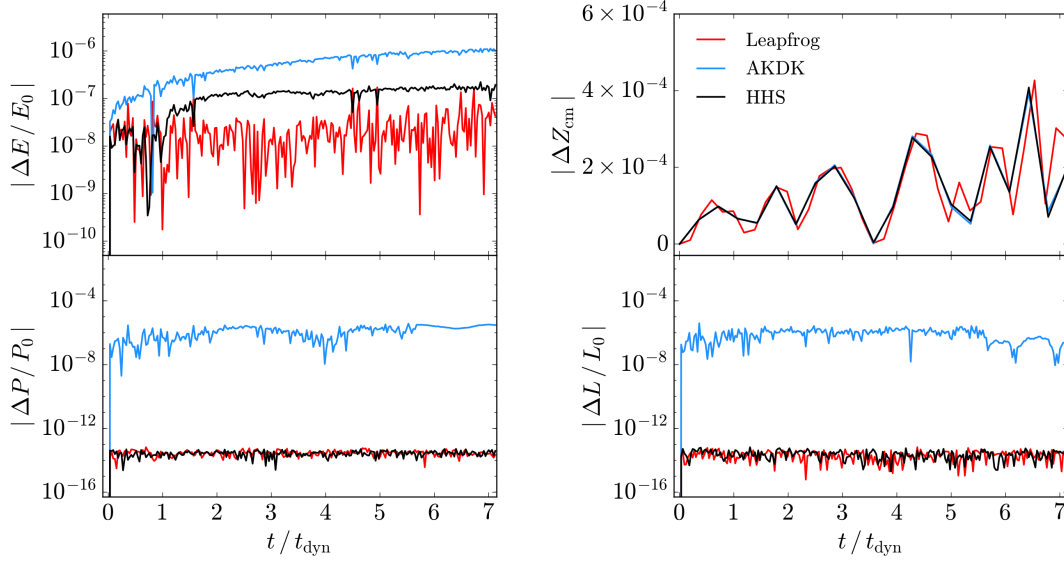


Fig. 3. Error in conserved quantities for a NFW halo with $N = 10^5$ particles plus a satellite simulated up to 7 dynamical times. Shown is the energy error (upper left panel), change in center of mass position (upper right panel), error in linear (lower left panel) and angular momentum (lower right panel) for the three different integrators: Leapfrog (red), AKDK (blue) and HHS (black). The color figure can be viewed online.

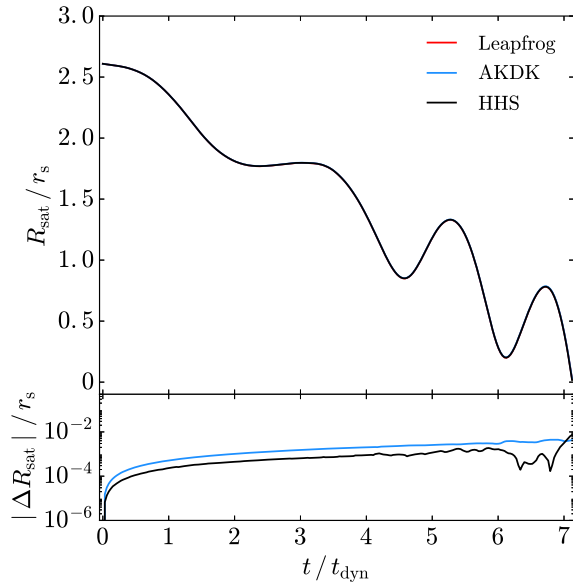


Fig. 4. Evolution of the satellite radial position (upper panel) for the sinking satellite test and for the three integrators: leapfrog (red), AKDK (blue) and HHS (black). When comparing with leapfrog (lower panel), the differences are below 1% between integrators. The color figure can be viewed online.

5. TIME-STEP SELECTION FUNCTION TESTS

As it has already been discussed some hierarchical/adaptive time-step integrators, like HHS and

AKDK, include a time-step selection function; such a prescription may help restoring the integrator symmetry. We may question if the approximated symmetric time-step selection function based on particle pairs given by equation 9 is only useful for a particular kind of simulation or code, and if we lose all the convenient properties of HHS, observed at this point, when the problem is not tractable by a direct summation code. To quantify such an effect we evolved the fiducial isolated halo switching the time-step selection function and we additionally performed test with the Tree/FMM code GADGET4.

5.1. Direct Summation Code

First, we consider our direct summation code implementation, simulating the fiducial isolated halo considering the HHS and AKDK integrators, as it can be seen in the upper panel of Figure 5. We take as a reference the AKDK integrator with an accuracy parameter $\eta_{\text{accel}} = 0.08$ (fiducial, solid blue line). The dotted black line shows HHS (with $\eta_{\text{FF}} = 0.055$), which is almost twice faster but slightly less accurate, and the dashed black line shows a case of HHS (with $\eta_{\text{FF}} = 0.015$) remarkably more accurate but 10% slower than the fiducial AKDK. We include another AKDK case (dashed blue) with a smaller accuracy parameter $\eta_{\text{accel}} = 0.049$, which is 20% less accurate than HHS (dashed black line) but 10% slower, and also is 20% slower and an order of magnitude more accurate than the fiducial AKDK

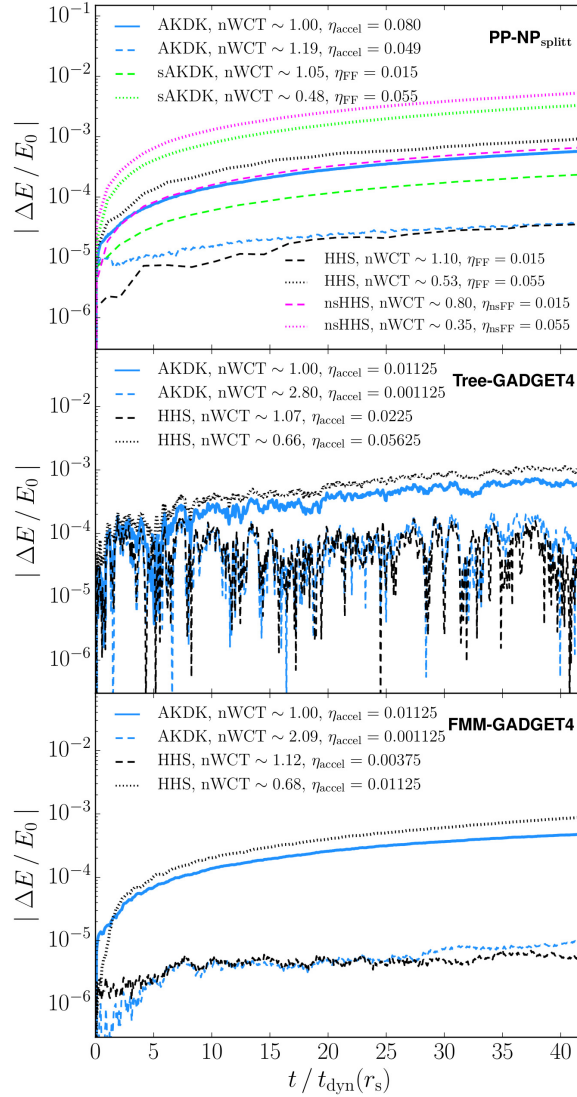


Fig. 5. Effect of time-step selection function and different acceleration codes. nWCT corresponds to the wall-clock time of each test normalized to the fiducial AKDK (solid blue line). Upper panel shows tests with our direct summation code. Solid blue line is the fiducial AKDK test and dotted black line is HHS, almost 50% faster. Dashed lines correspond to experiments with smaller accuracy parameter but reaching a limit where HHS is faster and more accurate than AKDK. Magenta dotted/dashed lines show the same HHS tests but neglecting the symmetrizing derivative term in equation 9; even going with smaller η_{nsFF} still may be competitive with AKDK. Green dotted/dashed lines show AKDK test with the symmetrized time-step selection function (equations 9 and 10) using the same parameters as HHS cases (black dotted/dashed lines, respectively). Middle panel shows experiments with GADGET4 using the Tree version. Results are consistent with the direct summation code. Solid blue line is the fiducial AKDK, dotted black line is HHS 7% slower and slightly less accurate. Dashed lines are AKDK and HHS, with almost flat behaviour, slightly better for HHS; however, AKDK is almost three times slower. Lower panel shows the equivalent tests but now for FMM GADGET4. As before, the AKDK for the flat case (dashed blue) is slightly worse in energy accuracy and almost twice slower as compared with HHS (dashed black). We conclude that, even for different time-step functions, there is still a regime where HHS is more efficient. The color figure can be viewed online.

case (solid blue). This means that considering even smaller values for the parameter η will not make AKDK more efficient than HHS. Next, we performed

some changes in the time-step selection function, we removed the derivative term from equation 9 which represents the symmetrizing correction for the HHS

integrator, we dubbed such tests nsHHS and they appear as the magenta lines in Figure 5. The energy drift is larger as compared with HHS but it is still acceptable for collisionless simulations, and it is faster. For completeness, we performed tests using equation 9 in AKDK (dubbed as sAKDK, green lines) with the same parameters (η_{FF} , rungs, etc.) as in the HHS tests. The energy drift is larger for the sAKDK test than the one corresponding to HHS; however, sAKDK is faster. Note that it is possible to match HHS accuracy by lowering the η_{FF} parameter in sAKDK tests, but it is slower (we do not show it because it does not add new information). So far, our tests suggest that HHS may benefit hybrid codes that use direct summation force calculation as part of their algorithm. For example, in the P3M technique (Hockney & Eastwood 1998) the most expensive part corresponds to direct summation, which runs in accelerators like GPUs (Habib et al. 2013, 2016; Cheng et al. 2020). Even using different time-step selection function, HHS may still obtain considerable performance. We analyze such a situation in the following sections, as well as the HHS performance in codes using approximated force computations (e.g. a tree code).

5.2. Tree Code: GADGET4

Recently, the 4th version of the publicly available code GADGET has implemented the HHS in the so called hierarchical gravity mode (Springel et al. 2021). The time-step selection function is similar to our equation 5 but the accuracy parameter η_{accel} is inside the square root. Changing the step function is a sensible choice because our equation 9, based on pair interactions, is not practical for very large numbers of particles. Also, in the GADGET4 HHS implementation, instead of using the DKD representation (as in our implementation), the authors adopted the KDK one (for further details we refer to Springel et al. 2021), in a similar way as Zhu (2017). Hence, this allow us to explore the case of an approximated gravitational acceleration code, such as a tree code (e.g. Barnes & Hut 1986), with different time-step selection function. For that purpose, we perform some tests using AKDK and HHS with the Tree version of GADGET4. As in the case of direct summation tests (§ 5.1), we simulated the fiducial isolated halo in such a way that we can directly compare with the direct summation code tests, including a non-symmetrized time-step function. The middle panel of Figure 5 shows the results for the Tree code version of GADGET4. For the corresponding fiducial AKDK (solid blue line), GADGET4 opens three time-step rungs,

and for its HHS implementation (dotted black line), it opens only two time-step rungs. Both integrators show an energy drift similar to 10^{-3} , however, HHS (dotted black line) is 66% faster, but less accurate. Motivated by this result, we ran a new HHS test decreasing the η_{accel} parameter (dashed black line); the energy is quite flat; therefore, energy conservation after $40 t_{\text{dyn}}$ is almost an order of magnitude better than the fiducial AKDK (solid blue line), but it is 7% slower. If we decrease η_{accel} for the AKDK integrator in order to match energy conservation (dashed blue line), the wall-clock time is considerably larger, by 50%. Although this is a particular example model, it is consistent with our previous tests. HHS is more stable and for medium and long-term integrations may be more efficient than AKDK, regardless of not using the approximated symmetric free-fall particle pairs time-step function (equations 9 and 10).

5.3. Fast Multipole Method Code: GADGET4

Gadget4 has implemented a different gravity solver based on the Fast Multipole Method expansion (FMM, e.g. Dehnen 2000, 2002). We ran the same fiducial isolated halo, as in the previous section, adopting the FMM scheme truncating the expansion at the quadrupole term. Results are presented in the lower panel of Figure 5. The blue solid line shows the fiducial case using AKDK ($\eta_{\text{accel}} = 0.01125$), the corresponding HHS case ($\eta_{\text{accel}} = 0.01125$, dotted black line) is relatively faster (66%); however, it is less accurate. We experimented lowering the η_{accel} parameter for HHS, and the energy evolution is flat (dashed black line). We also decreased η_{accel} for AKDK (dashed blue line); the energy accuracy is 10% worse but the wall-clock time is almost 100% larger; therefore, there is no point in trying smaller η_{accel} values. The experiments with the GADGET4 FMM version also confirm the conclusions from our direct summation tests.

6. PERFORMANCE

Although the adaptive nature of the HHS and AKDK integrators may imply a higher efficiency compared with the global-constant time-step leapfrog, the benefit of taking adaptive time-steps is evident only when the dynamical range is large. In comparison with AKDK, HHS has a computational overhead due to the recursive splitting of the Hamiltonian needed to build the time-step hierarchy.

We decided to make a short exploration of the simulation parameters (accuracy, rung number, and minimum time-step) with our direct summation code. We present the results in Figure 6, which

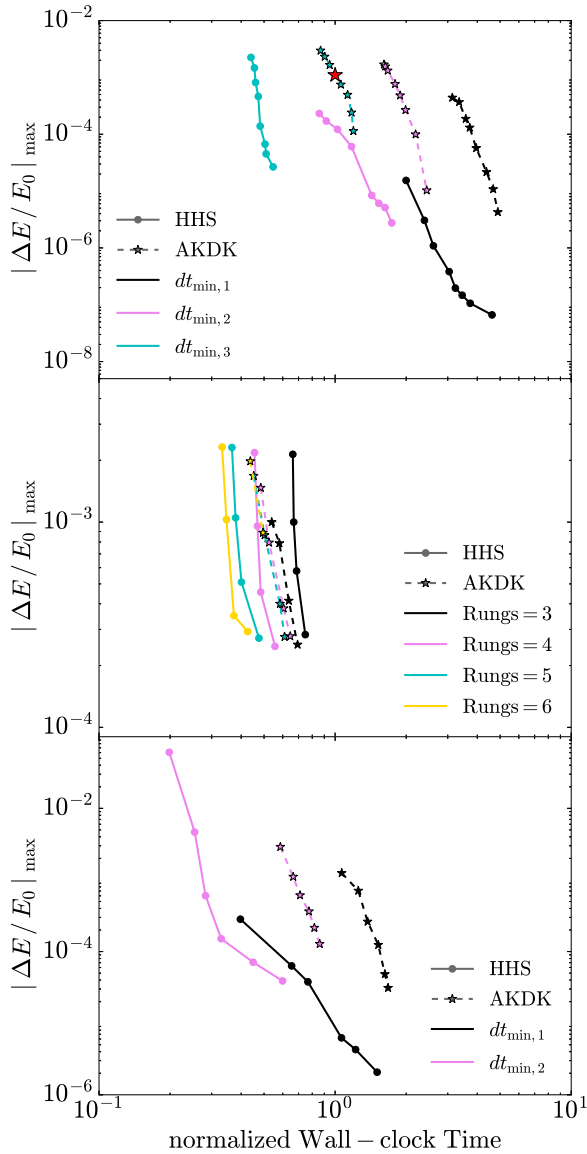


Fig. 6. Energy conservation as a function of wall-clock time (normalized with respect to the red star case in upper panel) for the fiducial isolated halo (upper and middle panels) and for a cuspy halo including four live cuspy satellites (bottom panel), for the HHS (solid circles) and AKDK (stars) integrators. In the upper panel, we used a Plummer softening $\epsilon = 0.007$, and we varied the minimum time step ($dt_{\min,1} = 5.4 \times 10^{-3}$, $dt_{\min,2} = 1.1 \times 10^{-2}$ and $dt_{\min,3} = 2.2 \times 10^{-2}$) but fixing the number of rungs (6 and 5 for HHS and AKDK, respectively). In the middle panel, we used $\epsilon = 0.01$, and we varied the number of rungs, but fixed the minimum time step ($dt_{\min} = 4.3 \times 10^{-2}$). For the bottom panel, we used $\epsilon = 0.004$, and we varied the minimum time step ($dt_{\min,1} = 6.4 \times 10^{-3}$ and $dt_{\min,2} = 1.3 \times 10^{-2}$) but fixing the number of rungs (6 and 3 for HHS and AKDK, respectively). The color figure can be viewed online

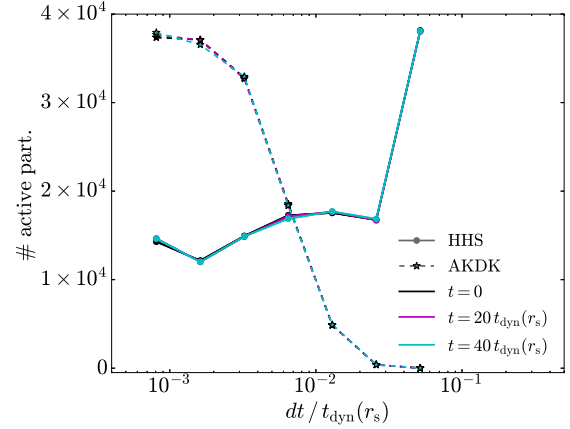


Fig. 7. Particle distribution across time-step rungs for different selection functions: acceleration criteria (equation 5, stars) and the approximated symmetric free-fall (equations 9 and 10, solid circles), for the fiducial isolated halo using the same parameters as in Figure 1. Note that the acceleration criterion has more particles with small time step and that the free-fall criterion is almost the opposite, with potential consequences for the performance. The color figure can be viewed online.

shows a pragmatic diagnostic of the integrator performance: energy conservation vs. wall-clock time. The upper and middle panels correspond to the fiducial isolated halo. In the upper panel we fixed the number of time-step rungs and we varied the minimum time-step; whereas in the middle panel, we fixed the minimum time-step (same for both integrators) and we varied the number of time-step rungs. The lower panel corresponds to the cuspy halo including four live cuspy satellites, a common situation in cosmological simulations that requires a large dynamical range. In many cases HHS outperforms AKDK. We may wonder what the reason is given the extra computations related with the splitting process. One possible suspect is the individual time-step distribution. To investigate that, we built the histogram of time steps for particles for the initial conditions and at later times (see Figure 7). For HHS (solid circles) it is clear that only a moderate fraction of particles are found in the deepest time-step rung. For AKDK the distribution is almost the opposite, there is a peak of particles in the three deepest rungs, which translates into many more time-steps than HHS. The difference in performance is partly due to the time-step selection function, in agreement with Zemp et al. (2007); Grudić & Hopkins (2020). Although tweaking parameters we may obtain differences in performance and accuracy, we noticed that for a defined energy conservation

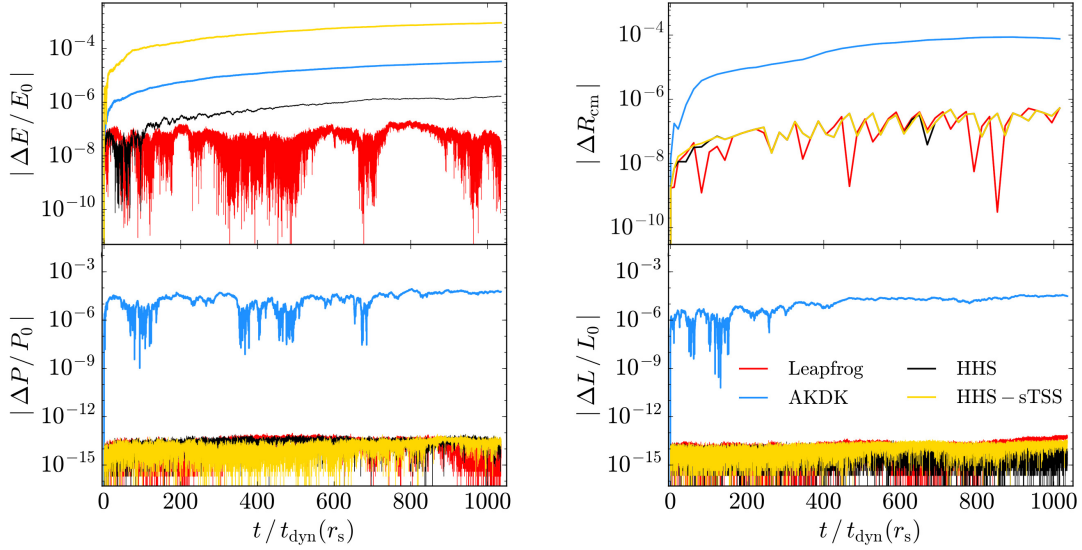


Fig. 8. As in Figure 1, but following the fiducial isolated halo up to 10^3 dynamical times (at scale radius). The color figure can be viewed online.

threshold in many cases HHS outperforms AKDK, because the energy growth is smaller for HHS than for the standard AKDK implementation, allowing HHS to use larger steps. Nevertheless, it is important to mention that if all the particles are similarly distributed in the time-step rungs for both integrators the computational overhead of HHS starts to play a more important role. This may happen for very low resolution runs where the dynamical range is artificially shortened. This is in agreement with the middle panel of the figure, showing that only when using more than three step runs HHS is faster than AKDK. The time-step histogram presented in Figure 7 is a handy tool to asses the situation.

Our conclusions are consistent with recent studies that published successful results using HHS with GADGET4 and reaching an extremely large dynamical range with multi-million particle numbers (Wang et al. 2020).

7. LONG-TERM STABILITY

At this point we have compared the accuracy and performance of the integrators for some dynamical times. A natural question arises, whether the HHS advantages are relevant for realistic long-term integration. Dark matter halos survive around 30 – 200 dynamical times in cosmological simulations depending on the merger/accretion history (Klypin et al. 2015). As before, we investigated the stability of en-

ergy, linear and angular momentum and density centroid for our fiducial isolated halo model, this time for hundreds of dynamical times (see Figure 8). Energy conservation of HHS (black) is quite close to the global-constant time-step leapfrog (red) behavior during the first 20 – 40 dynamical times (consistent with our previous tests). However, after that time it starts to slowly drift which seems to get slower at the end of the simulation ($\approx 700 t_{\text{dyn}}$). AKDK (blue) quickly drifts to a considerably larger energy error and keeps systematically growing. The yellow curve represents the HHS-sTSS version that delays the time-step hierarchy updating. As we observed before, it behaves as AKDK but with a smaller accuracy, although it is faster ($\approx 40\%$). For the linear and angular momentum all integrators preserve them. However, while HHS preserves them almost at machine precision, AKDK preservation is almost 8 orders of magnitude worse. A similar disparity is obtained by following the halo centroid. Seeking a cause of this difference in accuracy we tracked the circular velocity in experiments with a smaller number of particles ($N = 2000$) evolving the system for 400 dynamical times at $2.1 r_s$, where the circular velocity peaks. Figure 9 shows the circular velocity profile at several times. We found some differences, but they are all inside 10%. We conclude that, at the level of high accuracy, we do not expect important differences between integrators, and performance is the most relevant difference. As for as N -body simu-

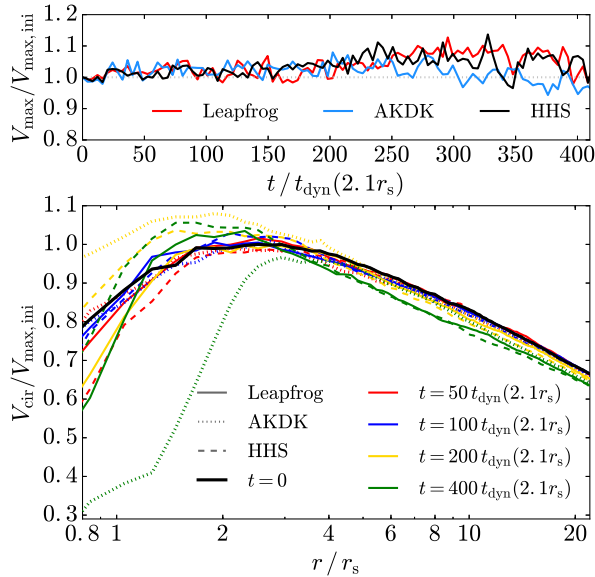


Fig. 9. Circular velocity curves for the fiducial isolated halo with 2000 particles following the system for long integration times. There is no systematic difference between different integrators. The energy conservation level is $\approx 10^{-5}$. The maximum circular velocity is scattered inside 10% at different moments. The color figure can be viewed online.

lations reaching a larger dynamical range, the smallest structures may live for a larger number of dynamical times; in this context HHS may offer a more stable option.

Recent studies regarding long-term N -body evolution (Hernandez et al. 2020), suggest that long-term integrations may be unstable to small changes in initial conditions realizations. This may be particularly critical for highly non-linear situations like the three-body problem. We generated a small ensemble of realizations for the fiducial isolated halo and for the sinking satellite problem. Results are shown in Figure 10 only for Leapfrog (red) and HHS (black). Indeed, some scatter is found; however, overall the results are robust.

8. REVERSIBILITY AND TIME SYMMETRY

The above numerical experiments show that there are certain parameter combinations where HHS is more accurate than AKDK or, alternatively, it is faster for a given energy accuracy. Because both integrators have different parameters it is natural to ask if there is a true advantage of HHS or if it is a misleading result, dependent on our implementation, accuracy or even particle number.

As we discussed in the introduction and in agreement with Hairer et al. (2003) we performed time symmetry and velocity reversibility tests using both HHS and AKDK integrators; we used leapfrog with a global-constant time-step as a reference case.

We chose the sinking satellite system as the test bed because the satellite orbit allows easily to track the system response in configuration space as well as in energy. At three different moments, termed BW1, BW2 and BW3, we reversed the velocity signs for all particles, and for one case instead of velocities we reversed the time sign; after that we continued the integration. Figure 11 shows the global result of forward (FW, solid lines) and backward (BW) evolution (i.e. inverting the sign of velocities) of the satellite distance to the halo center for all integrators, either for high (left panels) or low (right panels) energy conservation accuracy. For high energy conservation accuracy ($\approx 10^{-8}$, left panels), the differences in configuration space are in general small, which is consistent with Hernandez & Bertschinger (2018), where they discuss that AKDK preserves quantities like angular and linear momentum (see also Figure 3). However, there are still some differences as we can see in the lower panel. The satellite distance change with respect to its own forward evolution (lower panels) is a good diagnostic of reversibility. Clearly, the position difference in HHS (black) regarding the symplectic Leapfrog (red, global constant step) is below the simulation resolution determined by the softening (horizontal grey line), while for AKDK (blue) the calculated position difference is larger but close to the simulation softening. At a less accurate energy conservation but more common in collisionless simulations (10^{-3} , right panels), differences between forward and velocity reversal integration in Leapfrog (global constant step) and HHS are still below the simulation softening. However, AKDK has notable differences that are well above the simulation resolution and they are even detected in configuration space. We also tracked the fractional energy change (Figure 12). The first outstanding fact is the truly reversible behavior of the global-constant time-step leapfrog (upper panel); almost every peak and valley is reproduced after the velocity reversal. The middle panel shows the high accuracy tests for AKDK (blue lines) and HHS (black lines), and the bottom panel the corresponding low accuracy tests. For AKDK, there is a roughly systematic growth for both forward integration (blue solid opaque line) and also after reversing velocities, suggesting that AKDK is non-reversible. Instead, HHS is almost flat, suggesting that it is approximately reversible. We also ran a

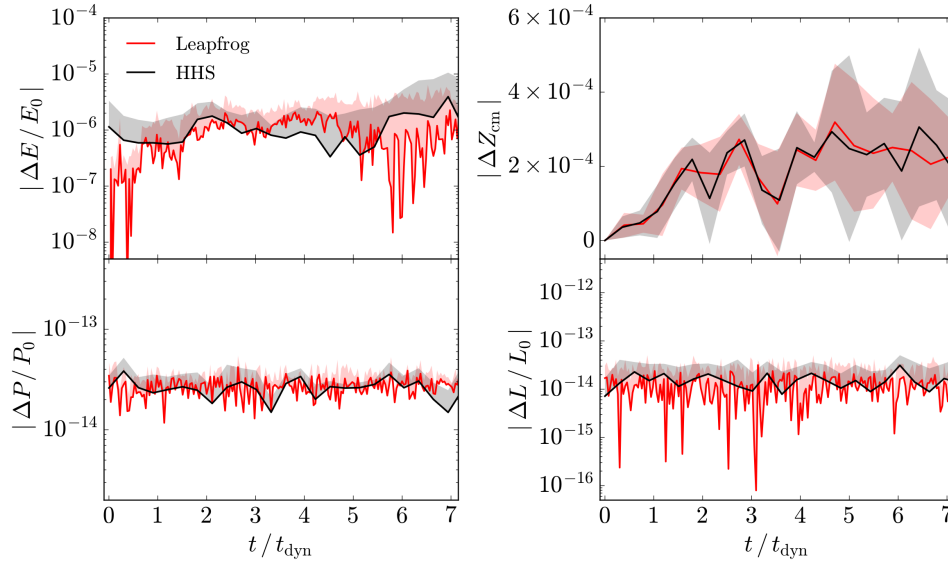


Fig. 10. Error in conserved quantities for a NFW halo with $N = 10^5$ particles plus a satellite simulated up to 7 dynamical times. Shown is the energy error (upper left panel), the change in center of mass position (upper right panel), the error in linear (lower left panel) and angular momentum (lower right panel) for the Leapfrog (red) and HHS (black) integrators. Shaded portions represent one sigma standard deviation propagated from different realizations ran under different random seeds. The color figure can be viewed online.

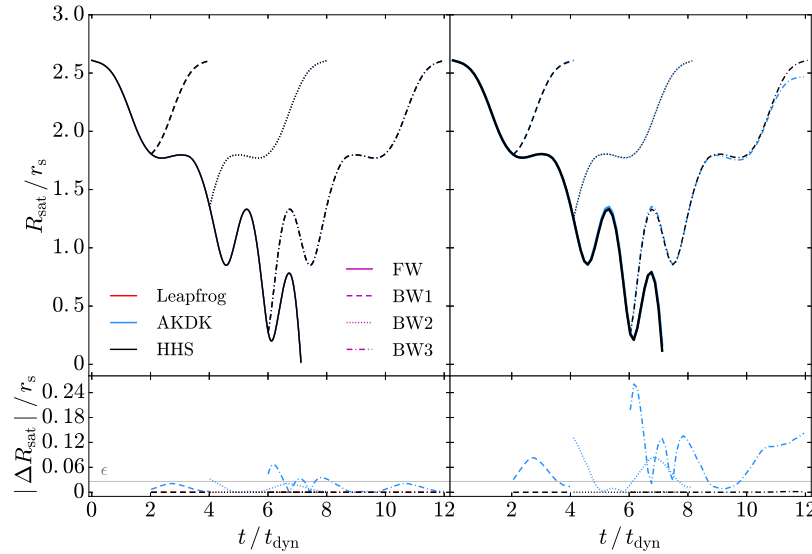


Fig. 11. Reversibility test. For the sinking satellite experiment we reversed the velocity sign at different moments, indicated by BW1 (dashed), BW2(dotted) and BW3 (dash-dot), and continued the integration. Solid lines represents the forward integration. Purple line labels only indicate the line-style corresponding to the start of each FW/BW integration. Upper panels show the normalized satellite distance as a function of time for the truly symplectic leapfrog (red lines), the adaptive one AKDK (blue lines) and HHS (black lines) integrators. Lower panels show the difference in position regarding the corresponding forward solution (solid lines). For high energy conservation accuracy ($\approx 10^{-8}$, left panels), there are some differences between integrators. However, they are inside (Leapfrog and HHS) or very close (AKDK) to the simulation softening (horizontal grey line). For a lower energy conservation accuracy ($\approx 10^{-3}$, right panels), still HHS and Leapfrog position differences are inside the simulation softening, whereas the AKDK case is above the simulation resolution. The color figure can be viewed online.

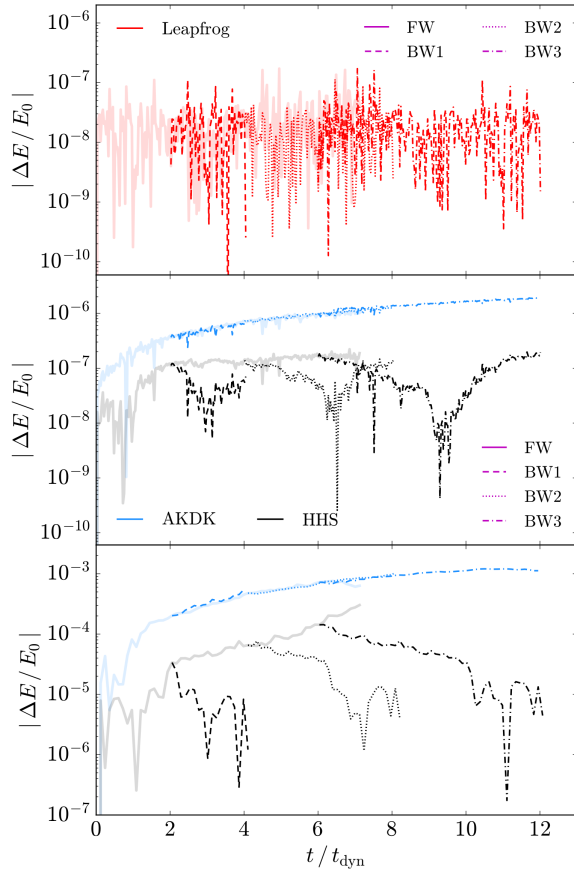


Fig. 12. Fractional energy error before (solid opaque lines) and after reversibility (dashed, dotted and dash-dot lines for BW1, BW2 and BW3 moments, respectively), for the same test of Figure 11. Top panel shows the global-constant time-step leapfrog, middle panel shows the higher accuracy in energy conservation tests, and the bottom panel the lower accuracy tests. Leapfrog is truly reversible. AKDK (blue lines) has a systematic growth of energy, suggesting that it is non-reversible. HHS (black lines) is almost flat with a small drift of energy after $\approx 2 t_{\text{dyn}}$ ($4.5 t_{\text{dyn}}$) for the high (low) accuracy test of the backward integrations, indicating that it is approximately reversible. Note that the purple line labels only indicate the line-style corresponding to the start of each FW/BW integration. The color figure can be viewed online.

test using HHS where we changed the time variable sign. In this case, the energy presents a systematic growth, showing that HHS is not time symmetric. However, for the sake of clarity, it was not included. We performed similar tests for the fiducial isolated halo and obtained similar results. The small slope showed in the energy drift suggests that HHS is approximately reversible. Furthermore the energy drift

is small compared to AKDK, which is non-reversible and non time-symmetric. This in agreement with Hairer et al. (2002) who showed that the symplectic Störmer-Verlet-LeapFrog (AKDK) performs poorly for an adaptive time-step integrator, unless the time-step assigning function is properly selected with a possible computational cost.

Figure 5 shows that even GADGET4 with the selection function given by equation 5 and its implementation of HHS allows, under certain conditions, for a faster or more accurate integration than AKDK. Figure 13 investigates the reversibility of HHS and AKDK in the Tree (upper panel) and FMM (lower panel) implementations using GADGET4. The forward (FW) evolution of both integrators is shown with solid opaque lines, and the backward (BW) evolution after changing the velocity sign, at $40 t_{\text{dyn}}$, is shown with dashed lines. For the Tree gravity solver using HHS, the energy drift for both forward and backward evolution is similar, particularly during the first $10 t_{\text{dyn}}$. However, although encouraging, we do not have enough evidence to claim that HHS is reversible. The time-step function adopted by GADGET4 may be the reason it is slightly different to our tests with a direct summation code. On the other hand, the reversed integration of AKDK shows a discontinuous change in its slope, indicating that it is not reversible. We conclude that Tree-HHS is more stable than Tree-AKDK. For the FMM gravity solver the test is not conclusive, because it does not show a significantly smaller slope in energy drift using the HHS scheme (Hierarchical Gravity).

9. DISCUSSION AND CONCLUSIONS

Using a GPU direct summation N -body code, we tested and characterized the Hierarchical Hamiltonian Splitting (HHS) integrator proposed by Pelupessy et al. (2012), but we focused on collisionless simulations. As a reference we compared with the global-constant time-step symplectic Leapfrog integrator and the widely used Adaptive one (AKDK). We also complemented our study using the HHS implementation in GADGET4 (dubbed as hierarchical gravity, Springel et al. 2021), which uses a different time-step selection function and approximate force solvers (Tree and FMM).

As recently discussed (e.g. Dehnen 2017), there is no general solution for a symplectic adaptive multi time-step integrator, although there are several proposals (e.g. Huang & Leimkuhler 1997; Hairer 1997; Calvo et al. 1998; Hardy et al. 1999; Farr & Bertschinger 2007). The problem is not exclu-

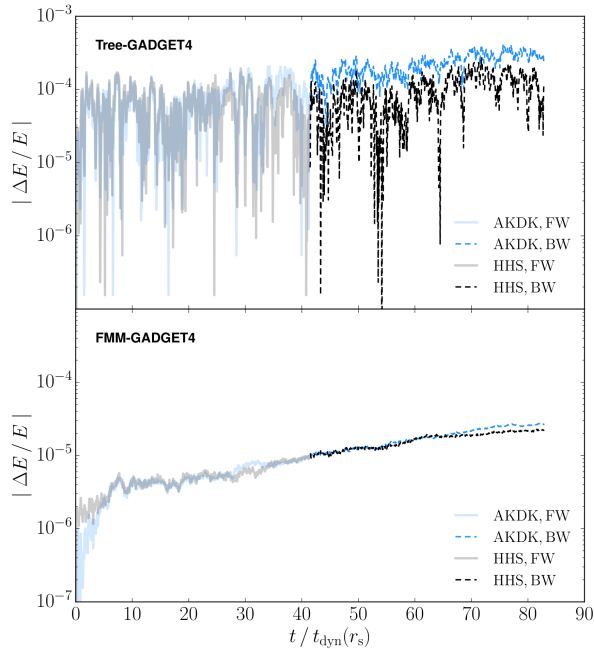


Fig. 13. Reversibility test for GADGET4. We followed the fiducial isolated halo using the GADGET4 code (shown with solid opaque lines) and we reversed the sign of particle velocities at around $40 t_{\text{dyn}}$ (dashed lines). Upper panel (Tree-GADGET4): for HHS with a non-symmetrized step function, remarkably up to $60 t_{\text{dyn}}$ the energy drift stays flat, then it slowly starts to grow. For AKDK the reversed integration just continues the forward systematic growth. Lower panel: For FMM with HHS and AKDK using a non-symmetrized step function, the energy drift grows systematically for both integrators. We can see that Tree-GADGET4 with HHS and the non-symmetrized step function could be approximately reversible or at least more stable. However, more studies are required. The color figure can be viewed online.

sive of astrophysics; the field of differential equations of dynamical systems has extensively reviewed the subject (Hairer et al. 2002). In particular, it is important to say that adaptive and multi-step techniques are not identical but they are related. Hernandez & Bertschinger (2018) address the important case of adaptive time steps, inspired by Hairer et al. (2002). They discuss what is called the “backwards error analysis” in order to explore commonly used integrators in astrophysics, concluding that symplecticity, time symmetry and reversibility are not the same and they are not always a guarantee of energy conservation. Nevertheless, the KAM (Kolmogorov-Arnold-Moser) theorem assures stability for symplectic (geometrical) and reversible in-

tegrators (Hairer et al. 2002) in contrast to non-reversible ones, like AKDK with the standard time-step selection function. The case of multi-step integration, requires extra conditions like the so called impulse (splitting) or averaging (less often force evaluation) techniques (Hairer et al. 2002). Similar problems have been discussed in the molecular dynamics field, and the r-RESPA method (Tuckerman et al. 1992) that is a splitting technique has been applied to the long-short range splitting case or multiple mass segregation with considerable advantage in performance. An important feature is that such approaches to the multi-step problem resulted in a symmetric or reversible method, not in a symplectic one. The major concrete benefit has been an improvement in the performance at a given energy accuracy. A similar situation applies to HHS, the case we study in this paper. HHS is a composition of *Fast* and *Slow* operators (Pelupessy et al. 2012) and based in our numerical experiments it is approximately reversible, which explains the performance advantage shown in § 6. The discussion in Hairer et al. (2002) and Hernandez & Bertschinger (2018) shows that the reversibility depends on the symmetry under a velocity sign change of hamiltonian and the corresponding time-step assigning function, and not on the accuracy of gravity calculation or particle number. The particular case of equation 10 is an approximate 1st order version of the one proposed by Hut et al. (1995) that depends only on the module of particle pairs relative velocities; therefore it is reversible. A future interesting avenue inspired by the r-RESPA method presented by Tuckerman et al. (1992) is the extension already discussed by Portegies Zwart et al. (2020). We experimented with the strategy motivated by the multi-step averaging technique (Hairer et al. 2002), updating the time-step hierarchy only at a given number of global time-steps (dubbed as HHS-sTSS, Figures 1 and 8). There is a gain in CPU time; however, the energy drift increases suggesting that further investigation is required.

Our results are summarized below:

1. Based on reversibility and time symmetry tests we concluded that HHS is not time symmetric but it is approximately reversible; it is also more stable than AKDK for a given energy accuracy. Although the exact correspondence between forward and backwards integration lasts only for few dynamical times, even for ten dynamical times the energy drift growth is small. In contrast, the AKDK energy drift grows systematically with time, clearly showing that it is non-reversible using the commonly used time-

step selection function. Based in our tests HHS reversibility explains the advantage in performance regarding AKDK. Based on the Hairer et al. (2002) discussion and the used time-step selection functions that depend only on the velocity module, such properties are independent of accuracy in gravity calculation and of particle number.

2. Our findings with the direct summation code may be also relevant for the high accuracy and costly section (PP) of codes using the P3M technique, as it has been also shown in molecular dynamics studies (Plimpton et al. 1997).
3. In agreement with our direct summation code tests, changing the time-step selection function for a non-symmetrized one, it is possible to find a combination of parameters in GADGET4 (using both the Tree and FMM code version) where HHS is more efficient than AKDK. We found approximate reversibility for the Tree Gadget4 test. However, for FMM Gadget4 our tests were inconclusive.
4. The population of particle histogram across the time-step rungs is useful to find a convenient parameter combination for the integrators.

GAA thanks V. Springel for nicely clarifying GADGET4 information. GAA and JCC thank Leobardo Ithehua Rico for the fruitful technical support and discussion. OV and GAA acknowledge support from UNAM PAPIIT Grant IN112518, IG101620 and IG101222. GAA and JAT thank support from CONACyT graduate fellowships 455336 and 825451, respectively. HV acknowledges support from IN101918 PAPIIT-UNAM Grant and from a Megaproyecto DGTIC-LANCAD for access to the Supercomputer MIZTLI. This research was partially supported through computational and human resources provided by the LAMOD UNAM project through the clusters Atocatl and Tochtli. LAMOD is a collaborative effort between the IA, ICN and IQ institutes at UNAM, and it acknowledges benefit from the MX28274 agreement with IBM. We thank CEDIA computing center for access to the DGX A100 cluster through an agreement with CUDI.

REFERENCES

- Aarseth, S. J. 1971, *Ap&SS*, 14, 20, <https://doi.org/10.1007/BF00649191>
- Angulo, R. E. & Hahn, O. 2021, arXiv e-prints, arXiv:2112.05165, <https://doi.org/10.48550/arxiv.2112.05165>
- Arca-Sedda, M. & Capuzzo-Dolcetta, R. 2016, *MNRAS*, 461, 4335, <https://doi.org/10.1093/mnras/stw1647>
- Bagla, J. S. 2002, *JApA*, 23, 185, <https://doi.org/10.1007/BF02702282>
- Barnes, J. & Hut, P. 1986, *Natur*, 324, 446, <https://doi.org/10.1038/324446a0>
- Bode, P. & Ostriker, J. P. 2003, *ApJS*, 145, 1, <https://doi.org/10.1086/345538>
- Bode, P., Ostriker, J. P., & Xu, G. 2000, *ApJS*, 128, 561, <https://doi.org/10.1086/313398>
- Calvo, M., López-Marcos, M., & Sanz-Serna, J. 1998, *Applied Numerical Mathematics*, 28, 1
- Channell, P. J. 1993, in *Proceedings of Symplectic Integrators Workshop*, Waterloo Ontario, Canada
- Cheng, S., Yu, H.-R., Inman, D., et al. 2020, in *Accepted for SCALE 2020*, colocated as part of the proceedings of CCGRID 2020; 2020 20th IEEE/ACM International Symposium on Cluster, Cloud and Internet Computing (CCGRID), <https://doi.org/10.1109/CCGrid49817.2020.00-22>, arXiv: 2003.03931
- Couchman, H. M. P. 1991, *ApJ*, 368, 23, <https://doi.org/10.1086/185939>
- Dehnen, W. 2000, *ApJ*, 536, 39, <https://doi.org/10.1086/312724>
- _____. 2002, *JCoPh*, 179, 27, <https://doi.org/10.1006/jcph.2002.7026>
- _____. 2017, *MNRAS*, 472, 1226, <https://doi.org/10.1093/mnras/stx1944>
- Dehnen, W. & Read, J. I. 2011, *EPJP*, 126, 55, <https://doi.org/10.1140/epjp/i2011-11055-3>
- Efstathiou, G., Davis, M., White, S. D. M., & Frenk, C. S. 1985, *ApJS*, 57, 241, <https://doi.org/10.1086/191003>
- Farr, W. M. & Bertschinger, E. 2007, *ApJ*, 663, 1420, <https://doi.org/10.1086/518641>
- Grudić, M. Y. & Hopkins, P. F. 2020, *MNRAS*, 495, 4306, <https://doi.org/10.1093/mnras/staa1453>
- Habib, S., Morozov, V., Frontera, N., et al. 2013, *SC'13 Proceedings of SC13: International Conference for High Performance Computing, Networking, Storage and Analysis*, 6, <https://doi.org/10.1145/2503210.2504566>
- Habib, S., Pope, A., Finkel, H., et al. 2016, *New A*, 42, 49, <https://doi.org/10.1016/j.newast.2015.06.003>
- Hairer, E. 1997, *ApNM*, 25, 219, [https://doi.org/10.1016/s0168-9274\(97\)00061-5](https://doi.org/10.1016/s0168-9274(97)00061-5)
- Hairer, E., Lubich, C., & Wanner, G. 2002, *Springer Series in Computational Mathematics*, 12, 399
- _____. 2003, *AcNum*, 12, 399, <https://doi.org/10.1017/s0962492902000144>
- Hardy, D. J., Okunbor, D. I., & Skeel, R. D. 1999, *ApNM*, 29, 19, [https://doi.org/10.1016/s0168-9274\(98\)00031-2](https://doi.org/10.1016/s0168-9274(98)00031-2)
- Hayli, A. 1967, *NASSP 153*, *The N-Body Gravitational Problem and the Simulation of Galactic Clusters*, 315
- Hernandez, D. M. & Bertschinger, E. 2018, *MNRAS*, 475, 5570, <https://doi.org/10.1093/mnras/sty184>

- Hernandez, D. M., Hadden, S., & Makino, J. 2020, *MNRAS*, 493, 1913, <https://doi.org/10.1093/mnras/staa388>
- Hernquist, L. & Katz, N. 1989, *ApJS*, 70, 419, <https://doi.org/10.1086/191344>
- Hockney, R. W. & Eastwood, J. W. 1998, *ISC Workshops*
- Huang, W. & Leimkuhler, B. 1997, *SIAM Journal on Scientific Computing*, 18, 239, <https://doi.org/10.1137/s1064827595284658>
- Hut, P. & McMillan, S. L. W. 1986, *The Use of Supercomputers in Stellar Dynamics*, (New York, NY: Springer), 267, <https://doi.org/10.1007/BFb0116387>
- Hut, P., Makino, J., & McMillan, S. 1995, *ApJ*, 443, 93, <https://doi.org/10.1086/187844>
- Jessop, C., Duncan, M., & Chau, W. Y. 1994, *JCoPh*, 115, 339, <https://doi.org/10.1006/jcph.1994.1200>
- Klypin, A. 2018, *Cosmological N-Body Simulations*, (World Scientific Series in Astrophysics), 27
- Klypin, A., Prada, F., Yepes, G., Heß, S., & Gottlöber, S. 2015, *MNRAS*, 447, 3693, <https://doi.org/10.1093/mnras/stu2685>
- Kravtsov, A. V., Klypin, A. A., & Khokhlov, A. M. 1997, *ApJS*, 111, 73, <https://doi.org/10.1086/313015>
- Makino, J. 1991, *ApJ*, 369, 200, <https://doi.org/10.1086/169751>
- Miller, T. B., van den Bosch, F. C., Green, S. B., & Ogiya, G. 2020, *MNRAS*, 495, 4496, <https://doi.org/10.1093/mnras/staa1450>
- Navarro, J. F., Frenk, C. S., & White, S. D. M. 1997, *ApJ*, 490, 493, <https://doi.org/10.1086/304888>
- Oshino, S., Funato, Y., & Makino, J. 2011, *PASJ*, 63, 881, <https://doi.org/10.1093/pasj/63.4.881>
- Pelupessy, F. I., Jänes, J., & Portegies Zwart, S. 2012, *New A*, 17, 711, <https://doi.org/10.1016/j.newast.2012.05.009>
- Plimpton, S. J., Pollock, R., & Stevens, M. J. 1997, *PPSC*
- Portegies Zwart, S., Pelupessy, I., Martínez-Barbosa, C., van Elteren, A., & McMillan, S. 2020, *CNSNS*, 85, 105240, <https://doi.org/10.1016/j.cnsns.2020.105240>
- Quinn, T., Katz, N., Stadel, J., & Lake, G. 1997, arXiv: astro-ph/9710043
- Sellwood, J. A. 1985, *MNRAS*, 217, 127, <https://doi.org/10.1093/mnras/217.1.127>
- Springel, V. 2005, *MNRAS*, 364, 1105, <https://doi.org/10.1111/j.1365-2966.2005.09655.x>
- Springel, V., Pakmor, R., Zier, O., & Reinecke, M. 2021, *MNRAS*, 506, 2871, <https://doi.org/10.1093/mnras/stab1855>
- Springel, V., Yoshida, N., & White, S. D. M. 2001, *New A*, 6, 79, [https://doi.org/10.1016/s1384-1076\(01\)00042-2](https://doi.org/10.1016/s1384-1076(01)00042-2)
- Stadel, J. G. 2001, *Cosmological N-body simulations and their analysis*, PhD Thesis, University of Washington
- Swope, W. C., Andersen, H. C., Berens, P. H., & Wilson, K. R. 1982, *JChPh*, 76, 637, <https://doi.org/10.1063/1.442716>
- Teyssier, R. 2002, *A&A*, 385, 337, <https://doi.org/10.1051/0004-6361:20011817>
- Tuckerman, M., Berne, B. J., & Martyna, G. J. 1992, *JChPh*, 97, 1990, <https://doi.org/10.1063/1.463137>
- Tuckerman, M. E., Martyna, G. J., & Berne, B. J. 1990, *JChPh*, 93, 1287, <https://doi.org/10.1063/1.459140>
- Verlet, L. 1967, *PhRv*, 159, 98, <https://doi.org/10.1103/PhysRev.159.98>
- Villumsen, J. V. 1989, *ApJS*, 71, 407, <https://doi.org/10.1086/191380>
- Wang, J., Bose, S., Frenk, C. S., et al. 2020, *Natur*, 585, 39, <https://doi.org/10.1038/s41586-020-2642-9>
- Weinberger, R., Springel, V., & Pakmor, R. 2020, *ApJS*, 248, 32, <https://doi.org/10.3847/1538-4365/ab908c>
- Xu, G. 1995, *ApJS*, 98, 355, <https://doi.org/10.1086/192166>
- Zemp, M., Stadel, J., Moore, B., & Carollo, C. M. 2007, *MNRAS*, 376, 273, <https://doi.org/10.1111/j.1365-2966.2007.11427.x>
- Zhu, Q. 2017, arXiv: 1712.10116, <https://doi.org/10.48550/arxiv.1712.10116>

THE BONDI-HOYLE ACCRETION TAIL OF POINT SOURCES TRAVELLING HYPERSONICALLY THROUGH A DENSE ENVIRONMENT

A. C. Raga¹, J. Cantó², A. Castellanos-Ramírez², A. Rodríguez-González¹, and P. R. Rivera-Ortiz³

Received December 16 2021; accepted March 21 2022

ABSTRACT

We present a model for the “Bondi-Hoyle tail” left behind by the hypersonic passage of a compact, massive object through a dense, radiative environment. We derive simple equations for the flow velocity and the mass along the tail, and obtain numerical and approximate analytical solutions for the steady state problem. We then study a time-dependent problem in which the source first travels within a dense cloud, and then emerges into a low density environment. This flow results in the production of a trail of dense gas joining the source at the point in which it emerged from the dense cloud. This trail has a linear velocity vs. position profile.

RESUMEN

Presentamos un modelo para una “cola de Bondi-Hoyle” producida por el pasaje hipersónico de un objeto compacto masivo a través de un medio ambiente radiativo. Derivamos ecuaciones sencillas para la velocidad y la masa del flujo a lo largo de la cola, y obtenemos soluciones numéricas y analíticas aproximadas del problema estacionario. Luego estudiamos el problema con dependencia temporal de una fuente que primero viaja dentro de una nube densa y luego emerge a un medio ambiente de baja densidad. Este flujo tiene como resultado la producción de una estela que conecta la fuente con el punto del cual ésta emergió de la nube densa. Esta estela tiene una velocidad que depende linealmente de la posición.

Key Words: accretion, accretion discs — hydrodynamics — ISM: jets and outflows — ISM: kinematics and dynamics — stars: winds, outflows

1. INTRODUCTION

The gravitational interactions due to a compact object moving through an environment were first studied by Bondi & Hoyle (1944). These interactions result in the deviation towards the symmetry axis of the streaming environment, and the formation of a “tail” of material behind the compact object (part of which ends up accreting onto the object). This flow is now called “Bondi-Hoyle (B-H) accretion”, and the trail of perturbed material left behind by the moving object is the “B-H tail”.

Most of the studies of B-H accretion have concentrated on evaluations of the gravitational drag on the compact object (see, e.g., Dokuchaev 1964; Ostriker 1999; Sánchez-Salcedo 2009; Cantó et al. 2011; Lee & Stahler 2014). This problem has recently gained

interest in the context of planets within accretion disks. Some of the relevant papers are:

- Cantó et al. (2013): a model for the drag on a point source within a disk with a Gaussian vertical density profile
- Thun et al. (2016): axisymmetric simulations from which they calculate the total hydrodynamic+gravitational drag on a rigid sphere,
- Masset & Velasco Romero (2017) and Velasco Romero & Masset (2020): show that radiative heating from emission of a point source can have strong effects on the gravitational drag.

In the present paper, we focus on the dynamics of the B-H tail left behind by a high velocity, compact object. This tail, seen in numerical simulations of hypersonic compact objects moving through a dense, highly radiative medium (see, e.g., Cantó et al. 2011) is formed by the convergence of the stream-

¹Instituto de Ciencias Nucleares, UNAM, CDMX, México.

²Instituto de Astronomía, UNAM, CDMX, México.

³Univ. Grenoble Alpes, Observatoire de Grenoble, Grenoble, France.

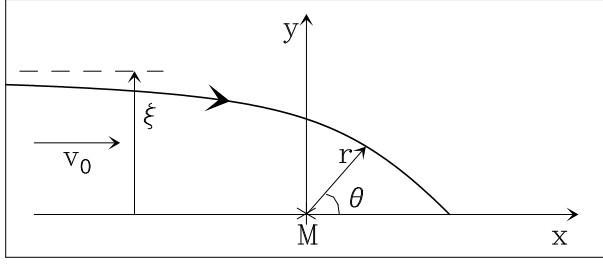


Fig. 1. Schematic diagram showing a plane flow traveling in the $+x$ direction with a velocity v_0 , which is perturbed by the gravitational attraction of a point source of mass M located at the origin of the xy -coordinate system. The thick curve shows the trajectory of a free-streaming fluid parcel with an initial impact parameter ξ .

ing environment onto the axis defined by the motion of the compact object.

Under the assumption of a locally well mixed flow, we derive the equations for the motion of the flow along the B-H tail, and derive a full numerical solution and an approximate analytic solution of the velocity and mass distribution of the tail (§ 2). We then study a time-dependent problem of the B-H tail left behind by compact object which first travels within a dense cloud, and then emerges into a low density environment (§ 4). The applicability of the B-H tail model to different kinds of compact objects is then discussed (§ 5). A discussion of the strong cooling assumption in our analytic model is presented in § 6. Finally, the results are summarized in § 7.

2. THE STEADY B-H TAIL

2.1. The Free-Streaming Trajectories

Let us consider a point mass M located at the origin of an xy -coordinate system, immersed in a hypersonic flow impinging along the x -axis, which is homogeneous and has a velocity v_0 for $x \rightarrow -\infty$. This situation is shown in the schematic diagram of Figure 1.

A fluid parcel impinging with an initial impact parameter ξ will follow the free-streaming trajectory

$$r = \frac{\xi^2}{\xi_0(1 + \cos \theta) + \xi \sin \theta}, \quad (1)$$

where

$$\xi_0 \equiv \frac{GM}{v_0^2} \approx [1.33 \times 10^{12} \text{ cm}] \left(\frac{M}{M_\odot} \right) \left(\frac{100 \text{ km s}^{-1}}{v_0} \right)^2, \quad (2)$$

G is the gravitational constant, θ the angle measured from the x -axis and r the spherical radius (see Figure 1).

The components of the velocity of the fluid parcel along this trajectory are:

$$v_x = \frac{v_0}{\xi} (\xi + \xi_0 \sin \theta); \quad v_y = -\frac{v_0 \xi_0}{\xi} (1 + \cos \theta), \quad (3)$$

The flow parcels with impact parameter ξ then intersect the x -axis at a position

$$x = \frac{\xi^2}{2\xi_0}, \quad (4)$$

with an axial velocity

$$v_x = v_0. \quad (5)$$

A more detailed derivation of these equations is given by Cantó et al. (2011).

The flow parcels arriving at the x -axis join a turbulent B-H tail into which they feed mass and momentum. This is described in the following subsection.

2.2. Mass and Momentum Fed into the B-H Tail

Let us consider the mass fed at position x in an interval Δx along the B-H tail. From equation (4) we obtain the range of impact parameters

$$\Delta \xi = \frac{\xi_0}{\xi} \Delta x = \sqrt{\frac{\xi_0}{2x}} \Delta x \quad (6)$$

of the flow parcels that arrive onto the axis inside Δx .

As the impinging flow is homogeneous (of density ρ_0), the mass injection rate of the flow parcels within the $\Delta \xi$ impact parameter range is:

$$\Delta \dot{M} = \rho_0 v_0 2\pi \xi \Delta \xi. \quad (7)$$

Combining equations (4), (6) and (7) we then obtain the mass rate fed per unit length into the tail:

$$\dot{m} = \frac{\Delta \dot{M}}{\Delta x} = 2\pi \xi_0 \rho_0 v_0, \quad (8)$$

which is independent of the position x along the tail. From equations (5) and (8) we find that the momentum injected per unit length into the tail is simply

$$\dot{m} v_0 = 2\pi \xi_0 \rho_0 v_0^2. \quad (9)$$

2.3. The Equations of Motion for the B-H Tail

The mass σ per unit length along the B-H tail satisfies continuity and momentum equations of the form:

$$\frac{\partial \sigma}{\partial t} + \frac{\partial \sigma v}{\partial x} = 2\pi \xi_0 \rho_0 v_0, \quad (10)$$

$$\frac{\partial \sigma v}{\partial t} + \frac{\partial \sigma v^2}{\partial x} = 2\pi \xi_0 \rho_0 v_0^2 - \frac{GM}{x^2} \sigma, \quad (11)$$

where v is the velocity along the B-H tail. In these equations we have considered the mass and momentum rates injected by the material accreting onto the tail (equations 8 and 9) and the gravitational force of the perturber. We have also neglected the pressure force along the axis of the B-H tail, as appropriate for a flow with strong radiative cooling.

We now define the dimensionless variables

$$t' \equiv \frac{t}{t_0}; \quad x' \equiv \frac{x}{\xi_0}; \quad v' \equiv \frac{v}{v_0}; \quad \sigma' \equiv \frac{\sigma}{\sigma_0}, \quad (12)$$

with ξ_0 given by equation (2) and

$$t_0 \equiv \frac{\xi_0}{v_0}; \quad \sigma_0 \equiv 2\pi \xi_0^2 \rho_0. \quad (13)$$

In terms of these dimensionless variables, equations (10-11) take the form:

$$\frac{\partial \sigma'}{\partial t'} + \frac{\partial \sigma' v'}{\partial x'} = 1, \quad (14)$$

$$\frac{\partial \sigma' v'}{\partial t'} + \frac{\partial \sigma' v'^2}{\partial x'} = 1 - \frac{\sigma'}{x'^2}, \quad (15)$$

in which the terms representing the mass and momentum incorporation into the tail take a unitary value.

2.4. The Stationary Case

The equations for a stationary B-H tail are obtained by setting the time derivative in equations (14-15) to zero, giving:

$$\frac{d\sigma' v'}{dx'} = 1, \quad (16)$$

$$\frac{d\sigma' v'^2}{dx'} = 1 - \frac{\sigma'}{x'^2}. \quad (17)$$

Equation (16) can be integrated to obtain:

$$\sigma' v' = x' - x'_0, \quad (18)$$

where x'_0 (an integration constant) is the position along the tail which separates a negative velocity region (for $x' < x'_0$, of material accreting onto the point mass) from a positive velocity region (for $x' > x'_0$, with tail material that escapes from the point mass).

Combining equations (17-18) we obtain a differential equation involving only the velocity:

$$\frac{dv'}{dx'} = \frac{(1 - v')x'^2 v' - (x' - x'_0)}{(x' - x'_0)x'^2 v'}. \quad (19)$$

This equation has a critical point at $[x' = x'_0, v' = 0]$, in which both the numerator and denominator of the right hand term are zero. The desired critical solution has to go through this critical point, smoothly joining the accreting $x' < x'_0$ region and the escaping $x' > x'_0$ region.

One can find the value of σ' at the critical point by first taking the $x' \rightarrow x'_0$ limit of equation (18):

$$\sigma'(x'_0) = \frac{1}{(dv'/dx')_{x'_0}}, \quad (20)$$

and in this limit equation (19) becomes:

$$\left(\frac{dv'}{dx'}\right)_{x'_0} = \frac{1}{x'^2_0}. \quad (21)$$

We therefore obtain:

$$\sigma'(x'_0) = x'^2_0. \quad (22)$$

We have been unable to find analytical expressions for the position x'_0 of the critical point nor for the $v'(x')$ solution of equation (19), and therefore proceed numerically. There are two standard options for finding critical solutions numerically:

- with a shooting method, in which successive integrations (of equation 19) starting at a small x' (integrating in the $+x'$ -direction) and at a large value of x' (in the $-x'$ -direction) are calculated with different initial v' values, until two solutions with a good match at the critical point are found,
- integrating the time-dependent equations (in our case, equations 14-15) and letting them relax to the stationary solution.

We have chosen this second possible approach. We integrated the time-dependent equations (14-15) with a simple, finite-difference method, starting with a ($\sigma' = 10^{-3}, v' = 0$) uniform initial condition. It would be more natural to choose a $\sigma' = 0$ initial condition (corresponding to a B-H with no initial mass), but this is unsuitable for carrying out the first integration step of the finite-difference method. We find that for a dominion of spatial extent x'_{max} , at a time $t'_{relax} \approx x'_{max}$, the solution converges to a stationary solution. We therefore integrate for a time = $10 x'_{max}$ to guarantee convergence.

The stationary solution obtained in this way is shown in Figure 2. We find that the critical point at which the flow velocity goes from negative to positive velocities is located at $x'_0 \approx 1.51$. At this point, the

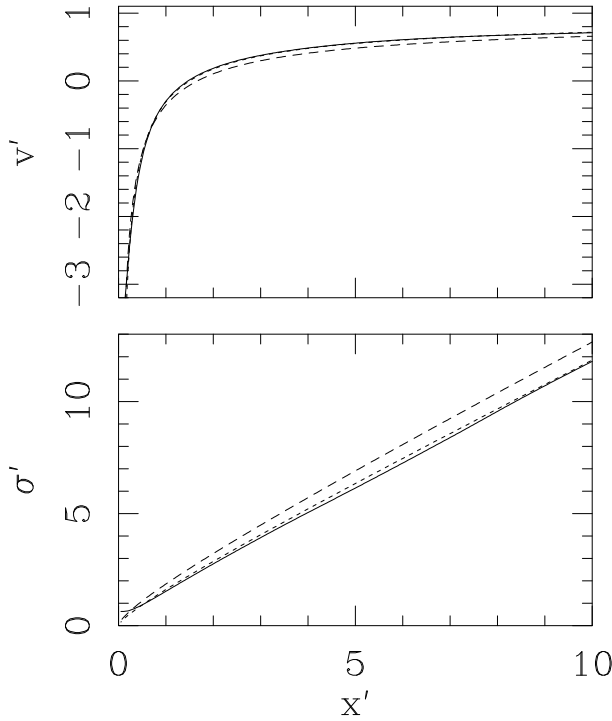


Fig. 2. Stationary solution for the dimensionless velocity v' (top) and mass per unit length σ' (bottom) as a function of dimensionless distance x' of the flow along a B-H tail. The solid lines correspond to the numerical solution, and the (barely distinguishable) short dash lines to the analytic approximation of equations (23-24). The long dash lines show our second analytic approximation given by equations (25) and (30).

density is $\sigma'_0 = 2.19$. These values of x'_0 and σ'_0 approximately satisfy equation (22).

We find that the $v'(x')$ stationary solution (obtained numerically, see above) can be well reproduced with a simple, single parameter fitting function of the form

$$v'_a(x') = 1 - \left(\frac{x'_0}{x'}\right)^{1/x'_0}, \quad (23)$$

with the $x'_0 \approx 3/2$ of the numerically determined critical point. The corresponding approximation for the dimensionless density σ' can then be calculated from equation (18), obtaining:

$$\sigma'_a(x') = \frac{x' - x'_0}{1 - (x'_0/x')^{1/x'_0}}. \quad (24)$$

The analytical approximations of equations (23-24) with $x'_0 = 3/2$ are shown in Figure 2.

We now present a purely analytic derivation of a similar approximate solution. This is done as follows:

- a. We consider a fitting function of the form:

$$v'_b(x') = 1 - \left(\frac{x'_0}{x'}\right)^\beta, \quad (25)$$

with arbitrary constants x'_0 and β ,

- b. From this equation we compute the first and second derivatives with respect to x' at position x'_0 :

$$\left(\frac{dv'_b}{dx'}\right)_{x'_0} = \frac{\beta}{x'_0}, \quad (26)$$

$$\left(\frac{d^2v'_b}{dx'^2}\right)_{x'_0} = -\frac{\beta(1+\beta)}{x'^2_0}, \quad (27)$$

- c. And then obtain the first and second derivative of $v'(x')$ at $x' = x'_0$ from equation (19) and its x' -derivative:

$$\left(\frac{dv'}{dx'}\right)_{x'_0} = \frac{1}{x'^2_0}, \quad (28)$$

$$\left(\frac{d^2v'}{dx'^2}\right)_{x'_0} = \frac{4(1-x'_0)}{x'^4_0}, \quad (29)$$

- d. Finally, equating (26) to (28) and (27) to (29) we obtain:

$$x'_0 = \frac{5}{3}; \quad \beta = \frac{1}{x'_0} = \frac{3}{5}. \quad (30)$$

The resulting $v'_b(x')$ (obtained substituting the values of equation 30 in equations 23 or 25) is shown in Figure 3. We see that it is a reasonable approximation for the numerically obtained $v'(x')$, but it is less accurate than the $x'_0 = 3/2$ fit to the numerical results (see above and Figure 2).

3. POINT MASS EMERGING FROM A DENSE CLOUD

Let us now consider the problem of the B-H tail produced by a point mass that first travels within a dense environment, and then suddenly emerges into a very low density environment. This situation can be modeled using equations (14-15) for the region of the flow within the dense cloud, and with similar equations with no mass/momentum deposition (i.e., setting to zero the unitary terms on the right hand side of equations 14-15).

We have carried out a numerical integration in which a dense environment of density ρ_0 (with which we normalize the equations, see equation 13) impinges on the point mass for a time $t'_0 = 100$ (corresponding to a displacement $x'_0 = 100$ of the point

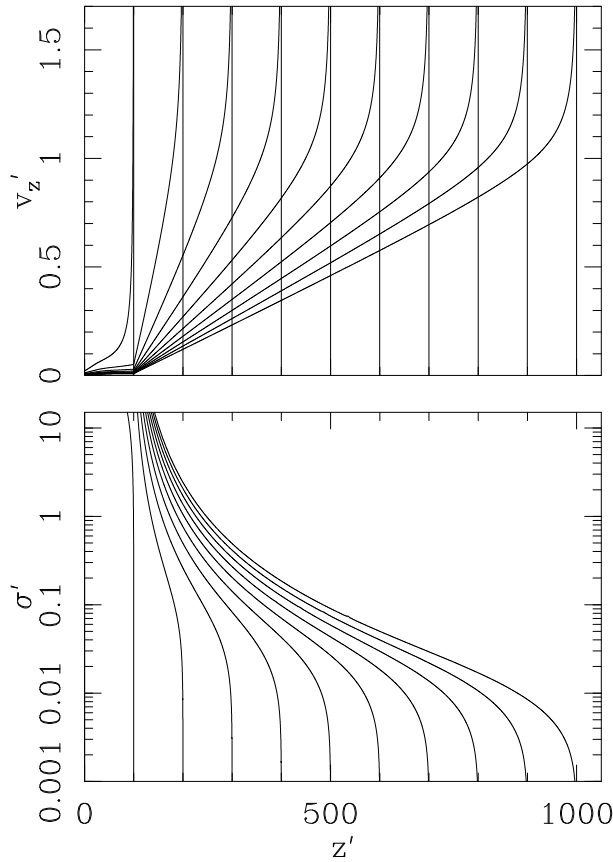


Fig. 3. Dimensionless velocity (top) and mass per unit length (bottom) as a function of distance (in a reference frame at rest with respect to the environment) for the time-dependent B-H tail produced by a point mass that emerges from a dense cloud (in the $z' < 100$ region) into a low density environment (for $z' > 100$). The left curves correspond to a time $t' = 100$, and the right curves to $t' = 1000$, with the successive curves at $\Delta t' = 100$ intervals.

mass with respect to the environmental gas), followed by a zero density impinging environment for $t' > t_0$. The chosen value for t'_0 allows an approximately stationary B-H tail to develop behind the point mass.

We plot the results in a reference system that is at rest with respect to the environmental gas. We therefore use $z' = t' - x'$ as spatial coordinate (with the point mass travelling in the $+z'$ direction) and a velocity $v'_z = 1 - v'$.

The results obtained from the simulation are shown in Figure 3. In this Figure, we show the velocity v'_z and the mass σ' along the B-H tail as a function of z' at time intervals $\Delta t' = 100$. The first curves (with the shortest z' extensions) correspond to $t' = 100$ (i.e., the moment at which the point

source emerges from the edge of the dense cloud, at a position $z' = 100$, see above), and the most extended curves correspond to $t' = 1000$.

The velocity distributions show a high peak close to the positions of the point mass, which correspond to the $v' \rightarrow -\infty$ material accreting onto the compact object. This region of high v'_z has very low mass per unit tail length σ' (as can be seen comparing the top and bottom frames of Figure 3).

In the region from the point of emergence from the cloud (at $z' = 100$, see above) to the point with $v'_z \approx 1$ the B-H tail develops a linear ramp of increasing velocities (top frame of Figure 3), due to a “velocity sorting” of the material in the free ($x' > x'_0$) region of the tail. This “Hubble velocity law” region has a mass σ' that rapidly drops for increasing z' values.

Through the velocity sorting mechanism, the B-H tail generated by the point mass when it was within the “dense cloud region” (i.e., in the $z' \leq 100$ region) at later times becomes very extended (e.g., from $z' \rightarrow 1000$ for $t' = 1000$), and might be easier to resolve with limited resolution observations. This long tail has a total mass that is somewhat smaller than the mass that is dragged out from the dense cloud, as part of the B-H tail is accreted onto the point mass.

4. APPLICABILITY OF THE MODEL

Let us now consider the nature of the “point mass” producing a B-H tail. The clear candidate for producing this flow would be a black hole or a neutron star. Also, runaway compact objects from planets to different types of star could in principle produce B-H tails under the conditions that are discussed below.

The region of the B-H tail following the motion of the source is produced by material with impact parameters $\leq \xi_0$ (see equations 1-2). Therefore, for this region of the tail to be formed the condition $R_* < \xi_0$ (where R_* is the radius of the source) has to be satisfied. Combining this condition with equation (2) we then see that the velocity v_0 of the source relative to the environment must satisfy the condition:

$$v_0 < v_{max} \equiv \sqrt{\frac{GM_*}{R_*}}. \quad (31)$$

Table 1 gives estimates of v_{max} for a selection of planets, main sequence stars and compact stars (a white dwarf and a neutron star). It is clear that an Earth-like planet will develop a B-H tail only if it is travelling at a velocity $< 8 \text{ km s}^{-1}$, and a “Jupiter”

TABLE 1

MAXIMUM VELOCITY AND MINIMUM ENVIRONMENTAL DENSITIES FOR DIFFERENT OBJECTS

	Earth	Jupiter	Sun	O7V	White dwarf	Neutron star
$M [M_\odot]$	3.0×10^{-6}	9.5×10^{-4}	1.0	40	1.0	1.5
$R_* [R_\odot]$	9.2×10^{-3}	0.10	1.0	$10 \cdot 10^{-2}$	1.4×10^{-5}	
$\dot{M} [M_\odot/\text{yr}]$	3×10^{-14}	10^{-6}	...	2×10^{-11}
$v_w [\text{km/s}]$	400	2500	...	$\sim 3 \times 10^5$
$v_{max} [\text{km/s}]$	7.9	42	440	880	4400	1.4×10^5
$n_c [\text{cm}^{-3}]$	1.6×10^4	2.1×10^9	...	0.3

at velocities $< 40 \text{ km s}^{-1}$ with respect to the surrounding environment.

If the source of the B-H tail has a stellar wind, we will have a wind/environment bow shock of characteristic size

$$R_{bs} = \sqrt{\frac{\dot{M} v_w}{4\pi \rho_0 v_0^2}}, \quad (32)$$

where v_w and \dot{M} are the terminal velocity and the mass loss rate (respectively) of the stellar wind. The bow shock will deflect the environmental material with impact parameters $< R_{bs}$, so for the inner part of the B-H tail to be formed, the condition $\xi_0 > R_{bs}$ has to be met. For a star (with v_w , \dot{M}) moving at a velocity v_0 , we then need an environmental density

$$\rho_0 > \rho_c \equiv \frac{\dot{M} v_w v_0^2}{4\pi G^2 M^2}, \quad (33)$$

where in the right hand term have set $R_{bs} = \xi_0$ (see equation 2) in equation (32).

In Table 1 we give the minimum number densities $n_c = \rho_c / (1.3 m_H)$ (where m_H is the hydrogen mass and we assume a 10% He abundance) obtained for a source velocity $v_0 = 100 \text{ km s}^{-1}$. We see that a ‘‘halo population’’ solar type star passing through the plane (with typical velocities $\approx 100 \text{ km s}^{-1}$ with respect to the galactic plane IMS), will only form a B-H tail when going through a particularly dense region (e.g., a molecular cloud) of $n > 10^4 \text{ cm}^{-3}$. On the other hand, because of its strong stellar wind, a runaway O star will never develop a B-H tail, as the required environmental densities for confining the bow shock are too high (see Table 1).

Clearly, the best potential candidates for producing observable B-H tails are white dwarfs and neutron stars (see Table 1). A standard white dwarf does not have a detectable wind, and a neutron star could have an appreciable relativistic wind (as implied by some of the observed pulsar wind nebulae,

see, e.g., Kargaltzev & Pavlov 2007). However, a relatively low density environment should be able to confine this wind (see the last row of Table 1). Of course, a black hole (not included in Table 1) will produce a B-H tail even if it is travelling at relativistic velocities.

5. THE STRONG RADIATIVE COOLING APPROXIMATION

In this section we discuss under which conditions there is strong radiative cooling in the B-H tail. In our solution, the characteristic size of the flow both across and along the symmetry axis is ξ_0 (see equation 2). The condition for radiative cooling to be important is that the cooling distance d_{cool} behind the shock (through which the material enters the shock) has to be smaller than ξ_0 . In the $d_{cool} \approx \xi_0$ limit, we will have a tail of radius also $\approx \xi_0$.

If the cross section of the tail has a cylindrical radius $\approx \xi_0$, the material (of impact parameter $\approx \xi_0$) entering the tail goes through a shock of velocity $\approx v_0$ (see equation 3) and preshock density $\approx n_0$ (see equation 8). The cooling distance behind this shock can be estimated using plane-parallel shock models. A possible analytic fit to the cooling distances of the conveniently well tabulated shock models of Hartigan et al, (1987) is:

$$d_{cool} = \left(\frac{100 \text{ cm}^{-3}}{n_0} \right) \left\{ [3 \times 10^{11} \text{ cm}] \left(\frac{v_0}{100 \text{ km s}^{-1}} \right)^{-6.4} + [8 \times 10^{13} \text{ cm}] \left(\frac{v_0}{100 \text{ km s}^{-1}} \right)^{5.5} \right\}, \quad (34)$$

appropriate for the $v_0 = 20 \rightarrow 400 \text{ km s}^{-1}$ shock velocity range.

Now, setting $d_{cool} = \xi_0$ and using equations (2) and (34), we find an estimate for the minimum environmental density n_{cool} for which the material in

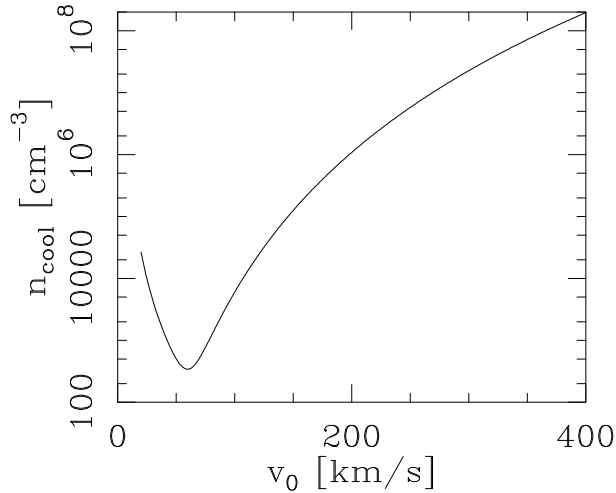


Fig. 4. Minimum environmental number density n_{cool} for producing a radiative, B-H tail as a function of the velocity v_0 of motion of a one solar mass point source. The density scales as the inverse of the mass of the point source (see equation 35).

the Bondi-Hoyle tail has substantial cooling:

$$\frac{n_{cool}}{100 \text{ cm}^{-3}} = \left(\frac{M_{\odot}}{M}\right) \left[0.224 \left(\frac{v_0}{100 \text{ km s}^{-1}}\right)^{-4.4} + 59.9 \left(\frac{v_0}{100 \text{ km s}^{-1}}\right)^{7.5}\right]. \quad (35)$$

In Figure 4, we give n_{cool} as a function of v_0 for a $1 M_{\odot}$ point mass source. We see that for a $1 M_{\odot}$ object travelling at a $\approx 100 \text{ km s}^{-1}$ velocity, an environmental density of at least $\approx 10^5 \text{ cm}^{-3}$ is necessary for the B-H tail to be radiative.

If this condition is not met, the tail will not be radiative, and the tail solutions of sections 2 and 3 are strictly not applicable. However, when comparing “thin flow solutions” (such as our present B-H tail solution) with numerical simulations, one finds that even for the case of non-radiative flows (in which the flow interaction regions are not narrow) the thin-flow solutions are still a reasonable approximation. This is the case, e.g., for stellar wind bow shocks (see, e.g., Raga et al. 1987). Further work will have to be done to see to what extent our present B-H tail analytic model agrees with non-radiative gas dynamic simulations.

6. SUMMARY

We have presented a model for the dynamics of the dense tail of material left behind by a point mass in hypersonic (but non-relativistic) motion with respect to the surrounding environment. Under the

assumptions of ballistic motion for the environment (before entering the tail) and locally well mixed material along the tail, the steady state is described by a quite simple differential equation (see equation 19).

We have been unable to find a full analytic solution for the steady B-H tail. However, we have numerically integrated the time-dependent equations to achieve the steady state (and therefore avoid finding the position of the critical point with a shooting method). We also find approximate analytic solutions that agree well with the numerical results.

We then studied the time-dependent problem of a B-H tail developed in the passage of the point source within a dense environment, followed by the emergence of the source into a very low density environment. This flow results in an extended “velocity sorted” (linear velocity vs. position) region of dragged out material joining the emerged source to the dense cloud.

Both of the solutions described in this paper have a constant velocity v_0 for the source. This, of course, limits the models to cases in which the perturbed environmental mass is small relative to the source mass. Clearly, it would be also possible to study cases in which the gravitational drag and the accretion modify the velocity of the source.

In order for the B-H tail to be produced, the motion v_0 has to be slower than the escape velocity from the surface of the source (as otherwise the source itself will directly accrete or displace the material that would form the tail, see section 4). Clearly, this does not introduce strong constraints on the motion in the case of neutron stars (with relativistic escape velocities) or black holes, but is an important limit for planetary or stellar sources.

Also, if the source has a stellar wind, it will produce a cometary bow shock that can stop the formation of the B-H tail. For a given motion v_0 , one can calculate the minimum value of the environmental density ρ_0 for which the bow shock will be confined to a small enough size. This condition implies high environmental densities (such as would be found in dense molecular clouds) in order for main sequence stars to be able to form B-H tails. We note that at least some pulsars have quite substantial relativistic winds (see, e.g., the review of Kargaltsev et al. 2017). However, these winds would be confined by relatively low density environments (see § 4).

We leave our model without a direct application to observed objects. It should be considered as a possibility for modelling runaway compact objects followed by trails of emitting gas, possibly joining them to a dense cloud from which they have emerged.

We will explore different possible objects in a future study.

This work was supported by the DGAPA (UNAM) grant IG100422. A.C.R. acknowledges support from a CONACyT postdoctoral fellowship. We acknowledge an anonymous referee for comments which (among other things) led to the results of § 5.

REFERENCES

- Bondi, H. & Hoyle, F. 1944, *MNRAS*, 104, 273, <https://doi.org/10.1093/mnras/104.5.273>
- Cantó, J., Esquivel, A., Sánchez-Salcedo, F. J., & Raga, A. C. 2013, *ApJ*, 762, 21, <https://doi.org/10.1088/0004-637x/762/1/21>
- Cantó, J., Raga, A. C., Esquivel, A., & Sánchez-Salcedo, J. 2011, *MNRAS*, 418, 1238, <https://doi.org/10.1111/j.1365-2966.2011.19574.x>
- Cantó, J., Raga, A. C., & Wilkin, F. P. 1996, *ApJ*, 469, 729, <https://doi.org/10.1086/177820>
- Dokuchaev, V. P. 1964, *SvA*, 8, 23
- Hartigan, P., Raymond, J., & Hartmann, L. 1987, *ApJ*, 316, 323, <https://doi.org/10.1086/165204>
- Kargaltsev, O., Pavlov, G. G., Klingler, N., & Rangelov, B. 2017, *JPIPh*, 83, 635830501, <https://doi.org/10.1017/S0022377817000630>
- Kargaltsev, O. & Pavlov, G. G. 2007, *ApJ*, 670, 655, <https://doi.org/10.1086/521814>
- Lee, A. T. & Stahler, S. W. 2014, *A&A*, 561, 84, <https://doi.org/10.1051/0004-6361/201322829>
- Masset, F. S. & Velasco Romero, D. A. 2017, *MNRAS*, 465, 3175, <https://doi.org/10.1093/mnras/stw3008>
- Ostriker, E. C. 1999, *ApJ*, 513, 252, <https://doi.org/10.1086/306858>
- Raga, A. C., Noriega-Crespo, A., Cantó, J., et al. 1997, *RMxAA*, 33, 73
- Sánchez-Salcedo, F. J. 2009, *MNRAS*, 392, 1573, <https://doi.org/10.1111/j.1365-2966.2008.14177.x>
- Thun, D., Kuiper, R., Schmidt, F., & Kley, W. 2016, *A&A*, 589, 10, <https://doi.org/10.1051/0004-6361/201527629>
- Velasco Romero, D. A. & Masset, F. S. 2020, *MNRAS*, 495, 2063, <https://doi.org/10.1093/mnras/staa1215>

J. Cantó and A. Castellanos-Ramírez: Instituto de Astronomía, Universidad Nacional Autónoma de México, Ap. 70-468, C. P. 04510, CDMX, México.

A. C. Raga and A. Rodríguez-González: Instituto de Ciencias Nucleares, Universidad Nacional Autónoma de México, Ap. 70-543, C. P. 04510, CDMX, México (raga@nucleares.unam.mx).

P. R. Rivera-Ortiz: Univ. Grenoble Alpes, CNRS, IPAG, 38000 Grenoble, France.

THE OVERCONTACT BINARY V563 LYRAE

Robert H. Nelson^{1,2,3}

Received January 16 2022; accepted March 27 2022

ABSTRACT

Radial velocity (RV) and light curve (LC) data for the overcontact binary V563 Lyr have been obtained and analysed with the 2003 version of the Wilson-Devinney (WD) code with results $K_1 = 147.4 \pm 2.1$ km/s, $K_2 = 247.2 \pm 1.1$ km/s, $RV_\gamma = 22.5 \pm 1.5$ km/s, $q_{\text{sp}} = 0.596 \pm 0.008$, $M_1 = 2.49(4)M_\odot$, $M_2 = 1.45(4)M_\odot$, $R_1 = 2.23(2)R_\odot$, $R_2 = 1.81(2)R_\odot$. A third component was identified, with radial velocity $RV_3 = 18.8 \pm 6.7$ km/s. Inserting the derived parameters of the eclipsing pair into a Log (L)-Log (T_{eff}) plot for each star using data from Yakut and Eggleton (2005) suggested that both stars are over-luminous and evolved to, and perhaps past, the terminal age main sequence (TAMS). The companion (star 3) has a spectral type of $A0 \pm 1$ spectral subclass but cannot be gravitationally bound to the eclipsing pair, as its flux would dominate that of the pair, which was not observed. The companion must lie at some other distance.

RESUMEN

Presentamos curvas de velocidad radial (RV) y de luz (LC) para la binaria en sobrecontacto V563 Lyr, y se analizan con la versión 2003 del código Wilson-Devinney (WD). Los resultados son: $K_1 = 147.4 \pm 2.1$ km/s, $K_2 = 247.2 \pm 1.1$ km/s, $RV_\gamma = 22.5 \pm 1.5$ km/s, $q_{\text{sp}} = 0.596 \pm 0.008$, $M_1 = 2.49(4)M_\odot$, $M_2 = 1.45(4)M_\odot$, $R_1 = 2.23(2)R_\odot$, $R_2 = 1.81(2)R_\odot$. Se identifica una tercera componente con velocidad radial $RV_3 = 18.8 \pm 6.7$ km/s. Al insertar los parámetros del par eclipsante en un diagrama Log (L)-Log (T_{eff}) para cada estrella usando los datos de Yakut y Eggleton (2005) se infiere que ambas estrellas son sobre-luminosas y han evolucionado hasta el punto terminal de la secuencia principal (TAMS), o más allá. La tercera estrella tiene un tipo espectral estimado de $A0 \pm 1$, pero no puede estar ligada gravitatoriamente al par eclipsante, pues su flujo dominaría al del par, lo cual no se observa. La tercera estrella tiene que estar a mayor distancia.

Key Words: binaries: close — stars: individual: V563 Lyrae — stars: variables: RR Lyrae — techniques: spectroscopic

1. INTRODUCTION

V563 Lyr (BD+40 3480, NSV 11321, NSVS 5499431, TYC 3122-495-1) was discovered by Hoffmeister (1965) as one of his many variables. It was later listed in the NSVS (Kukarkin & Kholopov 1982). There were 44 visual minimum estimates performed between 1995 to 1997 (Beltraminelli and Dalmazio 1999), and Beltraminelli et al. (1999) then obtained three new photoelectric

minimum timings, thereby refining the period. The latter also obtained photoelectric observations in B and V ; displayed the light curves in V and $B - V$, and concluded that the system was a contact binary belonging to the W UMa type. Based on the $B - V$ colour index, they estimated the spectral type to be F5.

After that there were many eclipsing timings reported in the literature, and Akerlof et al. (2001) indicated that the system was part of the ROTSE survey (Akerlof et al. 2000).

V563 Lyr was included in the multi-paper DDO radial velocity studies (Pribulla et al. 2009). However, they noted difficulty owing to the system's faintness (10.96 to 11.47 magnitudes in V) which re-

¹Mountain Ash Observatory, Prince George, BC, Canada.

²Desert Blooms Observatory, Benson, AZ.

³Guest User, Canadian Astronomy Data Centre, which is operated by the Dominion Astrophysical Observatory for the National Research Council of Canada's Herzberg Institute of Astrophysics.

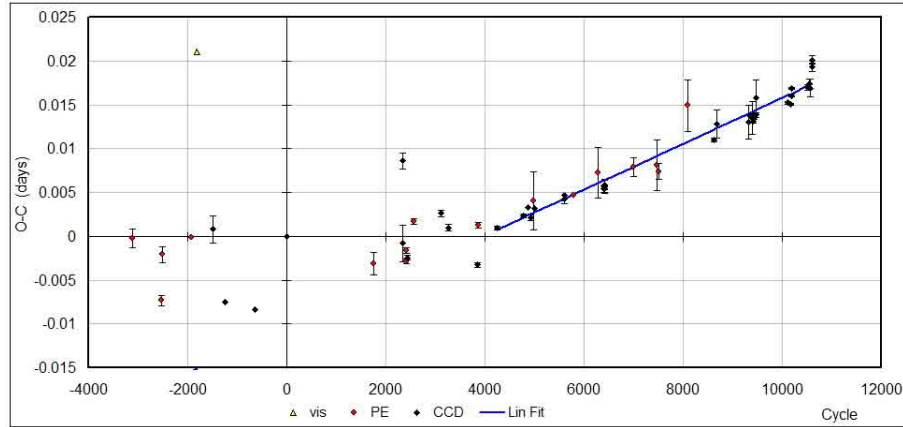


Fig. 1. The eclipse timing difference (O–C) plot for V563 Lyr. Open (yellow in the online version) triangle – visual; open (red) circle – photoelectric; black diamond – CCD. The elements used for phasing were [24 52500.2746, 0.5776412]. The data range is from 1997 to 2018. The colour figure can be viewed online.

sulted in “noisy spectra”. Further, they were able to obtain spectra at only the first quadrature (with a single exception); hence a spectroscopic mass ratio was not determinable. However, they did identify a third component in the spectra with velocity $RV_3 \approx 14$ km/s and ‘roughly’ estimated a mass ratio of 0.37. They also noted that the $J - K$ index (0.216) was more indicative of a spectral type F2-3 and that the (anomalously higher) $B - V$ index of 0.456 was likely due to interstellar extinction.

As there is no report of a Roche-based study involving both photometric and spectroscopic observation in the literature, this study was undertaken.

2. PERIOD VARIATION

An eclipse timing difference (O–C) plot is reproduced in Figure 1. The reader will notice a large scatter in the timings from cycle -4000 (1997) to 4000 (2008) which is puzzling, as all the timings but one are either photoelectric (PE) or CCD. After 2008, the period appears to be constant, but at a higher value. A few of the data points with errors > 0.005 days have been removed at the request of the referee.

The weighted least-squares best fit for the data after cycle 4000 yielded the following elements in equation 1, used for all phasing.

$$JDMinI(hel) = 2458629.64273(1) + 0.57764384(11) \cdot E. \quad (1)$$

An Excel worksheet containing all available timing data is available online at Nelson (2019 and 2020a).

3. SPECTROSCOPIC OBSERVATIONS

This observer obtained in 2016, 2018, 2019, and 2020 a total of 20 medium-resolution ($R \approx 10\,000$) spectra at the Dominion Astrophysical Observatory (DAO) in Victoria, British Columbia, Canada using the 1.83-m Plaskett telescope. Windows software *RaVeRe*, written by the author and available at (Nelson 2013, Nelson 2020a), was used for reduction. The radial velocities (RVs) were determined by the broadening functions (BF) routine (Ruciński 1992, 2004; Nelson 2010) as implemented in the Windows-based software *Broad* (Nelson 2013, 2020a). See Nelson (2020b) for further details. The elements used for all the phasing are given in equation 1 above.

A log of observations and the derived heliocentric radial velocities ($RV_{1,2,3}$) is presented in Table 1.

The calibrated one-dimensional spectra, sorted by phase, are presented in Figure 2.

As noted above, RV determination was by the broadening function method due to Rucinski. In most previous light curve modelling papers by this author (for example, Nelson 2017, Nelson 2020b), broadening functions were also used, and radial velocities extracted by smoothing the broadening function to remove noise, then centroiding the peaks that ensued. In the case of V563 Lyr, smoothing the peaks and centroiding is not appropriate owing to the likely presence of a third star, whose peak is obvious in the broadening functions, and which would contaminate the broadening functions from the other stars.

To disentangle the components, Gaussian profile curve fitting was developed in Excel (and later added to software *Broad*). The Gaussian profile for each of

TABLE 1
LOG OF DAO OBSERVATIONS AND RESULTS

DAO Image #	Mid-Time (HJD-2400000)	Exposure (sec)	Phase at Mid-exp	RV_1 (hel) (km/s)	RV_2 (hel) (km/s)	RV_3 (hel) (km/s)
20-19141	59090.7	3000	0.159	-127.0 (3.7)	238.1 (3.6)	6.1 (3.2)
20-19449	59098.8	3000	0.162	-107.4 (7.2)	240.0 (5.1)	16.7 (3.6)
18-5459	58241	2750*	0.170	-97.7 (3.8)	229.7 (3.6)	27.9 (3.2)
19-16500	58737.8	3000	0.181	-111.0 (8.3)	238.4 (8.1)	17.0 (7.6)
20-19574	59101.7	3000	0.182	-118.0 (3.6)	256.1 (3.2)	13.8 (4.0)
16-9400	57647.8	3600	0.218	-131.3 (5.5)	265.5 (4.1)	11.6 (2.1)
20-19396	59097.7	3000	0.274	-113.5 (3.8)	265.6 (8.9)	17.7 (3.4)
16-9347	57646.7	3600	0.288	-129.1 (3.8)	269.6 (3.9)	11.9 (1.6)
18-5305	58233	3000	0.309	-130.2 (7.7)	267.6 (2.4)	8.1 (4.8)
20-19583	59101.8	3000	0.342	-97.6 (4.2)	249.7 (5.7)	24.2 (3.4)
16-9365	57646.9	3600	0.647	159.1 (3.9)	-181.7 (3.3)	23.6 (4.8)
18-5384	58234.9	3000	0.651	144.0 (3.3)	-190.8 (4.0)	15.1 (3.8)
18-5489	58241.9	1798*	0.704	150.0 (2.3)	-216.1 (3.3)	17.6 (3.6)
16-9299	57645.8	3600	0.717	155.1 (3.1)	-212.7 (5.1)	21.8 (3.5)
16-9473	57652.7	3600	0.728	169.6 (6.1)	-220.0 (4.2)	29.6 (5.2)
20-19485	59099.7	3000	0.742	159.3 (6.5)	-217.5 (7.3)	25.8 (4.4)
18-5495	58241.9	3000	0.799	156.1 (4.8)	-206.9 (3.4)	22.3 (5.4)
20-19487	59099.7	3000	0.803	164.4 (7.3)	-199.4 (3.1)	27.6 (4.4)
20-19050	59088.8	3000	0.810	147.5 (6.7)	-192.7 (2.0)	22.7 (4.0)
19-16544	58745.6	2400	0.815	147.6 (9.0)	-192.5 (9.4)	14.6 (9.1)

* Clouds caused the exposure to be terminated early.

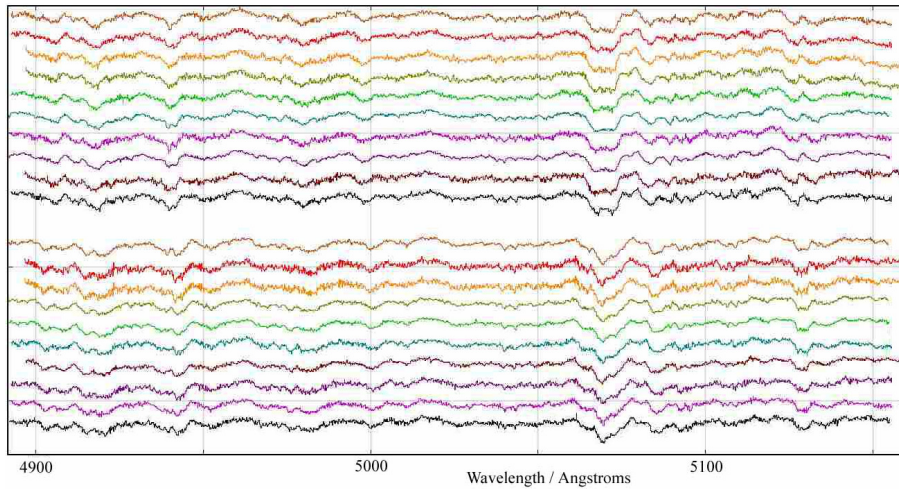


Fig. 2. V563 Lyr spectra, offset for clarity. The vertical scale is arbitrary. The phases (from top to bottom) correspond to those in Table 1, top to bottom. The colour figure can be viewed online.

the three stars required three parameters: central velocity v_0 , amplitude A , and ‘width’ w (the actual full width at half maximum of the Gaussian profile being $2 \cdot w \cdot \ln\{2^{1/2}\}$). The modified form of the stan-

dard Gaussian function is given in equation 2 (where i denotes the star index number $i = 1-3$).

$$G_i(v) = A_i \cdot \exp\{-(v - v_{0,i})^2/w_i^2\}. \quad (2)$$

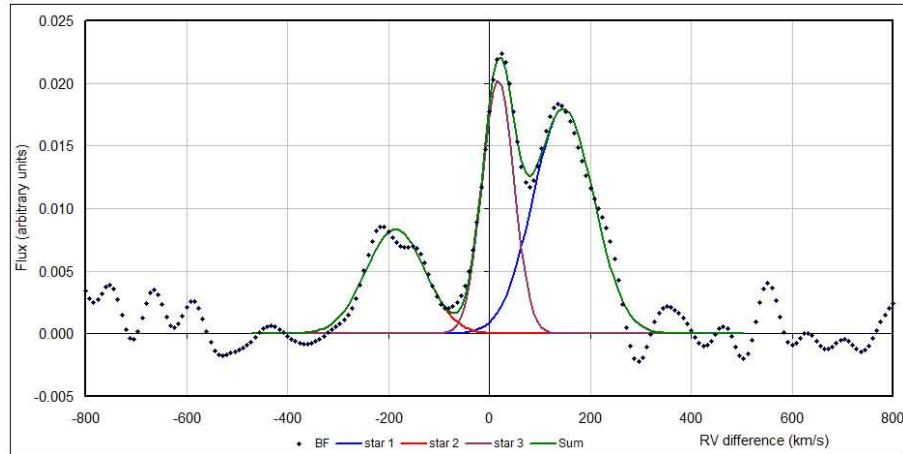


Fig. 3. Broadening function for V563 Lyr at phase 0.654 and the fitted Gaussian profiles. The standard spectrum is 18-5223 (HD 126053) and the program spectrum, 18-5384. The colour figure can be viewed online.

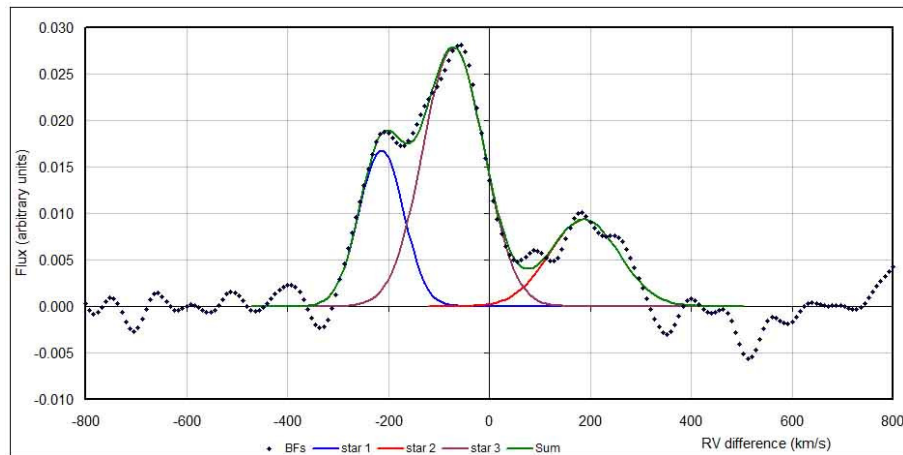


Fig. 4. Broadening function for V563 Lyr at phase 0.311 and the fitted Gaussian profiles. The standard spectrum is 18-5178 (HD 114762) and the program spectrum, 18-5305. (This corresponds to the third data line in Table 2). The colour figure can be viewed online.

The sum of the three functions was then taken as the theoretical curve, labelled in Figures 3-5 as ‘sum’, and the observed BF values, displayed as dots. The individual Gaussian components are also displayed. The sum of the differences squared (between the observed and theoretical values) was then optimized by adjusting the nine parameters. In Excel, the ‘Solver’ facility (which uses the Generalized Reduced Gradient code) was used, whereas software *Broad* uses the Levenberg-Marquardt (L-M) algorithm. (The former method is quite stable and almost always finds a solution, but may not be a relevant one, depending on the initial parameters, whereas the second requires a more critical choice to avoid crashes.) To avoid nonsensical results, care was taken to cut off

computation at certain lower and upper velocities. These cutoff values were usually set manually at the points where the observed BFs would first cross the x -axis (or nearly so) upon descent from the central peaks. (For example, in Figure 3, the lower limit was -220 and the upper, $+260$ km/s.). The results were found to be very insensitive to the choice of cutoff values, and any differences that resulted (typically 1 or 2 km/s) were well within error limits.

Note that, in Figure 3, the BF for the particular combination of comparison and program spectra, at phase 0.654, shows a clear separation of peaks. Note also the slight ‘peak pulling’ on the profile for Star 1 (on the right) due to the presence of the third

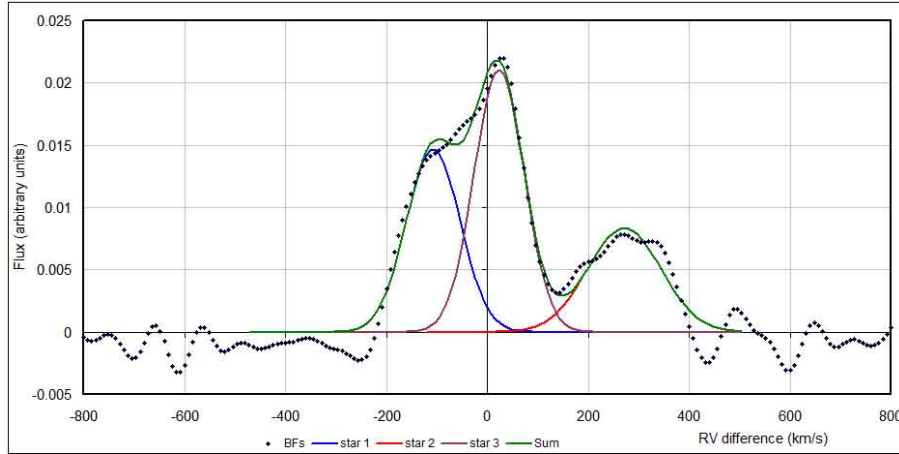


Fig. 5. Broadening function for V563 Lyr at phase 0.311 and the fitted Gaussian profiles. The standard spectrum is 18-5258 (HD 187691) and the program spectrum, 18-5305. (This corresponds to the sixth data line in Table 2). The colour figure can be viewed online.

star. Had the peak centroiding method been used, a distorted value for RV_1 would have ensued.

In view of the relatively long exposures relative to the period, a phase smearing correction was applied in each case. For details of, and a mathematical justification for, this procedure, the reader should consult Alton et al. (2020).

Figures 4 and 5 display the situation for the previous night when the opposite phases were experienced. Both are for the same program spectrum but use two different comparison spectra. For Figure 4, peak centroiding could again have been used, but again with peak pulling for Star 1.

In Figure 5 a different comparison spectrum was used but this time there is no definite peak for Star 1. One might wonder about the validity of the profiling method in this case. To compare results, we present in Table 2 the data for the one target spectrum and all seven different comparisons for that reduction.

The means and standard deviations for RV_1 , RV_2 , and RV_3 in this table are -127.2 (7.7), 261.3 (2.4), 11.1 (2.2) km/s, respectively. Note the very small scatter in RV_2 and RV_3 . The scatter in RV_1 is, in the experience of this observer, not excessive, but clearly the proximity of the stronger and sharper BF due to Star 3 complicates matters.

The reader will also note that, between Figure 4 and 5, the widths of the Gaussian functions for RV_3 are significantly different. This is somewhat troubling, as the heights and widths of the broadening peaks should reflect some physical values. The differences are likely due to the same errors in the Gaussian fitting approach—which rightly ought to be

TABLE 2
THE BF PROFILE-FITTING RESULTS FOR
PROGRAM SPECTRUM 18-5305*

Std File#	RV std name	RV_1 (Hel) km/s	RV_2 (Hel) km/s	RV_3 (Hel) km/s
18-5167	HD 089449	-125.2	263.6	9.9
18-5172	HD 102870	-130.6	263.9	10.2
18-5178	HD 114762	-141.8	263.4	9.2
18-5184	HD 140913	-121.4	261.3	14.3
18-5233	HD 126053	-122.3	260.1	12.2
18-5258	HD 187691	-119.1	259.0	13.6
18-5261	HD 154417	-129.7	257.9	8.6

*Converted to heliocentric RVs. The last column contains the RVs for the putative companion star. (See later discussion).

investigated thoroughly—but which would be better suited to a separate paper. In any case, the results seem reasonable.

Our mean value for RV_3 (for this target spectrum) is virtually consistent with the value (≈ 14 km/s, no error estimate) provided by Pribulla et al. (2009).

In § 5, we will need the ratio of the flux from Star 3 compared to the total flux (at phases 0.25 and 0.75). As the BF process is linear (Rucinski, undated private communication), we may obtain an estimate of the flux from a given component by taking the area under its Gaussian profile, which is proportional to amplitude A_i times width w_i as defined in equation 2; thus we have flux $F_i = k \cdot A_i \cdot w_i$ where k is a constant that drops out when ratios are

TABLE 3
THE VARIABLE, COMPARISON AND CHECK STARS FOR V563 LYR PHOTOMETRIC OBSERVATIONS

Object	TYC/GSC	RA (J2000)	Dec (J2000)	Spec.	V (mag)*	$(B-V)$ (mag)*
Variable	3122-495-1	18:45:06.6	+40:11:11.5	F5	11.112 (20)	0.282 (20)
Comparison	3122-1487	18:44:53.5	+40:10:03.5	—	11.944 (20)	1.147 (20)
Check	3122-2865	18:45:16.7	+40:12:26.9	—	12.128 (20)	0.749 (20)

*The APASS catalogue provided no error estimates, so 0.020 mag was assumed (in view of the faintness of the stars).

taken. The fraction of the flux contributed by the third star is then $F_3 / (F_1 + F_2 + F_3) = 0.29$ (7) in this case, averaged over the entire dataset (the figure in brackets is the standard deviation in units of the last digit). This value will be compared with the results from the photometric analysis which, of necessity, involves third light. The relevant photometric pass-band would be V , as it most closely approximates the wavelength range over which the spectra were taken.

The derived (heliocentric) RV values are listed in Table 1 along with the error estimate for each, the latter being the standard deviation of values from the different comparisons as presented above. The overall (i.e., through all phases) heliocentric radial velocity of the third star was $RV_3 = 18.8 \pm 6.7$ km/s. This is compatible with the centre of mass RV_γ of the eclipsing pair (see later discussion).

4. PHOTOMETRIC OBSERVATIONS

Photometric observations were carried out at Desert Blooms Observatory in 2019 (April-May). Obtained were a total of 742, 743, and 744 observations in B , V , and I_c respectively. The telescope is a 40 cm Schmidt-Cassegrain optical assembly operating at $f/6.8$; data acquisition was by a QSI 683 CCD camera (see Nelson 2020b for more details).

In Table 3, the coordinates for the stars of interest are presented, taken from the Tycho-2 Catalogue (Høg et al. 2000). The magnitudes are taken from the AAVSO Photometric All-Sky Survey (APASS, DR9; Henden et al. 2009). The colour index of the comparison was higher than one would like; however, most of the possible candidates in the field had similar values. The star chosen for the comparison had the advantage of close proximity and being close in brightness to the program star. (But see § 7 for a further discussion of comparison selection.) For all the runs, the difference $C - K$ was observed to be constant to within ≈ 0.01 magnitude, with no systematic variation.

As described in Nelson (2020b), automatic focusing was required to accommodate the large swings in temperature throughout each night.

The usual bias and dark subtraction, and flat fielding, as well as aperture photometry was accomplished with MIRA (by Mirametrics).

5. LIGHT CURVE ANALYSIS

Curve fitting was undertaken with the 2003 version of the Wilson-Devinney (WD) light curve and radial velocity analysis program with the Kurucz atmospheres (Wilson and Devinney 1971, Wilson 1990, Kurucz 1993, Kallrath et al. 1998, Kallrath & Milone 2009) as implemented in the Windows front-end software `WDwint56c` (Nelson 2013). RV and light curve data from the this paper were used in a simultaneous fit.

As mentioned above, the classification of Beltraminelli et al. (1999) was F5. Also, the 2MASS catalogue (Skrutskie et al. 2006) yielded values $J = 10.286$ (26) and $H = 10.120$ (31) so then $J - H = 0.166$ (40). Reference to interpolated tables from Cox (2000) as augmented with infrared data from Mihalas and Binney (1981) confirmed the designation. The tables of Pecaut and Mamajek (2013) yielded a temperature $T = 6510$ (120) K, and a $\log g = 4.355$ (8) (cgs) where the errors correspond to the differences over one spectral subclass. An interpolation program by Terrell (1994, available from Nelson 2013) gave the Van Hamme (1993) limb darkening values; and finally, a logarithmic (LD=2) law for the limb darkening coefficients was selected, appropriate for temperatures < 8500 K (ibid). The limb darkening coefficients are listed below in Table 4. Values for the gravity darkening exponent $g = 0.32$ and albedo $A = 0.5$ were chosen, appropriate for convective stars (Lucy 1967 and Ruciński 1969, respectively).

Based on the shape of the light curve, Mode 3 (overcontact binary) was selected. Initially, convergence by the method of multiple subsets was reached

TABLE 4

LIMB DARKENING VALUES FROM VAN HAMME (1993) BASED ON SPECTRAL TYPE F5, F5-6 FOR STARS 1 AND 2 RESPECTIVELY*

Band	Solution 1				Solution 2			
	x ₁	x ₂	y ₁	y ₂	x ₁	x ₂	y ₁	y ₂
<i>B</i>	0.806	0.813	0.233	0.213	0.835	0.841	0.153	0.129
<i>V</i>	0.710	0.723	0.275	0.269	0.756	0.767	0.240	0.223
<i>I_c</i>	0.553	0.567	0.276	0.271	0.601	0.612	0.254	0.242
Bol	0.639	0.640	0.241	0.234	0.646	0.648	0.214	0.203

*The same coefficients are listed for Solution 2 (discussed later) where the estimated spectral types are G1 and G4.

in a relatively small number of iterations. The subsets were: (a, Ω_1, L_1) , (i, T_2, q) , (T_2, Ω_1) , (T_2, q) , and $(a, V_{\text{gam}}, \varphi)$. In view of the fact that a companion was known to be present (from the spectra), it was appropriate to add third light (and also necessary to reach a solution). Therefore EL3 was a parameter, as was also a spot, added to Star 1. However, the correct choice of EL3 proved to be elusive, as the fit (as indicated by the sum of residuals squared) proved to be a weak function of the EL3 values selected, and differential corrections was unable to provide meaningful corrections. To overcome this problem, for each band, a value for EL3 was selected and the fit optimized by altering the other parameters (especially T_2 , q , and inclination i). Next, a new value for EL3 was chosen and the fit optimized again. In this way, the optimum value of EL3 for that band was determined. The procedure was then applied to the remaining bands.

In the original solutions there was a problem (picked up the referee) in that the values of EL3 were inconsistent with the ratio of fluxes derived from the broadening functions (see § 3), being an order of magnitude too low. This was despite the fact that the solution minimized the residuals and appeared to give a good fit visually. Thereafter, higher values of flux quantity EL3, starting with ≈ 0.2 for each band, were used in renewed modelling, and a grid search was followed, as above, to find a solution. The final values were EL3 = 0.257 (3), 0.256 (3), 0.245 (3) for *B*, *V*, *I_c* respectively. In determining the luminosity L_3 of star 3, one needs to assume that it radiates isotropically. If that assumption is made, we may take $L_3 = 4\pi \cdot \text{EL3}$ (Wilson and van Hamme 2013). The values for third light (luminosity) ratio $L_3/(L_1+L_2+L_3)$ are listed in Table 5 and repeated in Table 7 along with those for the other components.

Converting the EL3 (*B*) and EL3 (*V*) flux values to magnitudes and carrying through the errors

rigorously, we have $B - V = -0.004 \pm 0.036$ mags. With the estimated $B - V$ colour index of the third star at hand we have, using the tables of Pecaut and Mamajek (2013) we estimate the spectral type of Star 3 as A0 ± 1 spectral subclass. Note that the above derivation neglects interstellar absorption.

The above solution so achieved is presented in Table 5 as Solution 1.

Pribulla et al. (2009) estimated the luminosity ratio $L_3/(L_1+L_2) = 0.15$ (presumably in the *V* band). Taking the value in Table 5 of $L_3/(L_1+L_2+L_3)$ (*V*) = 0.271 (3) and using simple algebra we have $L_3 / (L_1 + L_2) = 0.371$ (4). The cause of the discrepancy between the two corresponding values is not clear.

The light curves, computed light curves and the residuals in the sense data-computed are plotted in Figure 6.

Next, the radial velocity data and solutions are plotted, starting with the RVs from this paper, in Figure 7. A simple double-sine fit yields values $K_1 = 147.4$ (2.1) km/s and $K_2 = 247.1$ (1.1) km/s, and $\text{RV}_\gamma = 22.5$ (1.5) km/s). The spectroscopic mass ratio is $q_{sp} = M_2/M_1 = K_1/K_2 = 0.596$ (8). Note that the mass ratio in Table 5 derived from combined (RV + LC) fitting differs somewhat from the spectroscopic mass ratio calculated from the ratios K_1/K_2 . This is normal; however, the former is considered more reliable as it is derived from all the data (Wilson 1990). In any case, the error bars virtually overlap.

A word about error estimation is appropriate here (all error values in this paper are one sigma). For the errors in K_1 and K_2 , the reader should consult Alton et al. (2020). For the individual RV data points in the present dataset, each RV is the mean of values obtained from eight different standards; the error estimate is simply the standard deviation of the group. Actual errors from systematic effects are obviously larger but not directly calculable. That is

TABLE 5

WILSON-DEVINNEY PARAMETERS FOR THE BEST-FIT SOLUTION FOR V563 LYR. SOLUTION 2 IS TO BE PREFERRED (SEE DISCUSSION)

WD Quantity	Sol'n 1	Sol'n 2	WD Quantity	Sol'n 1	Sol'n 2
Temperature T_1 (K)	6510*	5837*	$L_1/(L_1+L_2)$ (B)	0.634 (4)	0.646 (4)
Temperature T_2 (K)	6385 (7)	5689 (3)	$L_1/(L_1+L_2)$ (V)	0.628 (4)	0.637 (4)
$q = m_2/m_1$	0.583 (14)	0.563 (28)	$L_1/(L_1+L_2)$ (Ic)	0.622 (3)	0.629 (3)
Potential $\omega_1 = \omega_2$	2.797 (71)	2.797 (155)	$L_3/(L_1+L_2+L_3)$ (B)	0.276 (3)	0.276 (3)
Inclination i (degrees)	79.2 (2)	78.2 (1.1)	$L_3/(L_1+L_2+L_3)$ (V)	0.271 (3)	0.271 (3)
Semi-maj. axis, a (R_\odot)	4.61 (5)	4.61 (6)	$L_3/(L_1+L_2+L_3)$ (Ic)	0.259 (2)	0.259 (2)
Centre of mass RV_γ (km/s)	26.6 (1.8)	26.6 (9)	r_1 (pole) (orbital radii)	0.442 (14)	0.442 (14)
Fill-out factor f_1	0.685 (32)	0.685 (32)	r_1 (side) (orbital radii)	0.478 (20)	0.478 (20)
Spot co-latitude (deg)	38 (2)	36 (2)	r_1 (back) (orbital radii)	0.531 (31)	0.531 (32)
Spot longitude (deg)	173 (1)	173 (1)	r_2 (pole) (orbital radii)	0.354 (15)	0.354 (16)
Spot radius (deg)	20.5 (2)	20.7 (5)	r_2 (side) (orbital radii)	0.378 (20)	0.378 (20)
Spot temp. factor	0.852 (1)	0.846 (1)	r_2 (back) (orbital radii)	0.454 (49)	0.454 (50)
$\Sigma\omega_{res}^2$	0.23058	0.24186	—	—	—

*Held fixed.

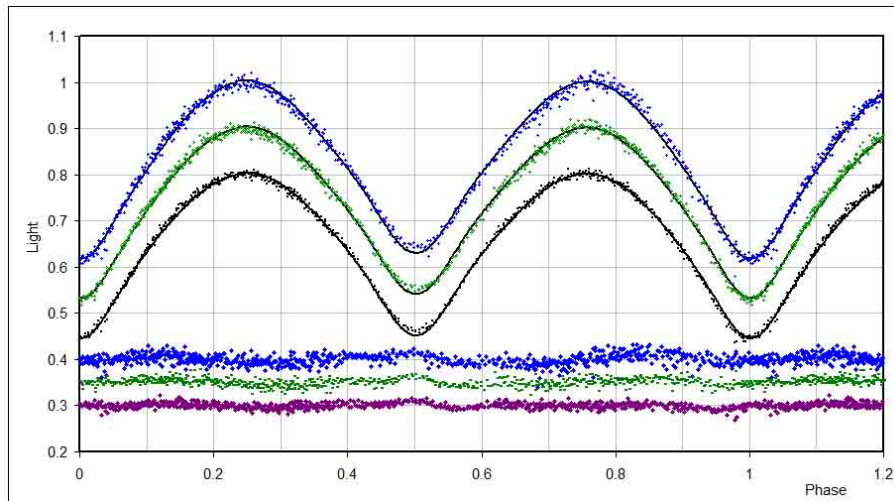


Fig. 6. V563 Lyr light curves and the WD results, separated by fixed offsets (0.1 light curve units). Plotted are, top to bottom: B , V , Ic . At the bottom of the figure, the differences in the sense observed-calculated; the order is the same as for the light curves. The colour figure can be viewed online.

why the sample standard deviation (i.e., sigma divided by root n) is not used, as it would imply a greater precision than what is experienced.

The visual representation of Binary Maker 3 (Bradstreet 1993) is presented in Figure 8.

The WD output fundamental parameters and errors are listed in Table 6. Most of the errors are output or derived estimates from the WD routines. These are statistical errors and known to be smaller

than total errors because the latter contain systematic errors not readily available.

In the last few light curve modelling papers by this author, it has been the norm to use differential photometry, the Gaia distance (Luri et al 2018), the interstellar absorption A_v , and the bolometric corrections (BCs) to estimate the luminosities. This independent calculation of the latter serves as a check on the spectral type and hence the effective temper-

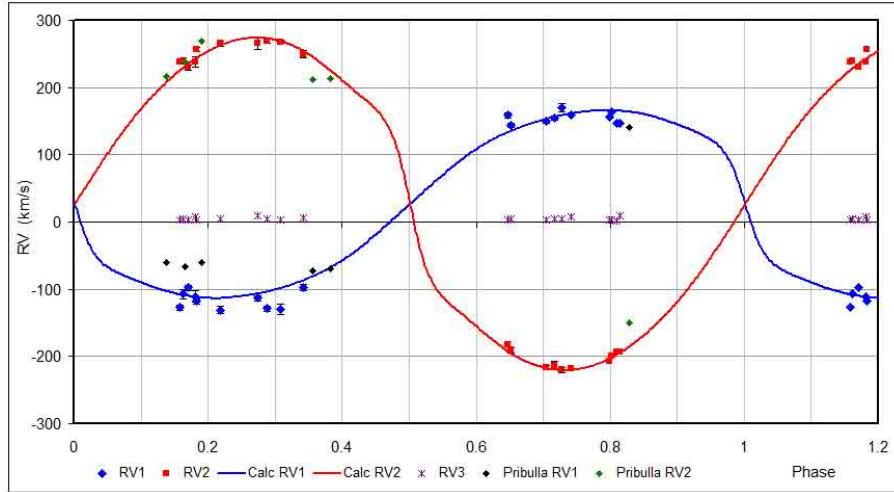


Fig. 7. V563 Lyr radial velocities and WD solution. The radial velocities of the third star appear near the x -axis. The RV_1 and RV_2 values from Pribulla et al. (2009) appear as the (black) and (green) diamonds, resp. From [ibid] there is a single point in the second half of the cycle. The colour figure can be viewed online.

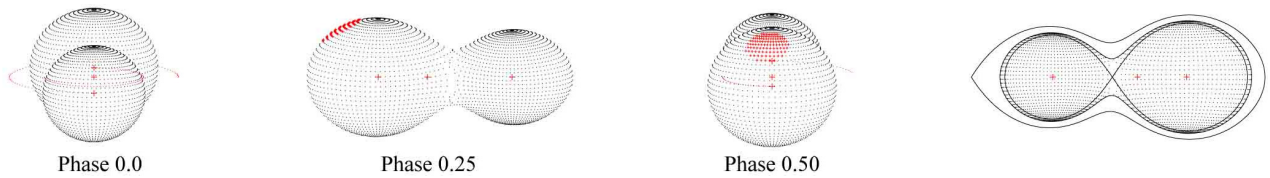


Fig. 8. V563 Lyr three-dimensional representation from Binary Maker 3, at the phases indicated, and the surface potentials. The colour figure can be viewed online.

TABLE 6

V563 LYR FUNDAMENTAL PARAMETERS. SOLUTION 2 IS TO BE PREFERRED (SEE LATER DISCUSSION)

Quantity	Solution 1		Solution 2	
	Star 1	Star 2	Star 1	Star 2
Spectral type	F5	F5-6	G1	G4
Temperature, T (K)	6510*	6385 (7)	5837*	5689 (3)
Mass, (M/M_{\odot})	2.49 (4)	1.45 (4)	2.49 (4)	1.45 (4)
Radius, R (R_{\odot})	2.23 (2)	1.81 (2)	2.23 (2)	1.81 (2)
M bol (mags)	2.52 (3)	3.06 (3)	3.00 (3)	3.56 (3)
Log g (cgs units)	4.14 (1)	4.08 (1)	4.14 (1)	4.08 (1)
Luminosity, L (L_{\odot})	7.73 (68)	4.70 (41)	4.97 (44)	2.96 (26)

ature of the more luminous component. We shall do so now. The calculation proceeds as follows:

Differential photometry at phases 0.23-0.27 and 0.73-0.77 (when both stars were visible broad-side) yielded the following instrumental differential magnitudes: $\Delta b = b_{\text{var}} - b_{\text{comp}} = -1.800 \pm 0.001$ mag and $\Delta v = v_{\text{var}} - v_{\text{comp}} = -0.995 \pm 0.006$ magnitudes.

The standard formulae for transformation from instrumental to Johnson magnitudes are given in equations 3 and 4 (Henden and Kaitchuk 1982):

$$V = v + \varepsilon(B - V) + \zeta, \tag{3}$$

$$B - V = \mu(b - v) + \zeta', \tag{4}$$

TABLE 7

RELATIVE LUMINOSITIES OF THE THREE COMPONENTS (ASSUMING A THIRD STAR, AND IF SO, THAT THE LATTER EMITS ISOTROPICALLY)

Band	$L_1 / (L_1+L_2+L_3)$	$L_2 / (L_1+L_2+L_3)$	$L_3 / (L_1+L_2+L_3)$
Blue, B	0.459 (3)	0.265 (1)	0.276 (3)
Visual, V	0.458 (2)	0.272 (1)	0.271 (3)
Infrared, I_c	0.461 (2)	0.280 (1)	0.259 (2)

where $\varepsilon = -0.032 \pm 0.001$ and $\mu = 1.086 \pm 0.010$ are the transformation coefficients for the camera + filter setup at DBO (Alton 2017). Operating differentially, the trailing constant ς drops out, and substituting equation 4 into 3 (and simplifying some subscripts) we have equation 5:

$$\begin{aligned} V &= V_c + \Delta v + \varepsilon \Delta(B - V) = \\ &V_c + \Delta v + \varepsilon \mu \Delta(b - v) = \\ &V_c + \Delta v + \varepsilon \mu (\Delta b - \Delta v), \end{aligned} \quad (5)$$

where $V_c = 11.944 \pm 0.020$ mags given in Table 3. Combining terms (with the errors added in quadrature) one obtains $V = 10.977 \pm 0.012$ mags.

Next, the presence of third light must be addressed. According to Wilson and van Hamme (2013), if one assumes that the third star emits light isotropically, one may write equation 6:

$$L = L_1 + L_2 + 4 \cdot \pi \cdot l_3 = L_1 + L_2 + L_3, \quad (6)$$

where l_3 is the same as EL3 used in the WD code and used above. Note that Wilson and van Hamme point out that simply listing EL3, as what one might want to do, is meaningless unless one also specifies the L_1 and L_2 values. As a result, we list $L_3/(L_1+L_2+L_3)$ in Table 7.

Using the computed luminosity ratios $L_1/(L_1+L_2+L_3)$ and $L_2/(L_1+L_2+L_3)$ for the V band, one finds the individual magnitudes $V_1 = 11.825$ (21), and $V_2 = 12.392$ (21) by using equation 7.

$$V_i = -2.5 \log[L_{iV}/(L_1 + L_2 + L_3)_V] + V \quad (7), \quad (7)$$

where $i = 1, 2$. Determination of the interstellar extinction was from the formulations of Amôres and Lepine (2005), and depending on the model, one obtains values of $A_v = 0.275, 0.248,$ and 0.124 mags with a mean value of 0.216 (71) mags, where the error is the sample standard deviation of the three values.

Then, using the standard formula (equation 8) applied to each star we have equation 8:

$$M_{bol, i} = V_i - A_v + BC_i - 5 \log(r/10), \quad (8)$$

whence the individual values for each star are $M_{bol,1} = 2.994(31)$ mags and $M_{bol,2} = 3.556$ (37). Converted to luminosities using the standard formula and making use of the bolometric magnitude of the Sun as $M_{bol,Sun} = 4.74$ mags (Cox 2000) we have the *photometric luminosities* $L_1 = 5.0$ (1.3) L_\odot and $L_2 = 3.0$ (9) L_\odot where the largest error source is from the Gaia distance. These values, are significantly lower than the WD output in Table 6.

Despite the rather large errors in the photometric luminosities, it seemed important to adjust the effective temperature T_1 . This is especially true because the spectral classification of Beltraminelli et al. (1999) was based on the colour index $(B - V)$ and, as we have seen, the flux received is contaminated by the significant contribution of the hot third star (spectral type $\approx A0$). Making use of the well-known black body law of equation 9

$$L \sim T^4 \cdot R^2, \quad (9)$$

we may write equation 10

$$T'_1 = T_1 \cdot (L'/L)^{1/4} = 6510 \cdot (5.0/7.73)^{1/4} = 5837 \text{ K}. \quad (10)$$

This is significantly lower than the original value and places the spectral type for Star 1 at $\approx G1$. Continuing on, and using this lower value for T_1 , a revised solution was derived in a relatively few steps. The final value for T_2 was 5689 K which would place the spectral type as $\approx G4$. The results are listed in Tables 5 and 6 as Solution 2.

6. EVOLUTIONARY STATUS

It is possible to investigate the evolutionary status of this system with the aid of data from Yakut and Eggleton (2005), who collected data for some 72 close binary systems for which reliable data existed. Types included were low-temperature over-contact binaries, near-contact binaries and detached

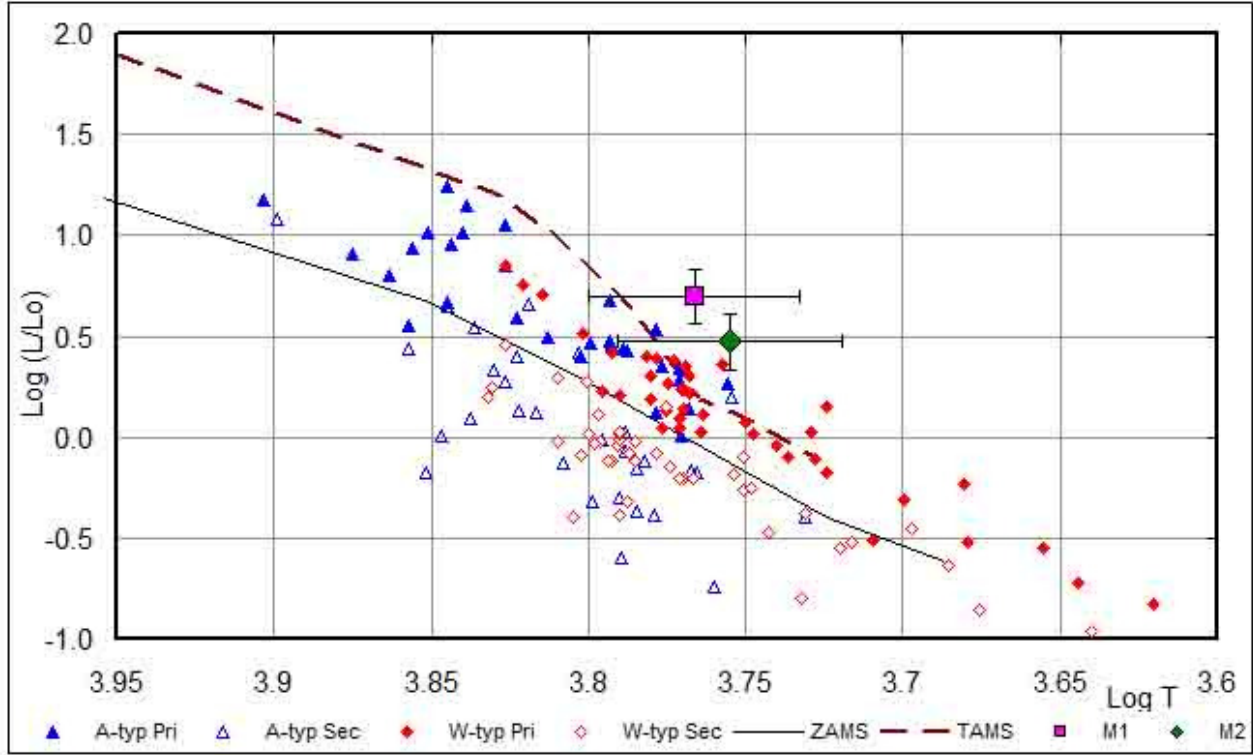


Fig. 9. Log L vs Log T plot for EW-type binaries from Yakut and Eggleton (2005). The ZAMS (solid line) and the TAMS are from the evolutionary tracks of the Geneva Group (Schaller et al. 1992) for $Z = 0.02$ (solar). The results from Solution 2 have been added: the large square (pink in the online version) is for Star 1 while the large (green) diamond is for Star 2. The (half) width of each error bar is the standard deviation of the values for $\log T_{1,2}$ and $\log L_{1,2}$ from each solution. The colour figure can be viewed online.

close binaries. Figure 9 reproduces their plot of $\log L$ vs $\log T$, with the zero-age main sequence (ZAMS) values for isolated stars from Cox (2000), and the terminal-age main sequence (TAMS) values from the evolutionary tracks of the Geneva Group (Schaller et al. 1992) for $Z = 0.02$ (solar).

This plot suggests both stars have evolved and might be past the TAMS. As a referee from a previous paper has noted, one should regard plots of this type with much caution, as we do not know the metallicity, and in any case there is a fairly large degree of uncertainty with the temperatures and luminosities for this system. The error bars hint at that uncertainty. What is needed is an analysis of a classification spectrum that would decompose the component spectra.

7. DISCUSSION

Further to the use of Gaussian profile fitting for extracting RVs from the broadening functions (rather than smoothing and peak centroiding), it has been found that, even for the detached peaks noted

in Nelson (202b), profile fitting gives more consistent results, and is now used on a regular basis by this observer for all RV determinations.

The matter of choice of the comparison star selection bears discussion. In light curve analyses, one rarely has the ideal comparison star which would be: (a) close in brightness, (b) close in spectral type, and (c) in close proximity in the image frame. If condition (a) is not followed and the stars are, say, more than a magnitude different in brightness, excessive shot noise will result because one of the stars will be underexposed. If condition (c) is not followed, less than ideal sky conditions may result in significant systematic deviations from the unaffected light curve from time to time, owing to significant variations in sky transparency over the sky area covered by the chip. For this observer, condition (b) is the one most readily relaxed. In answer to concerns by the referee of a previous paper regarding the choice of spectral type-matching of the comparison star, tests were rerun with a different comparison star considerably closer in colour; there were no sig-

nificant differences in the final parameters resulting from Wilson-Devinney modelling. Hence—within the limits of this test—the spectral-type matching of the comparison star would appear to be a non-issue.

Initial modelling runs of this system, as is so often the case for many overcontact systems, led to an early solution. However, the presence of spots and third light complicated matters (especially the latter), requiring many runs to achieve a convincing solution. Modelling with a bright spot at the back of Star 2 was attempted but gave poor results. The ready adoption of a solution that seemed to represent a minimum but for which there was an inconsistency between the strength of the third star BF and the weakness in the early adopted third star fluxes EL3 (for the phases 0.25 and 0.75) was problematic. Clearly the first solution was a local minimum; The takeaway from this is that modellers need to be aware that local minima exist and may not be represent consistency between all the observables. The lowest sum of residuals squared is not the only criterion.

The solution to the EL3 inconsistency was to start with some more realistic values ($EL3 = 0.2$) and do a grid search to find the optimum values; this was done and reasonable agreement between RV and photometric results was achieved. As noted above, the mean radial velocity (through all orbital phases of the eclipsing pair) of the putative third star ($RV_3 = 18.8 \pm 6.7$ km/s) and that of the centre of mass for the eclipsing pair ($RV_\gamma = 22.5 \pm 1.5$ km/s) are mutually consistent. At first glance, one might think that the third star would be in a mutual orbit with the eclipsing pair at inferior or superior conjunction, and therefore physically connected. However, based on the relative luminosities, it is likely a fairly early spectral type, estimated as $A0 \pm 1$ spectral subclass. Therefore its flux (were it at the same distance as the eclipsing pair, and a main-sequence type) would dominate that of the other two (G1 and G4). This was not observed. Therefore (Milone 2022) we are forced to the conclusion that the star is at a greater distance and therefore an accidental double. A high S/N classification spectrum at medium resolution might permit a disentangling of the spectral components which would settle the matter.

8. CONCLUSION

New radial velocity and photometric data for the overcontact binary V563 Lyr have been obtained and analysed with the 2003 version of the Wilson-Devinney code. Analysis of the radial velocity curves by fitting double sinusoidal curves yields values $K_1 = 147.4 \pm 2.1$ km/s, $K_2 = 247.2 \pm 1.1$ km/s,

$RV_\gamma = 22.5 \pm 1.5$ km/s, and $q_{sp} = 0.596 \pm 0.008$. A third component has been identified, with radial velocity $RV_3 = 18.8 \pm 6.7$ km/s which is in agreement with the findings of Pribulla et al. (2009) who found $RV_3 \approx 14$ km/s for the companion. Assuming an effective spectral type of F5, the following values for the masses, radii and luminosities of the eclipsing pair were obtained: $M_1 = 2.49(4) M_\odot$, $M_2 = 1.45(4) M_\odot$, $R_1 = 2.23(2) R_\odot$, $R_2 = 1.81(2) R_\odot$, $L_1 = 7.7(7) L_\odot$, and $L_2 = 4.7(4) L_\odot$. This has been labelled in Tables 5 and 6 as Solution 1.

However, a direct calculation of luminosities using photometry, the Gaia DR3 distance, the bolometric corrections, and estimated values for the interstellar extinction resulted in much lower luminosity values which were inconsistent with the values stated above (computed from WD modelling). As estimates of the spectral type of the companion were $\approx A0$ and the fact that its contribution to the overall flux were comparable to that of Star 2, that would imply that the spectral types of the eclipsing pair were much later than the F5 value of Beltraminelli et al. (1999) – that is, to make the average spectral type appear to be F5. An estimate of the corrected value for T_1 (based on the black body law) was 5837 ± 333 K, which would correspond to a spectral type of G1. Revised modelling with this lower T_1 value resulted in the revised luminosities of the eclipsing pair: $L_1 = 5.0(4) L_\odot$, and $L_2 = 3.0(3) L_\odot$.

Inserting the derived parameters of the eclipsing pair into a $\log(L) - \log(T_{eff})$ plot for each star using data from Yakut and Eggleton (2005) suggests that both stars are over-luminous and evolved to, and perhaps past, the terminal age main sequence.

The companion (Star 3) is estimated to have a spectral type $A0 \pm 1$ spectral subclass. If it were gravitationally bound, the flux from a main sequence A0 type would dominate the light curves and broadening functions, so that cannot be. Simple computations reveal that a white dwarf (WD) would contribute only a very small flux—too small for what was observed. In any case, the broadening functions from a WD would be much wider than what was observed (Milone 2022). Possibly, the companion could represent an optical double, and therefore be at any distance (Milone 2022).

A high S/N classification spectrum at medium resolution might permit a de-convolution of the spectral components which would settle the matter as to its nature.

It is a pleasure to thank the staff members at the DAO (David Bohlender, Dmitry Monen, and especially the late Les Saddlemyer) for their usual splen-

did help and assistance. Thanks are also due to Environment Canada for the website satellite images (see ‘Satellite images’ below) that were essential in predicting clear times for observing runs in this cloudy locale, and to Attila Danko for his Clear Sky Clocks, (see below). The author thanks the anonymous referee for pointing out some mistakes whose correction led to a much improved paper.

REFERENCES

- Akerlof, C., Amrose, S., Balsano, R., et al. 2000, *AJ*, 119, 1901, <https://doi.org/10.1086/301321>
- Alton, K. B. 2017, Personal Communication
- Alton, K. B., Nelson, R. H., & Kazimierz, S. 2020, *JApA*, 41, 26, <https://doi.org/10.1007/s12036-020-09641-y>
- Amôres, E. B. & Lepine, J. R. D. 2005, *AJ*, 130, 659, <https://doi.org/10.1086/430957>
- APASS, The AAVSO Photometric All-Sky Survey
- Beltraminelli, N. & Dalmazio, D. 1999, *GEOSE*, 25, 1
- Beltraminelli, N., Dalmazio, D., Remis, J., & Manna, A. 1999, *IBVS*, 4696, 1
- Bradstreet, D. H. 1993, in *Light Curve Modelling of Eclipsing Binary Stars*, ed. E. F. Milone, (New York, NY: Springer-Verlag), 151
- Cox, A. N. 2000, *Allen’s Astrophysical Quantities*, (New York, NY: Springer-Verlag)
- Danko, A. Clear Sky Clocks, <http://cleardarksky.com/>
- Henden, A. A. & Kaitchuk, R. H. 1982, *Astronomical Photometry* (New York, NY: Van Nostrand Reinhold)
- Henden, A. A., Welch, D. L., Terrell, D., & Levine, S. E. 2009, *AAS*, 41, 669
- Hoffmeister, C. 1965, *Mitt. Ver. Sterne*, B3, 113
- Høg, E., Fabricius, C., Makarov, V. V., et al. 2000, *A&A*, 355, 27
- Kallrath, J., Milone, E. F., Terrell, D., & Young, A. T. 1998, *ApJ*, 508, 308, <https://doi.org/10.1086/306375>
- Kallrath, J. & Milone, E. F. 2009, *Eclipsing Binary Stars: Modeling and Analysis*, (New York, NY: Springer Verlag)
- Kukarkin, B. V. & Kholopov, P. N. 1982, *New Catalogue of Suspected Variable Stars*, (Moscow: Publication Office “Nauka”)
- Kurucz, R. L. 1993, in *Light Curve Modelling of Eclipsing Binary Stars*, ed. E. F. Milone (New York, NY: Springer Verlag), 93
- Lucy, L. B. 1967, *ZA*, 65, 89
- Luri, X., Brown, G. A., Sarro, L. M., et al. 2018, *Gaia Data Release 3*, (available through Vizier)
- Mihalas, D. & Binney, J. 1981, *Galactic Astronomy, Structure and Kinematics*, (San Francisco, CA: Freeman)
- Milone, E. F. 2022, Personal Communication
- Mirametrics, <https://mirametrics.com>
- Nelson, R. H. 2010, in *The Alt-Az Initiative: Telescope and Instrument Developments*, eds. R. M. Genet, J. M. Johnson, & V. Wallen (Santa Margarita, CA: Collins Foundation Press)
- _____. 2013, Software by Bob Nelson, <http://binaries.boulder.swri.edu/binaries/>
- _____. 2017, *IBVS*, 6226, 1, <https://doi.org/10.22444/IBVS.6226>
- _____. 2019, Bob Nelson’s O-C Files, <http://www.aavso.org/>
- _____. 2020a, <http://binaries.boulder.swri.edu/binaries/>
- _____. 2020b, *NewA*, 77, 101362, <https://doi.org/10.1016/j.newast.2020.101362>
- Pecaut, M. J. & Mamajek, E. E. 2013, *ApJS*, 208, 9, <https://doi.org/10.1088/0067-0049/208/1/9>
- Pribulla, T., Rucinski, S. M., Blake, R. M., et al. 2009, *AJ*, 137, 3655, <https://doi.org/10.1088/0004-6256/137/3/3655>
- Ruciński, S. M. 1969, *AcA*, 19, 245
- _____. 1992, *AJ*, 104, 1968, <https://doi.org/10.1086/116372>
- _____. 2004, *IAUS 215, Stellar Rotation*, ed. A. Maeder and P. Eenens, (San Francisco, CA: IAUS), 17
- Satellite Images for North America, <http://www.cmc.ec.gc.ca/htmls/satellite.html>
- Schaller, G., Schaerer, D., Meynet, G., & Maeder, A. 1992, *A&AS*, 96, 269
- Skrutskie, M. F., Cutri, R. M., Stiening, R., et al. 2006, *AJ*, 131, 1163, <https://doi.org/10.1086/498708>
- Terrell, D. 1994, *Van Hamme Limb Darkening Tables*, vers. 1.1
- van Hamme, 1993, *AJ*, 106, 2096, <https://doi.org/10.1086/116788>
- Wilson, R. E. & Devinney, E. J. 1971, *ApJ*, 166, 605, <https://doi.org/10.1086/150986>
- Wilson, R. E. 1990, *ApJ*, 356, 613, <https://doi.org/10.1086/168867>
- Wilson, R. E. & van Hamme, W. 2013, *Computing Binary Star Observables*, (Reference Manual to the Wilson-Devinney Program), (Gainesville, FL: University of Florida)
- Yakut, K. & Eggleton, P. P. 2005, *ApJ*, 629, 1055, <https://doi.org/10.1086/431300>
- Robert H. Nelson: Mountain Ash Observatory, 1393 Garvin Street, Prince George, BC, Canada, V2M 3Z1 (bob.nelson@shaw.ca).
- Robert H. Nelson: Desert Blooms Observatory, Benson, AZ.
- Robert H. Nelson: Guest User, Canadian Astronomy Data Centre, which is operated by the Dominion Astrophysical Observatory for the National Research Council of Canada’s Herzberg Institute of Astrophysics.

PHOTOMETRIC ANALYSIS OF TWO K SPECTRAL TYPE CONTACT BINARY SYSTEMS

C. Barani¹, M. Martignoni¹, F. Acerbi¹, R. Michel², H. Aceves², and V. Popov³

Received January 17 2022; accepted March 28 2022

ABSTRACT

The first analysis of the light curves of contact binaries ROTSE J135349.8+305205 (CB1) and 1SWASP J150957.5-115308 (CB2) using the Wilson-Devinney code is presented. Both binary systems are of the A-subtype with a shallow fill-out (20.8% and 15.8% respectively) and a difference in temperatures between the components of < 200 K. A mass-ratio of 0.302 is found for CB1, while for CB2 the interesting value of 0.904 is found. The short periods, 0.246 d for CB1 and 0.229 d for CB2, and their spectral type K suggests that these systems are near the shortest period limit. The absolute elements are estimated using GAIA parallaxes. CB2 is found to be at the beginning of its evolution, while CB1 will approach the final evolutionary stage. The sum of the component masses of CB1 is $0.813 M_{\odot}$, below the mass limit of $1.0 - 1.2 M_{\odot}$ assumed for the known contact binary stars.

RESUMEN

Se presenta por primera vez el análisis, usando el código Wilson-Devinney, de las curvas de luz de las binarias de contacto ROTSE1 J135349.8+305205 (CB1) y 1SWASP J150957.5-115308 (CB2). Ambos sistemas son del subtipo-A con un relleno poco profundo (20.8% y 15.8%, respectivamente) y una diferencia en temperatura entre las componentes de < 200 K. Se encuentra que su razón de masas es de 0.302 para CB1, y para CB2 se encuentra el valor interesante de 0.904. Los periodos cortos, 0.246 d para CB1 y 0.229 d para CB2, y sus tipos espectrales K sugieren que estos sistemas están cercanos al límite de periodo más corto. Los elementos absolutos se estiman usando paralajes de GAIA. Se encuentra que CB2 está al comienzo del estadio evolutivo, mientras que CB1 se aproximará al estadio evolutivo final. La suma de las masas componentes de CB1 es $0.813 M_{\odot}$, debajo del límite de $1.0 - 1.2 M_{\odot}$ que se supone para las binarias de contacto conocidas.

Key Words: techniques: photometric — binaries: contact — stars: individual: ROTSE J135349.8+305205, 1SWASP J150957.5-115308

1. INTRODUCTION

A contact binary (CB) is a close binary star system where both components interact strongly, fill out their Roche lobes and share a common envelope (Kopal 1959; Eggleton 2006). Thermal energy is transferred from the hotter (primary) to the colder (secondary) star mainly through the common envelope leading to the establishment of a similar tem-

perature of the two stars. However, their mass ratio can be rather different.

The observational study of contact binaries allows the testing of theoretical models helping us to further understand of –for example– the merging process of stars and the evolution of their common envelope.

Contact binary systems usually belong to spectral types F, G and K, with orbital periods less than a day. The K-type binaries have been expected to have periods shorter than 0.3 days and show shallow characteristics. The rarity of this kind of binaries makes them very interesting systems for testing the

¹Stazione Astronomica Betelgeuse, Magnago, Italy.

²Instituto de Astronomía, UNAM, Ensenada, Baja California, México.

³Department of Physics and Astronomy, Shumen University, Bulgaria.

thermal relaxation theory (TRO, Lucy 1976; Flanery 1976; Robertson & Eggleton 1977).

ROTSE J135349.8+305205 (hereafter J135349) was found to be variable during the ROTSE I all-sky survey (Akerlof et al. 2000) as an EW system with an orbital period of 0.24698301 d. After J135349 was discovered it remained a neglected object. Here, the light curves of J135349 are analyzed and presented for the first time.

A light curve for ROTSE J150957.5-115308 = V373 Lib (hereafter J150957) was reported by Lohr et al. (2013), which presented the typical EW-type behavior and an orbital period of 0.2290205 d. The official name was assigned in the 82nd name-list of variable stars (Kazarovets et al. 2019).

With no previous studies of both these systems, the aim of the present work is to analyze their light curves using the latest version of the Wilson-Devinney code (Wilson & Devinney 1971; Wilson 1994; Wilson & van Hamme. 2016) and to determine the Roche configuration and their orbital parameters.

The outline of the paper is as follows. In § 2 we describe the observations made and their characteristics. In § 3 the times of minima and new ephemeris for our two contact binaries are reported. In § 4 the solution obtained with the Wilson-Devinney code is discussed and presented. In § 5 an estimation of physical parameters using Gaia parallax data is presented. Finally, in § 6 a discussion and final remarks are provided.

2. OBSERVATIONS

Observations done at the San Pedro Martir Observatory with the 0.84-m telescope, the Mexman filter-wheel and the *Spectral Instruments 1* CCD detector (an e2v CCD42-40 chip with a gain of $1.39 e^-/ADU$ and readout noise of $3.54 e^-$). The field of view was $7.6' \times 7.6'$ and a binning of 2×2 was employed during all the observations.

J135349 was observed on April 26 2017 for 7.4h, May 4 2018 for 6.1h and April 4 2021 for 2.2h. Alternated exposures in filters B , V , R_c and I_c , with exposure times of 60, 40, 15 and 15 seconds respectively, were taken in all the observing runs.

J150957 was observed on February 21 2017 for 3.8h, February 23 2017 for 3.6h, March 4 2019 for 3.4h, June 6 2019 for 2.5h, April 11 2021 for 3.2h and April 13 2021 for 6.6h. Alternated exposures in filters B , V and R_c , with exposure times of 60, 35 and 20 seconds respectively, were taken in all the observing runs. Flat field and bias images were also taken during all the nights.

TABLE 1

TIMES OF MINIMA FOR J135349 AND J150957

HJD	Epoch(1)	O-C(1)	Error	Source
<i>J135349:</i>				
2457869.7252	-0.5	-0.0001	0.0013	TW ^a
2457869.8489	0.0	0.0001	0.0015	"
2458242.8169	1510.0	-0.0008	0.0013	"
2458242.9419	1510.5	0.0008	0.0014	"
<i>J150957:</i>				
2455567.0550	0.0	-0.0026	0.0013	VSX ^b
2457805.9514	9776.0	0.0030	0.0012	TW ^a
2457808.0127	9785.0	0.0031	0.0012	"
2458640.8387	13421.5	0.0011	0.0012	"
2459315.9845	16369.5	-0.0013	0.0017	"
2459317.8165	16377.5	-0.0015	0.0021	"
2459317.9308	16378.0	-0.0017	0.0015	"

^aTW=This work. ^bVSX=Variable Star Index.

All images were processed using IRAF⁴ routines. Images were bias subtracted and flat field corrected before the instrumental magnitudes were computed with the standard aperture photometry method. These fields were also calibrated in the $UBV(RI)_c$ system with the help of some Landolt's photometric standards.

Based on the previous information, we decided to use star WISEJ135355.54+304735.9 ($U = 18.042$, $B = 16.936$, $V = 15.839$, $R_c = 15.148$ and $I_c = 14.549$) as comparison star for J135349 since it has a similar color (making differential extinction corrections negligible). For the case of J150957, star WISEJ150953.24-115045.3 ($U = 15.398$, $B = 14.587$, $V = 13.589$, $R_c = 12.931$ and $I_c = 12.446$) was employed. Any part of the data can be provided upon request.

3. TIMES OF MINIMA AND NEW EPHEMERIS

From our observations we were able to obtain 4 times of minimum (ToM) for J135349 and 6 for J150957, one ToM has been found in literature. All ToMs are presented in Table 1.

All ToMs are heliocentric and determined by the polynomial fit method. With these data we updated the ephemeris as follows. For J135349

$$\text{Min.}I(HJD) = 2457869.8488(5) + 0^d.24699835(5) \times E, \quad (1)$$

⁴IRAF is distributed by the National Optical Observatories, operated by the Association of Universities for Research in Astronomy, Inc., under cooperative agreement with the National Science Foundation.

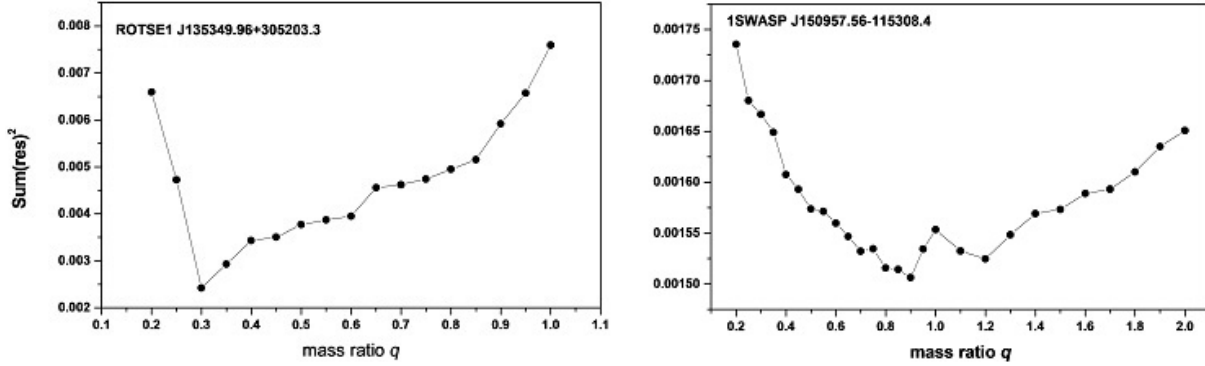


Fig. 1. The relation $\Sigma(res)^2$ versus mass ratio $q = M_2/M_1$ in Mode 3 of the W-D code for J135349 and J150957.

and for J150957

$$Min.I(HJD) = 2455567.0576(23) + 0^d.2290191(1) \times E. \quad (2)$$

4. PHOTOMETRIC SOLUTION WITH THE W-D METHOD

The light curves of both systems show clearly the EW behavior with continuous changes in the light. For this reason the Mode 3 of the Wilson-Devinney (W-D) code was used in the calculation.

Using our observations, we were able to determine the color index of both systems and, from the tables of Worthey & Lee (2011), the temperature of the primary component; that was xed at 4760 K for J135349, and 4220 K for J150957.

The temperatures of the components of the two systems suggest convective envelopes. Hence, we adopted the following atmospheric parameters: the gravity-darkening coecients $g_1 = g_2 = 0.32$ (Lucy 1967) and the bolometric albedos $A_1 = A_2 = 0.5$ (Ruciński 1973) were assigned; the limb-darkening parameters originate from van Hamme (1993) for $\log g = 4.0$, and solar abundances.

During the diifferential correction calculation in the W-D code we left as adjustable parameters the orbital inclination i , the mean surface eective temperature of the secondary component T_2 , the dimensionless surface potentials of the primary and secondary stars $\Omega_1 = \Omega_2$, the monochromatic luminosity of the primary component L_1 and the third light L_3 . In our solutions, we nd that the contribution of the third light is negligible.

The classical q -search method was used to nd the best initial value of the mass ratio to be used during the light curve analysis. The value of the mass ratio q was fixed in each iteration and increased after the

TABLE 2
LIGHT CURVES SOLUTION

	J135349	Error	J150957	Error
i ($^\circ$)	77.384	0.340	65.226	0.062
T_1 (K)	4760	fixed	4220	fixed
T_2 (K)	4690	14	4032	9
$\Omega_1 = \Omega_2$	2.6064	0.0120	3.5144	0.0023
q	0.3023	0.0047	0.9048	0.0011
f	0.209	0.006	0.158	0.008
L_{1B}	0.6673	0.0049	0.5478	0.0039
L_{2B}	0.2535	0.0051	0.3254	0.0036
L_{1V}	0.6809	0.0046	0.5306	0.0033
L_{2V}	0.2636	0.0044	0.3478	0.0031
L_{1R}	0.6739	0.0043	0.5388	0.0027
L_{2R}	0.2650	0.0040	0.3660	0.0026
L_{1I}	0.6849	0.0041	-	-
L_{2I}	0.2728	0.0037	-	-
Primary				
r (pole)	0.4481	0.0026	0.3748	0.0003
r (side)	0.4735	0.0035	0.3961	0.0004
r (back)	0.5023	0.0049	0.4320	0.0006
Secondary				
r (pole)	0.2861	0.0041	0.3582	0.0003
r (side)	0.2991	0.0051	0.3777	0.0004
r (back)	0.3365	0.0093	0.4147	0.0006
$\Sigma(Res)^2$	0.0023052		0.0014944	

sum of residuals showed a minimum number. As one can see from Figure 1, where the sum of squares of residuals ($\Sigma(res)^2$) versus mass ratio q is shown, the best mass ratio for J135349 is found at $q = 0.3$ and for J150957 at $q = 0.9$. These values of q were also treated as free parameters in the successive step of our analysis.

The final results obtained are listed in Table 2, while the obtained fit is shown in Figure 2.

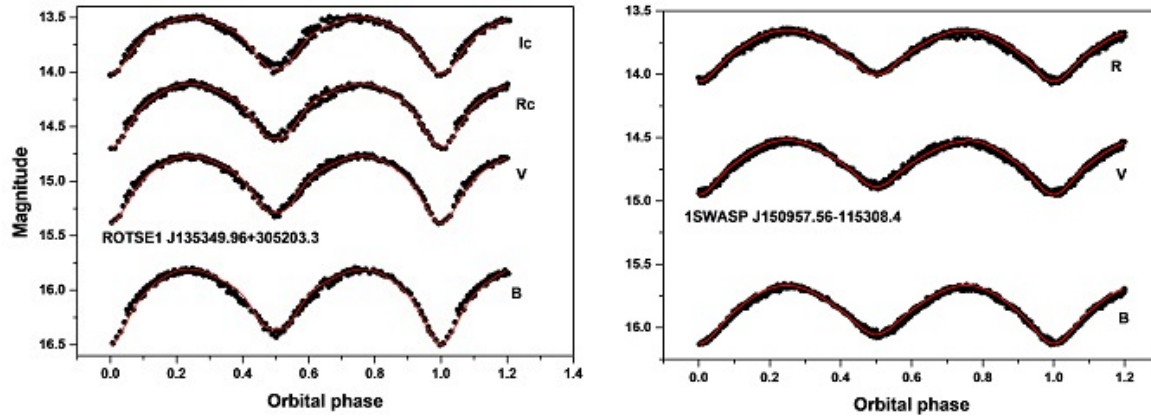


Fig. 2. CCD filtered light curves for the systems at different wavelengths. Points are the original observations while lines represent the theoretical light curves obtained in our modeling. The color figure can be viewed online.

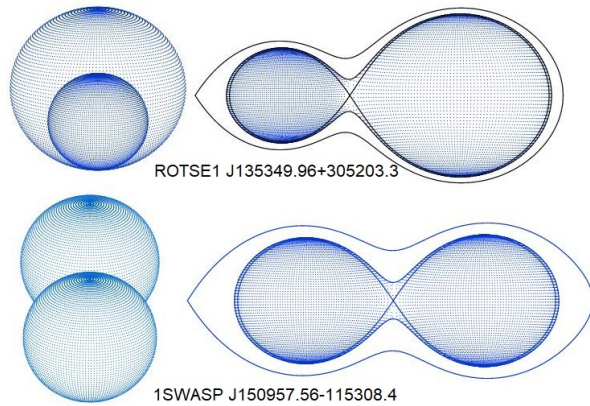


Fig. 3. Model representation of the CBs J135349 ($q = 0.3$) and J150957 ($q = 0.9$). The configuration at the primary minimum (left) and the Roche geometry (right) of these systems resulting from our modeling are shown. The color figure can be viewed online.

The values of the mass ratio for both systems indicate that they are typical A-subtype contact binaries in the Binnendijk (1965) classification. In Figure 3 the graphical representation of the systems and the relative Roche geometries are displayed.

By examining Table 2 the following information can be obtained. Both systems are of the A-subtype and in good thermal contact. The temperature of the components suggests that they are of the K spectral type. We note that it is somewhat strange to find a spectral K-type in A-subtype contact systems.

Systems of late spectral type generally belong to the W-subtype of W UMa contact binaries, but there are some exceptions that belong to the A-subtype as 2MASS J11201034-2201340 (Hu et al. 2016), ES Cep

(Zhu et al. 2014), NSV 395 (Samec et al. 2016), and AP UMi (Awadalla et al. 2016).

Our two systems, despite having temperatures consistent with late spectral type K, show the characteristics of the subtype-A contact binaries; i.e., $T_1 > T_2$, transit at primary minimum, and a mass ratio $q < 1$.

CB J150957, having a mass ratio near unity, can be considered to be a high mass ratio system. High mass ratio systems, proposed firstly by Csizmadia & Klagyivik (2004) are a subgroup of contact binaries with mass ratio $q > 0.72$.

For the H-type the rate of energy transfer is less efficient than for other contact binaries at a given luminosity ratio. Having a mass ratio close to unity, less luminosity should be transferred in order to equalize their surface temperature.

Both binary systems show a low fill-out value. The low fill-out value is not a common feature among A-subtype contact binaries, and only a few A-subtype contact binaries are found to have a high mass ratio and a shallow common envelope (see Table 5 of Han et al. 2019). Contact binary J150957, which shows the same peculiar characteristics, can be added to this short list.

Note that the errors of the parameters given in Table 2 are the formal errors from the W-D code. For a discussion see Barani et al. (2017).

5. ESTIMATION OF THE PHYSICAL PARAMETERS WITH THE GAIA PARALLAX

Physical parameters such as mass, radius and luminosity are very important information for a contact binary system. Hence it is necessary to es-

timate them. Here we will indicate how we have estimated the physical parameters of J135349 and J150957 without radial velocity curves, using the parallax known by Gaia (Gaia Collaboration et al. 2018).

First, we calculated the Galactic extinction obtained using different methods from which an average value of the A_V (Masda et al. 2018) was extracted; in detail:

1. Simple and spiral model from Amôres & Lépine (2005) using the code GALExtin.⁵
2. Equation 1 from Iglesias-Marzoa et al. (2019).
3. Dust tables by Schlegel et al. (1998) in the NASA IPAC (NASA 2015); proceeding therefore to deredden the visual magnitudes in quadratures.⁶

Using the parallax from Gaia we calculated the visual absolute magnitude using the relation

$$M_V = m_V(\text{max}) - 5 \log D + 5 - A_V, \quad (3)$$

and the bolometric magnitude $M_{\text{bol}} = M_V + BC_V$, where BC_V is the bolometric correction obtained from the Pecaut et al. (2012) and Pecaut & Mamajek (2013) tables. This allowed us to obtain the total luminosity of the systems as

$$L_T = L_1 + L_2 = 10^{-0.4(M_{\text{bol}} - 4.7554)}, \quad (4)$$

and also the individual luminosities of the components.

Knowing the temperatures of the first and second component of each system we obtained their radii, and finally the total mass of the system; by using the value of the mass ratio obtained from the Wilson-Devinney analysis, the single masses M_1 and M_2 as shown in Table 3 were obtained.

We used the absolute elements of the primary and secondary components of both systems (Table 3) to estimate their evolutionary status by means of the $\log T_{\text{eff}} - \log L$ (i.e. HertzsprungRussell) diagram on the evolutionary tracks of Girardi et al. (2000). The results are shown in Figure 4.

It is possible to see from Figure 4 that both the primary and the secondary components of J150957 are undermassive, with a luminosity comparable to that of a zero age main sequence (ZAMS) star.

For J135349 the primary component is located in the region between the ZAMS and TAMS (terminal

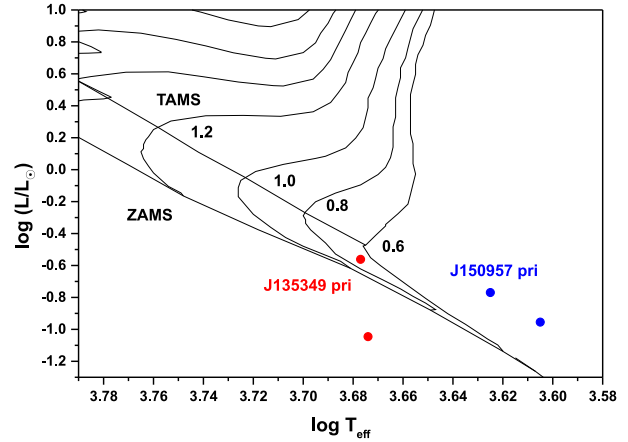


Fig. 4. Components of our binary systems plotted in the HR diagram. Zero age main sequence (ZAMS), terminal age main sequence (TAMS), evolutionary tracks and isochrones were taken from Girardi et al. (2000) for a solar chemical composition. The numbers denote initial masses. The color figure can be viewed online.

age main sequence) near the evolutionary track of 0.6, but it is underluminous given its mass. The secondary component, located under the ZAMS, is overmassive and slightly underluminous.

These results suggest that both systems consist of two stars of similar surface brightness, but in different evolutionary stages.

According to Flannery (1976) the stability parameter \mathfrak{S} for the mass-exchange in a CB can be defined as:

$$\mathfrak{S} = \ln \left[\frac{R_p(0.38 + 0.2 \log q)}{R_s(0.38 - 0.2 \log q)} \right], \quad (5)$$

where R_p refers to the primary's radius and R_s to the secondary. If $\mathfrak{S}=0$ no mass transfer occurs; if $\mathfrak{S} > 0$ an unbalanced pressure gradient will force gas from the primary to secondary, and vice versa if $\mathfrak{S} < 0$.

In our case we obtain $\mathfrak{S}=0.074$ for J150957; hence there is mass transfer from primary to the secondary; the contrary is true for J135349 where we obtain $\mathfrak{S} = -0.019$. In both CBs the value of \mathfrak{S} indicates a poor mass exchange between the components.

6. DISCUSSION AND FINAL REMARKS

The results of our analysis lead to two contact binary systems of the A-subtype that are in good thermal contact and have a shallow degree of contact between their components.

J150957, with a mass ratio $q = 0.905$, belongs to the high mass ratio type contact binaries (i.e. an H-type).

⁵http://www.galexin.org/interstellar_extinction.php

⁶<http://irsa.ipac.caltech.edu/applications/DUST>

TABLE 3
ESTIMATED ABSOLUTE ELEMENTS

Target	$L_1(L_\odot)$	$L_2(L_\odot)$	$R_1(R_\odot)$	$R_2(R_\odot)$
J150957	0.170 ± 0.003	0.111 ± 0.007	0.771 ± 0.007	0.684 ± 0.025
J135349	0.275 ± 0.005	0.090 ± 0.008	0.770 ± 0.007	0.448 ± 0.023
	$a(R_\odot)$	$M_1(M_\odot)$	$M_2(M_\odot)$	ρ_1 (g cm^{-3})
J150957	1.922 ± 0.020	0.953 ± 0.030	0.862 ± 0.028	1.27
J135349	1.546 ± 0.020	0.624 ± 0.027	0.189 ± 0.011	1.92
	ρ_2 (g cm^{-3})	Mag Max V	M_V	M_{bol}
J150957	3.03	14.52	7.04	6.13
J130349	2.90	14.77	6.32	5.85
	J	$\log J$	$\log J_{lim}$	J_{lim}
J150957	5.11^{51}	51.71	51.78	6.06^{51}
J130349	9.71^{50}	50.99	51.17	1.48^{51}

The spectral type K for all the components of the binary systems is somewhat strange for the A-subtype, but there are few A-subtype systems of K-type.

In our analysis we found no significant evidence of spots on the surfaces of the two components, the OConnell effect. This fact could be explained by a period of magnetic quiescence in the CBs (Zhang et al. 2011).

Using the absolute elements provided in Table 3 the dynamical evolution of contact binaries can be inferred via the determination of the orbital angular momentum J_0 (Eker et al. 2006).

In Figure 5 it is possible to see the position our systems occupy in the $\log J_0 - \log M$ diagram. The curved borderline separates the detached from the contact region and provides a check of the Roche configurations of J150957 and J130349. The values of $\log J_0$ place J150957 near the borderline of this diagram, while J130349 is in the well defined region of contact systems.

An exhaustive characterization of contact binaries, via the period-temperature relation, was recently conducted by Qian et al. (2020). In Figure 6 (Figure 4 in the original paper) we show the position of J150957 and J135349 in the period-temperature plot. Systems near the lower line are marginal contact systems while systems near the upper line are deep-contact ones. Between the two lines there are normal contact systems.

J150957 is near the lower boundary at the beginning of the evolutionary stage of contact binary evolution (Figure 6). It is also shown in the

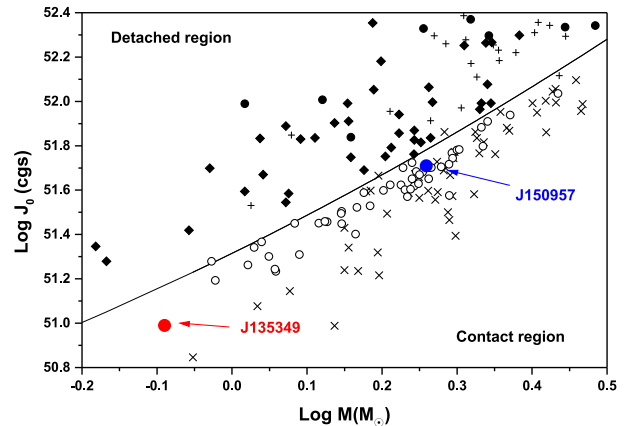


Fig. 5. Position of J150957 and J135349 in the $\log J_0 - \log M$ diagram. Symbols are described in Figure 1 of the original paper of Eker et al. (2006). The color figure can be viewed online.

$\log J_0 - \log M$ plot where the system is slightly under the borderline, in the contact region. This assumption is endorsed by the high mass ratio ($q = 0.9$) and the low fill-out (15.6%).

The other system, J135349 is well inside the boundaries for normal EW (Figures 5 and 6) and, with its small mass ratio ($q = 0.38$), its fill-out value (20.9%) and the almost equal temperature of the components, it follows that it is approaching the final evolutionary stage of the contact binary evolution.

The total mass determined for J150957 is over the minimum total mass limit for W UMa systems of 1.0-1.2 M_\odot (Sępień 2006), while J135349, with its total

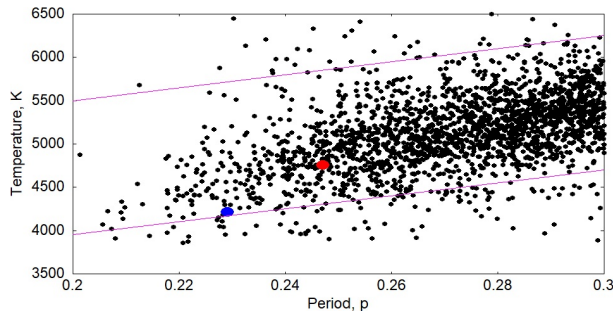


Fig. 6. Correlation between the orbital period P (days) and temperature T (K), based on parameters of 8510 contact binaries from Qian et al. (2020). The position J150957 is marked in blue, and that of J135349 in red. The color figure can be viewed online.

mass $M_{tot} = 0.813 M_{\odot}$, is under this limit. This means a mass loss, and may imply a late evolutionary stage of this contact binary system.

This work made use of data from the European Space Agency (ESA) mission Gaia,⁷ and processed by the Gaia Data Processing and Analysis Consortium (DPAC).⁸

Use of the International Variable Star Index (VSX) database has been made (operated at AAVSO Cambridge, Massachusetts, USA), as well as of the AAVSO Photometric All-Sky Survey (APASS) funded by the Robert Martin Ayers Sciences Fund. Also, use has been made of the VizieR catalogue access tool, CDS, Strasbourg, France. The original description of the VizieR service was published in A&AS 143, 23.

Based upon observations carried out at the Observatorio Astronómico Nacional on the Sierra San Pedro Mártir (OAN-SPM), Baja California, México.

REFERENCES

- Akerlof, C., Amrose, S., Balsano, R., et al. 2000, *AJ*, 119, 1901, <https://doi.org/10.1086/301321>
- Amôres, E. B. & Lépine, J. R. 2005, *AJ*, 130, 659, <https://doi.org/10.1086/430957>
- Awadalla, N. S., Hanna, M. A., Ismail, M. N., Hassan, I. A., & Elkhamisy, M. A. 2016, *JKAS*, 49, 65, <https://doi.org/10.5303/JKAS.2016.49.3.065>
- Barani, C., Martignoni, M., & Acerbi, F. 2017, *NewA*, 50, 73, <https://doi.org/10.1016/j.newast.2016.07.010>
- Binnendijk, L. 1965, The Position of Variable Stars in the Hertzsprung-Russell Diagram, *VeBam*, 27, 36

⁷<https://www.cosmos.esa.int/gaia>.

⁸<https://www.cosmos.esa.int/web/gaia/dpac/consortium>.

- Csizmadia, S. & Klagyivik, P. 2004, *A&A*, 426, 1001, <https://doi.org/10.1051/0004-6361:20040430>
- Eker, Z., Demircan, O., Bilir, S., & Karataş, Y. 2006, *MNRAS*, 373, 1483, <https://doi.org/10.1111/j.1365-2966.2006.11073.x>
- Eggleton, P. 2006, *Evolutionary Processes in Binary and Multiple Stars*, (Cambridge, UK: CUP)
- Flannery, B. P. 1976, *ApJ*, 205, 217, <https://doi.org/10.1086/154266>
- Gaia Collaboration, Brown, A. G. A., Vallenari, A., et al. 2018, *A&A*, 616, 1, <https://doi.org/10.1051/0004-6361/201833051>
- Girardi, L., Bressan, A., Bertelli, G., & Chiosi, C. 2000, *A&AS*, 141, 371, <https://doi.org/10.1051/aas:2000126>
- Han, Q.-W., Li, L.-F., & Jiang, D.-K. 2019, *RAA*, 19, 174, <https://doi.org/10.1088/1674-4527/19/12/174>
- Hu, C.-P., Yang, T.-C., Chou, Y., et al. 2016, *AJ*, 151, 170, <https://doi.org/10.3847/0004-6256/151/6/170>
- Iglesias-Marzoa, R., Arévalo, M. J., López-Morales, M., et al. 2019, *A&A*, 627, 153, <https://doi.org/10.1051/0004-6361/201935516>
- Kazarovets, E. V., Samus, N. N., Durlevich, O. V., et al. 2019, *IBVS*, 6261, 1, <https://doi.org/10.22444/IBVS.6261>
- Kopal, Z. 1959, *Close binary systems*, (London, UK: The International Astrophysics Series, Chapman & Hall)
- Lohr, M. E., Norton, A. J., Kolb, U. C., et al. 2013, *A&A*, 549, 86, <https://doi.org/10.1051/0004-6361/201220562>
- Lucy, L. B. 1967, *ZA*, 65, 89
- . 1976, *ApJ*, 205, 208, <https://doi.org/10.1086/154265>
- Masda, S. G., Al-Wardat, M. A., & Pathan, J. M. 2018, *JApA*, 39, 58, <https://doi.org/10.1007/s12036-018-9548-z>
- Pecaut, M. J., Mamajek, E. E., & Bubar, E. J. 2012, *ApJ*, 746, 154, <https://doi.org/10.1088/0004-637X/746/2/154>
- Pecaut, M. J. & Mamajek, E. E. 2013, *ApJS*, 208, 9, <https://doi.org/10.1088/0067-0049/208/1/9>
- Qian, S.-B., Zhu, L.-Y., Liu, L., et al. 2020, *RAA*, 20, 163, <https://doi.org/10.1088/1674-4527/20/10/163>
- Robertson, J. A. & Eggleton, P. P. 1977, *MNRAS*, 179, 359, <https://doi.org/10.1093/mnras/179.3.359>
- Ruciński, S. M. 1973, *AcA*, 23, 79
- Samec, R. G., Clark, J., Maloney, D., et al. 2016, *JAAVSO*, 44, 101
- Schlegel, D. J., Finkbeiner, D. P., & Davis, M. 1998, *ApJ*, 500, 525, <https://doi.org/10.1086/305772>
- Stepień, K. 2006, *AcA*, 56, 347
- van Hamme, W. 1993, *AJ*, 106, 2096, <https://doi.org/10.1086/116788>
- Wilson, R. E. & Devinney, E. J. 1971, *ApJ*, 166, 605, <https://doi.org/10.1086/150986>

- Wilson, R. E. 1994, *PASP*, 106, 921, <https://doi.org/10.1086/133464>
- Wilson, R. E. & van Hamme, W. 2016, *Computing Binary Stars Observables*. <ftp.astro.ufl.edu>, directory pub/wilson/lcdc2015
- Worthey, G. & Lee, H.-ch. 2011, *ApJS*, 193, 1, <https://doi.org/10.1088/0067-0049/193/1/1>
- Zhang, X.-B., Ren, A.-B., Luo, C.-Q., & Luo, Y.-P. 2011, *RAA*, 11, 583, <https://doi.org/10.1088/1674-4527/11/5/008>
- Zhu, L. Y., Qian, S. B., Soonthornthum, B., et al. 2014, *AJ*, 147, 42, <https://doi.org/10.1088/0004-6256/147/2/42>

- F. Acerbi: Via Zoncada 51, Codogno, LO, 26845, Italy (acerbifr@tin.it).
- H. Aceves: Instituto de Astronomía, UNAM. A.P. 877, 22800 Ensenada, BC, Mexico (aceves@astro.unam.mx).
- C. Barani: Via Molinetto 35, Triulza di Codogno, LO, 26845, Italy (cvbarani@alice.it).
- M. Martignoni: Via Don G. Minzoni 26/D, Magnago, MI, 20020, Italy (massimiliano.martignoni@outlook.it).
- R. Michel: Instituto de Astronomía, UNAM. A.P. 877, 22800 Ensenada, BC, Mexico (rmm@astro.unam.mx).
- V. Popov: Department of Physics and Astronomy, Shumen University, 115 Universitetska str., 9700 Shumen, Bulgaria (velimir.popov@elateobservatory.com)

A NON-SINGULAR CLOSED BOUNCING UNIVERSE WITHOUT VIOLATION OF NULL ENERGY CONDITION

Nasr Ahmed^{1,2}, Tarek M. Kamel², and Mohamed I. Nouh²

Received November 16 2021; accepted March 28 2022

ABSTRACT

A matter bouncing entropy-corrected cosmological model has been suggested. The model allows only positive curvature with negative pressure and no violation of the null energy condition. The result obtained in this paper is supported by some recent theoretical works where the combination of positive spatial curvature and vacuum energy leads to non-singular bounces with no violation of the null energy condition. An important feature of the current model is that evolutions of the cosmic pressure, energy density and equation of state parameter are independent of the values of the prefactors α and β in the corrected entropy-area relation. The validity of the classical and the new nonlinear energy conditions has been discussed. The cosmographic parameters have been analyzed.

RESUMEN

Sugerimos un modelo cosmológico con materia en rebote y entropía corregida. El modelo permite sólo curvatura positiva con presión negativa, y no viola la condición de energía nula. El resultado que obtenemos se ve apoyado por trabajos teóricos recientes en los que la combinación de curvatura espacial positiva y energía de vacío conduce a rebotes no singulares sin violar la condición de energía nula. Un rasgo importante del modelo actual es que la evolución de la presión cósmica, la densidad de energía y el parámetro de la ecuación de estado son independientes de los valores de los prefactores α y β en la relación corregida entropía-área. Se discute la validez de las condiciones de energía clásica y de la nueva energía no lineal. Se analizan también los parámetros cosmográficos.

Key Words: cosmology: theory — cosmology: parameters

1. INTRODUCTION AND MOTIVATION

A major challenge in gravity and modern cosmology is the late-time cosmic acceleration (Perlmutter et al. 1999, Percival et al. 2001, Stern et al. 2010). The existence of 'Dark Energy' (DE) with negative pressure which represents a repulsive gravity is one possible explanation. A variety of DE models have been suggested through modified gravity theories (Tsujikawa 2013, Kamenshchik et al. 2001, Caldwell 2002, Chiba 2000, Sen 2002, Arkani-Hamed et al. 2004, Ahmed 2018) and dynamical scalar fields (Harko et al. 2011, Nojiri et al. 2017, Nojiri and Odintsov 2006, Nojiri et al. 2008, Ferraro and Fiorini 2007, Bengochea and Ferraro 2009, De Felice and Tsujikawa 2010, Alves et al. 2011, Maeder 2017, Gagnon et al. 2011, Ahmed and Moss 2008, Ahmed and Moss 2010). Gravity also has a deep connection with thermodynamics; this connection has been proved through the entropy-area formula $S = \frac{A}{4G}$ where S is the black hole's entropy and A is its horizon area (Hawking 1975). The FRW cosmological equations can also be derived from the first law of thermodynamics (Cai and Kim 2005, Bousso 1999, Nojiri and Odintsov 2006). When higher order curvature terms appear, the entropy-area formula, which holds only for GR, needs corrections. Modified FRW equations have been given in Cai and Cao (2008) using the corrected entropy-area relation

¹Mathematics Department, Faculty of Science, Taibah University, Saudi Arabia.

²Astronomy Department, National Research Institute of Astronomy and Geophysics, Helwan, Cairo, Egypt.

$$S = \frac{A}{4G} + \alpha \ln \frac{A}{4G} + \beta \frac{4G}{A}. \quad (1)$$

The values of the two dimensionless constants α and β are in debate and not yet determined (Salehi and Fard 2018, Jing and Yan 2002). While positive and negative values of α and β have been suggested by some authors, it has been argued in (Gour 2002, Hod 2004, Xia et al. 2013, Yang and Xu 2014, Medved 2005) that the "best guess" might simply be zero. A detailed discussion for all possible values has been introduced in Ahmed and Alamri (2019, 2019a) based on cosmological and stability arguments.

In spite of its success, the standard Big Bang model suffers from a number of problems such as the flatness problem, the horizon problem and the initial singularity problem. Although some problems have been addressed in the inflationary scenario in which the universe undergoes an exponential expansion for a very short interval of time, the initial singularity problem still remained unanswered (Guth 1981, Starobinsky 1980). An alternative theory free from the initial singularity is the Big Bounce, in which the universe arises from a prior contracting phase. In other words, the universe initially contracts to a minimal size before it starts to expand again (Novello and Bergliaffa 2008, Ijjas and Steinhardt 2018, Sahoo et al. 2020, Nojiri et al. 2019) (see Brandenberger and Peter, 2017 for a review of earlier bouncing scenarios). Such a contraction-expansion process may be repeated forever, which also gives the name cyclic cosmology to such models. Bouncing cosmology has been discussed in the framework of many modified gravity theories such as $f(R)$ gravity, $f(T)$ gravity, $f(G)$ gravity, $f(R, T)$ gravity (Bamba, et al. 2014, Bamba, et al. 2014, Bamba, et al. 2015, Bamba, et al. 2016, Tripathy et al. 2019) and teleparallel gravity (de la Cruz-Dombriz, et al., 2018).

While many bouncing models have been introduced, a special attention has been paid to the Matter Bounce Scenario (MBS) (de Haro and Cai 2015, Cai et al., 2013, Quintin et al., 2014, de Haro 2012, Wilson-Ewing 2013) which leads to a nearly scale invariant power spectrum of primordial curvature perturbations. In this scenario, the universe is nearly matter-dominated at very early times in the contracting phase and gradually evolves towards a bounce. At the bounce, all parts of the universe are supposed to be in causal contact which means no horizon problem (Nojiri et al., 2019). After that, a regular expansion starts in agreement with the behavior of the standard Big Bang model. Some unclear conceptual issues of the Matter Bounce Scenario have been discussed in detail in Nojiri et al. (2019). Although there has been a wide observational and theoretical support for the flat universe (Tegmark et al. 2004, Bennett et al. 2003, Spergel et al. 2003a, Ahmed et al. 2020), some other recent observations of cosmic microwave background anisotropies also suggest that our universe may be closed rather than flat (Di Valentino et al. 2020, Handley 2021, Planck Collaboration et al. 2020a, 2020b). The present theoretical work supports positive curvature; we show that the existence of a stable entropy-corrected bouncing cosmology implies a closed universe.

The paper is organized as follows: In § 2, a matter-bounce solution to the modified entropy-corrected cosmological equations is provided with the expressions for the pressure p , energy density ρ , EoS parameter ω , deceleration and the jerk parameters j and q . A complete analysis for the evolution of these functions with cosmic time is studied for different values of α and β for the three values of the curvature κ ($= +1, 0, -1$). § 3 is dedicated to the study of the stability of the model and § 4 to cosmography. The final conclusion is included in § 5.

2. COSMOLOGICAL EQUATIONS AND SOLUTIONS

Taking (1) into account, the following FRW equations can be obtained (Cai et al., 2008)

$$H^2 + \frac{k}{a^2} + \frac{\alpha G}{2\pi} \left(H^2 + \frac{k}{a^2}\right)^2 - \frac{\beta G^2}{3\pi^2} \left(H^2 + \frac{k}{a^2}\right)^3 = \frac{8\pi G}{3} \rho. \quad (2)$$

$$2 \left(\dot{H} - \frac{k}{a^2}\right) \left(1 + \frac{\alpha G}{\pi} \left(H^2 + \frac{k}{a^2}\right) - \frac{\beta G^2}{\pi^2} \left(H^2 + \frac{k}{a^2}\right)^2\right) = -8\pi G(\rho + p). \quad (3)$$

A general FRW model has been constructed in (Ahmed and Alamri, 2019a) where equations (2) and (3) have been solved using the hyperbolic ansatz $a(t) = A\sqrt{\sinh(\zeta t)}$ which allows the cosmic deceleration-acceleration transition. Using this hyperbolic solution, the evolution of the equation of state parameter also suggests zero

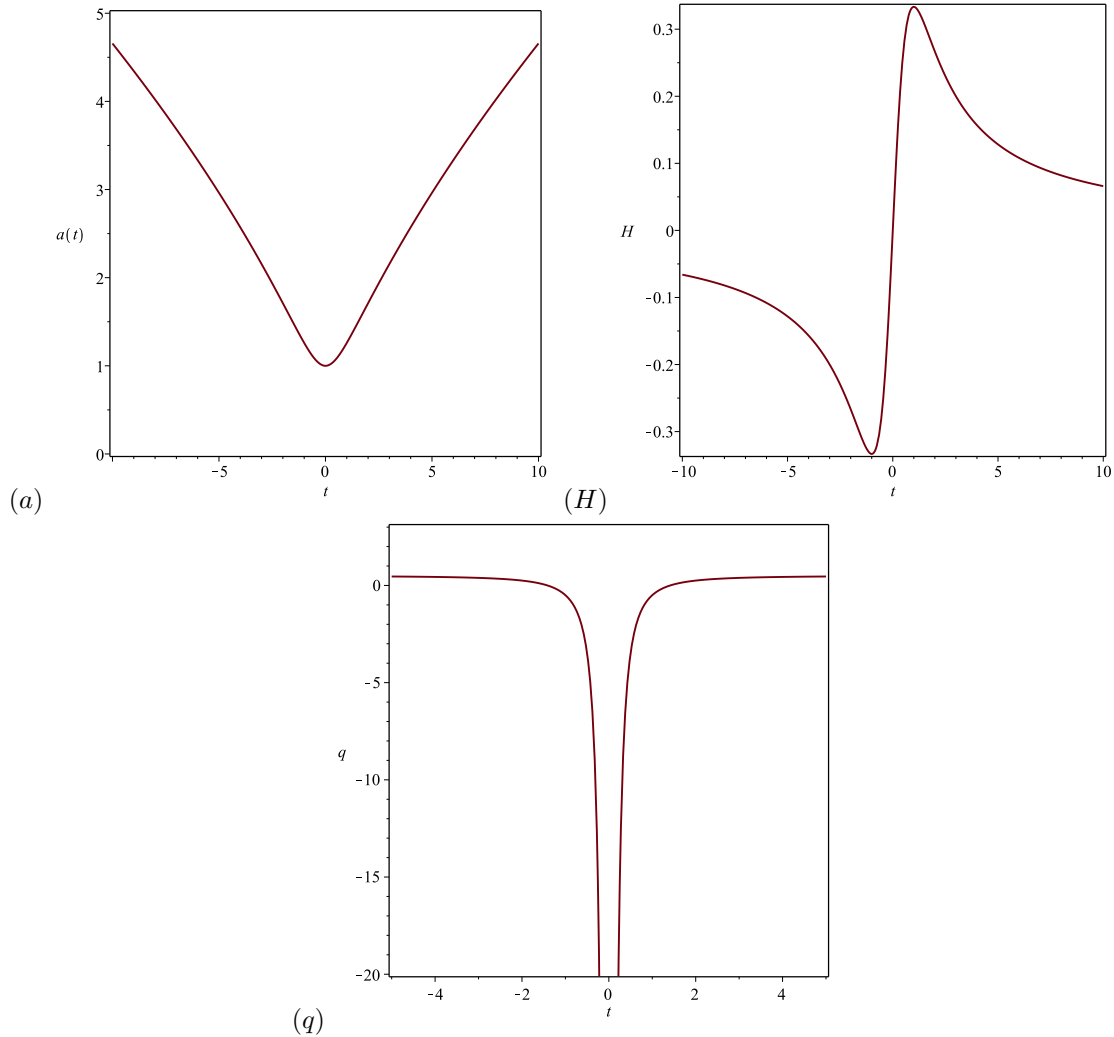


Fig. 1. The scale factor, Hubble and deceleration parameters for the MBS ($n = \frac{1}{3}$). The Hubble parameter is negative before the bounce, positive after the bounce and zero at the bounce. The color figure can be viewed online.

values of the two prefactors. A similar result was reached in Ahmed and Alamri (2019b), where the zero values are required to avoid the causality violation. Exploring relation (1) in different cosmological contexts helps to provide an accurate estimation of the values of α and β . Depending on the values of α and β , the bouncing solutions (2) and (3) were investigated in Salehi and Fard (2018). The modified FRW equations obtained from relation (1) without the β term were introduced in Cai et al. (2008). Considering the following scale factor for a variant non-singular bounce (Nojiri et al., 2019)

$$a(t) = (At^2 + 1)^n, \tag{4}$$

the Matter Bounce Scenario can be explored via this ansatz when $n = \frac{1}{3}$. The expressions for deceleration and Hubble parameters q and H can now be written as

$$q(t) = -\frac{\ddot{a}a}{\dot{a}^2} = -\frac{(2n-1)At^2 + 1}{2nAt^2}, \quad H(t) = \frac{2nAt}{At^2 + 1}. \tag{5}$$

The formulas for the pressure $p(t)$ and energy density $\rho(t)$ are

$$\begin{aligned}
p(t) = & \frac{-1}{16\pi^3 (A^6 t^{12} + 6A^5 t^{10} + 15A^4 t^8 + 20A^3 t^6 + 15A^2 t^4 + 6At^2 + 1)} \\
& \times (128\beta A^6 n^5 t^6 - 128\beta A^5 n^5 t^4 - 128\beta A^6 n^6 t^6 - 32\alpha\pi A^6 n^3 t^8 - 32\alpha\pi A^5 n^3 t^6 \\
& + 32\alpha\pi A^4 n^3 t^4 + 32\alpha\pi A^3 n^3 t^2 + 48\alpha\pi A n^4 t^8 + 96\alpha\pi A^5 n^4 t^6 + 48\alpha\pi A^4 n^4 t^4 - 8A^6 \pi^2 t^{10} n \\
& - 24A^5 \pi^2 t^8 n - 16A^4 \pi^2 t^6 n + 16A^3 \pi^2 t^4 n + 24A^2 \pi^2 t^2 n + 24n^2 A^2 t^2 \pi^2 + 24n^2 A^6 \pi^2 t^{10} \\
& + 96n^2 A^5 \pi^2 t^8 + 144n^2 A^4 \pi^2 t^6 + 96n^2 A^3 t^4 \pi^2 + 8\pi^2 n A + (At^2 + 1)^{-2n} (12A^5 \pi^2 t^{10} k \\
& + 30A^4 \pi^2 t^8 k + 40A^3 \pi^2 t^6 k + 30A^2 \pi^2 t^4 k + 12A \pi^2 t^2 k + 8\alpha\pi A^6 n^2 t^{10} k + 32\alpha\pi A^5 n^2 t^8 k \\
& + 48\alpha\pi A^4 n^2 t^6 k - 8\alpha\pi A^6 n t^{10} k - 24\alpha\pi A^5 n t^8 k + 32\alpha\pi A^3 n^2 t^4 k + 8\alpha\pi A^2 n^2 t^2 k \\
& + 16\alpha\pi A^3 n t^4 k + 24\alpha\pi A^2 n t^2 k - 16\alpha\pi A^4 n t^6 k + \pi^2 k - 32\beta A^6 n^4 t^8 k \\
& - 64\beta A^5 n^4 t^6 k - 32\beta A^4 n^4 t^4 k + 64\beta A^6 n^3 t^8 k + 64\beta A^5 n^3 t^6 k - 64\beta A^4 n^3 t^4 k \\
& - 64\beta A^3 n^3 t^2 k + 8\alpha\pi k n A) + (At^2 + 1)^{-4n} (-8\beta k^2 n A - \alpha\pi k^2 \\
& - 16\beta A^3 k^2 t^4 n + 8\beta A^6 k^2 t^{10} n^2 + 32\beta A^5 k^2 t^8 n^2 + 48\beta A^4 k^2 t^6 n^2 + 8\beta A^6 k^2 t^{10} n \\
& + 24\beta A^5 k^2 t^8 n + 32\beta A^3 k^2 t^4 n^2 + 16\beta A^4 k^2 t^6 n + 8\beta A^2 k^2 t^2 n^2 - 24\beta A^2 k^2 t^2 n \\
& - \alpha\pi A^6 k^2 t^{12} - 6\alpha\pi A^5 k^2 t^{10} - 15\alpha\pi A^4 k^2 t^8 - 20\alpha\pi A^3 k^2 t^6 - 15\alpha\pi A^2 k^2 t^4 \\
& - 6\alpha\pi A k^2 t^2) + (At^2 + 1)^{-6n} (2\beta A^6 k^3 t^{12} + 12\beta A^5 k^3 t^{10} + 30\beta A^4 k^3 t^8 \\
& + 40\beta A^3 k^3 t^6 + 30\beta A^2 k^3 t^4 + 12\beta A k^3 t^2 + 2\beta k^3).
\end{aligned} \tag{6}$$

$$\begin{aligned}
\rho(t) = & \frac{-1}{16\pi^3 (A^6 t^{12} + 6A^5 t^{10} + 15A^4 t^8 + 20A^3 t^6 + 15A^2 t^4 + 6At^2 + 1)} \\
& \times (128\beta A^6 n^6 t^6 - 48\alpha\pi A^6 n^4 t^8 - 96\alpha\pi A^5 n^4 t^6 - 48\alpha\pi A^4 n^4 t^4 - 24n^2 A^2 t^2 \pi^2 \\
& - 24n^2 A^6 t^{10} \pi^2 - 96n^2 A^5 t^8 \pi^2 - 144n^2 A^4 t^6 \pi^2 - 96n^2 A^3 t^4 \pi^2 \\
& + (At^2 + 1)^{-2n} (-6A^6 \pi^2 t^{12} k - 36A^5 \pi^2 t^{10} k - 90A^4 \pi^2 t^8 k - 120A^3 \pi^2 t^6 k - 90A^2 \pi^2 t^4 k \\
& - 36A \pi^2 t^2 k - 24\alpha A^6 \pi n^2 t^{10} k - 96\alpha A^5 \pi n^2 t^8 k - 144\alpha A^4 \pi n^2 t^6 k - 96\alpha A^3 \pi n^2 t^4 k \\
& - 24\alpha A^2 \pi n^2 t^2 k - 6\pi^2 k + 96\beta A^6 n^4 t^8 k + 192\beta A^5 n^4 t^6 k + 96\beta A^4 n^4 t^4 k) \\
& + (At^2 + 1)^{-4n} (-3\alpha\pi k^2 + 24\beta A^6 k^2 n^2 t^{10} + 96\beta A^5 k^2 n^2 t^8 + 144\beta A^4 k^2 n^2 t^6 \\
& + 96\beta A^3 k^2 n^2 t^4 + 24\beta A^2 k^2 n^2 t^2 - 3\alpha\pi A^6 k^2 t^{12} - 18\alpha\pi A^5 k^2 t^{10} - 45\alpha\pi A^4 k^2 t^8 \\
& - 60\alpha\pi A^3 k^2 t^6 - 45\alpha\pi A^2 k^2 t^4 - 18\alpha\pi A k^2 t^2) \\
& + (At^2 + 1)^{-6n} (2\beta A^6 k^3 t^{12} + 12\beta A^5 k^3 t^{10} + 30\beta A^4 k^3 t^8 + 40\beta A^3 k^3 t^6 + 30\beta A^2 k^3 t^4 \\
& + 12\beta A k^3 t^2 + 2\beta k^3).
\end{aligned} \tag{7}$$

Figure 2 shows the evolution of the energy density, the pressure and the equation of state parameter with cosmic time. The evolution of $\rho(t)$ shows that the only case allowed physically is the one with positive curvature $k = +1$. The plots of $p(t)$ and $\omega(t)$ shows a Quintessence-dominated universe along with negative pressure. The existence of negative pressure agrees with the 'dark energy assumption' which implies a negative pressure. Such evolutions of the three parameters have been found to be independent of the values of the prefactors α and β as shown in Table(2). The jerk parameter has the asymptotic value $j = 1$ at late-time. After making use of the relation between the scale factor and the redshift $a = \frac{1}{1+z}$ to express ω in terms of z , we find that $\omega(z) = -1$ at the current epoch where $z = 0$.

3. STABILITY OF THE MODEL

In this section, we discuss the validity of the classical linear energy conditions (Hawking and Ellis 1973, Wald 1984) and the new nonlinear energy conditions (ECs) (Martin-Moruno and Visser 2013, Abreu et al. 2011, Martin-Moruno and Visser 2013a, Martin-Moruno and Visser 2013b). The classical linear ECs (the null

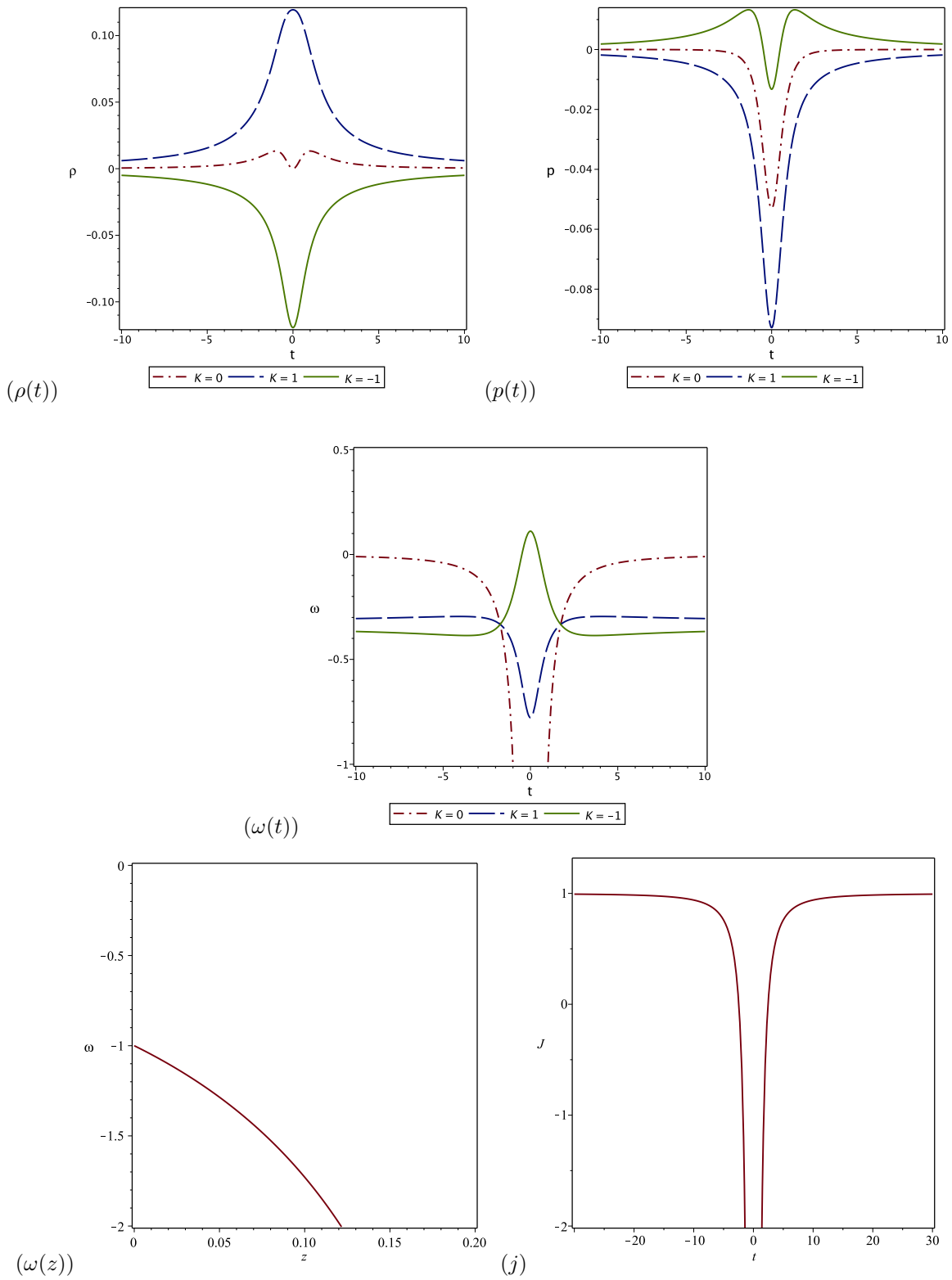


Fig. 2. Evolution of ρ , p and ω for the matter bounce scenario ($n = \frac{1}{3}$). (a) The physically accepted behavior of energy density exists only for a closed universe. (b) The pressure is always negative. (c) The equation of state parameter for a closed universe lies in the range $-1 < \omega < 0$ which means a Quintessence-dominated universe. The same behavior of ρ , p and ω has been obtained for different values of α and β (Table 1). (d) Equation of state parameter ω as a function of the redshift z ; we see that $\omega(z) = -1$ at $z = 0$. (e) The jerk parameter has the asymptotic value $j = 1$ at late-time. Here $A = 1.5$. The color figure can be viewed online.

TABLE 1
 IN THE CURRENT BOUNCING MODEL, EVOLUTIONS OF ρ , P AND ω ARE INDEPENDENT OF
 THE VALUES OF α AND β

α	0.1	0	0.2	-0.1	0	-0.5	0	0.01	0
β	0.1	0.3	0	-0.1	-0.7	0	0.02	-0.001	0
Same behav- ior of $\rho(t)$?	!	!	!	!	!	!	!	!	!
	for all								
	k								
Same behav- ior of $p(t)$?	!	!	!	!	!	!	!	!	!
	for all								
	k								
Same behav- ior of $\omega(t)$?	!	!	!	!	!	!	!	!	!
	for all								
	k								

$\rho + p \geq 0$; weak $\rho \geq 0$, $\rho + p \geq 0$; strong $\rho + 3p \geq 0$ and dominant $\rho \geq |p|$ energy conditions) should be replaced by other nonlinear ECs when semiclassical quantum effects are taken into account (Martin-Moruno and Visser 2013a, Martin-Moruno and Visser 2013b). In the current work, we consider the following nonlinear ECs: (i) The flux EC (FEC): $\rho^2 \geq p_i^2$ (Aberu et al. 2011, Martin-Moruno and Visser 2013), first presented in Aberu et al. (2011). (ii) The determinant EC (DETEC): $\rho \cdot \Pi p_i \geq 0$ (Martin-Moruno and Visser 2013b). (iii) The trace-of-square EC (TOSEC): $\rho^2 + \sum p_i^2 \geq 0$ (Martin-Moruno and Visser 2013).

According to the strong energy condition (SEC), gravity should always be attractive. But this ‘highly restrictive’ condition fails when describing the current cosmic accelerated epoch and during inflation (Visser 1997a, Visser 1997b, Visser 1997c). In the current model we have a negative pressure which represents a repulsive gravity and, consequently, the SEC is not expected to be satisfied as indicated in Figure 3b. Only for the closed universe ($K = +1$), the null energy condition (NEC) (Figure 3a) and the dominant energy condition (Figure 3c) are satisfied all the time. Although most models of non-singular cosmologies require a violation of the NEC ($\rho + p \geq 0$), avoiding such a violation would be preferable, if possible. The NEC is the most fundamental of the ECs and on which many key results are based, such as the singularity theorems (Alexandre and Polonyi 2021). Violation of NEC automatically implies the violation of all other point-wise energy conditions.

A classical non-singular bouncing cosmological model in which the NEC is not violated was introduced in Gungor and Starkman (2021). A detailed discussion on the relation between the enforcement of the NEC and the occurrence of bouncing universes was given in Giovannini (2017). It has been shown in Bramberger and Jean-Luc Lehnars (2019) that a combination of positive spatial curvature and vacuum energy (violating the SEC) leads to non-singular bounces with no violation of the NEC. Recalling the definition of Dark Energy as a component of negative pressure, our result in the current work agrees with the result obtained in Dunsby and O. Luongo (2016). We also obtain a combination of positive curvature, violation of the SEC, and a bouncing universe without violation of the NEC. A non-singular bouncing cosmological model with positive spatial curvature and flat scalar potential was constructed in Capozziello (2019). The behavior of the new nonlinear ECs is plotted in Figure 3d, e, f. For the closed universe, both the flux and trace-of-square ECs are satisfied.

4. COSMOGRAPHIC ANALYSIS

The cosmography of the universe has recently been an attractive area of research (Visser 2005, Capozziello et al. 2019) where cosmological parameters can be described in terms of kinematics only. Consequently, cosmographic analysis is model-independent with no need to assuming an equation of state in order to explore the cosmic dynamics (Visser, 2005). The Taylor expansion of the scale factor $a(t)$ around the present time t_0 can be written as

$$a(t) = a_0 \left[1 + \sum_{n=1}^{\infty} \frac{1}{n!} \frac{d^n a}{dt^n} (t - t_0)^n \right]. \quad (8)$$

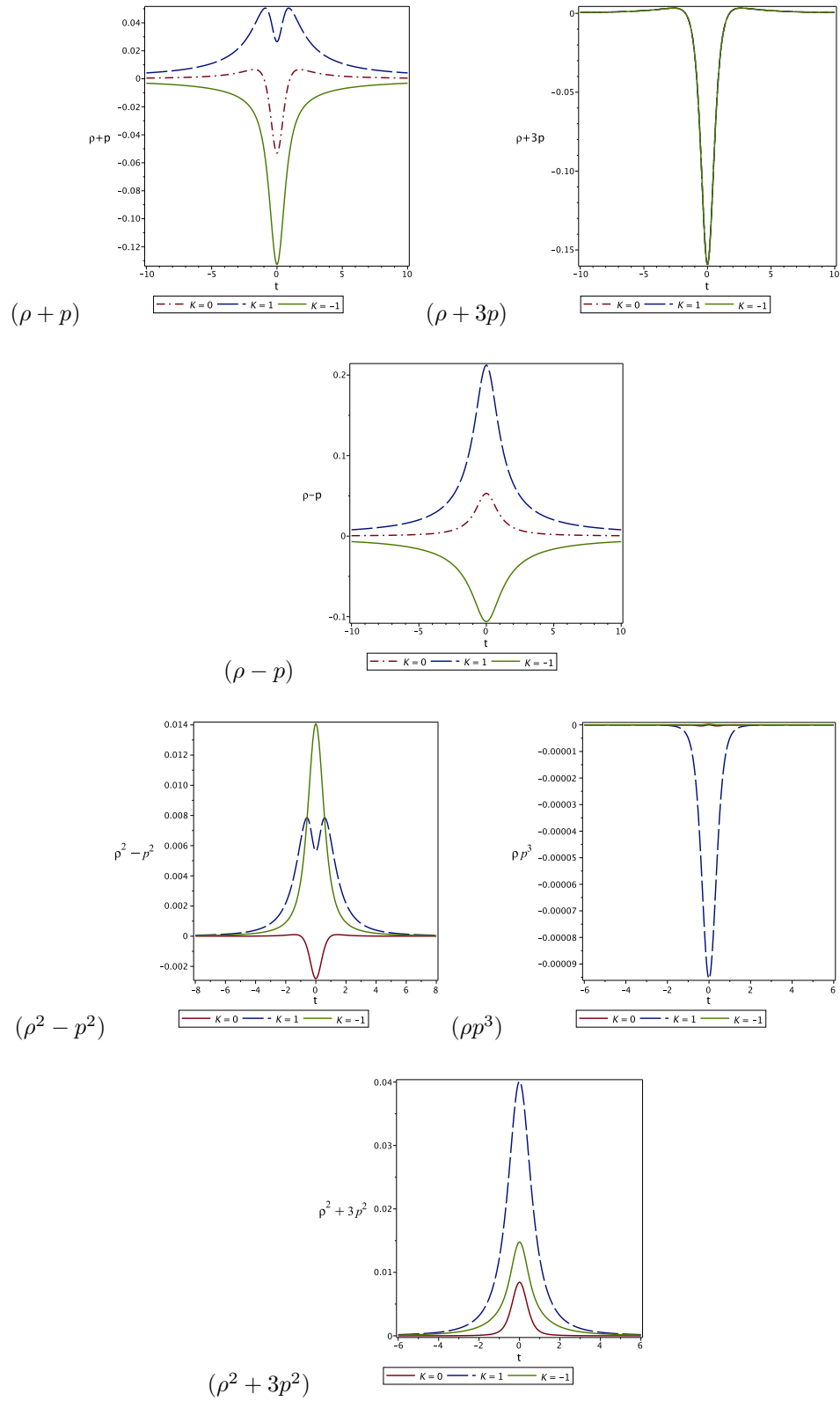


Fig. 3. Classical and nonlinear ECs: No violations of NEC and DEC for $k = +1$. The color figure can be viewed online.

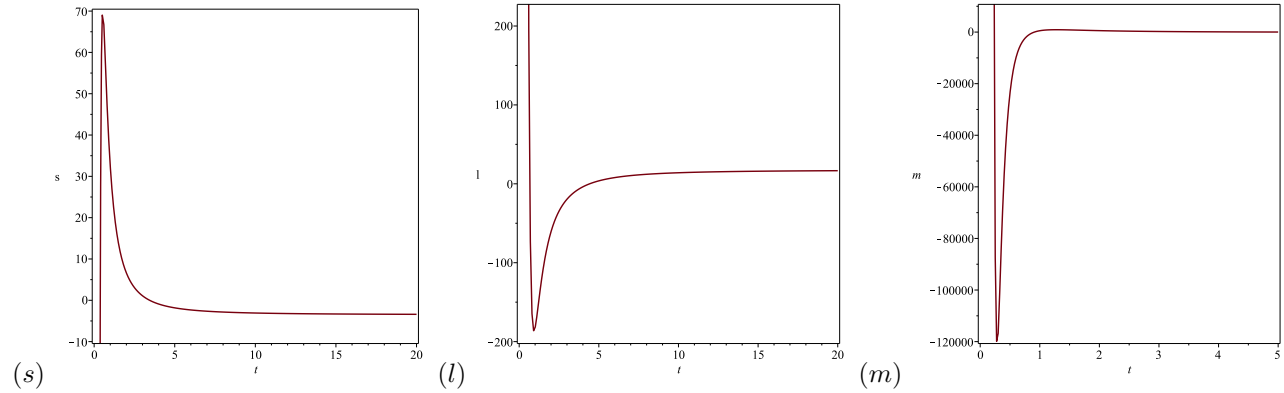


Fig. 4. Evolution of the cosmographic parameters s , l and m with time. The color figure can be viewed online.

The following cosmographic coefficients of the series (8) are recognized respectively as the Hubble parameter H , the deceleration parameter q , the jerk j , the snap s , the lerk l and the max-out m parameters

$$\begin{aligned} H &= \frac{1}{a} \frac{da}{dt}, \quad q = -\frac{1}{aH^2} \frac{d^2a}{dt^2}, \quad j = \frac{1}{aH^3} \frac{d^3a}{dt^3}, \\ s &= \frac{1}{aH^4} \frac{d^4a}{dt^4}, \quad l = \frac{1}{aH^5} \frac{d^5a}{dt^5}, \quad m = \frac{1}{aH^6} \frac{d^6a}{dt^6}. \end{aligned} \quad (9)$$

For the current model, the expressions for H and q have been given in (5). The expressions for j , s , l and m are given as

$$j = \frac{1}{2} [(2n^2 - 3n + 1)at^2 + 3(n - 1)], \quad (10)$$

$$s = \frac{1}{4A^2n^3t^4} [(4n^3 - 12n^2 + 11n - 3)A^2t^4 + (12n^2 - 30n + 18)At^2 + 3(n - 1)], \quad (11)$$

$$\begin{aligned} l &= \frac{1}{4A^2n^4t^4} [(n^4 - 20n^3 + 35n^2 - 25n + 6)A^2t^4 + (20n^3 - 90n^2 + 130n - 60)At^2 \\ &+ 15(n^2 - 3n + 2)], \end{aligned} \quad (12)$$

$$\begin{aligned} m &= \frac{1}{8A^3n^5t^6} [(8n^5 - 60n^4 + 170n^3 - 225n^2 + 137n - 30)A^3t^6 + (60n^4 - 420n^3 \\ &+ 1065n^2 - 1155n + 450)A^2t^4 + (90n^3 - 495n^2 + 855n - 450)At^2 + 15(n^2 - 3n + 2)]. \end{aligned} \quad (13)$$

The sign of q determines whether the expansion is accelerating (negative sign) or decelerating (positive sign). j represents a suitable way to describe models close to Λ CDM (Visser, 2005). The sign of j is also important; the positive sign shows the existence of a transition time when cosmic expansion gets modified; the value of s is necessary to determine the dark energy evolution. In spite of its advantages, a useful discussion on the limits and drawbacks of the cosmographic approach has been given in Visser (2005).

5. CONCLUSION

In this paper, we have constructed a matter bouncing entropy-corrected model using a special ansatz for a variant non-singular bounce (Nojiri et al., 2019). The main features of the present model are as follows:

- Only a closed universe is allowed in the model. While the strong energy condition is violated, the null and dominant energy conditions are satisfied all the time only for $K = +1$. Although most models of non-singular cosmologies require a violation of the NEC, it is highly preferable to avoid such violation if possible. The new nonlinear energy conditions has also been investigated.

- The evolution of the equation of state parameter and of the cosmic pressure shows a Quintessence-dominated universe along with negative pressure. In the current model we get $\omega(z) = -1$ at the present epoch where $z = 0$, as it should be according to observations.
- The result obtained in the current work agrees with the result obtained in Bramberger and Jean-Luc Lehnars (2019), where the combination of positive spatial curvature and vacuum energy (violating the strong energy condition) leads to non-singular bounces with no violation of the null energy condition. Our result also agrees with the works of Giovannini (2017), Matsui et al. (2019). This represents a strong support for the current work, where similar results have been obtained in different work frames.
- We have examined many positive, negative and zero values for α and β and found no change in the behavior of the cosmic pressure, energy density and equation of state parameter. This is another interesting feature of this entropy-corrected bouncing model, where the evolutions of p , ρ and ω are independent of the constants α and β .
- The cosmographic parameters have been analyzed.

We are so grateful to the reviewer for many valuable suggestions and comments that significantly improved the paper. This paper is based upon work supported by Science, Technology & Innovation Funding Authority (STDF) under Grant number 37122.

REFERENCES

- Abreu, G., Barceló, C., & Visser, M. 2011, JHEP, 12, 92, [https://doi.org/10.1007/JHEP12\(2011\)092](https://doi.org/10.1007/JHEP12(2011)092)
- Ahmed, N. & Alamri, S. 2018, RAA, 18, 123, <https://doi.org/10.1088/1674-4527/18/10/123>
- _____. 2019, CAJPh, 97, 1075, <https://doi.org/10.1139/cjp-2018-0635>
- _____. 2019a, IJGMM, 16, <https://doi.org/10.1142/s0219887819501597>
- _____. 2019b, ApSS, 364, 100, <https://doi.org/10.1007/s10509-019-3590-4>
- Ahmed, N. & Moss, I. G. 2008, JHEP, 12, 108, <https://doi.org/10.1088/1126-6708/2008/12/108>
- _____. 2010, NuPhB, 833, 133, <https://doi.org/10.1016/j.nuclphysb.2010.03.008>
- Ahmed, N., Bamba, K., & Salama, F. 2020, IJGMM, 17, 2050075-268, <https://doi.org/10.1142/s0219887820500759>
- Alexandre, J. & Polonyi, J., 2021, PhRvD, 103, 105020, <https://doi.org/10.1103/PhysRevD.103.105020>
- Alves, M. E. S., Miranda, O. D., & de Araujo, J. C. N. 2011, PhLB, 700, 283, <https://doi.org/10.1016/j.physletb.2011.05.022>
- Arkani-Hamed, N., Cheng, H.-C, Luty, M. A., & Mukohyama, S. 2004, JHEP, 05, 074, <https://doi.org/10.1088/1126-6708/2004/05/074>
- Bamba, K., MaLarenko, A. N., Myagky, A. N., Nojiri, S., & Odintsov, S. D. 2014, JCAP, 01, 008, <https://doi.org/10.1088/1475-7516/2014/01/008>
- Bamba, K., Makarenko, A. N., Myagky, A. N., & Odintsov, S. D. 2014, PhLB, 732, 349, <https://doi.org/10.1016/j.physletb.2014.04.004>
- _____. 2015, JCAP, 04, 001, <https://doi.org/10.1088/1475-7516/2015/04/001>
- Bamba, K., Nashed, G. G. L., El Hanafy, W., & Ibraheem, Sh. K. 2016, PhRvD, 94, 083513, <https://doi.org/10.1103/PhysRevD.94.083513>
- Bengochea, G. R. & Ferraro, R. 2009, PhRvD, 79, 124019, <https://doi.org/10.1103/PhysRevD.79.124019>
- Bennett, C. L., Halpern, M., Hinshaw, G., et al. 2003, ApJS, 148, 1, <https://doi.org/10.1086/377253>
- Bousso, R. 1999, JHEP, 9907, 004, <https://doi.org/10.1088/1126-6708/1999/07/004>
- Brandenberger, R. & Peter, P. 2017, FoPh, 47, 797, <https://doi.org/10.1007/s10701-016-0057-0>
- Bramberger, S. F. & Lehnars, J.-L. 2019, PhRvD, 99, 123523, <https://doi.org/10.1103/PhysRevD.99.123523>
- Cai, R. G. & Kim, S. P. 2005, JHEP, 02, 050, <https://doi.org/10.1088/1126-6708/2005/02/050>
- Cai, R. G., Cao, L. M., & Hu, Y.-P. 2008, JHEP 08, 090, <https://doi.org/10.1088/1126-6708/2008/08/090>
- Cai, Y. F., McDonough, E., Duplessis, F., & Brandenberger, R. H. 2013, JCAP, 10, 024, <https://doi.org/10.1088/1475-7516/2013/10/024>
- Caldwell, R. R. 2002, PhLB, 545, 23, [https://doi.org/10.1016/s0370-2693\(02\)02589-3](https://doi.org/10.1016/s0370-2693(02)02589-3)
- Capozziello, S., D'Agostino, R., & Luongo, O. 2019, IJMPD, 28, 1930016, <https://doi.org/10.1142/s0218271819300167>
- Chiba, T., Okabe, T., & Yamaguchi, M. 2000, PhRvD, 62, 023511, <https://doi.org/10.1103/PhysRevD.62.023511>
- De Felice, A. & Tsujikawa, S. 2010, LRR, 13, 3, <https://doi.org/10.12942/lrr-2010-3>
- de Haro, J., 2012, JCAP, 11, 037, <https://doi.org/10.1088/1475-7516/2012/11/037>

- de Haro, J. & Cai, Y.-F. 2015, *GReGr*, 47, 95, <https://doi.org/10.1007/s10714-015-1936-y>
- de la Cruz, A., Farrugia, G., Said, J. L., & Gómez, D. S. 2018, *PhRvD*, 97, 104040, <https://doi.org/10.1103/PhysRevD.97.104040>
- Di Valentino, E., Melchiorri, A., & Silk, J. 2020, *NatAs*, 4, 196, <https://doi.org/10.1038/s41550-019-0906-9>
- Dunsby, P. K. S. & Luongo, O. 2016, *IJGMM*, 13, 1630002-606, <https://doi.org/10.1142/s0219887816300026>
- Ferraro, R. & Fiorini, F. 2007, *PhRvD*, 75, 084031, <https://doi.org/10.1103/PhysRevD.75.084031>
- Gagnon, J. & Lesgourgues, J. 2011, *JCAP*, 09, 26, <https://doi.org/10.1088/1475-7516/2011/09/026>
- Giovannini, M. 2017, *PhRvD*, 96, 101302, <https://doi.org/10.1103/PhysRevD.96.101302>
- Gour, G. 2002, *PhRvD*, 66, 104022, <https://doi.org/10.1103/PhysRevD.66.104022>
- Güngör, Ö. & Starkman, G. D. 2021, *JCAP*, 04, 003, <https://doi.org/10.1088/1475-7516/2021/04/003>
- Guth, A. 1981, *PhRvD*, 23, 347, <https://doi.org/10.1103/PhysRevD.23.347>
- Handley, W. 2021, *PhRvD*, 103, 041301, <https://doi.org/10.1103/PhysRevD.103.L041301>
- Harko, T., Lobo, F. S. N., Nojiri, S., & Odintsov, S. D. 2011, *PhRvD*, 84, 024020, <https://doi.org/10.1103/PhysRevD.84.024020>
- Hawking, S. W. & Ellis, G. F. R. 1973, *The large-scale structure of space-time* (Cambridge, UK: CUP)
- Hawking, S. W. 1975, *CMAPh*, 43, 199, <https://doi.org/10.1007/BF02345020>
- Hod, S. 2004, *CQGra*, 21, 97, <https://doi.org/10.1088/0264-9381/21/14/L01>
- Ijjas, A. & Steinhardt, P. J. 2018, *CQGra*, 35, 135004, <https://doi.org/10.1088/1361-6382/aac482>
- Jing, J. L. & Yan, M. L. 2001, *PhRvD*, 63, 024003, <https://doi.org/10.1103/PhysRevD.63.024003>
- Kamenshchik, A., Moschella, U., & Pasquier, V. 2001, *PhLB*, 511, 265, [https://doi.org/10.1016/50370-2693\(01\)00571-8](https://doi.org/10.1016/50370-2693(01)00571-8)
- Maeder, A. 2017, *ApJ*, 849, 158, <https://doi.org/10.3847/1538-4357/aa92cc>
- Martín-Moruno, P. & Visser, M. 2013, *JHEP*, 2013, 50, [https://doi.org/10.1007/JHEP09\(2013\)050](https://doi.org/10.1007/JHEP09(2013)050)
- _____. 2013, *PhRvD*, 88, 061701, <https://doi.org/10.1103/PhysRevD.88.061701>
- Matsui, H., Takahashi, F., & Terada, T. 2019, *PhLB*, 795, 152, <https://doi.org/10.1016/j.physletb.2019.06.013>
- Medved, A. J. M. 2005, *CQGra*, 22, 133, <https://doi.org/10.1088/0264-9381-22-1-009>
- Nojiri, S., Odintsov, S. D., & Oikonomou, V. K. 2017, *PhR*, 692, 1, <https://doi.org/10.1016/j.physrep.2017.06.001>
- Nojiri, S. & Odintsov, S. D. 2006, *PhRvD*, 74, 086005, <https://doi.org/10.1103/PhysRevD.74.086005>
- _____. 2006, *GReGr*, 38, 1285, <https://doi.org/10.1007/s10714-006-0301-6>
- Nojiri, S., Odintsov, S. D., & Tretyakov, P. V. 2008, *ThPS*, 172, 81, <https://doi.org/10.1143/PTPS.172.81>
- Nojiri, S., Odintsov, S. D., Oikonomou, V. K., & Paul, T. 2019, *PhRvD*, 100, 084056, <https://doi.org/10.1103/PhysRevD.100.084056>
- Novello, M. & Bergliaffa, S. E. P. 2008, *PhR*, 463, 127, <https://doi.org/10.1016/j.physrep.2008.04.006>
- Percival, W. J., Baugh, C. M., & Bland-Hawthorn, J. 2001, *MNRAS*, 327, 1297, <https://doi.org/10.1046/j.1365-8711.2001.04827.x>
- Perlmutter, S., Aldering, G., Goldhaber, G., et al. 1999, *AJ*, 517, 565, <https://doi.org/10.1086/307221>
- Planck Collaboration, Aghanim, N., Akrami, Y., et al. 2020a, *A&A*, 641, 6, <https://doi.org/10.1051/0004-6361/201833910>
- Planck Collaboration, Aghanim, N., Akrami, Y., et al. 2020b, *A&A*, 614, 5, <https://doi.org/10.1051/0004-6361/201936386>
- Quintin, J., Cai, Y. F., & Brandenberger, R. H. 2014, *PhRvD*, 90, 063507, <https://doi.org/10.1103/PhysRevD.90.063507>
- Sahoo, P., Bhattacharjee, S., Tripathy, S. K., & Sahoo, P. K. 2020, *PMLA*, 35, 2050095, <https://doi.org/10.1142/s021773205000952>
- Salehi, A. & Mahmoudi-Fard, M. 2018, *EPJC*, 78, 232, <https://doi.org/10.1140/epjc/s10052-018-5727-y>
- Sen, A. 2002, *JHEP*, 07, 065, <https://doi.org/10.1088/1126-6708/2002/07/065>
- Spergel, D. N., Verde, L., Peiris, H. V., et al. 2003a, *ApJS*, 148, 175, <https://doi.org/10.1086/377226>
- Stern, D., Jimenez, R., Verde, L., Kamionkowski, M., & Stanford, S. A. 2010, *JCAP*, 02, 008, <https://doi.org/10.1088/1475-7516/2010/02/008>
- Starobinsky, A. A. 1980, *PhLB*, 91, 99, [https://doi.org/10.1016/0370-2693\(80\)90670-x](https://doi.org/10.1016/0370-2693(80)90670-x)
- Tegmark, M., Satruss, M. A., Blanton, M. R., et al. 2004, *PhRvD*, 69, 103501, <https://doi.org/10.1103/PhysRevD.69.103501>
- Tripathy, S. K., Khuntia, R. K., & Parida, P. 2019, *EPJP*, 134, 504, <https://doi.org/10.1140/epjp/i2019-12879-3>
- Tsujikawa, S. 2013, *CQGra*, 30, 4003, <https://doi.org/10.1188/0264-9381/30/21/214003>
- Visser, M. 1997, *Sci*, 276, 88, <https://doi.org/10.1126/science.276.5309.88>
- _____. 1997, *PhRvD*, 56, 7578, <https://doi.org/10.1103/PhysRevD.56.7578>
- _____. [arXiv:gr-qc/9710010](https://arxiv.org/abs/gr-qc/9710010)
- _____. 2005, *GReGr*, 37, 154, <https://doi.org/10.1007/s10714-005-0134-8>
- Wald, R. M. 1984, *General relativity* (Chicago, IL: University of Chicago Press)
- Wei, H. 2009, *CoTPh*, 52, 743, <https://doi.org/10.1088/0253-6102/52/4/35>
- Wilson-Ewing, E. 2013, *JCAP*, 03, 026, <https://doi.org/10.1088/1475-7516/2013/03/026>
- Xia, J. Q., Li, H., & Zhang, X. 2013, *PhRvD*, 88, 06351, <https://doi.org/10.1103/PhysRevD.88.063501>
- Yang, W. & Xu, L. 2014, *PhRvD*, 89, 3517, <https://doi.org/10.1103/PhysRevD.89.083517>

Nasr Ahmed: Mathematics Department, Faculty of Science, Taibah University, Saudi Arabia.

Nasr Ahmed, Tarek M. Kamel, and Mohamed I. Nouh: Astronomy Department, National Research Institute of Astronomy and Geophysics, Helwan, Cairo, Egypt.

A VINDICATION OF THE RR LYRAE FOURIER LIGHT CURVE DECOMPOSITION FOR THE CALCULATION OF METALLICITY AND DISTANCE IN GLOBULAR CLUSTERS

A. Arellano Ferro

Instituto de Astronomía, Universidad Nacional Autónoma de México, Ciudad Universitaria, México.

Received February 3 2022; accepted April 1 2022

ABSTRACT

We report the mean metallicity and absolute magnitude of RR Lyrae stars in a sample of 37 globular clusters, calculated via the Fourier decomposition of their light curves and *ad hoc* semi-empirical calibrations, in an unprecedented homogeneous approach. This enabled a new discussion of the metallicity dependence of the horizontal branch (HB) luminosity, as a fundamental distance indicator. The calibration for the RRab and RRc stars should be treated separately. For the RRab the dispersion is larger and non-linear. For the RRc stars the correlation is less steep, very tight and linear. The relevance of the HB structural parameter \mathcal{L} , is highlighted and we offer a non-linear calibration of the form $M_V([\text{Fe}/\text{H}], \mathcal{L})$. Excellent agreement is found between values of $[\text{Fe}/\text{H}]$ and M_V from the light curve decomposition with spectroscopic values and distances obtained via Gaia-DR3 and HST. The variables census in 35 clusters includes 326 stars found by our program.

RESUMEN

Reportamos valores medios de la metalicidad y magnitud absoluta de estrellas RR Lyrae en 37 cúmulos globulares (CGs), calculados homogéneamente por medio de la descomposición de Fourier de las curvas de luz y de calibraciones *ad hoc* semi empíricas. Lo anterior permitió un nuevo análisis de la luminosidad de la rama horizontal (RH) y su dependencia de la metalicidad, como indicador fundamental de distancia. La calibración para estrellas RRab y RRc debe tratarse por separado. Para las RRab no es lineal y presenta mayor dispersión. Para las RRc la correlación es lineal y estrecha. La relevancia del parámetro de estructura de la RH, \mathcal{L} para las RRab, es evidente. Ofrecemos una calibración de la forma $M_V([\text{Fe}/\text{H}], \mathcal{L})$. Los valores de $[\text{Fe}/\text{H}]$ y M_V comparan muy bien con valores espectroscópicos y determinaciones de distancia obtenidas con datos de Gaia-DR3 and HST. El censo de variables en 35 cúmulos incluye 326 descubiertas por nuestro programa.

Key Words: globular clusters: general — stars: horizontal branch — stars: distances — stars: fundamental parameters — stars: variables: RR Lyrae

1. A BRIEF PANORAMA OF THE M_V - $[\text{Fe}/\text{H}]$ RELATION

The relevance of RR Lyrae (RRL) stars as distance indicators has been well known since the early 20th century. Shapley (1917) recognized that “the median magnitude of the short-period variables [RR Lyrae stars] apparently has a rigorously constant value in each globular cluster” and “the observed differences in the mean values then become sensitive criteria of distance, and the relative parallaxes of these remote systems can be known with an accu-

racy...”, a fact that was used later by Shapley himself to describe the Galactic distribution of globular clusters (Shapley 1918). This apparently constant value of the mean magnitude of the RRL can now be interpreted as the luminosity level of the horizontal branch (HB) being constant in all globular clusters. The fact that this is not exactly the case, but instead that metallicity plays a role in determining the luminosity level of the HB, has been demonstrated from theoretical and observational grounds. Sandage (1981); Lee et al. (1990); Sandage (1990)

provided a calibration of the M_V -[Fe/H] relation. Lee et al. (1990) discussed its dependence on helium abundance. Other empirical calibrations followed in the works of Walker (1992), Carney et al. (1992), Sandage (1993) and Benedict et al. (2011). Complete summaries on the calibration of the M_V -[Fe/H] relation can be found in the works of Chaboyer (1999), Cacciari & Clementini (2003) and Sandage & Tamman (2006).

While the relation has been considered to be linear in most empirical works, a non-linear nature is advocated by theoretical approaches, e.g. Cassisi et al. (1999) and VandenBerg et al. (2000). A linear relation of the form $M_V = a + b[\text{Fe}/\text{H}]$ has been broadly accepted in the literature and the slope, resulting from a variety of independent calibrations, ranges a wide span (0.13 - 0.30) as different strategies have been adopted, mainly towards the calculation of M_V . The relevance of the slope and zero point of this relation on the relative and absolute ages of the globular clusters has been amply discussed by Chaboyer et al. (1996, 1998) and Demarque et al. (2000). That a linear relation may be an over simplification (Catelan & Smith 2015) becomes very clear from the theoretical analysis of Demarque et al. (2000), that clearly demonstrates the role of the HB structure and that the slope itself is a function of metallicity. The higher complexity of the HB luminosity and metallicity interconnection has however defied clear empirical demonstrations and calibrations, for which, a very extensive and homogeneous endeavor is required.

Our approach to the determination of mean M_V and [Fe/H] of RRL stars has been the Fourier light curve decomposition of both the fundamental mode and first overtone pulsators RRab and RRc respectively. This followed by the employment of solidly established semi-empirical calibrations between the Fourier parameters and the physical quantities. As early as 2002, our group started studying individual clusters in great detail from CCD time-series imaging through the Johnson-Kron-Cousins *VI* bands. Each cluster in the sample has been the subject of a dedicated study, and the discussions include several key aspects of the nature of the globular clusters, such as distinction of likely cluster members from field stars, structure of the colour-magnitude diagram (CMD), pulsating mode distribution on the HB, and theoretical approaches to the mass loss events in the red giant branch and the subsequent mass distribution at the stage of core He-burning (zero age horizontal branch or ZAHB) and post ZAHB evolution.

In 2017, Arellano Ferro et al. (2017) (hereinafter ABG17) summarized the results of a 15-year old program dedicated to study the variable star populations in globular clusters. The program was mainly aimed to the determination of the mean distance and metallicity of the clusters in a homogeneous way, via the Fourier decomposition of the light curves of their RRL stars and the use of well tested semi-empirical calibrations of the Fourier parameters in terms of luminosity and [Fe/H]. The program is based on the Johnson-Kron-Cousins *VI* CCD time-series imaging, and their subsequent scrutiny via the difference images analysis (DIA), that produces accurate photometry even in the crowded central regions of the globular clusters. In the process numerous variables of virtually all types typically present in globular clusters were discovered, of which ABG17 gave a detailed account.

Presently, five years after ABG17 paper, our group has systematically continued enlarging the sample of studied clusters which has increased from 25 to 34. This should enable a better sustained discussion of the M_V -[Fe/H] relation, i.e. the metallicity dependence of the luminosity of the horizontal branch (HB), and the influence of the cluster Oosterhoff type and the HB structure (Demarque et al. 2000). In the present paper we update our discussion of the nature and calibration of the M_V -[Fe/H] relation, and introduce the role of the HB structure parameter \mathcal{L} which is shown to be of obvious relevance. We also perform a census of variable stars per cluster per variable type and reinforce the resulting cluster distance scale from the Fourier approach via the comparison with independent distances recently obtained from *Gaia* and HST accurate data.

We shall mention at this point that the parameters listed in the tables below for specific clusters and number of variables may occasionally differ slightly from the equivalent tables in ABG17, as a result of a critical evaluation of the original samples. The present tables supersede the previous ones.

2. OBSERVATIONS AND IMAGE REDUCTIONS

2.1. Observations

The observations involved in the program have been obtained in several observatories and telescopes in the 0.8-2.15 m range. The majority of the observations have been performed with the 2.0 m Himalayan Chandra Telescope (HCT) of the Indian Astronomical Observatory (IAO), Hanle, India. We have also used the 0.84 m of San Pedro Mártir Observatory (SPM) Mexico, the 2.15 m telescope of the Complejo Astronómico El Leoncito (CASLEO), San Juan, and

the 1.52 m telescope of Bosque Alegre of the Córdoba Observatory, Argentina, the Danish 1.54 m telescope at La Silla, Chile, the SWOPE 1.0 m telescope of Las Campanas Observatory, Chile, the LCOGT 1 m telescope network at the South African Astronomical Observatory (SAAO) in Sutherland, South Africa, at the Side Spring Observatory (SSO) in New South Wales, Australia, and at Cerro Tololo Inter-American Observatory (CTIO), Chile.

2.2. Transformation to the Standard System

All observations have been transformed from the instrumental to the standard Johnson-Kron-Cousins photometric system (Landolt 1992) *VI*, using local standard stars in the fields of the target clusters. These standard stars have been taken from the extensive collection of Stetson (2000)¹. Typically between 30 and 200 standard stars were available per globular cluster.

2.3. Difference Image Analysis

All the image photometric treatment has been performed using the Difference Image Analysis with the *DanDIA* pipeline (Bramich 2008; Bramich et al. 2013, 2015).

3. CALCULATION OF M_V AND $[Fe/H]$

Our approach to the calculation of mean M_V and $[Fe/H]$ for each GC in the sample has been through the RRL light curve Fourier decomposition, and the application of *ad hoc*, well tested, semi empirical calibrations. The Fourier decomposition of the RRL light curves is performed by fitting the observed light curve in *V*-band with a Fourier series model of the form:

$$m(t) = A_0 + \sum_{k=1}^N A_k \cos \left(\frac{2\pi}{P} k (t - E) + \phi_k \right), \quad (1)$$

where $m(t)$ is the magnitude at time t , P is the period, and E is the epoch. A linear minimization routine is used to derive the best-fit values of the amplitudes A_k and phases ϕ_k of the sinusoidal components. From the amplitudes and phases of the harmonics in equation 1, the Fourier parameters, defined as $\phi_{ij} = j\phi_i - i\phi_j$, and $R_{ij} = A_i/A_j$, are computed.

Subsequently, the low-order Fourier parameters can be used in combination with semi-empirical calibrations to calculate $[Fe/H]$ and M_V for each RRL,

and hence the mean values of the metallicity and absolute magnitude for the RRL population in the host cluster.

The specific calibrations and zero points used for RRab and RRC stars for this purpose are described in § 3.1. Numerous Fourier decompositions of RRL light curves can be found in the literature. However, over the years, each author has used different calibrations and zero points to estimate M_V and $[Fe/H]$. Our group has also used slightly different equations in the earlier papers but in the work by Arellano Ferro et al. (2010) zero points of the M_V calibrations (see their § 4.2), were discussed and adopted, and we have used them subsequently. In the present paper we have recalculated M_V and $[Fe/H]$ for all clusters in the sample, using the calibrations described in the following section.

The final values found for M_V and $[Fe/H]$, the later expressed in the three different scales defined in § 3.1, are listed in Table 1, which is organized by Oosterhoff types; Oosterhoff (1939, 1944) realized that the periods of fundamental-mode RRL, or RRab stars in a given cluster, group around two values; 0.55 d (Oosterhoff Type I or OoI) and 0.65 d (Oosterhoff Type II or OoII). OoI clusters are systematically more metal-rich than OoII clusters. A third Oosterhoff class (OoIII) (Pritzl et al. 2000), which presently contains only two GCs, NGC 6388 and NGC 6441, is represented by very metal-rich systems, where the periods of their RRab stars average about 0.75 d. A few clusters have been classified as of the intermediate type or OoInt, since the average periods of their RRab stars and their mean $[Fe/H]$ fall between those of Type I and Type II clusters; it has been argued that OoInt clusters may be associated to an extragalactic origin (Catelan 2009) due to their similarity to dSph galaxies, satellites of the Milky Way, and their respective clusters. In Table 1 we include of 16 OoI, 14 OoII, 2 OoIII and 2 OoInt clusters. The calculations have been performed independently for RRab and RRC stars. For clusters with differential reddening, i.e. NGC 1904, NGC 3201, NGC 6333 and NGC 6401, care has been taken in calculating the individual reddening for each RRL. The interested reader is referred to the original papers for a detailed discussion on that subject.

3.1. $[Fe/H]$ and M_V Calibrations

For the calculation of $[Fe/H]$ we adopted the following calibrations:

$$[Fe/H]_j = -5.038 - 5.394P + 1.345\phi_{31}^{(s)}, \quad (2)$$

¹<http://www3.cadc-ccda.hia-ihh.nrc-cnrc.gc.ca/community/STETSON/standards>

TABLE 1
MEAN VALUES OF [Fe/H], GIVEN IN THREE DIFFERENT SCALES, AND M_V FROM A
HOMOGENEOUS FOURIER DECOMPOSITION OF THE LIGHT CURVES OF RR LYRAE CLUSTER
MEMBERS¹

GC	Oo	[Fe/H] _{ZW}	[Fe/H] _{UV}	[Fe/H] _N	M_V	N	[Fe/H] _{ZW}	[Fe/H] _{UV}	[Fe/H] _N	M_V	N	Ref.	$E(B-V)$	\mathcal{L}
NGC (M)		RRab					RRc							
1261	I	-1.48±0.05	-1.38	-1.27	0.59±0.04	6	-1.51±0.13	-1.38	-1.41	0.55±0.02	4	25	0.01	-0.67
1851	I	-1.44±0.10	-1.33	-1.18	0.54±0.03	10	-1.40±0.13	-1.28	-1.28	0.59±0.02	5	23	0.02	-0.20
3201	I	-1.49±0.10	-1.39	-1.29	0.60±0.04	19	-1.47±0.08	-1.37	-1.36	0.58±0.01	2	3	diff.	+0.08
4147	I	-1.56±0.17	-1.47	-1.44	0.57±0.03	5	-1.72±0.26	-1.68	-1.66	0.57±0.05	6	4	0.01	+0.38
5272 (M3)	I	-1.56±0.16	-1.46	-1.46	0.59±0.05	59	-1.65±0.14	-1.57	-1.56	0.56±0.06	23	24	0.01	+0.18
5904 (M5)	I	-1.44±0.09	-1.33	-1.19	0.57±0.08	35	-1.49±0.11	-1.39	-1.38	0.58±0.03	22	19	0.03	+0.31
6171 (M107)	I	-1.33±0.12	-1.22	-0.98	0.62±0.04	6	-1.02±0.18	-0.90	-0.88	0.59±0.03	4	22	0.33	-0.74
6229	I	-1.42±0.07	-1.32	-1.13	0.61±0.06	12	-1.45±0.19	-1.32	-1.58	0.53±0.10	8	20	0.01	+0.14
6362	I	-1.20±0.13	-1.06	-0.73	0.66±0.07	5	-1.21±0.16	-1.09	-1.10	0.59±0.05	6	27	0.06	-0.58
6366	I	-0.84	-0.77	-	0.71	1	-	-	-	-	-	11 ²	0.80	-0.9
6401	I	-1.36±0.09	-1.24	-1.04	0.60±0.07	19	-1.27±0.23	-1.09	-1.16	0.58±0.03	9	21	diff.	+0.13
6712	I	-1.25±0.06	-1.13	-0.82	0.55±0.03	6	-1.10±0.04	-0.95	-0.96	0.57±0.18	3	30	0.35	-0.44
6934	I	-1.56±0.14	-1.46	-1.49	0.58±0.05	15	-1.53±0.12	-1.41	-1.50	0.59±0.03	5	26	0.10	+0.25
6981 (M72)	I	-1.48±0.11	-1.37	-1.28	0.63±0.02	12	-1.66±0.08	-1.60	-1.55	0.57±0.04	4	14	0.06	+0.14
7006	I	-1.51±0.13	-1.40	-1.36	0.61±0.03	31	-1.81±0.27	-1.75	-1.78	0.59±0.04	3	33	0.08	-0.28
Pal13	I	-1.64±0.15	-1.56	-1.67	0.65±0.05	4	-	-	-	-	-	28	0.10	-0.3
288	II	-1.85 ³	-1.87	-1.42	0.38	1	-1.59	-1.52	-1.54	0.58	1	1	0.03	+0.88
1904 (M79)	II	-1.84±0.13 ³	-1.86	-1.46	0.41±0.05	5	-1.71	-1.66	-1.69	0.58	1	2	diff.	+0.74
4590 (M68)	II	-2.07±0.09 ³	-2.21	-2.01	0.49±0.07	5	-2.09±0.03	-2.24	-2.23	0.53±0.01	15	5	0.05	+0.17
5024 (M53)	II	-1.94±0.06 ³	-2.00	-1.68	0.45±0.05	18	-1.84±0.13	-1.85	-1.85	0.52±0.06	3	6	0.02	+0.81
5053	II	-2.05±0.14 ³	-2.18	-2.07	0.46±0.08	3	-2.00±0.18	-2.05	-2.06	0.55±0.05	4	7	0.18	+0.52
5466	II	-2.04±0.14 ³	-2.16	-2.01	0.44±0.09	8	-1.90±0.21	-1.89	-1.96	0.53±0.06	5	8	0.00	+0.58
6205 (M13)	II	-1.60	-1.54	-1.00	0.38	1	-1.70±0.20	-1.63	-1.71	0.59±0.05	3	29	0.02	+0.95
6254 (M10)	II?	-	-	-	-	-	-1.59	-1.52	-1.52	0.52	1	32	0.25	+0.92
6333 (M9)	II	-1.91±0.13 ³	-1.96	-1.72	0.47±0.04	7	-1.71±0.23	-1.66	-1.66	0.55±0.04	6	9	diff.	+0.87
6341 (M92)	II	-2.12±0.18 ³	-2.16 ⁵	-2.26	0.45±0.03	9	-2.01±0.11	-2.11	-2.17	0.53±0.06	3	10	0.02	+0.91
7078 (M15)	II	-2.22±0.19 ³	-2.46	-2.65	0.51±0.04	9	-2.10±0.07	-2.24	-2.27	0.52±0.03	8	15	0.08	+0.67
7089 (M2)	II	-1.60±0.18	-1.51	-1.25	0.53±0.13	10	-1.76±0.16	-1.73	-1.76	0.51±0.08	2	16	0.06	+0.11
7099 (M30)	II	-2.07±0.05 ³	-2.21	-1.88	0.40±0.04	3	-2.03	-2.14	-2.07	0.54	1	17	0.03	+0.77
7492	II	-1.89 ^{3,4}	-1.93	-0.83	0.37	1	-	-	-	-	-	18 ⁵	0.00	+0.76
6402 (M14)	Int	-1.44±0.17	-1.32	-1.17	0.53±0.07	24	-1.23±0.21	-1.12	-1.12	0.58±0.05	36	32	0.57	+0.56
6779 (M56)	Int	-1.76	-1.74	-1.74	0.53	1	-1.96	-2.03	-2.05	0.51	1	34	0.26	+0.82
6388	III	-1.35±0.05	-1.23	-1.00	0.53±0.04	2	-0.67±0.24	-0.64	-0.56	0.61±0.07	6	12	0.40	-0.69
6441	III	-1.35±0.17	-1.23	-0.80	0.43±0.08	7	-1.02±0.34	-0.82	-1.00	0.55±0.08	8	13	0.51	-0.73

Notes: ¹ Quoted uncertainties are 1- σ errors calculated from the scatter in the data for each cluster. The number of stars considered in the calculations is given by N. ² The only RRL V1 is probably not a cluster member. ³ This value has a -0.21 dex added, see § 1 for a discussion. ⁴ Adopted since published Fourier coefficients are insufficient. ⁵ Based on one light curve not fully covered.

References are the source of the Fourier coefficients: 1. Arellano Ferro et al. (2013b); 2. Kains et al. (2012); 3. Arellano Ferro et al. (2014); 4. Arellano Ferro et al. (2018b); 5. Kains et al. (2015); 6. Arellano Ferro et al. (2011); 7. Arellano Ferro et al. (2010); 8. Arellano Ferro et al. (2008b); 9. Arellano Ferro et al. (2013a); 10. Yepez et al. (2020); 11. Arellano Ferro et al. (2008a); 12. Pritzl et al. (2002); 13. Pritzl et al. (2001); 14. Bramich et al. (2011); 15. Arellano Ferro et al. (2006); 16. Lázaro et al. (2006); 17. Kains et al. (2013); 18. Figuera Jaimes et al. (2013); 19. Arellano Ferro et al. (2016); 20. Arellano Ferro et al. (2015b); 21. Tsapras et al. (2017); 22. Deras et al. (2018); 23. Walker (1998); 24. Cacciari et al. (2005); 25. Arellano Ferro et al. (2019); 26. Yepez et al. (2018); 27. Arellano Ferro et al. (2018a); 28. Yepez et al. (2019); 29. Deras et al. (2019); 30. Deras et al. (2020); 31. Arellano Ferro et al. (2020); 32. Yepez et al. (2022); 33. Rojas Galindo et al. (2021); 34. Deras et al. (2022)

$$[\text{Fe}/\text{H}]_{\text{ZW}} = 52.466P^2 - 30.075P + 0.131\phi_{31}^{(c)2} - 0.982\phi_{31}^{(c)} - 4.198\phi_{31}^{(c)}P + 2.424, \quad (3)$$

from Jurcsik & Kovács (1996) and Morgan et al. (2007) for RRab and RRc stars, respectively. In the above equations, $\phi^{(c)}$ and $\phi^{(s)}$ are the phases calculated either on a cosine or a sine series respectively,

and they are correlated as $\phi^{(s)} = \phi^{(c)} - \pi$. The iron abundance on the Jurcsik & Kovács (1996) scale can be converted into the Zinn & West (1984) scale using the equation $[\text{Fe}/\text{H}]_{\text{J}} = 1.431[\text{Fe}/\text{H}]_{\text{ZW}} + 0.88$ (Jurcsik 1995). Then, the $[\text{Fe}/\text{H}]_{\text{ZW}}$ can be transformed into the spectroscopic scale $[\text{Fe}/\text{H}]_{\text{UV}}$ defined by Carretta et al. (2009) from high resolution spec-

troscopic determinations of the iron abundance, via the relation: $[\text{Fe}/\text{H}]_{\text{UV}} = -0.413 + 0.130 [\text{Fe}/\text{H}]_{\text{ZW}} - 0.356 [\text{Fe}/\text{H}]_{\text{ZW}}^2$.

Nemec et al. (2013) calculated non-linear calibrations of $[\text{Fe}/\text{H}]$ in terms of ϕ_{31} and pulsating period, using as calibrators the iron to hydrogen abundances of 26 RRab and 110 RRC stars calculated from high dispersion spectroscopy. For the RRC stars they added four RRC stars to the original 106 used by Morgan et al. (2007) (equation 3), and removed *a posteriori* nine outlier stars. Nemec’s calibrations for the RRab and RRC stars are respectively of the form;

$$[\text{Fe}/\text{H}]_{\text{N}} = -8.65 - 40.12P + 5.96\phi_{31}^{(s)}(K) + 6.27\phi_{31}^{(s)}(K)P - 0.72\phi_{31}^{(s)}(K)^2, \quad (4)$$

where $\phi_{31}^{(s)}(K) = \phi_{31}^{(s)} + 0.151$ is given in the *Kepler* scale (Nemec et al. 2013), and

$$[\text{Fe}/\text{H}]_{\text{N}} = 1.70 - 15.67P + 0.20\phi_{31}^{(c)} - 2.41\phi_{31}^{(c)}P + 18.0P^2 + 0.17\phi_{31}^{(c)2}. \quad (5)$$

As pointed out by Nemec et al. (2013), since the above calibrations are based on high resolution spectroscopic determinations of $[\text{Fe}/\text{H}]$, the derived values $[\text{Fe}/\text{H}]_{\text{N}}$ are on the UV scale of Carretta et al. (2009). Thus, they should be comparable to the values $[\text{Fe}/\text{H}]_{\text{UV}}$, a point on which we shall comment below.

For the calculation of M_V we adopted the calibrations:

$$M_V = -1.876 \log P - 1.158A_1 + 0.821A_3 + 0.41, \quad (6)$$

$$M_V = -0.961P - 0.044\phi_{21}^{(s)} - 4.447A_4 + 1.061, \quad (7)$$

from Kovács & Walker (2001) and Kovács & Kanbur (1998) for the RRab and RRC stars, respectively. The zero points of equations 6 and 7 have been calculated to scale the luminosities of RRab and RRC stars to the distance modulus of 18.5 mag for the Large Magellanic Cloud (LMC) (see the discussion in § 4.2 of Arellano Ferro et al. (2010).

In Table 1 we list the globular clusters studied by our team and the resulting $[\text{Fe}/\text{H}]$ in the scales of Zinn & West (1984), Carretta et al. (2009) and Nemec et al. (2013), i.e. $[\text{Fe}/\text{H}]_{\text{ZW}}$, $[\text{Fe}/\text{H}]_{\text{UV}}$ and $[\text{Fe}/\text{H}]_{\text{N}}$ and M_V , estimated via the Fourier decomposition of the light curves of the RRab and RRC stars. To this end, we have taken the Fourier parameters published in the original papers and applied the above calibrations for the sake of homogeneity. We have also included the two metal-rich

clusters NGC 6388 and NGC 6441 studied by Pritzl et al. (2002, 2001), NGC 1851 (Walker 1998) and NGC 5272 (M3) (Cacciari et al. 2005) since the light curve Fourier decomposition parameters are available in those papers. In order to increase the sample, the clusters NGC 5286, NGC 6266 and NGC 6809, have been added. For these, Fourier-based physical parameters have been reported by Zorotovic et al. (2010), Contreras et al. (2010) and Olech et al. (1999) respectively and the results have been duly transformed to the proper scales by Kains et al. (2012). In all these calculation of the Fourier-based physical parameters, we have systematically avoided clear Blazhko variables or any amplitude modulated stars. All the relevant papers are recorded in the notes to Table 1.

The use of the above equations and their zero points forms the basis of the discussion of the M_V - $[\text{Fe}/\text{H}]$ relation and the cluster distances on a homogeneous scale, which we present in the following sections.

4. VINDICATION OF THE PHOTOMETRIC APPROACH TO THE METALLICITIES

There is absolutely no doubt that the most precise approach to the determination of metallicities of heavenly bodies is via high-resolution spectroscopy. The practical limitations to that technique are several however; to reach deep in magnitude, typical of the HB in most globular clusters, long exposure times with large telescopes are required, making it unaffordable. The spectroscopic values for 19 clusters listed by Carretta et al. (2009) were obtained in numerous previous papers cited by these authors. The analyses were carried on luminous red giants of $V \approx 14 - 16$ mag, i.e. 2-3 magnitudes brighter than RRL stars at the HB, and after an enormous compromise of observational and computational resources. While this situation may change with the advent of in-orbit high resolution spectrographs, the competition for access to the instrumentation will likely remain tough. The photometric approach to the metallicity and luminosity calculation in RRL stars was envisaged in the 1980’s (Simon & Teays 1982), and became a popular alternative since it reaches as low as $V \approx 20$ mag with sufficient accuracy with very short exposure times on 1-2 m-class telescopes, enabling the access to larger samples of clusters. The Fourier decomposition approach was further developed to produce the calibrations in § 3 employed in this paper.

Our goal in this section is to compare the photometric values reported in this work with the spectroscopic values of Carretta et al. (2009). Figure 1

shows the photometric based values of $[\text{Fe}/\text{H}]$ in the UV and Nemec scales (Table 1) for the RRab and RRc stars, plotted versus the spectroscopic values given by Carretta et al. (2009). In Panels (a) and (b) it is clear that the comparison is satisfactory for the case of $[\text{Fe}/\text{H}]_{\text{UV}}$. However, for $[\text{Fe}/\text{H}]_{\text{N}}$ the RRab calibration seems to systematically overestimate the metallicity relative to the spectroscopic values. The iron values from Nemec's calibration for RRc stars also compare well with the spectroscopic values. There is a mild suggestion in both panels (b) and (d) that the calibrations for the RRc stars of equations 3 and 5, which are in fact based on the same set of calibrators, may require a small adjustment of about -0.2 dex for iron values smaller than -2.0 .

5. THE M_V - $[\text{Fe}/\text{H}]$ CORRELATION

It has been argued that equation 2 overestimates $[\text{Fe}/\text{H}]$ for metal-poor clusters. This problem has been addressed by Jurcsik & Kovács (1996), Schwarzenberg-Czerny & Kaluzny (1998), Kovács (2002), Nemec (2004) and Arellano Ferro et al. (2010). It is difficult to quantify a correction to be applied, and it is likely also a function of the metallicity. However, empirical estimations in the above papers point to a value between -0.2 and -0.3 dex on the scale of equation 2. We have adopted -0.3 dex, which on the ZW scale is equivalent to -0.21 dex. Equally difficult is to define a value of $[\text{Fe}/\text{H}]_{\text{ZW}}$ below which the corrections should be applied. Guided by the metallicity values of globular clusters in the spectroscopic scale of Carretta et al. (2009), we estimated that a reasonable limit would be $[\text{Fe}/\text{H}]_{\text{ZW}} < -1.7$. Therefore, the values listed in Table 1 for clusters with $[\text{Fe}/\text{H}]_{\text{ZW}} < -1.7$ dex were obtained by adding -0.21 dex to the value of $[\text{Fe}/\text{H}]_{\text{ZW}}$ found via equation 2. As a consequence the $[\text{Fe}/\text{H}]_{\text{UV}}$ values for these clusters are also affected by this correction. Note that the good comparison between the photometric $[\text{Fe}/\text{H}]_{\text{UV}}$ and the spectroscopic values displayed in Figure 1 (a) was obtained after the application of the correction above.

In Figure 2 we show the distribution of clusters in the M_V - $[\text{Fe}/\text{H}]$ plane obtained from the RRab stars (left panel) and the RRc stars (right panel). In each of these panels we display the resulting distributions for the three involved scales $[\text{Fe}/\text{H}]_{\text{ZW}}$, $[\text{Fe}/\text{H}]_{\text{UV}}$ and $[\text{Fe}/\text{H}]_{\text{N}}$. In the middle and bottom boxes, for the spectroscopic scales $[\text{Fe}/\text{H}]_{\text{UV}}$ and $[\text{Fe}/\text{H}]_{\text{N}}$, we include as reference, in gray colour, two theoretical, non-linear, versions of the M_V - $[\text{Fe}/\text{H}]$ relation of Cassisi et al. (1999) and Vandenberg et al. (2000).

We shall discuss these correlations separately for the RRab and RRc stars.

5.1. From RRab Stars in Globular Clusters

The trend between $[\text{Fe}/\text{H}]$ in all scales and M_V is evident, as much as the large scatter. There are a few outliers, labeled in the figure, that were not considered in the calculations of the fitted regressions (with the exception of M15). However, some evidence of non-linearity is suggested in the central and bottom panels of Figure 2, particularly oriented by the presence of M15 that is the most metal-poor cluster in the sample; hence its relevance. It is also worth noting that Nemec et al. (2013) calibration, equation 4, includes a wider selection of calibrators with metallicities below -2.0 , and as low as $[\text{Fe}/\text{H}] \approx -2.68$ (for star X Ari). Since the number of stars involved in the calculation of the physical parameters varies from cluster to cluster, all the fits below have been weighted by $1/(\sigma_i^2/N_i)$. The quadratic fits for $[\text{Fe}/\text{H}]_{\text{UV}}$ and $[\text{Fe}/\text{H}]_{\text{N}}$ are of the form:

$$M_V = 1.016(\pm 0.170) + 0.428(\pm 0.207)[\text{Fe}/\text{H}]_{\text{UV}} + 0.081(\pm 0.060)[\text{Fe}/\text{H}]_{\text{UV}}^2, \quad (8)$$

with an rms=0.060 mag, and

$$M_V = 0.740(\pm 0.056) + 0.141(\pm 0.077)[\text{Fe}/\text{H}]_{\text{N}} + 0.013(\pm 0.026)[\text{Fe}/\text{H}]_{\text{N}}^2, \quad (9)$$

with an rms=0.060 mag.

The quadratic empirical solutions for $[\text{Fe}/\text{H}]_{\text{UV}}$, shown in Figure 2 (b), is remarkably similar to the theoretical predictions of Vandenberg et al. (2000) and Cassisi et al. (1999), in shape and luminosity level. To our knowledge, this is the first empirical solution that reproduces the theoretical predictions of the non-linear nature of the correlation, which it has likely been enabled by the homogeneous treatment of a large number of clusters, and the distinction of RRab and RRc stars.

We call attention to the inclusion of the metal rich cluster NGC 6366 ($-0.77, 0.71$) in the UV correlation for the RRab, in spite of its metallicity being derived from a single star that might not be a cluster member (Arellano Ferro et al. 2008b). However, excluding it or employing the value $[\text{Fe}/\text{H}]=-0.59$ listed by Harris (1996) makes no significant variation in the correlation.

5.2. From RRc Stars in Globular Clusters

The mean $[\text{Fe}/\text{H}]$ and M_V determined from the RRc stars in the family of studied globular clusters

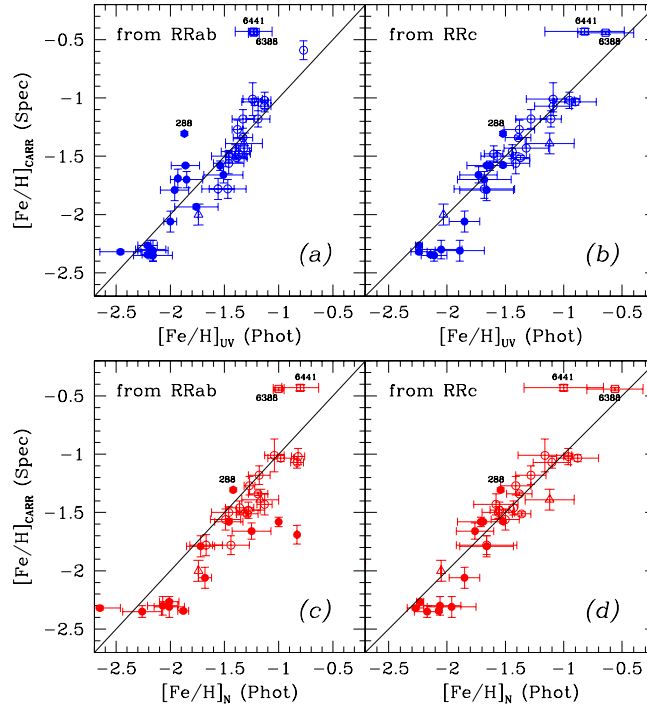


Fig. 1. Comparison of the Fourier based $[\text{Fe}/\text{H}]$ (Table 1), with those from high-resolution spectroscopy based values from Carretta et al. (2009). Filled and empty circles represent OoII and OoI clusters respectively. Open triangles and squares represent OoInt and OoIII clusters. See § 4 for a discussion. The color figure can be viewed online.

are correlated, as shown in the right panel of Figure 2. Immediate differences are seen when compared to the cases from the RRab stars: the slopes are milder, the distributions in the three metallicity scales are all very similar, the correlations are strikingly tight, in spite of which no suggestion of a non-linear correlation is evident. It should also be noted that the Oo-int (triangles) and the OoIII clusters (squares) follow the trends well.

The linear correlations for the $[\text{Fe}/\text{H}]_{\text{UV}}$ and $[\text{Fe}/\text{H}]_{\text{N}}$ can be expressed as:

$$M_V = 0.034(\pm 0.009)[\text{Fe}/\text{H}]_{\text{UV}} + 0.601(\pm 0.015), \quad (10)$$

and

$$M_V = 0.050(\pm 0.004)[\text{Fe}/\text{H}]_{\text{N}} + 0.641(\pm 0.006), \quad (11)$$

with an rms=0.022 mag.

Equations 10 and 11 are basically identical. The reason is that, although the values of $[\text{Fe}/\text{H}]_{\text{UV}}$ and $[\text{Fe}/\text{H}]_{\text{N}}$, come from different formulations (equations 3 and 5), both calibrations come essentially from the same set of calibrator stars, since Nemec et al. (2013) took the calibrators from Morgan et al.

(2007), and added four stars, for a total sample of 101 stars.

The remarkable difference of the cluster distribution on the M_V - $[\text{Fe}/\text{H}]$ plane for the luminosity and metallicity determinations from the Fourier decomposition for RRab and RRc stars, does require some considerations. Naturally one may wonder if this is an artifact of the calibrations employed to transform Fourier parameters into physical parameters. However, the good agreement of the photometric metallicities $[\text{Fe}/\text{H}]_{\text{UV}}$ and the spectroscopic values (Figure 1 (a)), and also the good cluster distance agreement with independent high-quality determinations presented below in § 6, offer support to the photometric calibrations given in § 3 and their results in Table 1. In our opinion, the run of $[\text{Fe}/\text{H}]$ with M_V and the scatter seen in RRab stars are a consequence of the interconnection of the following: RRab stars are larger amplitude variables with a more complex light curve morphology; often the light maximum is very acute, and they are prone to display amplitude and phase modulations. Therefore, their Fourier decomposition is subject to further uncertainties as they require a larger number of harmonics for a proper representation. Their larger periods may also limit a proper coverage of their pul-

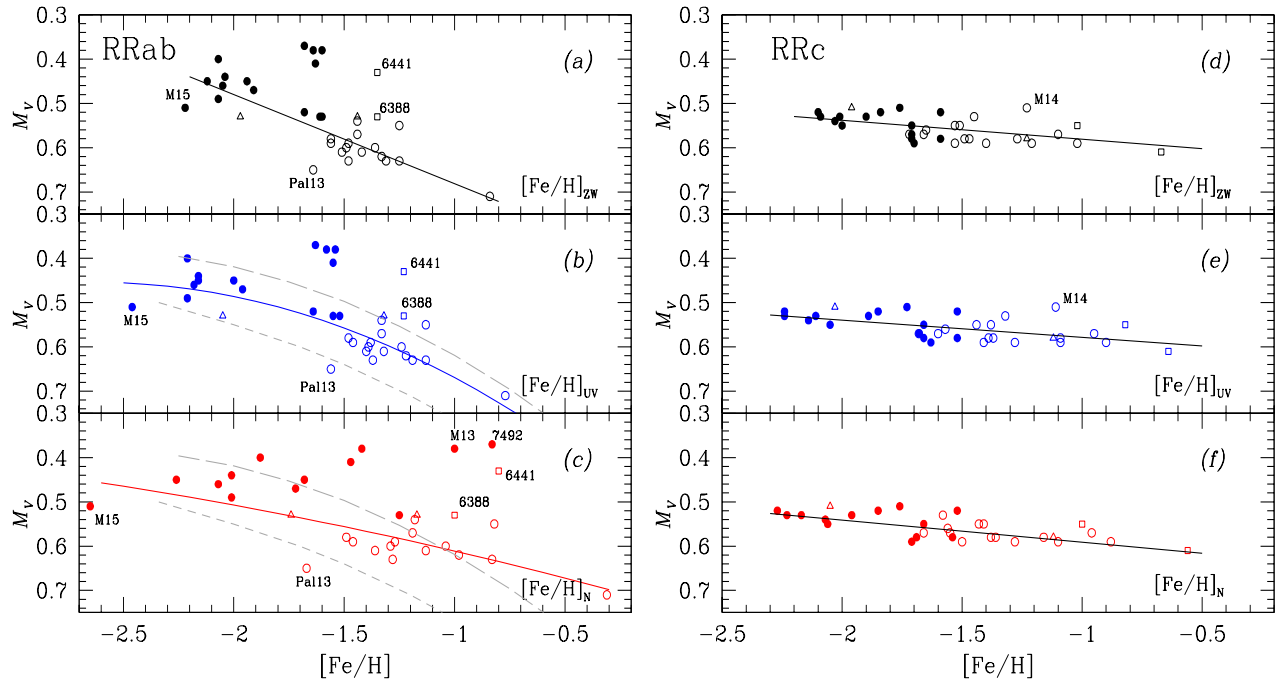


Fig. 2. The $[\text{Fe}/\text{H}]$ versus M_V correlations for RRab and RRc stars. The involved metallicity scale is, from top to bottom panels, $[\text{Fe}/\text{H}]_{\text{ZW}}$, $[\text{Fe}/\text{H}]_{\text{UV}}$ and $[\text{Fe}/\text{H}]_{\text{N}}$. Filled and open circles represent OoII and OoI clusters respectively. Open triangles and squares represent OoInt and OoIII clusters. All fits have been weighted by the number of stars included in each cluster. In the left panel, the gray curves are the theoretical predictions of Cassisi et al. (1999) (long dash) and VandenBerg et al. (2000) (short dash), which are strikingly similar to the photometric solution in panel (b). The color figure can be viewed online.

sating cycle. Also, RRab stars in a given cluster may display small evolutionary stage differences, spreading a luminosity range. These circumstances have their impact on the calibration of the Fourier parameters and on the resultant scatter in the M_V - $[\text{Fe}/\text{H}]$ plane. On the other hand, RRc stars have simpler light curves, mostly sinusoidal, and are more concentrated towards the ZAHB; thus, their Fourier and physical parameters tend to be better correlated.

In summary, the HB luminosity-metallicity correlation seen from the RRab stars is steeper (a fact that had already been reported by ABG17), more scattered and non-linear, whereas from the RRc stars the relation is milder but better defined and linear. RRab and RRc stars should not be mixed for the purpose of studying or applying the correlation as a distance indicator instrument. Therefore, for the sake of estimating a globular cluster distance from its RRL, given its metallicity, one should prefer the RRc stars whenever possible, and either equations 10 or 11.

5.3. The Role of the HB Structure Parameter

Demarque et al. (2000), have argued on theoretical grounds that the overall structure of the HB plays

a relevant role and may be interconnected with the HB luminosity and the metallicity of the parental globular cluster. Here we explore the role of the HB type parameter, or Zinn-Lee parameter, defined as $\mathcal{L} = (B - R)/(B + V + R)$ (Zinn 1986; Lee 1990), from empirical arguments. B , V and R represent the number of stars to the blue of the instability strip (IS), the number of RRL stars, and to the red of the IS respectively. For a better calculation of \mathcal{L} , it is convenient to include, as far as possible, only cluster member stars in the counting. Since the list of \mathcal{L} values for a large number of clusters presented by Torelli et al. (2019) is the result of membership considerations, we have adopted them for the subsequent analysis. When a cluster is not included in the above list we used the value reported by Catelan (2009). The one exception is NGC 7079 (M2). For this cluster, the reported value is $\mathcal{L}=+0.96$. The analysis of the projected positions and proper motions available in the *Gaia*-eDR3 data base, and the application of the method of Bustos Fierro & Calderón (2019), kindly performed by Dr. Bustos Fierro, renders a CMD of very likely cluster member stars, with a substantial population of red HB stars for $\mathcal{L}=+0.34$, which shall

be adopted. For a few other clusters where similar analyses have been carried out, \mathcal{L} values close to those of Torelli et al. (2019) were found.

Figure 3 illustrates the correlation between \mathcal{L} and M_V , the latter as obtained from the Fourier decomposition for RRab stars (top panel) and RRC stars (bottom panel). In the case of the RRab stars the correlation clearly shows a quadratic trend, once the two Oo-Int clusters, NGC 6388 and NGC 6441, were excluded. In the case of the RRC stars the correlation appears linear with a very mild slope. The corresponding fits in Figure 3 are of the form:

$$M_V = 0.620(\pm 0.011) - 0.029(\pm 0.018)\mathcal{L} - 0.135(\pm 0.036)\mathcal{L}^2, \quad (12)$$

with an rms = 0.058, and

$$M_V = 0.558(\pm 0.006) - 0.019(\pm 0.013)\mathcal{L}, \quad (13)$$

with an rms = 0.026.

Considering the trends in Figure 2 for the RRab and RRC, both for the $[\text{Fe}/\text{H}]_{\text{UV}}$ values (middle panels), and in Figure 3, the dependence of M_V on the metallicity $[\text{Fe}/\text{H}]$ and HB structure parameter \mathcal{L} , can be expressed, for the RRab and RRC respectively as:

$$M_V = A + B[\text{Fe}/\text{H}]_{\text{UV}} + C[\text{Fe}/\text{H}]_{\text{UV}}^2 + D\mathcal{L} + E\mathcal{L}^2, \quad (14)$$

with $A=+1.096(\pm 0.141)$, $B=+0.519(\pm 0.172)$, $C=+0.119(\pm 0.050)$, $D=+0.006(\pm 0.014)$, $E=-0.111(\pm 0.029)$, and rms = 0.053 mag.

$$M_V = +0.609(\pm 0.016) + 0.032(\pm 0.009)[\text{Fe}/\text{H}]_{\text{UV}} + 0.015(\pm 0.011)\mathcal{L}, \quad (15)$$

with rms = 0.024 mag.

The equivalent calibrations in terms of the metallicity in the scale of Nemec et al. (2013), $[\text{Fe}/\text{H}]_{\text{N}}$ are:

$$M_V = A + B[\text{Fe}/\text{H}]_{\text{N}} + C[\text{Fe}/\text{H}]_{\text{N}}^2 + D\mathcal{L} + E\mathcal{L}^2, \quad (16)$$

with $A=+0.720(\pm 0.082)$, $B=+0.130(\pm 0.098)$, $C=+0.033(\pm 0.029)$, $D=-0.043(\pm 0.020)$, $E=-0.145(\pm 0.030)$, and rms = 0.055 mag.

$$M_V = +0.655(\pm 0.019) + 0.063(\pm 0.013)[\text{Fe}/\text{H}]_{\text{N}} + 0.012(\pm 0.009)\mathcal{L}, \quad (17)$$

with rms = 0.019 mag.

For the calibration of equations 14 and 16 from the RRab solutions, the terms involving \mathcal{L} are small but significant. On the contrary, equations 15 and

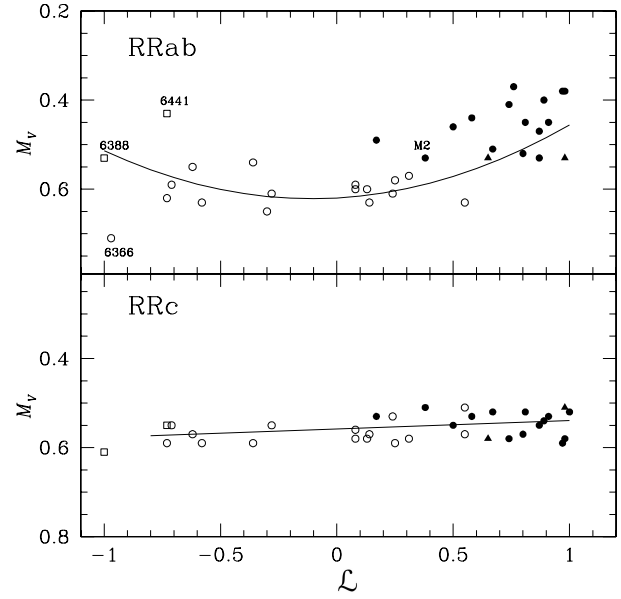


Fig. 3. The HB structure parameter \mathcal{L} vs. mean M_V for a family of clusters coded as in Figure 1. Two open squares for the OoIII clusters were not considered in the weighted fits.

17 from the RRC solutions, the last term is insignificant, and in fact, for instance equations 10 and 15 in the UV scale, or equations 11 and 17 in the Nemec's scale, are, within the uncertainties, indistinguishable, confirming the linearity and sufficiency of an M_V - $[\text{Fe}/\text{H}]$ relation for the RRC stars.

Therefore, the empirical M_V - $[\text{Fe}/\text{H}]$ relation as worked out from the Fourier decomposition of RRab stars light curves, has turned out to be much more complex, with the metallicity and HB structure playing a measurable role, and equations 14 and 16 are a good representation.

For the RRC stars, with simpler light curves and generally being more confined near the ZAHB, the M_V - $[\text{Fe}/\text{H}]$ relation remains linear and simple, and the structure of the HB does not seem to play any pertinent role; equation 10 and 11, or for any purpose equations 15 and 17, are good empirical calibrations, with a well established slope around 0.06.

6. GLOBULAR CLUSTER DISTANCES

Once the mean absolute magnitude M_V for the HB is obtained for a given cluster, its distance can be estimated for an assumed value of $E(B-V)$. Using the values listed in Table 1 the distances were calculated and are listed in Table 2 as they were obtained either for the RRab or RRC stars from equations 6 and 7 respectively. We perform a comparison with accurate mean distances recently estimated

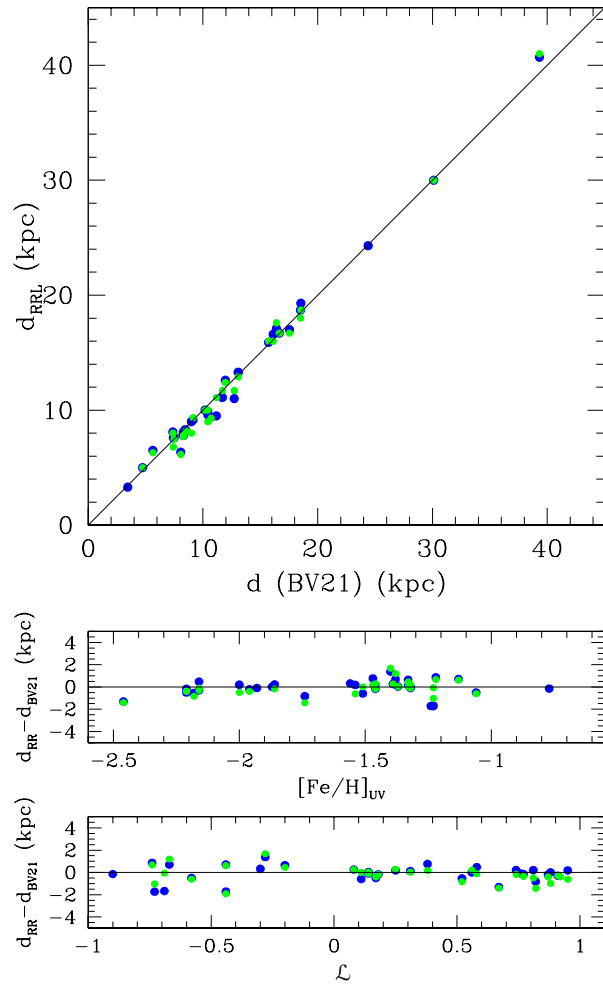


Fig. 4. Comparison of distances obtained from the RRL Fourier decomposition and those of BV21. Blue and green symbols stand for distances derived from RRab and RRc Fourier light curve treatment, respectively. The color figure can be viewed online.

by Baumgardt & Vasiliev (2021) (hereinafter BV21), calculated for a large sample of globular clusters using the data from *Gaia*-eDR3, *HST* and selected literature distances.

It should be obvious from Table 2 that the distances derived from our Fourier approach (Columns 2 and 3) agree with those of BV21. Figure 4 is a graphical comparison and shows how the distance differences do not correlate either with the metallicity or with the HB structure parameter. The Fourier and the BV21 distances differences are all smaller than 1.7 kpc and display a standard deviation of 0.7 kpc.

The agreement is remarkably good considering that the distance determinations come from completely independent approaches. We note that the

distances obtained from the M_V calibrations for RRab and RRc stars, are also independent, as they come from different and independent calibrations. This gives further support to the M_V calibrations of equations 6 and 7 and to their zero points (Arellano Ferro et al. 2010).

The accurate distances of individual globular clusters obtained from the RRL stars listed in Table 4, can serve as a frame of comparison of other independent methods to calculate cluster distances. Given that SX Phe stars are common in globular clusters, they can be used as secondary distance indicators through their well established P-L relation, of which, however, different calibrations are found in the literature. We shall explore the consistency of the results. We considered the calibrations of Arellano Ferro et al. (2011) (AF11), and Cohen & Sarajedini (2012) (CS12). The resulting distances from these two calibrations of 13 clusters with well observed SX Phe stars are listed in Columns 4 and 6 of Table 2, Column 5 indicates the number of member SX Phe stars available in each cluster. We should emphasize that the two calibrations lead to distances agreeing within 1.3 kpc, except for NGC 6934 where the distance differences is ≈ 2.0 kpc for the CS12 calibration. The SX Phe distances agree with the RRL results well within 1 kpc, i.e. the average RRL and SX Phe distance match in average by $\approx 4\%$ of the corresponding distance.

7. VARIABLE STARS IN OUR SAMPLE OF GLOBULAR CLUSTERS

Once a CCD time-series photometry is performed on a given cluster, a by-product of the exercise is the discovery of previously undetected variables. In the work carried by our group, we have systematically searched for variables via a variety of approaches described in the individual papers, e.g. Arellano Ferro et al. (2013b). In Table 3 we summarize the number of variables, and their types, known in the globular clusters of our sample, noting the ones found by our work. We have found 326 new variables in the field of the clusters, 23 of them are either considered field stars or have not been classified. The most numerous families are in order RRab, RRc, SR, SX Phe, eclipsing binaries, CW and double mode RRd stars. The total number of variables detected in these clusters is 2047 but only 1886 are likely to be truly cluster members. Thus, about 16% of the variables in this sample of clusters has been found by our VI CCD time-series imaging program.

TABLE 2

DISTANCES FOR A SAMPLE OF GLOBULAR CLUSTERS ESTIMATED HOMOGENEOUSLY FROM THE RRL STARS LIGHT CURVE FOURIER DECOMPOSITIONS

GC NGC(M)	$d(kpc)$ (RRab)	$d(kpc)$ (RRc)	$d(kpc)$ (SX Phe) P-L AF11	No. of SX Phe	$d(kpc)$ (SX Phe) P-L CS12	$E(B - V)$	$d(kpc)$ BV21
288	9.0±0.2	8.0	8.8±0.4	6	9.4±0.6	0.03	8.988
1261	17.1±0.4	17.6±0.7	–	–	–	0.01	16.400
1851	12.6±0.2	12.4±0.2	–	–	–	0.02	11.951
1904 (M79)	13.3±0.4	12.9	–	–	–	0.01	13.078
3201	5.0±0.2	5.0±0.1	4.9±0.3	16	5.2±0.4	dif	4.737
4147	19.3	18.7±0.5	–	–	–	0.02	18.535
4590 (M68)	9.9±0.3	10.0±0.2	9.8±0.5	6	–	0.05	10.404
5024 (M53)	18.7±0.4	18.0±0.5	18.7±0.6	13	20.0±0.8	0.02	18.498
5053	17.0±0.4	16.7±0.4	17.1±1.1	12	17.7±1.2	0.02	17.537
5272	10.0±0.2	10.0±0.4	–	–	–	0.01	10.175
5466	16.6±0.2	16.0±0.6	15.4±1.3	5	16.4±1.3	0.00	16.120
5904 (M5)	7.6±0.2	7.5±0.3	6.7±0.5	3	7.5±0.2	0.03	7.479
6205 (M13)	7.6	6.8±0.3	7.2±0.7	4	–	0.02	7.419
6171	6.5±0.3	6.3±0.2	–	–	–	0.33	5.631
6229	30.0±1.5	30.0±1.1	27.9	1	28.9	0.01	30.106
6254 (M10)	–	4.7	5.2±0.3	15	5.6±0.3	0.25	5.067
6333 (M9)	8.1±0.2	7.9±0.3	–	–	–	dif	8.300
6341 (M92)	8.2±0.2	8.2±0.4	–	–	–	0.02	8.501
6362	7.8±0.1	7.7±0.2	7.1±0.2	6	7.6±0.2	0.09	8.300
6366	3.3	–	–	–	–	0.80	3.444
6388	9.5±1.2	11.1±1.1	–	–	–	0.40	11.171
6401	6.35±0.7	6.15±1.4	–	–	–	dif	8.064
6402 (M14)	9.1±0.9	9.3±0.5	–	–	–	0.57	9.144
6441	11.0±1.8	11.7±1.0	–	–	–	0.51	12.728
6712	8.1±0.2	8.0±0.3	–	–	–	0.35	7.382
6779 (M56)	9.6	9.0	–	–	–	0.26	10.430
6934	15.9±0.4	16.0±0.6	15.8	1	18.0	0.10	15.716
6981 (M72)	16.7±0.4	16.7±0.4	16.8±1.6	3	18.0±1.0	0.06	16.661
7006	40.7±1.6	41.0±1.6	–	–	–	0.08	39.318
7078 (M15)	9.4±0.4	9.3±0.6	–	–	–	0.08	10.709
7089 (M2)	11.1±0.6	11.7±0.02	–	–	–	0.06	11.693
7099 (M30)	8.32±0.3	8.1	8.0	1	8.3	0.03	8.458
7492	24.3	–	22.1±3.2	2	24.1±3.7	0.00	24.390
Pal 13	23.8±0.6	–	–	–	–	0.10	23.475

8. CONCLUSIONS

A homogeneous approach towards the determination of mean M_V and $[Fe/H]$ from the Fourier decomposition of the cluster member RRL light curves, enables a new empirical exploration of the nature of the M_V - $[Fe/H]$ relation, which describes the dependence of the luminosity of the HB on the metallicity. Although numerous efforts, from assorted strategies, have been performed to establish the zero point and slope of the relation, universal values have been elusive. We found that, if the RRL stars are to be used as indicators of the form of the relation, or if this is to be employed as a distance indicator instrument, it should be treated independently for RRab and RRc stars. The reason is that the relation displays a different nature; for the RRab stars it is non linear with considerable scatter, while for the RRc it is tight, linear and the slope is mild.

Following the suggestion of theoretical works (Demarque et al. 2000), the inclusion of the HB structural parameter \mathcal{L} demonstrates that M_V is also correlated with \mathcal{L} , in a nonlinear fashion for the RRab analysis. For the RRc the role of \mathcal{L} is negligible. We offer a calibration M_V - $[Fe/H]$ - \mathcal{L} , with $[Fe/H]$ in the spectroscopic scale of Carretta et al. (2009) (equation 14) or in the Nemec et al. (2013) scale (equation 16) valid for RRab stars, and linear calibrations M_V - $[Fe/H]$ in the above two scales (equation 10 or equation 11) valid for RRc stars.

We find pertinent at this point to recall a well established result: that globular clusters harbour more than one generation of stars (e.g. Bedin et al. 2004; Piotto et al. 2005, 2007), and that each generation has a measurable different chemical abundance; particularly, the He content increases in later generations (Milone et al. 2018). As a result of different evolutionary sequences, the objects on the HB

TABLE 3

NUMBER OF PRESENTLY KNOWN VARIABLES PER CLUSTER FOR THE MOST COMMON VARIABLE TYPES, IN A SAMPLE OF GLOBULAR CLUSTERS STUDIED BY OUR GROUP†

GC NGC (M)	RRab	RRc	RRd	SX Phe	Binaries	CW-(AC)-RV	SR, L,M	Spotted	Unclass others *	Total per cluster	Ref.
288	0/1	0/1	0/0	0/6	0/1	0/0	0/1			0/10	1
1261	0/16	0/6	0/0	0/3	0/1	0/0	0/3			0/29	22
1904 (M79)	0/6	1/5	0/0	0/5	0/1	0/1	0/14		0/1	1/32	
3201	0/72	0/7	0/0	3/24	0/11	0/0	0/8	0/2	0/7	3/124	3
4147	0/5	0/19	0/1	0/0	0/14	0/0	2/2		0/3	2/41	4,23,35
4590 (M68)	0/14	0/16	0/12	4/6	0/0	0/0	0/0		1/2	4/48	5
5024 (M53)	0/29	2/35	0/0	13/28	0/0	0/0	1/12			16/104	6,7
5053	0/6	0/4	0/0	0/5	0/0	0/0	0/0			0/15	8
5466	0/13	0/8	0/0	0/9	0/3	0/1	0/0		2/2	0/34	9
5904 (M5)	2/89	1/40	0/0	1/6	1/3	0/2	11/12		0/1	16/152	17,18
6171 (M107)	0/15	0/6	0/0	0/1	0/0	0/0	2/3		0/3	2/25	24
6205 (M13)	0/1	1/7	2/2	2/6	1/3	0/3	3/22		0/4	9/44	25
6229	10/42	5/15	0/0	1/1	0/0	2/5	6/6		0/1	24/69	19
6254 (M10)	0/0	0/1	0/0	1/15	2/10	0/3	0/5		0/2	3/34	26
6333 (M9)	0/8	2/10	1/1	0/0	3/4	1/1	5/6		3/4	12/30	10
6341 (M92)	0/9	0/5	1/1	1/6	0/0	0/1	1/1		0/6	3/23	27
6362	0/16	0/15	1/3	0/6	0/12	0/0	0/0	0/3	0/22	1/55	28
6366	0/1	0/0	0/0	1/1	1/1	1/1	3/4			6/8	11
6388	1/14	2/23	0/0	0/1	0/10	1/11	42/58			46/117	21
6397	0/0	0/0	0/0	0/5	0/15	0/0	0/1		0/13	0/21	29
6401	6/23	6/11	0/0	0/0	0/14	0/1	3/3		14/14	15/52	20
6402 (M14)	0/55	3/56	1/1	1/1	0/3	0/6	18/32			23/154	30
6441	2/50	0/28	0/1	0/0	0/17	2/9	43/82		0/10	47/187	21
6528	1/1	1/1	0/0	0/0	1/1	0/0	4/4			7/7	21
6638	3/10	2/18	0/0	0/0	0/0	0/0	3/9		0/25	8/37	21
6652	0/3	0/1	0/0	0/0	1/2	0/1	0/2		1/5	1/9	21
6712	0/10	0/4	0/0	0/0	2/2	0/0	5/11		0/8	7/27	31
6779 (M56)	0/1	0/2	0/0	1/1	3/3	0/2	0/3		1/6	4/12	32
6934	3/68	0/12	0/0	3/4	0/0	2/3	3/5		1/6	11/92	33
6981 (M72)	8/37	3/7	0/0	3/3	0/0	0/0	0/1			14/48	12
7078 (M15)	0/65	0/67	0/32	0/4	0/3	0/2	0/3		0/11	0/176	13
7089 (M2)	5/23	3/15	0/0	0/2	0/0	0/4	0/0		0/12	8/44	14
7099 (M30)	1/4	2/2	0/0	2/2	1/6	0/0	0/0		0/3	6/14	17
7492	0/1	0/2	0/0	2/2	0/0	0/0	1/2			3/7	16
Pal 13	0/4	0/0	0/0	0/0	0/0	0/0	1/1			1/5	34
Total per type	41/713	35/448	6/54	39/153	16/140	9/57	157/316	0/5	23/161	303/1886	

†The variable star types are adopted from the General Catalog of Variable Stars (Kazarovets et al. 2009; Samus et al. 2009). Entries expressed as M/N indicate the M variables found or reclassified by our program and the total number N of presently known variables. Column 11 indicates the relevant papers on a given clusters.

*Numbers from this column are not considered in the totals. Here we include unclassified variables or likely field variables in the FoV of the cluster.

References: 1. Arellano Ferro et al. (2013a); 2. Kains et al. (2012); 3. Arellano Ferro et al. (2014a); 4. Arellano Ferro et al. (2004); 5. Kains et al. (2015); 6. Arellano Ferro et al. (2011); 7. Bramich & Freudling (2012); 8. Arellano Ferro et al. (2010); 9. Arellano Ferro et al. (2008a), 10. Arellano Ferro et al. (2013a), 11. Arellano Ferro et al. (2008b), 12. Bramich et al. (2011); 13. Arellano Ferro et al. (2006); 14. Lázaro et al. (2006); 15. Kains et al. (2013); 16. Figuera Jaimes et al. (2013); 17. Arellano Ferro et al. (2015a), 18. Arellano Ferro et al. (2016); 19. Arellano Ferro et al. (2015b); 20. Tsapras et al. (2017); 21. Skottfelt et al. (2015); 22. Arellano Ferro et al. (2019); 23. Arellano Ferro et al. (2018b); 24. Deras et al. (2018); 25. Deras et al. (2019); 26. Arellano Ferro et al. (2020); 27. Yepez et al. (2020); 28. Arellano Ferro et al. (2018a); 29. Ahumada et al. (2021); 30. Yepez et al. (2022); 31. Deras et al. (2020); 32. Deras et al. (2022); 33. Yepez et al. (2018); 34. Yepez et al. (2019); 35. Lata et al. (2019).

have a large range of He abundance causing the observed HB structure, particularly the color range, and the breadth; the higher the value of Y, the more luminous the corresponding ZAHB would be. Recently it has been shown that small variations in the He-burning core mass would also contribute to

the observed breadth of the HB (Yepez et al. 2022). Hence, the values of the \mathcal{L} parameter employed in the present investigation may be responding to these effects, which in turn may be responsible, at least partially, of the scatter observed in the correlations. Therefore, while it is helpful to identify the cluster

star members, as we have done, the identification of stars belonging to the different generations in each cluster might offer an important improvement on the calibration of the M_V -[Fe/H]- \mathcal{L} correlation.

To give support to our results, we compared the Fourier determinations of [Fe/H] with the spectroscopic values in the scale of Carretta et al. (2009) and found them to be in excellent agreement. The distances obtained from the mean Fourier M_V calibrations, and their zero points, have proven to match within 1.7 kpc and to display a difference dispersion with an rms of 0.7 kpc, with the independent and also homogeneous distances determined by Baumgardt & Vasiliev (2021) from *Gaia*-eDR3 and HST data.

The CCD time-series photometric study of globular clusters, in combination with difference image analysis, has been very fruitful in the discovery of new variables. Following the latest version of the Catalogue of Variable Stars in Globular Clusters (Clement et al. 2001), we updated in Table 3 the number of known variables per type and per cluster and indicated the numbers of variables found and classified by our program over the years, for a total of 303 out of the 1886 variables, likely to be cluster members, presently known in the family of the 35 clusters considered.

I am indebted to all my colleagues that have coauthored the numerous papers cited here, for their sincere dedication and implementation of their expertise to the several astrophysical fronts involved in the project. My special thanks to Prof. Sunetra Giridhar and Dr. Dan Bramich for extended discussions and very useful suggestions. A warm acknowledgement to Dr. Ivan Bustos Fierro for his willingness to decipher the stellar membership status in several clusters. I recognize with gratitude the many corrections and comments made by a very attentive anonymous referee, which triggered relevant modifications in the manuscripts. I am grateful to the institutions operating the employed telescopes for the time granted to our project, and to the many support staff members in all these observatories for making possible and efficient all our data gathering. The facilities at IAO and CREST are operated by the Indian Institute of Astrophysics, Bangalore. The project has been generously supported through the years by the program PAPIIT of the DGAPA-UNAM, México via several grants, the most recent being IG100620.

DATA AVAILABILITY

The data underlying this article shall be made available on request to the author (armando@astro.unam.mx).

REFERENCES

- Ahumada, J. A., Arellano Ferro, A., Bustos Fierro, I. H., et al. 2021, *New A*, 88, 101607, <https://doi.org/10.1016/j.newast.2021.101607>
- Arellano Ferro, A., Ahumada, J. A., Bustos Fierro, I. H., Calderón, J. H., & Morrell, N. I. 2018a, *AN*, 339, 183, <https://doi.org/10.1002/asna.201813465>
- Arellano Ferro, A., Ahumada, J. A., Calderón, J. H., & Kains, N. 2014, *RMxAA*, 50, 307
- Arellano Ferro, A., Bramich, D. M., Figuera Jaimes, R., et al. 2013a, *MNRAS*, 434, 1220, <https://doi.org/10.1093/mnras/stt1080>
- Arellano Ferro, A., Bramich, D. M., Giridhar, S., et al. 2013b, *AcA*, 63, 429
- Arellano Ferro, A., Bramich, D. M., & Giridhar, S. 2017, *RMxAA*, 53, 121
- Arellano Ferro, A., Bramich, D. M., Giridhar, S., Luna, A., & Muneer, S. 2015a, *IBVS*, 6137, 1
- Arellano Ferro, A., Bustos Fierro, I. H., Calderón, J. H., & Ahumada, J. A. 2019, *RMxAA*, 55, 337, <https://doi.org/10.22201/ia.01851101p.2019.55.02.18>
- Arellano Ferro, A., Figuera Jaimes, R., Giridhar, S., et al. 2011, *MNRAS*, 416, 2265, <https://doi.org/10.1111/j.1365-2966.2011.19201.x>
- Arellano Ferro, A., García Lugo, G., & Rosenzweig, P. 2006, *RMxAA*, 42, 75
- Arellano Ferro, A., Giridhar, S., & Bramich, D. M. 2010, *MNRAS*, 402, 226, <https://doi.org/10.1111/j.1365-2966.2009.15931.x>
- Arellano Ferro, A., Giridhar, S., Rojas López, V., et al. 2008a, *RMxAA*, 44, 365
- Arellano Ferro, A., Luna, A., Bramich, D. M., et al. 2016, *Ap&SS*, 361, 175, <https://doi.org/10.1007/s10509-016-2757-5>
- Arellano Ferro, A., Mancera Piña, P. E., Bramich, D. M., et al. 2015b, *MNRAS*, 452, 727, <https://doi.org/10.1093/mnras/stv1299>
- Arellano Ferro, A., Rojas Galindo, F. C., Muneer, S., & Giridhar, S. 2018b, *RMxAA*, 54, 325
- Arellano Ferro, A., Rojas López, V., Giridhar, S., & Bramich, D. M. 2008b, *MNRAS*, 384, 1444, <https://doi.org/10.1111/j.1365-2966.2007.12760.x>
- Arellano Ferro, A., Yepez, M. A., Muneer, S., et al. 2020, *MNRAS*, 499, 4026, <https://doi.org/10.1093/mnras/staa2977>
- Baumgardt, H. & Vasiliev, E. 2021, *MNRAS*, 505, 5957, <https://doi.org/10.1093/mnras/stab1474>
- Bedin, L. R., Piotto, G., Anderson, J., et al. 2004, *ApJ*, 605, 125, <https://doi.org/10.1086/420847>

- Benedict, G. F., McArthur, B. E., Feast, M. W., et al. 2011, *AJ*, 142, 187, <https://doi.org/10.1088/0004-6256/142/6/187>
- Bramich, D. M. 2008, *MNRAS*, 386, 77, <https://doi.org/10.1111/j.1745-3933.2008.00464.x>
- Bramich, D. M., Bachelet, E., Alsubai, K. A., Mislis, D., & Parley, N. 2015, *A&A*, 577, 108, <https://doi.org/10.1051/0004-6361/201526025>
- Bramich, D. M., Figuera Jaimes, R., Giridhar, S., & Arellano Ferro, A. 2011, *MNRAS*, 413, 1275, <https://doi.org/10.1111/j.1365-2966.2011.18213.x>
- Bramich, D. M. & Freudling, W. 2012, *MNRAS*, 424, 1584, <https://doi.org/10.1111/j.1365-2966.2012.21385.x>
- Bramich, D. M., Horne, K., Albrow, M. D., et al. 2013, *MNRAS*, 428, 2275, <https://doi.org/10.1093/mnras/sts184>
- Bustos Fierro, I. H. & Calderón, J. H. 2019, *MNRAS*, 488, 3024, <https://doi.org/10.1093/mnras/stz1879>
- Cacciari, C. & Clementini, G. 2003, *Stellar Candles for the Extragalactic Distance Scale*, ed. D. Alloin and W. Gieren, *LNP*, 635, 105
- Cacciari, C., Corwin, T. M., & Carney, B. W. 2005, *AJ*, 129, 267, <https://doi.org/10.1086/426325>
- Carretta, E., Bragaglia, A., Gratton, R., D’Orazi, V., & Lucatello, S. 2009, *A&A*, 508, 695, <https://doi.org/10.1051/0004-6361/200913003>
- Cassisi, S., Castellani, V., degl’Innocenti, S., Salaris, M., & Weiss, A. 1999, *A&AS*, 134, 103, <https://doi.org/10.1051/aas:1999126>
- Catelan, M. 2009, *Ap&SS*, 320, 261, <https://doi.org/10.1007/s1059-009-9987-8>
- Catelan, M. & Smith, H. A. 2015, *Pulsating Stars* (Weinheim, Germany: Wiley-VCH Verlag GmbH & Co)
- Chaboyer, B. 1999, *Globular Cluster Distance Determinations in Post-Hipparcos Cosmic Candles*, ed. A. Heck & F. Caputo (Boston, MA: Kluwer Academic Publishers), 111, https://doi.org/10.1007/978-94-011-4734-7_7
- Chaboyer, B., Demarque, P., Kernan, P. J., & Krauss, L. M. 1998, *ApJ*, 494, 96, <https://doi.org/10.1086/305201>
- Chaboyer, B., Demarque, P., & Sarajedini, A. 1996, *ApJ*, 459, 558, <https://doi.org/10.1086/176921>
- Clement, C. M., Muzzin, A., Dufton, Q., et al. 2001, *AJ*, 122, 2587, <https://doi.org/10.1086/323719>
- Cohen, R. E. & Sarajedini, A. 2012, *MNRAS*, 419, 342, <https://doi.org/10.1111/j.1365-2966.2011.19697.x>
- Contreras, R., Catelan, M., Smith, H. A., et al. 2010, *AJ*, 140, 1766, <https://doi.org/10.1088/0004-6256/140/6/1766>
- Demarque, P., Zinn, R., Lee, Y.-W., & Yi, S. 2000, *AJ*, 119, 1398, <https://doi.org/10.1086/301261>
- Deras, D., Arellano Ferro, A., Bustos Fierro, I. H., & Yezpez, M. A. 2022, *RMxAA*, 58, 121, <https://doi.org/10.22201/ia.01851101p.2022.58.01.10>
- Deras, D., Arellano Ferro, A., Lázaro, C., et al. 2019, *MNRAS*, 486, 2791, <https://doi.org/10.1093/mnras/stz642>
- _____. 2020, *MNRAS*, 493, 1996, <https://doi.org/10.1093/mnras/staa196>
- Deras, D., Arellano Ferro, A., Muneer, S., Giridhar, S., & Michel, R. 2018, *AN*, 339, 603, <https://doi.org/10.1002/asna.201813489>
- Figuera Jaimes, R., Arellano Ferro, A., Bramich, D. M., Giridhar, S., & Kuppuswamy, K. 2013, *A&A*, 556, 20, <https://doi.org/10.1051/0004-6361/201220824>
- Harris, W. E. 1996, *AJ*, 112, 1487, <https://doi.org/10.1086/118116>
- Jurcsik, J. & Kovács, G. 1996, *A&A*, 312, 111
- Kains, N., Arellano Ferro, A., Figuera Jaimes, R., et al. 2015, *A&A*, 578, 128, <https://doi.org/10.1051/0004-6361/201424600>
- Kains, N., Bramich, D. M., Arellano Ferro, A., et al. 2013, *A&A*, 555, 36, <https://doi.org/10.1051/0004-6361/201321819>
- Kains, N., Bramich, D. M., Figuera Jaimes, R., et al. 2012, *A&A*, 548, 92, <https://doi.org/10.1051/0004-6361/201220217>
- Kovács, G. 2002, *ASPC* 265, *Omega Centauri, A Unique Window into Astrophysics*, ed. F. van Leeuwen, J. D. Hughes, & G. Piotto (San Francisco, CA: ASPC), 163
- Kovács, G. & Kanbur, S. M. 1998, *MNRAS*, 295, 834, <https://doi.org/10.1046/j.1365-8711.1998.01271.x>
- Kovács, G. & Walker, A. R. 2001, *A&A*, 374, 264, <https://doi.org/10.1051/0004-6361:20010844>
- Landolt, A. U. 1992, *AJ*, 104, 340, <https://doi.org/10.1086/116242>
- Lata, S., Pandey, A. K., Pandey, J. C., et al. 2019, *AJ*, 158, 51, <https://doi.org/10.3847/1538-3881/ab22a6>
- Lázaro, C., Arellano Ferro, A., Arévalo, M. J., et al. 2006, *MNRAS*, 372, 69, <https://doi.org/10.1111/j.1365-2966.2006.10742.x>
- Lee, Y.-W. 1990, *ApJ*, 363, 159, <https://doi.org/10.1086/169326>
- Lee, Y.-W., Demarque, P., & Zinn, R. 1990, *ApJ*, 350, 155, <https://doi.org/10.1086/168370>
- Milone, A. P., Marino, A. F., Renzini, A., et al. 2018, *MNRAS*, 481, 5098, <https://doi.org/10.1093/mnras/sty2573>
- Morgan, S. M., Wahl, J. N., & Wieckhorst, R. M. 2007, *MNRAS*, 374, 1421, <https://doi.org/10.1111/j.1365-2966.2006.11247.x>
- Nemec, J. M. 2004, *AJ*, 127, 2185, <https://doi.org/10.1086/382903>
- Nemec, J. M., Cohen, J. G., Ripepi, V., et al. 2013, *ApJ*, 773, 181, <https://doi.org/10.1088/0004-637x/773/2/181>
- Olech, A., Kaluzny, J., Thompson, I. B., et al. 1999, *AJ*, 118, 442, <https://doi.org/10.1086/300917>
- Piotto, G., Bedin, L. R., Anderson, J., et al. 2007, *ApJ*, 661, 53, <https://doi.org/10.1086/518503>

- Piotto, G., Villanova, S., Bedin, L. R., et al. 2005, *ApJ*, 621, 777, <https://doi.org/10.1086/427796>
- Pritzl, B. J., Smith, H. A., Catelan, M., & Sweigart, A. V. 2001, *AJ*, 122, 2600, <https://doi.org/10.1086/323447>
- _____. 2002, *AJ*, 124, 949, <https://doi.org/10.1086/341381>
- Rojas Galindo, F., Arellano Ferro, A., Bustos Fierro, I. H., & Yepez, M. A. 2021, in prep
- Sandage, A. 1981, *ApJ*, 248, 161, <https://doi.org/10.1086/159140>
- _____. 1990, *ApJ*, 350, 631, <https://doi.org/10.1086/168416>
- Sandage, A. & Tammann, G. A. 2006, *ARA&A*, 44, 93, <https://doi.org/10.1146/annurev.astro.43.072103.150612>
- Schwarzenberg-Czerny, A. & Kaluzny, J. 1998, *MNRAS*, 300, 251, <https://doi.org/10.1046/j.1365-8711.1998.01895.x>
- Shapley, H. 1917, *PNAS*, 3, 479, <https://doi.org/10.1073/pnas.3.7.479>
- _____. 1918, *ApJ*, 48, 154, <https://doi.org/10.1086/142423>
- Simon, N. R. & Teays, T. J. 1982, *ApJ*, 261, 586, <https://doi.org/10.1086/160369>
- Skottfelt, J., Bramich, D. M., Figuera Jaimes, J. R., et al. 2015, *A&A*, 573, 103, <https://doi.org/10.1051/0004-6361/201424967>
- Stetson, P. B. 2000, *PASP*, 112, 925, <https://doi.org/10.1086/316595>
- Torelli, M., Iannicola, G., Stetson, P. B., et al. 2019, *A&A*, 629, 53, <https://doi.org/10.1051/0004-6361/201935995>
- Tsapras, Y., Arellano Ferro, A., Bramich, D. M., et al. 2017, *MNRAS*, 465, 2489, <https://doi.org/10.1093/mnras/stw2773>
- VandenBerg, D. A., Swenson, F. J., Rogers, F. J., Iglesias, C. A., & Alexander, D. R. 2000, *ApJ*, 532, 430, <https://doi.org/10.1086/308544>
- Walker, A. R. 1992, *ApJ*, 390, 81, <https://doi.org/10.1086/186377>
- _____. 1998, *AJ*, 116, 220, <https://doi.org/10.1086/300432>
- Yepez, M. A., Arellano Ferro, A., & Deras, D. 2020, *MNRAS*, 494, 3212, <https://doi.org/10.1093/mnras/staa637>
- Yepez, M. A., Arellano Ferro, A., Deras, D., et al. 2022, arXiv e-prints, arXiv:2201.02160, <https://doi.org/10.48550/arXiv.2201.02160>
- Yepez, M. A., Arellano Ferro, A., Muneer, S., & Giridhar, S. 2018, *RMxAA*, 54, 15
- Yepez, M. A., Arellano Ferro, A., Schröder, K.-P., et al. 2019, *NewA*, 71, 1, <https://doi.org/10.1016/j.newast.2019.02.006>
- Zinn, R. 1987, *Stellar Populations*, ed. C. A. Norman, A. Renzini, & M. Tosi (New York, NY: CUP), 73
- Zinn, R. & West, M. J. 1984, *ApJS*, 55, 45, <https://doi.org/10.1086/190947>
- Zorotovic, M., Catelan, M., Smith, H. A., et al. 2010, *AJ*, 139, 357, <https://doi.org/10.1088/0004-6256/139/2/357>

SIMULATIONS OF UNEQUAL BINARY COLLISIONS EMBEDDED IN A TURBULENT GAS CLOUD FAR FROM A MASSIVE GRAVITATIONAL CENTER

Guillermo Arreaga-García

Departamento de Investigación en Física, Universidad de Sonora, México.

Received January 5 2022; accepted April 6 2022

ABSTRACT

We simulate the collapse of a turbulent gas cloud, in which we choose two sub-clouds. A translational velocity \vec{v}_L or \vec{v}_R is added, so that the sub-clouds move towards each other to collide. The radius and pre-collision velocity of the sub-clouds are chosen to be unequal, and both head-on and oblique collisions are considered. The simulations are all calibrated to have the same total mass and initial energy ratio $\alpha = 0.16$, which is defined as the ratio of thermal energy to gravitational energy. We compare low- β models to a high- β models, where β is defined as the ratio of kinetic energy to gravitational energy. Finally, we consider the turbulent cloud to be under the gravitational influence of an object located far enough, in order to approximate the tidal effects by means of an azimuthal velocity V_{cir} added to the cloud particles apart from the translational and turbulent velocities mentioned above. We compare a low- V_{cir} model with a high- V_{cir} one.

RESUMEN

Se simula el colapso de una nube turbulenta de gas con dos subnubes. Se agrega una velocidad traslacional \vec{v}_L o \vec{v}_R tal que las subnubes se muevan una hacia la otra para chocar. El radio y la velocidad pre-colisión de las subnubes se escogen desiguales y se consideran colisiones frontales y oblicuas. Las simulaciones se calibran para tener la misma masa total y razón de energía inicial $\alpha = 0.16$, definida como la razón de la energía térmica a la energía gravitacional. Comparamos modelos de baja- β y alta- β , con β igual a la razón de la energía cinética a la energía gravitacional. Consideramos también que la nube esté bajo la influencia gravitacional de un objeto lejano, para aproximar los efectos de marea por medio de una velocidad azimutal V_{cir} agregada a las partículas de la nube, además de las velocidades traslacional y turbulenta. Comparamos un modelo de baja- V_{cir} con uno de alta- V_{cir} .

Key Words: hydrodynamics — stars: formation — turbulence — methods: numerical

1. INTRODUCTION

There is ample observational evidence of the occurrence of cloud-cloud collisions, see Testi et al. (2000), Churchwell et al. (2006), Furukawa et al. (2009), Torii et al. (2011), Takahira et al. (2014) and Yamada et al. (2021). Regions such as RCW49, Westerlund2, and NGC 3603 are examples of cloud-cloud collisions. Collision between clouds are widely expected, because clouds moving at random directions have been observed in the plane of the Milky Way, see Roslowsky et al. (2003) and Bolatto et al.

(2008). As a star formation mechanism, some observations indicate that cloud-cloud collisions are the external agent to trigger the initial gas condensation at the interface of the colliding clouds. This star formation mechanism seems to be a very important step to explain the formation of high-mass stars and clusters of stars. For low-mass stars, the most relevant mechanism of formation seems to be the gravitational collapse of cloud cores, that is induced by an internal agent, such as the expansion of HII regions, see Scoville et al. (1986).

The G0.253 + 0.016 molecular cloud, which is also called the Brick, has attracted much attention and is believed to be formed by a cloud-cloud collision. This cloud is massive ($\approx 10^5 M_\odot$) and compact (3 pc), located in the Central Molecular Zone of the Milky Way (CMZ). The Brick can be considered to be a possible progenitor cloud of a young massive cluster (YMC) of stars; that is, the Brick represents the initial conditions out of which high-mass proto-stars can be formed through gravitational collapse, see Petkova et al. (2006).

Longmore et al. (2012) presented deep, multiple-filter, near-IR observations of the Brick, to ascertain its dynamical state. Longmore et al. (2012) noted that large-scale emission from shocked-gas was detected toward the Brick, which indicates that this cloud could have been formed by the convergence of large-scale flows of gas or by a cloud-cloud collision.

Using ALMA line emission observations of sulfur monoxide, Higuchi et al. (2014) compared the filamentary structures observed in the cloud G0.253+0.016 with a cloud collision model. Consequently, the shell structure was obtained theoretically, which is similar to that shell-like structure observed in the G0.253+0.016 cloud. The model proposed by Higuchi et al. (2014) considered that the giant G0.253+0.016 molecular cloud may have formed due to a cloud collision between two unequal clouds. The small cloud had a radius of 1.5 pc and a mass of $0.5 \times 10^5 M_\odot$; the larger cloud had a radius of 3 pc and a mass of $2 \times 10^5 M_\odot$. Their approaching pre-collision velocity was from 30 to 60 km/s.

Using the Combined Array for Research in Millimeter-wave Astronomy (CARMA), Kauffmann et al. (2013) presented high-resolution interferometric molecular line and dust emission maps for the G0.253+0.016 cloud. They estimated the virial parameter of the the G0.253+0.016 cloud, which yields a value of $\alpha_{\text{vir}} < 0.8$. In addition, Rathborne et al. (2015) used ALMA observations of the Brick to investigate its physical conditions.

Many surveys have reported the physical conditions of gas structures of the ISM on the verge of collapse; see for instance, Caselli et al. (2002) and Jijina et al. (1999). The dimensionless ratios α and β , which are defined as the ratio of thermal energy to gravitational energy and the ratio of kinetic energy to gravitational energy, respectively- are very useful to characterize the physical state of these gas structures. Observations seem to favor the statistical occurrence of low- β clumps. However, recent observations have found a gas cloud with a high value of β , see for example Jackson et al. (2018). In addition, for

clouds in the CMZ, the gas is observed to be highly turbulent, with large non-thermal line-widths in the range from 20 to 50 km/s. Consequently, considering an isothermal sound speed from 0.3 to 0.6 km/s and gas temperatures from 30 to 100 K, the typical Mach numbers are in the range from 10 to 60, which is a highly-supersonic turbulence, see Bally et al. (1998) and Mills (2017).

From the theoretical side, many simulations that aim to study a cloud-cloud collision process have appeared in the last three decades, for instance, Hausman (1981), Lattanzio et al. (1985), Kimura and Tosa (1996), Klein and Woods (1998) and Marinho and Lépine (2000). However, these early simulations were done with low resolution. Simulations with much better resolution were done more recently by Burkert and Alves (2009) and Anathpindika (2009a). Colliding gas structures starting from hydrodynamical equilibrium were considered by Kitsionas and Whitworth (2007) and Anathpindika (2009b). Anathpindika (2010) considered collisions between unequal gas structures. Gómez et al. (2007), Vazquez-Semamedi et al. (2007) and other authors studied the generation of turbulence at the shock front of head-on collisions.

Lis and Menten (1998) proposed a model that was based on a cloud-cloud collision that aimed to explain far-infrared continuum emission observations of the G0.253+0.016 molecular cloud. The simulation presented by Habe and Ohta (1992) assumed that the mass ratio of the non-identical colliding clouds was 1:4 and the radius ratio was 1:2.

Dale et al. (2019) and Kruijssen et al. (2019) proposed hydrodynamical simulations of a gas cloud orbiting in the gravitational potential of the CMZ, in the radial range from 1 to 300 pc. In these simulations, each SPH particle was given an additional external force to take the external potential of the CMZ into account.

Anathpindika (2010) studied a head-on collision between two clouds of different sizes: one cloud was modeled as a Bonnor-Ebert sphere and the second cloud was modeled as a uniform density sphere. The cloud's pre-collision translation velocities were also unequal: one moves at 10 km/s while the second cloud moves at -15 km/s. The formation of a bow-shock is the main outcome of these simulations. The bow-shock continues collapsing, so that the models showed a lot of fragmentation while other models with slow collision velocities showed no sign of fragmentation. In addition, the author noted that this behavior (whether or not fragmentation is present) also depends on the simulation resolution.

In this paper we aim to study the collision process of several un-equal sub-clouds, which are initially embedded within a parent turbulent cloud. The set up of this paper is similar to the physical conditions mentioned by Anathpindika (2010), Higuchi et al. (2014) and Kauffmann et al. (2013), so that the system of interest resembles the Brick. In addition, we want to see what role the initial turbulence of the cloud can have on the overall collision process. While Anathpindika (2010) and other authors have considered two separate clouds that collide, we emphasize that in this paper that the initial cloud entirely contains the two sub-clouds that collide. We consider both kinds of clouds to simulate: low and high β turbulent models, so that $\beta = 0.5$ or $\beta = 50$. In both cases, the cloud will collapse once the initial turbulence has been dissipated. It has been shown by Arreaga (2018) that the β ratio can reach very high values, and yet the simulations of these clouds show that they still collapse globally.

The models considered in this paper are clearly incomplete given that they do not take into account the environment of the cloud, so that the models are taken as isolated systems, which is a common practice in numerical simulations of cloud collapse and evolution. In the case of the Brick, or in general of a cloud located in the CMZ, a tidal force will be exerted upon the clouds from a massive central object, see Molinari et al. (2011).

For this reason, we introduce an approximate model to mimic the gravitational influence of a central massive object on the cloud, in addition to the collision process described earlier. In this approximate model, an additional velocity is added to each SPH particle of the cloud, so that this velocity is directly related to the escape velocity induced by the massive central object on the cloud. The result obtained with this simple model has allowed us to conclude that the collapse of the cloud is accelerated by the presence of the external object, as was already pointed out by Dale et al. (2019) and Kruijssen et al. (2019), using a more complete model.

It must be emphasized that this simple approximate model produces a central condensation during the very early evolution of the cloud, which is decisive in the subsequent evolution. The results obtained from these simulations are in agreement with observations (Hillenbrand and Hartmann, 1998) and simulations (Kirk et al., 2014), which indicate that the most massive member of a star cluster is always located at the center of the cluster.

It must be noted that the gas particles of all the models include three types of velocities, which are

the turbulent velocity spectrum, the translational velocity and the azimuthal velocity; all of them are given as initial conditions of the SPH particles. The particles are then allowed to evolve as gas described by the Navier-Stokes hydrodynamic equations under the influence of their own gravitational interaction.

The outline of this paper is as follows. In § 2 we describe the initial cloud, within which all the collision models will take place. The initial conditions given to the simulation particles are explained in § 2.1 and § 2.2. We define the azimuthal velocity in § 2.3. Then, in § 2.4 we give the details of the collision geometry and define the models to be studied. We describe the GADGET2 code, the resolution of the simulations and the equation of state in S 2.6, § 2.7 and S 2.8, respectively. In § 3, we describe the most important features of the time evolution of our simulations by means of two-dimensional (2D) and three-dimensional (3D) plots. A dynamical characterization of the simulation outcomes is undertaken in § 4. Finally, in § 5 and § 6 we discuss the relevance of our results in view of those reported by previous papers, and we make some concluding remarks.

2. THE PHYSICAL SYSTEM AND COMPUTATIONAL CONSIDERATIONS

The gas cloud that is considered in this paper is a uniform sphere with a radius of $R_0 = 3.0$ pc and a mass of $M_0 = 1.0 \times 10^5 M_\odot$. The average density and the free-fall time of this cloud are $\rho_0 = 5.9 \times 10^{-20}$ g cm $^{-3}$ and $t_{ff} = 8.64 \times 10^{12}$ s or 0.27 Myr (2.7×10^5 yr), respectively. The values of R_0 and M_0 have been taken from Kauffmann et al. (2013) and Higuchi et al. (2014), to draw comparisons with their models of the Brick. The number density of the cloud considered here is $n_0 = 15352$ particles per cm 3 ; a mean molecular weight of 2.4 for the hydrogen molecule is assumed. Therefore, its mean mass is 3.9×10^{-24} g.

It should be emphasized that these physical properties of density, mass and radius are typical of the gas structures, so-called “clumps”, in the cloud classification framework of Jijina et al. (1999) and Bergin et al. (2007) of the ISM, with a number density within the range $10^3 - 10^4$ cm 3 . With respect to the mass, the gas structure of this paper would better correspond to a “cloud”, because the typical mass of clouds is within the range $10^3 - 10^4 M_\odot$ while that of the clumps is in the range $50 - 500 M_\odot$.

We therefore use the term cloud to refer to the gas structure considered here, although it is clearly much denser than a typical cloud. For a cloud structure near the CMZ, the physical properties are ob-

served to be more extreme, so that the number density and the temperature are in general higher than in the clouds of ISM in the galactic disc, see Longmore et al. (2013).

2.1. The Initial Conditions of the Simulation Particles

2.1.1. The Initial Positions

The gas particles are initially located in a simulation volume, which is divided into small cubic elements, with a volume given by $\Delta x \Delta y \Delta z$. A gas particle is placed at the center of each cubic element. Next, each particle is displaced a distance of the order $\Delta/4.0$ in a random spatial direction within each cubic element. The total number of particles is 13,366,240. Therefore, the mass of a simulation particle is given by $m_p = 7.48 \times 10^{-3} M_\odot$.

2.1.2. The Initial Turbulent Velocity Spectrum

To generate the turbulent velocity spectrum, we set up a mesh with a side length equal to 2 times the cloud radius, $L_0 = 2R_0$, so that the size of each grid element of this mesh is $\delta = L_0/N_g$ and the mesh partition is determined by $N_g = 64$. In Fourier space, the partition is given by $\delta K = 1/L_0$, so that each wave-number vector \vec{K} has the components $K_x = i_x \delta K$, $K_y = i_y \delta K$ and $K_z = i_z \delta K$, where the indices i_x, i_y, i_z in equation 1 take integer values in the range $[-N_g/2, N_g/2]$ to cover all of the mesh.

A velocity vector $\vec{v}(\vec{r}) = (v_x, v_y, v_z)$ must be assigned for a SPH particle located at position $\vec{r} = (x, y, z)$, which is given by

$$\vec{v}(\vec{r}) \approx \sum_{i_x, i_y, i_z} \left| \vec{K} \right|^{\frac{-n-2}{2}} \vec{K} \sin(\vec{K} \cdot \vec{r} + \Phi_K), \quad (1)$$

where n is the spectral index. It must be noted that this kind of curl-free velocity spectrum is known as a curl-free (CF) type. A method to obtain a divergence-free (DF) type of turbulence spectrum has been shown in Dobbs et al. (2005). Arreaga (2017) examined the effects on the collapse of cores due to variation of the number and size of the Fourier modes, for each turbulence type, whether divergence-free or curl-free. Arreaga (2017) demonstrated that the results of the core collapse are not substantially different. Arreaga (2018) presented simulations in which the velocity vector given to each SPH particle was formed by a combination of the two types of turbulent spectra $\vec{v} = \frac{1}{2} \vec{v}_{DF} + \frac{1}{2} \vec{v}_{CF}$.

The initial power of the velocity field for both types of turbulence is given by:

$$P(\vec{K}) = \langle |v(\vec{K})|^2 \rangle = |\vec{K}|^{-n}. \quad (2)$$

The spectral index has been fixed in our simulations to the value $n = -1$ and thus we will have $P \approx K$ and $v^2 \approx K^{-1}$. Other authors have used other values for the spectral index, for instance $n = 2$, so that their power and velocity go as $P \approx K^{-2}$ and $v^2 \approx K^{-2}$, respectively, see Dobbs et al. (2005).

Finally, the level of turbulence can be adjusted by introducing a multiplicative constant in front of the right-hand side of equation 1, whose value is fixed, as we explain it in the next § 2.2. Later, we will show that the velocity spectrum proposed in § 2.1.2 has some of the well-known characteristics of turbulence, see § 5.1.

2.2. Initial Energies

In a particle-based simulation, the thermal, kinetic and gravitational energies are given by

$$\begin{aligned} E_{\text{ther}} &= \frac{3}{2} \sum_i m_i \frac{P_i}{\rho_i}, \\ E_{\text{kin}} &= \frac{1}{2} \sum_i m_i v_i^2, \\ E_{\text{grav}} &= \frac{1}{2} \sum_i m_i \Phi_i, \end{aligned} \quad (3)$$

where P_i is the pressure and Φ_i is the gravitational potential at the location of particle i , with velocity v_i and mass m_i . It should be emphasized that all of the SPH particles of a simulation must be used in the summation of equation 3.

Let α be defined as the ratio of the thermal energy to the gravitational energy and let β be the ratio of the kinetic energy to the gravitational energy, so that

$$\alpha \equiv \frac{E_{\text{ther}}}{|E_{\text{grav}}|}, \quad (4)$$

and

$$\beta \equiv \frac{E_{\text{kin}}}{|E_{\text{grav}}|}. \quad (5)$$

The value of the speed of sound c_0 has been fixed at 225,000 cm/s, so that the initial turbulent cloud has the α_0 ratio given by 0.16, for all the collision models. The multiplicative constant mentioned in § 2.1.2 has been adjusted so that the initial turbulent cloud has a β_0 ratio given by 0.5.¹

¹We also consider models with a very high value of the ratio of the kinetic energy to the gravitational energy; in addition, there is observational interest in these kinds of model, see § 2.2.1 below.

Higuchi et al. (2014) presented line emission observations of the Brick using the Atacama Large Millimeter/Submillimeter Array and considered values of $\beta_0 = 0.1$ and $\alpha_0 = 0.02$ taking into account a cloud mass of $2 \times 10^5 M_\odot$, radius of 2.8 pc, a temperature of 20 K and a one-dimensional velocity dispersion of 4 km/s.

The virial parameter is very useful when characterizing the physical state of a gas structure, which is defined observationally by

$$\beta_{\text{vir}} \equiv \frac{5 \sigma_{1D}^2 R}{G M}, \quad (6)$$

where G is Newton's gravitational constant, M and R are the mass and radius of the gas structure, and σ_{1D} is the intrinsic one-dimensional velocity dispersion of the hydrogen molecule. Assuming isotropic motions, a 3D velocity dispersion can be simply related by $\sigma_{3D} = \sqrt{3} \sigma_{1D}$. It should be noted that a gas structure in virial equilibrium would have $\beta_{\text{vir}} = 1$.

The empirical relation between the virial parameter is $\beta_{\text{vir}} = 2a\beta$, where β is the dimensionless ratio defined in equation 5 and a is a numerical factor that is empirically included to take modifications of non-homogeneous and non-spherical density distributions into account. According to this empirical relation, the virial parameter of the simulation of this paper is approximately 1.

Later, the virial theorem will be useful to show the level of virialization of the simulation outcome. In general terms, for a gas structure in virial equilibrium, the energy ratios defined above in equations 4 and 5 satisfy the relation

$$\alpha + \beta = \frac{1}{2}. \quad (7)$$

It is expected that if a gaseous system has $\alpha + \beta > 1/2$, then it will expand; in the other case, if $\alpha + \beta < 1/2$, then the system will collapse. It must be mentioned that Miyama et al. (1984), Hachisu and Heriguchi (1984) and Hachisu and Heriguchi (1985) obtained a criterion of the type $\alpha \times \beta < 0.2$ to predict the output of a given simulation.

2.2.1. Observational Evidence for Models with Extreme Initial Kinetic Energy.

Large kinetic energy molecular clouds have recently been observed. For example, Jackson et al. (2018), reported unusually large line-widths of the G337.342-0.119 gas structure, which is also known as the Pebble. These kinds of clouds are expected

not to collapse in terms of the virial theorem, because a gas structure such as the Pebble reaches a virial parameter of 3.7.²

In spite of this, numerical simulations have shown that there are gas structures with a large kinetic energy, so that their virial parameter is around or greater than 2, and are in a state of global collapse, see for instance Ballesteros et al. (2018). In addition, Arreaga (2018) determined the extreme kinetic energy allowed for a turbulent core to collapse under the influence of its own self-gravity. The results that these authors found are given in terms of the ratio β , which is defined here in equation 5 of § 2.2, so that a turbulent core can have an initial β as high as 2 – 8 and with an initial Mach number within 3 – 9 and still finish its evolution in a collapsed state.

For clouds in the CMZ, the gas is observed to be highly turbulent, with high non-thermal line-widths in the range from 20 to 50 km/s. Considering an isothermal sound speed within the range from 0.3 to 0.6 km/s for gas temperatures from 30 to 100 K, the typical Mach numbers are in the range from 10 to 60, which is a highly supersonic turbulence, see Bally et al. (1998) and Mills (2017).

2.3. The Azimuthal Velocity

Let us consider a massive agent, such as a dwarf spheroidal galaxy, which is located at the origin of a coordinate system. Let us place the molecular cloud of interest here to be in the z -axis, at a distance Z_C . This massive agent induces an escape velocity at each radius R (with respect to the center of the massive agent), so that

$$V_{\text{cir}} = \sqrt{2GM(R)/R}, \quad (8)$$

where $M(R)$ is the mass contained up to the radius R and G is Newton's gravitational constant. In spherical coordinates R , θ and ϕ , the velocity vector \vec{V} has components V_R , V_θ and V_ϕ , respectively. These spherical components are related to the Cartesian components of velocity V_x , V_y and V_z by three simultaneous equations, whose coefficients are given in terms of the sine and cosine of the polar and azimuthal angles θ and ϕ , as follows:

$$\begin{aligned} V_R &= V_x \sin(\theta) \cos(\phi) + V_y \sin(\theta) \sin(\phi) + V_z \cos(\theta), \\ V_\theta &= V_x \cos(\theta) \cos(\phi) + V_y \cos(\theta) \sin(\phi) - V_z \sin(\theta), \\ V_\phi &= -V_x \sin(\phi) + V_y \cos(\phi). \end{aligned} \quad (9)$$

²Recall that the virial theorem states that a gas structure with a virial parameter less than 1 will collapse; otherwise, if the virial parameter is greater than 1, then a gas structure will not collapse.

Let us assume that Z_C and the radius of the cloud (which is defined in § 2 $R_0 = 3$ pc with respect to the center of the cloud), satisfy the relation $R_0/Z_C \ll 1$, then as $\sin(\theta) = R_0/R \approx R_0/Z_C \ll 1$ then $\theta \approx 0$, for which $\cos(\theta) \approx 1$ and $\sin(\theta) \approx 0$. In addition, in the particular case that the cloud follows a circular orbit around the massive center at radius R , then the velocity vector would only have a non-zero polar velocity component, V_θ , while the radial and azimuthal components V_R and V_ϕ are zero. Let us denote this velocity as $V_\theta = -V_{\text{cir}}$, where the minus sign indicates that the assumed rotation of the cloud is counter-clock-wise in its orbit around the massive agent. Under these simplifications, the relations 9 between Cartesian and spherical components of velocity are reduced to

$$\begin{aligned} V_x &= -V_{\text{cir}} \cos(\phi), \\ V_y &= -V_{\text{cir}} \sin(\phi), \\ V_z &= 0, \end{aligned} \quad (10)$$

so that the magnitude of the velocity of a particle located at any radius R is therefore always given by $\sqrt{V_x^2 + V_y^2} = V_{\text{cir}}$. These Cartesian components of the velocity will be added to the particle velocity defined in equation 1 to generate four new models in which this approximation will be implemented. It should be noted that the azimuthal angles have the same projection in both coordinate systems: the first is based on the cloud center and the second is located at the gravitational agent center.

We will call this velocity the “azimuthal velocity” because it is given only in terms of the azimuthal angle ϕ . Then, the approximation that replaces the tidal force by an azimuthal velocity, as described in equation 10, does not depend explicitly on the distance of the massive center to the cloud as long as ratio between the cloud radius to this distance is quite small.

Following with the model of a cloud of the CMZ, the mass of this massive agent has been fixed at $M_B = 3.6 \times 10^6 M_\odot$, which corresponds to the black hole located at the center of the Milky Way. In this case, the escape velocity at 500 pc is 5.57 km/s. To compare this velocity with those displayed at Figure 2, in terms of the speed of sound c_0 defined in § 2.2, we have a Mach number of $V_{\text{cir}} = 2.47$. It must be noted that the magnitude of this circular velocity V_{cir} is quite small as compared to that proposed by Molinari et al. (2011), in which a model for the orbit of the gas stream near the massive center Sgr B2 is around 80 km/s. For this reason, we have also included a second set of models in which

the massive agent is considered to be molecular gas concentrated in the nuclear bulge of the Milky Way, see Launhardt et al. (2002), so that the total mass is $M_H = 8.4 \times 10^8 M_\odot$, see also Mills (2017), for which the escape velocity at 500 pc is 85 km/s, such that the normalized velocity in terms of the speed of sound 37.82.

2.4. The Collision Models

It is important to emphasize that the cloud entirely contains the two subsets of particles that are going to collide. Let us call these subsets the pre-collision sub-clouds. They are located initially along the x -axis, so that the centers are: for the left-hand clump $(-2.55, 0, 0)$ pc and for the right-hand clump $(2.55, 0, 0)$ pc.

The radius of the pre-collision sub-clouds are chosen to be equal for two models, and different for another two models. The former models are head-on collisions. An impact parameter b has also been considered for the latter models, so that they are oblique collisions, in which b takes the value 1.5 pc along the y -axis. Bekki and Couch (2004) have demonstrated observationally that the most likely impact parameter b in cloud collisions in the Large Magellanic Cloud and the Small Magellanic Cloud is $0.5 D < b < D$ where D is the diameter of the cloud. For the radius R_0 of the cloud considered in this paper, b has been chosen such that $b = 0.25 D$.

We show all these models in Table 1. The label is shown in Column one. The impact parameter value is shown in Column two. In Columns three and four, the relationship of the radius and translational velocities are shown, for the left-hand and right-hand sub-clouds, respectively. It is important to emphasize that the relative pre-collision velocity of the sub-clouds is 29 km/s and is formed for non-identical velocities for the left-hand and right-hand sub-clouds. In Column five, the value of the ratio of the kinetic energy to the gravitational energy for the initial configuration of particles is shown, see equation 5. Finally, Column six gives the value of the azimuthal velocity added to the cloud particles, see § 2.3. It must be clarified that these models are a sample from a larger set of models that was considered in a first manuscript, so that the numbers of the labels do not show any ordering.

2.4.1. A Note on the Physical Parameters chosen for the Sub-clouds.

As we mentioned in § 1, the idea that the Brick could be formed by a non-identical cloud-cloud collision has been explored for some time. Habe and

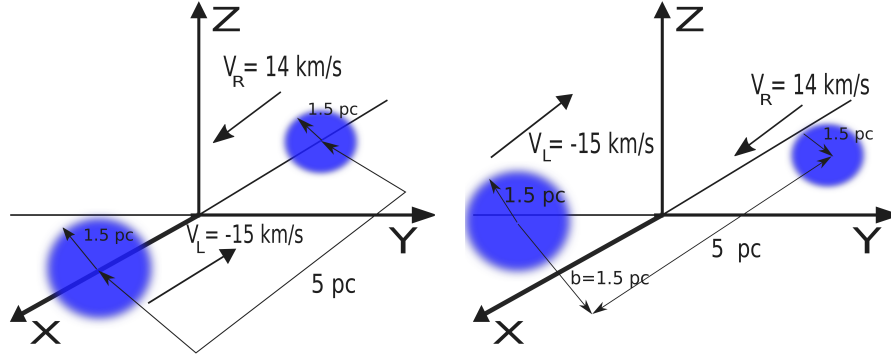


Fig. 1. Schematic diagram of the pre-collision geometry for a head-on collision (left-hand panel) and an oblique collision (right-hand panel). The color figure can be viewed online.

TABLE 1
THE COLLISION MODELS

Model	b [pc]	$r_L : r_R$ [pc]	$v_L : v_R$ [km/s]	β_0	V_{cir}/c_0
U5	0	0.75:1.5	14:-15	0.5	0
U13	0	1.5:1.5	14:-15	0.5	0
U9	1.5	0.75:1.5	14:-15	0.5	0
U11	1.5	1.5:1.5	14:-15	0.5	0
U5b	0	0.75:1.5	14:-15	50	0
U13b	0	1.5:1.5	14:-15	50	0
U9b	1.5	0.75:1.5	14:-15	50	0
U11b	1.5	1.5:1.5	14:-15	50	0
U5r	0	0.75:1.5	14:-15	0.5	2.47
U13r	0	1.5:1.5	14:-15	0.5	2.47
U9r	1.5	0.75:1.5	14:-15	0.5	2.47
U11r	1.5	1.5:1.5	14:-15	0.5	2.47
U5rb	0	0.75:1.5	14:-15	0.5	37.82
U13rb	0	1.5:1.5	14:-15	0.5	37.82
U9rb	1.5	0.75:1.5	14:-15	0.5	37.82
U11rb	1.5	1.5:1.5	14:-15	0.5	37.82

b is the impact parameter; $r_L : r_R$ is the initial relation of the colliding sub-cloud radii; $v_L : v_R$ is the relation of the translational velocities or pre-collision velocities; β_0 is the initial ratio of kinetic energy to gravitational energy; and V_{cir}/c_0 is the ratio between the azimuthal velocity and the speed of sound.

Ohta (1992) assumed that the mass ratio of the colliding clouds is 1:4 and the radius ratio is 1:2. Later, Lis and Menten (1998) followed this collision model, so that their pre-collision velocities of the clouds are

taken for this paper exactly as these authors introduced them.

More recently, using observations, Kauffmann et al. (2013) estimated that the virial parameter of the Brick is around $\beta_{\text{vir}} \leq 0.8$ and considered the same geometry of un-equal clouds at the same relation proposed by Habe and Ohta (1992) and Lis and Menten (1998). In this paper, we have taken the value of $\beta_0 = 0.5$, so that we expect to have a value of the virial parameter of ≈ 1 , see § 2.2.

Shortly after, Higuchi et al. (2014) reconsidered this idea and continued the exploration of a cloud-cloud collision model in which the relative speed of colliding clouds was within the range from 30 to 60 km/s, and the radii were of 1.5 and 3 pc, for the small and big clouds, respectively.

In this paper, the translation velocity shown in Table 1, $v_L : v_R$, is given in terms of the sound speed c_0 by 6.2:6.6 Mach, so that the relative velocity of approach is a little greater than 12 Mach.

To allow comparison of the results of the present paper with Lis and Menten (1998), Kauffmann et al. (2013) and Higuchi et al. (2014), we use here the same values for the mass, radius and translation velocity of the cloud-cloud collision model that were used by these authors.

It must be noted that the gas particles of all the models described in Table 1 include the Cartesian components of velocity described in equation 1, which are the turbulent velocity spectrum and the translation velocity $v_L : v_R$ of the sub-clouds. However, only the last four models include a third set of velocity components already described equation 10, which are needed to implement the approximation

that replaces the tidal force by an azimuthal velocity. All three types of velocities enter as initial conditions of the SPH particles, as we will describe in § 2.5.

2.5. Characterization of the Initial Turbulence

To show the nature of the turbulence that is implemented in § 2.1.2, we consider the distribution functions of the initial velocity.

In Figure 2, we show the distribution functions of the radial component of the velocity at the initial snapshot, so that in the vertical axis the fraction f of the simulation particles whose magnitude of the velocity is smaller than that value shown in the horizontal axis. The radial component has been calculated with respect to the origin of the coordinates located in the center of the cloud, which is located at the center of the simulation box.

According to the left-hand column panels of Figure 2 that is, for models U and Ub , half of the simulation particles have a negative radial velocity component, while the other half have a positive radial component. This symmetry is expected from the random process described in § 2.1 to generate the direction of the velocity vectors.

It must be emphasized that for the right-hand column panels of Figure 2 that is, for models Ur and Urb , which include an azimuthal velocity, the symmetry of the curves with respect to the positive and negative radial components has been lost. These panels indicate that the azimuthal velocity favors that 80 percent of the particles have negative radial component of the velocity.

It must also be emphasized that both types of models U , Ur and Urb have the same initial turbulent velocity spectrum with the same level of energy, as defined in § 2.1 and § 2.2, and have the same translational velocity. The only difference between them is whether or not they include the azimuthal velocity, as described in § 2.3. It is observed in Figure 2 that the distribution function of the models U shows a magnitude of the velocity 12 percent smaller than that of models Ur .

Later, we will compare these curves at the initial snapshot with curves obtained for an snapshot of the final evolution stage.

A brief description of the dynamics of the isolated cloud is given in § 5.1.

2.6. The Evolution Code

The simulations of this paper are evolved using the particle-based Gadget2 code, which implements the SPH method to solve the Euler equations of hydrodynamics; see Springel (2005). Gadget2 has a

Monaghan-Balsara form for the artificial viscosity, see Balsara (1995), so that the strength of the viscosity is regulated by setting the parameter $\alpha_\nu = 0.75$ and $\beta_\nu = \frac{1}{2} \times \alpha_\nu$, see Equations 11 and 14 in Springel (2005). The Courant factor has been fixed at 0.1.

The SPH sums are evaluated using the spherically symmetric M4 kernel and so gravity is spline-softened with this same kernel. The smoothing length h establishes the compact support, so that only a finite number of neighbors to each particle contribute to the SPH sums. The smoothing length changes with time for each particle, so that the mass contained in the kernel volume is a constant for the estimated density. Particles also have gravity softening lengths ϵ , which change step by step with the smoothing length h , so that the ratio ϵ/h is of order unity. In Gadget2, ϵ is set equal to the minimum smoothing length h_{\min} , which is calculated over all particles at the end of each time step.

2.7. Resolution

Truelove et al. (1997) demonstrated that the resolution requirement of a hydrodynamic simulation can be expressed in terms of the Jeans wavelength λ_J , which is given by

$$\lambda_J = \sqrt{\frac{\pi c^2}{G \rho}}, \quad (11)$$

where G is Newton's gravitation constant, c is the instantaneous sound speed and ρ is the local density, so that a mesh-based simulation must always have its grid length scale l such that $l < \lambda_J/4$.

Bate and Burkert (1997) demonstrated that the resolution requirement for a particle-based code, the Jeans wavelength λ_J is better written in terms of the spherical Jeans mass M_J , which is defined by

$$M_J \equiv \frac{4}{3} \pi \rho \left(\frac{\lambda_J}{2} \right)^3 = \frac{\pi^{\frac{5}{2}} c^3}{6 \sqrt{G^3 \rho}}, \quad (12)$$

so that an SPH code will produce correct results as long as the minimum resolvable mass m_r is always less than the Jeans mass M_J . The mass m_r is given by $m_r \approx M_J/(2N_{\text{neigh}})$, where N_{neigh} is the number of particles included in the SPH kernel (i.e., the number of neighbors). Therefore, our simulations will comply with this resolution requirement if the particle mass m_p is such that $m_p/m_r < 1$.

As we mentioned in § 2.1, we have $N = 13366240$ SPH particles in each simulation and therefore $m_p = 7.4 \times 10^{-3} M_\odot$. Now, if we consider that the highest peak density in our collision models is $\rho_{\max} = 5.0 \times 10^{-12} \text{ g/cm}^3$, then the minimum Jeans

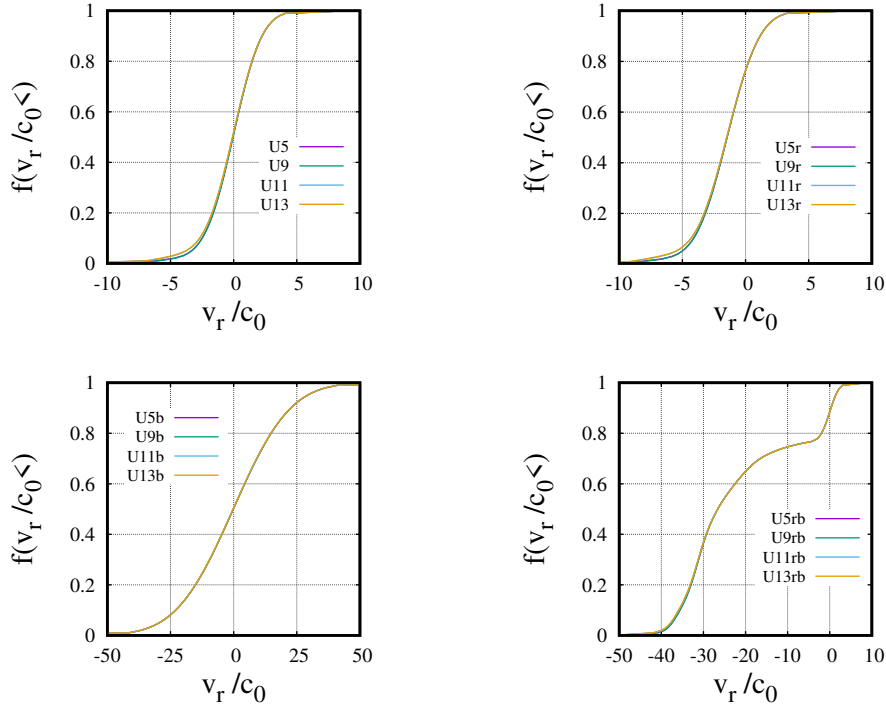


Fig. 2. Distribution function for the radial component of the velocity at the initial snapshot at $t/t_{ff} = 0$, for the model (top left-hand) U with a low level of turbulence; (top right-hand) U_r with a small azimuthal velocity; (bottom left-hand) U_b with a high level of turbulence and (bottom right-hand) U_{rb} with a large azimuthal velocity. f is the fraction of particles whose magnitude of the velocity v_r/c_0 (normalized with the sound speed) is smaller than that value shown in the horizontal axis. The color figure can be viewed online.

mass would be given by $(M_J)_{\min} \approx 0.594048 M_\odot$, so that we obtain $m_r = 7.4 \times 10^{-3} M_\odot$. Thus, for that peak density the ratio $m_p/m_r \leq 1$, and the Jeans resolution requirement is satisfied. In this sense, we are sure to avoid the growth of numerical instabilities or the occurrence of artificial fragmentation in all our simulations, up to densities smaller or equal than ρ_{\max} . In the next sections, we will present our results in terms of a normalized density, so that $\log(\rho_{\max}/\rho_0)$ is given by 7.9, where ρ_0 is the average density of the initial cloud, as we mentioned in § 2.

2.8. Equation of State

Most simulations in the field of collapse used an ideal equation of state or a barotropic equation of state (BEOS), as was proposed by Boss et al. (2000):

$$p = c_0^2 \rho \left[1 + \left(\frac{\rho}{\rho_{\text{crit}}} \right)^{\gamma-1} \right], \quad (13)$$

where $\gamma \equiv 5/3$ and ρ_{crit} is a critical density, a parameter which we explain now. This BEOS takes into account the increase in temperature of the gas as it begins to heat once gravity has produced a substantial contraction of the cloud. In this paper, we

also use this BEOS scheme for simplicity with a critical density $\rho_{\text{crit}} = 5.0 \times 10^{-14} \text{ g/cm}^3$, which is 100 times smaller than the peak density considered in § 2.7 for the resolution requirement estimate; that is, ρ_{\max} . However, it should be emphasized that it is only an approximation. Consequently, to describe correctly the transition from the ideal to the adiabatic regime, one needs to solve the radiative transfer problem coupled to gravity in a self-consistent way.

3. RESULTS

3.1. Evolution of the Density Peak

In Figure 3 we show the time evolution of the global density peak, irrespective of where the particle with the highest density is located in the simulation volume. As can be seen in this figure, all models collapse at different times (as expected).

Let us consider the top left-hand panel of Figure 3, the models with a low level of turbulence. The fastest collapse is that of Model U_{13} ; followed by the collapse of Models U_9 and U_5 , respectively. The slowest collapse is that of Model U_{11} .

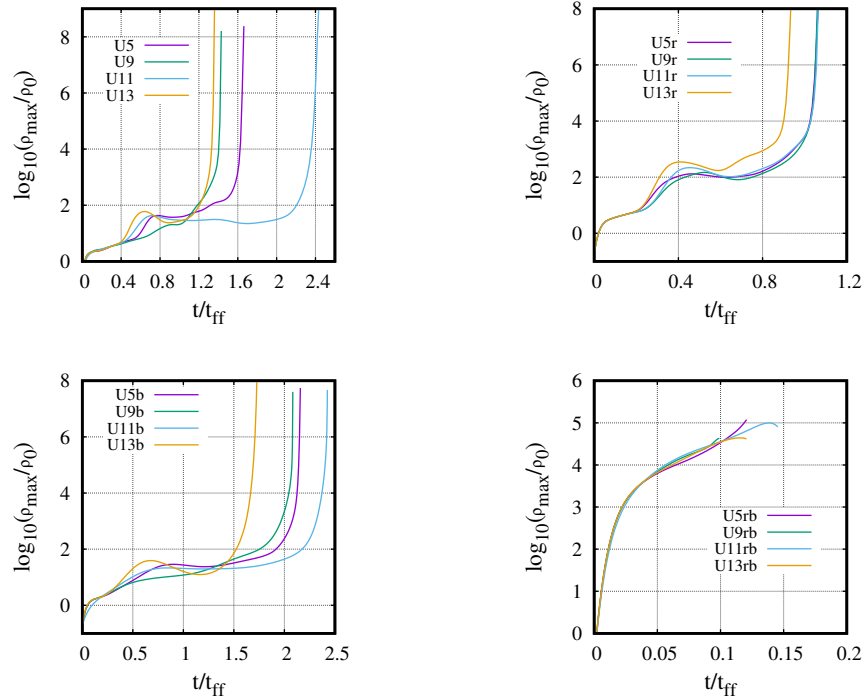


Fig. 3. Evolution of the density peak for all the models (top left-hand) U with low level of turbulence; (top right-hand) Ur with a small azimuthal velocity (bottom left-hand) Ub with high level of turbulence and (bottom right-hand) Urb with a large azimuthal velocity. The color figure can be viewed online.

This ordering seems to be a consequence of the gas dragging, which is caused by the asymmetry in radius and velocity. Consequently, as the gas flows, it is more difficult to condense by the action of the gravity. Model $U13$ does not show any sign of gas dragging, because the gas remains of the head-on collision is still around of the pre-collision center. This is the reason why this model collapses first.

The density peak curve of Model $U9$ very closely follows that of Model $U13$; This happens because the right-hand sub-cloud acts as a primary member in the binary system formed, which is only slightly perturbed by the left-hand sub-cloud, that acts as a secondary member of the binary. The collapse takes place first in the primary, which is more massive.

The density peak curve of Model $U5$ is the third to reach the collapse. This happens because the right-hand sub-cloud entirely swallows the left-hand sub-cloud during the collision, so it produces a mass perturbation in the central region, which must first settle down for the collapse to continue. The slowest collapse is that of Model $U11$. This happens because the dragging of the colliding sub-clouds is maximum, so the mass does not stack easily.

Let us now consider the bottom left-hand panel of Figure 3, the Models Ub with a high level of turbulence. In this case, the behavior of all of the curves is the same as that explained earlier for the top panel, but for the panel of Model Ub there is a slight shift to the right to longer evolution times, above all for the Models $U5b, U9b$ and $U13b$. The collapse time of Model $U11b$ is almost similar to that observed in Model $U11$.

We observe a very significant change in the time scale for the right column panels of Figure 3; in the top right-hand panel, Models Ur that include a low azimuthal velocity, the collapse is accelerated, so that the collapse time is shorter than the previous models U and Ub by 40 percent, approximately. In the bottom right-hand panel, Models Urb that include a high azimuthal velocity, the collapse is extremely fast and the time scale has been reduced to a range from 0.1 to 0.15 t/t_{ff} . In addition, the curves for Models Urb do not show any sign of the early random collisions between the SPH particles, due to the turbulence spectrum induced on each particle velocity.

3.2. Column Density Plots

The main outcome of the collision models is shown by means of column density plots of a thin slice of gas, parallel to the x - y plane. To make a proper comparison between the different models, we have selected for each model a snapshot whose peak density is such that $\log(\rho_{\max}/\rho_0) \approx 5$.

In Model $U5$, once the head-on collision between the left-hand and right-hand sub-clouds has taken place, the asymmetry in the original sub-clouds in both radius and translational velocity, makes the right-hand sub-cloud (the biggest and the fastest cloud) swallow and drag the left-hand sub-cloud (the smallest and slowest cloud). The resulting stirred gas oscillates from the left-hand side to the right-hand side along the x -axis. The spatial symmetry in the original configuration of the right-hand sub-cloud is translated to the symmetry in the arms developed around the central cloudlet, as can be seen in the top left-hand panel of Figure 4. In § 3.1, this phenomenon was simply referred to as gas dragging, which was a useful way to explain the time of collapse by means of the density peak curves.

When the asymmetry in the radius is removed, the final result is a central cloudlet, that is elongated along the x -axis, with a strong bipolar outflow along the y -axis, as can be seen in the top right-hand panel of Figure 4, which is the outcome of Model $U13$. Because of this result, we note that the asymmetry in the velocities of the collision model is not as important as the asymmetry in the radii with respect to the outcome of the simulations.

Different results are obtained when an impact parameter is taken into account. In the case of Model $U9$, as illustrated in the bottom left-hand panel of Figure 4, the asymmetry in the radii and velocities together with an impact parameter produce a weak binary system, in which the left-hand sub-cloud (the smallest and slowest cloud) passes by and is attracted by the right-hand sub-cloud (the biggest and fastest cloud), so that part of the mass of the former is pulled out. Nevertheless, an arm is still visible around the remains of the pre-collision left-hand sub-cloud and a long arm also develops around the central cloudlet, which is analogous in origin to the arm formed in Model $U5$.

In the case of Model $U11$, when the symmetry in the radii of the pre-collision sub-clouds is restored but still in the presence of the impact parameter as in Model $U9$, a binary system is formed as the main outcome, in which several gas bridges are seen to be strongly connecting the remains of the two collid-

ing clumps, as can be seen in the bottom right-hand panel of Figure 4.

In Figure 5 we show the column density plots of Models Ub , with a high level of turbulence. As expected, there is a lot of similarity with the previous Models U , with a low level of turbulence, because the initial structure of the velocity spectrum is the same for both Models U and Ub . The only difference is the magnitude of the velocity. The larger magnitude of the velocity for Models Urb makes the arms and tails larger and better defined than those in Models U .

Let us now consider the iso-density plots for Models Ur , which are shown in the Figure 6. In this case, we show two columns of density plots. In the right-hand column of Figure 6, we show the density plots for the snapshots with almost the same density peak shown in Figure 4 to allow comparison with Models U and Ub . We only observe an homogeneous and spherical collapse as the final result of simulations Ur .

In the left-hand column of Figure 6, we choose snapshots of the first stage of evolution, to show the early development of a central lump of gas, which is a direct consequence of the azimuthal velocity added to the particle velocity, see § 2.3. This central lump of gas makes the collapse of the cloud faster, as can be seen in Figure 3, because it acts as a centrally located mass attractor.

Finally, let us consider the iso-density plots for Models Urb , which are shown in Figure 7. We observe the formation of a massive lump of gas at the cloud center, at the beginning of the evolution, similarly to those shown in the left-hand column of Figure 6. However, for each Model Urb , the massive lump of gas is quite bigger than for models Ur . This is a direct consequence of the higher azimuthal velocity added to the particle velocity, see § 2.3. This massive central lump of gas makes the collapse quite faster than that observed for Models Ur , as we notice happens in the bottom right-hand panel of Figure 3.

3.3. 3D Rendered Plots

In Figure 8, we show the spatial structure of the models U using 3D plots, for the same time and density chosen for the snapshot shown in Figure 4. Until now, the figures displayed in § 3.2, have been cuts parallel to the equatorial plane of the initial sphere, so that around of 10,000 particles are included in the slice shown. For the 3D plots, all of the particles with a density greater than $\log(\rho_{\max}/\rho_0) \approx 0.7$ and located within the region $[-2.5, 2.5]$ in the three Cartesian coordinates x, y, z , entered in the 3D plots.

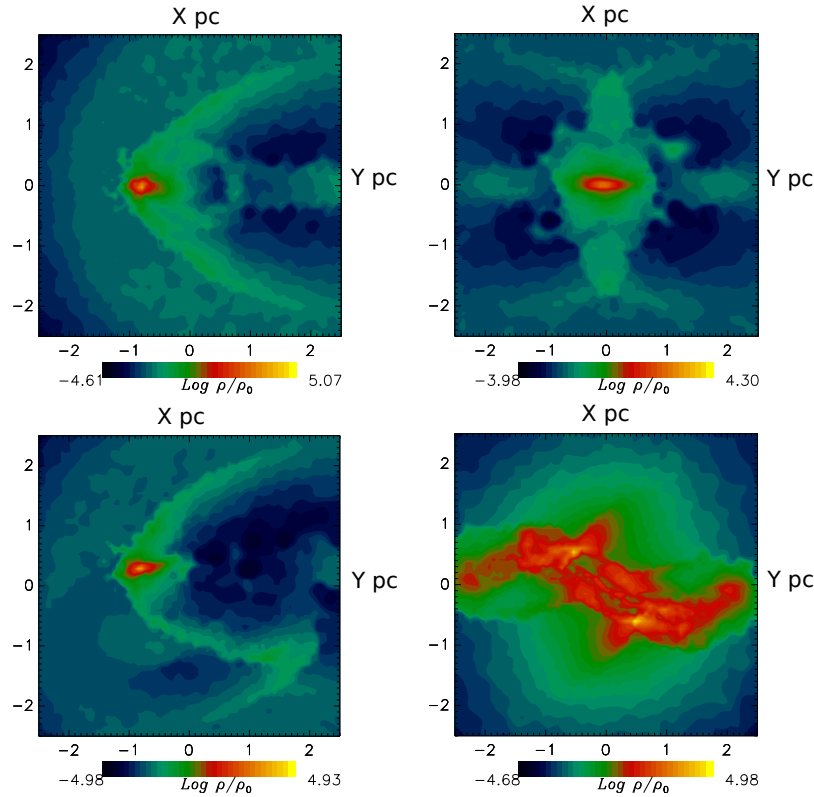


Fig. 4. Column density plots of the collision models U , for a thin slice of gas parallel to the x - y plane. The unit of length is one parsec. The models are shown in panels as follows: (top left-hand) $U5$ (at time $t/t_{ff} = 1.65$ and peak density $\log(\rho_{\max}/\rho_0) = 5.0$); (top right-hand) $U13$ (at time $t/t_{ff} = 1.34$ and peak density $\log(\rho_{\max}/\rho_0) = 4.3$); (bottom left-hand) $U9$ (at time $t/t_{ff} = 1.42$ and peak density $\log(\rho_{\max}/\rho_0) = 5.0$); (bottom right-hand) $U11$ (at time $t/t_{ff} = 2.4$ and peak density $\log(\rho_{\max}/\rho_0) = 5.0$). The color figure can be viewed online.

In this case, the number of particles that are used to make the 3D plots ranges from 181266 to 5616884. The log of the density is rendered in the 3D plots by assigning a color and a vertical bar located in the bottom right-hand corner of each panel. It must be noted that an arbitrary rotation is done on the Cartesian coordinates to show some of the details of the spatial structure.

In the top left-hand panel of Figure 8, we see the remains of Model $U5$, view from the rear (along the positive x -axis), in which one can see an elongated bulb. In the region where the unequal sub-cloud collision takes place, on the negative side of the x -axis, one can see a thick disk of gas surrounding the elongated bulb. This structure looks like a mushroom pointing toward the negative x -axis.

In the top right-hand panel of Figure 8, we see the remains of Model $U13$; recall that this collision is head-on along the x -axis between two equal sized sub-clouds. For this reason, one can see an elongated solid tube of gas along the x -axis, surrounded by an almost spherical gas region, which is formed by the

particles bounced from the collision, most of which escape away along the y -axis in both directions, positive and negative.

In the bottom left-hand panel of Figure 8, we see the remains of Model $U9$, in which two unequal sized sub-clouds have an oblique collision. One can see only the remains of each separate sub-clouds, after their close encounter, so one can notice that the bottom sub-cloud is almost destroyed by the tidal force caused by the top sub-cloud.

In the bottom right-hand panel of Figure 8, we see the remains of Model $U11$, in which two equal-sized sub-clouds have an oblique collision. For this reason, the symmetry is evident between the top and bottom gas tubes, which are formed as the tracks of the original colliding sub-clouds. There is a complex bridge of gas connecting these top and bottom tubes. A disk of gas is surrounding the bridge.

3.4. Distribution Function of the Radial Component of Velocity

In Figure 9 we show in the vertical axis the fraction of particles with a velocity smaller than that

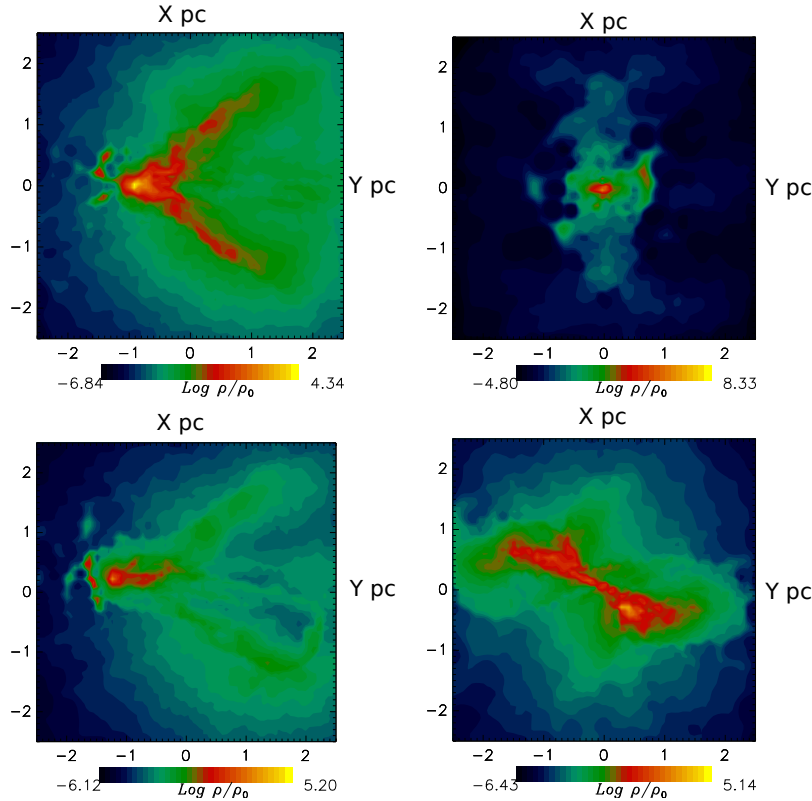


Fig. 5. Column density plots of the collision models Ub , for a thin slice of gas parallel to the x-y plane. The unit of length is one parsec. The models are shown in panels as follows: (top left-hand) $U5b$ (at time $t/t_{ff} = 2.15$ and peak density $\log(\rho_{\max}/\rho_0) = 4.34$); (top right-hand) $U13b$ (at time $t/t_{ff} = 1.73$ and peak density $\log(\rho_{\max}/\rho_0) = 8.63$); (bottom left-hand) $U9b$ (at time $t/t_{ff} = 2.08$ and peak density $\log(\rho_{\max}/\rho_0) = 5.20$); (bottom right-hand) $U11b$ (at time $t/t_{ff} = 2.42$ and peak density $\log(\rho_{\max}/\rho_0) = 5.14$). The color figure can be viewed online.

shown in the horizontal axis. This distribution function of the velocity is taken at the same time and density as the snapshots shown in Figures 4, 5, 6 and 7. We consider only the radial component of the velocity, which is calculated with respect to the center of the cloud.

By comparing with the panels of Figure 2 in § 2.5, one can see that the fraction of the simulation particles with a negative component of the radial velocity has increased from 0.5 at time $t/t_{ff} = 0$ for all the models, to 0.9 for Models U , at time of the Figure 4; to 0.8 for Models Ub and to 0.9 for Models Ur . This means that a high fraction of the simulation particles have likely reached already (Models $U5$, $U9$ and $U13$) or are flowing towards (Model $U11$) an accretion center.

4. DYNAMIC CHARACTERIZATION OF THE SIMULATIONS OUTCOME

Let us define a cloudlet as the densest region of a simulation outcome, whose physical properties must be determined. The center of the cloudlet and a ra-

dius are the main parameters to delimit the cloudlet region and calculate its physical properties. These centers do not coincide in general the center of mass of each simulation, although both kind of centers are close to each other, as can be seen in Figure 10, in which we show the center of each cloudlet in Models U .

4.1. Radial Profile of the Density and Mass

In Figure 11 we show the radial profile of the density (in the left-hand column) and the mass (in the right-hand column), calculated with respect to the center of each cloudlet as defined in Figure 10.

It must be clarified that the density $\rho_{\text{bin}}(r)$ and mass $M(r)_{\text{bin}}$, shown in the vertical axis of Figure 11, are determined by taking into account only those particles located within the radii r and δr , where δr is given by $4/500$ pc per bin, and r goes from $r = 0$ (the cloudlet center) to $r_{\text{max}} = 4$ pc (even further than the edge of the cloudlet, because we want to study the environment of the cloudlets as well).

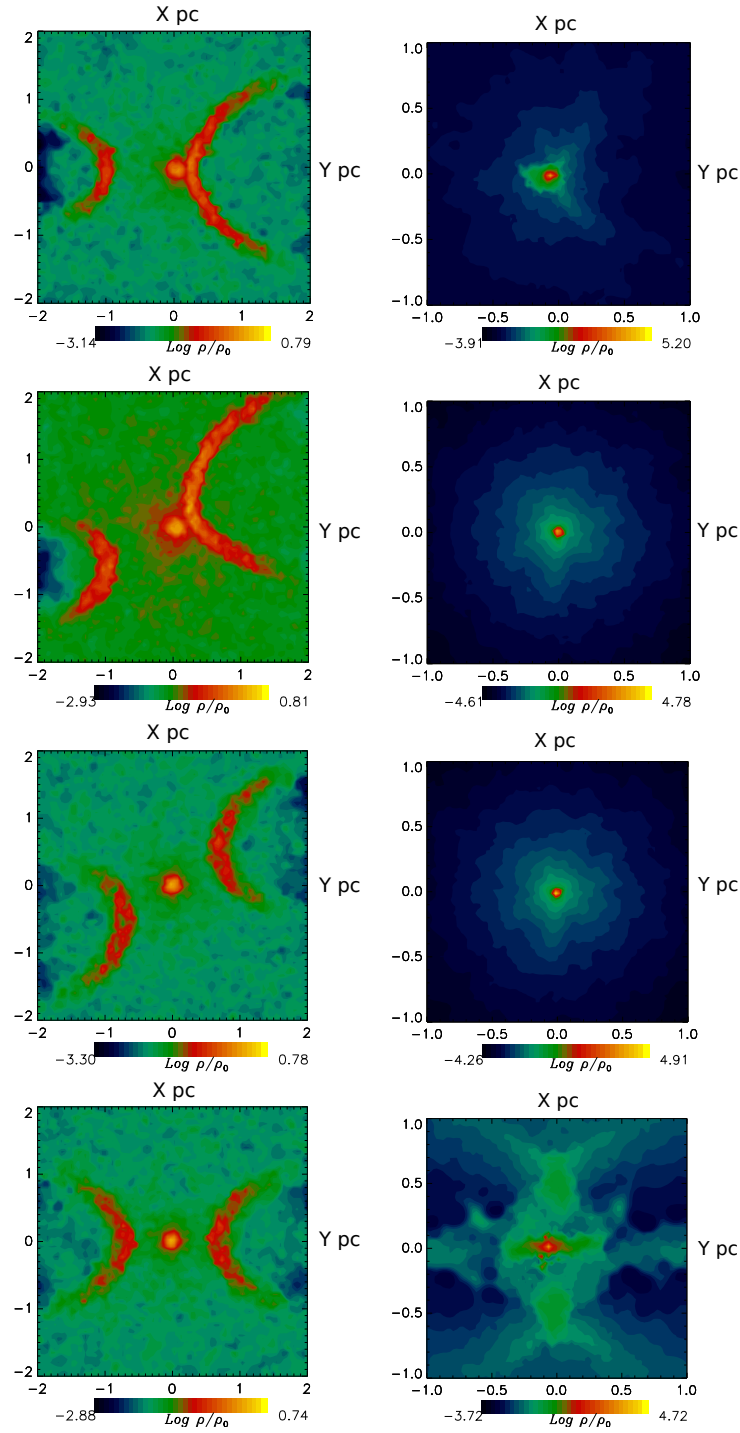


Fig. 6. Column density plots of the collision models U_r , with an azimuthal velocity included, see § 2.3. The models are shown in panels (from top to bottom) as follows: (first line) Model $U5r$, (left) at time $t/t_{ff} = 0.24$, peak density $\text{log}(\rho_{\text{max}}/\rho_0) = 0.79$ and (right) at time $t/t_{ff} = 1.05$, peak density $\text{log}(\rho_{\text{max}}/\rho_0) = 5.2$; (second top line) Model $U9r$, (left) at time $t/t_{ff} = 0.25$, peak density $\text{log}(\rho_{\text{max}}/\rho_0) = 0.8$ and (right) at time $t/t_{ff} = 1.05$, peak density $\text{log}(\rho_{\text{max}}/\rho_0) = 4.8$; (third line) Model $U11r$, (left) at time $t/t_{ff} = 0.23$, peak density $\text{log}(\rho_{\text{max}}/\rho_0) = 0.78$ and (right) at time $t/t_{ff} = 1.05$, peak density $\text{log}(\rho_{\text{max}}/\rho_0) = 4.9$; (fourth line) Model $U13r$, (left) at time $t/t_{ff} = 0.22$, peak density $\text{log}(\rho_{\text{max}}/\rho_0) = 0.74$ and (right) at time $t/t_{ff} = 0.92$, peak density $\text{log}(\rho_{\text{max}}/\rho_0) = 4.7$. The color figure can be viewed online.

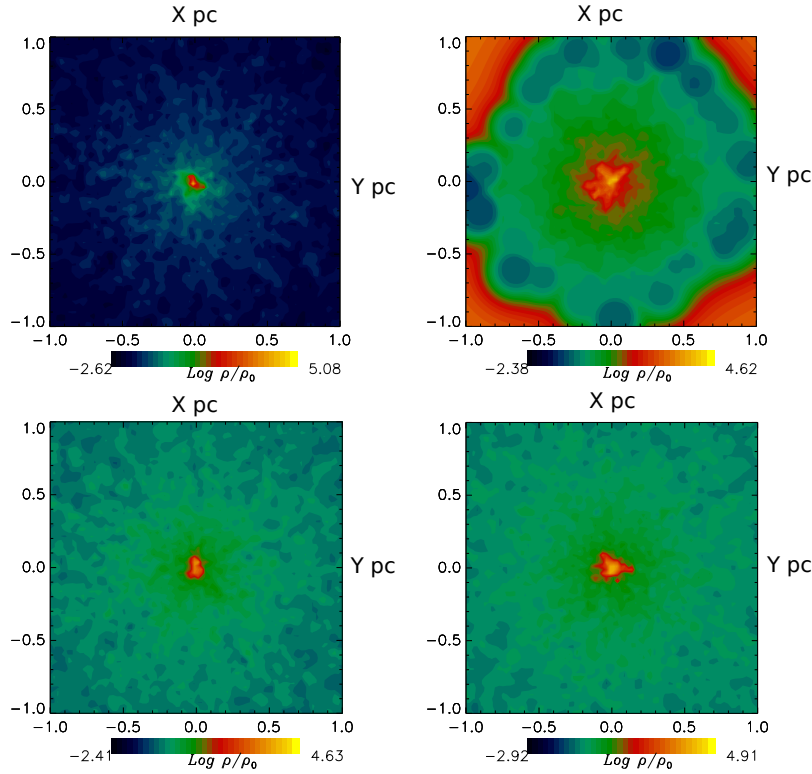


Fig. 7. Column density plots of the collision models Urb , for a thin slice of gas parallel to the x-y plane. The unit of length is one parsec. The models are shown in panels as follows: (top left-hand) $U5rb$ (at time $t/t_{ff} = 0.12$ and peak density $\log(\rho_{\max}/\rho_0) = 5.0$); (top right-hand) $U13rb$ (at time $t/t_{ff} = 0.12$ and peak density $\log(\rho_{\max}/\rho_0) = 4.62$); (bottom left-hand) $U9rb$ (at time $t/t_{ff} = 0.09$ and peak density $\log(\rho_{\max}/\rho_0) = 4.63$); (bottom right-hand) $U11rb$ (at time $t/t_{ff} = 0.15$ and peak density $\log(\rho_{\max}/\rho_0) = 4.62$). The color figure can be viewed online.

Let us consider the top line of Figure 11 for Models U . For Model $U11$, there are two cloudlets. Consequently, we label the cloudlet located to the left of the vertical axis and above the horizontal axis, as Cloudlet “a” (in the upper left-hand region). We label the cloudlet located to the right of the y-axis and below the x-axis as Cloudlet “b”, as can be seen in the bottom right-hand panel of Figure 10.

The curves of ρ_{bin} for Models $U5$, $U9$, $U11a$ and $U11b$ are not steep, as opposed to the curve for Model $U13$. This means that the cloudlets of these models must have a mass increasing with radius, as can be seen in the right-hand panel of the top line of Figure 11.

Model $U13$ is the only one that shows a density curve $\rho_{\text{bin}}(r)$ decreasing significantly with radius r . For this behavior, the mass $M(r)_{\text{bin}}(r)$ is almost kept constant for a wide range of radii. This would be the standard behavior of a dense cloudlet formed by gravitational attraction in a simulation.

In the second and third lines of Figure 11, from top to bottom, we show the curves for Models Ub

and Ur , respectively. The behavior observed here is quite similar to the one described earlier for Model U . In the bottom line, we show the curves for Models Urb , which include a high azimuthal velocity and as we have seen in § 3.2, the simulation outcome changed significantly. In this case, the density curves are kept constant and the mass curves are slightly increasing functions of the radius, above all in the range of radius 0-3 pc.

Rathborne et al. (2015) found curves for the radial profile of the mass and density of the Brick, such that the mass curve is always an increasing function of their effective radius, while the density curve is always a decreasing function, both curves extending up to a effective radius of 2 pc. For instance, the mass contained within its central one pc is approximately $6 \cdot 10^3 M_{\odot}$, while the density curve follows a power-law over radii $r^{-1.2}$.

The increasing mass curves shown in the right-hand column of Figure 11 are of the same order of magnitude as those reported by Rathborne et al. (2015), taking into account that the curves of Fig-

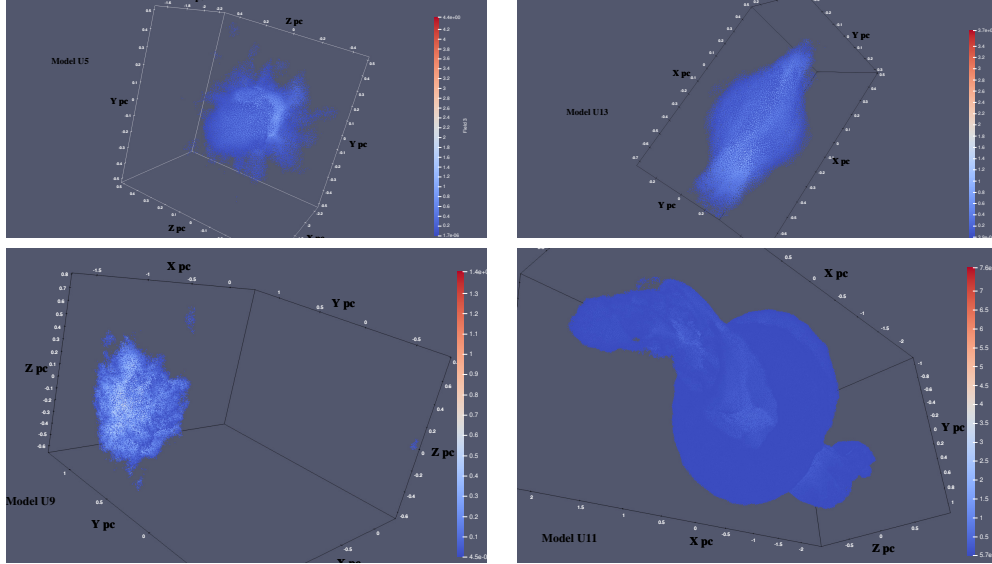


Fig. 8. 3D-plots of the collision Models U for the same snapshots of Figure 4, rotated arbitrarily to reveal more details of the configurations, in a window of spatial dimension from -2.5 to 2.5 , in each of the axis- xyz , in which only those particles with $\log(\rho_{\max}/\rho_0) > 0.7$ have entered to make the plot. The panels and the number of particles entered are shown as follows: (top left-hand) $U5$ with 243455 particles; (top right-hand) $U13$ with 287037 particles; (bottom left-hand) $U9$ with 181266 particles and (bottom right-hand) $U11$ with 5616884 particles. The color figure can be viewed online.

ure 11 are not cumulative (as we mentioned earlier). Therefore, the exterior layers (outside of the densest central region) of the cloud, contain a substantial amount of mass.

4.2. Radial Profile of the Radial and Tangential Components of the Velocity

In Figure 12, we show the radial profile of the radial (left-hand column) and tangential (right-hand column) components of the velocity. We apply here the same radial partition described in § 4.1; that is, from the cloudlet center up to 4 pc.

Let us clarify the meaning of the tangential component of the velocity. In spherical coordinates (r, θ, ϕ) , a gas particle has a magnitude of the velocity vector v_p with the components v_r, v_θ and v_ϕ . Then, we split the components of the velocity into radial v_r and tangential $v_t = (v_\theta + v_\phi)/2$, so that we can follow both components separately. We do this separation because the radial component can be associated with a collapse trend while the tangential component can be considered as a manifestation of turbulence, see Guerrero and Vázquez (2020).

The left-hand column panels Figure 12 indicate that many particles move to the cloudlet center, mostly from the innermost region of the cloud. The right-hand column panels Figure 12 indicate that

there is a non-zero, almost constant, tangential component of the velocity. These observations indicate that a lot of particles are falling towards the cloudlet center in trajectories that are slightly curved (i.e., not from a purely radial direction, such as in a free-fall).

Let us recall the behavior of a test particle and let its velocity magnitude be given by v_g . This v_g is determined by $v_g = \sqrt{2GM(r)/r}$, where $M(r)$ is the mass contained up to radius r and G is Newton's gravitational constant. This v_g can be considered as the velocity when a test particle arrives at distance r from the central mass M , having started from rest at infinity, where its gravitational potential is zero. As is well known, for a spatially bounded mass of radius R_g , the velocity v_g must increase with the radius r , such that $0 < r < R_g$. Once the radial coordinate r is outside the bounded mass, that is, for $r > R_g$ the velocity v_g simply decreases.

It must be noted that a significant fraction of the total velocity magnitude v_p comes from its radial component v_r , though a minor fraction of v_p comes from the tangential components grouped in v_t . Then, we can think about a curve of v_p if we see a curve of v_r , because we only need to transform from v_r to v_p by changing the velocity sign, from

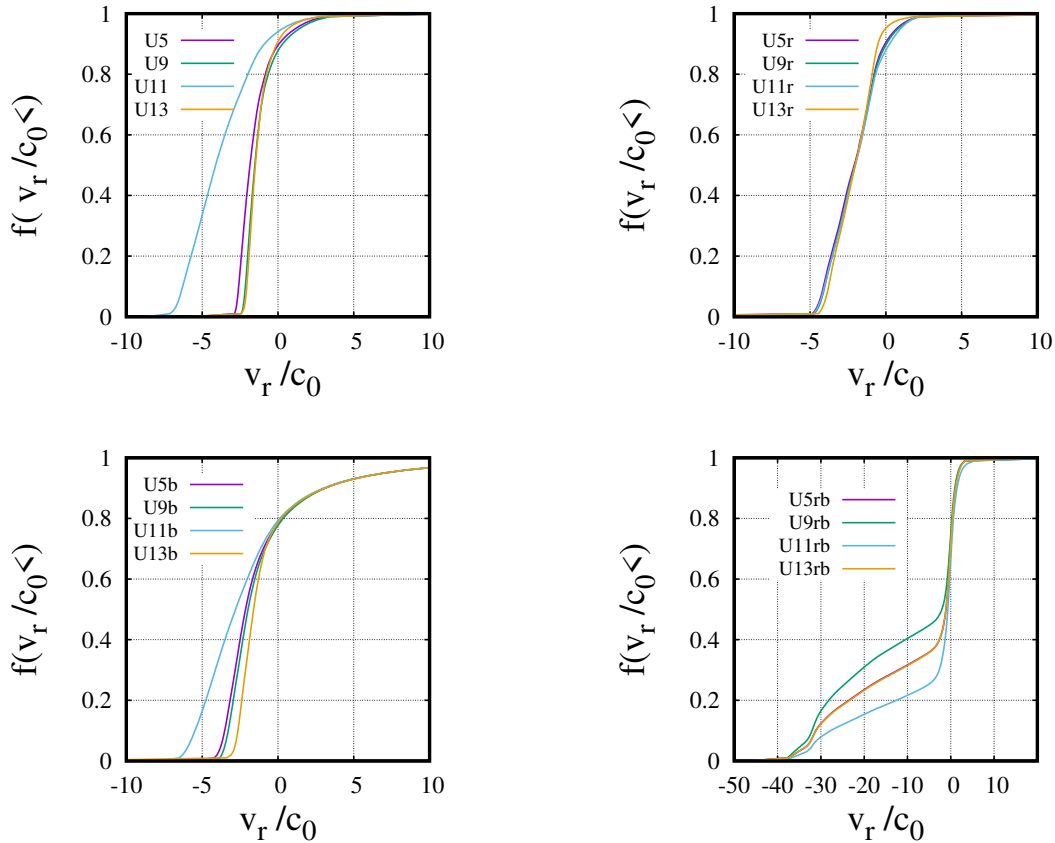


Fig. 9. Distribution function of the the radial component of the velocity, calculated with respect to the center of the cloud. The snapshots are taken at the same time and density as the snapshots shown in Figure 4, 5, 6 and Figure 7. (top left-hand) Models U with a low level of turbulence; (top right)-hand Ur with a low azimuthal velocity (bottom left-hand) Ub with high level of turbulence and (bottom right-hand) Urb with a high azimuthal velocity. The color figure can be viewed online.

negative to positive values, so that the behavior of both curves, v_r and v_p , would be very similar.

Let us consider the panels of the top line of Figure 12, which are for Models U . In terms of the “imagined curves” of $v_p(r)$, the cloudlets $U11a$ and $U11b$ follow the behavior expected for the test particle velocity, indicating that the cloudlet radius R (the analog of the bonded mass) is around 1 pc for both cloudlets of Model $U11$. The curves for Models $U9$ and $U13$ indicate that the bounded mass has a very small radius R , which is slightly smaller than 0.5 pc. For Model $U5$, the resolution of the radial partition is not fine enough to indicate a radius R of the cloudlet found. This bounded mass can be identified with the size of the region from the center of the cloud, which is a particle reservoir, out of which the particles flow towards the cloud center. The core of the collapsing cloud, which is formed by the parti-

cles with higher density of the simulation, is located in these cloud centers.

The panels of the second line of Figure 12, from top to bottom, show the curves for the Models Ub , which are very similar to those already described for Models U .

The panels of the third line of Figure 12, which are for Models Ur , with a low azimuthal velocity, indicate a behavior very similar to that observed for Models $U9$ and $U13$, that is, a region of particle reservoir is about 1 pc in radius from the center of the cloud. These behaviors can be better seen in the panels on the bottom line of Figure 12, which are for Models Urb . Models Urb have a high azimuthal velocity, whose effect is more clearly seen because the in-fall velocity is quite higher than in the previous Models U , Ub and Ur . Instead of a bounded mass, the size of the region of strong in-fall gas is deter-

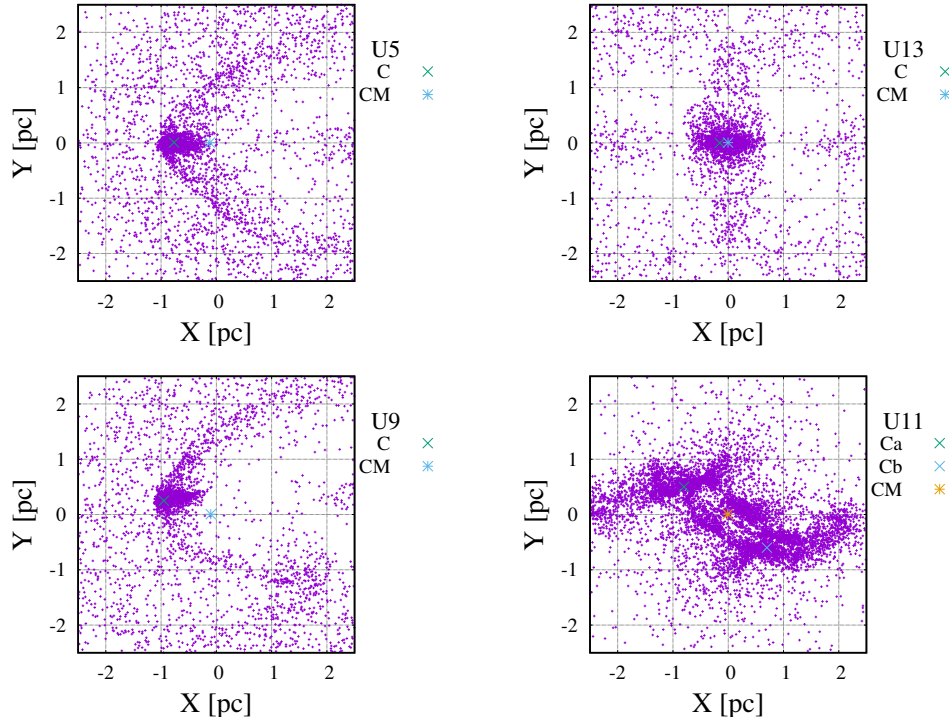


Fig. 10. Cloud centers are marked with a symbol “x”; the center of mass is marked with the symbol “*”; both of them are located in a thin slice parallel to the xy plane, in which the symbol “+” represents a gas particle. The models are as follows: (top left-hand) $U5$; (top right-hand) $U13$; (bottom left-hand) $U9$ and (bottom right-hand) $U11$. The color figure can be viewed online.

mined by the size of the centrally located lump of gas induced by the azimuthal velocity, see the left-hand column of Figure 6, for an illustration.

4.3. Integral Properties of the Cloudlets

In Figure 13 we show the values of the dimensionless ratios α and β , respectively, calculated only for a cloud region that includes the cloudlets and their surroundings. Two parameters are used: the first parameter is $\log(\rho_{\min})$, which is a lower bound for density; and the second parameter r_{\max} is a maximum radius, which is taken with respect to the cloudlet’s center. To calculate the ratios α_f and β_f for the cloudlets, we consider only those particles that have a density greater than $\log(\rho_{\min})$ and are located at a radius smaller than r_{\max} . To make a comparison between all the models and to calculate the properties of all the models shown in Figure 13, we have used the following values $\log(\rho_{\min}) = 0.0$ and $r_{\max} = 1.5$ pc.

One can see in the top left-hand panel of Figure 13 that Models $U5$, $U9$ and $U13$ have a similar value for the ratio α_f , which is around 0.1. For the cloudlets “a” and “b” of Model $U11$ (i.e.,

$U11a$ and $U11b$) α_f is around 0.05. The values of the ratio β_f ranges from 0.1 for Model $U13$, around 0.13 for Model $U5$, and a little higher than 0.2 for Model $U9$. Cloudlets $U11a$ and $U11b$ have the highest values of $\beta_f \approx 0.55$. Cloudlets $U11a$ and $U11b$ are the only ones over-virialized, because their sum $\alpha_f + \beta_f > 1/2$; while Models $U5$, $U9$ and $U13$ are sub-virialized, because their sum $\alpha_f + \beta_f < 1/2$. The same behavior is observed for Models U_b , with a high turbulence, as can be seen in the bottom left-hand panel of Figure 13.

In both the top right-hand panel and the bottom left-hand panel of Figure 13, we see that curves for the Models U_r and U_b , respectively, show a behavior that is very similar to that already observed for the curves of Models U . For all Models U_r and U_b the ratio α_f is around the value 0.09, with a clear tendency to lower values. The ratio β_f for these models ranges from 0.1 to 0.5. Models U_r , U_r5 , U_r9 and U_r13 are sub-virialized, because their sum $\alpha_f + \beta_f < 1/2$. Meanwhile, the two cloudlets of Model U_r11 are over-virialized, because their sum $\alpha_f + \beta_f > 1/2$. The same behavior is observed for Models U_b .

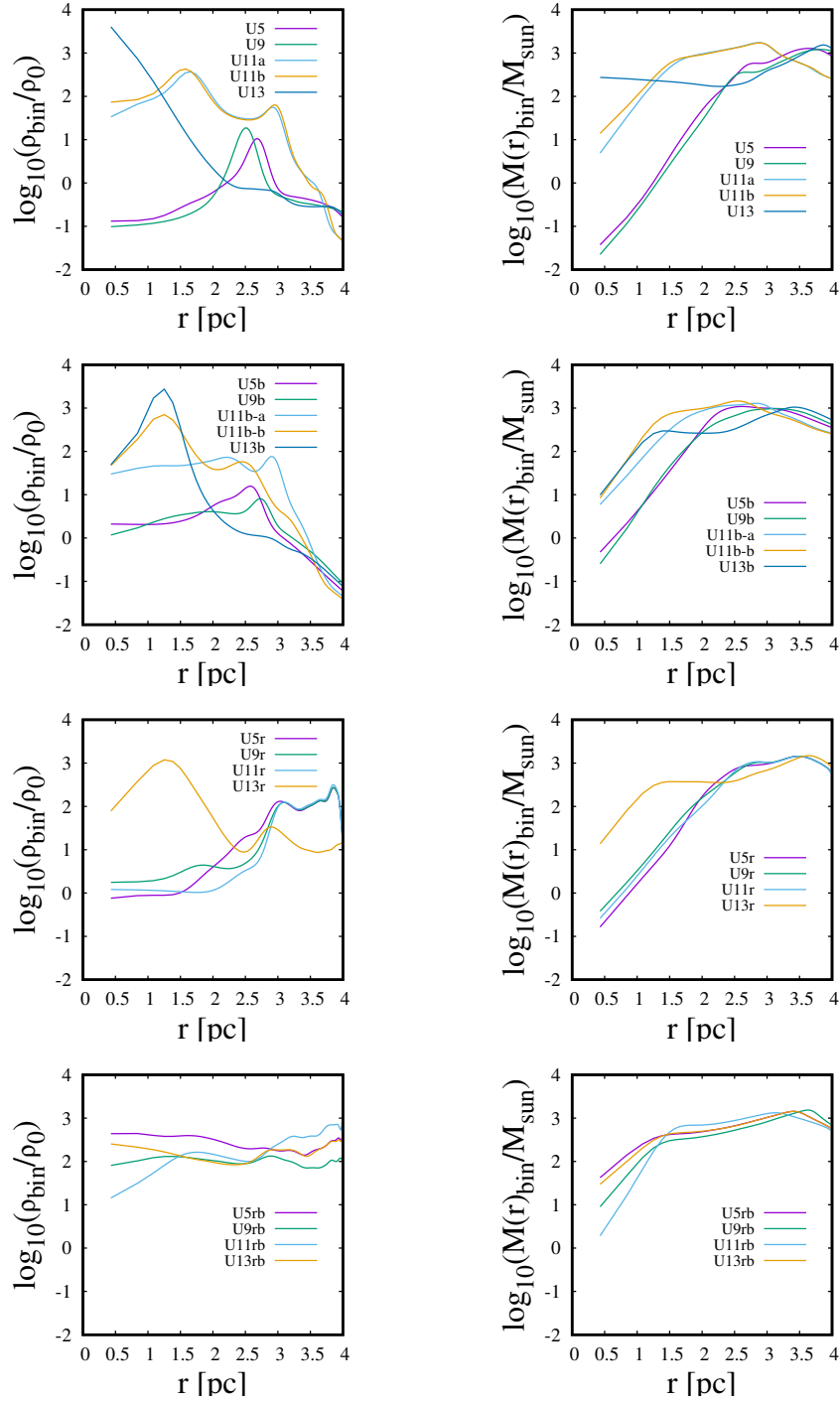


Fig. 11. (Left-hand panel) Radial profile of the density and (right-hand panel) radial profile of the mass. In the vertical axis we show the mass and density averaged over those particles located within the radial spherical shell defined by r , so that these functions are not cumulative. In the horizontal axis, r starts at 0, the center of each cloudlet, as illustrated in Figure 10 for Models U and analogously calculated for all the other models. The panels on the top line are for Models U ; the panels on the middle line are for Models Ur and the panels on the bottom line are for Models Urb . The snapshots are taken at the same time and peak density as in Figure 4, Figure 5, Figure 6 and Figure 7, respectively. The color figure can be viewed online.

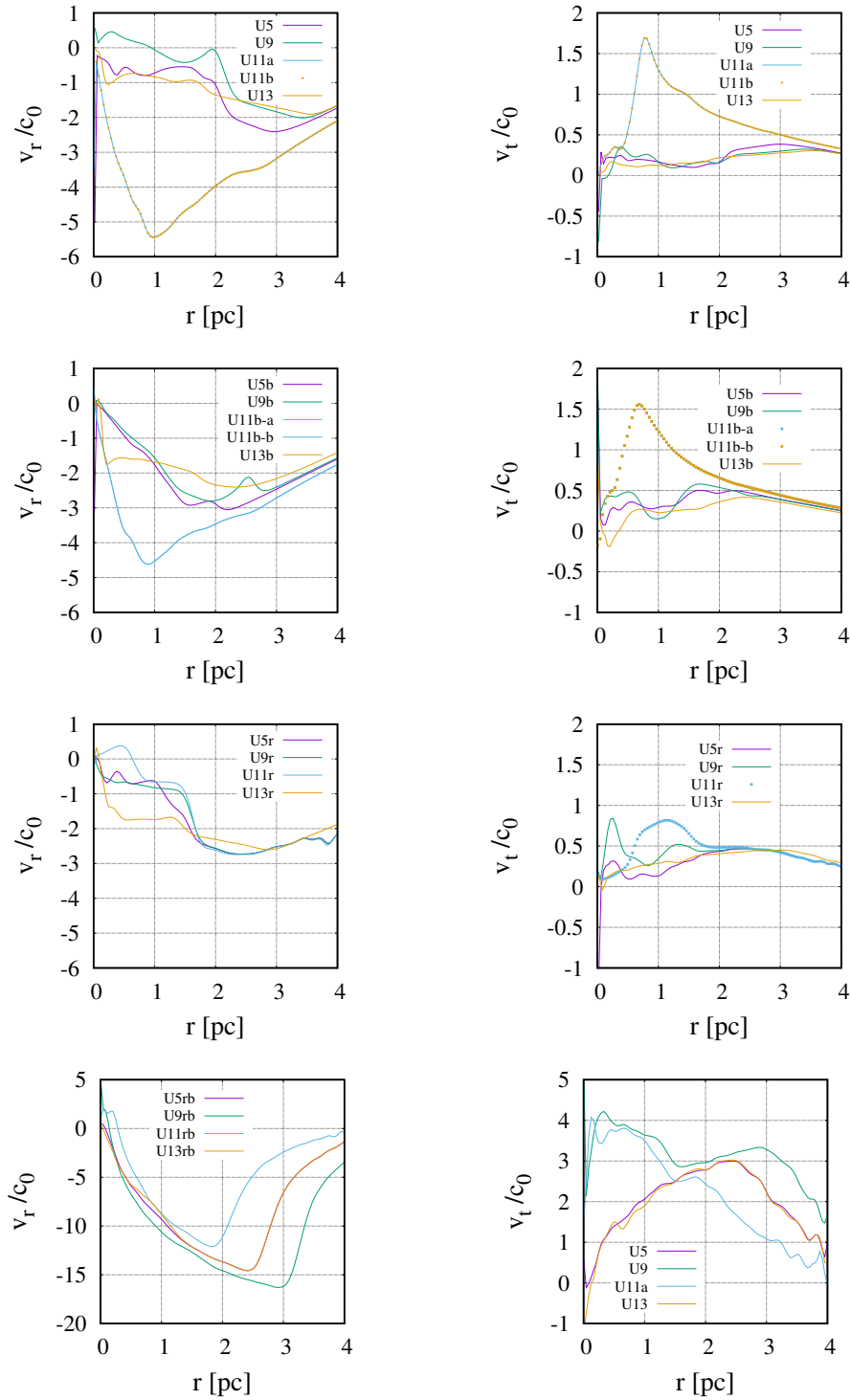


Fig. 12. (Left-hand column) Radial profile of the radial component of the particle velocity and (right-hand column) the radial profile of the tangential component of the particle velocity, both calculated with respect the center of each cloudlet illustrated in Figure 10 and normalized with the speed of sound. From top to bottom, the first line of panels is for Models U ; the second line for Models Ub and the third and four lines for Models Ur and Urb , respectively. The snapshots considered for these calculations are taken at the same time and peak density shown in Figure 4, Figure 5, Figure 6 and Figure 7, respectively. The color figure can be viewed online.

On the opposite side, all Models *Urb*, as shown in the bottom right-hand panel of Figure 13, are over-virialized, because the high initial azimuthal velocity is manifested in the excess of kinetic energy, such that the β_f ratio for these models is in the range 7-11. In spite of this excess of kinetic energy, all Models *Urb* have collapsed.

We show the mass associated with the cloudlets of the models on the vertical axis of Figure 14. We have considered the mass of only those particles that entered into the calculation of the physical properties shown in § 4. In the horizontal axis, we show Models from 1 to 4, ordering the models in the following way: *U5*, *U9*, *U11* and *U13*, respectively.

The mass of the cloudlets for Models *U5*, *U9* and *U13* are shown in the top left-hand panel, so that the mass ranges from $\log(M_f/M_\odot) = 3.6$ to 3.8. Two cloudlets of Model *U11* have the largest masses, around $\log(M_f/M_\odot) = 4.6$.

In contrast to what we have observed when compared to other physical properties of Models *U* with *Ub*, the behavior is different; in the case of the mass of the cloudlets, without any trend.

The mass of the cloudlets for Model *Ur* is shown in the top right-hand panel of Figure 14. We see that Models *Ur5*, *Ur9* and *Ur11* all have similar cloudlet masses, which are around $\log(M_f/M_\odot) = 4.5$. Meanwhile, the cloudlet mass for Model *Ur13* is a little smaller than the mass of the other models, $\approx \log(M_f/M_\odot) = 4.4$.

Given that Models *Urb* have the highest in-fall radial velocity of the all the models, as can be seen in 12, then their mass accretion rate must be the highest too; for this, the mass enclosed is systematically higher than in the other models, although there is not much difference in the mass values observed in the panels of Figure 14 when compared to the big difference in the infall radial velocity.

It must be emphasized that the mass scale shown in Figure 14 is in agreement with the mass observed for an open cluster of stars, which is around $10^4 M_\odot$, while the mass scale of a globular cluster of stars is around $10^5 M_\odot$, see Kumai et al. (1993).

The results of the collapse of a gas core (e.g., in the so called “standard isothermal simulation”) are identified as protostars (Boss (1995), Boss et al. (2000), Burkert and Alves (2009) and Arreaga (2007)). In the same sense, the gas structures obtained from the simulations of the present paper and whose properties are shown in § 4 can be called a proto-cluster of protostars. As is well-known for simulations of the collapse of a gas core, the mass of the proto-stars depends on the mass of the parent

cloud, see for instance Arreaga (2016). The same is expected to be true for proto-clusters.

Finally, it must be recalled that the results displayed in Figure 13 and Figure 14 are taken when the collapse is still ongoing, so that the peak density is around $\log(\rho_{\max}/\rho_0) \approx 5$. As we have seen in § 3.1, the final state of the collapse reaches a peak density around $\log(\rho_{\max}/\rho_0) \approx 8$.

5. DISCUSSION

Although the dynamics of an isolated turbulent cloud is well-known (see for instance Goodwin et al. 2001a, Goodwin et al. 2004b and Goodwin 2006), in § 5.1 we begin by describing the evolution of the isolated turbulent cloud, to discuss its influence on the collision models considered in § 5.2, § 5.3 and § 5.4. After this, we commence the discussion about the most important features of the collision models presented in § 3.

5.1. *The Collapse of the Isolated Turbulent Cloud*

We mentioned in § 1 and § 2.2 that the initial conditions of the isolated cloud are chosen to favor its gravitational collapse. The curve of the peak density for the isolated cloud develops a small peak at a time smaller than $t/t_{ff} = 0.1$. This increase of density happens because of the multitude of gas lumps formed by the collisions between gas particles that occur simultaneously throughout the cloud. This density peak does not appear for low levels of initial kinetic energies, which is measured by the β ratio defined in equation 5; for high values of the β ratio, this early peak is quite noticeable.

In contrast, the time required by the isolated cloud to reach the highest density values, for instance $\log(\rho_{\max}/\rho_0) \approx 6$, does not depend significantly on the level of the initial energy, at least for a wide range of the initial β ratio. This is due to the fact that almost all of the kinetic energy available is equally dissipated by the random collision of particles, as described in the previous paragraph. The time required for the cloud to reach its highest peak density is around $t/t_{ff} = 2.5$, which is of the same order of time that can be seen in Figure 3 for the collapse of the collision models.

In the time interval between $0.1 < t/t_{ff} < 2.0$, a relaxation of the small gas lumps occurs throughout the cloud, so that the peak density curve decreases quickly. From there, it increases very slowly, up to times $t/t_{ff} > 2.0$, at which the final collapse takes place very quickly.

From the point of view of the column density plots, the occurrence of collisions between gas particles, as a consequence of the turbulent velocity field

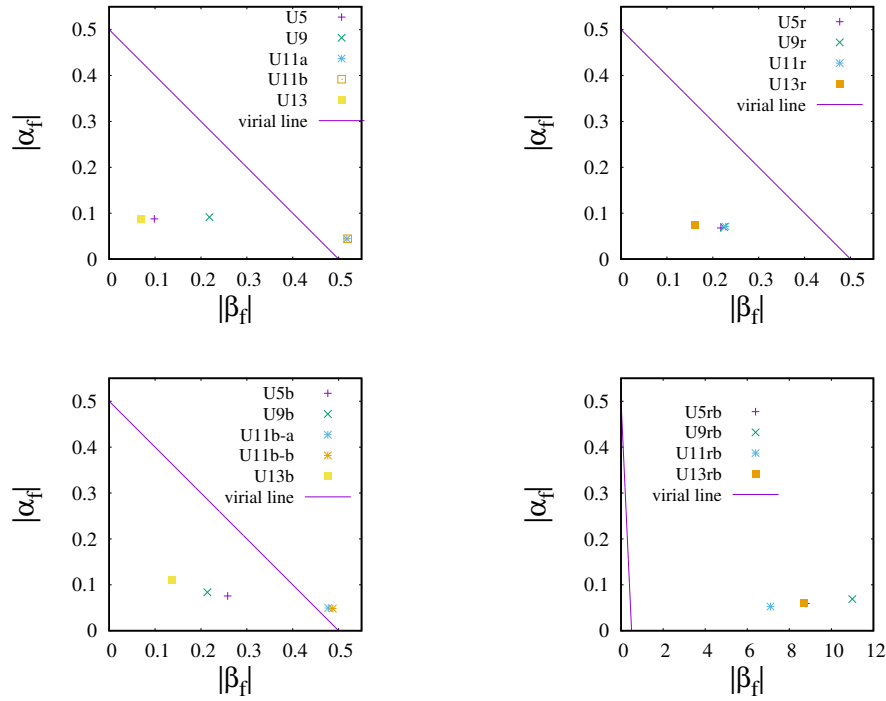


Fig. 13. The ratio of the thermal energy to the gravitational energy α versus the ratio of the kinetic energy to the gravitational energy β , of the cloudlets defined in § 4.3, at the same time as the snapshots shown in Figure 4, Figure 5, Figure 6 and Figure 7, respectively. (top left-hand) U with a low level of turbulence; (top right-hand) U_r with a low azimuthal velocity; (bottom left-hand) U_b with a high level of turbulence and (bottom right-hand) U_{rb} with a high azimuthal velocity. The color figure can be viewed online.

implemented initially, is seen as a random formation of many over-dense lumps of gas, which are homogeneously distributed across the entire cloud volume, see the left-hand panel of Figure 15. Later, when the initial kinetic energy of the cloud is dissipated, the cloud reaches a physical state similar to a free-fall collapse, which is seen as a clear tendency to a global collapse towards its central region. However, at the final evolution stage that could be followed in this paper, the mass accretion with spherical symmetry is lost, so that a central dense filamentary structure forms that is highly anisotropic and with a high possibility of fragmenting, see the right-hand panel of Figure 15. The behavior described in this section is paradigmatic of turbulence.

5.2. Does the Turbulence make a Difference in the Collision Simulations ?

The occurrence of the collision between the sub-clouds induced by the translation velocity $v_L : v_R$ prevents the gas particles from forming small lumps of gas throughout the cloud by means of early random collisions; as explained in § 5.1.

There is over-dense gas in the contact region between the colliding sub-clouds. This over-density accelerates the collapse of the remaining gas of the cloud, so that the turbulence does not have time enough to get relaxed by dissipation of the kinetic energy. For this reason, the turbulence does not play a fundamental role in the outcome of the simulations, such as U and U_b . In fact, if one turns off the turbulence and keeps only the collision process of the sub-clouds in these models, then the results are basically the same.

5.3. Does the Level of Turbulence make a Difference in the Collision Simulations ?

We recall that the level of turbulence in the simulations can be modified by introducing an arbitrary multiplicative constant in equation 1. As we mentioned in § 2.2.1, there is interest in considering models of turbulent clouds with extreme initial kinetic energy in addition to those clouds with low-level turbulence, which are more favored statistically. Consequently, we have studied the effect of the level of turbulence on the simulations (i.e., Models U_b), as can be seen in Table 1.

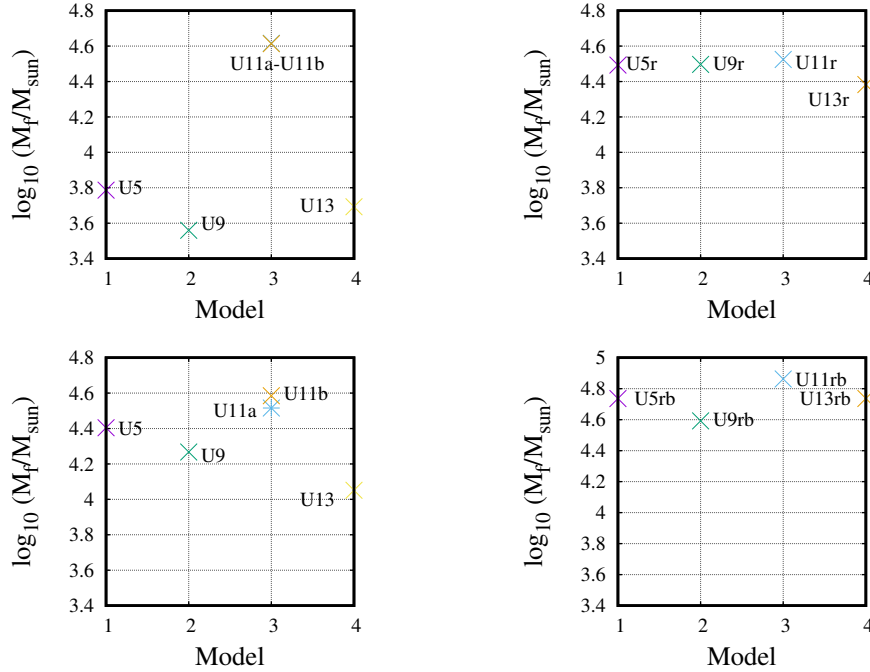


Fig. 14. The log of the mass of the cloudlets defined in § 4.3, at the same time as the snapshots shown in Figure 4, Figure 5, Figure 6 and Figure 7, respectively. (Top left-hand) U with a low level of turbulence; (top right-hand) Ur with a small azimuthal velocity; (bottom left-hand) Ub with a high level of turbulence and (bottom right-hand) Urb with a large azimuthal velocity. The color figure can be viewed online.

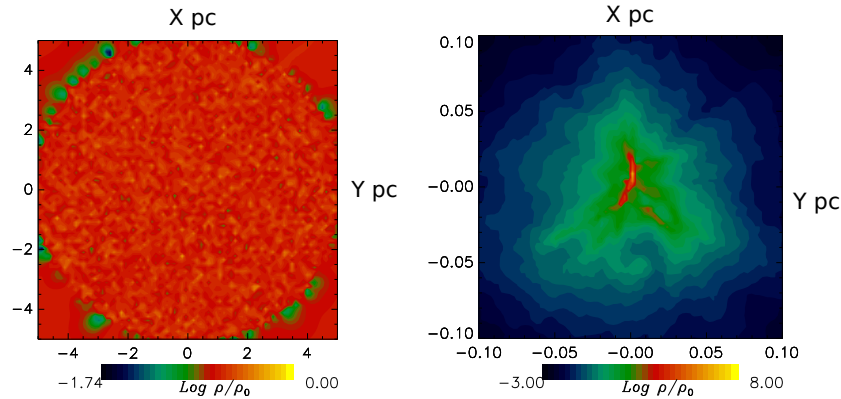


Fig. 15. Column density plots of the isolated turbulent cloud, for a thin slice of gas parallel to the x - y plane. The unit of length is one parsec. The plots are shown in panels as follows: (left-hand) at time $t/t_{ff} = 0.02$ and peak density $\log(\rho_{\max}/\rho_0) = 0.53$; (right-hand) at time $t/t_{ff} = 2.5$ and peak density $\log(\rho_{\max}/\rho_0) = 8.0$. The color figure can be viewed online.

The average Mach velocity \mathcal{M}_p of the gas particles for the low-level of turbulence Models U is around $\mathcal{M}_p \approx 2.9$. For the radial component of the velocity (calculated with respect to the origin of coordinates of the simulation box), the average Mach number is $\mathcal{M}_r \approx -0.13$. For the tangential component of the velocity, the average Mach number is $\mathcal{M}_t \approx 0.01$. In the meantime, the translational ve-

locities (around 15 km/s) given to the particles that are to collide are of order $\mathcal{M}_c \approx 6.6$. Then, for Models U , $\mathcal{M}_c \gg \mathcal{M}_{p,r,t}$.

For the high-level of turbulence Models Ub , we have an average $\mathcal{M}_p \approx 25$. Despite this significant increase of the magnitude of the velocity, the average radial and tangential components do not change appreciably with respect to those of Models U ; that

is, $\mathcal{M}_r \approx -0.12$ and $\mathcal{M}_t \approx 0.01$. In contrast, for Models *Ub* we have $\mathcal{M}_c \ll \mathcal{M}_p$.

In spite of the opposite features in the relation of Mach numbers for Models *U* and *Ub* with respect to the translational velocity, the outcome of the simulations *U* and *Ub* do not show any significant difference with respect to the final configuration of Models *U5*, *U9* and *U13*. The only differences that can be observed are: (i) that the double bridge of gas formed in Model *U11* becomes only one bridge in Model *U11b*; and (ii) that the density peak curves, shown in Figure 3, for the *Ub* models are displaced to the right-hand side at large free-fall times, so that the collapse takes a little longer than for Models *U*.

5.4. *How Useful is the Approximation of an Azimuthal Velocity to Mimic Tidal Forces in the Collision Simulations ?*

There is an obvious problem with the approximation of a velocity instead of a tidal force, as described in § 2.3, which is that the azimuthal velocity entered only once in the simulations, as an initial condition of the gas particles. Obviously, this is a severe limitation of the model, similar to that of the turbulence, which is not replenished continually during a simulation. Therefore, the effect of the tidal interaction must be activated during all the simulation time.

However, we observe in Figure 6 that the immediate effect of the azimuthal velocity on the simulated cloud is a strong tendency for the gas to be accumulated quickly at the cloud's center. In this case, if the azimuthal velocity terms given in equation 10 were implemented at every time step of the simulation, then to model more appropriately the tidal force over all the simulation time one would expect this tendency to accelerate the central collapse of the cloud.

It should be emphasized that the previous statement is based on the results of a very naive model, in which the only information about the massive center exerting a gravitational force on the cloud is by means of the circular velocity, which is given by $\sqrt{2GM(R)/R}$, as described in § 2.3.

According to § 2.3, the approximation of the azimuthal velocity is valid as long as the ratio between the cloud radius to the distance to the gravitational center is quite small. A way to check the applicability of this approximation is obviously to make the calculation without the approximation. However, this is not an immediate calculation. The main difficulty is the difference in length and mass scales when considering a small cloud (with very few parsecs of radius) near a massive object (probably with a scale

of kpc in radius, separated from the cloud by several hundreds of pc, or even a kpc, and whose mass can quite greater than that of the cloud), both of which must have evolved together in the same simulation code.

For instance, Gnedin (2003) resorts to a re-simulation technique, so that a low-resolution simulation of the massive object (e.g., a central dwarf galaxy) is first carried out to obtain an approximate gravitational potential. This is then used in a second high-resolution simulation of the cloud, in which this potential is taken into account as an external time-varying field on the gas particles. However, applying this technique to the problem presented in this work would require a future paper.

5.5. *A Brief Review of the Literature on this Subject*

Many papers have simulated isolated clouds and followed their collisions. However, simulations of clouds under the influence of an external gravitational potential are limited in number.

Let us now mention briefly some results of more accurate calculation methods of the tidal effects on clouds, which is a subject that has a long history. For instance, Sigalotti and Klapp (1992) used a time-varying gravitational potential to calculate the equal-sized cloud-cloud tidal interaction of clouds that are in an elliptic orbit, and reported configuration transformations on the clouds in their course to collapse.

More recently, Longmore et al. (2013) proposed that the collapse of the Brick is a progenitor of a star cluster, whose collapse was triggered as a consequence of the tidal compression exerted by Sgr B2 during the most recent peri-center passage of the Brick.

Kruijssen et al. (2015) determined a realistic orbit of a dense gas streams in the CMZ. In a subsequent paper, Kruijssen et al. (2019) calculated the tidal interaction of the galactic center on the orbit followed by the dense gas streams of the CMZ. They found that the tidal interaction acting upon the clouds makes a compression on the vertical direction, which causes the clouds to become pancake-like structures.

Later, Dale et al. (2019) simulated the evolution of turbulent clouds in orbit at the CMZ. The authors assumed a similar magnitude of the kinetic energy to the gravitational energy and found that the clouds collapse rapidly. This paper is a mature way of simulating tidal force in cloud dynamic evolutions by introducing the tidal force potential.

5.6. Applicability of these Simulations to Represent the Evolved Clouds of the CMZ

In view of § 5.2 and § 5.3, the collision process (and its parameters) is clearly the dominant physical mechanism in shaping the appearance of the cloud in the simulation outcome. It is possible that this collision of sub-clouds, with the cloud's self-gravity, is the dominant process of the cloud evolution, even over the tidal interaction with the massive center, and above all, for the small scale of the circular velocity that is induced, as compared to the magnitude of the other velocities involved, which are the turbulent and the translational velocities, see § 2.3.

For Models *U5*, *U9*, and *U13*, the geometry of the resulting configuration can be well characterized by defining a center and a radius of a cloudlet. For Model *U11*, this spherical structure does not make sense, as can be seen in Figures 4 and 8. The outcome of Model *U11* is a complex, structured molecular gas cloud that exhibits an interconnected network of components. This is the only model that can be compared or approximated to the cloud configuration called the Brick.

In fact, for the Brick, a shell-like structure with radius of 1.3 pc has been revealed from observations in the integrated intensity map of SO. For instance, see Figures 1 and 3 of Longmore et al. (2012); Figures 1 and 3 of Kauffmann et al. (2013); Figures 1 and 2 of Higuchi et al. (2014). Kruijssen et al. (2019) presented three panels in their Figure 6, to compare the results of ALMA observations of the Brick to a synthetic observation obtained from a numerical simulation. A complex gas structure can be seen in these panels, in which the gas condenses in a persistent diagonal direction with many twisted and bending filaments connected in a messy way. Model *U11* of this paper clearly shows a similar diagonal direction of the dense gas.

It may seem that there is a huge problem with Models *Ur*, given that all of the different structures obtained as a result of the collision process in Model *U* are destroyed because of the azimuthal velocity of Models *Ur*. However, the configuration obtained in Models *Ur* can be well recognized as the final outcome of the formation process of a YMC, which is observed to be a strong central condensation of gas, with an enclosed mass of stars of about $10^4 M_{\odot}$ with a size of one pc; see for instance Rathborne et al. (2015). The Arches cloud is an example of this kind of observed configuration; see Portegies et al. (2010).

6. CONCLUDING REMARKS

We examined models with three kinds of velocities, namely turbulent, translational and azimuthal.

These velocities were introduced as initial conditions of the simulation particles. Then, the particles were left to evolve as a self-gravitating gas by using the public hydrodynamic code Gadget2.

The role played by these velocities determines the subsequent evolution of the cloud. It must be emphasized that all the models considered in this paper include the same turbulent velocity spectrum (calibrated to fix the initial energies and physical properties which favors the global collapse of the cloud) and the same translational velocity (which produces the collision between two dissimilar sub-clouds).

In Models *U* with a low level of turbulence, we observed the coalescence of the sub-clouds, enriched by the asymmetry in radii and translational velocities of the sub-clouds. When the impact parameter was introduced, the model produced a binary system with interconnected arms and with a complex structure. In Models *Ub*, with a high level of turbulence, we obtained a similar structure to that observed in models *U*. However, in Model *Ub*, the arms and tails are larger than those of Models *U*. The most significant change between these simulations was observed in Models *U11* and *U11b*, such that the double bridge of gas found in Model *U11* becomes a single bridge in Model *U11b*.

The free parameters of Models *U* and *Ub* (i.e., the impact parameter, the radii and the translational velocities of the sub-clouds) have been kept fixed. If these parameters were allowed to vary, then certainly more interesting configuration outcomes will be produced.

In addition to the turbulent and the translational velocities, the last models, *Ur* and *Urb*, also include a small and a large azimuthal velocity, respectively. The purpose of this azimuthal velocity was to mimic, at least initially, the effect of the tidal force on the cloud. The magnitude of the azimuthal velocity induced in the cloud depends explicitly on the distance R from the cloud and the mass M of the gravitational center by means of the circular velocity $\sqrt{2GM(R)/R}$.

We observed that the presence of this azimuthal velocity in the simulation always induces a centrally located lump of gas in the cloud. If V_{cir} is small, then the collision process of the sub-clouds dominates the dynamics of the cloud, even over the turbulence and therefore the cloud evolution changes little compared to that observed without the azimuthal velocity. However, if V_{cir} is large compared with the other velocities involved, then the cloud evolution changes significantly: reducing too much the collapsing time, suppressing any sign of the collision

of the sub-clouds, and producing a central condensation, so that the different structures obtained as a result of the collision process are destroyed. In fact, we observed that the cloud collapses faster when the azimuthal velocity is larger.

We recall that this approximation is only valid when the ratio between the cloud radius to the distance to the gravitational center is quite small; in other words, only for spatially compact clouds. For this kind of cloud, the observation described above is in good agreement with the known fact that clouds in the CMZ are observed to be denser than clouds in the ISM. Furthermore, because gravity is an ubiquitous force, this azimuthal velocity approximation allows us to explain why centrally condensed clouds are more abundant than uniform clouds in the ISM, see Ward-Thompson (1994) and André et al. (1998).

In addition to information on shapes, we have also provided information about the physical properties of the final collapse products and their surrounding region, which include the density, mass and velocity profile. As mentioned in § 5.6, we have found proto-cluster structures that are still in their formation process. Furthermore, by the mass scale and the radius of the resulting centrally condensed configurations, the outcomes of Models Ur and Urb can be identified with the final process of the formation of a young massive proto-cluster. Basically, the models show a strong flow of particles towards the cloud center, at different radial velocities (a few Mach) and with some bending trajectories.

The author gratefully acknowledges the computer resources, technical expertise, and support provided by the Laboratorio Nacional de Supercomputo del Sureste de México through Grant number 202201010N.

REFERENCES

- Anathpindika, S. 2009a, *A&A*, 504, 437, <https://doi.org/10.1051/0004-6361/200911748>
- Anathpindika, S. 2009b, *A&A*, 504, 451, <https://doi.org/10.1051/0004-6361/200911762>
- _____. 2010, *MNRAS*, 405, 1431, <https://doi.org/10.1111/j.1365-2966.2010.16541.x>
- André, P., Bacmann, A., Motte, F., & Ward-Thompson, D. 1998, *The Physics and Chemistry of the Interstellar Medium*, ed. V. Ossenkopf, J. Stutzki, & G. Winnewisser (GCA-Verlag Herdecke), 241
- Arreaga-García, G., Klapp, J., Sigalotti, L. D. G., & Gabbasov, R. 2007, *ApJ*, 666, 290, <https://doi.org/10.1086/520492>
- Arreaga-García, G. 2016, *RMxAA*, 52, 155
- _____. 2017, *RMxAA*, 53, 361
- _____. 2018, *Ap&SS*, 363, 157, <https://doi.org/10.1007/s10509-018-3379-x>
- Balsara, D. 1995, *JCoPh*, 121, 357, [https://doi.org/10.1016/S0021-9991\(95\)90221-x](https://doi.org/10.1016/S0021-9991(95)90221-x)
- Ballesteros-Paredes, J., Vázquez-Semadeni, E., Palau, A., & Klessen, R. S. 2018, *MNRAS*, 479, 2112, <https://doi.org/10.1093/mnras/sty1515>
- Bally J., Stark A. A., Wilson R. W., & Henkel Ch. 1988, *ApJ*, 324, 223, <https://doi.org/10.1086/165891>
- Bate, M. R. & Burkert, A. 1997, *MNRAS*, 288, 1060, <https://doi.org/10.1093/mnras/288.4.1060>
- Bekki, K., Beasley, M. A., & Couch, W. J. 2004, *ApJ*, 602, 730, <https://doi.org/10.1086/381171>
- Bergin, E. A. & Tafalla, M. 2007, *ARA&A*, 45, 339, <https://doi.org/10.1146/annurev.astro.45.071206.100404>
- Bolatto, A. D., Leroy A. K., Roslowsky, E., Walter, F., & Blitz L. 2008, *ApJ*, 686, 948, <https://doi.org/10.1086/591513>
- Boss, A. P. 1995, *ApJ*, 439, 224, <https://doi.org/10.1086/175166>
- Boss, A. P., Fisher, R. T., Klein, R. I. & McKee, C. F. 2000, *ApJ*, 528, 325, <https://doi.org/10.1086/308160>
- Burkert, A. & Alves, J. 2009, *ApJ*, 695, 1308, <https://doi.org/10.1088/0004-637x/695/2/1308>
- Caselli, P., Benson, P. J., Myers, P. C., & Tafalla, M. 2002, *ApJ*, 572, 238, <https://doi.org/10.1086/340195>
- Churchwell, E., Povich, M.S., Allen, D., et al. 2006, *ApJ*, 649, 759, <https://doi.org/10.1086/507015>
- Dale, J.E., I. A. Bonnell, I.A. and Whitworth, A.P., 2007, *MNRAS*, 375, 1291, <https://doi.org/10.1111/j.1365-2966.2006.11368.x>
- Dale, J. E., Kruijssen, J. M. D. & Longmore, S. N. 2019, *MNRAS*, 486, 3307, <https://doi.org/10.1093/mnras/stz888>
- Dobbs, C. L., Bonnell, I. A., & Clark, P. C. 2005, *MNRAS*, 360, 2, <https://doi.org/10.1111/j.1365-2966.2005.08941.x>
- Furukawa, N., Dawson, J. R., Ohama, A., et al. 2009, *ApJ*, 696, 115, <https://doi.org/10.1088/0004-637x/696/2/L115>
- Gnedin, O. Y. 2003, *ApJ*, 582, 141, <https://doi.org/10.1086/344636>
- Gómez, G. C., Vázquez-Semadeni, E., Shadmehri, M., & Ballesteros-Paredes, J. 2007, *ApJ*, 669, 1042, <https://doi.org/10.1086/521620>
- Goodwin, S. P., Whitworth, A. P., & Ward-Thompson, D., 2004a, *A&A*, 414, 633, <https://doi.org/10.1051/0004-6361:20031594>
- _____. 2004b, *A&A*, 423, 169, <https://doi.org/10.1051/0004-6361:20040285>
- _____. 2006, *A&A*, 452, 487, <https://doi.org/10.1051/0004-6361:20054026>
- Guerrero-Gamboa, R. & Vázquez-Semadeni, E. 2020, *ApJ*, 903, 136, <https://doi.org/10.3847/1538-4357/abba1f>

- Habe, A. & Ohta, K. 1992, PASJ, 44, 203
- Hachisu, I. & Heriguchi, Y. 1984, A&A, 140, 259
- _____. 1985, A&A, 143, 355
- Hausman, M. A. 1981, ApJ, 245, 72, <https://doi.org/10.1086/158787>
- Higuchi, A. E., Chibueze, J. O., Habe, A., Takahira, K., & Takano, S. 2014, AJ, 147, 141, <https://doi.org/10.1088/004-6256/147/6/141>
- Hillenbrand, L. A. & Hartmann, L. W. 1998, ApJ, 492, 540, <https://doi.org/10.1086/305076>
- Jackson, J. M., Contreras, Y., Rathborne, J. M., et al., 2018, ApJ, 869, 102, <https://doi.org/10.3847/1538-4357/aae7c7>
- Jijina, J., Myers, P. C., & Adams, F. C. 1999, ApJS, 125, 161, <https://doi.org/10.1086/313268>
- Kauffmann, J., Pillai, T., & Goldsmith, P. F. 2013, ApJ, 779, 185, <https://doi.org/10.1088/0004-637x/779/2/185>
- Kimura, T. & Tosa, M. 1996, A&A, 308, 979
- Kirk, H., Offner, S. S. R., & Redmond, K. J. 2014, MNRAS, 439, 1765, <https://doi.org/10.1093/mnras/stuu52>
- Kitsionas, S. & Whitworth, A. P. 2007, MNRAS, 378, 507, <https://doi.org/10.1111/j.1365-2966.2007.11707.x>
- Klein, R. I. & Woods, D. T. 1998, ApJ, 497, 777, <https://doi.org/10.1086/305488>
- Kruijssen, J. M. D., Dale, J. E., & Longmore, S. N. 2015, MNRAS, 447, 1059, <https://doi.org/10.1093/mnras/stu2526>
- Kruijssen, J. M. D., Dale, J. E., Longmore, S. N., et al. 2019, MNRAS, 484, 5734, <https://doi.org/10.1093/mnras/stz381>
- Kumai, Y., Basu, B., & Fujimoto, M. 1993, ApJ, 404, 144, <https://doi.org/10.1086/172265>
- Lattanzio, J. C., Monaghan, J. J., Pongracic, H., & Schwarz, M. P. 1985, MNRAS, 215, 125, <https://doi.org/10.1093/mnras/215.2.125>
- Launhardt, R., Zylka, R., & Mezger, P. G. 2002, A&A, 384, 112, <https://doi.org/10.1051/0004-6361:20020017>
- Lis, D. C. & Menten, K. M. 1998, ApJ, 507, 794, <https://doi.org/10.1086/306366>
- Longmore, S. N., Rathborne, J., Bastian, N., et al. 2012, ApJ, 746, 117, <https://doi.org/10.1088/0004-637x/746/2/117>
- Longmore, S. N., Bally, J., Testi, L., et al. 2013, MNRAS, 429, 987, <https://doi.org/10.1093/mnras/sts376>
- Longmore, S. N., Kruijssen, J. M. D., Bally, J., et al. 2013, MNRAS, 433, 15, <https://doi.org/10.1093/mnras/slt048>
- Marinho, E. P. & Lépine, J. R. D. 2000, A&AS, 142, 165, <https://doi.org/10.1051/aas:2000327>
- Mills, E. A. C. 2017, arXiv: 1705.05332
- Miyama, S. M., Hayashi, C., & Narita, S. 1984, ApJ, 279, 621, <https://doi.org/10.1086/161926>
- Molinari, S., Bally, J., Noriega-Crespo, A., et al. 2011, ApJ, 735, 33, <https://doi.org/10.1088/2041-8205/735/2/L33>
- Petkova, M. A., Kruijssen, J. M. D., Kluge, A. L., et al. 2021, arXiv: 2104.09558
- Portegies Zwart, S. F., McMillan, S. L. W., & Gieles, M. 2010, ARA&A, 48, 431, <https://doi.org/10.1146/annurev-astro-081309-130834>
- Rathborne, J. M., Longmore, S. N., Jackson, J. M., et al. 2015, ApJ, 802, 125, <https://doi.org/10.1088/0004-637x/802/2/125>
- Roslowky, E., Engargiola, G., Plambeck, R., & Blitz, L. 2003, ApJ, 599, 258, <https://doi.org/10.1086/379166>
- Scoville, N. Z., Sanders, D. B., & Clemens, D. P. 1986, ApJ, 310, 77, <https://doi.org/10.1086/184785>
- Sigalotti, L. D. & Klapp, J. 1992, MNRAS, 254, 111, <https://doi.org/10.1093/mnras/254.1.111>
- Springel, V. 2005, MNRAS, 364, 1105, <https://doi.org/10.1111/j.1365-2966.2005.09655.x>
- Tafalla, M., Mardones, D., Myers, P. C., et al. 1998, ApJ, 504, 900, <https://doi.org/10.1086/306115>
- Takahira, K., Tasker, E. J., & Habe, A. 2014, ApJ, 792, 63, <https://doi.org/10.1088/0004-637x/792/1/63>
- Testi, L., Sargent, A. I., Olmi, L., & Onello, J. S. 2000, ApJ, 540, 53, <https://doi.org/10.1086/312858>
- Torii, K., Enokiya, R., Sano, H., et al. 2011, ApJ, 738, 46, <https://doi.org/10.1088/0004-637x/738/1/46>
- Truelove, J. K., Klein, R. I., McKee, Ch. F., et al. 1997, ApJ, 489, 179, <https://doi.org/10.1086/310975>
- Vazquez-Semamedi, E., Gómez, G. C., Jappsen, A. K., et al. 2007, ApJ, 657, 870, <https://doi.org/10.1086/510771>
- Ward-Thompson, D., Scott, P. F., Hills, R. E., & André, P. 1994, MNRAS, 268, 276, <https://doi.org/10.1093/mnras/268.1.276>
- Yamada, R. I., Fukui, Y., Sano, H., et al. 2021, arXiv: 2106.01852

MILDLY RELATIVISTIC, BALLISTIC CORKSCREW JETS AS ROTATED SPIRALS

A. C. Raga¹ and J. Cantó²

Received March 30 2022; accepted June 7 2022

ABSTRACT

Relativistic, corkscrew jets are produced by some Galactic compact objects (notably, the SS433 outflow) and by some of the central monsters of quasars or AGN. As the result of arrival time-delay effects, the projections of the outflow locus onto the observed plane of the sky are remarkably different for the (blueshifted) jet and the (redshifted) counterjet. In terms of a ballistic, precessing jet model, we show that for a range of outflow parameters these relativistic effects correspond to apparent changes in: the orientation angle of the precession axis, the opening angle of the precession cone and the flow velocity. This description is appropriate for outflows with $v/c \leq 0.5$.

RESUMEN

Jets relativistas en forma de tirabuzón se producen por algunos objetos compactos galácticos (notablemente, el flujo de SS433) y por algunos de los monstruos centrales de cuásares y AGN. Como resultado de efectos de tiempos de arribo de la luz, las proyecciones de los flujos sobre el plano del cielo observado son llamativamente distintas para el jet (corrido al rojo) y para el contrajet (corrido al azul). En términos de un modelo de jet precesante balístico, mostramos que para un intervalo de parámetros del flujo estos efectos relativistas corresponden a cambios aparentes en: la orientación del eje de precesión, el ángulo de apertura del cono de precesión y la velocidad del flujo. Esta descripción es apropiada para flujos con $v/c \leq 0.5$.

Key Words: HII regions — hydrodynamics — stars: winds, outflows

1. INTRODUCTION

Observations of the remarkable, mildly relativistic bipolar outflow from SS 433 (see the early papers of Ryle et al. 1978 and Margon et al. 1979) showing an unusual precession signature (Hjellming & Johnston 1981a), led to the study of the dynamics of ballistic, “corkscrew” (i.e., precessing) jets. This simple problem was lucidly addressed by Hjellming & Johnston (1981b) and Gower et al. (1982).

The analytic treatment of relativistic, corkscrew jets has been extended including the effect of a magnetic field (Kochanek 1991) and considering a “ram pressure braking term” (Panferov 2014). Also, more complex time evolutions of the ejection direction (e.g., including a “nodding” superposed on the precession) have been explored (e.g., Stirling et al. 2002). Relativistic gasdynamical simulations have

also been done (see, e.g., Horton et al. 2020; Barkov & Bosch-Ramon 2021).

These models are naturally relevant for modelling SS 433, which has continued to be actively observed through the years (see, e.g., Bell et al. 2010; Jeffrey et al. 2016; Martí et al. 2018; Blundell et al. 2018), and for other galactic “microquasars” with precessing jets (see, e.g., Luque-Escamilla et al. 2015; Coriat et al. 2019). Also, some of the early papers on models of relativistic corkscrew jets were directed to outflows from quasars or from AGN (Gower et al. 1982; Baryshev 1983), and observations of such jets have naturally continued over the years (see, e.g., An et al. 2010; Kharb et al. 2019).

Our present paper studies a specific feature of the ballistic corkscrew jet model. As pointed out by Gower et al. (1982), an increase in v/c has the effect of an apparent rotation of the precession axis, with the projected (i.e., blueshifted) jet lobe appearing to lie closer to the plane of the sky. Through an analysis

¹Instituto de Ciencias Nucleares, UNAM, México.

²Instituto de Astronomía, UNAM, México.

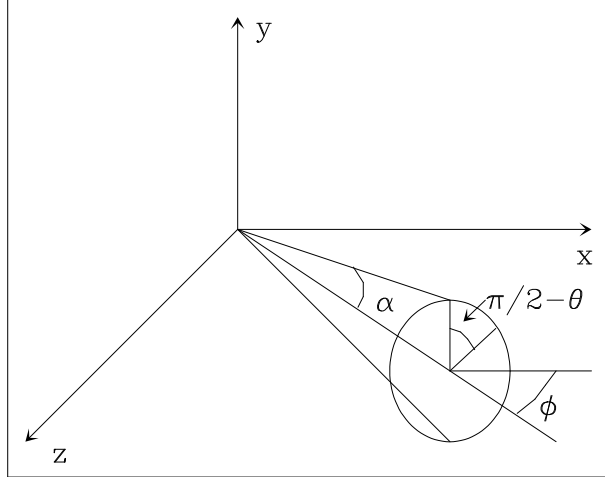


Fig. 1. Schematic diagram showing the precession cone of the ballistic jet model. The xy -plane is parallel to the plane of the sky, and the z -axis points towards the observer. The half-opening angle of the cone is α , and the precession axis points towards the observer at an angle ϕ from the plane of the sky. There is also an oppositely directed counterjet which is not shown in the figure.

of the ballistic, precessing jet equations we show that this is indeed the case, and obtain the value of the rotation angle as a function of the flow parameters.

The paper is organized as follows. In § 2, we present the ballistic, precessing jet model of Hjellming & Johnston (1981b) and Gower et al. (1982). In § 3, we derive the conditions under which a “classical jet spiral” (projected onto the plane of the sky without considering time-delay effects) approximately coincides with the projection of a relativistic, corkscrew jet. In § 4 we explore the parameter space of the problem, and derive the range of parameters in which the “equivalent, rotated spiral model” is an appropriate description of the relativistic jet. Finally, the results are summarized in § 5.

2. RELATIVISTIC, FREE-STREAMING EQUATIONS

Let us consider a bipolar jet source located at the origin of the (x, y, z) coordinate system, with (x, y) on the plane of the sky and z pointing towards the observer. The ejection axis precesses on a cone of half-opening angle α , and the axis of the cone lies at an angle ϕ from the plane of the sky towards the observer, as shown in the schematic diagram of Figure 1. The precession phase (with origin on the xz -plane) is:

$$\theta(\tau) = \Omega\tau + \theta_0, \quad (1)$$

where τ is the time of ejection, θ_0 is the precession phase at $\tau = 0$ and $\Omega = \pm 2\pi/\tau_p$, with τ_p being the precession period (the positive sign corresponding to a counterclockwise and the negative sign to a clockwise precession).

The ballistic trajectory of the ejected fluid parcels is given by:

$$x = v(t' - \tau)[\cos \alpha \cos \phi + \sin \alpha \sin \phi \cos \theta(\tau)], \quad (2)$$

$$y = v(t' - \tau) \sin \alpha \sin \theta(\tau), \quad (3)$$

$$z = v(t' - \tau)[\cos \alpha \sin \phi - \sin \alpha \cos \phi \cos \theta(\tau)], \quad (4)$$

where t' is the evolutionary time of the jet, $\tau \leq t'$ is the time at which the fluid parcels were ejected and v is the (constant) ejection velocity. The locus of the oppositely directed counterjet is obtained with the $v \rightarrow -v$ change in equations (2-4).

An observation of the shape of the precessing jet (projected onto the plane of the sky), is done at a fixed arrival time t (of the emitted light at the observer). Setting $t = 0$ for $t' = 0$ these two times obey the relation:

$$t = t' - \frac{z}{c}, \quad (5)$$

where c is the speed of light and z is given by equation (4).

Combining equations (2-5) one obtains the plane of the sky jet locus

$$x = \frac{v(t - \tau)}{1 - \frac{v}{c} A(\tau)} [\cos \alpha \cos \phi + \sin \alpha \sin \phi \cos \theta(\tau)], \quad (6)$$

$$y = \frac{v(t - \tau)}{1 - \frac{v}{c} A(\tau)} \sin \alpha \sin \theta(\tau), \quad (7)$$

with

$$A(\tau) = \cos \alpha \sin \phi - \sin \alpha \cos \phi \cos \theta(\tau). \quad (8)$$

The locus of the counterjet is obtained by setting a negative v .

Equations (6-8) give the plane of the sky locus of the jet in a parametric way, with the parameter being the ejection time τ (with $\tau \leq t$). These equations have been derived and explored by Hjellming & Johnston (1981b) and by Gower et al. (1982).

Interestingly, the y/x ratio is independent of v and v/c (see equations 6-7). This ratio has a series of alternative maxima and minima, which correspond to the maximum excursions from the projected precession axis of the projected spiral. These maxima fall at rotation angles:

$$\cos \theta_m = -\tan \alpha \tan \phi, \quad (9)$$

and all have the same value

$$\tan \alpha_0 = \left(\frac{y}{x}\right)_m = \frac{\sin \alpha}{\sqrt{\cos^2 \alpha - \sin^2 \phi}}. \quad (10)$$

Therefore, the observed path of the projected jet lies within a triangle of half-opening angle α_0 (given by equation 10), regardless of the value of v/c . One should note that these successive maxima in y/x only appear if the $\alpha + \phi \leq \pi/2$ condition is met.

3. THE EQUIVALENT CLASSICAL SPIRAL

A classical, $v \ll c$ precessing jet has a projected path given by equations (6-7) with $v/c = 0$ in the denominator. In this section we search for a “classical jet spiral” with velocity v_1 , half-opening angle α_1 and orientation ϕ_1 (with respect to the plane of the sky) that produces the same plane of the sky locus as a relativistic jet (of arbitrary v/c) with corresponding parameters v , α and ϕ .

Setting $\phi_1 = \phi + \Delta\phi$, the $v/c = 0$ limit of equations (6-7) can be written as:

$$x = v_1(t - \tau) \cos \Delta\phi(t - \tau) [\cos \alpha_1 \cos \phi + \sin \alpha_1 \cos \theta(\tau) \sin \phi - \tan \Delta\phi A(\tau)], \quad (11)$$

$$y = v_1(t - \tau) \sin \alpha_1 \sin \theta(\tau), \quad (12)$$

with θ given by equation (1) and $A(\tau)$ by equation (8) with $\alpha = \alpha_1$.

It can be straightforwardly shown that if one chooses:

$$\Delta\phi = -\tan^{-1} \left(\frac{v}{c} \cos \phi \cos \alpha\right), \quad (13)$$

$$\alpha_1 = \sin^{-1} \left[\cos \Delta\phi \sin \alpha \left(1 + \frac{v}{c} \cos \alpha \sin \phi\right)\right], \quad (14)$$

$$v_1 = \frac{v}{\cos \Delta\phi}, \quad (15)$$

then equations (6-7) coincide with equations (11-12) to first order in the terms of

$$\beta = v/c \text{ and } \epsilon = \sin \alpha \sin \phi \cos \theta(\tau). \quad (16)$$

Therefore, for small values of β and ϵ the plane of the sky projection of a relativistic, precessing jet corresponds to the projection of a spiral with an orientation $\phi_1 = \phi + \Delta\phi$, half opening angle α_1 and velocity v_1 (see equations 13-15) that differ from the ϕ , α , v values of the relativistic flow.

The “rotated spiral” description (equations 11-15) is appropriate for $v/c \ll 1$ and/or $\epsilon \ll 1$ (see equation 16). This latter condition can be obtained by having $\alpha \ll 1$ and/or $\phi \ll 1$, as the $\cos \theta(\tau)$ term

TABLE 1

PHYSICAL CONDITIONS FOR THE NUMERICAL SIMULATIONS.

Fig.	v/c	ϕ	α	$\Delta\phi$	$\Delta\alpha$	v_1/v
2	0.1	0	10	-5.62	-0.05, -0.05	1.00
2	0.1	20	10	-5.29	0.30, -0.38	1.00
2	0.1	40	10	-4.31	0.61, -0.67	1.00
2	0.1	60	10	-2.82	0.85, -0.87	1.00
2	0.1	80	10	-0.98	0.98, -0.98	1.00
3	0.2	0	10	-11.14	-0.19, -0.19	1.02
3	0.2	20	10	-10.49	0.50, -0.83	1.02
3	0.2	40	10	-8.58	1.15, -1.38	1.01
3	0.2	60	10	-5.62	1.67, -1.76	1.00
3	0.2	80	10	-1.96	1.96, -1.96	1.00
4	0.26	10	20	-13.53	0.28, -1.43	1.03
5	0.2	10	20	-10.49	0.32, -1.01	1.02
5	0.4	10	20	-20.31	-0.02, -2.55	1.07
5	0.6	10	20	-29.04	-0.83, -4.35	1.14
5	0.8	10	20	-36.52	-1.89, -6.17	1.24
6	0.26	10	30	-12.50	0.48, -2.03	1.02
6	0.26	10	50	-9.35	1.06, -2.78	1.01
6	0.26	10	70	-5.00	1.91, -2.83	1.00
6	0.26	45	30	-9.05	4.92, -5.47	1.01
6	0.26	45	50	-6.74	8.28, -7.87	1.01
6	0.26	45	70	-3.60	15.42, -8.49	1.00

*The values of $\Delta\phi$ and v_1 correspond to the jet (directed towards the observer). The oppositely directed counterjet has a $\Delta\phi$ equal to $(-1)\times$ the values given in this table. The two values given for $\Delta\alpha$ correspond to the jet and the counterjet. All of the angles are given in degrees.

adopts all values from -1 to 1 along the jet locus. In the following section, we explore quantitatively the agreement of equations (11-12) with equations (6-7) for different values of the parameters of the precessing jet flow.

4. EXPLORATION OF PARAMETER SPACE

We now carry out a comparison between the rotated spiral description and the relativistic plane of the sky projection of corkscrew jets for a range of model parameters. We have chosen the 21 parameter combinations listed in Table 1. The first column of this table gives the number of the figure in which each model is displayed. Columns 2-4 give the v/c , orientation angle ϕ and half-opening angle α that fix each of the models. The remaining columns give the values that determine the rotated spiral description:

$\Delta\phi$ (equation 13, the value for the jet is given, the counterjet having a positive $\Delta\phi$ with the same module), $\Delta\alpha = \alpha_1 - \alpha$ (see equation 14, the first value corresponding to the jet and the second one to the counterjet) and v_1/v (see equation 15, the counterjet having a negative value with the same module).

We first consider a jet with $v/c = 0.1$ and $\alpha = 10^\circ$. In Figure 2 we show the locus of the jet projected on the plane of the sky for different orientation angles ϕ . We have assumed that the ejection direction has a $\theta_0 = 0$ initial phase (see equation 1). In the plots, we have the jet (directed towards the observer) for $x > 0$ and the counterjet (directed away from the plane of the sky) for $x < 0$.

From Figure 2 we see that (at the resolution of the plots), the “rotated spiral” description of the flow (equations 11-15) coincides with the relativistic jet (equations 6-7) except for $\phi = 80^\circ$ for which small differences between the two solutions are seen.

In Figure 3, we show the projected locus of a jet with $v/c = 0.2$ and $\alpha = 10^\circ$. As expected, we see that there are somewhat larger deviations between the “rotated spiral” and the relativistic solutions. However, a reasonable qualitative agreement is obtained for all values of ϕ (the largest deviations appearing in the $\phi = 80^\circ$ projection).

The results shown in Figures 2 and 3 demonstrate that for relatively low values of v/c and α (so that β and ϵ are small, see equation 16) there is a good agreement between the “rotated spiral” and relativistic solutions for all orientation angles $\phi \leq 80^\circ$.

We now choose the $v/c = 0.26$, $\alpha = 20^\circ$, $\phi = 10^\circ$ parameters derived by Hjellming & Johnston (1981) for the SS 433 outflow. It is clear that this jet indeed corresponds to our “rotated spiral” solution (see Figure 4).

In order to further explore the limits of our approximate rotated spiral solution, we now fix the $\alpha = 20^\circ$ and $\phi = 10^\circ$ “SS 433 parameters” and play with the value of v/c . The results of this exercise (see Figure 5) show that while for $v/c = 0.2$ and 0.4 we obtain a good quantitative agreement between the relativistic and “rotated spiral” solutions, for $v/c = 0.6$ and 0.8 the two solutions only show a qualitative resemblance. Therefore, we see that the rotated spiral solution provides a good description of the jet solution only for velocities smaller than $v \approx 0.5$.

Finally, we calculate models with $v/c = 0.26$, two orientation angles $\phi = 10$ and 45° and half-opening angles $\alpha = 30, 50,$ and 70° . The results of this exercise (see Figure 6) show that while the discrepancies between the relativistic and “rotated spiral”

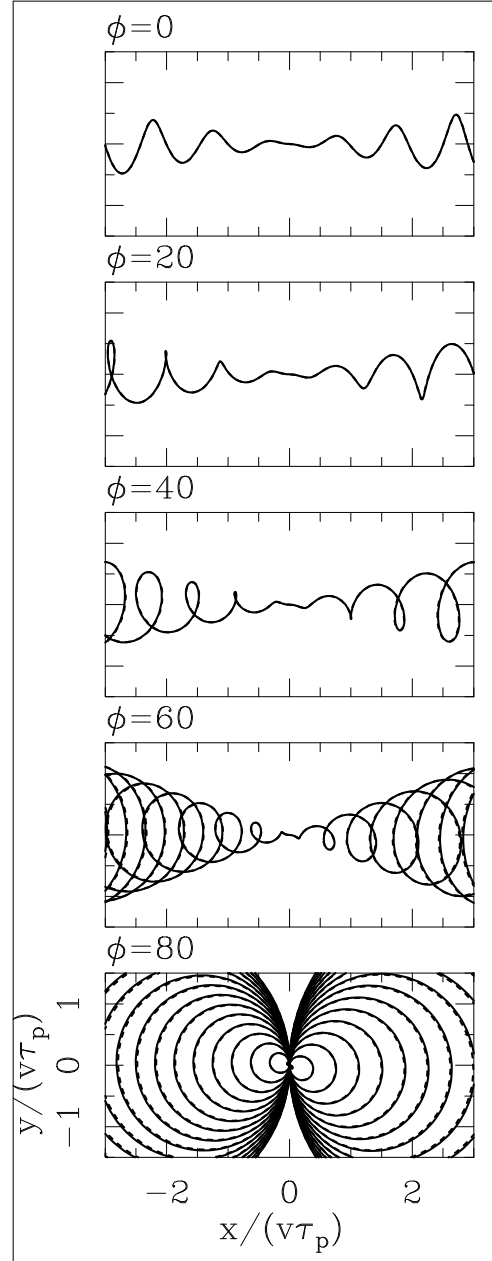


Fig. 2. The projection of the jet locus onto the plane of the sky for jet/counterjet systems with $v/c = 0.1$, $\alpha = 10^\circ$ and different values of the angle ϕ between the precession axis with respect to the plane of the sky. The blueshifted jet is shown with $x > 0$ and the redshifted counterjet with $x < 0$. The exact solution to the relativistic problem is shown with a solid line, and the approximate “rotated spiral description” is shown with a dashed line. Both solutions almost coincide at the resolution of the plots. The plane of the sky coordinates are normalized with the product $v\tau_p$ of the outflow velocity times the precession period. An initial $\theta_0 = 0$ phase for the precession has been assumed.

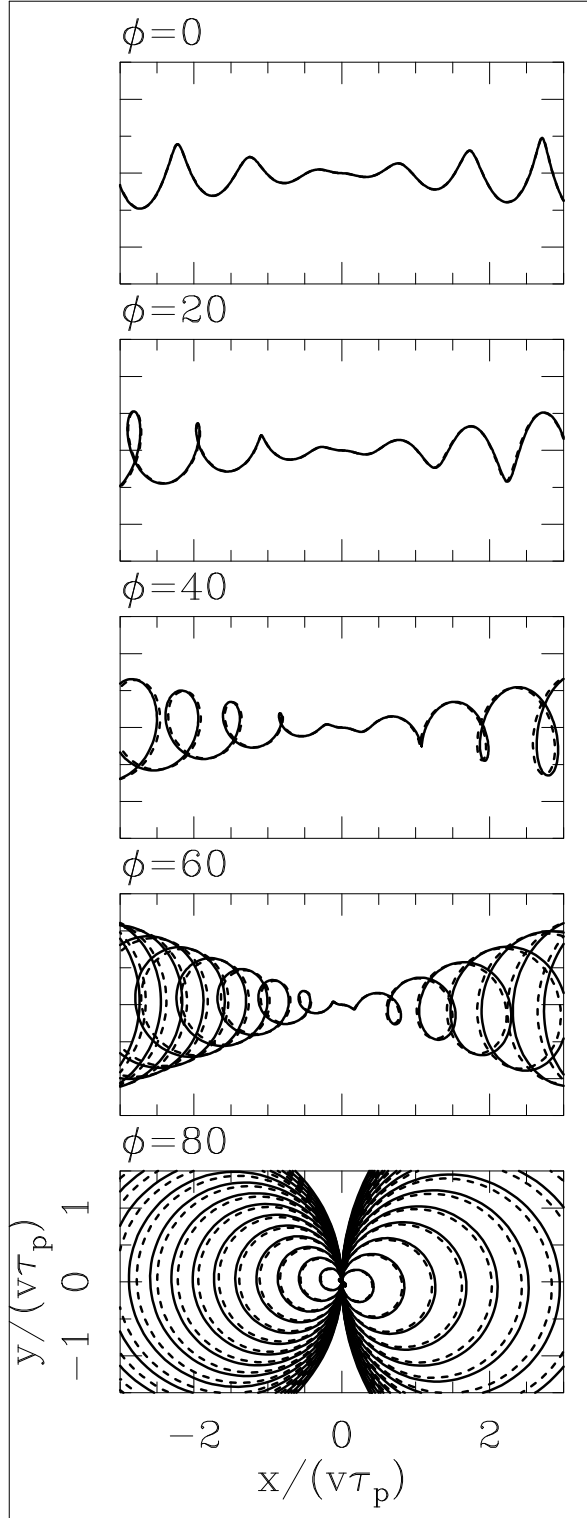


Fig. 3. The same as Figure 2 but for flows with $v/c = 0.2$. Larger differences between the full solution (solid lines) and the “rotated spiral description” (dashed lines) are seen.

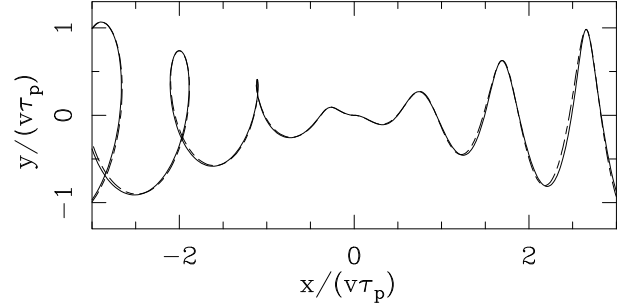


Fig. 4. Outflow with the “SS 433 parameters” $v/c = 0.26$, $\alpha = 20^\circ$, $\phi = 10^\circ$ parameters derived of Hjellming & Johnston (1981). A good agreement is found between the full solution (solid line) and the “rotated spiral description” (dashed line). Again a $\theta_0 = 0$ initial phase has been assumed.

solutions grow with increasing α , a reasonable qualitative agreement is obtained except for the $\alpha = 70^\circ$, $\phi = 45^\circ$ model.

5. SUMMARY

We find that, independent of the v/c value, the projection of a precessing jet on the plane of the sky lies within a triangle of half-opening angle α_0 given by equation (10), provided that the $\alpha + \phi \leq \pi/2$ condition is met (where α is the precession half-opening angle and ϕ the angle between the precession axis and the plane of the sky).

We also find that mildly relativistic precessing jet/counterjet systems on the plane of the sky correspond to the (classical) projection of a spiral with an orientation angle $\phi_1 = \phi + \Delta\phi$, half-opening angle $\alpha_1 = \alpha + \Delta\alpha$ and flow velocity v_1 which differ from the corresponding ϕ , α and v of the outflow.

As can be seen in Table 1, the rotated spiral has:

- velocity correction: generally $v_1/v \approx 1$, except for the $v/c = 0.6, 0.8$ models (see Figure 5), for which the “rotated spiral” description does not work well;
- opening angle correction: $\Delta\alpha = \alpha_1 - \alpha$ is generally small ($< 2^\circ$), except for the higher v/c and α models (see figures 5 and 6);
- rotation: this is clearly the main correction that has to be done so that the classical plane of the sky projection of a spiral agrees with the relativistic, time-delayed projection. The axes of the jet and the counterjet are both rotated (by the same $\Delta\phi$) away from the observer. Because of this, in the models with $\phi \geq 10^\circ$ the counterjet axis (directed away from the observer) increases its angle with respect to the plane of

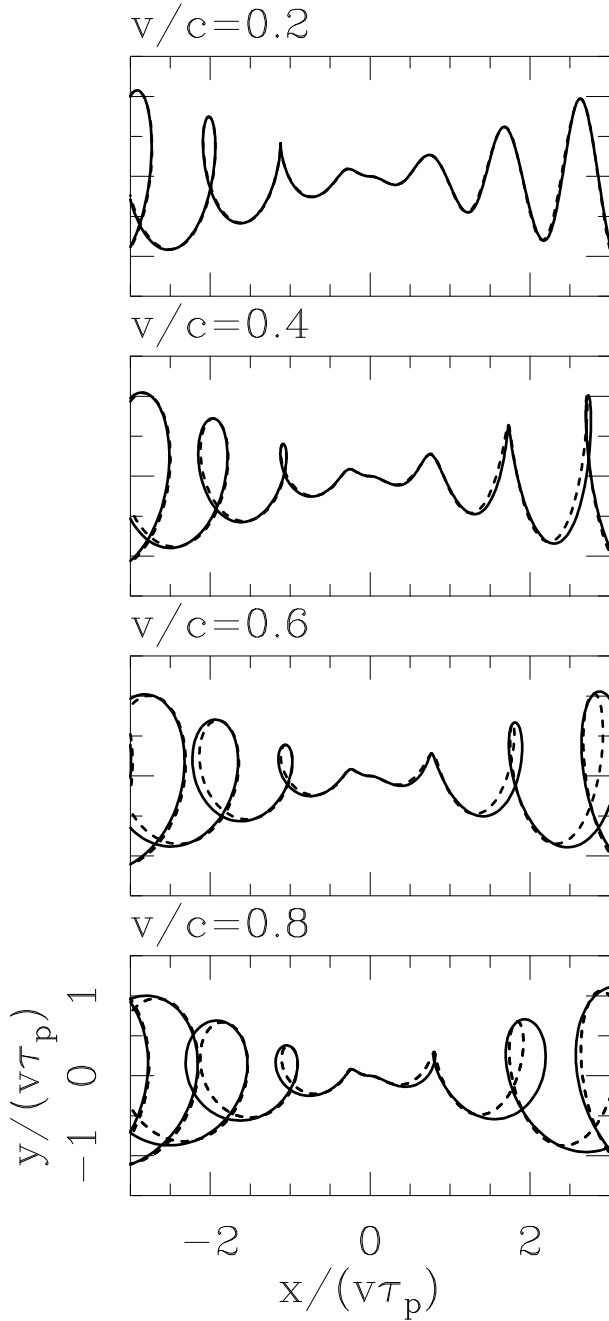


Fig. 5. Precessing jet flows with $\alpha = 20^\circ$ and $\phi = 10^\circ$, and with different values of v/c (given by the labels at the top left of each frame). The full solution (solid lines) and the “rotated spiral description” (dashed lines) show a good agreement for $v/c \leq 0.5$.

the sky, and the jet axis (directed towards the observer) approaches the plane of the sky.

Even though the “rotated spiral” description is based on a linearization of the relativistic free-streaming equations (with respect to the β and ϵ

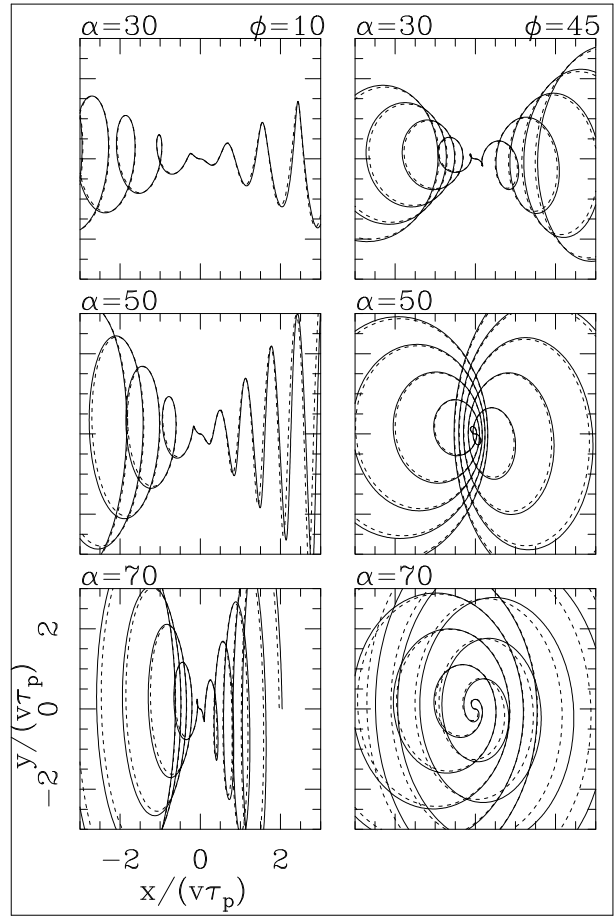


Fig. 6. Jet flows with $v/c = 0.26$, two orientations ($\phi = 10^\circ$ for the left and $\phi = 45^\circ$ for the right column) and three half-opening angles (top: $\alpha = 30^\circ$; center: $\alpha = 50^\circ$; bottom: $\alpha = 70^\circ$). One can appreciate the increasing differences for larger α values between the full solution (solid lines) and the “rotated spiral description” (dashed lines). To avoid confusion, we only show the locus of the material ejected during five precession periods.

variables, see equation 16), we find that it provides a qualitatively correct approximation to the projected, relativistic corkscrew when $v/c < 0.5$ (see § 4 and Figure 5). Provided that this condition is met, the rotated spiral description is good approximation for all orientation angles (see Figures 2 and 3), and for half-opening angles $\alpha \leq 50^\circ$ (see Figure 6). Also, it is a definitely good approximation for the parameters of the SS433 flow (see Figure 4).

These results are clearly not of ground-breaking importance. However, we think that they provide an interesting advance in the qualitative understanding of the observed morphologies of mildly relativistic, corkscrew jets.

This work was supported by the DGAPA (UNAM) grant IG100422. We thank an anonymous referee for comments which led (among other things) to the inclusion of Table 1.

REFERENCES

- An, T., Hong, X. Y., Hardcastle, M. J. et al. 2010, MNRAS, 402, 87, <https://doi.org/10.1111/j.1365-2966.2009.15899>
- Barkov, M. V. & Bosch-Ramon, V. 2022, MNRAS, 510, 3479, <https://doi.org/10.1093/mnras/stab3609>
- Baryshev, I. V. 1983, SvAL, 9, 307
- Bell, M. R., Roberts, D. H., & Wardle, J. F. C., 2011, ApJ, 736, 118, <https://doi.org/10.1088/0004-637x/736/2/118>
- Blundell, K. M., Laing, R., Lee, S., Richards, A. 2018, ApJ, 867, 25, <https://doi.org/10.3847/2041-8213/aae890>
- Coriat, M., Fender, R. P., Tasse, C. et al. 2019, MNRAS, 484, 1672, <https://doi.org/10.1093/mnras/stz099>
- Gower, A. C., Gregory, P. C., Unruh, W. G., & Hutchings, J. B. 1982, ApJ, 262, 478, <https://doi.org/10.1086/160442>
- Hjellming, R. M. & Johnston, K. J. 1981a, Natur, 290, 100, <https://doi.org/10.1038/290100a0>
- _____. 1981b, ApJ, 246, 141, <https://doi.org/10.1086/183571>
- Horton, M. A., Krause, M. G. H., & Hardcastle, M. J. 2020, MNRAS, 499, 5765, <https://doi.org/10.1093/mnras/sta3020>
- Jeffrey, R. M., Blundell, K. M., Trushkin, S. A., & Mioduszewski, A. J. 2016, MNRAS, 461, 312, <https://doi.org/10.1093/mnras/stw1322>
- Kharb, P., Vaddi, S., Sebastian, B., et al. 2019, ApJ, 871, 249, <https://doi.org/10.3847/1538-4357/aafad7>
- Kochanek, C. S. 1991, ApJ, 371, 289, <https://doi.org/10.1086/169892>
- Luque-Escamilla, P. L., Martí, J., & Martínez-Aroza, J., 2015, A&A, 584, 122, <https://doi.org/10.1051/0004-6361/201527238>
- Margon, B., Ford, H. C., Katz, J. I., et al. 1979, ApJ, 230, 41, <https://doi.org/10.1086/182958>
- Martí, J., Bujalance-Fernández, I., Luque-Escamilla, P. L. et al. 2018, A&A, 619, 40, <https://doi.org/10.1051/0004-6361/201833733>
- Panferov, A. 2014, A&A, 562, 130, <https://doi.org/10.1051/0004-6361/201322456>
- Ryle, M., Caswell, J. L., Hine, G., & Shakeshaft, J. 1978, Natur, 276, 571, <https://doi.org/10.1038/276571a0>
- Stirling, A. M., Jowett, F. H., Spencer, R. E., et al. 2002, MNRAS, 337, 657, <https://doi.org/10.1046/j.1365-8711.2002.05944.x>

A. C. Raga: Instituto de Ciencias Nucleares, Universidad Nacional Autónoma de México, Ap. 70-543, 04510 CDMX, México (raga@nucleares.unam.mx)

J. Cantó: Instituto de Astronomía, Universidad Nacional Autónoma de México, Ap. 70-468, 04510 CDMX, México

A NEW ORBIT FOR COMET C/1830 F1 (GREAT MARCH COMET)

Richard L. Branham Jr.

Instituto Argentino de Nivología, Glaciología y Ciencias Ambientales (Ianigla), Centro Científico Tecnológico - Mendoza, Mendoza, Argentina.

Received April 7 2022; accepted June 24 2022

ABSTRACT

Comet C/1830 F1 (Great March comet) is one of a large number of comets with parabolic orbits. Given that there are sufficient observations of the comet, (428 in right ascension and 424 in declination), it proves possible to calculate a better orbit. The calculations are based on a 12th order predictor-corrector method. The comet's orbit is highly elliptical, $e=0.99792$ and, from calculated mean errors, statistically different from a parabola. The comet will not return for thousands of years and thus represents no immediate NEO threat.

RESUMEN

El cometa C/1830 F1 (Gran Cometa de Marzo) es uno entre un gran número de cometas con órbitas parabólicas. Puesto que hay muchas observaciones del cometa, (428 en ascensión recta y 424 en declinación), es posible calcular una órbita mejor. Los cálculos se basan en un método predictor-corrector de orden 12. La órbita es altamente elíptica, $e=0.99792$ y, según los errores medios calculados, distinta de una parábola. El cometa no regresará durante miles de años y por ende no representa ninguna amenaza NEO.

Key Words: celestial mechanics — comets: individual: C/1830 F1 — methods: data analysis

1. INTRODUCTION

This paper continues a series on orbits of comets with catalogued parabolic orbits (Marsden and Williams 2003), but which nevertheless possess sufficient observations to do a better calculation. Various reasons exist for studying these comets. A comet with a parabolic orbit *may* be, depending on factors such as perihelion distance, a Near Earth Object (NEO). A non-parabolic orbit decides the matter. If a more refined orbit proves to be a hyperbola, the comet might potentially be of extra-solar origin. This should be addressed. Many, perhaps most, parabolic orbits were calculated by the method of Olbers (Dubyago 1961, Ch. 8) as a computational convenience and used normal places. With modern computers normal places are an anachronism that degrades, if only slightly, the solution. Better can be done. And better orbits mean better statistics for studying the origin of comets. But perhaps most importantly is professionalism. It is disconcerting that a great comet should be catalogued with an or-

bit calculated in 1873. We can do much better with modern computational techniques.

Why study Comet C/1830 F1 (Great March comet), hereafter simply “the comet”, in particular? Numerous observations, over 400, are available. The perihelion distance of 0.9210 au and eccentricity of 0.99792 mean that the object *could* be an NEO, but the calculation of the orbit, given shortly, shows that the comet never comes closer than 0.147 au from the earth. Its period of over 9,000 yr renders nugatory any preoccupation over a possible close approach. The comet, nevertheless, was observed for five months and professionalism dictates a better than 19th century orbit.

2. PRELIMINARY DATA REDUCTION AND EPHEMERIDES

Gambart (1830) discovered the comet in Marseille on 22 April, although it had apparently been seen previous to perihelion passage near the south equatorial pole (Schulze 1873). I conducted a literature search of the journals published in the 19th

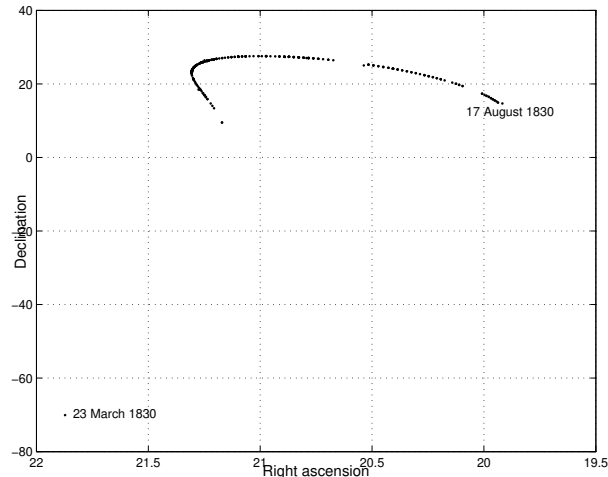


Fig. 1. The observations.

century that include comet observations and also annual reports of some of the major observatories. The search proved vexing, not only because the 1830 date precluded use of a number of journals that were founded later, such as *The Astronomical Journal*, but also because some of the formats were unusual. Mayer in Vienna, for example, refers to “observation lines” “Beobachtungsreihen” to which corrections in α and δ are made. It is unclear to me exactly how he is reducing the observations, which are neither ring nor filar micrometer observations. Likewise, the Florence observations contain times of entry and egress from the inner and outer rings of a ring micrometer for the comet, but also for an accompanying star. This star cannot be a reference star because insufficient information is given to calculate the comet’s position from the reference star’s position; see Chauvenet (1962, Vol. 2, pp. 436-438). It appears as if the observer merely wished to publish the comet’s position along with that for a star. Schulze mentions that three transit circle observations of the comet were made at the Cape Observatory before perihelion passage, but he does not publish the original observations, only a normal place based on the three. I could find no reference to the original observations in the literature and therefore treated the normal place as a genuine observation.

This search yielded a total of 428 observations in right ascension (α) and 424 in declination (δ). Some observations were made in one coordinate only. Two observations, the Cape normal place and one of the Vienna observations, were made with a transit circle. Their data processing differs slightly from the others because transit circle observations are traditionally reduced to the geocenter rather than to the topocen-

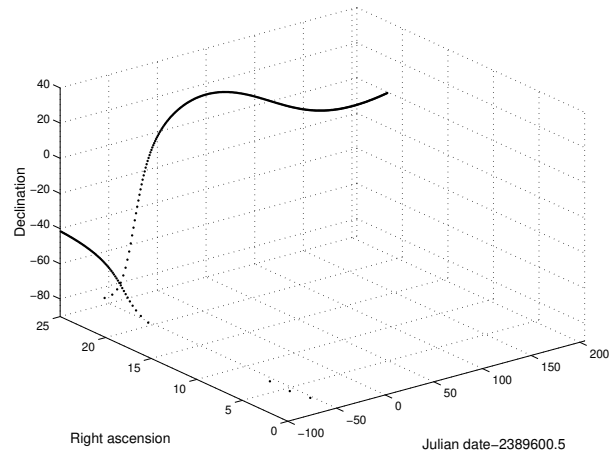


Fig. 2. Computed alpha and delta versus time.

ter and of course the time of observation is the same as α . Table 1 summarizes the observations for each observatory and Figure 1 graphs them. One notices that the Cape observation, really three observations, lies far from the others, but nevertheless seems to follow the general pattern of the post-perihelion observations if one projects them backwards. This is shown in Figure 2, where one sees that near an x -axis value of -65 the value for α is $\simeq 21^h$ and the value for $\delta \simeq -70^\circ$.

Because most of the observers use local mean or sidereal time and some express α in degrees rather than hours, minutes, and seconds all of the observations were reduced to the common format of Terrestrial Time, α , and δ . None of the observations employed north polar distance in lieu of δ . Whenever a specific reference star was given to which the comet observation had been referred, as happened for 53 observations, its position was recalculated, with modern positions taken from the Tycho-2 catalog (Høg et al. 2000), using the algorithm in Kaplan et al. (1989). If differences in α and δ from the reference star, $\Delta\alpha$ and $\Delta\delta$, were given, they were applied, corrected for differential aberration and refraction, to the new position. Sometimes it was not evident if an observation had already been corrected for differential aberration or refraction. I calculated two final sets of residuals, both with and without these corrections, but the results were nearly the same. If $\Delta\alpha$ and $\Delta\delta$ were not given but a reference star was (21 observations) the differences in the positions between the older catalog and Tycho-2 were applied to the published positions of the comet. Observations for which no reference star was given, the remaining observations, were taken as published. Because the observations are 19th century, they were corrected

TABLE 1
OBSERVATIONS BY OBSERVATORY

Observatory	Obs. in α	Obs. in δ	Reference ¹
Altona, Germany	7	4	AN, 1830, 8, 365
Bremen, Germany	7	6	AN, 1830, 8, 285
Cape, South Africa	1	1	AN, 1873, 82, 975
Crakow, Poland	84	87	AN, 1830, 8, 477
Florence, Italy	132	132	AN, 1831, 9, 149
Göttingen, Germany	3	3	AN, 1830, 8, 253
Königsberg, Germany	21	21	AN, 1831, 9, 165
Kremsmünster, Austria	16	16	AN, 1831, 9, 291
Mannheim, Germany	18	18	AN, 1830, 8, 337
			MN, 1830, 1, 180
Marseilles, France	7	7	AN, 1830, 8, 319
			AN, 1830, 8, 251
Padua, Italy.	66	66	AN, 1831, 9, 285
Prague, Czech Rep	16	16	AN, 1830, 8, 285
			AN, 1830, 8, 315
Speyer, Germany	10	7	AN, 1830, 8, 299
Vienna, Austria	40	40	AN, 1830, 8, 437

¹AN: *Astron. Nachr.*; MN: *Monthly Notices RAS*

for the E-terms of the aberration if the observation was derived from a mean position. See Scott (1964) for a discussion of the E-terms.

Rectangular coordinates needed to calculate observed minus calculated positions, $(O-C)$'s, were initially generated, along with numerically integrated partial derivatives to correct the comet's orbit, from a 12th order predictor-corrector integrator. This is generally referred to as Moulton's method, for which Branham (1979) gives more detail. The coordinates are heliocentric and the Moon is carried as a separate body.

3. ERRORS OR MISSING INFORMATION IN THE OBSERVATIONS

Processing 19th century observations is a far from trivial task because the observations are published in different languages, English, French, German, Italian, and even Latin, do not conform to a standard format, and contain many errors. The reader may refer to an article of mine that discusses the matter in detail (Branham 2011a) and includes various examples. Common errors include mistaking a 3 for a 5 or 8, a 2 for a 7, transposing numbers, 35 for 53, misidentifying a reference star, or an error in time that affects both the $(O-C)$, observed minus calculated position, in α and also in δ in such a manner that one can identify the error in time. With previous comets that I have studied over half of the bad

$(O-C)$'s could be corrected to produce reasonable values. Unfortunately, for the Great March comet this turned out not to be the situation. For example, an observation made at Marseilles on 11 May gave an $(O-C)_\delta$ close to $120''$. A change in the minutes of the observation from 56 to 54 would eliminate this large $(O-C)$, but misreading a 6 for a 4 seems unlikely, and I left the observation alone. Likewise, declination observations, two made on 11 July and another two on 13 July in Florence, had $(O-C)_\delta$'s between $120''$ and $134''$. These are close to a two arc-minute error, but it seems unlikely that all of the observations would have this sort of error. In any event there is insufficient evidence in the observations themselves to suggest a possible source of error and thus the observations remain untouched. Therefore, unlike all of my previous studies of 19th century comets, no changes were made to the observations as published.

4. TREATMENT OF THE OBSERVATIONS

The observations of Table 1 result in 852 equations of condition, calculated from the numerically integrated partial derivatives, and hence the residuals necessary to correct the orbit. Assigning weights to the observations, necessary because of the disparity in their quality, remains similar to that of my previous publications on comet orbits. The first orbits were calculated by use of the robust L_1 criterion

(Branham 1990, Ch. 6) to minimize the effect of discordant observations. Then the final orbit came from weighting the residuals with the biweight function. If \mathbf{r} represents the vector of the post-fit residuals, scale an individual residual r_i by the median of the absolute values of the residuals, $r_i = r_i / \text{median}(|\mathbf{r}|)$. Then calculate weighting factors w_i by:

$$w_i = [1 - (r_i/4.685)^2]^2, \quad |r_i| \leq 4.685; \quad (1)$$

$$w_i = 0, \quad |r_i| > 4.685.$$

Equation (1) incorporates the advantages of being impersonal, recognizes that smaller residuals are more probable than larger ones, and assigns them higher weight. Figure 3 shows a histogram of the weights. The amount of trimming, 8.1% of the weights, lower than the machine epsilon of $2.22 \cdot 10^{-16}$, is acceptable, especially considering that 81.6% of the weight are greater than 0.5 and 51.5% great than 0.9. With the biweight the final mean error of unit weight becomes $\sigma(1) = 14.''77$, a value that falls somewhat on the high side compared with other 19th century comets, but is still acceptable. The Windsor, Australia, observations of the Great Southern comet (Branham 2018), for example, have $\sigma(1) = 16.''47$, although with all of the observations for that comet we find $\sigma(1) = 10.''80$. Other 19th century comets have mean errors over $10''$. Comet C/1819 N1 (Great comet of 1819) has $\sigma(1) = 11.''23$ (Branham 2017) and comet C/1857 D1 (d'Arrest) has $\sigma(1) = 10.''25$ (Branham 2011b). If the 11 and 13 July observations in Florence could be corrected by $120''$, or simply eliminated, the mean error would undoubtedly decrease. But in lieu of unavailable specific details there remains no justification for such an arbitrary action, and one must accept the observations as given. Such a procedure seems more objective than that adopted by Peck for his 1904 computation of a parabolic orbit of comet C/1845 L1 (Great June comet) (Branham 2009), where observations from Kremsmünster, Austria, and Modena and Padua in Italy were discarded as being “worthless”, “poor quality”, and “untrustworthy”, but no statistical evidence was offered for such pejorative adjectives.

Figure 4 shows the distribution of the residuals from the final solution and Figure 5 a histogram of the residuals. The distribution appears far from Gaussian (normal, bell shaped): a skewness of -1.12, (0 for a normal distribution), indicating an excess of negative residuals; a kurtosis of -0.25 (0 for the normal) shows a platykurtic distribution, and the Q factor of 0.15 (2.54 for the normal), shows tails not

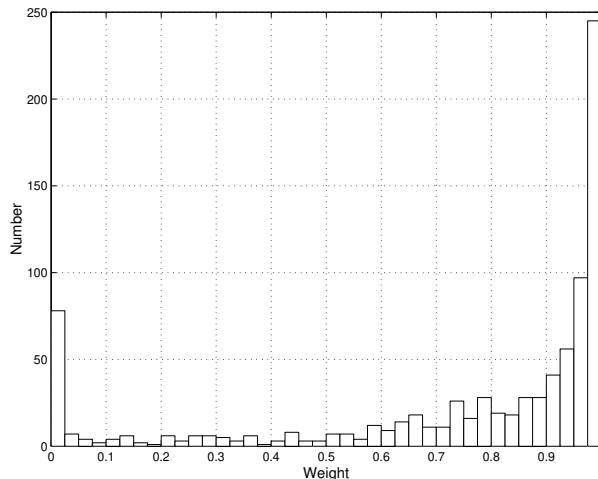


Fig. 3. Histogram of weights.

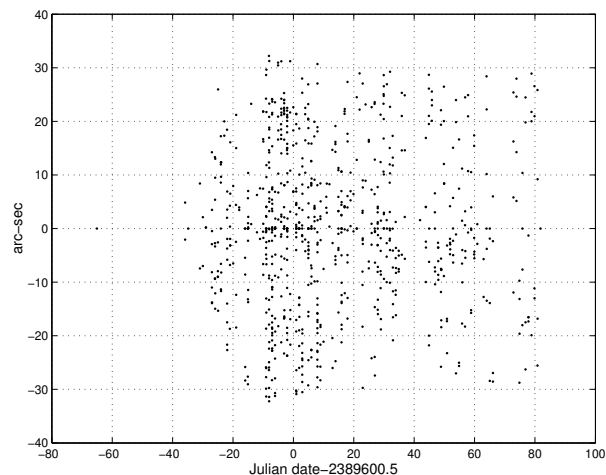


Fig. 4. Distribution of residuals.

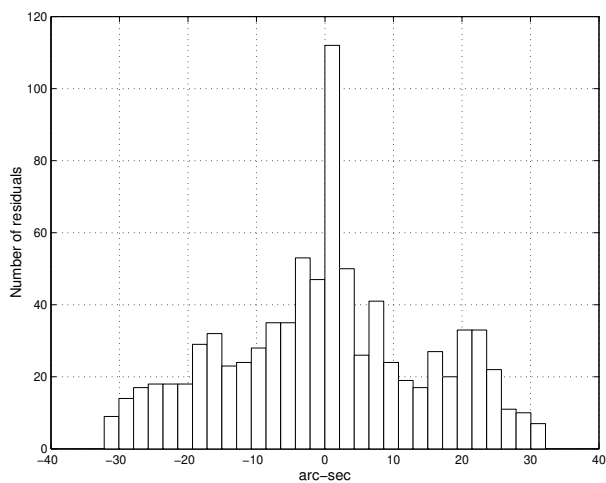


Fig. 5. Histogram of residuals.

TABLE 2

RECTANGULAR COORDINATES AND VELOCITIES: (EPOCH JD 2389600.5, EQUINOX J2000)

Unknown	Solution	Mean Error
x_0	9.088867e-02	3.801770e-06
y_0	-1.239522e+00	3.387994e-06
z_0	-8.837712e-02	6.926546e-04
\dot{x}_0	1.921819e-02	1.514776e-07
\dot{y}_0	-9.942274e-03	2.259179e-07
\dot{z}_0	2.475755e-03	7.067256e-05
$\sigma(1)$	14.''73	

TABLE 3

COVARIANCE (UPPER TRIANGLE) AND CORRELATION (SUBDIAGONAL) MATRICES

0.0028	-0.0006	0.0735	-0.0000	-0.0000	0.0093
-0.2422	0.0023	-0.2986	-0.0000	0.0000	-0.0192
0.1423	-0.6489	94.0689	0.0025	-0.0228	8.3848
-0.1563	-0.0352	0.1203	0.0000	-0.0000	0.0001
-0.0878	0.2829	-0.7436	-0.1261	0.0000	-0.0027
0.1774	-0.4099	0.8736	0.0365	-0.8784	0.9793

too heavy considering the height of the distribution near 0. Thus, the distribution is far from normal, but nevertheless random. Application of a runs test for randomness of the non-zero residuals, eliminated by the biwright function, (Wonnacott & Wonnacott 1972, pp. 409-411) indicates 363 runs out of an expected 365, or an 84.2% chance of being random. Randomness remains more important than normality for the goodness of fit of a distribution.

5. THE SOLUTION

Table 2 shows the final solution for the rectangular coordinates, x_0 , y_0 , z_0 , and velocities, \dot{x}_0 , \dot{y}_0 , \dot{z}_0 , along with their mean errors for epoch JD 2389600.5 and the mean error of unit weight, $\sigma(1)$.

Table 3 shows the covariances and the correlations. Some correlations are high, but the condition number of the matrix of the equations of condition, 4.67×10^7 , remains moderate. Moreover, Eichhorn's efficiency of 0.52 implies that the linear system seems well-conditioned and should result in a reliable solution. Eichhorn's efficiency (Eichhorn 1990) varies from 0 for completely dependent columns of a linear system to 1 for completely independent columns.

TABLE 4

ORBITAL ELEMENTS AND MEAN ERRORS: EPOCH JD 2389600.5; EQUINOX J2000

Unknown	Value	Mean Error
	0.°0050907	
M_0	JD 2389552.20502 (1830 April 09.70502)	0.0039517
a	443.80734	229.34518
e	0.99792	0.00107
q	0.92100	0.25039
Ω	295.°97864	27.°96157
i	104.°94660	0.°72621
ω	227.°85682	11.°62836

Table 4 gives the orbital elements corresponding with the rectangular coordinates of Table 3: the mean anomaly of perihelion passage, M_0 ; the eccentricity, e ; the semi-major axis, a ; perihelion distance, q ; the inclination, i ; the node, Ω ; and the argument of perihelion, ω . Rice's procedure (1902), expressed in modern notation, calculates the mean errors for the elliptical elements and uses \mathbf{C} , the covariance matrix from the least squares solution for the rectangular coordinates and velocities.

Identify the errors in a quantity such as the node Ω with the differential of the quantity, $d\Omega$. Let \mathbf{V} be the vector of the partial derivatives $\left(\partial\Omega/\partial x_0 \quad \partial\Omega/\partial y_0 \quad \cdots \quad \partial\Omega/\partial \dot{z}_0 \right)$. Then the error can be found from

$$(d\Omega)^2 = \sigma^2(1)\mathbf{V} \cdot \mathbf{C} \cdot \mathbf{V}^T. \tag{2}$$

The partial derivatives in equation (2) are calculated from the well known expressions linking orbital elements, whether elliptical or hyperbolic, with their rectangular counterparts. The solution shows a highly elliptical orbit, and the mean errors indicate that the ellipse is statistically distinguishable from a parabola.

The comet's period P comes from the relation

$$P = 2\pi a^{1.5}/k, \tag{3}$$

where k is the Gaussian gravitational constant. From equation (2), equation (3), and the values in Table 3 we calculate $P = 9351 \pm 7098$ yr, a large formal mean error but one consistent with the substantial error in the semi-major axis. It also seems evident that no close approach to the earth will take place in the future.

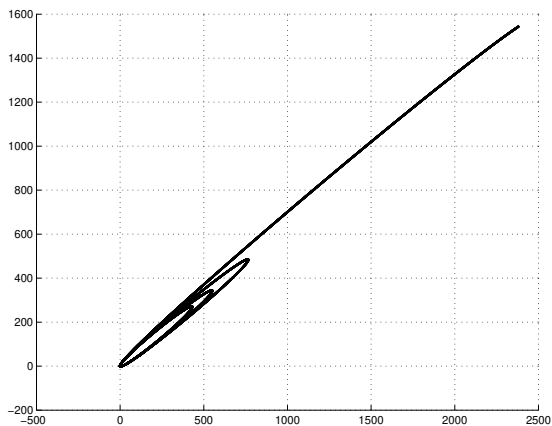


Fig. 6. Orbit from JD -5805999.5 to JD 9806000.5.

Given that the orbit is highly elliptic, could the comet possibly be of extra-solar origin, an initially hyperbolic orbit converted by planetary perturbations to elliptical? To check this possibility I integrated the orbit backwards to JD -5805999.5, an interval of a little over 22,400 years. The integration uses once again heliocentric coordinates. Such long integrations generally employ barycentric coordinates because they permit a longer time interval. But given the speed of modern computers such a concern becomes secondary. Barycentric coordinates are needed for calculations involving stellar aberration such as the determination of aberration day numbers.

Figure 6 shows the results of the integration in the x - y plane. The comet finds itself 2889 au from the Sun at JD -5805999.5 with a still elliptic orbit, $a = 1494$ au. Thus, the comet is not hyperbolic and comes from the Oort cloud. The closest approach to the Earth is 0.147 au at JD 9736510.5, and thus the comet represents no threat in the future. It is evident that the orbit has become substantially modified over thousands of years as Figure 6 shows. Something similar occurred with comet C/1857 D1 (d'Arrest); see Figure 5 in Branham (2011b). This is most likely caused by the effects of the Jovian planets, but the Great March comet's mediocre orbit quality hardly justifies an intensive investigation.

6. CONCLUSIONS

An orbit for Comet C/ 1830 F1 (Great March comet), based on available observations, 428 in α and 424 in δ , is given. The orbit is highly elliptical and statistically different from a parabola. The comet cannot be considered a NEO. Nor is it likely that the comet has an extra-solar origin, but rather originated in the Oort cloud.

REFERENCES

- Branham, R. L. Jr. 1979, *AstP*, 21, 167
- _____. 1990, *Scientific Data Analysis. An Introduction to Overdetermined Systems*, (New York, NY: Springer), <https://doi.org/10.1007/978-1-4612-3362-6>
- _____. 2007, *AN*, 328, 137, <https://doi.org/10.1002/asna.200610665>
- _____. 2009, *AN*, 330, 346, <https://doi.org/10.1002/asna.200811033>
- _____. 2011a, in *Comets: characteristics, composition, and orbits*, ed. Peter G. Melark (Hauppauge, NY: Nova Science Publishers), 123
- _____. 2011b, *AN*, 332, 676, <https://doi.org/10.1002/asna.201111577>
- _____. 2017, *RMxAA*, 53, 53
- _____. 2018, *RMxAA*, 54, 163
- Dubyago, A. D. 1961, *The Determination of Orbits*, (New York, NY: Macmillan)
- Eichhorn, H. 1990, in *Errors Bias and Uncertainties*, Proceedings held in Strasbourg, September 1989, ed. C. Jaschek & F. Murtagh (CUP), 133
- Gambart, 1830, *AN*, 8, 251
- Høg, E., Fabricius, C., Markarov, V. V., et al. 2000, *A&A*, 355, 27
- Kaplan, G. H., Hughes, J. A., Seidelmann, P. K., & Smith, C. A. 1989, *AJ*, 97, 1197, <https://doi.org/10.1086/115063>
- Marsden, B. G. & Williams, G. V. 2003, *Catalog of Cometary Orbits, XVth*, (Cambridge, MA: Smithsonian Astrophysical Obs.)
- Rice, H. L. 1902, *AJ*, 22, 149, <https://doi.org/10.1086/103399>
- Scott, F.P. 1964, *AJ*, 69, 372, <https://doi.org/10.1086/109287>
- Schulze, L. R. 1873, *AN*, 82, 97
- Wonnacott, T. H. & Wonnacott, R. J. 1972, *Introductory Statistics*, 2nd ed. (New York, NY: Wiley)

Richard L. Branham Jr.: Emeritus investigator, Instituto Argentino de Nivología, Glaciología y Ciencias Ambientales (Ianigla), Centro Científico Tecnológico - Mendoza, C.C. 330, Mendoza, Argentina (richardbranham_1943@yahoo.com).

THE HIPPARCOS PLEIADES PARALLAX ERROR IS ALSO A PROPER MOTION ERROR

Valeri V. Makarov

U.S. Naval Observatory, Washington, DC 20392-5420, USA.

Received May 4 2022; accepted June 29 2022

ABSTRACT

The mean parallax of the Pleiades open cluster from the Hipparcos catalog is larger than the true value by approximately 1 mas. The origin of this error, as well as a possible algorithm of correcting it, was proposed by Makarov (2002). The problem is reassessed using the more accurate Gaia data with a focus on the predicted correction to the Pleiades proper motions. The accurately determined differences Gaia – Hipparcos for 52 common stars are close to these estimates within the formal uncertainties for all three parameters, which strongly suggests that the proposed interpretation was correct. With adjustments for the systematic vector field fitted with 126 vector spherical harmonics to degree 7, these differences amount to $(+0.39, -0.74)$ mas yr⁻¹. The implications of small-scale proper motion and position errors in Hipparcos for present day astrometry are briefly discussed.

RESUMEN

La paralaje media del cúmulo abierto de las Pléyades obtenida del catálogo Hipparcos es aproximadamente 1 mas mayor que el valor verdadero. Makarov (2002) propuso una razón para este error y un algoritmo para corregirlo. El problema se examina aquí de nuevo, usando los datos más precisos de Gaia y con hincapié en la corrección predicha para los movimientos propios en las Pléyades. Las diferencias Gaia – Hipparcos determinadas con precisión para 52 estrellas en común son muy parecidas a las estimaciones (dentro de las incertidumbres formales de los tres parámetros), lo cual sugiere que la interpretación propuesta es correcta. Al realizar ajustes para el vector de campo sistemático con 126 armónicos esféricos vectoriales y grado 7 estas diferencias resultan ser de $(+0.39, -0.74)$ mas año⁻¹. Se discuten brevemente las implicaciones de pequeños errores en las posiciones y los movimientos propios del Hipparcos para la astrometría moderna.

Key Words: astrometry — parallaxes — proper motions — reference systems

1. INTRODUCTION

The publication of the Hipparcos star catalog and its supporting data sets (ESA 1997) marked the beginning of a new golden age of astrometry and fostered even bolder ideas setting more ambitious goals. The impact of this space mission across the diverse areas of astronomy and astrophysics is summarized by Perryman (2008). The advent of space astrometry was not incontrovertible, however. Perhaps, the most contentious issue discussed for at least a decade was the conspicuous discrepancy between the mean trigonometric parallax of the Pleiades open cluster and the previously adopted distance value, which

had crystallized from numerous observational and theoretical investigations (Mermilliod et al. 1997). The Hipparcos parallax is too large at approximately 8.6 mas, placing the Pleiades main sequence about 0.5 mag fainter with respect to the well-established main sequence at its metallicity. After careful analysis of possible astrophysical causes, such as incorrectly determined reddening, abnormal helium abundance, a systematic error of ≈ 1 mas in the Hipparcos data was proposed, which is well outside of the 3σ statistical range (Pinsonneault et al. 1998; Soderblom et al. 1998). The first important clue toward a consistent explanation of the discrepancy

was provided by Narayanan & Gould (1999), who used the convergent point method and the resulting kinematic parallaxes (significantly more precise than the trigonometric parallaxes) for the Pleiades and Hyades to reveal the presence of *sky-correlated* errors in the Hipparcos data on angular scales 2° – 3° .

The presence of such a large error in Hipparcos astrometry had been initially doubted by some authors privy to the mission (van Leeuwen 1999; Robichon et al. 1999). Very soon, mounting evidence to the contrary of astrometric (Gatewood et al. 2000; Pan et al. 2004; Zwahlen et al. 2004; Soderblom et al. 2005; Melis et al. 2014; Galli et al. 2017) and astrophysical nature (Stello & Nissen 2001; Munari et al. 2004; Percival et al. 2005; Fox Machado et al. 2006; An et al. 2007; Miller et al. 2013; Kim et al. 2016; Madler et al. 2016) was provided. One could say that the bottom line of this discussion was drawn by the Gaia astrometric mission (Gaia Collaboration et al. 2016) of much superior precision, which already in its first data release (DR1, Gaia Collaboration et al. 2016) unambiguously confirmed that both the principal Hipparcos catalog and its later re-reduction failed to provide an accurate mean parallax of the Pleiades. A very accurate trigonometric parallax of the Pleiades was also obtained from Gaia Data Release 2 (Gaia Collaboration et al. 2018).

One of the goals of this paper is to show that the correct interpretation of the origin of this spectacular error has been presented by Makarov (2002). The topic is revisited because Hipparcos continues to be important for many studies related to positions and motions of brighter stars, as well as for practical applications (Kopeikin & Makarov 2021). Understanding past mistakes is also essential for planning of future space astrometry missions, and generally, of large astrometric catalogs. The other objective is to draw the attention of the research community to the fact that Hipparcos proper motions of the brighter stars contain significant position correlated errors at a range of angular scales. These proper motions are being used in a number of important projects, for example, for detecting accelerating astrometric binaries with unresolved or dim companions (e.g., Kervella et al. 2019).

2. LOCALLY WEAK CONDITION

The main principles of self-calibrating all-sky space astrometry, originally formulated by P. Lacroute in 1966 (see Kovalevsky 1984) are based on the concept of a telescope with split viewing directions separated by a fixed “basic angle” Γ . One-

dimensional positions of stars (called abscissae) are measured on the detector as they drift across the two fields of view. Linearized condition equations include only small differences “observed minus calculated” of the measured abscissae and the derived astrometric parameters are therefore corrections to a set of nominal values. Likewise, the results for other unknowns involved in this adjustment are also small corrections to some previously estimated or assumed functions of time. Without the basic angle, the condition equations would be nearly degenerate to a wide range of perturbations. The ability to reference each target star to a large number of other stars observed almost simultaneously at a large angular distance is pivotal in improving the condition of space astrometry equations. Trigonometric parallaxes, in particular, become absolute (Makarov 1998), while the propagation of large-scale sky-correlated errors of proper motions and positions (outside of the well-known 6–rank deficiency) is greatly reduced (Makarov et al. 2012).

This theoretical advantage had yet to be realized in a carefully designed data processing pipeline where the tasks of instrument calibration, attitude reconstruction, and astrometric adjustment were divided into stages of a complex iterative process and performed by different teams. The one-dimensional along-scan attitude was modeled by piece-wise cubic spline functions of time. The characteristic scale of these functions was a few degrees, matching the angular diameter of a nearby cluster. As explained in detail in Makarov (2002), setting the weights of individual measurements depending on the measured flux gives rise to a strong imbalance between the data from the two fields of view and a locally weak condition. An imprecise initial assumption about the true abscissae of the Pleiades, for example, would not be corrected because of a poor convergence of the iterative adjustment. The proposed fix was to re-estimate the instantaneous position of the bisector assigning a greater weight to the fainter stars simultaneously observed in the other field of view.

3. THE MEAN PLEIADES PARALLAX AND PROPER MOTION IN GAIA DR3

Gaia DR3 (Gaia Collaboration et al. 2021) includes many more members of the Pleiades cluster than Hipparcos because of the fainter magnitude limit. For the purpose of unbiased comparison, however, we have to use the same sample of stars as in Makarov (2002). It includes 53 bona fide Pleiades members with H_p magnitudes between

2.85 and 10.87 and a median magnitude 8.32. The brightest star, Alcione = HIP 17702, however, does not have proper motion or parallax determinations in Gaia DR3. It is eliminated from the analysis leaving 52 stars. Some of these stars have fainter companions within 10'' resolved in DR3, with three companions being likely members of the cluster and possibly binary companions according to the astrometric information. In each case, the closer match is much brighter removing any ambiguity in cross-identification.

The mean differences of parallax and proper motion components, $\Delta\varpi$, $\Delta\mu_{\alpha*}$, and $\Delta\mu_{\delta}$, are computed in the sense ‘‘Gaia – Hipparcos’’ with weights w_i inversely proportional to the combined formal variances as given in the two catalogs, e.g.,

$$\Delta\varpi = \frac{\sum_{i=1}^{52} (\varpi_{\text{DR3},i} - \varpi_{\text{HIP},i}) / (\sigma_{\varpi_{\text{DR3},i}}^2 + \sigma_{\varpi_{\text{HIP},i}}^2)}{\sum_{i=1}^{52} (\sigma_{\varpi_{\text{DR3},i}}^2 + \sigma_{\varpi_{\text{HIP},i}}^2)^{-1}}. \quad (1)$$

The standard error of the mean is then computed as

$$\sigma_{\Delta\varpi} = \left(\sum_{i=1}^{52} (\sigma_{\varpi_{\text{DR3},i}}^2 + \sigma_{\varpi_{\text{HIP},i}}^2)^{-1} \right)^{-\frac{1}{2}}, \quad (2)$$

and the same formulae are applied to the proper motion components $\mu_{\alpha*}$ and μ_{δ} .

In application to proper motions, this is a simplified way of estimating statistical differences, which includes only the coordinate projections of the proper motion vector $\mu_{\alpha*}$ and μ_{δ} . A mathematically more consistent method is to compute for each star the vector differences $\delta_{\mu} = \mu_{\text{DR3}} - \mu_{\text{HIP}}$ and their normalized bivariate values

$$\chi_{\mu} = \left(\delta_{\mu}^T \mathbf{C}_{\mu}^{-1} \delta_{\mu} \right)^{\frac{1}{2}}, \quad (3)$$

where \mathbf{C}_{μ} is the sum of the corresponding 2×2 covariance matrices of the proper motion vectors in Gaia and Hipparcos. The statistics χ_{μ} are expected to be distributed as $\chi(1)$. For an adequate comparison with the results from Makarov (2002), however, the simplified method is required because the full covariance matrix of the updated Hipparcos proper motion was not available.

We note that the weights of proper motion component differences are dominated by the uncertainties in Hipparcos, where the formal errors are much greater than in Gaia DR3. This is seen from the error bars in Figure 1, which shows the δ components of the 52 proper motions in DR3 plotted versus the

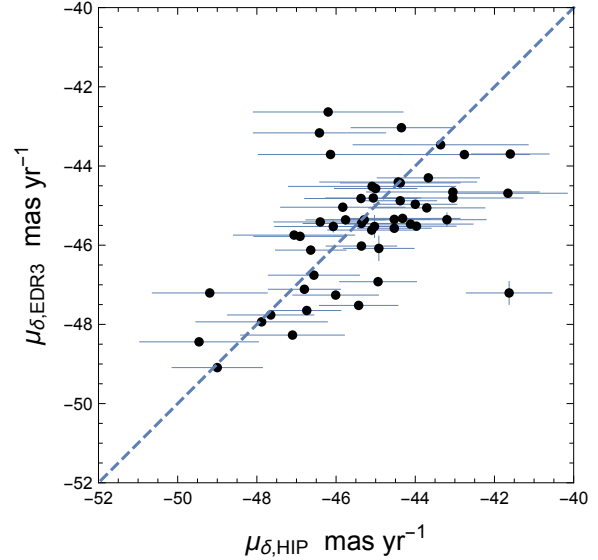


Fig. 1. Declination components of proper motions of 52 Pleiades members in Gaia DR3 and Hipparcos.

corresponding values in Hipparcos. The straight diagonal line shows the location of data points when the determinations in the two catalogs are ideally consistent. More points are shifted below this line, reflecting the significant difference between the mean proper motions.

The mean differences thus computed are $\Delta\varpi = -1.00 \pm 0.17$ mas, $\Delta\mu_{\alpha*} = +0.34 \pm 0.17$ mas yr⁻¹, and $\Delta\mu_{\delta} = -0.62 \pm 0.13$ mas yr⁻¹. The corresponding confidence bounds for these mean values assuming a normal distribution of errors are 1, 0.9772, and 1, respectively. These values are statistically close to the corrections intrinsically derived by Makarov (2002) from the Hipparcos data: -0.71 ± 0.14 mas, $+0.45 \pm 0.14$ mas yr⁻¹, -0.66 ± 0.11 mas yr⁻¹, respectively. The formal confidence bounds for these estimates are 1, 0.9993, and 1, respectively. We note that the probability of the null hypothesis that these updates coincide within $1.7 \cdot \sigma$ or better in all the three parameters by accident is practically zero.

The Gaia DR3 and Hipparcos proper motion systems for brighter stars are known to have systematic, or large-scale sky-correlated differences. They include a substantial rigid 3D rotation, which can be viewed as a spin of the entire frame with an angular acceleration. The pattern of Gaia–Hipparcos proper motion differences, however, is not limited to this rigid rotation. To estimate the contribution of the large-scale vector field to the Pleiades-specific proper motion differences, a dedicated analysis of the proper motion systems was performed. The Hip-

parcos catalog positions and their covariances were transferred onto the mean epoch of Gaia DR3 (2016) and all common stars were cross-matched. After removal of a large number of known binary and double stars, as well as statistically perturbed unresolved astrometric binaries, some 75,000 well-behaved stars with proper motions in both catalogs remained. A set of 126 vector spherical harmonics (which is a complete set up to degree 7) was fitted to the observed Gaia–Hipparcos vector field using the formal covariance matrices for optimal weights. Each vector spherical harmonic represents a specific vector field pattern on the sky, and its coefficient defines the estimated amplitude. The result revealed a spectrum of harmonics with statistically significant signal-to-noise ratios, where the three magnetic (or, toroidal) harmonics of degree 1 were by far the greatest contributors. The median vector length of the fitted field is $191 \mu\text{as yr}^{-1}$. At the location of the Pleiades cluster, the fitted value is $(-48, +123) \mu\text{as yr}^{-1}$. In order to correct for the large-scale distortion pattern, this vector should be subtracted from the above quoted mean proper motion differences. The result $(+0.39, -0.74) \text{ mas yr}^{-1}$ is marginally closer to the estimates from Makarov (2002).

4. DISCUSSION

For nearly two decades, the Hipparcos catalog provided an optical realization of the International Celestial Reference System. Its emergence motivated fundamental changes in the definition of the celestial reference frame with a decisive move from the dynamic mean equinox of J2000 to a mathematically fixed, precession-free origin on the similarly defined equator (Seidemann & Kovalevsky 2002). The endeavor of achieving a maximally inertial (non-rotating) reference system of celestial coordinates resulted in the shift of paradigm from referencing stellar positions to the solar system ephemerides. The valued quasi-inertiality is based on a complex and indirect link to the extragalactic reference frame (Kovalevsky et al. 1997). This link is much more robust and straightforward for Gaia, which observed $\approx 10^6$ optical quasars and AGNs, as well as a few thousand optical counterparts of ICRF3 (Gaia Collaboration et al. 2018). Unfortunately, because of essentially separate calibration pipelines for bright stars and fainter sources, this link does not fully apply to the sample of Hipparcos stars. This may be one of the reasons for significant global and large-scale proper motion differences. Gaia DR3 proper motions of brighter stars, in particular, may have

significant rigid spin components with respect to the better constrained fainter stars (Cantat-Gaudin & Brandt 2021).

Hipparcos astrometry acquires a pivotal role of the first-epoch realization of a quasi-inertial celestial reference frame. Any distortions of its position and proper motion systems affect the long-term viability of this frame. One application is the detection of $\Delta\mu$ binaries (Wielen et al. 1999), which are unresolved astrometric binaries with variable proper motion. The increased sensitivity of this method allows us to detect Jupiter-mass planets in long-period orbits around nearby stars. It is also relevant for maintaining the optical reference frame, because only truly single stars can be stable astrometric standards. The present follow-up study shows that Hipparcos parallaxes and proper motions are burdened by small-scale error of technical origin, which is, in principle, correctable. It is likely that the mean positions in Hipparcos are also affected in certain parts of the celestial sphere by similar or larger amounts. Such errors are bound to propagate into the most precise Hipparcos–Gaia (HG) proper motions, which are central to the anticipated detection of long-period companions of planetary mass or inactive black hole companions of stellar mass (Mashian & Loeb 2017). This error overhead coming from unaccounted perturbations of Hipparcos positions may exceed the intrinsic formal error of short-term Gaia proper motions, so its presence is bound to perturb the detection results toward increased occurrence of false positives at the most affected locations. Ongoing investigations of the Gaia–Hipparcos proper motion field should at a minimum take into account possible sky-correlated deviations. A more ambitious goal would be to devise ways of correcting Hipparcos astrometry once we have understood the origin of its main weakness. A complete reprocessing of Hipparcos mission data starting with the Intermediate Astrometry Data (HIAD) and using Gaia results for certified stable and single astrometric standards can be considered. Such a reprocessing effort should focus on improving the attitude, basic angle Γ , and reference great circle zero-points solutions. The technical feasibility of such a solution for the latter data type has been demonstrated by Zacharias et al. (2022) using precision astrometric data from modern ground-based observations. In the same paper, the technical possibility of reprocessing the available Hipparcos data and solving for an improved set of abscissae zero-points has been demonstrated. Gaia positions of the fainter Hipparcos stars can be extrapolated back to 1991.25 using corrected Gaia proper motions

and used as additional constraints in such a global solution, potentially improving the system of Hipparcos positions on the largest spatial scale including rotation. Another possibility is to improve the Hipparcos proper motion system *a posteriori* at the cost of removing the option of external verification of Gaia. The main obstacle on this way is the existence of similar sky-correlated errors in Gaia, including a possible rigid spin of the entire proper motion system already seen in the Gaia Data Release 2 (Makarov & Berghea 2019). Although these imperfections are much smaller in Gaia than in Hipparcos, they create ambiguity in the interpretation of obvious differences between the two catalogs. A deeper insight into the propagation of correlated errors in Hipparcos may help to disentangle this ambiguity.

The anonymous referee is thanked for useful and constructive suggestions. This work has made use of data from the European Space Agency (ESA) mission *Gaia* (<https://www.cosmos.esa.int/gaia>), processed by the *Gaia* Data Processing and Analysis Consortium (DPAC, <https://www.cosmos.esa.int/web/gaia/dpac/consortium>). Funding for the DPAC has been provided by national institutions, in particular the institutions participating in the *Gaia* Multilateral Agreement.

REFERENCES

- An, D., Terndrup, D. M., Pinsonneault, M. H., et al. 2007, *ApJ*, 655, 233, <https://doi.org/10.1086/509653>
- Cantat-Gaudin, T. & Brandt, T. D. 2021, *A&A*, 649, 124, <https://doi.org/10.1051/0004-6361/202140807>
- ESA 1997, The HIPPARCOS and TYCHO catalogues. Astrometric and photometric star catalogues derived from the ESA HIPPARCOS Space Astrometry Mission (Noordwijk, Netherlands : ESA Publications Division), 1200
- Fox Machado, L., Pérez Hernández, F., Suárez, J. C., Michel, E., & Lebreton, Y. 2006, *MmSAI*, 77, 455
- Gaia Collaboration, Babusiaux, C., van Leeuwen, F., et al. 2018, *A&A*, 616, 10, <https://doi.org/10.1051/0004-6361/201832843>
- Gaia Collaboration, Mignard, F., Klioner, S. A., et al. 2018, *A&A*, 616, 14, <https://doi.org/10.1051/0004-6361/201832916>
- Gaia Collaboration, Brown, A. G. A., Vallenari, A., et al. 2016, *A&A*, 595, 2, <https://doi.org/10.1051/0004-6361/201629512>
- Gaia Collaboration, Prusti, T., de Bruijne, J. H. J., et al. 2016, *A&A*, 595, 1, <https://doi.org/10.1051/0004-6361/201629272>
- Gaia Collaboration, Brown, A. G. A., Vallenari, A., et al. 2021, *A&A*, 649, 1, <https://doi.org/10.1051/0004-6361/202039657>
- Galli, P. A. B., Moraux, E., Bouy, H., et al. 2017, *A&A*, 598, 48, <https://doi.org/10.1051/0004-6361/201629239>
- Gatewood, G., de Jonge, J. K., & Han, I. 2000, *ApJ*, 533, 938, <https://doi.org/10.1086/308679>
- Kervella, P., Arenou, F., Mignard, F., et al. 2019, *A&A*, 623, 72, <https://doi.org/10.1051/0004-6361/201834371>
- Kim, B., An, D., Stauffer, J. R., et al. 2016, *ApJS*, 222, 19, <https://doi.org/10.3847/0067-0049/222/2/19>
- Kopeikin, S. M. & Makarov, V. V. 2021, *FrASS*, 8, 9, <https://doi.org/10.3389/frspas.2021.639706>
- Kovalevsky, J. 1984, *MitAG*, 62, 63
- Kovalevsky, J., Lindegren, L., Perryman, M. A. C., et al. 1997, *A&A*, 323, 620
- Mädler, T., Jofré, P., Gilmore, G., et al. 2016, *A&A*, 595, 59, <https://doi.org/10.1051/0004-6361/201629091>
- Makarov, V. V. 1998, *A&A*, 340, 309
- . 2002, *AJ*, 124, 3299, <https://doi.org/10.1086/344683>
- Makarov, V. V., Dorland, B. N., Gaume, R. A., et al. 2012, *AJ*, 144, 22, <https://doi.org/10.1088/0004-6256/144/1/22>
- Makarov, V. & Berghea, C. 2019, *The Gaia Universe*, 25, <https://doi.org/10.5281/zenodo.2648649>
- Mashian, N. & Loeb, A. 2017, *MNRAS*, 470, 2611, <https://doi.org/10.1093/mnras/stx1410>
- Melis, C., Reid, M. J., Mioduszewski, A. J., et al. 2014, *Science*, 345, 1029, <https://doi.org/10.1126/science.1256101>
- Mermilliod, J.-C., Turon, C., Robichon, N., Avenou, F., & Lebreton, Y. 1997, *ESASP, Hipparcos - Venice '97'*, 402, 643
- Miller, B., King, J. R., Chen, Y., et al. 2013, *PASP*, 125, 1297, <https://doi.org/10.1086/673922>
- Munari, U., Dallaporta, S., Siviero, A., et al. 2004, *A&A*, 418, 31, <https://doi.org/10.1051/0004-6361:20040124>
- Narayanan, V. K. & Gould, A. 1999, *ApJ*, 523, 328, <https://doi.org/10.1086/307716>
- Pan, X., Shao, M., & Kulkarni, S. R. 2004, *Natur*, 427, 326, <https://doi.org/10.1038/nature02296>
- Percival, S. M., Salaris, M., & Groenewegen, M. A. T. 2005, *A&A*, 429, 887, <https://doi.org/10.1051/0004-6361:20041694>
- Perryman, M. 2008, *Astronomical Applications of Astrometry* (Cambridge, UK: CUP), <https://doi.org/10.1017/CB09780511575242>
- Pinsonneault, M. H., Stauffer, J., Soderblom, D. R., et al. 1998, *ApJ*, 504, 170, <https://doi.org/10.1086/306077>
- Robichon, N., Arenou, F., Mermilliod, J.-C., & Turon, C. 1999, *A&A*, 345, 471

- Seidelmann, P. K. & Kovalevsky, J. 2002, *A&A*, 392, 341, <https://doi.org/10.1051/0004-6361:20020931>
- Soderblom, D. R., King, J. R., Hanson, R. B., et al. 1998, *ApJ*, 504, 192, <https://doi.org/10.1086/306073>
- Soderblom, D. R., Nelan, E., Benedict, G. F., et al. 2005, *AJ*, 129, 1616, <https://doi.org/10.1086/427860>
- Stello, D. & Nissen, P. E. 2001, *A&A*, 374, 105, <https://doi.org/10.1051/0004-6361:20010665>
- van Leeuwen, F. 1999, *A&A*, 341, 71
- Wielen, R., Dettbarn, C., Jahrei, H., Lenhardt, M., & Schwan, H. 1999, *A&A*, 346, 675
- Zacharias, N., Makarov, V. V., Finch, C. T., et al. 2022, arXiv:2204.09080, <https://doi.org/10.48550/arXiv.2204.09080>
- Zwahlen, N., North, P., Debernardi, Y., et al. 2004, *A&A*, 425, 45, <https://doi.org/10.1051/0004-6361:200400062>

ANN AND ANALYTICAL SOLUTIONS TO RELATIVISTIC ISOTHERMAL GAS SPHERES

Mohamed I. Nouh¹, Yosry A. Azzam¹, Emad A-B Abdel-Salam², Farag I. Elnagahy¹, and Tarek M. Kamel¹

Received May 19 2022; accepted July 7 2022

ABSTRACT

Relativistic isothermal gas spheres are a powerful tool to model many astronomical objects, like compact stars and clusters of galaxies. In the present paper, we introduce an artificial neural network (ANN) algorithm and Taylor series to model the relativistic gas spheres using Tolman-Oppenheimer-Volkoff differential equations (TOV). Comparing the analytical solutions with the numerical ones revealed good agreement with maximum relative errors of 10^{-3} . The ANN algorithm implements a three-layer feed-forward neural network built using a back-propagation learning technique that is based on the gradient descent rule. We analyzed the mass-radius relations and the density profiles of the relativistic isothermal gas spheres against different relativistic parameters and compared the ANN solutions with the analytical ones. The comparison between the two solutions reflects the efficiency of using the ANN to solve TOV equations.

RESUMEN

Las esferas isotérmicas relativistas son una herramienta poderosa para modelar objetos astronómicos, tales como estrellas compactas y cúmulos de galaxias. En este trabajo presentamos un algoritmo basado en una red neuronal artificial (ANN) y series de Taylor para modelar esferas de gas relativistas usando las ecuaciones diferenciales de Tolman-Oppenheimer-Volkoff (TOV). La comparación de las soluciones analíticas con las numéricas muestra una buena concordancia, con errores relativos máximos de 10^{-3} . El algoritmo ANN implementa una red neuronal de tres niveles con pro-alimentación, construida usando una técnica de aprendizaje con retro-propagación basada en la regla del gradiente descendente. Analizamos las relaciones masa-radio y los perfiles de densidad de las esferas relativistas isotérmicas y comparamos las soluciones ANN con las analíticas. Esta comparación muestra la eficiencia de ANN para resolver las ecuaciones TOV.

Key Words: methods: analytical — methods: miscellaneous — relativistic processes — stars: interiors

1. INTRODUCTION

Many astrophysical issues, particularly those involving star structure and galactic dynamics, benefit from the use of isothermal models (Binney & Tremaine 1987; Chandrasekhar 1939). In terms of stellar structure and evolution theory, isothermal self-gravitating spheres may be used to calculate the behaviour of physical variables.

There are a lot of studies concerning the isothermal spheres in the framework of Newtonian mechanics (non-relativistic) (Milgrom 1984; Liu 1996; Natarajan & Lynden-Bell 1997; Roxburgh & Stockman 1999; Hunter 2001; Raga et al. 2013). Several works have conducted numerical investigations on relativistic isothermal spheres within the framework of general relativity theory. Chavanis (2002) explored the structure and stability of

¹Astronomy Department, National Research Institute of Astronomy and Geophysics (NRIAG), Cairo, Egypt.

²Department of Mathematics, Faculty of Science, New Valley University, Egypt.

isothermal gas spheres using a linear equation of state in the context of general relativity. Sharma (1990) used the Pade approximation technique to provide straightforward and accessible approximate analytical solutions to the TOV equation of hydrostatic equilibrium, and his results indicate that general relativity isothermal arrangements have a limited extent. Saad (2017) proposed a novel approximate analytical solution to the TOV equation using a combination of the Euler-Abel transformation and the Pade approximation. Besides the numerical and analytical solutions of similar nonlinear differential equations similar to TOV equations, artificial intelligence approaches presented reliable results in many problems arising in astrophysics. In this context, Morawski & Bejger (2020) proposed a unique method based on ANN algorithms for reconstructing the neutron star equation of state from the observed mass-radius relationship. Nouh et al. (2020) presented a neural network-based computational approach for solving fractional Lane-Emden differential equation problems. Azzam et al. (2021) used an artificial neural network (ANN) approach and simulate the conformable fractional isothermal gas spheres and compared them with the results of the analytical solution deduced using the Taylor series. Abdel-Salam et al. (2021) presented the neural network (NN) mathematical model and developed a neural network approach for simulating the helium burning network using a feed-forward mechanism.

In the present article, we solve TOV equations by the ANN and analytically by an accelerated Taylor series. We employ an ordinary feed-forward neural network to estimate the solution of TOV equations for the ANN simulation, which has been shown to outperform competing computational approaches. A three-layer feed-forward neural network is used, which was trained using a back-propagation learning approach based on the gradient descent rule. The following is the paper's structure: The relativistic isothermal polytrope is discussed in § 2. The analytical solution to the TOV equation is found in § 3. The mathematical modelling of the ANN is covered in § 4. § 5 summarizes the results obtained, and § 6 presents the conclusion.

2. THE RELATIVISTIC ISOTHERMAL GAS SPHERE (RIGS)

In the polytropic equation of state ($P = K\rho^{1+1/n}$, where P is the pressure, ρ is the density, and K is the polytropic constant), the polytropic index n ranges from 0 to ∞ . When n approaches or equals ∞ , the isothermal equation of state $P = K\rho$ emerges. By combining the isothermal equation of state with the equation of the hydrostatic equilibrium in the frame of the general relativity, the TOV equation of the isothermal gas sphere could be given as (Sharma 1990),

$$\frac{dP}{dr} = - \left(\frac{GM_r}{r^2} \right) \frac{\rho + (P/c^2)(1 + (4\pi Pr^3/M_r c^2))}{(1 - (2GM_r/rc^2))}, \quad (1)$$

where M_r is the total mass energy or 'effective mass' of the star of radius r including its gravitational field is given by

$$M_r = \frac{4\pi}{c^2} \int_0^r \rho c^2 r^2 dr. \quad (2)$$

Define the variables, χ , ν , u , and the relativistic parameter s , by

$$\begin{aligned} \chi &= rA; \\ A^2 &= 4\pi G\rho_c/sc^2; \\ s &= \frac{P_c}{\rho_c c^2}, \end{aligned} \quad (3)$$

where ρ_c and P_c are the central density and central pressure of the star respectively, $u(x)$ and $\nu(x)$ are the Emden and is the mass functions of radius, and c is the speed of light. Equations (1) and (2) can be transformed into the dimensionless forms in the (x, u) plane as

$$\frac{(1 - 2s\nu(x)/x)}{1 + \sigma} + x^2 \frac{du}{dx} - \nu(x) - se^{-u}x^3 = 0 \quad (4)$$

$$\frac{d\nu}{dx} = x^2 e^{-u}, \quad (5)$$

which satisfy the initial conditions

$$u(0) = 0; \frac{du(0)}{dx} = 0; \nu(0) = 0. \quad (6)$$

If the pressure is substantially lower than the energy density at the center of a star (i.e., goes to zero), as in the non-relativistic case, the system of equations (4) and (5) simplifies to the Newtonian isothermal structure equations

$$\frac{1}{x^2} \frac{d}{dx} \left(x^2 \frac{du}{dx} \right) = e^{-u}. \quad (7)$$

One can calculate physical parameters of the stellar models like radius (R), density (ρ), and mass M_r using the following equations

$$\begin{aligned} R &= xc \sqrt{\frac{s}{4\pi G \rho_c}} \\ \rho &= \rho_c e^{-u}; \\ M_r &= \frac{4\pi \rho_c}{A^2} \nu(x). \end{aligned} \quad (8)$$

3. ANALYTICAL SOLUTION TO EQUATION (4)

Rearrange equations (4) and (5) as

$$\begin{aligned} x^2 \frac{du}{dx} - 2svx \frac{du}{dx} - \nu - \nu s - sx^3 e^{-u} - s^2 x^3 e^{-u} &= 0, \\ \frac{d\nu}{dx} &= x^2 e^{-u}, \end{aligned} \quad (9)$$

where the initial conditions are

$$u(0) = 0; \quad \frac{du(0)}{dx} = 0; \quad \nu(0) = 0.$$

Write the Taylor series for the function $u(x)$ as

$$u(x) = u(0) + D_x u(0)x + \frac{D_x^2 u(0)}{2!} x^2 + \frac{D_x^3 u(0)}{3!} x^3 + \frac{D_x^4 u(0)}{4!} x^4 + \frac{D_x^5 u(0)}{5!} x^5 + \dots, \quad (10)$$

at $x = 0$ the first derivative is given by

$$\nu'_0 = (0)^2 e^{-u(0)} = 0,$$

and the second derivative is

$$\nu''_0 = 2(0)e^{-u(0)} - (0)^2 e^{-u(0)} u'_0 = 0,$$

differentiating another time, we have

$$\nu''' = 2e^{-u} - 4xe^{-u}u' + x^2e^{-u}u'^2 - x^2e^{-u}u''; \quad (11)$$

when $x = 0$ we have

$$\nu'''_0 = 2e^{-u(0)} - 4(0)e^{-u(0)}u'(0) + (0)^2e^{-u(0)}u'(0)^2 - (0)^2e^{-u(0)}u''(0) = 2(1) = 2;$$

the fourth derivative is given by

$$\nu^{(4)} = -6e^{-u}u' + 6xe^{-u}u'^2 - 6xe^{-u}u'' - x^2e^{-u}u'^3 + 3x^2e^{-u}u'u'' - x^2e^{-u}u''', \quad (12)$$

when $x = 0$ we have $\nu^{(4)}_0 = 0$;

the fifth derivative is given by

$$\begin{aligned} \nu^{(5)} &= 6e^{-u}u'^2 - 6e^{-u}u'' + 6e^{-u}u'^2 - 6xe^{-u}u'^3 + 12xe^{-u}u'u'' - 6e^{-u}u'' + 6xe^{-u}u'u'' \\ &\quad - 6xe^{-u}u''' - 2xe^{-u}u'^3 + x^2e^{-u}u'^4 - 3x^2e^{-u}u'^2u'' + 6xe^{-u}u'u'' - 3x^2e^{-u}u'^2u'' \\ &\quad + 3x^2e^{-u}u''^2 + 3x^2e^{-u}u'u''' - 2xe^{-u}u''' + x^2e^{-u}u'u''' - x^2e^{-u}u^{(4)}. \end{aligned}$$

Substituting $x = 0$ we have

$$\nu_0^{(5)} = 12e^{-u_0}(u_0')^2 - 12e^{-u_0}u_0'' = -12u_0'',$$

and so on. Now write the first TOV equation of equation (9) as

$$x^2u' - 2svxu' - v - \nu s - sx^3e^{-u} - s^2x^3e^{-u} = 0. \quad (13)$$

Differentiating equation (13) for x we have

$$2xu' + x^2u'' - 2svu' - 2sv'xu' - 2svxu'' - \nu' - s\nu' - 3sx^2e^{-u} + sx^3e^{-u}u' = 0; \quad (14)$$

when $x = 0$ all terms are equal to zero.

Differentiating equation (14) for x we have

$$\begin{aligned} &2u' + 2xu'' + 2xu''' + x^2u'''' - 2sv'u' - 2svu'' - 2sv'u' - 2sv''xu' - 2sv'xu'' \\ &- 2svu''' - 2sv'xu''' - 2s\zeta xu'''' - \nu'' - s\nu'' - 6sxe^{-u} + 3sx^2e^{-u}u' + 3sx^2e^{-u}u'' \\ &- sx^3e^{-u}u'^2 + sx^3e^{-u}u'' = 0; \end{aligned}$$

which can be simplified into

$$\begin{aligned} &2u' + 4xu'' + x^2u'''' - 4sv'u' - 4svu'' - 2sv''xu' - 4sv'xu'' - 2svxu''' \\ &- \nu'' - s\nu'' - 6sxe^{-u} + 6sx^2e^{-u}u' - sx^3e^{-u}u'^2 + sx^3e^{-u}u'' = 0. \end{aligned} \quad (15)$$

Putting $x = 0$ we have

$$\begin{aligned} &2u_0' + 4(0)u_0'' + (0)^2u_0'''' - 4sv_0'u_0' - 4sv_0u_0'' - 2s(0)\nu_0''u_0' - 4s(0)\nu_0'u_0'' \\ &- 2s(0)\nu_0u_0''' - \nu_0'' - s\nu_0'' - 6s(0)e^{-u_0} + 6s(0)^2e^{-u_0}u_0' - s(0)^3e^{-u_0}(u_0')^2 + s(0)^3e^{-u_0}u_0'' = 0. \end{aligned}$$

Since

$$u_0 = 0, \nu_0 = 0, \nu_0' = 0, \nu_0'' = 0,$$

this gives

$$u_0' = 0.$$

By differentiating equation (15) and putting $x = 0$ this gives

$$u_0'' = \frac{1}{3} + \frac{1}{3}s + s + s^2 = \frac{1}{3}(1 + s)(1 + 3s).$$

Following the same procedure mentioned above, we obtained the values of $u_0''', u_0^{(4)}, u_0^{(5)}, \nu_0^{(6)}, u_0^{(6)}$ and so on. Substituting these values into the Taylor series, equation (10), the Emden function is given by

$$u(x) = \frac{1}{6}(1 + s)(1 + 3s)x^2 + \dots \quad (16)$$

4. THE ANN ALGORITHM

4.1. Simulation of the RIGS

The proposed ANN simulation scheme of the RIGS is plotted in Figure 1. First, we assume $u_t = (x, p)$ to be the neural network's approximate solution to equation (4), which may be expressed as follows (Yadav et al. 2015):

$$u_t(x, p) = f(x, N(x, p)) + A(x), \quad (17)$$

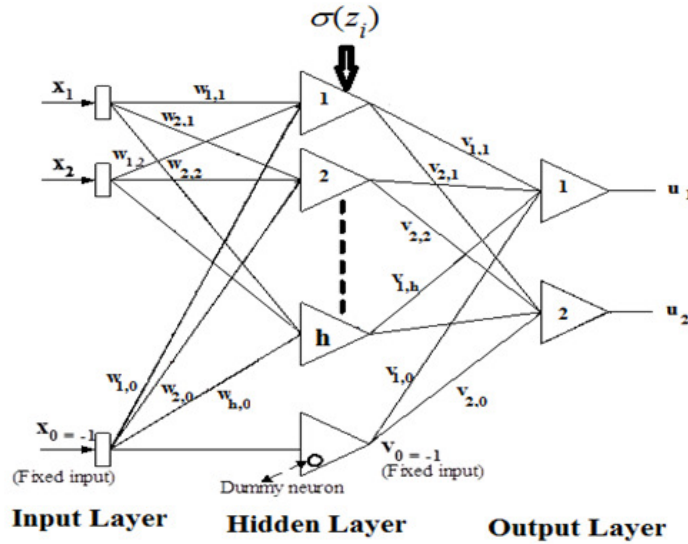


Fig. 1. Proposed ANN architecture for simulating the isothermal gas sphere.

where the first term represents a feed-forward neural network with input vector x and p is the corresponding vector of adjustable weight parameters, and the second term represents the boundary or initial value. The ANN output, $N(x, p)$, is provided by

$$N(x, p) = \sum_{i=1}^H \nu_i \sigma(z_i), \quad (18)$$

where $z_j = \sum_{i=1}^n w_{ij} x_j + \beta_i$, and w_{ij} represents the weight from the input unit j to the hidden unit i , ν_i represents the weight from the hidden unit i to the output, β_i is the bias of the i^{th} hidden unit, and $\sigma(z_i)$ is the sigmoid activation function that has the form $\sigma(x) = \frac{1}{1+e^{-x}}$.

Write the derivative of networks output N for the input vector x_j as

$$\begin{aligned} D_{x_j} N(x, p) &= D_{x_j} \left(\sum_{i=1}^H \nu_i \sigma(z_j = \sum_{i=1}^n w_{ij} x_j + \beta_i,) \right) \\ &= \sum_{i=1}^h \nu_i w_{ij} \sigma^1, \sigma^1 = D_x \sigma(x) \end{aligned} \quad (19)$$

and the n^{th} derivative of N , equation (18), is

$$D_{x_j}^{(n)} N(x, p) = \sum_{i=1}^n \nu_i P_i \sigma_i^{(n)}, \quad (20)$$

where

$$P_i = \prod_{k=1}^n w_{ik}, \sigma_i = \sigma(z_i).$$

As a result, the proposed solution for the TOV equations is given by

$$u_t(x, p) = x^2 N(x, p), \quad (21)$$

$$\nu_t(x, p) = x^3 M(x, p), \quad (22)$$

this fulfills the initial conditions as

$$u_t(0, p) = 0 \cdot N(0, p) = 0, \nu_t(0, p) = (0)^3 M(0, p) = 0.$$

And

$$\begin{aligned} D_x u_t(x, p) &= 2xN(x, p) + x^2 D_x N(x, p), \\ D_x \nu_t(x, p) &= 3x^2 M(x, p) + x^3 D_x M(x, p), \end{aligned} \quad (23)$$

$$\begin{aligned} D_x u_t(0, p) &= 2(0)N(0, p) + 0 \cdot D_x N(0, p), \\ D_x \nu_t(0, p) &= 3(0)^2 M(0, p) + (0)^3 D_x M(0, p). \end{aligned} \quad (24)$$

4.2. ANN Gradient Computations and Updating the Parameters

When we examine the solution presented by equations (21), we transform the problem to an unconstrained optimization one, and the error to be minimised is given by (Yadav et al. 2015).

$$\begin{aligned} E(x) &= \sum_i \{x^2 D_x u_t(x_i, p) - 2\sigma x \nu_t(x_i, p) D_x u_t(x_i, p) - \nu_t(x_i, p) \\ &\quad - \sigma \nu_t(x_i, p) u_t(x_i, p) - \sigma x^3 e^{-u_t(x_i, p)} - \sigma^2 x^3 e^{-u_t(x_i, p)}\}^2 \\ &\quad + \sum_i \{D_x \nu_t(x_i, p) - x^2 e^{-u_t(x_i, p)}\}^2, \end{aligned} \quad (25)$$

where

$$\begin{aligned} D_x u_t(x, p) &= 2xN(x, p) + x^2 D_x^\alpha N(x, p), \\ D_x \nu_t(x, p) &= 3x^2 M(x, p) + x^3 D_x M(x, p). \end{aligned} \quad (26)$$

To upgrade network parameters, we calculate the NN derivative for both input and the parameters of the network and train the NN for the optimum parameter value. Once the network has been trained, one can optimize the network parameters and compute $u_t(x, p)u_t(x, p) = x^2 N(x, p)$.

The derivative of any of its inputs is analogous to the feed-forward neural network N with one hidden layer, the same weights w_{ij} , and thresholds β_i , and each weight ν_i replaced with $\nu_i P_i$ where $P_i = \prod_{k=1}^n w_{ik}^{\alpha k}$. Moreover, the sigmoid function's nth order derivative is substituted for the transfer function of each hidden unit. As a result, the gradient with respect to the original network parameters may be determined as follows:

$$\begin{aligned} D_{\nu_i} N &= P_i \sigma_i^{(n)}, \\ D_{\beta_i} N &= \nu_i P_i \sigma_i^{(n+1)}, \\ D_{w_{ij}} N &= x_i \nu_i P_i \sigma_i^{(n+1)} + \nu_i (\prod_{k=1, k \neq j} w_{ik}) \sigma_i^{(n)}. \end{aligned} \quad (27)$$

The updating rule of the network parameters will be given as follows

$$\nu_i(x+1) = \nu_i(x) + a D_{\nu_i} N, \quad (28)$$

$$\beta_i(x+1) = \beta_i(x) + b D_{\beta_i} N, \quad (29)$$

$$w_{ij}(x+1) = w_{ij}(x) + c D_{w_{ij}} N, \quad (30)$$

where a, b, c are learning rates, $i = 1, 2, \dots, n$, and $j = 1, 2, \dots, h$.

An ANN's main processing unit is the neuron, which is capable of carrying out local information and processing local memory. The net input (z) of each neuron is calculated by adding the weights it receives to form a weighted sum of such inputs and then adding them with a bias (β). The net input (z) is then processed by an activation function, which is likely to result in neuron output (shown in Figure 1).

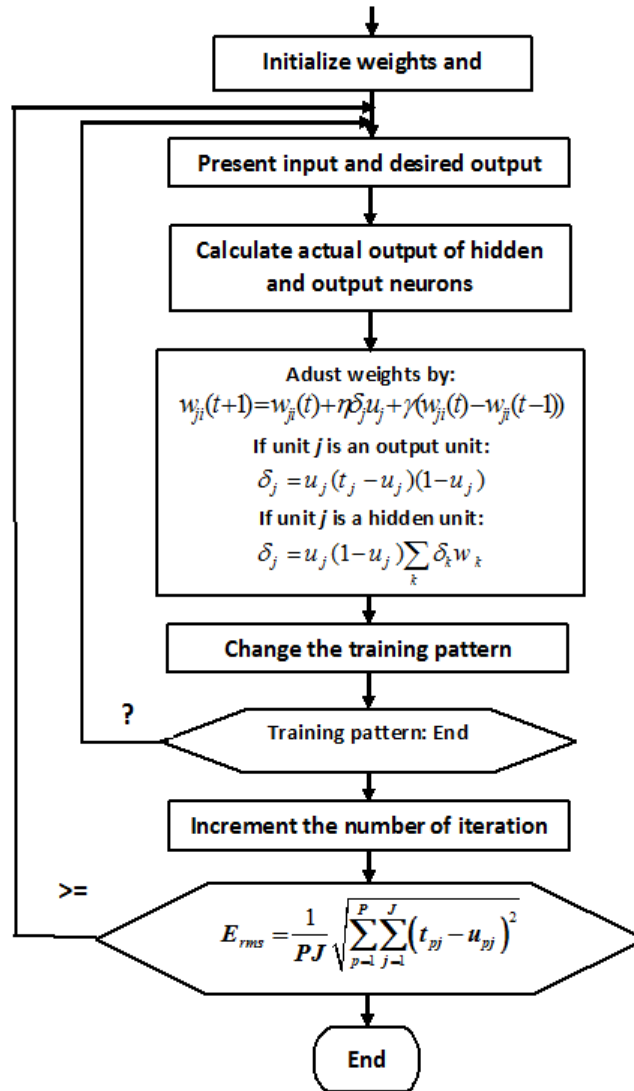


Fig. 2. Proposed ANN architecture for simulating the isothermal gas sphere.

4.3. Back-Propagation Learning Algorithm

Back-propagation (BP) is a gradient technique that seeks to minimize the mean square error between the actual and predicted outputs of a feed-forward net. It demands continuously differentiable non-linearity. Figure 2 depicts a flow chart of a back-propagation offline learning method (Leshno et al. 1993). We used a recursive technique that started with the output units and moved back to the first concealed layer. To compare the output u_j at the output layer to the desired output t_j , an error function of the following kind is used:

$$\delta_j = u_j(t_j - u_j)(1 - u_j). \quad (31)$$

For the hidden layer, the error function takes the form:

$$\delta_j = u_j(1 - u_j) \sum_k \delta_k w_k. \quad (32)$$

where δ_j is the error term in the output layer and w_k is the weight between the hidden and output layers. The error is replicated backward from the output layer to the input layer as follows to modify the weight of each connection:

$$w_{ji}(t+1) = w_{ji}(t) + \eta \delta_j u_j + \gamma (w_{ji}(t) - w_{ji}(t-1)). \quad (33)$$

The rate of learning η must be chosen so that it is neither too small, resulting in a slow convergence, nor too large, resulting in misleading results. The momentum term in equation (33) is added with the momentum constant γ to accelerate the convergence of the back-propagation learning algorithm error and to aid in stomping the changes over local increases in the energy function and trying to push the weights to follow the overall downhill direction (Leshno et al. 1993). This term adds a percentage of the most recent weight adjustment to the current weight adjustments. At the start of the training phase, both η and γ terms are allocated and determine the network stability and speed (Elminir et al. 2007; Basheer & Hajmeer 2000; El-Mallawany et al. 2014).

The procedure is repeated for each input pattern until the network output error falls below a preset threshold. The final weights are frozen during the test session and utilized to calculate the precise values of both the density profile and mass-radius relation. To evaluate the training's success and quality, the error is computed for the entire batch of training patterns using the root-mean-square normalised error, which is defined as:

$$E_{rms} = \frac{1}{PJ} \sqrt{\sum_{p=1}^P \sum_{j=1}^J (t_{pj} - u_{pj})^2}, \quad (34)$$

where P is the number of training patterns, J is the number of output units, t_{pj} is the target output at unit j , and u_{pj} is the actual output at the same unit j . Zero error would indicate that all of the ANN's output patterns completely match the predicted values and that the ANN is completely trained. Internal unit thresholds are also modified by assuming they are connection weights on links derived from an auxiliary constant-valued input.

5. RESULTS AND DISCUSSIONS

5.1. Training Data Preparation

To prepare the data for the ANN simulation of the problem, we elaborated a Mathematica code to derive the Emden and mass functions of the relativistic isothermal gas spheres using the Taylor series. We performed the calculations for the range of the dimensionless parameter $x = 0 - 35$; this upper limit of x corresponds to an isothermal sphere on the verge of gravothermal collapse (Antonov 1985). To obtain an accurate result for these analytical physical parameters, we accelerated both the series expansions of the Emden function (u) and the mass function (ν) by the accelerated scheme suggested by Nouh (2004); Saad et al. (2021). The radius, density, and mass of the gas sphere are calculated using equations (8).

We calculated 50 gas models for the range of the relativistic parameter $\sigma = 0 - 0.5$ with step 0.01. The radius, density, and mass of the star are calculated for the typical neutron star physical parameters: mass $M_* = 1.5M_\odot$, central density $\rho_c = 5.75 \times 10^{14} \text{ g cm}^{-3}$, central pressure $P_c = 2 \times 10^{33} \text{ par}$, and radius $R_* = 1.4 \times 10^6 \text{ cm}$. We plotted in Figure 3 the density profiles and the mass-radius relations of the relativistic isothermal gas spheres. Because the effect of the relativistic parameter on the Emden function is smaller than that on the mass function (the relation between the density and the Emden function is given by $\rho = \rho_c e^{-u}$), we plotted the density profiles for the relativistic parameter values $\sigma = 0.1, 0.2, 0.3,$ and 0.4 only.

5.2. Network Training

The data calculated in the previous section have been used to train the NN we used to simulate the Emden and mass functions of the relativistic isothermal gas spheres. We trained the ANN that has the architecture previously shown in Figure 1 for such a purpose. The network is composed of three layers which are the input layer, the hidden layer, and the output layer. The input layer has two inputs which symbolize the relativistic parameter (σ) and the ratio (R/R_*), where R_* is the radius of the typical neutron star which is equal to $R_* = 1.4 \times 10^6 \text{ cm}$. This ratio takes values from 0 to 1 in steps of 0.02. The output layer has also two outputs which represent the Emden function (density profile) and the mass-radius relation of the relativistic isothermal gas spheres. We checked three configurations for the number of hidden layer neurons by testing 20, 50, and 100 neurons in that layer to find which of them was the best. The data values for the relativistic function (σ) that have been used for the training and testing of the adopted neural network are shown in Table 1.

After checking the three configurations of the hidden layer neurons, we concluded that the best number of those neurons was 50. This number of the hidden layer neurons gave the least RMS error of 0.000156 in almost

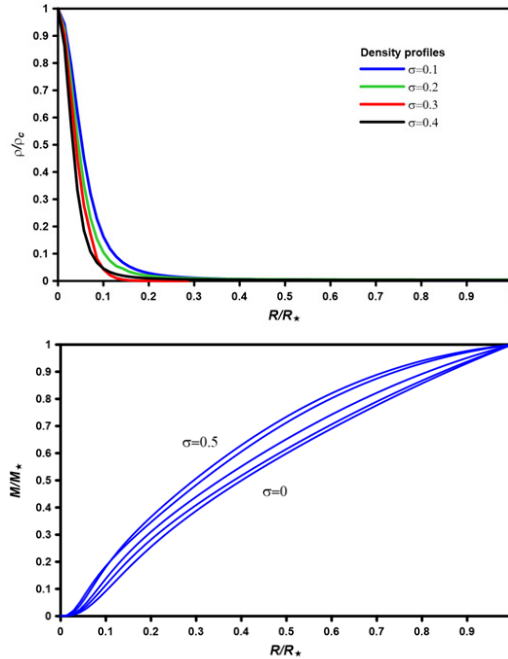


Fig. 3. The density profiles (upper panel) and the mass-radius relations (lower panel) of the relativistic isothermal gas spheres. The color figure can be viewed online.

TABLE 1

TRAINING AND TESTING DATA FOR THE NN ADOPTED TO SIMULATE THE EMDEN AND MASS FUNCTIONS OF THE RELATIVISTIC ISOTHERMAL GAS SPHERES

Training Data					Testing Data				
σ					σ				
0.01	0.02	0.03	0.05	0.06	0.04	0.08	0.12	0.16	0.20
0.07	0.09	0.10	0.11	0.13	0.24	0.28	0.32	0.36	0.40
0.14	0.15	0.17	0.18	0.19					
0.21	0.22	0.23	0.25	0.26					
0.27	0.29	0.30	0.31	0.34					
0.35	0.37	0.38	0.39	0.41					
0.42	0.43	0.45	0.46	0.49					
				0.50					

the same number of training iterations. So, the configuration of the NN adopted to simulate the Emden and mass functions of the relativistic isothermal gas spheres was 2-50-2.

While in the training phase of the NN, we used a value of the momentum ($\gamma = 0.5$) and a value for the learning rate ($\eta = 0.03$). Those values of γ and η were found to speed up the convergence of the back-propagation training algorithm without exceeding the solution. The convergence and stability behaviors of the input layer weights, bias, and output layer weights (w_i , β_i , and ν_i) were studied during the training phase which is shown in Figure 4. The weight values were initialised to random values, which can be seen in such figures, and after a number of iterations, they converged to stable values.

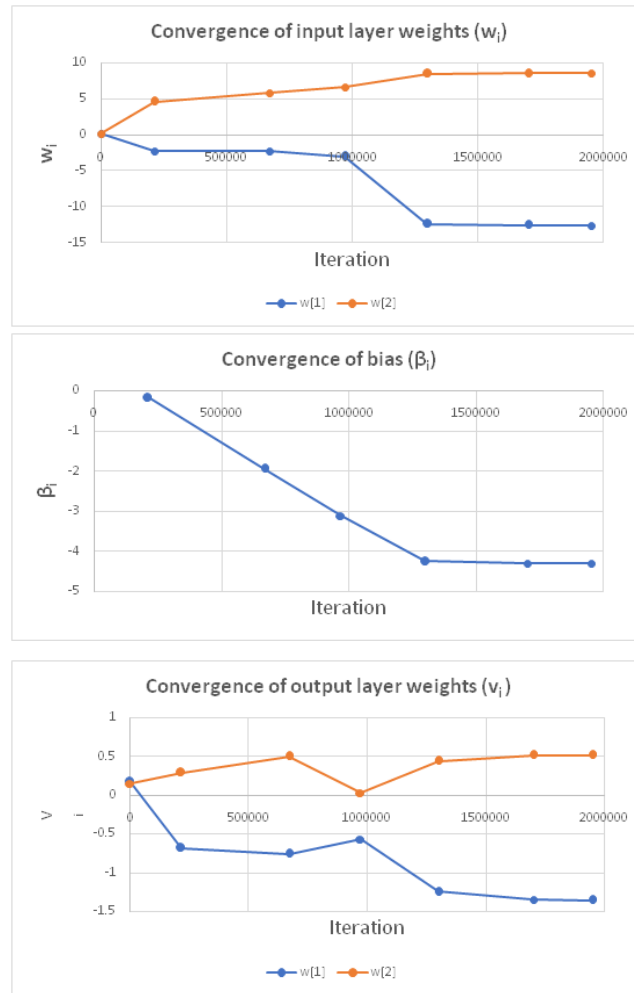


Fig. 4. The density profiles (upper panel) and the mass-radius relations (lower panel) of the relativistic isothermal gas spheres. The color figure can be viewed online.

5.3. Comparison with the Analytical Model

After the training phase is completed, we can use the code with its frozen weight values to compute the Emden and mass functions of the RIGS. To compare the analytical models and the ANN ones, we calculated the isothermal gas models for the relativistic parameters shown in Column 2 of Table 1. The results of these comparisons are displayed in Figure 5, which shows the identical overlap between the density profiles and their relevant ANN models. The figures also show the limited discrepancies between the ANN model and their relevant mass-radius relations. In general, we obtained good agreement with a maximum absolute error for the density profiles and mass-radius relations of 1% and 5%, respectively.

According to Nouh et al. (2020), the large discrepancy in the curve of the mass-radius relations can be attributed to numerical instability caused by the mass function's (ν) acceleration process.

6. CONCLUSIONS

In the present paper, the Taylor series and an artificial neural network (ANN) approach were used to solve the relativistic isothermal gas sphere. We wrote a Mathematica code to derive the symbolic expressions for the Emden and the relativistic functions. Then, the radii, densities, and masses of the gas spheres were calculated and the convergence of the analytical models was accelerated using Euler-Abel and Pade transformations. A

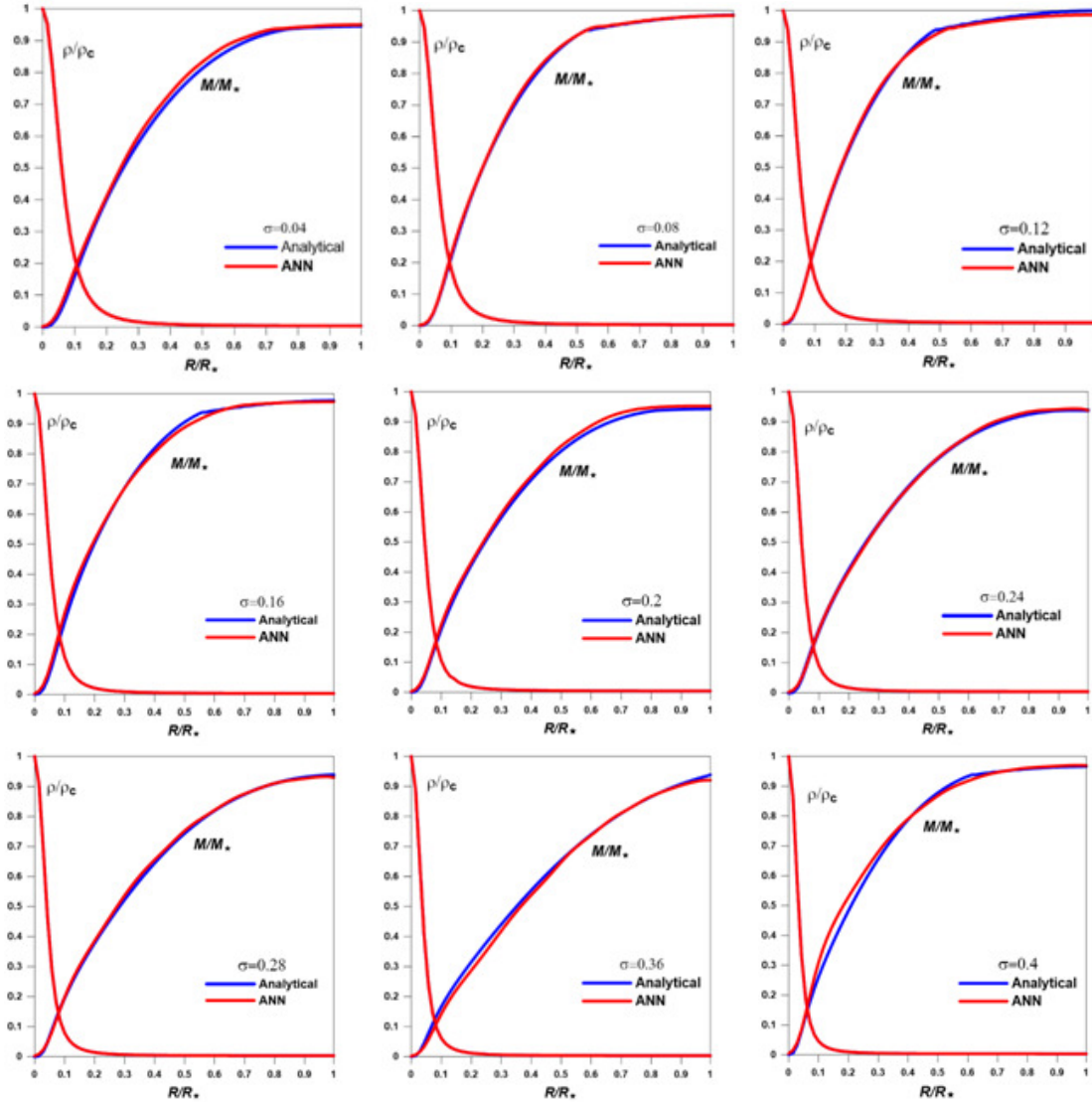


Fig. 5. The mass-radius relation and density profile were calculated for the relativistic parameter range $\sigma=0.04, 0.08, 0.12, 0.16, 0.2, 0.24, 0.28, 0.36$, and 0.4 . The red lines represent the accelerated Taylor series solutions, while the blue lines represent the ANN solutions. The color figure can be viewed online.

total sum of 50 analytical gas models was calculated for the range of the relativistic parameter $\sigma = 0 - 0.5$ with step 0.01 and compared to the numerical ones which indicated that the maximum relative errors are 1% and 3% for the density profiles and mass-radius relations, respectively.

For the ANN calculations, we developed a C++ code that implemented the feed-forward back-propagation learning scheme. Training and testing of the ANN algorithm were performed for the density profiles and mass-radius relation of the neutron stars. The efficiency and accuracy of the presented algorithm were evaluated by running it through 10 relativistic isothermal gas models and comparing them to analytical models. The ANN calculations yielded results that were in very good agreement with the analytical results, demonstrating that using the ANN method is effective, accurate, and may outmatch other methods.

Acknowledgment: We are so grateful to the reviewer for his/her many valuable suggestions and comments that significantly improved the paper. This paper is based upon work supported by Science, Technology & Innovation Funding Authority (STDF) Egypt, under Grant Number 37122.

REFERENCES

- Abdel-Salam, E. A.-B, Nouh, M. I., Azzam, Y. A., & Jazmati, M. S. 2021, in *AdAst*2021, 12, <https://doi.org/10.1155/2021/6662217>
- Antonov, V. A. 1985, in *Dynamics of star clusters*, IAUS 113 (Princeton, NJ: Dordrecht-Reidl), 7, 135
- Azzam, Y. A., Abdel-Salam, E. A.-B, & Nouh, M. I. 2021, *RMxAA*, 57, 189, <https://doi.org/10.22201/ia.01851101p.2021.57.01.14>
- Basheer, I. A. & Hajmeer, M. 2000, *Journal Of Microbiological Methods*, 43, 3, [https://doi.org/10.1016/s0167-7012\(00\)00201-3](https://doi.org/10.1016/s0167-7012(00)00201-3)
- Binney, J. & Tremaine, S. 1987, *Galactic Dynamics* (Princeton, NJ: PUP)
- Chandrasekhar, S. 1939, *An Introduction to the study of stellar structure*, (Chicago, Ill: UCP)
- Chavanis, P. H. 2002, *A&A*, 381, 709, <https://doi.org/10.1051/0004-6361:20011424>
- El-Mallawany, R., Gaafar, M. S., & Azzam, Y. A. 2014, *Chalcogenide Letters*, 11, 227
- Elminir, H. K., Azzam, Y. A. & Younes, F. I. 2007, *Energy*, 32, 1513, <https://doi.org/10.1016/j.energy.2006.10.010>
- Hunter, C. 2001, *MNRAS*, 328, 839, <https://doi.org/10.1046/j.1365-8711.2001.04914.x>
- Leshno, M., Lin, V., Pinkus, A., & Schocken, S. 1993, *Neural Networks*, 6, 861, [https://doi.org/10.1016/s0893-6080\(05\)80131-5](https://doi.org/10.1016/s0893-6080(05)80131-5)
- Liu, F. K. 1996, *MNRAS*, 281, 1197, <https://doi.org/10.1093/mnras/281.4.1197>
- Milgrom, M. 1984, *ApJ*, 287, 571, <https://doi.org/10.1086/162716>
- Morawski, F. & Bejger, M. 2020, *A&A*, 642, 78, <https://doi.org/10.1051/0004-6361/202038130>
- Natarajan, P. & Lynden-Bell, D. 1997, *MNRAS*, 286, 268, <https://doi.org/10.1093/mnras/286.2.268>
- Nouh, M. I. 2004, *NewA*, 9, 467, <https://doi.org/10.1016/j.newast.2004.02.003>
- Nouh, M., Abdel-Salam, E., & Azzam, Y. 2022, *Artificial Neural Network Approach versus Analytical Solutions for Relativistic Polytopes*, *Research Square Platform, LCC*, <https://doi.org/10.21203/rs.3.rs-1340444/v1>
- Nouh, M. I., Azzam, Y. A., & Abdel-Salam, E. A.-B. 2020, *Modeling Fractional Polytropic Gas Spheres Using Artificial Neural Network*, *arXiv:2006.15445*, <https://doi.org/10.48550/arXiv.2006.15445>
- Raga, A. C., Rodríguez-Ramírez, J. C., Villasante, M., Rodríguez-González, A., & Lora, V. 2013, *RMxAA*, 49, 63
- Roxburgh, I. W. & Stockman, L. M. 1999, *MNRAS*, 303, 466, <https://doi.org/10.1046/j.1365-8711.1999.02219.x>
- Saad, A., Nouh, M. I., Shaker, A. A., & Kamel, T. M. 2017, *RMxAA*, 53, 247
- _____. 2021, *RMxAA*, 57, 407, <https://doi.org/10.22201/ia.01851101p.2021.57.02.13>
- Sharma, J. P. 1990, *Ap&SS*, 163, 109
- Yadav, N., Yadav, A., & Kumar, M. 2015, *An Introduction to Neural Network Methods for Differential Equations*, (Springer Dordrecht), <https://doi.org/10.1007/978-94-017-9816-7>

Yosry A. Azzam, Farag I. Elnagahy, Tarek M. Kamel, and Mohamed I. Nouh: Astronomy Department, National Research Institute of Astronomy and Geophysics (NRIAG), 11421 Helwan, Cairo, Egypt.

Emad A-B Abdel-Salam: Department of Mathematics, Faculty of Science, New Valley University, El-Kharja 72511, Egypt.

A STUDY OF THE NGC 1193 AND NGC 1798 OPEN CLUSTERS USING CCD *UBV* PHOTOMETRIC AND GAIA EDR3 DATA

Talar Yontan¹, Hikmet Çakmak¹, Selçuk Bilir¹, Timothy Banks^{2,3}, Michel Raúl⁴, Remziye Canbay⁵, Seliz Koç⁵, Seval Taşdemir⁵, Hülya Erçay⁵, Burçin Tanık Öztürk⁵, and Deniz Cennet Dursun⁵

Received June 1 2022; accepted July 14 2022

ABSTRACT

We present photometric, astrometric, and kinematic studies of the old open star clusters NGC 1193 and NGC 1798. Both of the clusters are investigated by combining data sets from *Gaia* Early Data Release 3 (EDR3) and CCD *UBV* observational data. $E(B - V)$ color excesses are derived for NGC 1193 as 0.150 ± 0.037 and for NGC 1798 as 0.505 ± 0.100 mag through the use of two-color diagrams. Photometric metallicities are also determined from two-color diagrams with the results of $[\text{Fe}/\text{H}] = -0.30 \pm 0.06$ dex for NGC 1193 and $[\text{Fe}/\text{H}] = -0.20 \pm 0.07$ dex for NGC 1798. The isochrone fitting distance and age of NGC 1193 are 5562 ± 381 pc and 4.6 ± 1 Gyr, respectively. For NGC 1798, these parameters are 4451 ± 728 pc and 1.3 ± 0.2 Gyr. Kinematic and dynamic orbital calculations indicate that NGC 1193 and NGC 1798 belong to the thick-disk and thin-disk populations, respectively.

RESUMEN

Presentamos un estudio fotométrico, astrométrico y cinemático de los cúmulos abiertos viejos NGC 1193 y NGC 1798. Ambos cúmulos se estudian combinando datos de *Gaia* Early Data Release 3 (EDR3) con datos CCD *UBV*. Mediante el uso de diagramas de dos colores se obtienen excesos de color $E(B - V)$ para NGC 1193 de 0.150 ± 0.037 mag, y para NGC 1798 de 0.505 ± 0.100 mag. Se determinan las metalicidades fotométricas con los mismos diagramas, y resultan ser de $[\text{Fe}/\text{H}] = -0.30 \pm 0.06$ dex para NGC 1193 y de $[\text{Fe}/\text{H}] = -0.20 \pm 0.07$ dex para NGC 1798. La distancia y la edad obtenidas con el ajuste de isocronas para NGC 1193 son de 5562 ± 381 pc y 4.6 ± 1 giga-años, respectivamente. Para NGC 1798 estos parámetros tienen valores de 4451 ± 728 pc y 1.3 ± 0.2 giga-años, respectivamente. Los cálculos cinemáticos y orbitales indican que NGC 1193 pertenece a la población de disco grueso y NGC 1798 a la de disco delgado.

Key Words: open cluster and associations: individual: NGC 1193, NGC 1798 — Galaxy: disc — Hertzsprung-Russell and colour-magnitude

1. GENERAL

Open clusters are identified as groupings of stars, beyond those found in a single multiple star system, that are bound together by their weak self-gravitational forces. As cluster stars are formed by the collapse of the same molecular cloud, their basic astrophysical parameters, such as color excess, dis-

tance, metal abundance, and age are similar while their masses and luminosities can range widely. This paper concentrates on open star clusters inside our own galaxy's disk, which are often called 'galactic clusters'. These properties make such open clusters important tools to investigate the structure, formation, and evolution of the Galactic disk, as well as to give opportunities to enhance our understanding of stellar evolution models. In particular, the study of old open clusters can give insight into the kinematic properties and chemical structure of the Galactic disk (Friel 1995).

¹Department of Astronomy & Space Sciences, Istanbul University, Istanbul, Turkey.

²Nielsen, Chicago, USA.

³Harper College, Illinois, USA.

⁴Observatorio Astronómico Nacional, Universidad Nacional Autónoma de México, Ensenada, México.

⁵Institute of Graduate Studies in Science, Istanbul University, Istanbul, Turkey.

1.1. NGC 1193

In 1786 William Herschel discovered the open cluster NGC 1193 ($\alpha = 03^{\text{h}} 05^{\text{m}} 56^{\text{s}}.64$, $\delta = +44^{\circ} 22' 58''.80$, $l = 146^{\circ}.8143$, $b = -12^{\circ}.1624$), located in the constellation of Perseus (Dreyer 1888). Together with an angular size of $2'$, NGC 1193 has a dense central stellar concentration and is classified as II3m (Ruprecht 1966). King (1962) reported that NGC 1193 is likely to be old. In the study of Janes & Adler (1982), NGC 1193 was identified as a dense, poorly studied open cluster with an angular diameter of $2'$. Kaluzny (1988) presented the first CCD BV photometric study of NGC 1193, identifying five possible blue straggler stars in the cluster. By BV isochrone fitting to the color magnitude diagram (CMD), they determined the color excess and distance to be $0.12 \leq E(B - V) \leq 0.23$ mag and $4.2 \leq d \leq 4.9$ kpc, respectively. Additionally the metallicity, distance module, and age of the cluster were adopted as $Z = 0.01$, $(m - M)_V = 13.8$ mag, and $t = 8 \times 10^9$ years. Through investigation of the cluster's color-magnitude diagram, Kaluzny (1988) indicated that subgiant branch stars are more populous than red giant branch stars. Utilizing spectroscopic observations, Friel, Liu, & Janes (1989) calculated the first radial velocity estimate for the cluster as $\langle V_r \rangle = -82$ km s $^{-1}$. Friel & Janes (1993) performed medium resolution spectroscopic analyses and estimated the cluster metallicity as $[\text{Fe}/\text{H}] = -0.50 \pm 0.18$ dex from four giant members. They also calculated the radial velocities of stars whose values lie within $-64 \leq V_r \leq -103$ km s $^{-1}$. Tadross (2005) used photometric data of Kaluzny (1988) and astrometric data from the USNO-B1.0 catalog of Monet et al. (2003) to determine the cluster's color excess $E(B - V) = 0.10 \pm 0.06$, distance modulus $\mu = 13.90 \pm 0.10$ mag, distance $d = 5.25 \pm 0.24$ kpc, age $t = 8$ Gyr, and metallicity as $Z = 0.008$. Moreover, Tadross (2005) analysed the cluster with regard to the radial profile of van den Bergh & Sher (1960) and estimated the core radius as $r_c = 1'.4$ and the limiting radius as $r_{\text{lim}} = 6'.5$. Kyeong et al. (2008) applied a fitting procedure of the theoretical isochrones of Bertelli et al. (1994) to the color-magnitude diagrams based on CCD $UBVI$ photometric data of NGC 1193. They calculated the color excess as $E(B - V) = 0.19 \pm 0.04$ mag, the metallicity $[\text{Fe}/\text{H}] = -0.45 \pm 0.12$ dex, the true distance module $(m - M_V)_0 = 13.30 \pm 0.15$ mag, and the cluster age as $\log t(\text{yr}) = 9.7 \pm 0.1$.

The *Gaia* mission (Gaia collaboration et al. 2016) has led to substantial improvements in the quality and precision of astrometric, photometric,

and spectroscopic data. *Gaia* has provided precise astrometric, photometric, and spectroscopic data of nearly 1.8 billion stars. Cantat-Gaudin et al. (2018) identified 215 most likely cluster members, using astrometric and photometric data of stars across the locality of NGC 1193. In the study, they determined the mean proper motion of the cluster as $(\mu_\alpha \cos \delta, \mu_\delta) = (-0.125 \pm 0.023, -0.329 \pm 0.019)$ mas yr $^{-1}$ and the trigonometric parallax as $\varpi = 0.159 \pm 0.009$ mas. Soubiran et al. (2018) used the second *Gaia* data release (*Gaia* DR2; Gaia collaboration et al. 2018) spectroscopy to identify a radial velocity measurement for one member star of NGC 1193, calculating its radial velocity as $\langle V_r \rangle = -83.24 \pm 0.51$ km s $^{-1}$. In addition, Carrera et al. (2019) determined the mean radial velocity of the cluster as $\langle V_r \rangle = -85.16$ km s $^{-1}$, based on APOGEE spectroscopic data for two member stars of the cluster. Donor et al. (2020) analysed three cluster member stars using APOGEE DR16 spectroscopic data and calculated the radial velocity and metallicity of the NGC 1193 as $\langle V_r \rangle = -84.7 \pm 0.2$ km s $^{-1}$ and $[\text{Fe}/\text{H}] = -0.34 \pm 0.01$ dex, respectively. Using *Gaia* DR2 data, they determined the mean proper motion components of the cluster as $(\mu_\alpha \cos \delta, \mu_\delta) = (-0.22 \pm 0.10, -0.36 \pm 0.07)$ mas yr $^{-1}$.

1.2. NGC 1798

The open cluster NGC 1798 ($\alpha = 05^{\text{h}} 11^{\text{m}} 39^{\text{s}}.36$, $\delta = +47^{\circ} 41' 27''.60$, $l = 160^{\circ}.7043$, $b = +04^{\circ}.8500$) was discovered in 1885 by Edward Barnard, located in the Auriga constellation (Dreyer 1888). With an angular size of about 5 arcmin, this cluster is classified as II2m with a central dense stellar concentration (Ruprecht 1966). Examination of the cluster's CMD reveals that the regions of the main sequence and red clump (RC) stars are more distinct than the red giant branch (RGB). Based on this morphological feature, Janes & Phelps (1994) gave the age of NGC 1798 as 1.5 Gyr and the distance as 3.44 kpc.

The first CCD $UBVI$ photometric observations of the NGC 1798 were made by Park & Lee (1999). The angular diameter of the cluster was given as 8.3 arcmin (10.2 pc), the color excess $E(B - V) = 0.51 \pm 0.04$ magnitude, the distance $d = 4.2 \pm 0.3$ kpc, the metallicity $[\text{Fe}/\text{H}] = -0.47 \pm 0.15$ dex, and the age $t = 1.4 \pm 0.2$ Gyr. Lata et al. (2002) used the data of Park & Lee (1999) to determine the absolute magnitude and color indices for the I band as $I(M_V) = -4.86$, $I(U - V)_0 = 0.97$, $I(B - V)_0 = 0.82$, and $I(V - I)_0 = 1.14$ mag. Maciejewski & Niedzielski (2007) obtained the structural and astrophysical parameters of 42 open clus-

ters with CCD BV photometry. They determined the cluster's limiting radius $r_{\text{lim}} = 9$ arcmin, the core radius $r_c = 1.3 \pm 0.1$ arcmin, the central stellar density $f_0 = 9.5 \pm 0.28$ star arcmin $^{-2}$, and the background stellar density $f_{\text{bg}} = 3.14 \pm 0.05$ stars per arcmin 2 . These researchers used the isochrones of Bertelli et al. (1994), obtaining the color excess of the cluster as $E(B - V) = 0.37^{+0.10}_{-0.09}$, the distance modulus as $(m - M) = 13.90^{+0.26}_{-0.63}$ mag, the distance as $d = 3.55^{+0.64}_{-1.22}$ kpc, and the age being $\log t$ (yr) = 9.2. Ahumada & Lapasset (2007) examined 1,887 blue straggler star (BSS) candidates in 427 open clusters and identified 24 BSS in the direction of NGC 1798. They indicated that six of these BSS are massive and 18 are low mass stars. Carrera (2012) calculated the radial velocities of four open clusters including NGC 1798 by analyzing spectroscopic data of their member stars. By measuring Ca II lines, Carrera (2012) determined the mean radial velocity of NGC 1798 as $\langle V_r \rangle = 2 \pm 10$ km s $^{-1}$. They used six member stars in total, consisting of five RGB stars and one main sequence turn-off star. Oralhan et al. (2015) analyzed CCD $UBVRI$ photometric observations of 20 open clusters and obtained their astrophysical parameters. They determined the reddening, photometric metallicity, distance modulus, distance, and age of the NGC 1798 as $E(B - V) = 0.47 \pm 0.07$ mag, $[\text{Fe}/\text{H}] = -0.50 \pm 0.28$ dex, $(m - M)_0 = 12.70 \pm 0.04$ mag, $d = 3.47 \pm 0.06$ kpc, and $t = 1.78 \pm 0.22$ Gyr.

Cantat-Gaudin et al. (2020) used photometric and astrometric data from the *Gaia* DR2 (Gaia collaboration et al. 2018) to determine astrometric and astrophysical parameters of 2,017 open clusters. They identified 218 member stars in NGC 1798. Considering these members they calculated mean proper-motion components and trigonometric parallaxes of the cluster as $(\mu_\alpha \cos \delta, \mu_\delta) = (0.913 \pm 0.011, -0.318 \pm 0.010)$ mas yr $^{-1}$ and $\varpi = 0.178 \pm 0.005$ mas. Liu & Pang (2019) used astrometric and photometric data of 78 member stars of NGC 1798 to calculate the mean proper-motion components, trigonometric parallaxes, and age of the cluster as $(\mu_\alpha \cos \delta, \mu_\delta) = (0.903 \pm 0.026, -0.400 \pm 0.295)$ mas yr $^{-1}$, $\varpi = 0.241 \pm 0.026$ mas, and $t = 1.7 \pm 0.1$ Gyr.

A number of studies explored open clusters using ground-based telescopes within the scope of spectroscopic survey programs (Gilmore et al. 2012; Conrad et al. 2014; Maciejewski & Niedzielski 2007; Kos et al. 2018). Within the context of the APOGEE survey, Donor et al. (2018) utilized spectral observations of 259 cluster member stars in 19 open clusters including NGC 1798 and obtained the radial ve-

locity and different metal abundance values of the stars. Analysing nine member stars in NGC 1798 Donor et al. (2018) determined the mean radial velocity as $\langle V_r \rangle = 2 \pm 1.7$ km s $^{-1}$ and the iron abundance $[\text{Fe}/\text{H}] = -0.18 \pm 0.02$ dex. Soubiran et al. (2018) analysed *Gaia* DR2 spectroscopic data of four member stars in the cluster and obtained the mean radial velocity as $\langle V_r \rangle = 2.60 \pm 0.41$ km s $^{-1}$. Donor et al. (2020) analysed eight cluster member stars using APOGEE DR16 spectroscopic data and calculated the radial velocity and metallicity of the NGC 1798 as $\langle V_r \rangle = 2.7 \pm 0.8$ km s $^{-1}$ and $[\text{Fe}/\text{H}] = -0.27 \pm 0.03$ dex, respectively. Using *Gaia* DR2 data, they determined the mean proper motion components of the cluster as $(\mu_\alpha \cos \delta, \mu_\delta) = (0.83 \pm 0.04, -0.31 \pm 0.04)$ mas yr $^{-1}$.

2. OBSERVATIONS AND DATA REDUCTIONS

2.1. CCD UBV Photometric Data

The observations of these two clusters, along with many others, were carried out at the San Pedro Martir Observatory,⁶ as part of an ongoing $UBVRI$ photometric survey of Galactic stellar clusters. The 84-cm ($f/15$) Ritchey-Chretien telescope was employed in combination with the Mexman filter wheel.

NGC 1193 was observed on 2013-09-19 with the ESPO CCD detector (a 2048×2048 $13.5\text{-}\mu\text{m}$ square-pixels E2V CCD42-40 with a gain of 1.65 e $^-$ /ADU and a readout noise of 3.8 e $^-$ at the 2×2 binning employed, providing an unvignetted field of view of 7.4×9.3 arcmin 2). Short and long exposures were taken to properly measure both the bright and faint stars of the fields. Exposure times were 2, 12, 120s for both I and R ; 6, 30, 200 for V ; 30, 100, 700s for B ; and 60 and 1800s for U .

NGC 1798 was observed on 2009-11-01 with the SITE3 detector (a Photometrics 1024×1024 $24\text{-}\mu\text{m}$ square-pixels with a gain of 1.3 e $^-$ /ADU and a readout noise of 6.8 e $^-$, giving an unvignetted field of view of 6.8×6.8 arcmin 2). Exposure times for I and R were 2, 12 and 120s in duration; 6, 30 and 200s for V ; 30, 100 and 700s for B ; and 60 and 1800s for U .

Landolt's standard stars (Landolt 2009) were also observed in good sky conditions, at the meridian and at about two air masses, to properly determine the atmospheric extinction coefficients. Flat fields were taken at the beginning and the end of each night and bias images were obtained between cluster observations. Data reduction with point spread function (PSF) photometry was carried out by one of

⁶<https://www.astrossp.unam.mx/en/home/>.

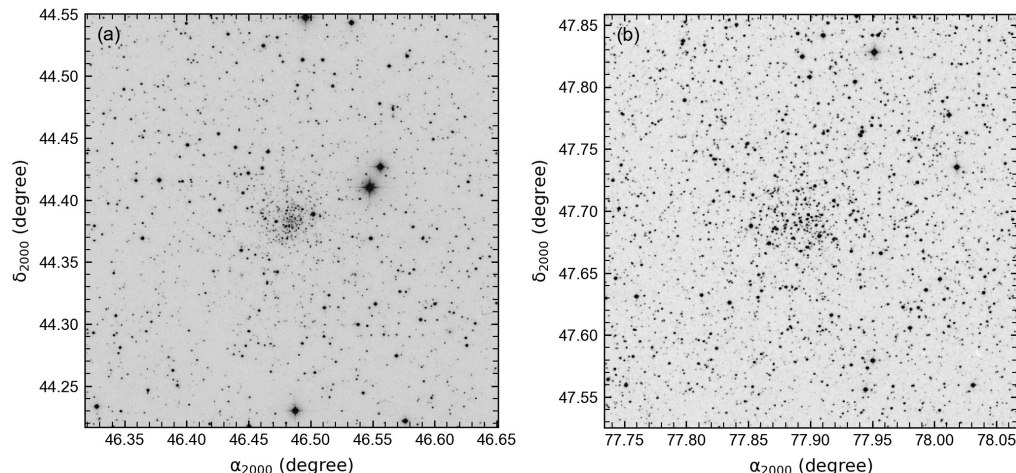


Fig. 1. Identification charts for NGC 1193 (left panel) and NGC 1798 (right panel), taken from the Leicester database and archive service (LEDAS).

the authors (RM) with the IRAF/DAOPHOT packages (Stetson 1987) and employing the transformation equations recommended, in their Appendix B, by Stetson et al. (2019).

3. DATA ANALYSIS

3.1. *Gaia* Astrometric and Photometric Data

The (early) third data release of *Gaia* (hereafter *Gaia* EDR3, *Gaia* collaboration et al. 2021) provides high quality astrometric and photometric data of nearly 1.5 billion celestial objects. Together with ground-based CCD *UBV* photometry we took into account *Gaia* EDR3 astrometric and photometric data to perform astrometric, photometric, and kinematic analyses of NGC 1193 and NGC 1798. We extracted such EDR3 data for all stars within regions of 20 arcmins about the centres of each cluster, using the coordinates given by Cantat-Gaudin et al. (2020) ($\alpha = 03^{\text{h}}05^{\text{m}}56^{\text{s}}.64$, $\delta = +44^{\circ}22'58''.80$ for NGC 1193 and $\alpha = 05^{\text{h}}11^{\text{m}}39^{\text{s}}.36$, $\delta = +47^{\circ}41'27''.60$ for NGC 1798). Thus we reached 9,141 stars within the magnitude range $7 < G < 23$ mag for NGC 1193 and 14,834 stars within $8 < G < 21$ mag for NGC 1798, respectively. 20 arcmin field of view optical images for the two clusters are presented in Figure 1. To construct photometric and astrometric catalogues for each cluster, we matched the *UBV* data to that from the *Gaia* EDR3 catalogue using stellar equatorial coordinates considering distances less than 5 arcsec. The mean difference in distances between the coordinates of stars in the matched catalogues was ≈ 0.08 arc seconds for both clusters. Both resulting catalogues contain positions (α, δ), *UBV* observational data (apparent *V* magnitudes, color indices $U - B$, $B - V$), *Gaia* EDR3

astrometric ($\mu_{\alpha} \cos \delta, \mu_{\delta}, \varpi$) and photometric data ($G, G_{\text{BP}} - G_{\text{RP}}$), and membership probabilities (P) as calculated in this study (Table 1). Catalogues of CCD *UBV* photometric as well as *Gaia* photometric and astrometric data for all the detected stars in the cluster regions are available electronically for NGC 1193 and NGC 1798⁷. Errors of the *UBV* and *Gaia* EDR3 photometric data were adopted as internal errors, being the uncertainties in the determination of the instrumental magnitudes of the stars. We calculated the mean photometric errors separately as functions of *V* and *G* intervals, listing the results in Table 2 (on page 338). It can be seen from the table that the mean internal *UBV* errors reach 0.08 mag for stars brighter than $V = 20$ mag for both clusters. The mean internal errors of *Gaia* EDR3 photometry for stars brighter than $G = 21$ mag reach 0.011 mag for NGC 1193 and 0.007 mag for NGC 1798.

To obtain precise astrophysical parameters, we identified photometric completeness limits for each cluster. Stars fainter than these limits were not included in further analyses. *G* and *V* magnitude histograms were constructed to determine the photometric completeness limits for each clusters (see Figure 2). Stellar counts decrease for magnitudes fainter than $G = 20$ for both NGC 1193 (Figure 2a) and NGC 1798 (Figure 2c). Stellar counts decrease for magnitudes fainter than $V = 19$ for NGC 1193 (Figure 2b) and NGC 1798 (Figure 2d), indicating that incompleteness (of stellar recovery) has set in. Thus, for both clusters, we adopted these values as the cluster photometric completeness limits.

⁷The complete tables can be obtained from VizieR electronically.

TABLE 1: THE PHOTOMETRIC AND ASTROMETRIC CATALOGUES FOR NGC 1193 and NGC 1798

NGC 1193											
ID	RA (hh:mm:ss.ss)	DEC (dd:mm:ss.ss)	V (mag)	U - B (mag)	B - V (mag)	G (mag)	G _{BP} - G _{RP} (mag)	$\mu_{\alpha} \cos \delta$ (mas yr ⁻¹)	μ_{δ} (mas yr ⁻¹)	ϖ (mas)	P
001	03:05:36.67	+44:22:00.62	19.194(0.062)	—	1.155(0.120)	21.929(0.049)	1.693(0.116)	—	—	—	—
002	03:05:37.44	+44:22:01.67	18.984(0.044)	—	0.893(0.083)	18.777(0.003)	1.080(0.043)	-0.587(0.247)	-0.251(0.223)	-0.083(0.241)	0.80
003	03:05:38.33	+44:19:33.12	19.162(0.056)	—	1.475(0.140)	18.254(0.003)	2.116(0.035)	-4.640(0.181)	-0.566(0.165)	1.009(0.177)	0.00
004	03:05:38.40	+44:21:46.02	19.286(0.067)	—	1.262(0.137)	18.592(0.003)	1.759(0.040)	-4.072(0.220)	-2.553(0.200)	0.640(0.214)	0.00
005	03:05:38.74	+44:24:25.10	18.631(0.034)	0.194(0.170)	0.993(0.065)	18.418(0.003)	0.969(0.032)	-0.426(0.220)	-0.410(0.235)	0.185(0.220)	1.00
...
565	03:06:18.54	+44:18:51.83	17.758(0.017)	0.458(0.088)	0.881(0.026)	17.510(0.003)	1.137(0.014)	1.640(0.128)	-2.394(0.097)	0.433(0.119)	0.00
566	03:06:19.07	+44:24:53.68	17.558(0.014)	0.042(0.042)	0.616(0.020)	17.463(0.003)	0.786(0.020)	-0.717(0.177)	-0.447(0.122)	0.149(0.121)	0.30
567	03:06:19.29	+44:19:29.22	15.451(0.006)	0.058(0.011)	0.697(0.008)	15.287(0.003)	0.908(0.005)	-5.602(0.039)	-2.523(0.030)	0.604(0.036)	0.00
568	03:06:19.45	+44:27:38.77	16.806(0.042)	0.534(0.156)	0.941(0.044)	16.465(0.003)	1.235(0.008)	5.074(0.078)	-1.965(0.062)	0.799(0.068)	0.00
569	03:06:19.77	+44:18:25.54	19.881(0.101)	—	0.658(0.152)	19.655(0.005)	1.061(0.069)	0.254(0.530)	0.166(0.412)	0.264(0.521)	0.40
...
NGC 1798											
ID	RA (hh:mm:ss.ss)	DEC (dd:mm:ss.ss)	V (mag)	U - B (mag)	B - V (mag)	G (mag)	G _{BP} - G _{RP} (mag)	$\mu_{\alpha} \cos \delta$ (mas yr ⁻¹)	μ_{δ} (mas yr ⁻¹)	ϖ (mas)	P
001	05:11:19.70	+47:39:52.01	20.254(0.135)	—	0.563(0.192)	19.499(0.004)	1.573(0.056)	0.968(0.426)	-0.986(0.343)	0.270(0.344)	0.32
002	05:11:19.73	+47:38:35.08	19.765(0.089)	—	1.182(0.171)	19.278(0.004)	1.575(0.048)	0.919(0.372)	-0.611(0.283)	-0.051(0.289)	0.29
003	05:11:19.79	+47:41:26.68	18.623(0.041)	—	1.046(0.074)	18.215(0.003)	1.471(0.024)	-0.020(0.175)	-0.596(0.137)	0.083(0.140)	0.00
004	05:11:20.00	+47:43:15.08	20.046(0.151)	—	0.920(0.208)	19.369(0.004)	1.604(0.057)	1.623(0.331)	-2.917(0.270)	0.418(0.279)	0.00
005	05:11:20.13	+47:44:05.70	18.459(0.045)	-0.360(0.265)	1.050(0.071)	18.291(0.003)	1.315(0.025)	0.913(0.171)	-1.461(0.141)	0.144(0.143)	0.35
...
523	05:11:58.51	+47:38:31.88	17.366(0.020)	0.807(0.267)	1.321(0.046)	16.766(0.003)	1.623(0.008)	0.843(0.073)	-1.241(0.059)	0.119(0.059)	0.80
524	05:11:58.73	+47:38:58.99	17.628(0.024)	0.286(0.162)	0.913(0.040)	17.158(0.003)	1.322(0.008)	0.805(0.098)	-3.354(0.077)	0.354(0.074)	0.00
525	05:11:58.88	+47:38:05.24	15.629(0.040)	0.281(0.038)	0.551(0.043)	15.582(0.003)	0.870(0.005)	0.701(0.056)	-0.518(0.043)	0.289(0.043)	0.98
526	05:11:59.04	+47:39:49.94	19.197(0.028)	—	1.848(0.043)	19.037(0.004)	1.875(0.036)	-1.779(0.431)	-1.480(0.356)	0.947(0.336)	0.00
527	05:11:59.15	+47:42:42.85	20.344(0.191)	—	0.931(0.298)	19.339(0.004)	1.461(0.057)	0.414(0.358)	0.057(0.294)	0.906(0.305)	0.00

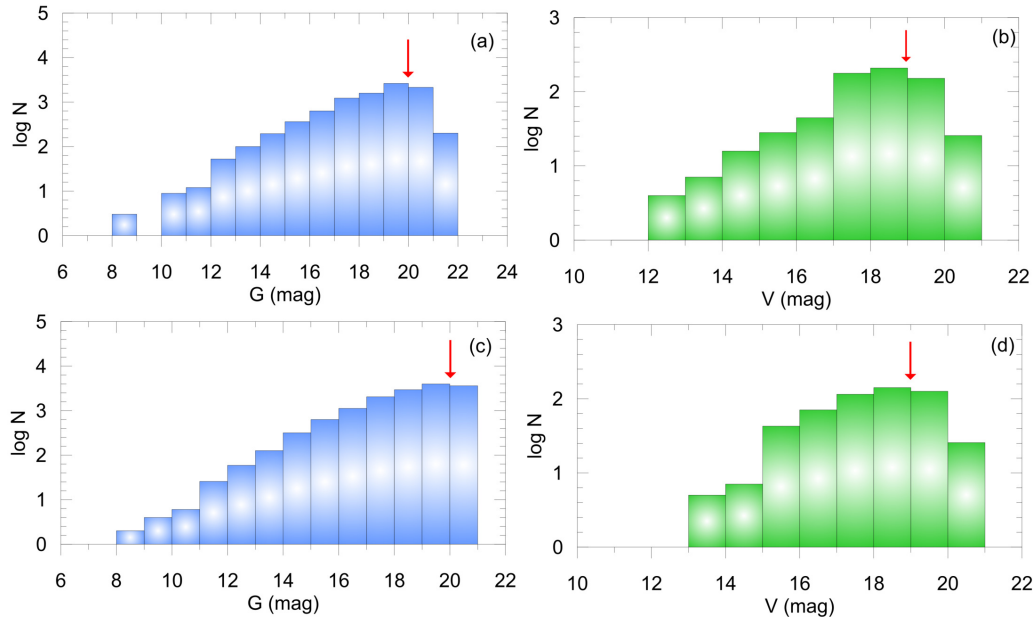


Fig. 2. Interval G and V -band magnitude histograms of NGC 1193 (a, b) and NGC 1798 (c, d): The red arrows show the faint limiting apparent magnitudes in G and V -bands. The color figure can be viewed online.

TABLE 2
THE MEAN INTERNAL PHOTOMETRIC ERRORS FOR EACH CLUSTER

NGC 1193					NGC 1798			
V	N	σ_V	σ_{U-B}	σ_{B-V}	N	σ_V	σ_{U-B}	σ_{B-V}
(8, 12]	—	—	—	—	—	—	—	—
(12, 14]	9	0.017	0.020	0.022	5	0.024	0.047	0.045
(14, 15]	14	0.008	0.012	0.010	5	0.027	0.054	0.038
(15, 16]	22	0.007	0.018	0.010	41	0.021	0.055	0.032
(16, 17]	36	0.011	0.037	0.015	70	0.020	0.070	0.033
(17, 18]	147	0.018	0.065	0.027	114	0.023	0.148	0.037
(18, 19]	177	0.034	0.122	0.057	140	0.045	0.230	0.075
(19, 20]	140	0.075	0.234	0.130	126	0.077	—	0.141
(20, 21]	24	0.145	—	0.244	26	0.136	—	0.242
NGC 1193					NGC 1798			
G	N	σ_G	$\sigma_{G_{BP}-G_{RP}}$	N	σ_G	$\sigma_{G_{BP}-G_{RP}}$		
(5, 10]	5	0.003	0.006	6	0.003	0.005		
(10, 12]	21	0.003	0.005	32	0.003	0.005		
(12, 13]	52	0.003	0.005	59	0.003	0.005		
(13, 14]	101	0.003	0.005	125	0.003	0.005		
(14, 15]	196	0.003	0.006	315	0.003	0.005		
(15, 16]	366	0.003	0.006	630	0.003	0.006		
(16, 17]	634	0.003	0.010	1115	0.003	0.009		
(17, 18]	1219	0.003	0.019	2026	0.003	0.017		
(18, 19]	1588	0.004	0.044	2936	0.003	0.035		
(19, 20]	2616	0.005	0.155	3943	0.004	0.075		
(20, 21]	2144	0.011	0.232	3647	0.007	0.152		
(21, 23]	198	0.027	0.378	—	—	—		

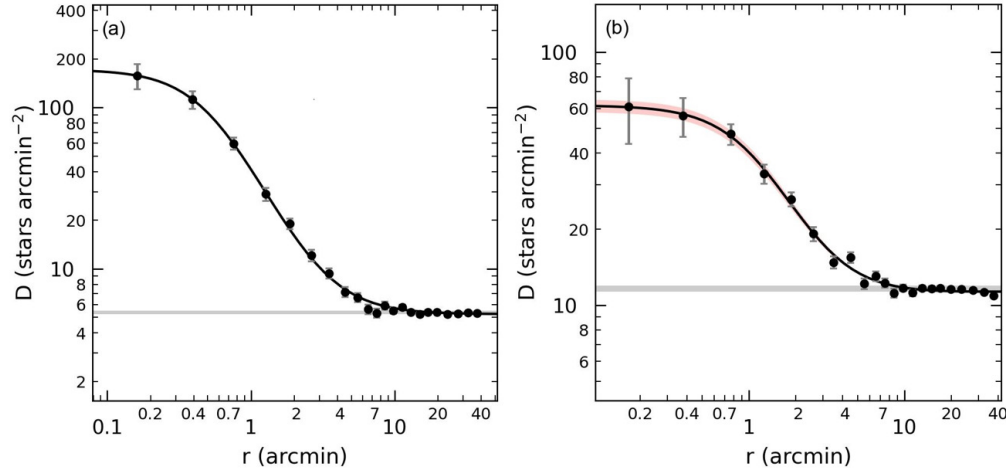


Fig. 3. Radial density profiles for NGC 1193 (a) and NGC 1798 (b). Errors were derived using the equation of $1/\sqrt{N}$, where N represents the number of stars used in the density estimation. The solid lines represents the optimal King (1962) profiles. The background density level and its errors are the horizontal grey bands. The King fit uncertainty (1σ) is shown by the red shaded region. The color figure can be viewed online.

3.2. Structural Parameters of the Clusters

We utilized Radial Density Profile (RDP) analysis to determine the structural parameters of the clusters. First, we specified many concentric rings outwards from the cluster center, using the central coordinates given by Cantat-Gaudin et al. (2020). Stellar densities (ρ) were estimated for each ring by dividing the number of stars within the photometric completeness limit ($G \leq 20$ mag) in it by the ring area. The resulting RDPs were fitted with King (1962) models via χ^2 minimisation, giving estimates for the core, limiting, and effective radii of each cluster. The King (1962) model is described as $\rho(r) = f_{bg} + [f_0/(1 + (r/r_c)^2)]$ where r is the radius from the cluster centre, f_{bg} the background density, f_0 the central density, and r_c the core radius. See Figure 3 for each cluster's RDP together with the best fitting King (1962) model to it. As a result of the fitting procedure, we inferred central stellar density, core radius and background stellar density as $f_0 = 166.865 \pm 1.573$ stars arcmin $^{-2}$, $r_c = 0.526 \pm 0.009$ arcmin and $f_{bg} = 5.225 \pm 0.124$ stars arcmin $^{-2}$ for NGC 1193 and $f_0 = 53.597 \pm 3.789$ stars arcmin $^{-2}$, $r_c = 1.190 \pm 0.056$ arcmin and $f_{bg} = 11.318 \pm 0.321$ stars arcmin $^{-2}$ for NGC 1798, respectively. At the $r = 8$ arcmin limiting radius, the stellar density becomes similar to the background density (a grey horizontal line) as seen in Figure 3a (NGC 1193) and Figure 3b (NGC 1798). Therefore, we concluded that the limiting radii for both clusters are $r_{lim} = 8$ arcmin. We considered only the stars inside these limiting radii in further analyses.

3.3. CMDs and Membership Probabilities of Stars

The membership probabilities (P) of stars located in each of two cluster regions were calculated applying the Unsupervised Photometric Membership Assignment in Stellar Cluster program (UPMASK; Krone-Martins & Moitinho 2014). UPMASK uses k -means clustering, where k is the number of clusters, to detect spatially concentrated groups and identify the most likely cluster members. An integer k -means is not adjusted directly by the user and the best result from the UPMASK methodology is achieved when the k -means value is within 6 to 25 (Krone-Martins & Moitinho 2014; Cantat-Gaudin et al. 2020). We applied UPMASK to calculate stellar membership probabilities by considering each star's five-dimensional astrometric parameters from *Gaia* EDR3 (Gaia collaboration et al. 2021), which contains equatorial coordinates (α , δ), proper motion components ($\mu_\alpha \cos \delta$, μ_δ), trigonometric parallaxes (ϖ), and their uncertainties. During application we scaled these five parameters to unit variance and ran 100 iterations for each clusters to assess cluster membership. The membership probability of a star is defined by the frequency of the group in which it is clustered. We reached the best results when k was set to 12 for NGC 1193 and 15 for NGC 1798. We identified as possible cluster members those stars brighter than $G = 20$ mag with membership probabilities $P \geq 0.5$ that we identified as possible members of clusters. This led to 735 possible members for NGC 1193 and 1,536 for NGC 1798. Cantat-Gaudin et al. (2020) give the number of stars brighter than $G = 18$ mag

with the membership probabilities $P > 0.5$ as 215 for NGC 1193 and 218 for NGC 1798. The dissimilarity can be explained by lower precision in the astrometric *Gaia* DR2 data compared to *Gaia* EDR3, as well as the G magnitude limit of stars used in the analyses. With the release of *Gaia* EDR3 data, the precision of astrometric and photometric measurements increased with respect to *Gaia* EDR2 data. For the *Gaia* EDR3 release the accuracy of trigonometric parallaxes increased by 30 percent and the uncertainties decreased by nearly 40%, the proper motion accuracy increased by a factor of 2 and the associated uncertainties improved by a factor ≈ 2.5 . Moreover, the precision of photometric data and celestial positions are better in terms of homogeneity (Gaia collaboration et al. 2021).

To take into consideration the impact of binary stars in the main-sequences of the studied clusters, we plotted the $V \times (B - V)$ CMDs of the stars within the cluster limiting radii (r_{lim}) which we had obtained for the clusters and then fitted the Zero Age Main-Sequence (ZAMS) of Sung et al. (2013) to these diagrams. The ZAMS fitting was by eye according to the stars with the membership probability $P \geq 0.5$ and shifted 0.75 mag towards brighter magnitudes in order to account for the most likely cluster binary stars (4a and c). During the ZAMS fitting we made sure for each cluster that the main-sequence, turn-off, and giant stars with membership probabilities $P \geq 0.5$ were selected. The process resulted in 181 likely member stars for NGC 1193 and 161 for NGC 1798 which lie between the fitted ZAMS curves and are located inside the r_{lim} radii. We used these stars to determine astrophysical parameters of the two clusters. Figure 4 shows the $V \times (B - V)$ CMDs with the best fitted ZAMS (Figures 4a and c) and $G \times (G_{\text{BP}} - G_{\text{RP}})$ CMDs (Figures 4b and d) with the background and most likely member stars. Figure 5 presents histograms of the number of stars located through the two cluster fields versus their membership probabilities. Vector-Point Diagrams (VPDs) were plotted for the stars within the limiting radii and are shown as Figure 6. It can be seen from the figure that NGC 1193 (Figure 6a) and NGC 1798 (Figure 6b) are affected by field stars but with the membership selection criteria, the ‘most likely’ cluster stars (shown as the color-scaled points in Figure 6) can be separated from field stars (grey dots in Figure 6). The mean proper motion components of the most likely cluster members are $(\mu_{\alpha} \cos \delta, \mu_{\delta}) = (-0.207 \pm 0.009, -0.431 \pm 0.008)$ for NGC 1193 and $(\mu_{\alpha} \cos \delta, \mu_{\delta}) = (0.793 \pm 0.006, -0.373 \pm 0.005)$ mas yr $^{-1}$ for NGC 1798.

Moreover, using these members we obtained mean trigonometric parallaxes of NGC 1193 and NGC 1798 as $\varpi_{\text{Gaia}} = 0.191 \pm 0.157$ mas and $\varpi_{\text{Gaia}} = 0.203 \pm 0.099$ mas, respectively.

4. ASTROPHYSICAL PARAMETERS OF THE CLUSTERS

We summarize in this section the processes we performed to determine the astrophysical parameters of NGC 1193 and NGC 1798 (for detailed descriptions on the methodology see Yontan et al. 2015, 2019, 2021; Ak et al. 2016; Bilir et al. 2006, 2010, 2016; Bostancı et al. 2015, 2018; Banks et al. 2020; Akbulut et al. 2021; Koç et al. 2022). Color excesses and metallicities of the clusters were derived using two-color diagrams (TCDs), whereas we obtained distance moduli and ages individually by fitting theoretical models on CMDs.

4.1. Reddening

The $E(U - B)$ and $E(B - V)$ color excesses for NGC 1193 and NGC 1798 were derived using $(U - B) \times (B - V)$ TCDs. We selected the main-sequence stars for which simultaneous U , B , and V magnitudes were available, as well as with membership probabilities $P \geq 0.5$. As shown in Figure 7, we constructed TCDs for these stars and compared their positions by fitting the solar metallicity dereddened ZAMS of Sung et al. (2013). The ZAMS was fitted according to the equation $E(U - B) = 0.72 \times E(B - V) + 0.05 \times E(B - V)^2$ (Garcia et al. 1988) by applying χ^2 optimisation with steps of 0.001 mag. The best solutions for $E(B - V)$ and $E(U - B)$ values are those corresponding to the minimum χ^2 , being $E(B - V) = 0.150 \pm 0.037$ mag for NGC 1193 and $E(B - V) = 0.505 \pm 0.100$ mag for NGC 1798. The errors of color excesses are determined as $\pm 1\sigma$ deviations, and are presented as the green lines in Figure 7. When we compared the reddening estimated for NGC 1193, we concluded that it is in a good agreement within the errors with the values ($0.10 \leq E(B - V) \leq 0.19$ mag) given by different authors (Kaluzny 1988; Tadross 2005; Kyeong et al. 2008). For NGC 1798, our finding result is compatible with the values given by Park & Lee (1999, $E(B - V) = 0.51 \pm 0.04$ mag) and Oralhan et al. (2015, $E(B - V) = 0.47 \pm 0.07$ mag).

4.2. Metallicities

The determination of photometric metallicities of the two clusters employed the method given by Karaali et al. (2003a,b, 2011). This

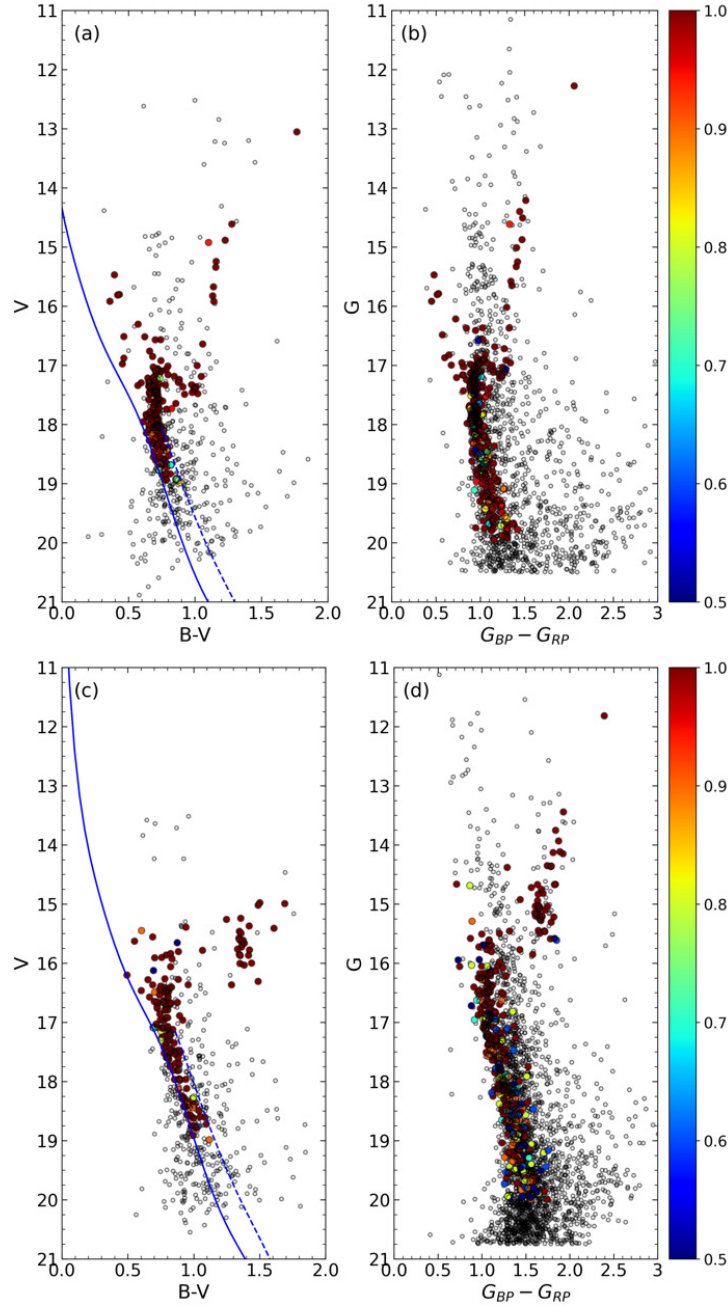


Fig. 4. $V \times (B - V)$ and $G \times (G_{BP} - G_{RP})$ CMDs of NGC 1193 (a, b) and NGC 1798 (c, d). The blue dot-dashed lines represent the ZAMS (Sung et al. 2013) including the binary star effect. The membership probabilities of stars that lie within the fitted ZAMS are shown with different colors according to the color scales shown to the right of the figure. These member stars are located within $r_{\text{lim}} = 8$ arcmin of the cluster centres calculated for NGC 1193 and NGC 1798. Grey dots indicate low probability members ($P < 0.5$), or field stars ($P = 0$). The color figure can be viewed online.

method is based on F and G type main-sequence stars and their UV-excesses as well as on stars whose color index range correspond to $0.3 \leq (B - V)_0 \leq 0.6$ mag (Eker et al. 2018, 2020). We selected F-G type main-sequence stars within

the range $0.3 \leq (B - V)_0 \leq 0.6$ mag after calculating the intrinsic $(B - V)_0$ and $(U - B)_0$ colors of the most likely cluster member ($P \geq 0.5$) stars. To determine the difference between the $(U - B)_0$ color indices of cluster stars and the Hyades main sequence

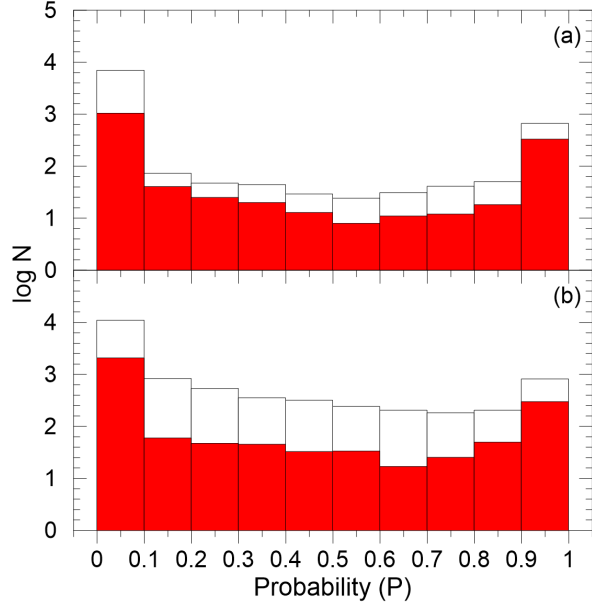


Fig. 5. Histograms of the membership probabilities for NGC 1193 (a) and NGC 1798 (b). The red colored shading denotes the stars that lie within the main-sequence band and effective cluster radii ($r_{\text{lim}} \leq 8'$), while the white colored bars indicate the membership probabilities of all stars in each cluster's direction. The color figure can be viewed online.

which corresponds to the same $(B - V)_0$ color indices, we constructed $(U - B)_0 \times (B - V)_0$ TCDs. This difference between cluster and Hyades stars is defined as the UV-excess which is expressed by the equation of $\delta = (U - B)_{0,H} - (U - B)_{0,S}$, where H and S denote the Hyades and cluster stars respectively, which implies the same $(B - V)_0$ color indices. By calibrating $(B - V)_0$ of stars to $(B - V)_0 = 0.6$ mag (i.e., $\delta_{0.6}$) we normalised the UV excess and plotted the histogram of normalised $\delta_{0.6}$ values. To calculate the mean $\delta_{0.6}$, we fitted a Gaussian to the distribution. Taking into account the Gaussian peak, the photometric metallicities of the studied clusters are obtained from the equation given by Karaali et al. (2011):

$$[\text{Fe}/\text{H}] = -14.316(1.919)\delta_{0.6}^2 - 3.557(0.285)\delta_{0.6} + 0.105(0.039). \quad (1)$$

We identified 12 and 7 F-G type main-sequence stars to calculate the photometric metallicity of NGC 1193 and NGC 1798, respectively. TCDs and the distributions of normalised $\delta_{0.6}$ UV excesses for two clusters are shown in Figure 8. The calculated mean $\delta_{0.6}$ values of NGC 1193 and NGC 1798 are 0.085 ± 0.010 mag and 0.068 ± 0.011 mag, respec-

tively. The photometric metallicity $[\text{Fe}/\text{H}]$ value for NGC 1193 is $[\text{Fe}/\text{H}] = -0.30 \pm 0.06$ dex and for NGC 1798 it is $[\text{Fe}/\text{H}] = -0.20 \pm 0.07$ dex, which correspond to their peak values in the $\delta_{0.6}$ distribution.

The $[\text{Fe}/\text{H}]$ metallicities were transformed to the mass fraction Z to derive ages of the clusters. For this, the analytic equations of Bovy^{8,9} for PARSEC (Bressan et al. 2012) models were used, namely:

$$z_x = 10^{[\text{Fe}/\text{H}] + \log\left(\frac{z_\odot}{1 - 0.248 - 2.78 \times z_\odot}\right)}, \quad (2)$$

and

$$z = \frac{(z_x - 0.2485 \times z_x)}{(2.78 \times z_x + 1)}. \quad (3)$$

z and z_x are the elements heavier than helium and the intermediate operation function, respectively. z_\odot is the solar metallicity which was adopted as 0.0152 (Bressan et al. 2012). We calculated $z = 0.008$ for NGC 1193 and $z = 0.010$ for NGC 1798.

Many authors obtained spectroscopic metallicities of NGC 1193 and NGC 1798 based on ground-based observations, as listed in Table 3. Photometric metallicities calculated in this study are well supported by the spectroscopic studies presented in the literature. We conclude that our metallicity findings are reliable. Thus, we adopted our results for the determination of distance moduli and age.

4.3. Distance Moduli and Age Estimation

We used PARSEC isochrones (Bressan et al. 2012), which contain UBV filters as well as *Gaia* passbands, to obtain the distance moduli and ages of the studied clusters simultaneously. To do this, we selected the PARSEC models considering the mass fractions (z) estimated for each cluster and compared them to the $V \times (U - B)$, $V \times (B - V)$, and $G \times (G_{\text{BP}} - G_{\text{RP}})$ CMDs according to member stars ($P \geq 0.5$). Selected isochrones were fitted to CMDs visually by attaching importance to 'most likely' member stars which make up the main-sequence, turn-off and giant regions of each cluster. During the fitting process of PARSEC models to the UBV data, we used the $E(B - V)$ values derived above by this study, while for the *Gaia* EDR3 data we considered the equation of $E(G_{\text{BP}} - G_{\text{RP}}) = 1.41 \times E(B - V)$ (Sun et al. 2021). We obtained the error of the distance moduli and distances using the relation given by Carraro et al. (2017). We fitted two more isochrones

⁸<https://github.com/jobovy/isodist/blob/master/isodist/Isochrone.py>.

⁹The equations are given in lines between 199 and 207 in the code.

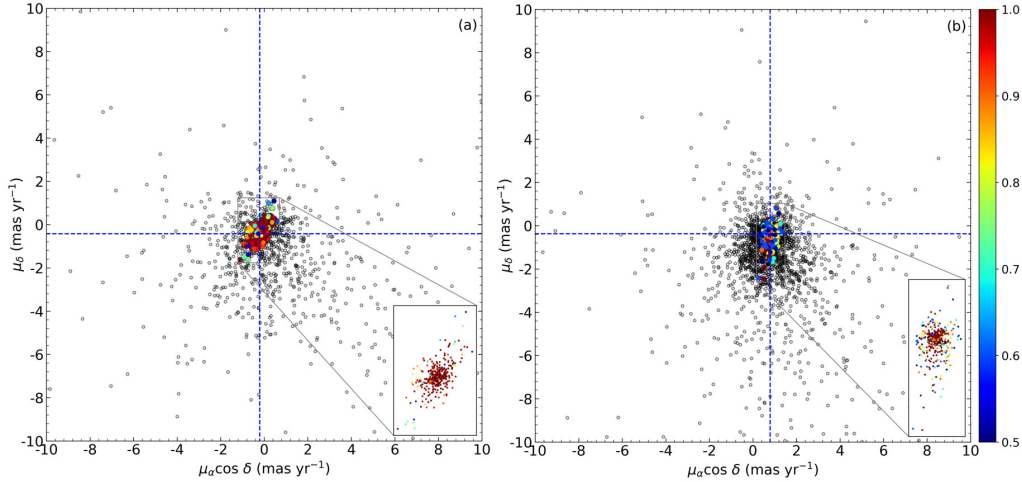


Fig. 6. VPDs of NGC 1193 (a) and NGC 1798 (b). Colored dots identify the membership probabilities of the most likely cluster members according to the color scale shown on the right. The zoomed box in the panels represents the region of condensation for both clusters in the VPD. Dashed lines are the intersection of the mean proper motion values. The color figure can be viewed online.

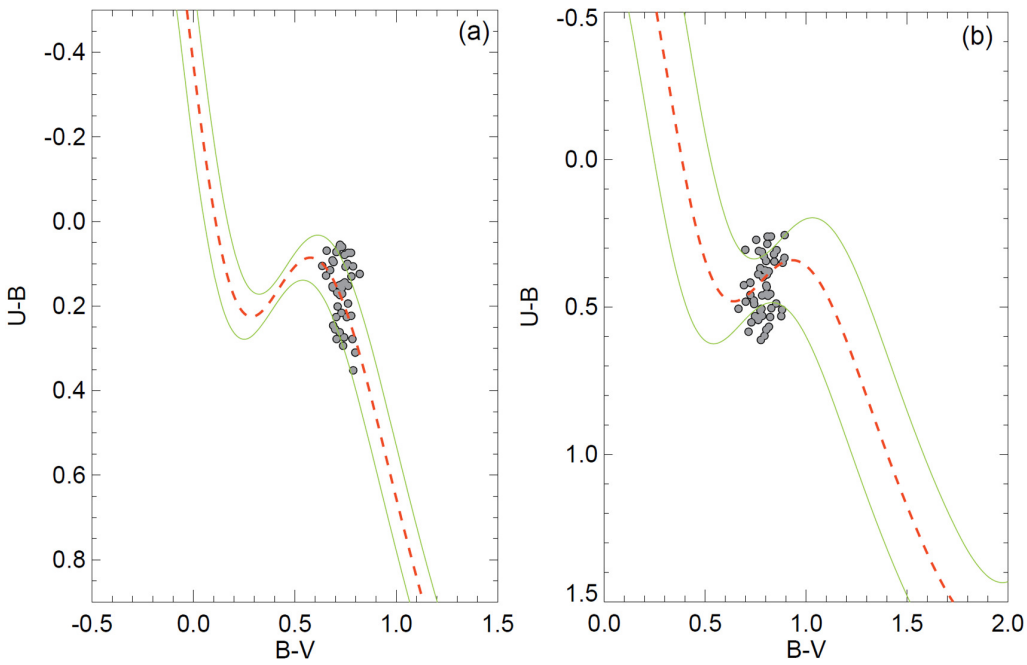


Fig. 7. Two-color diagrams of the most probable member main-sequence stars in the regions of NGC 1193 (a) and NGC 1798 (b). Red dashed and green solid curves represent the reddened ZAMS given by Sung et al. (2013) and $\pm 1\sigma$ standard deviations, respectively. The color figure can be viewed online.

to estimate age uncertainties considering the spread of the most likely member stars in the turn-off and sub-giant regions of the cluster. The ages of such selected isochrones give the higher and lower acceptable values for the estimated cluster ages. The best fit with $z = 0.008$ gave the distance moduli and age

of NGC 1193 as $\mu = 14.191 \pm 0.149$ mag and $t = 4.6 \pm 1.0$ Gyr. For NGC 1798, the best fit of $z = 0.010$ gave these values as $\mu = 14.808 \pm 0.332$ mag and $t = 1.3 \pm 0.2$ Gyr, respectively. The distances of the clusters corresponding to the estimated distance moduli are also $d_{iso} = 5562 \pm 381$ pc for NGC 1193

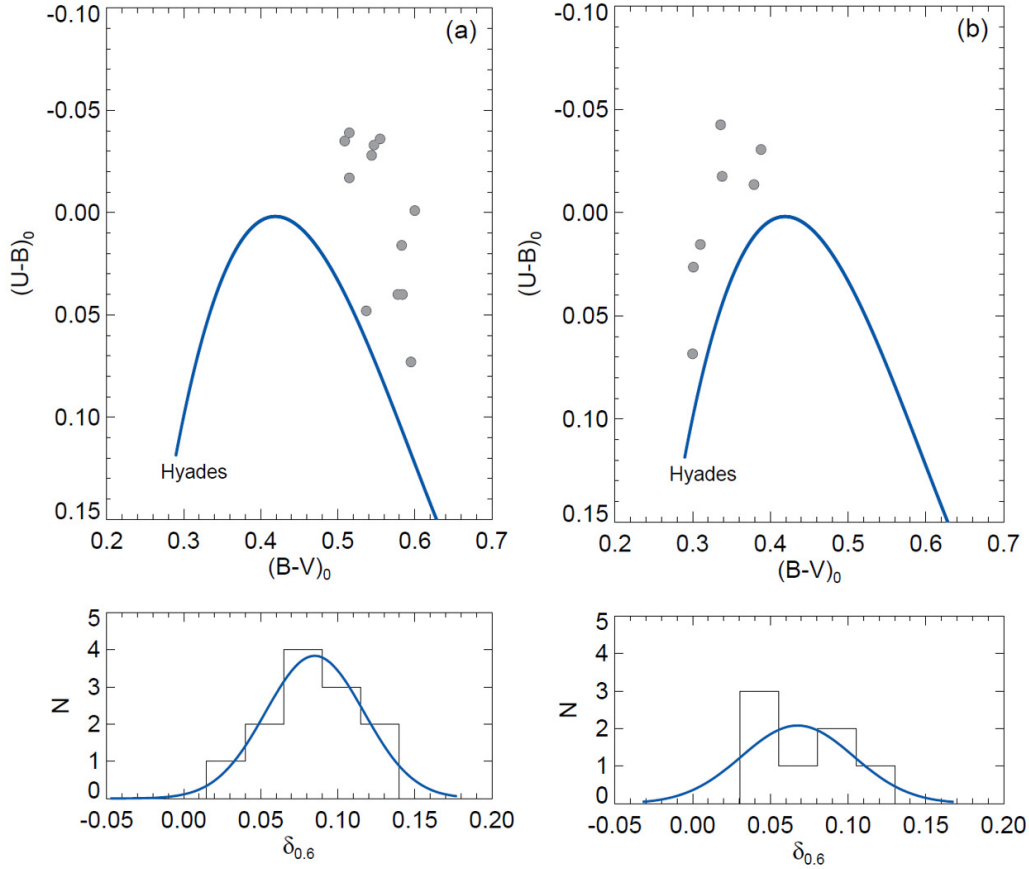


Fig. 8. Two-color diagrams (upper panels) and the distributions of normalised $\delta_{0.6}$ (lower panels) for NGC 1193 (a) and NGC 1798 (b). The solid blue lines in the upper and lower panels represent the main-sequence of Hyades and Gaussian models which were fitted to the histograms, respectively. The color figure can be viewed online.

and $d_{\text{iso}} = 4451 \pm 728$ pc for NGC 1798. The $V \times (U - B)$, $V \times (B - V)$, and $G \times (G_{\text{BP}} - G_{\text{RP}})$ CMDs with the best fit isochrones and associated errors are shown in Figure 9.

The isochrone-based distance for NGC 1193 as estimated by this study is compatible with the result given by Tadross (2005, $d = 5.25 \pm 0.24$ kpc). As well, the estimated age of the cluster is in a good agreement with the value of Kyeong et al. (2008, $t = 5.0 \pm 1.3$ Gyr). For NGC 1798, the derived distance matches well within the errors with the result of Park & Lee (1999, $d = 4.2 \pm 0.3$ kpc). The age of the cluster is coherent with the findings given by Park & Lee (1999, $t = 1.4 \pm 0.2$ Gyr) and Maciejewski & Niedzielski (2007, $t = 1.6$ Gyr).

Applying the linear equation of ϖ (mas) = $1000/d$ (pc), we converted isochrone distances to trigonometric parallaxes for the two clusters. This indicated that the parallax distances of NGC 1193 and NGC 1798 are $\varpi_{\text{iso}} = 0.180 \pm 0.012$ mas and $\varpi_{\text{iso}} = 0.225 \pm 0.037$ mas, respectively. It is con-

cluded that these values are in good agreement with the *Gaia* EDR3 trigonometric parallax distances for both clusters.

5. KINEMATICS AND GALACTIC ORBIT PARAMETERS OF CLUSTERS

The MWPOENTIAL2014 (Bovy 2015) algorithm, one of the potential functions defined in GALPY (the galactic dynamics library, Bovy 2015¹⁰), was applied to calculate the space velocity components and galactic orbital parameters for NGC 1193 and NGC 1798. The algorithm assumes an axisymmetric potential for the Milky Way galaxy. We adopted the galactocentric distance to be $R_{\text{GC}} = 8$ kpc, the Solar circular velocity of $V_{\text{rot}} = 220$ km s⁻¹ (Bovy 2015; Bovy & Tremaine 2012), and the Solar distance from the galactic plane as 27 ± 4 pc (Chen et al. 2000). Since the MWPOENTIAL2014 code comprises bulge, disk, and halo

¹⁰See also <https://galpy.readthedocs.io/en/v1.5.0/>

TABLE 3

METALLICITIES CALCULATED FOR TWO CLUSTERS. N IS THE NUMBER OF MEMBER STARS USED IN THE ANALYSES

NGC 1193					NGC 1798				
$\langle[\text{Fe}/\text{H}]\rangle$	(dex)	N	Survey/Catalog/Telescope	Ref	$\langle[\text{Fe}/\text{H}]\rangle$	(dex)	N	Survey/Catalog/Telescope	Ref
-0.51 ± 0.09		4	KPNO	(01)	-0.18 ± 0.02		4	KPNO	(10)
-0.22 ± 0.14		2	HET	(02)	-0.165		4	KPNO	(11)
-0.17 ± 0.13		1	HET	(03)	-0.18 ± 0.01		4	KPNO	(06)
-0.22 ± 0.01		1	PASTEL	(04)	-0.294		4	KPNO	(12)
-0.17		1	HET	(05)	-0.34 ± 0.01		4	KPNO	(13)
-0.25 ± 0.01		2	APOGEE DR14	(06)	-0.200 ± 0.006		4	KPNO	(14)
-0.34 ± 0.01		3	APOGEE DR16	(07)	-0.30 ± 0.02		4	KPNO	(15)
-0.320 ± 0.012		1	GALAH DR3	(08)	-0.27 ± 0.03		4	KPNO	(07)
-0.30 ± 0.06		12	SPMO	(09)	-0.267 ± 0.007		4	KPNO	(08)
					-0.20 ± 0.07		7	SPMO	(09)

(01) Friel et al. (2002), (02) Friel, Jacobson, & Pilachowski (2010), (03) Jacobson & Friel (2013), (04) Heiter et al. (2014), (05) Overbeek, Friel, & Jacobson (2016), (06) Carrera et al. (2019), (07) Donor et al. (2020), (08) Spina et al. (2021), (09) This study, (10) Donor et al. (2018), (11) Ting, Hawkins, & Rix (2018), (12) Ting & Rix (2019), (13) Hasselquist et al. (2020), (14) Sit & Ness (2020), (15) Olney et al. (2020).

potentials of the Milky Way, we assumed that it well represents the Galaxy.

Bovy (2015) defined the bulge component as a spherical power law density profile, given as follows:

$$\rho(r) = A \left(\frac{r_1}{r}\right)^\alpha \exp\left[-\left(\frac{r}{r_c}\right)^2\right], \quad (4)$$

where r_1 is the present reference radius, r_c the cut-off radius, A the amplitude that is applied to the potential in mass density units, and α is the inner power. We adopted the potential presented by Miyamoto & Nagai (1975) for the galactic disk component:

$$\Phi_{\text{disk}}(R_{\text{GC}}, Z) = -\frac{GM_{\text{d}}}{\sqrt{R_{\text{GC}}^2 + \left(a_{\text{d}} + \sqrt{Z^2 + b_{\text{d}}^2}\right)^2}}. \quad (5)$$

R_{GC} is the distance from the galactic center, Z the vertical distance from the galactic plane, G the universal gravitational constant, M_{d} the mass of the galactic disk, and a_{d} and b_{d} are the scale-length and scale-height of the disk, respectively.

The potential for the halo component was obtained by Navarro et al. (1996) as:

$$\Phi_{\text{halo}}(r) = -\frac{GM_{\text{s}}}{R_{\text{GC}}} \ln\left(1 + \frac{R_{\text{GC}}}{r_{\text{s}}}\right), \quad (6)$$

where M_{s} is the mass of the dark matter halo of the Milky Way and r_{s} is its radius.

To determine the spacial velocities and galactic orbit parameters of NGC 1193 and NGC 1798, we used the equatorial coordinates, proper motion components, distances, and radial velocity data with their uncertainties in the calculations. These values are listed in Table 4. We performed kinematic and dynamic analyses with 1 Myr steps over a 3.5 Gyr integration time. We considered the proper motion components and distances of the two clusters as derived by this study (see § 3.3), while for the radial velocities we used the data of Donor et al. (2020) who gave $\langle V_r \rangle = -84.7 \pm 0.2 \text{ km s}^{-1}$ for NGC 1193 and $\langle V_r \rangle = 2.7 \pm 0.8 \text{ km s}^{-1}$ for NGC 1798. As a result, we obtained for both clusters estimates of apogalactic distance R_{a} , perigalactic distance R_{p} , eccentricity e , maximum vertical distance from galactic plane Z_{max} , galactic space velocity components (U , V , W), and orbital period T . These estimates are listed in Table 4. The space velocity components (U, V, W) were calculated as $(70.95 \pm 0.16, -47.62 \pm 0.10, 5.56 \pm 0.59) \text{ km s}^{-1}$ for NGC 1193 and $(-7.18 \pm 1.50, -14.64 \pm 2.27, 9.13 \pm 1.69) \text{ km s}^{-1}$ for NGC 1798. In their study based on *Gaia* DR2 astrometric data (Gaia collaboration et al. 2018), Soubiran et al. (2018) derived the space velocity components for NGC 1193 as $(U, V, W) = (68.84 \pm 0.53, -46.77 \pm 0.54, 9.00 \pm 0.65) \text{ km s}^{-1}$ and for NGC 1798 as $(U, V, W) = (7.50 \pm 0.41, -16.63 \pm 0.50, 12.85 \pm 0.39) \text{ km s}^{-1}$. These results are in good agreement with the values cal-

TABLE 4
FUNDAMENTAL PARAMETERS OF NGC 1193 AND NGC 1798

Parameter	NGC 1193	NGC 1798
$(\alpha, \delta)_{J2000}$ (Sexagesimal)	03:05:56.64, +44:22:58.80	05:11:39.36, +47:41:27.60
$(l, b)_{J2000}$ (Decimal)	146.8143, -12.1624	160.7043, +04.8500
f_0 (stars arcmin $^{-2}$)	166.865 ± 1.573	53.597 ± 3.789
r_c (arcmin)	0.526 ± 0.009	1.190 ± 0.057
f_{bg} (stars arcmin $^{-2}$)	5.225 ± 0.124	11.318 ± 0.321
r_{lim} (arcmin)	8	8
r (pc)	12.95	10.36
$\mu_\alpha \cos \delta$ (mas yr $^{-1}$)	-0.207 ± 0.009	0.793 ± 0.006
μ_δ (mas yr $^{-1}$)	-0.431 ± 0.008	-0.373 ± 0.005
Cluster members ($P \geq 0.5$)	181	161
ϖ (mas)	0.191 ± 0.157	0.203 ± 0.099
$E(B - V)$ (mag)	0.150 ± 0.037	0.505 ± 0.100
$E(U - B)$ (mag)	0.109 ± 0.027	0.376 ± 0.073
A_V (mag)	0.465 ± 0.084	1.566 ± 0.310
[Fe/H] (dex)	-0.30 ± 0.06	-0.20 ± 0.07
Age (Gyr)	4.6 ± 1.0	1.3 ± 0.2
Distance modulus (mag)	14.191 ± 0.149	14.808 ± 0.332
Isochrone distance (pc)	5562 \pm 381	4451 \pm 728
$(X, Y, Z)_\odot$ (pc)	(-4550, 2976, 1172)	(-4186, 1466, 376)
R_{GC} (kpc)	12.90	12.27
PDMF slope	-1.38 ± 2.16	-1.30 ± 0.21
U_{LSR} (km/s)	79.78 ± 0.29	1.65 ± 1.51
V_{LSR} (km/s)	-33.43 ± 0.35	-0.45 ± 2.30
W_{LSR} (km/s)	12.13 ± 0.62	15.70 ± 1.70
S_{LSR} (km/s)	87.35 ± 0.77	15.79 ± 3.23
R_a (kpc)	14.44 ± 0.34	14.11 ± 0.30
R_p (kpc)	10.80 ± 0.43	11.72 ± 0.50
z_{max} (pc)	1342 \pm 77	725 \pm 148
e	0.144 ± 0.008	0.092 ± 0.011
T (Myr)	370 \pm 12	381 \pm 23
Birthplace (kpc)	10.86	11.82

culated in the study. The correction to the local standard of rest (LSR), given by Coşkunoğlu et al. (2011) as $(U, V, W) = (8.83 \pm 0.24, 14.19 \pm 0.34, 6.57 \pm 0.21)$ km s $^{-1}$, was applied to the space velocity components. The derived LSR corrected space velocity components are $(U, V, W)_{LSR} = (79.78 \pm 0.29, -33.43 \pm 0.35, 12.13 \pm 0.62)$ km s $^{-1}$ for NGC 1193 and $(U, V, W)_{LSR} = (1.65 \pm 1.51, -0.45 \pm 2.30, 15.70 \pm 1.70)$ km s $^{-1}$ for NGC 1798. Moreover, the space velocities of NGC 1193 were calculated to be 87.35 ± 0.77 km s $^{-1}$ and 15.79 ± 3.23 km s $^{-1}$ for NGC 1798.

Considering the space velocity components of stars in different Galactic populations, Schuster et al. (2012) divided the stars into thin disk ($-50 < V_{LSR}$ km/s), thick disk ($-180 < V_{LSR} \leq -50$ km/s) and halo ($V_{LSR} \leq 180$ km/s) groups. Figure 10 shows the positions of the clusters according to the Schuster et al. (2012)'s kinematic criteria. According to these criteria, the open clusters NGC 1193

and NGC 1798 appear to be members of the thick disk and thin disk populations, respectively. Considering the metal abundance range of NGC 1193 ($-0.51 \leq [Fe/H] \leq -0.17$ dex, see Table 3), it is concluded that the cluster belongs to the metal-rich side of the thick-disk population.

Figure 11 presents the orbits of NGC 1193 (Figure 11a) and NGC 1798 (Figure 11c) as functions of distance from the galactic center and the galactic plane ($Z \times R_{GC}$ and $R_{GC} \times t$). The birth and present-day locations for the two clusters are marked with yellow triangles and circles in sub-figures 11b and 11d. Figures 11a and 11c show that both of the clusters entirely orbit outside the solar circle. The orbital eccentricities of NGC 1193 and NGC 1798 are smaller than 0.15, thus their orbits are close to circular. The results of orbital integrations imply that NGC 1193 reaches its maximum vertical distance from the galactic plane at $Z_{max} = 1342 \pm 77$ pc

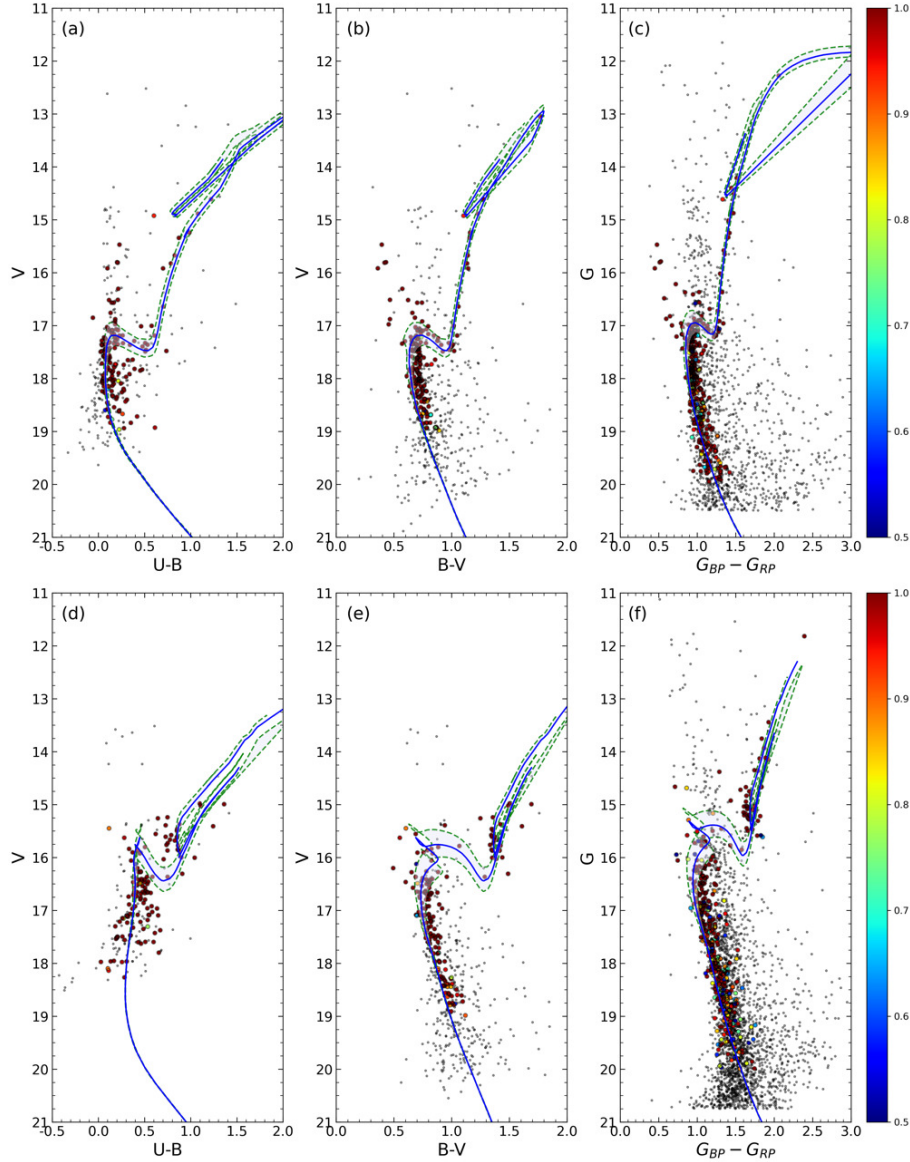


Fig. 9. CMDs for the NGC 1193 (Panels a, b, and c) and NGC 1798 (Panels d, e, and f). The differently colored dots represent the membership probabilities according to the color scales shown on the right side of the diagrams. Grey dots indicate low probability members ($P < 0.5$), or field stars ($P = 0$). The blue lines show the PARSEC isochrones, while the shaded areas surrounding these lines are their associated errors. The color figure can be viewed online.

with an orbital period $T = 370 \pm 12$ Myr, and these values correspond to $Z_{\max} = 725 \pm 148$ pc and $T = 381 \pm 23$ Myr for NGC 1798. Considering the age values determined in this study for the clusters, we ran the GALPY program backwards in time and examined the resulting birth-places. The program indicated that the birth-place radial distances are 10.86 kpc and 11.82 kpc for NGC 1193 and NGC 1798, respectively, meaning that the clusters were born in the metal-poor region outside the solar circle.

6. LUMINOSITY AND PRESENT-DAY MASS FUNCTIONS

The distribution of stars according to their brightness is defined as the luminosity function (LF). We used *Gaia* EDR3 photometric data to determine LFs for the two clusters. For this, main-sequence stars located inside the 8 arcmin limiting radii, as derived above, were selected for the two clusters. The magnitude ranges of the chosen stars are within the $17.25 \leq G \leq 20$ mag for NGC 1193 and $16.5 \leq G \leq 20$ mag for NGC 1798. We converted the G mag-

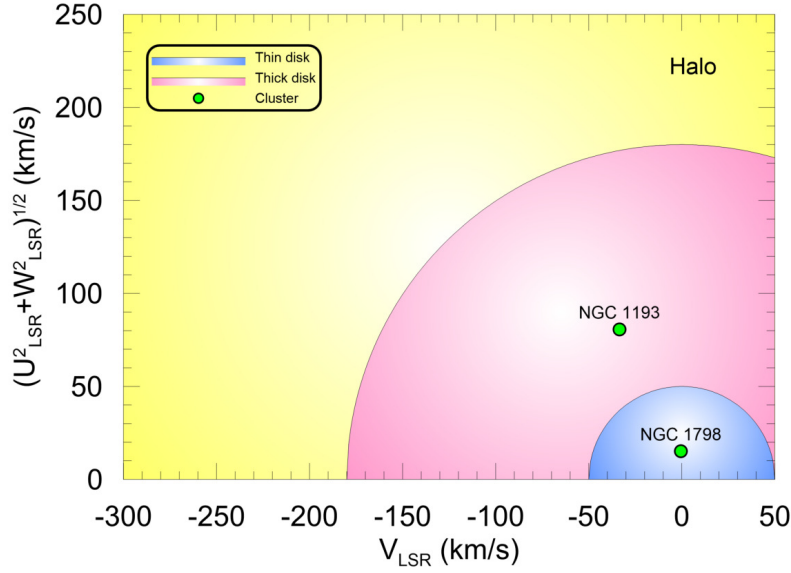


Fig. 10. Toomre diagram for NGC 1193 and NGC 1798. Blue, pink and yellow regions show thin disk, thick disk and halo populations, respectively. The color figure can be viewed online.

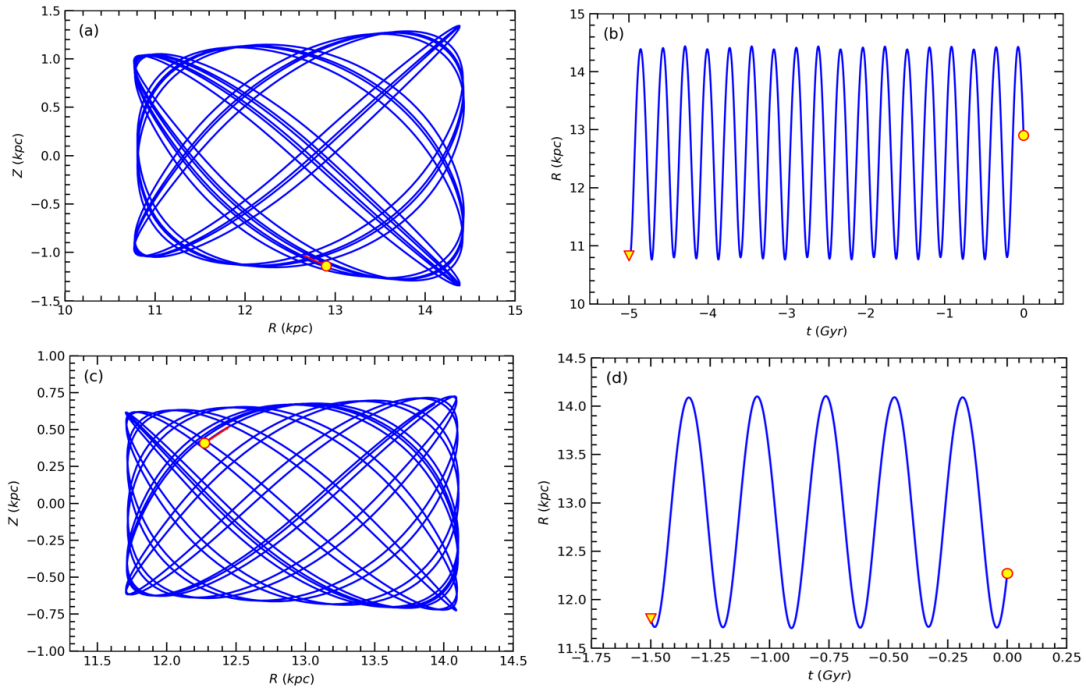


Fig. 11. The galactic orbits and birth radii of NGC 1193 (a,b) and NGC 1798 (c,d) in the $Z \times R_{GC}$ and $R_{GC} \times t$ planes. The filled yellow circles and triangles show the present day and birth positions, respectively. Red arrows are the motion vectors of OCs. The color figure can be viewed online.

nitudes of the selected stars to absolute magnitudes with the equation $M_G = G - 5 \times \log d + 5 + A_G$, where G is the apparent magnitude and d the distance derived earlier in this study. A_G is the extinction for G

magnitudes and is represented by $A_G = 0.84 \times A_V$ (Sun et al. 2021) (here A_V is the extinction for V magnitudes). This led to the absolute magnitude ranges being limited within the $2.5 < M_G < 5.5$ and

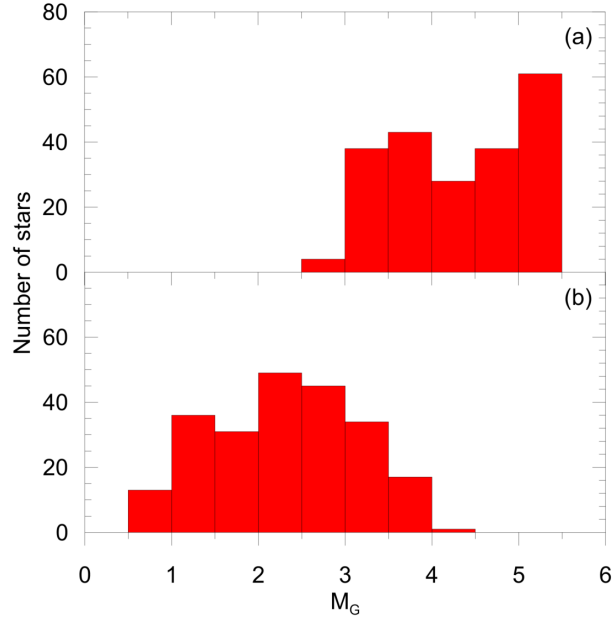


Fig. 12. The luminosity functions of NGC 1193 (a) and NGC 1798 (b). The histograms show the absolute magnitudes of the main-sequence stars belonging to the clusters. The color figure can be viewed online.

$0.5 < M_G < 4.5$ mag for NGC 1193 and NGC 1798, respectively. We constructed LF histograms with the step-size 0.5 mag, as shown as Figure 12 for both clusters.

To convert these LFs to present day mass functions (PDMFs) we employed the PARSEC isochrones (Bressan et al. 2012), which give the ages and metal abundances (z) of the clusters. We utilized a high degree polynomial equation between G -band absolute magnitudes and masses of theoretical main-sequence stars. The resulting absolute magnitude-mass relation was used to transform the observational absolute G band magnitudes to masses. The number, mass range, and mean mass of main-sequence stars that resulted are 212, $0.85 \leq M/M_\odot \leq 1.2$, and $0.99M_\odot$ for NGC 1193, and 226, $1.1 \leq M/M_\odot \leq 2$, and $1.53 M_\odot$ for NGC 1798. The mass function PDMF can be approximated by a power law defined as by Salpeter (1955):

$$\log\left(\frac{dN}{dM}\right) = -(1 + \Gamma) \times \log(M) + \text{constant}. \quad (7)$$

Here dN is the number of stars in a mass bin of width dM with a central mass M and Γ being the slope of the PDMF. We estimated the slope of the PDMF in both clusters for apparent $G \leq 20$ mag, which

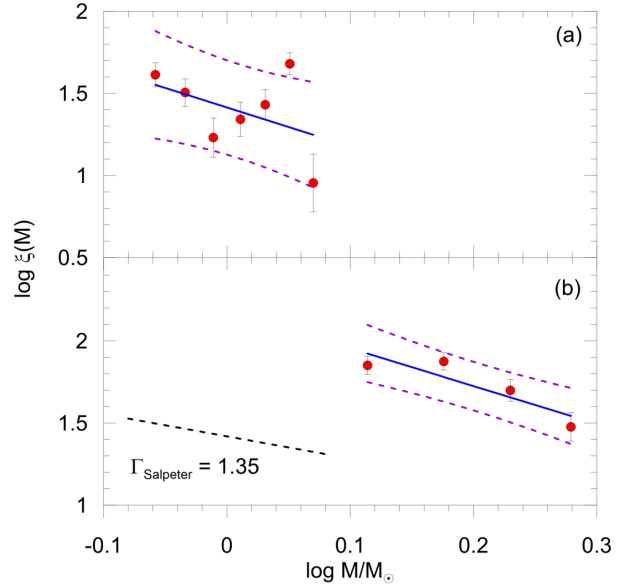


Fig. 13. Present-day mass functions of NGC 1193 (a) and NGC 1798 (b) derived from all samples (red circle). The blue and dashed lines represent the mass functions of the open clusters and Salpeter (1955)'s mass function, respectively. The purple dashed lines show $\pm 1\sigma$ prediction levels. The color figure can be viewed online.

corresponds to stars more massive than $0.85 M_\odot$ in NGC 1193 and $1.1 M_\odot$ for NGC 1798. The resulting PDMFs with the best fits are presented in Figure 13. We calculated the slope values to be $\Gamma = 1.38 \pm 2.16$ for NGC 1193 and as $\Gamma = 1.30 \pm 0.21$ for NGC 1798. Since the NGC 1193 cluster is about 5.5 kpc from the Sun, the magnitudes of the main-sequence stars are within a narrow range. This causes the mass range of the main-sequence stars to be limited and the distribution of the mass function to show a large scatter. While the PDMF of the NGC 1193 is compatible with Salpeter (1955)'s result of $\Gamma = 1.35$, the error of the PDMF is large. This situation is different for NGC 1798. Considering the value and error of the PDMF for NGC 1798, it is in agreement with Salpeter's result.

7. SUMMARY AND CONCLUSION

We performed photometric, astrometric, and kinematic studies of two old age open clusters, NGC 1193 and NGC 1798, using CCD UBV and *Gaia* EDR3 data. We examined the cluster structure, obtaining basic astrophysical parameters as well as properties of galactic orbits for two clusters. Outcomes of the study are listed in Table 4 and summarised as follows:

1. Performing the RDP analyses, we determined the limiting radii $r_{\text{lim}} = 8$ arcmin for both clusters. This value corresponds to limiting radii of 12.95 pc and 10.36 pc for NGC 1193 and NGC 1798, respectively. We considered the stars within these limiting radii as potential cluster members and restricted subsequent analysis to this set of stars.
2. The calculation of membership probabilities of stars was made using the UPMASK program together with a five-dimensional parameter space containing the stars' proper motion components, trigonometric parallaxes, and their uncertainties. We considered the stars with probabilities $P \geq 0.5$ to be cluster members. Additionally we adopted two more criteria to clarify cluster membership:
 - (a) binary star contamination in the cluster main-sequences which was interpreted by the de-reddened ZAMS fitted to $V \times (B - V)$ CMDs with a shift of +0.75 mag in the V band, and
 - (b) within the limiting radii determined in the study (as per step 1).

Consequently, we selected the stars inside the clusters' limiting radii, within best-fitting ZAMS and with the membership probability $P \geq 0.5$ as 'real' members of two clusters. Thus we identified 361 and 428 stars as most likely members of NGC 1193 and NGC 1798, respectively.
3. The reddening and photometric metallicities of the two clusters were derived separately using CCD UBV TCDs. The reddening analyses were performed by fitting de-reddened ZAMS to main sequence member stars. Photometric metallicity was based on the comparison of F-G type main sequence members with the Hyades main-sequence. The reddening and photometric metallicity for NGC 1193 are $E(B - V) = 0.150 \pm 0.037$ mag and $[\text{Fe}/\text{H}] = -0.30 \pm 0.06$ dex, respectively. The corresponding values for NGC 1798 are $E(B - V) = 0.505 \pm 0.100$ mag and $[\text{Fe}/\text{H}] = -0.20 \pm 0.07$ dex.
4. The distance moduli, distance, and age of the NGC 1193 were derived as $\mu_V = 14.191 \pm 0.149$ mag, $d = 5562 \pm 381$ pc, and $t = 4.6 \pm 1$ Gyr, respectively. Similarly $\mu_V = 14.808 \pm 0.332$ mag, $d = 4451 \pm 728$ pc, and $t = 1.3 \pm 0.2$ Gyr were calculated for NGC 1798. These results were obtained by simultaneously fitting PARSEC isochrones on the UBV and *Gaia* EDR3 photometric CMDs utilizing the most likely member stars according to reddening and metallicities derived in the study.
5. Mean proper motion components were calculated as $(\mu_\alpha \cos \delta, \mu_\delta) = (-0.207 \pm 0.009, -0.431 \pm 0.008)$ mas yr⁻¹ for NGC 1193 as well as $(\mu_\alpha \cos \delta, \mu_\delta) = (0.793 \pm 0.006, -0.373 \pm 0.005)$ mas yr⁻¹ for NGC 1798.
6. We estimated mean trigonometric parallaxes using *Gaia* EDR3 data of most likely members for two clusters. The results are $\varpi_{\text{Gaia}} = 0.191 \pm 0.157$ mas for NGC 1193 and $\varpi_{\text{Gaia}} = 0.203 \pm 0.099$ mas for NGC 1798. We also converted isochrones distances to trigonometric parallaxes by applying the linear equation ϖ (mas) = 1000/ d (pc) and found $\varpi_{\text{iso}} = 0.180 \pm 0.012$ mas for NGC 1193 and $\varpi_{\text{iso}} = 0.225 \pm 0.037$ mas for NGC 1798. For both clusters our derived trigonometric parallaxes values calculated from isochrone fitting distances are well supported by the values determined from *Gaia* EDR3 trigonometric parallaxes of member stars.
7. Space velocities and galactic orbital parameters show that NGC 1193 belongs to the thick-disk population, whereas NGC 1798 is a member of the thin-disk population. Moreover, both clusters orbit completely outside the solar circle.
8. We found that NGC 1193 and NGC 1798 were born outside the solar circle with the birth radii of 10.86 and 11.82 kpc from the Galactic center, respectively. These birth radii indicate the metal-poor formation region and support the metallicities calculated in the study for the two clusters.
9. Present day mass function slopes of $\Gamma = 1.38 \pm 2.16$ and $\Gamma = 1.30 \pm 0.21$ were derived for NGC 1193 and NGC 1798, respectively. While the results for two clusters are in good agreement with the value of Salpeter (1955), that for NGC 1193 possesses a large uncertainty. We concluded that because of its distance, the main-sequence stars of NGC 1193 are limited within a narrow range of magnitudes.

The observations of this publication were made at the National Astronomical Observatory, San Pedro Mártir, Baja California, México, and the authors wish to thank the staff of the Observatory for their assistance during these observations. This research has made use of the WEBDA database, operated at the Department of Theoretical Physics and Astrophysics of the Masaryk University. This research has made use of NASA's Astrophysics Data System. We also made use of VizieR and Simbad databases at CDS, Strasbourg, France as well as data from the European Space Agency (ESA) mission *Gaia*¹¹, processed by the *Gaia* Data Processing and Analysis Consortium (DPAC)¹². Funding for DPAC has been provided by national institutions, in particular the institutions participating in the *Gaia* Multilateral Agreement. IRAF was distributed by the National Optical Astronomy Observatory, which was operated by the Association of Universities for Research in Astronomy (AURA) under a cooperative agreement with the National Science Foundation. PyRAF is a product of the Space Telescope Science Institute, which is operated by AURA for NASA. We thank the University of Queensland for collaboration software.

REFERENCES

- Ahumada, J. A. & Lapasset, E. 2007, *A&A*, 463, 789, <https://doi.org/10.1051/0004-6361:20054590>
- Ak, T., Bostancı, Z. F., Yontan, T., et al. 2016, *Ap&SS*, 361, 126, <https://doi.org/10.1007/s10509-016-2707-2>
- Akbulut, B., Ak, S., Yontan, T., et al. 2021, *Ap&SS*, 366, 68, <https://doi.org/10.1007/s10509-021-03975-x>
- Banks, T., Yontan, T., Bilir, S. & Canbay, R. 2020, *JApA*, 41, 6, <https://doi.org/10.1007/s12036-020-9621-2>
- Bertelli, G., Bressan, A., Chiosi, C., Fagotto, F. & Nasi, E. 1994, *A&AS*, 106, 275
- Bressan, A., Marigo, P., Girardi, L., et al. 2012, *MNRAS*, 427, 127, <https://doi.org/10.1111/j.1365-2966.2012.21948.x>
- Bilir, S., Güver, T. & Aslan, M. 2006, *AN*, 327, 693, <https://doi.org/10.1002/asna.200510614>
- Bilir, S., Güver, T., Khamitov, I., Ak, T., Ak, S., Coşkunoglu, K. B., Paunzen, E. & Yaz, E. 2010, *Ap&SS*, 326, 139, <https://doi.org/10.1007/s10509-009-0233-1>
- Bilir, S., Bostancı, Z. F., Yontan, T., et al. 2016, *AdSpR*, 58, 1900, <https://doi.org/10.1016/j.asr.2016.06.039>
- Bostancı, Z. F., Ak, T., Yontan, T., et al. 2015, *MNRAS*, 453, 1095, <https://doi.org/10.1093/mnras/stv1665>
- Bostancı, Z. F., Yontan, T., Bilir, S., et al. 2018, *Ap&SS*, 363, 143, <https://doi.org/10.1007/s10509-018-3364-4>
- Bovy, J. & Tremaine, S. 2012, *ApJ*, 756, 89, <https://doi.org/10.1088/0004-637X/756/1/89>
- Bovy, J. 2015, *ApJS*, 216, 29, <https://doi.org/10.1088/0067-0049/216/2/29>
- Cantat-Gaudin, T., Jordi, C., Vallenari, A., et al. 2018, *A&A*, 618, 93, <https://doi.org/10.1051/0004-6361/201833476>
- Cantat-Gaudin, T., Anders, F., Castro-Ginard, A., et al. 2020, *A&A*, 640, 1, <https://doi.org/10.1051/0004-6361/202038192>
- Carraro, G., Sales Silva, J. V., Moni Bidin, C. & Vazquez, R. A. 2017, *ApJ*, 153, 99, <https://doi.org/10.3847/1538-3881/153/3/99>
- Carrera, R. 2012, *A&A*, 544, 109, <https://doi.org/10.1051/0004-6361/201219625>
- Carrera, R., Bragaglia, A., Cantat-Gaudin, T., et al. 2019, *A&A*, 623, 80, <https://doi.org/10.1051/0004-6361/201834546>
- Chen, Y. Q., Nissen, P. E., Zhao, G., Zhang, H. W. & Benoni, T. 2000, *A&AS*, 141, 491, <https://doi.org/10.1051/aas:2000124>
- Conrad, C., Scholz, R.-D., Kharchenko, N. V., et al. 2014, *A&A*, 562, 54, <https://doi.org/10.1051/0004-6361/201322070>
- Coşkunoglu, B., Ak S., Bilir, S., et al. 2011, *MNRAS*, 412, 1237, <https://doi.org/10.1111/j.1365-2966.2010.17983.x>
- Donor, J., Frinchaboy, P. M., Cunha, K., et al. 2018, *AJ*, 156, 142, <https://doi.org/10.3847/1538-3881/aad635>
- Donor, J., Frinchaboy, P. M., Cunha, K., et al. 2020, *AJ*, 159, 199, <https://doi.org/10.3847/1538-3881/ab77bc>
- Dreyer, J. L. E. 1888, *MmRAS*, 49, 1
- Eker, Z., Bakış, V., Bilir, S., et al. 2018, *MNRAS*, 479, 5491, <https://doi.org/10.1093/mnras/sty1834>
- Eker, Z., Soyduğan, F., Bilir, S., et al. 2020, *MNRAS*, 496, 3887, <https://doi.org/10.1093/mnras/staa1659>
- Friel, E. D., Liu, T. & Janes, K. A. 1989, *PASP*, 101, 1105, <https://doi.org/10.1086/132583>
- Friel, E. D. & Janes, K. A. 1993, *A&A*, 267, 75
- Friel, E. D. 1995, *ARA&A*, 33, 381, <https://doi.org/10.1146/annurev.aa.33.090195.002121>
- Friel, E. D., Janes, K. A., Tavarez, M., et al. 2002, *AJ*, 124, 2693, <https://doi.org/10.1086/344161>
- Friel, E. D., Jacobson, H. R. & Pilachowski, C. A. 2010, *AJ*, 139, 1942, <https://doi.org/10.1088/0004-6256/139/5/1942>
- Gaia Collaboration, Prusti, T., de Bruijne, J. H. J. et al. 2016, *A&A*, 595, 1, <https://doi.org/10.1051/0004-6361/201629272>
- Gaia Collaboration, Brown, A. G. A., Vallenari, A., Prusti, T., et al. 2018, *A&A*, 616, 1, <https://doi.org/10.1051/0004-6361/201833051>

¹¹<https://www.cosmos.esa.int/gaia>

¹²<https://www.cosmos.esa.int/web/gaia/dpac/consortium>

- Gaia Collaboration, Brown, A. G. A., Vallenari, A., Prusti, T., et al. 2021, *A&A*, 649, 1, <https://doi.org/10.1051/0004-6361/202039657>
- Garcia, B., Claria, J. J. & Levato, H. 1988, *Ap&SS*, 143, 317, <https://doi.org/10.1007/BF00637143>
- Gilmore, G., Randich, S., Asplund, M., et al. 2012, *Msngr*, 147, 25
- Hasselquist, S., Zasowski, G., Feuillet, D. K., et al. 2020, *ApJ*, 901, 109, <https://doi.org/10.3847/1538-4357/abaeae>
- Heiter, U., Soubiran, C., Netopil, M. & Paunzen, E. 2014, *A&A*, 561, 93, <https://doi.org/10.1051/0004-6361/201322559>
- Jacobson, H. R. & Friel, E. D. 2013, *AJ*, 145, 107, <https://doi.org/10.1088/0004-6256/145/4/107>
- Janes, K. & Adler, D. 1982, *ApJS*, 49, 425, <https://doi.org/10.1086/190805>
- Janes, K. A. & Phelps, R. L. 1994, *AJ*, 108, 1773, <https://doi.org/10.1086/117192>
- Kaluzny, J. 1988, *AcA*, 38, 339
- Karaali, S., Bilir, S., Karataş, Y. & Ak, S. G. 2003a, *PASA*, 20, 165, <https://doi.org/10.1071/AS02028>
- Karaali, S., Ak, S. G., Bilir, S., Karataş, Y. & Gilmore, G. 2003b, *MNRAS*, 343, 1013, <https://doi.org/10.1046/j.1365-8711.2003.06743.x>
- Karaali, S., Bilir, S., Ak, S., Yaz, E. & Coşkunoglu, B. 2011, *PASA*, 28, 95, <https://doi.org/10.1071/AS10026>
- King, I. 1962, *AJ*, 67, 471, <https://doi.org/10.1086/108756>
- Kog, S., Yontan, T., Bilir, S., et al. 2022, *AJ*, 163, 191, <https://doi.org/10.3847/1538-3881/ac58a0>
- Kos, J., de Silva, G., Buder, S., et al. 2018, *MNRAS*, 480, 5242, <https://doi.org/10.1093/mnras/sty2171>
- Krone-Martins, A. & Moitinho, A. 2014, *A&A*, 561, 57, <https://doi.org/10.1051/0004-6361/201321143>
- Kyeong, J., Kim, S. C., Hiriart, D. & Sung, E.-C. 2008, *JKAS*, 41, 147, <https://doi.org/10.5303/JKAS.2008.41.6.147>
- Landolt, A. U. 2009, *AJ*, 137, 4186, <https://doi.org/10.1088/0004-6256/137/5/4186>
- Lata, S., Pandey, A. K., Sagar, R. & Mohan, V. 2002, *A&A*, 388, 158, <https://doi.org/10.1051/0004-6361:20020450>
- Liu, L. & Pang, X. 2019, *ApJS*, 245, 32, <https://doi.org/10.3847/1538-4365/ab530a>
- Maciejewski, G. & Niedzielski, A. 2007, *A&A*, 467, 1065, <https://doi.org/10.1051/0004-6361:20066588>
- Miyamoto, M. & Nagai, R. 1975, *PASJ*, 27, 533
- Monet, D. G., Levine, S. E., Canzian, B., et al. 2003, *AJ*, 125, 984, <https://doi.org/10.1086/345888>
- Navarro, J. F., Frenk, C. S. & White, S. D. M. 1996, *ApJ*, 462, 563, <https://doi.org/10.1086/177173>
- Olney, R., Kounkel, M., Schillinger, C., et al. 2020, *AJ*, 159, 182, <https://doi.org/10.3847/1538-3881/ab7a97>
- Oralhan, İ. A., Karataş, Y., Schuster, W. J., Michel, R. & Chavarría, C. 2015, *NewA*, 34, 195, <https://doi.org/10.1016/j.newast.2014.06.011>
- Overbeek, J. C., Friel, E. D. & Jacobson, H. R. 2016, *ApJ*, 824, 75, <https://doi.org/10.3847/0004-637X/824/2/75>
- Park, H. S. & Lee, M. G. 1999, *MNRAS*, 304, 883, <https://doi.org/10.1046/j.1365-8711.1999.02366.x>
- Ruprecht, J. 1966, *BAICz*, 17, 33
- Salpeter, E. E. 1955, *ApJ*, 121, 161, <https://doi.org/10.1086/145971>
- Schuster, W. J., Moreno, E., Nissen, P. E. & Pichardo, B. 2012, *A&A*, 538, 21, <https://doi.org/10.1051/0004-6361/201118035>
- Sit, T. & Ness, M. K. 2020, *ApJ*, 900, 4, <https://doi.org/10.3847/1538-4357/ab9ff6>
- Soubiran, C., Cantat-Gaudin, T., Romero-Gómez, M., et al. 2018, *A&A*, 619, 155, <https://doi.org/10.1051/0004-6361/201834020>
- Spina, L., Ting, Y.-S., De Silva, G. M., et al. 2021, *MNRAS*, 503, 3279, <https://doi.org/10.1093/mnras/stab471>
- Stetson, P. B. 1987, *PASP*, 99, 191, <https://doi.org/10.1086/131977>
- Stetson, P. B., Pancino, E., Zocchi, A., Sanna, N. & Monelli, M. 2019, *MNRAS*, 485, 3042, <https://doi.org/10.1093/mnras/stz585>
- Sun, M., Jiang, B., Yuan, H. & Li, J. 2021, *ApJS*, 254, 38, <https://doi.org/10.3847/1538-4365/abf929>
- Sung, H., Lim, B., Bessell, M. S., et al. 2013, *JKAS*, 46, 103, <https://doi.org/10.5303/JKAS.2013.46.3.103>
- Tadross, A. L. 2005, *AN*, 326, 19, <https://doi.org/10.1002/asna.200410335>
- Ting, Y.-S., Hawkins, K. & Rix, H.-W. 2018, *ApJL*, 858, 7, <https://doi.org/10.3847/2041-8213/aabf8e>
- Ting, Y.-S. & Rix, H.-W. 2019, *ApJ*, 878, 2, <https://doi.org/10.3847/1538-4357/ab1ea5>
- van den Bergh, S. & Sher, D. 1960, *PDDO*, 2, 203
- Yontan, T., Bilir, S., Bostancı, Z. F., et al. 2015, *Ap&SS*, 355, 267, <https://doi.org/10.1007/s10509-014-2175-5>
- Yontan, T., Bilir, S., Bostancı, Z. F., et al. 2019, *Ap&SS*, 364, 152, <https://doi.org/10.1007/s10509-019-3640-y>
- Yontan, T., Bilir, S., Ak, T., et al. 2021, *AN*, 342, 538, <https://doi.org/10.1002/asna.202113837>

Talar Yontan, Hikmet Çakmak & Selçuk Bilir: Istanbul University, Faculty of Science, Department of Astronomy and Space Sciences, 34119, Beyazıt, Istanbul, Turkey (talar.yontan@istanbul.edu.tr, hcakmak@istanbul.edu.tr, sbilir@istanbul.edu.tr).

Timothy Banks: Nielsen, 200 W Jackson Blvd, Chicago, IL 60606, USA (tim.banks@nielsen.com); Department of Physical Science & Engineering, Harper College, 1200 W Algonquin Rd, Palatine, IL 60067, USA (tbanks@harpercollege.edu).

Michel Raúl: Observatorio Astronomico Naciona, Universidad Nacional Autonoma de Mexico, Ensenada, Mexico (rmm@astro.unam.mx).

Remziye Canbay, Seliz Koç, Seval Taşdemir, Hülya Erçay, Burçin Tanık Öztürk, & Deniz Cennet Dursun: Istanbul University, Institute of Graduate Studies in Science, Programme of Astronomy and Space Sciences, 34116, Beyazıt, Istanbul, Turkey (rmzycnby@gmail.com, seliskoc@gmail.com, tasdemir.seval@ogr.iu.edu.tr, hulyaercay5@gmail.com, burcin.tanik@istanbul.edu.tr, denizcdursun@gmail.com).

CEN X–3 AS SEEN BY MAXI DURING SIX YEARS

Á. Torregrosa², J. J. Rodes-Roca^{1,2}, J. M. Torrejón^{1,2}, G. Sanjurjo-Ferrín², and G. Bernabéu^{1,2}

Received November 11 2021; accepted July 21 2022

ABSTRACT

The aim of this work is to study both light curve and orbital phase spectroscopy of Cen X-3 taking advantage of the *MAXI*/GSC observation strategy. These studies allow delimiting the stellar wind properties and its interactions with the compact object. From the analysis of the light curve, we have estimated the orbital period of the binary system and also found possible QPOs around a super-orbital period of $P_{\text{superorb}} = 220 \pm 5$ days. Both orbital phase-averaged and phase-resolved spectra were extracted and analysed in the 2.0–20.0 keV energy range. Two models have described spectra satisfactorily, a partial absorbed Comptonization of cool photons on hot electrons plus a power law, and a partial absorbed blackbody plus a power law, both modified by adding Gaussian lines. The high value of the X-ray luminosity in the averaged spectrum indicates that the accretion mode is not only due to the stellar wind.

RESUMEN

Se pretende estudiar la curva de luz y la espectroscopía en fase orbital de Cen X-3 gracias a la estrategia de observación de *MAXI*/GSC. Estos estudios permiten delimitar las propiedades del viento estelar y sus interacciones con el objeto compacto. Por medio de este análisis hemos estimado el período orbital del sistema y hemos encontrado posibles QPOs alrededor de un superperíodo orbital de $P_{\text{superorb}} = 220 \pm 5$ días. Hemos extraído y analizado los espectros medio y en fase orbital en el intervalo 2.0–20.0 keV por medio de dos modelos: una comptonización parcialmente absorbida de fotones fríos en electrones calientes más una ley de potencias y un cuerpo negro parcialmente absorbido más una ley de potencias, ambos modificados por líneas Gaussianas. El alto valor de la luminosidad del espectro medio indica un modo de acreción no debido solamente al viento estelar.

Key Words: pulsars: individual: Cen X–3 — stars: supergiants — X-rays: binaries

1. INTRODUCTION

Cen X-3 is an eclipsing high-mass X-ray binary system formed by an O-type donor star and a neutron star. Its complex X-ray behaviour makes both its temporal and spectral analysis extremely important to better understand its properties. So far, it is the only high-mass X-ray binary (HMXB) system in the Milky Way where mass transfer onto a neutron star occurs directly from the surface of the donor star (via Roche lobe overflow). The source was discovered in 1967 (Chodil et al. 1967) and Krzeminski (1974) estimated the distance as ≈ 8 kpc. The distance to Cen X-3 obtained from the European Space Agency

(ESA) mission Gaia³ Early Data Release 3 (GEDR3) is $d(\text{kpc}) = 6.8_{-0.5}^{+0.6}$. It has been derived by using the parallax measure, the source’s G-band magnitude and BP-RP colour (Bailer-Jones et al. 2021), called by them “photogeometric” distance.

It consists of a neutron star (NS) and a giant star O6–8 III companion called V779 Cen (Hutchings et al. 1979) with mass $\approx 20 M_{\odot}$ (van der Meer et al. 2007) and radius $\approx 12 R_{\odot}$ (Naik et al. 2011). Rawls et al. (2011) calculated the NS mass by using a Monte Carlo method and assuming a Roche lobe filling factor between 0.9 and 1.0, $M_{\text{NS}} = (1.35 \pm 0.15) M_{\odot}$. However, applying another technique based on eclipsing light curve analysis and including an accretion disc around the NS, they de-

¹Department of Physics, Systems Engineering and Signal Theory, University of Alicante, 03080 Alicante, Spain.

²University Institute of Physics Applied to Sciences and Technologies, University of Alicante, 03080 Alicante, Spain.

³<https://www.cosmos.esa.int/gaia>

rived a final mass for this system of $(1.49 \pm 0.08) M_{\odot}$. The binary orbit is almost circular, eccentricity $e < 0.0016$ (Bildsten et al. 1997), with an orbital period of ≈ 2.1 days, determined from regular X-ray eclipses (Schreier et al. 1972).

The observed average high X-ray emission $\approx 10^{37}$ erg s $^{-1}$ compared to that observed in wind-fed accreting systems $\approx 10^{36}$ erg s $^{-1}$ (Martínez-Núñez et al. 2017; Kretschmar et al. 2019) suggests additional structures in the NS environment. Studies of the light curve of Cen X-3 (Tjemkes et al. 1986) and the observed overall NS spin-up trend of 1.135 ms yr $^{-1}$ with fluctuations on time scales of years (Tsunemi et al. 1996), together with the detection of quasi periodic oscillations (QPOs) from the source (Takeshima et al. 1991; Raichur & Paul 2008b) showed evidences of an accretion disk, due to Roche lobe overflow. Other structures such as an additional gas stream or an accretion wake might also be present in the accretion scenario in this source (Stevens 1988; Suchy et al. 2008).

Thus, variability of model parameters along the orbital phase allow us not only to investigate the characteristics of the circumstellar matter around the NS but also to trace permanent wind structures. Many authors have reported on the iron emission lines of Cen X-3 (Ebisawa et al. 1996; Iaria et al. 2005; Naik & Paul 2012; Rodes et al. 2017; Aftab et al. 2019) around the orbital period. Although *MAXI* was able to detect the Fe $K\alpha$, it cannot resolve it properly. However, changes in the central energy of the iron line with the orbital phase pointed to a coexistence of two iron lines at different energies (Rodes et al. 2017). Therefore, by using *ASCA* description of the iron emission lines of Cen X-3 we fitted three Gaussian profiles to the *MAXI*/*GSC* data, fixing some of the line parameters to estimate their equivalent widths.

In this paper we present the spectroscopic and light curve analysis of Cen X-3 observed with *MAXI*. *MAXI*/*GSC* data covers the entire orbit and extends over more than six years. Orbital phase-averaged and phase-resolved spectroscopy were performed applying several models in the 2–20 keV energy range. Observations and data reduction are described in § 2, timing analysis is presented in § 3, orbital phase-averaged spectrum and orbital phase-resolved spectra results are discussed in § 4, and § 5 contains the summary of the main findings.

2. OBSERVATIONS AND DATA

MAXI is an X-ray monitor on board the International Space Station (ISS) since August 2009 (Mat-

TABLE 1
EPHEMERIS DATA USED FOR TIMING CALCULATIONS

$T_{0,ecl}$ (MJD)	$50506.788423 \pm 0.000007$
P_{orb} (d)	$2.08704106 \pm 0.00000003$ *
\dot{P}_{orb}/P_{orb} (10^{-6} yr $^{-1}$)	-1.800 ± 0.001

*Falanga et al. 2015.

suoka et al. 2009). Every ≈ 92 minutes it scans almost the entire sky in each ISS orbit, observing a particular source for about 40–150 s (Sugizaki et al. 2011) depending on the position of the object. It consists of two types of X-ray slit cameras, the Gas Slit Camera (GSC, Mihara et al. 2011) in the 2.0–20.0 keV, and the Solid-state Slit Camera (SSC, Tomida et al. 2011) operating in the 0.7–7.0 keV energy range. The in-orbit performance of GSC and SSC is presented in Sugizaki et al. (2011) and Tsunemi et al. (2010), respectively.

3. TIMING ANALYSIS

Firstly, we have extracted the *MAXI*/*GSC* on-demand light curves of Cen X-3 with a time resolution of one ISS orbit in five energy bands, 2.0–20.0, 2.0–4.0, 4.0–10.0, 10.0–20.0 and 5.7–7.5 keV. To analyse the light curves we used *Python* and the *Starlink* software package⁴.

Secondly, we have used the Lomb-Scargle technique (Press & Rybicki 1989) to determine the orbital period from the original light curve 2.0–20.0 keV and have obtained $P_{orb} = 2.0870 \pm 0.0005$ days (Figure 2), which is comparable to that obtained by Nagase et al. (1992), Raichur & Paul (2010), Falanga et al. (2015) or Rodes et al. (2017). The errors in the periods were estimated using the *Peaks* tool inside the time-series analysis package *Period* in *Starlink*. The effect of the barycentric correction on the light curves was found to be negligible and did not need to be taken into consideration. Then, we folded the light curves with the best orbital period to produce energy-resolved orbital intensity profiles using the ephemeris from Falanga et al. (2015). In Table 1 we compiled the ephemeris data used for timing calculations.

As a sample, the resulting orbital light curve between 10.0–20.0 keV is plotted in Figure 1 where the strongest changes are observed as the NS ingresses and egresses from eclipse. We defined ten orbital phase bins corresponding to phase intervals

⁴<http://starlink.eao.hawaii.edu/starlink>.

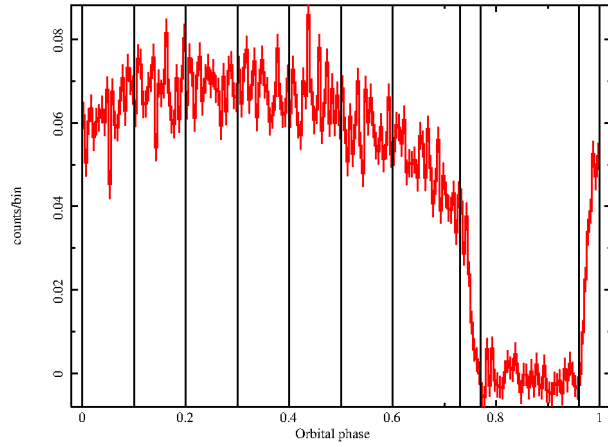


Fig. 1. Background subtracted light curve in 10.0–20.0 keV energy range. The color figure can be viewed online.

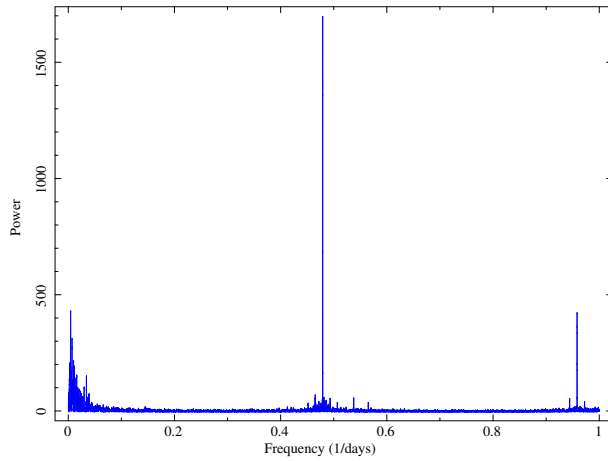


Fig. 2. Lomb-Scargle periodogram of the 2.0–20.0 keV light curve. The color figure can be viewed online.

[0.0–0.1] (post-egress), [0.1–0.2], [0.2–0.3], [0.3–0.4], [0.4–0.5], [0.5–0.6], [0.6–0.73] (pre-ingress), [0.73–0.77] (ingress), [0.77–0.96] (which corresponds to the total eclipse) and [0.96–1.0] (egress).

Another two maximum peaks were present in the Lomb-Scargle periodogram. The first one with a power of 430.03 corresponds to a period of 220 ± 5 days, which might be consistent with the superorbital period of 93.3–435.1 days reported by Sugimoto et al. (2014). The second one with a power of 422.48 corresponds to a period of ≈ 1.04 days, which is a harmonic of the orbital period. In addition, around the superorbital period, there are a few more peaks that can be interpreted as QPOs (Figure 3), as also pointed out by Raichur & Paul (2008a), Raichur & Paul (2008b), Takeshima et al. (1991) and Priedhorsky & Terrell (1983).

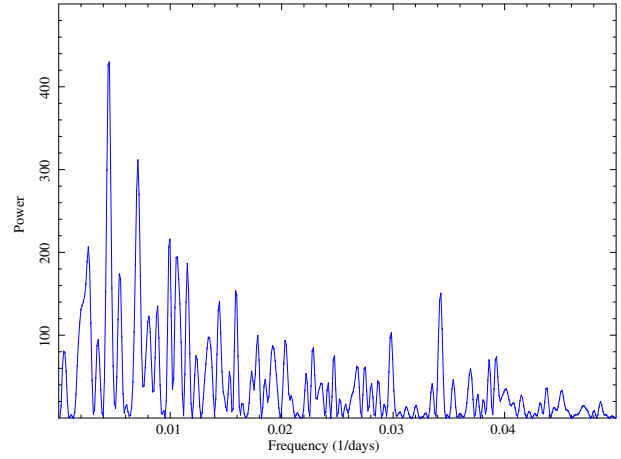


Fig. 3. Zoom of the QPOs in the original 2.0–20.0 keV light curve. The color figure can be viewed online.

It is expected that HMXBs show strong absorption at low energies (below 4 keV), complex iron emission lines between 6.4 keV and 7.2 keV and an energy cutoff at high energies (greater than 10 keV). In order to analyse the light curves variability the *MAXI/GSC* energy range (2.0–20.0 keV) has been divided into 2.0–4.0 keV (low energy), 4.0–10.0 keV (medium energy), 5.7–7.5 keV (iron complex emission lines) and 10.0–20.0 keV (high energy) bands. Therefore, we have calculated the hardness ratio defined as H/S , where H are the net counts in the hard band and S are those obtained in the soft band, between the light curves: (5.7–7.5 keV) / (2.0–4.0 keV), (4.0–10.0 keV) / (5.7–7.5 keV), (10.0–20.0 keV) / (5.7–7.5 keV), (10.0–20.0 keV) / (2.0–4.0 keV), (10.0–20.0 keV) / (4.0–10.0 keV) and (4.0–10.0 keV) / (2.0–4.0 keV).

From the folded light curve, the hardness ratio measurements obtained for each pointing along the orbit had large error bars. Therefore, they were averaged over 150 points and the uncertainties were estimated using error propagation. The overall profile shape was quite similar and consistent with a constant value, so we could not identify any morphology or tendency (see Figure 4, top panel). Figure 4, bottom panel, shows the hardness ratio using a weighted average over 150 bins. The hardness ratio is consistent with a constant ($HR \approx 0.75$) for the out of eclipse indicating there is no significant change in the spectral shape. On the other hand, during the eclipse the brightness of Cen X-3 is also consistent with a constant value ($HR \approx 0.3$) but 2.5 times lower than out of eclipse. Both the drop in brightness at eclipse ingress and the rise in brightness at eclipse egress are quite sharp.

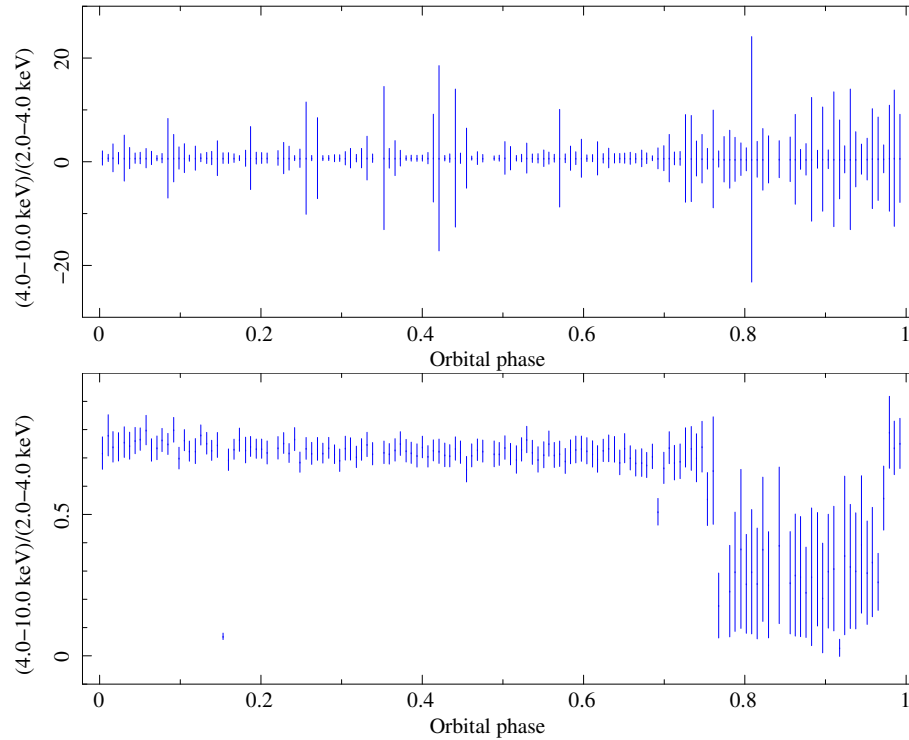


Fig. 4. Hardness ratio $H/S = (4.0 - 10.0 \text{ keV})/(2.0 - 4.0 \text{ keV})$. *Top panel*: using simple average. *Bottom panel*: using weighted average. The color figure can be viewed online.

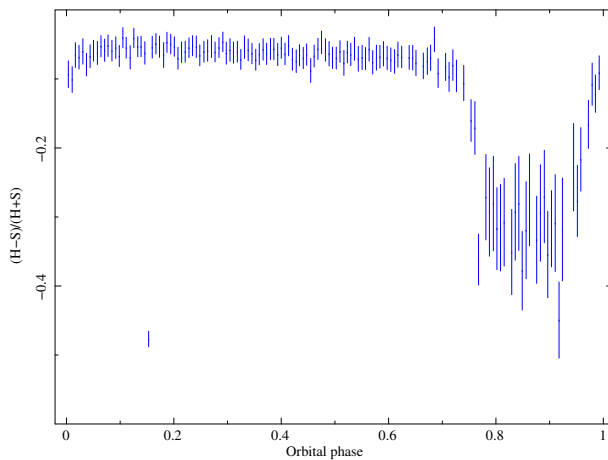


Fig. 5. Hardness curve $(H - S)/(H + S)$ using weighted average, where $H = 4.0 - 10.0 \text{ keV}$ and $S = 2.0 - 4.0 \text{ keV}$ energy bands. The color figure can be viewed online.

The process to obtain the hardness curves $(H - S)/(H + S)$ is the same used to calculate H/S , where $H = 4.0 - 10.0 \text{ keV}$ and $S = 2.0 - 4.0 \text{ keV}$ (Figure 5). The general trend of the hardness curve is very similar to that of the hardness ratio, although the decrease and increase before and after the eclipse is smoother. Moreover, as can be seen in Figures 14

(equation 2) and 15 (equation 5) it is consistent with the behaviour of the unabsorbed flux variation.

During an orbital period of Cen X-3, *MAXI/GSC* can perform up to 33 observations of the object (an example is shown in Figure 6). However, for individual point X-ray sources, the *MAXI/GSC* detector has very short exposures of about 60 s fifteen times a day which is not long enough to extract orbital phase-resolved spectra. As a consequence, it is necessary to accumulate observations in each orbital phase to obtain spectra with a good signal-to-noise ratio.

4. SPECTRAL ANALYSIS

4.1. Orbital Phase Averaged Spectrum

We have extracted the orbital phase averaged spectrum of Cen X-3 (see Figure 7) with *MAXI/GSC* using the *MAXI* on-demand processing⁵, carefully excluding any contamination by nearby brighter sources. For spectral analysis we used the *XSPEC* fitting package, released as a part of *XANADU* in the *HEASoft* tools. We tested both phenomenological and physical models commonly applied to accreting X-ray pulsars and rebinned all extracted spectra to obtain spectral bins by Gaussian distribution.

⁵<http://maxi.riken.jp/mxondem>

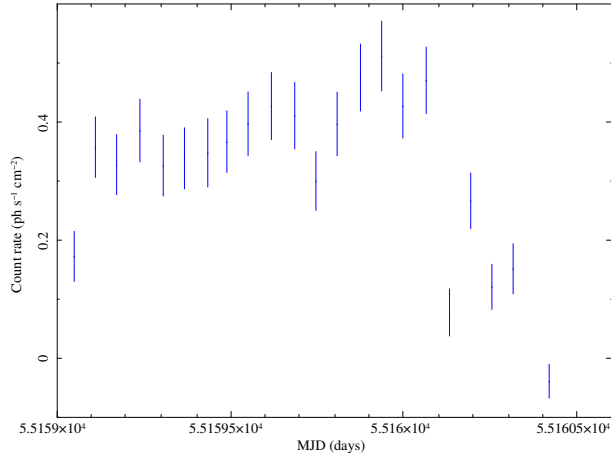


Fig. 6. Light curve in 2.0–20.0 keV energy range for an orbital period of Cen X-3. The color figure can be viewed online.

Absorbed Comptonisation models have been successfully applied to HMXBs in the 2.0–20.0 keV energy range covered by *MAXI/GSC*, such as Vela X-1 (Doroshenko et al. 2013), 4U 1538-52 (Rodes-Roca et al. 2015) and Cen X-3 (Rodes et al. 2017). We started to describe the orbital phase-averaged spectrum using a simple partial absorbed Comptonisation model modified by a Gaussian absorption line at ≈ 5 keV to compensate the incompleteness of the *MAXI/GSC* response (Nakahira private communication). An iron fluorescence emission line present in the spectrum is modelled with a Gaussian component, Fe $K\alpha$ at 6.4 keV. This model is described by equation (1).

$$F(E) = pcfabs \times gabs \times compST + \text{Gaussian line} \quad (1)$$

where, in terms of XSPEC, *pcfabs* is a partial covering fraction absorption that affects only a fraction *f* of the model component multiplied by it, *gabs* is the Gaussian absorption line component, *compST* is the Comptonisation of cool photons on hot electrons (Sunyaev & Titarchuk 1980), and the Gaussian line is added to describe the Fe $K\alpha$ line. The absorption cross sections were taken from Verner & Yakovlev (1995) and the abundances were set to those of Wilms et al. (2000).

Although this model describes the averaged spectra between 2.0–20.0 keV well ($\chi_r^2 = 1.09$), it cannot offer a good statistical and/or physical solution for all orbital phase-resolved spectra. For example, fitting the eclipse spectrum, i.e. when the direct X-ray emission is totally blocked by the companion, we obtained that the covering fraction factor was $f \approx 0$. Model parameters were also not well constrained. As the aim was to satisfactorily describe both the aver-

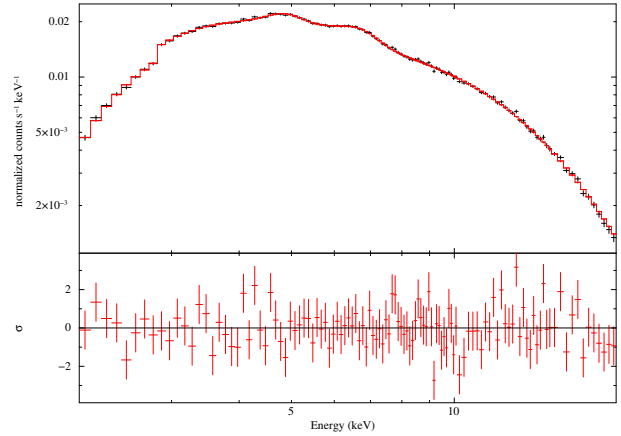


Fig. 7. Orbital phase averaged spectrum of Cen X-3 in the 2.0–20.0 keV band. *Top panel*: data and best-fit model described by equation (2). *Bottom panel*: residuals between the spectrum and the model. The resulting fit parameters are reported in Table 2. The color figure can be viewed online.

aged spectrum and the orbital phase-resolved spectra with the same model, it was decided to reject it.

Recently, Aftab et al. (2019) and Sanjurjo-Ferrín et al. (2021) carried out spectral analysis of *XMM-Newton* data in the eclipse and out-of-eclipse phases in the energy band (0.8–10.0 keV). They obtained best fits by combining blackbody and power-law components and used them to describe both eclipse and out-of-eclipse spectra. In addition, Wojdowski et al. (2001) argued that the stellar wind in the system is smooth and concluded that the wind is most likely driven by X-ray heating of the illuminated surface of the companion star as proposed by Day & Stevens (1993). Compared to previous studies, thanks to *MAXI/GSC*'s observation strategy, a large number of complete orbits have been observed and divided into 10 orbital phase intervals. According to the previous discussion, finally, models including either a blackbody component (*bbody* in XSPEC) or a Comptonisation component (*compST* in XSPEC) have been combined to describe the average spectrum.

Interstellar medium (ISM) absorption and local absorption components have been included by means of a partial covering fraction defined through the parameter *C*. The *tbnew*⁶ component is a recent version of the Tübingen-Boulder absorption model which updates the absorption cross sections and abundances (Wilms et al. 2000); the *gabs* factor has been described above; *po* is a simple photon power

⁶<https://pulsar.sternwarte.uni-erlangen.de/wilms/research/tbabs/>

TABLE 2
BEST-FIT MODEL PARAMETERS FOR THE
AVERAGED SPECTRUM^a

Component	Parameter	Value
P.c.f.	C	0.71 ± 0.08
$tbnew$	N_H^1 [10^{22} atoms cm^{-2}]	19_{-3}^{+4}
	N_H^2 [10^{22} atoms cm^{-2}]	$2.5_{-0.5}^{+0.6}$
$gabs$	E[keV]	5.12 ± 0.05
	σ [keV]	0.02 (<i>frozen</i>)
	line depth	$0.7_{-0.4}^{+1.2}$
<i>Power law</i>	Photon index Γ	2.16 ± 0.15
	norm [$\text{keV}^{-1} \text{s}^{-1} \text{cm}^{-2}$]	$0.44_{-0.11}^{+0.14}$
$bbody$	kT [keV]	3.46 ± 0.04
	norm [L_{39}/D_{10}^2]	$0.0171_{-0.0018}^{+0.0021}$
Fe $K\alpha$	Line E [keV]	6.42 (<i>frozen</i>)
	σ [keV]	0.01 (<i>frozen</i>)
	EW [keV]	0.023 ± 0.004
	norm [$10^{-4} \text{ph s}^{-1} \text{cm}^{-2}$]	8.0 ± 1.3
Fe XXV	Line E [keV]	6.69 (<i>frozen</i>)
	σ [keV]	0.01 (<i>frozen</i>)
	EW [keV]	0.025 ± 0.004
	norm [$10^{-4} \text{ph s}^{-1} \text{cm}^{-2}$]	8.4 ± 1.3
Fe XXVI	Line E [keV]	6.99 (<i>frozen</i>)
	σ [keV]	0.01 (<i>frozen</i>)
	EW [keV]	0.017 ± 0.004
	norm [$10^{-4} \text{ph s}^{-1} \text{cm}^{-2}$]	5.2 ± 1.3
χ_r^2	$\chi^2/(\text{d.o.f.}) = 115/106 = 1.1$	

^aParameters for equation (2). P.c.f. is the partial covering fraction. EW represents the equivalent width of the emission line. Uncertainties are given at the 90% ($\Delta\chi^2 = 2.71$) confidence limit and d.o.f is degrees of freedom.

law consisting of a dimensionless photon index (Γ) and the normalisation constant (K), the spectral photons $\text{keV}^{-1} \text{cm}^{-2} \text{s}^{-1}$ at 1 keV; $bbody$ corresponds to a blackbody model whose parameters include the temperature kT_{bb} in keV and the normalisation $norm$, defined as L_{39}/D_{10}^2 , where L_{39} is the source luminosity in units of $10^{39} \text{erg s}^{-1}$ and D_{10}^2 is the distance to the source in units of 10 kpc. This model is given by equation (2).

$$F(E) = (C \times tbnew + (1 - C) \times tbnew) [gabs \times (po + bbody + GL)], \quad (2)$$

where GL represents the Gaussian functions added to account for the emission lines. Here, parameters

derived from ASCA data by Ebisawa et al. (1996) were used to describe the Fe $K\alpha$ complex.

Fitted parameters for the continuum model are listed in Table 2 where it is also included the equivalent width (EW) of the Gaussian emission lines. Figure 7 shows the data, the best-fit model described by equation (2), and residuals as the difference between observed flux and model flux divided by the uncertainty of the observed flux.

Since the surface luminosity of a blackbody only depends on its temperature, it is possible to calculate the radius of the emitting region, R_{bb} , by using the expression:

$$R_{\text{bb}}(\text{km}) = 3.04 \times 10^4 \frac{D\sqrt{F_{\text{bb}}}}{T_{\text{bb}}^2}, \quad (3)$$

where D is the distance to the source in kpc, F_{bb} is the unabsorbed flux in $\text{erg s}^{-1} \text{cm}^{-2}$ in the energy range 2.0–20.0 keV, T_{bb} the temperature in keV. Taking into account the distance to the source given by *GAI A (E)DR3* $d(\text{kpc}) = 6.8_{-0.5}^{+0.6}$, and an unabsorbed flux of $(1.7_{-0.4}^{+0.5}) \times 10^{-9} \text{erg s}^{-1} \text{cm}^{-2}$ in the *MAXI/GSC* energy band, from equation (3) we found a radius of the emitting surface of $R_{\text{bb}} = 0.71_{-0.16}^{+0.19} \text{km}$. If we assume thermal emission from the NS polar cap, this radius may be consistent with the expected size (also compatible with Sanjurjo-Ferrín et al. 2021).

The intrinsic bolometric X-ray luminosity is a key parameter to infer the stellar wind parameters and the details of the accretion processes. It is usually estimated from the measured X-ray flux of the source by using equation (4). Although the accretion flow is not expected to be as isotropic as the stellar wind, here, it is assumed that the system is emitting isotropically. A few cautions should be kept in mind when using this assumption: in accreting neutron stars, the bulk of the x-rays are produced in the accretion columns near the two magnetic poles; the emission profiles of these regions are not well known; the bolometric flux is measured on a small energy band and derived from phenomenological rather than physically justified models (see Martínez-Núñez et al. (2017) for a review of stellar winds from massive stars).

$$L_X = 4\pi D^2 f_{\text{no-abs}}, \quad (4)$$

where L_X is the X-ray luminosity, D is the distance to the source and $f_{\text{no-abs}}$ is the unabsorbed flux in the 2.0–20.0 keV energy band. We obtained $L_X = (1.9_{-0.8}^{+1.0}) \times 10^{37} \text{erg s}^{-1}$, $f_{\text{no-abs}} = (3.5_{-0.9}^{+1.1}) \times 10^{-9} \text{erg s}^{-1} \text{cm}^{-2}$, indicating

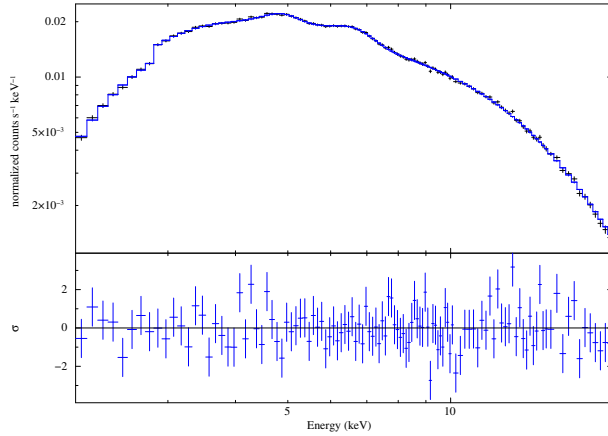


Fig. 8. Orbital phase averaged spectra of Cen X-3 in the 2.0–20.0 keV band. *Top panel*: data and best-fit model (equation (5)). *Bottom panel*: residuals between the spectrum and the model. The resulting fit parameters are reported in Table 3. The color figure can be viewed online.

that the accretion mode is not only due to the stellar wind ($> 10^{36}$ erg s $^{-1}$) but should also be enhanced by disk accretion or gas stream accretion.

From the *bbody* normalization, L_{39}/D_{10}^2 , a value of $0.04^{+0.09}_{-0.08}$ is derived, which is consistent with the experimental result if we take into account the uncertainties of the parameters.

Another model has been also tested by replacing the blackbody by a Comptonisation model, maintaining the rest of the components unchanged. This model is described by equation (5).

$$F(E) = (C \times tbnew + (1 - C) \times tbnew) [gabs \times (po + compST + GL)]. \quad (5)$$

Best-fit model parameters are listed in Table 3 and Figure 8 shows the averaged spectrum. From the model, the inferred unabsorbed flux was $(3^{+6}_{-1}) \times 10^{-9}$ erg s $^{-1}$ cm $^{-2}$ in the MAXI/GSC energy band, corresponding to an X-ray luminosity of $L_X = (2^{+3}_{-1}) \times 10^{37}$ erg s $^{-1}$ which agrees completely with the previous result.

The Comptonisation parameter $y = kT\tau^2/(m_e c^2)$, where k is the Boltzmann constant, T is the temperature, τ is the optical depth, m_e is the electron mass and c is the light speed, determines the efficiency of the Comptonisation process (Titarchuk 1994; Prat et al. 2008), and its value from the averaged spectrum $y = 2.7^{+0.2}_{-0.3}$ indicates an efficient process that corresponds to a moderate accretion rate.

The iron fluorescence emission line shows an interesting evolution along the orbital phase: it is

TABLE 3
BEST-FIT MODEL PARAMETERS FOR THE AVERAGED SPECTRUM^a

Component	Parameter	Value
P.c.f.	C	$0.80^{+0.09}_{-0.08}$
<i>tbnew</i>	N_H^1 [10^{22} atoms cm $^{-2}$]	15^{+4}_{-3}
	N_H^2 [10^{22} atoms cm $^{-2}$]	$1.9^{+1.2}_{-0.8}$
<i>gabs</i>	E[keV]	5.12 ± 0.05
	σ [keV]	0.02 (<i>frozen</i>)
	line depth	$0.5^{+0.8}_{-0.3}$
<i>Power law</i>	Γ	$2.6^{+0.8}_{-0.5}$
	norm [$\text{keV}^{-1} \text{s}^{-1} \text{cm}^{-2}$]	$0.3^{+0.5}_{-0.1}$
<i>compST</i>	kT [keV]	3.935 ± 0.009
	τ	$18.6^{+0.8}_{-1.0}$
	norm	$0.08^{+0.03}_{-0.02}$
Fe K α	Line E [keV]	6.42 (<i>frozen</i>)
	σ [keV]	0.01 (<i>frozen</i>)
	EW [keV]	0.035 ± 0.004
	norm [10^{-3} ph s $^{-1}$ cm $^{-2}$]	1.05 ± 0.11
Fe XXV	Line E [keV]	6.69 (<i>frozen</i>)
	σ [keV]	0.01 (<i>frozen</i>)
	EW [keV]	0.016 ± 0.004
	norm [10^{-4} ph s $^{-1}$ cm $^{-2}$]	4.8 ± 1.1
Fe XXVI	Line E [keV]	6.99 (<i>frozen</i>)
	σ [keV]	0.01 (<i>frozen</i>)
	EW [keV]	0.021 ± 0.004
	norm [10^{-4} ph s $^{-1}$ cm $^{-2}$]	5.2 ± 1.1
χ_r^2	$\chi^2/(\text{d.o.f.}) = 112/105 = 1.1$	

^aParameters for equation (5). P.c.f. is the partial covering fraction. EW represents the equivalent width of the emission line. Uncertainties are given at the 90% confidence limit and d.o.f is degrees of freedom.

centred at 6.4 keV out-of-eclipse but it is shifted to 6.7 keV at the ingress suggesting the coexistence of two iron lines at different energies (Rodes et al. 2017). Sensitive X-ray observatories such as *ASCA* and *XMM-Newton* have detected and resolved the Fe complex in Cen X-3 (Ebisawa et al. 1996; Sanjurjo-Ferrín et al. 2021, respectively). In contrast, MAXI/GSC is not able to resolve it and therefore the values obtained for these lines by Ebisawa et al. (1996) have been used to fit them. For this purpose, all their parameters except the line intensities were fixed (see Tables 2 and 3). The line flux ratio $[\text{Fe XXVI}]/[\text{Fe XXV}]$ can be used to estimate the ionisation state of the emitting plasma.

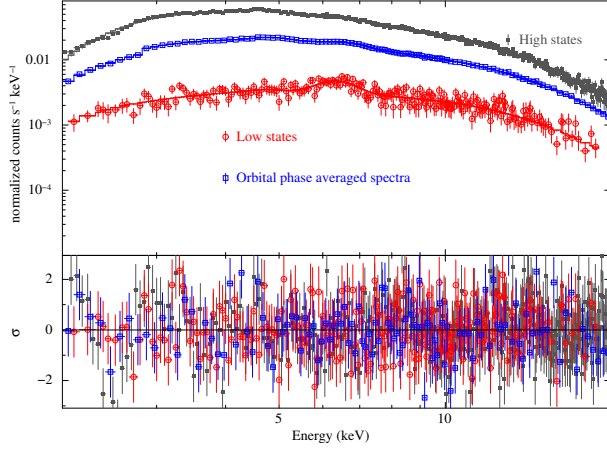


Fig. 9. Orbital phase averaged, high states and low states spectra of Cen X-3 in the 2.0–20.0 keV band. *Top panel:* Data and best-fit models (defined by equation (2)). *Bottom panel:* residuals for the model. The resulting fit parameters are reported in Table 4. The color figure can be viewed online.

The results obtained in the averaged spectrum for both models were 0.6 ± 0.3 (equation 2) and 1.1 ± 0.5 (equation 5), respectively. Assuming that this procedure is an approximation of the ionisation state of the system, these average values point to a highly ionised plasma with $\log \xi \approx (3.4 - 3.8)$, according to the ionisation parameter calculated by Ebisawa et al. (1996, their Figure 8, upper panel).

Since the partial covering fraction modifies the continuum at low energies, two hydrogen column components were applied: one to describe the ISM towards the system, N_H^2 , and the other to describe the ISM plus local absorption, N_H^1 . The mean value of the Galactic column density of hydrogen $N_{H,tot}$ in the direction of Cen X-3 is $1.16 \times 10^{22} \text{ cm}^{-2}$ (Willingale et al. 2013). Valencic & Smith (2015) reported an ISM absorption towards this source of $(1.6 \pm 0.3) \times 10^{22} \text{ cm}^{-2}$. The column N_H^2 derived from both models are compatible taking into account its uncertainties.

4.2. Orbital Phase Averaged, High and Low States Spectra with MAXI/GSC

As a consequence of the large variability of the light curve, high and low states have been defined. Thus, the good time intervals (GTIs) of both states have been identified in the energy range 2.0–20.0 keV and their respective averaged spectra have been extracted. In this analysis, we fitted the high and low states spectra with the same models as we used in the orbital phase-averaged spectrum, except that only a single Gaussian has been included here. The fits are shown in Figures 9 and 10; meanwhile, the best-fit

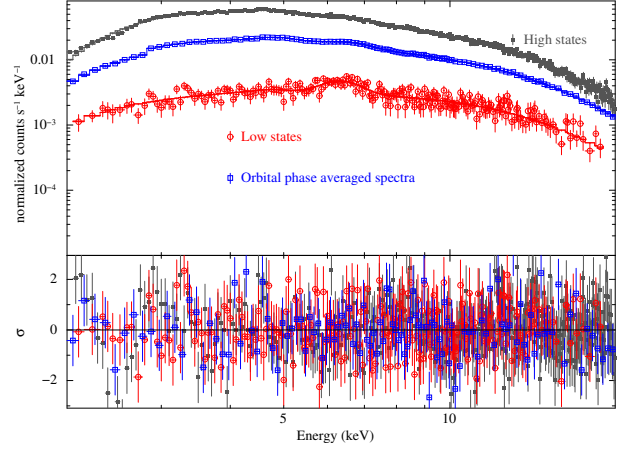


Fig. 10. Orbital phase averaged, high states and low states spectra of Cen X-3 in the 2.0–20.0 keV band. *Top panel:* Data and best-fit models (defined by equation (5)). *Bottom panel:* residuals for the model. The resulting fit parameters are reported in Table 5. The color figure can be viewed online.

model parameters are listed in Tables 4 (equation 2) and 5 (equation 5).

To determine the periods of high and low activity we established a number of counts greater than $\approx 0.5 \text{ photons s}^{-1} \text{ cm}^{-2}$ and less than $\approx 0.3 \text{ photons s}^{-1} \text{ cm}^{-2}$, respectively. Then, more than 100 bins (one bin $\approx 0.1 \text{ MJD}$) were accumulated to calculate the low-activity intervals and grouped 10 bins by 10 bins for the high-activity events.

The unabsorbed fluxes of the orbital phase-averaged, high and low activity spectra in units of $\text{erg s}^{-1} \text{ cm}^{-2}$ are $(1.72 \pm 0.03) \times 10^{-9}$, $(4.1^{+1.3}_{-1.0}) \times 10^{-9}$ and $(5.4^{+1.5}_{-1.2}) \times 10^{-10}$, respectively. For such fluxes, the radius of the blackbody emitting area is found $R_{bb} = 0.71^{+0.07}_{-0.06} \text{ km}$ (averaged spectra), $R_{bb} = 1.6 \pm 0.5 \text{ km}$ (high states) and $R_{bb} = 0.36^{+0.12}_{-0.10} \text{ km}$ (low states). All values are on the order of 1 to 2 km which is compatible with a hot spot on the NS surface (Sanjurjo-Ferrín et al. 2021).

Using the definition of the *bbody* normalization, L_{39}/D_{10}^2 , we have derived its value in the three spectra: $0.04^{+0.08}_{-0.07}$ (averaged spectra), 0.1 ± 0.3 (high states) and $0.009^{+0.019}_{-0.016}$ (low states). These values are consistent with the experimental ones, taking the uncertainties into account (see Table 4).

The Comptonisation parameter y (see Table 6) shows an efficient process that corresponds to a moderate accretion rate if we take into account the uncertainties.

TABLE 4

BEST-FIT MODEL PARAMETERS FOR THE AVERAGED, HIGH STATES AND LOW STATES SPECTRA^a

Component	Parameter	Value
P.c.f.	C	0.809 ± 0.003
<i>tbnew</i>	$N_H^1 [10^{22} \text{ atoms cm}^{-2}]$	18.8 ± 0.6
	$N_H^2 [10^{22} \text{ atoms cm}^{-2}]$	2.57 ± 0.07
<i>gabs</i>	E[keV]	5.12 (<i>frozen</i>)
	σ [keV]	0.02 (<i>frozen</i>)
	line depth	0.7 (<i>frozen</i>)
<i>Power law</i>	Γ	2.184 ± 0.009
	norm [$\text{keV}^{-1} \text{ s}^{-1} \text{ cm}^{-2}$]	0.405 ± 0.006
<i>bbody</i>	kT [keV]	3.4628 ± 0.0023
	norm [L_{39}/D_{10}^2]	0.01527 ± 0.00014
Fe $K\alpha$	Line E [keV]	6.67 ± 0.05
	σ [keV]	$0.28_{-0.08}^{+0.07}$
	EW [keV]	0.070 ± 0.004
	norm [$10^{-3} \text{ ph s}^{-1} \text{ cm}^{-2}$]	1.98 ± 0.12
χ_r^2	$\chi^2/(\text{d.o.f.}) = 115/108 = 1.1$	
P.c.f.	C	0.800 ± 0.003
<i>tbnew</i>	$N_H^1 [10^{22} \text{ atoms cm}^{-2}]$	63_{-11}^{+17}
	$N_H^2 [10^{22} \text{ atoms cm}^{-2}]$	6.9 ± 0.5
<i>gabs</i>	E[keV]	5.12 (<i>frozen</i>)
	σ [keV]	0.02 (<i>frozen</i>)
	line depth	0.7 (<i>frozen</i>)
<i>Power law</i>	Γ	$2.65_{-0.21}^{+0.22}$
	norm [$\text{keV}^{-1} \text{ s}^{-1} \text{ cm}^{-2}$]	$3.8_{-0.9}^{+1.2}$
<i>bbody</i>	kT [keV]	$2.87_{-0.18}^{+0.09}$
	norm [L_{39}/D_{10}^2]	0.033 ± 0.004
χ_r^2	$\chi^2/(\text{d.o.f.}) = 452/351 = 1.3$	

During the high state, when L_X is close to $10^{38} \text{ erg s}^{-1}$, the Fe $K\alpha$ is not present in the spectrum. Moreover, the EW of the Fe $K\alpha$ is three times higher during the low states than that in the averaged spectra. These facts suggest that the strong x-ray radiation may mask the possible presence of iron emission lines.

The unabsorbed flux is found to vary with a similar trend for both models. In fact, the X-ray luminosity is the same, taking the uncertainties into account (see Table 6, Column 2 corresponds to equation 2 and Column 3 corresponds to equation 5). On the one hand, it indicates (for averaged spectra and high states) that the accretion mode is not only due to the stellar wind ($> 10^{36} \text{ erg s}^{-1}$) but should also be enhanced by disk accretion or gas stream accretion. On the other hand, the luminosity indicates that the accretion mode in low states spectra is due

TABLE 4 (CONTINUED)

BEST-FIT MODEL PARAMETERS FOR THE AVERAGED, HIGH STATES AND LOW STATES SPECTRA^a

Component	Parameter	Value
P.c.f.	C	0.80 ± 0.03
<i>tbnew</i>	$N_H^1 [10^{22} \text{ atoms cm}^{-2}]$	18_{-5}^{+7}
	$N_H^2 [10^{22} \text{ atoms cm}^{-2}]$	$1.4_{-0.7}^{+0.9}$
<i>gabs</i>	E[keV]	5.12 (<i>frozen</i>)
	σ [keV]	0.02 (<i>frozen</i>)
	line depth	0.69 (<i>frozen</i>)
<i>Power law</i>	Γ	2.55 ± 0.18
	norm [$\text{keV}^{-1} \text{ s}^{-1} \text{ cm}^{-2}$]	$0.071_{-0.016}^{+0.020}$
<i>bbody</i>	kT [keV]	$3.67_{-0.17}^{+0.18}$
	norm [L_{39}/D_{10}^2]	$0.0050_{-0.0003}^{+0.0004}$
Fe $K\alpha$	Line E [keV]	6.31 ± 0.10
	σ [keV]	$0.22_{-0.22}^{+0.19}$
	EW [keV]	0.22 ± 0.04
	norm [$10^{-3} \text{ ph s}^{-1} \text{ cm}^{-2}$]	1.6 ± 0.3
χ_r^2	$\chi^2/(\text{d.o.f.}) = 206/220 = 0.9$	

^aParameters for equation (2). P.c.f. is the partial covering fraction. EW represents the equivalent width of the emission line. Uncertainties are given at the 90% confidence limit and d.o.f is degrees of freedom.

to stellar wind. Therefore, the difference in X-ray luminosity between the high and low states can be attributed to a decrease in the accretion rate rather than an overall rise in absorption.

Tables 7 and 8 show the unabsorbed flux and the luminosity of each model component (equations 2 and 5, respectively) as well as the total unabsorbed fluxes and luminosities whose values agree with those given in Table 6.

4.3. Orbital Phase-Resolved Spectra with MAXI/GSC

Previous studies following this direction of analysis have been performed in one or two orbits (Nagase et al. 1992; Suchy et al. 2008) or over shorter orbital phases (Ebisawa et al. 1996; Audley et al. 1996; Woźdowski et al. 2001; Aftab et al. 2019; Sanjurjo-Ferrín et al. 2021). We have obtained orbital phase-resolved spectra of the HMXB pulsar Cen X-3, accumulating the 60 s duration scans into ten orbital phase bins covering entirely its orbit (Rodes-Roca et al. 2015).

Based on the results from § 4.1, we fitted the orbital phase-resolved spectra with the same two models as we used in the orbital phase-averaged spectrum. Both models gave acceptable fits to observational data and the results are shown in Figures 11 and 12 for selected orbital phase-resolved spectra.

TABLE 5
BEST-FIT MODEL PARAMETERS FOR THE
AVERAGED, HIGH STATES AND LOW STATES
SPECTRA^a

Component	Parameter	Value
P.c.f.	C	0.813 ± 0.004
<i>tbnew</i>	$N_H^1 [10^{22} \text{ atoms cm}^{-2}]$	15.9 ± 0.5
	$N_H^2 [10^{22} \text{ atoms cm}^{-2}]$	2.22 ± 0.08
<i>gabs</i>	E[keV]	5.12 (<i>frozen</i>)
	σ [keV]	0.02 (<i>frozen</i>)
	line depth	0.5 (<i>frozen</i>)
<i>Power law</i>	Γ	2.612 ± 0.023
	norm [$\text{keV}^{-1} \text{ s}^{-1} \text{ cm}^{-2}$]	0.323 ± 0.011
<i>compST</i>	kT [keV]	3.90 ± 0.04
	τ	$19.26^{+0.24}_{-0.23}$
	norm	0.0709 ± 0.0013
Fe $K\alpha$	Line E [keV]	6.65 ± 0.04
	σ [keV]	0.28 ± 0.07
	EW [keV]	0.074 ± 0.004
	norm [$10^{-3} \text{ ph s}^{-1} \text{ cm}^{-2}$]	2.04 ± 0.12
χ_r^2	$\chi^2/(\text{d.o.f.}) = 111/107 = 1.0$	
P.c.f.	C	$0.840^{+0.012}_{-0.011}$
<i>tbnew</i>	$N_H^1 [10^{22} \text{ atoms cm}^{-2}]$	66^{+4}_{-3}
	$N_H^2 [10^{22} \text{ atoms cm}^{-2}]$	$6.87^{+0.12}_{-0.11}$
<i>gabs</i>	E[keV]	5.12 (<i>frozen</i>)
	σ [keV]	0.02 (<i>frozen</i>)
	line depth	0.5 (<i>frozen</i>)
<i>Power law</i>	Γ	2.603 ± 0.012
	norm [$\text{keV}^{-1} \text{ s}^{-1} \text{ cm}^{-2}$]	3.42 ± 0.07
<i>compST</i>	kT [keV]	2.85 ± 0.05
	τ	48^{+8}_{-6}
	norm	$0.023^{+0.006}_{-0.005}$
χ_r^2	$\chi^2/(\text{d.o.f.}) = 452/350 = 1.3$	

The degeneracy between the properties of the accretion rate and the physical parameters of the NS in all available models produces a certain degree of degeneracy between fit parameters. The behaviour of different parameters of the model described by equation (5) towards eclipse suggests degeneracies between them. To better explore the photon index variation, we constrained its value to the interval obtained between orbital phase 0.0 to 0.6, i.e. $1.90 < \Gamma < 2.85$, and fitted the spectra of pre-ingress, ingress, eclipse and egress orbital phases again. The errors were obtained with the *error* task, provided by XSPEC, and with propagation of uncertainties. The new values obtained by this procedure differed only slightly from the previous values within errors. However, the photon index was not

TABLE 5 (CONTINUED)
BEST-FIT MODEL PARAMETERS FOR THE
AVERAGED, HIGH STATES AND LOW STATES
SPECTRA^a

Component	Parameter	Value
P.c.f.	C	$0.80^{+0.04}_{-0.03}$
<i>tbnew</i>	$N_H^1 [10^{22} \text{ atoms cm}^{-2}]$	18^{+7}_{-5}
	$N_H^2 [10^{22} \text{ atoms cm}^{-2}]$	$1.1^{+0.9}_{-0.7}$
<i>gabs</i>	E[keV]	5.12 (<i>frozen</i>)
	σ [keV]	0.02 (<i>frozen</i>)
	line depth	0.5 (<i>frozen</i>)
<i>Power law</i>	Γ	2.37 ± 0.17
	norm [$\text{keV}^{-1} \text{ s}^{-1} \text{ cm}^{-2}$]	$0.055^{+0.015}_{-0.012}$
<i>compST</i>	kT [keV]	3.7 ± 0.3
	τ	43^{+22}_{-9}
	norm	$0.0026^{+0.0014}_{-0.0013}$
Fe $K\alpha$	Line E [keV]	6.31 ± 0.10
	σ [keV]	$0.22^{+0.17}_{-0.22}$
	EW [keV]	0.22 ± 0.03
	norm [$10^{-3} \text{ ph s}^{-1} \text{ cm}^{-2}$]	1.61 ± 0.23
χ_r^2	$\chi^2/(\text{d.o.f.}) = 206/219 = 0.9$	

^aParameters for equation (5). P.c.f. is the partial covering fraction. EW represents the equivalent width of the emission line. Uncertainties are given at the 90% confidence limit and d.o.f is degrees of freedom.

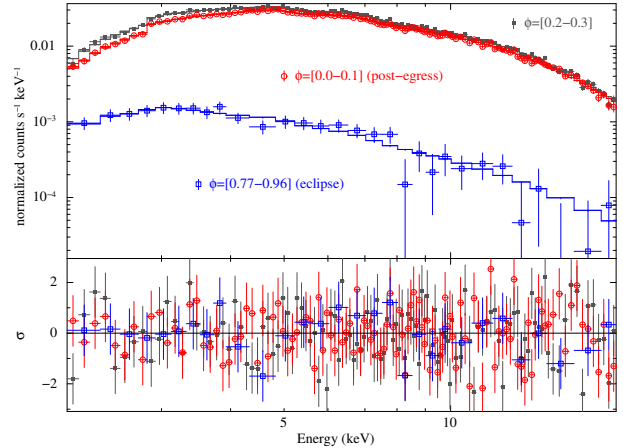


Fig. 11. Orbital phase-resolved spectra of Cen X-3 in the 2.0–20.0 keV band. *Top panel*: Selected spectra and best-fit models (defined by equation (2)). *Bottom panel*: residuals for the model. The color figure can be viewed online.

well constrained and exhibited relatively large errors. Our results are marked with open blue circles in Figures 14–18 and 20, where filled red squares represent the initial parameter values. The possible degeneracy between the spectral photon index Γ and absorption spectral parameters is known. Therefore,

TABLE 6
X-RAY LUMINOSITY (10^{37} ERG S $^{-1}$) AND COMPTONISATION PARAMETER

Orbital phase	L_x (equation 2)	L_x (equation 5)	$y = k T \tau^2 / (m_e c^2)$
Averaged	$1.9^{+0.4}_{-0.3}$	$1.9^{+0.4}_{-0.3}$	2.83 ± 0.10
High states	6 ± 3	$6.3^{+1.3}_{-1.0}$	13^{+5}_{-3}
Low states	$0.40^{+0.18}_{-0.15}$	$0.40^{+0.18}_{-0.14}$	13^{+15}_{-7}

TABLE 7
UNABSORBED FLUX (10^{-9} ERG S $^{-1}$ CM $^{-2}$)
AND LUMINOSITY (10^{37} ERG S $^{-1}$)*

Component	Unabs. flux (equation 2)	L_x (equation 2)
<i>Power law</i>	1.72 ± 0.03	$0.95^{+0.19}_{-0.15}$
<i>bbody</i>	1.72 ± 0.03	$0.95^{+0.19}_{-0.15}$
Fe K α	0.0343 ± 0.0005	$0.019^{+0.004}_{-0.003}$
Total	3.47 ± 0.06	$1.9^{+0.4}_{-0.3}$
<i>Power law</i>	$7.3^{+2.3}_{-1.7}$	4.1 ± 2.0
<i>bbody</i>	$4.1^{+1.3}_{-1.0}$	$2.2^{+1.1}_{-0.9}$
Total	11^{+4}_{-3}	6 ± 3
<i>Power law</i>	0.16 ± 0.04	$0.09^{+0.04}_{-0.03}$
<i>bbody</i>	$0.54^{+0.15}_{-0.12}$	$0.30^{+0.14}_{-0.11}$
Fe K α	$0.026^{+0.007}_{-0.006}$	$0.014^{+0.007}_{-0.005}$
Total	$0.73^{+0.20}_{-0.17}$	$0.40^{+0.19}_{-0.15}$

*For the model components for the averaged, high states and low states spectra.

TABLE 8
UNABSORBED FLUX (10^{-9} ERG S $^{-1}$ CM $^{-2}$)
AND LUMINOSITY (10^{37} ERG S $^{-1}$)*

Component	Unabs. flux (equation 5)	L_x (equation 5)
<i>Power law</i>	0.676 ± 0.023	$0.37^{+0.08}_{-0.07}$
<i>compST</i>	2.67 ± 0.09	1.5 ± 0.3
Fe K α	0.0353 ± 0.0012	$0.020^{+0.004}_{-0.003}$
Total	3.38 ± 0.11	1.9 ± 0.4
<i>Power law</i>	7.49 ± 0.15	$4.2^{+0.8}_{-0.7}$
<i>compST</i>	3.94 ± 0.08	2.2 ± 0.4
Total	11.43 ± 0.23	$6.4^{+1.2}_{-1.1}$
<i>Power law</i>	$0.17^{+0.05}_{-0.04}$	$0.09^{+0.04}_{-0.03}$
<i>compST</i>	$0.52^{+0.14}_{-0.11}$	$0.29^{+0.13}_{-0.10}$
Fe K α	$0.026^{+0.007}_{-0.006}$	$0.014^{+0.007}_{-0.005}$
Total	$0.72^{+0.20}_{-0.17}$	$0.39^{+0.18}_{-0.14}$

*For the model components for the averaged, high states and low states spectra.

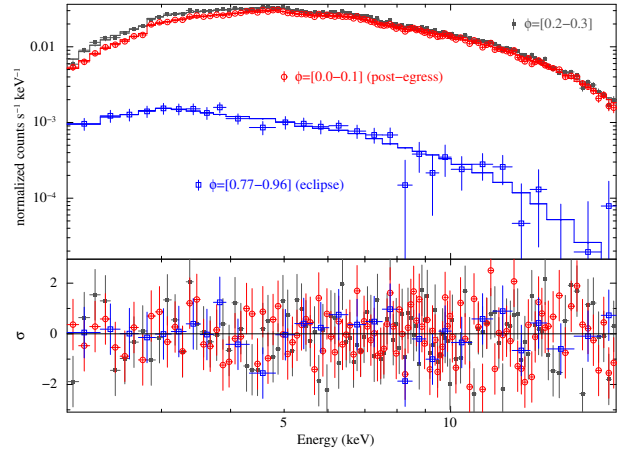


Fig. 12. Orbital phase-resolved spectra of Cen X-3 in the 2.0–20.0 keV band. *Top panel*: Selected spectra and best-fit models (defined by equation (5)). *Bottom panel*: residuals for the model. The color figure can be viewed online.

we produced χ^2 contour plots of Γ and N_H^1 for both models (see Figure 13). It is clear from this figure that the value of N_H^1 is moderately correlated to that of Γ as expected. However, the narrow energy band of MAXI/GSC as well as the observational mode makes it extremely difficult to remove this degeneracy through spectral fitting. In the following, we discuss the orbital phase spectral variation of the model parameters described by equations (2) and (5).

In Figures 14–18 and 20–21, we show the evolution of the relevant parameters of both models throughout orbital phase. The temperature of the blackbody is almost constant, decreasing drastically in the eclipse and increasing in the eclipse-egress. That implies that the emission zone of this component should be large. The normalisation of the blackbody component shows a smooth decrease, which could be compatible with a constant value, reaching the minimum value at eclipse (Figure 14). The radius of the emission zone is of the order of 1 to 3 km whereas in eclipse it is about 9 ± 3 km (Figure 14). This fact could suggest soft X-ray reflection

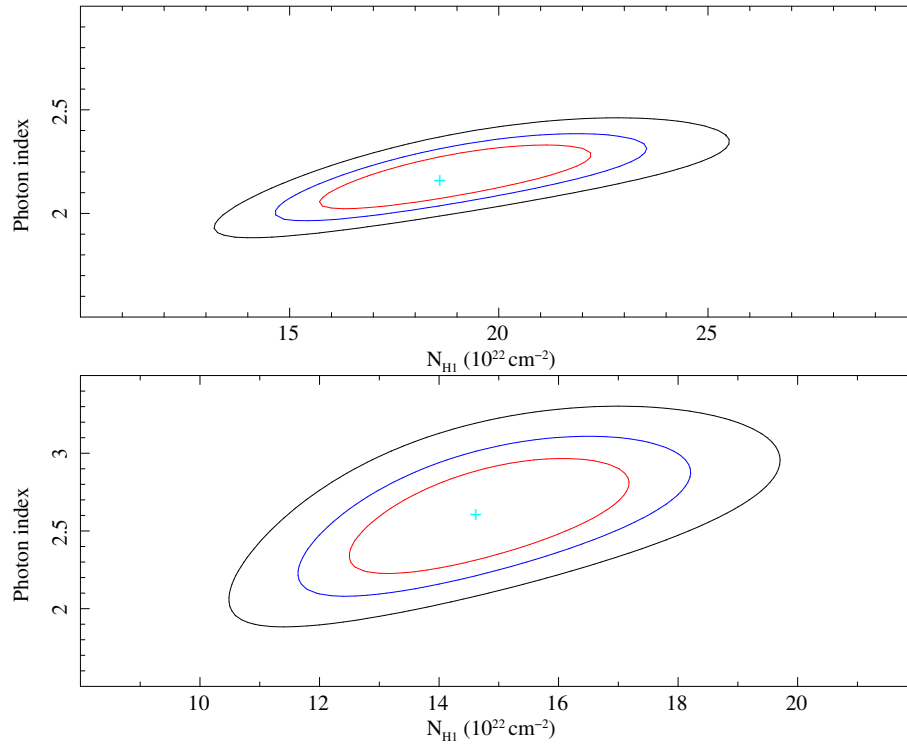


Fig. 13. The ellipses are χ^2 -contours for two parameters (N_H^1 and Γ). The contours are 68%, 90% and 99% confidence levels for two interesting parameters. *Top panel*: averaged spectrum fitted by equation (2). *Bottom panel*: averaged spectrum fitted by equation (5). The color figure can be viewed online.

from the inner accretion disk region and agree with that reported by Sanjurjo-Ferrín et al. (2021).

When the neutron star is embedded into the stellar wind of the donor, the hydrogen column density shows a modulation along the orbit. Therefore, besides the interstellar medium absorption component (consistent with a constant value), we also allowed for the presence of a local absorber, modulated by a partial covering fraction that acts as a proxy for some features of the stellar wind of the donor star or the surroundings of the compact object.

For the model defined by equation (2), the normalisation of the power law decreases smoothly during out-of-eclipse before reaching a minimum during pre-eclipse, eclipse and eclipse-egress (Figure 14). The power-law photon index is rather stable during all orbital phases ($\Gamma \approx 2.1$), but it drops to ≈ 1.3 in the eclipse-egress ([0.96-1.0]) (Figure 20, top panel).

For the model defined by equation (5), the normalisation of the power law (Figure 15) shows a similar pattern to that of the photon index (Figure 20, fourth panel), showing a flat behaviour out-of-eclipse, increasing as ingress takes place and decreasing at egress. Apparently, the evolution along the orbit of the power-law parameters seems to be

different. However, if the range of photon index is constrained, the values obtained with the new fits become consistent with each other taking into account the uncertainties. This would suggest that there is a certain degree of degeneracy between model parameters. The orbital variation of temperature and Comptonisation normalisation have two local peaks and the lowest value occurs at the eclipse.

The orbital evolution of unabsorbed flux for both models shows a very similar trend. In fact, the corresponding X-ray luminosities are the same taken into account uncertainties (see in Table 9, Column 2 corresponds to equation 2 and Column 3 corresponds to equation 5). The unabsorbed flux is consistent with a constant value, except for eclipse and eclipse-egress. Although for an almost circular orbit and disc accretion no orbital modulation in the amount of material to accrete is expected, variations of the flux can be due to local absorption produced by an emerging accretion stream (eclipse-egress), probably corotating with the compact object, and/or a decrease in the accretion rate, most likely associated to instabilities at the inner edge of the disc interacting with the neutron star magnetosphere.

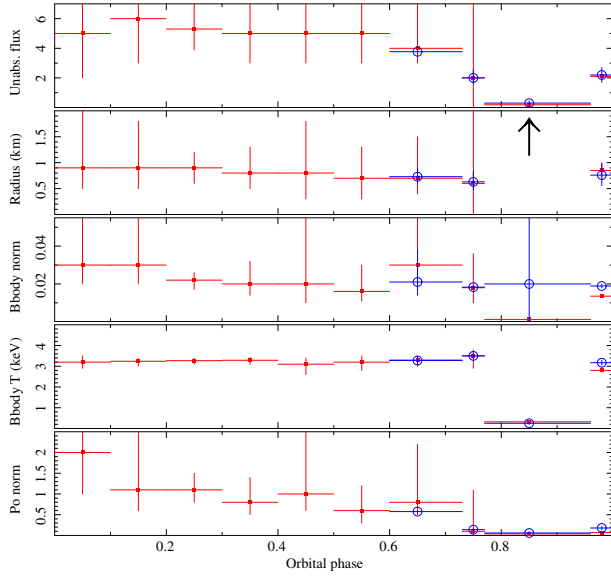


Fig. 14. Evolution of some parameters of the model described by equation (2). Unabsorbed flux is in units of 10^{-9} erg cm $^{-2}$ s $^{-1}$. Bbody norm is in units of L_{39}/D_{10}^2 . Power-law normalisation is expressed in units of keV $^{-1}$ s $^{-1}$ cm $^{-2}$. Filled red squares: initial values. Open blue circles: values obtained by constraining the range of values of the photon index (pre-ingress, ingress, eclipse and egress). The color figure can be viewed online.

The X-ray continuum is modified by a partial covering fraction where the column N_H^2 corresponds to the ISM towards the source and N_H^1 represents the ISM plus the circumstellar environment absorption (Figure 20). We have depicted the variation of the covering fraction measured from our models in Figure 18. It is seen that the covering fraction tends for most of the orbit to have values lower than 0.8, $0.4 < C < 0.9$, which means that there are large inhomogeneities in the stellar wind of the giant star. Although both models seem to follow the same trend in the covering fraction, the orbital variation of C , given by equation (5), shows a certain modulation while the error bars obtained in equation (2) prevent us from confirming this orbital modulation. Nevertheless, taking into account uncertainties, most data points are consistent with 0.8 in both models. The covering factor variation from 0.76 to 0.9 is compatible with the compact object being deeply embedded into the stellar wind of the companion according to Sanjurjo-Ferrín et al. (2021). From the long-term observations used here $C > 0.8$ at orbital phases [0.2-0.3] and eclipse.

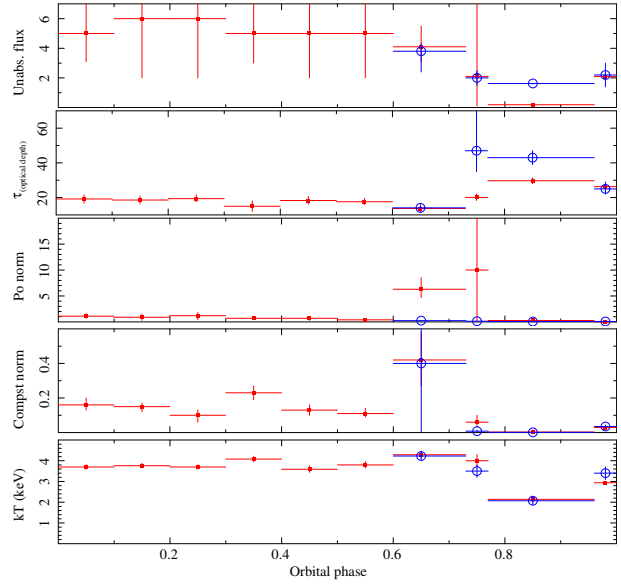


Fig. 15. Evolution of some parameters of the model described by equation (5). Unabsorbed flux is in units of 10^{-9} erg cm $^{-2}$ s $^{-1}$. Power-law normalisation is expressed in units of keV $^{-1}$ s $^{-1}$ cm $^{-2}$. Filled red squares: initial values. Open blue circles: values obtained by constraining the range of values of the photon index (pre-ingress, ingress, eclipse and egress). The color figure can be viewed online.

4.4. Iron Line Complex

The spectral resolution of *MAXI/GSC* is not good enough to resolve the iron line complex, i.e. fluorescence emission lines (Fe K α at ≈ 6.4 keV, Fe K β at ≈ 7.1 keV) and recombination emission lines (Fe XXV at ≈ 6.7 keV and Fe XXVI at ≈ 6.9 keV). From *MAXI/GSC* observations, the iron line feature is found to peak, in general, at ≈ 6.5 keV in the out-of-eclipse phase and peak at higher energies ≈ 6.7 keV in the ingress phase. This suggests the presence of both Fe K α and recombination lines. The high spectral resolution provided by other missions such as *ASCA*, *XMM-Newton* or *Chandra*, proved to be instrumental in resolving these emission lines, if present (Ebisawa et al. 1996; Aftab et al. 2019; Sanjurjo-Ferrín et al. 2021). Other sources where this dichotomy has been reported are Vela X-1 (Martínez-Núñez et al. 2014; Doroshenko et al. 2013; Malacaria et al. 2016), 4U 1538-52 (Rodes-Roca et al. 2011, 2015) and GX 301-2 (Fürst et al. 2011; Islam & Paul 2014). Therefore, to describe the Fe complex, values obtained from *ASCA* observations were adopted and used to fit our orbital

TABLE 9
X-RAY LUMINOSITY (10^{37} ERG S $^{-1}$) AND COMPTONISATION PARAMETER

Orbital phase	L_x (equation 2)	L_x (equation 5)	$y = kT\tau^2/(m_e c^2)$
Post-egress	3_{-2}^{+14}	$2.9_{-1.5}^{+1.8}$	2.7 ± 0.7
[0.1 – 0.2]	3_{-2}^{+6}	3 ± 3	2.5 ± 0.7
[0.2 – 0.3]	$2.9_{-1.2}^{+1.6}$	3_{-3}^{+2}	$2.7_{-0.6}^{+0.7}$
[0.3 – 0.4]	3_{-2}^{+3}	$3.0_{-1.7}^{+2.3}$	1.8 ± 0.8
[0.4 – 0.5]	3_{-2}^{+6}	$3.0_{-2.1}^{+1.8}$	2.4 ± 0.7
[0.5 – 0.6]	3_{-2}^{+3}	2.6 ± 1.8	2.3 ± 0.6
Pre-ingress	2_{-1}^{+4}	$2.3_{-0.9}^{+1.2}$	1.6 ± 0.6
Ingress	1_{-1}^{+11}	1_{-1}^{+7}	$3.2_{-0.8}^{+0.9}$
Eclipse	$0.10_{-0.02}^{+0.03}$	0.10 ± 0.03	3.7 ± 0.7
Egress	$1.2_{-0.2}^{+0.3}$	$1.2_{-0.2}^{+0.3}$	3.98 ± 0.16

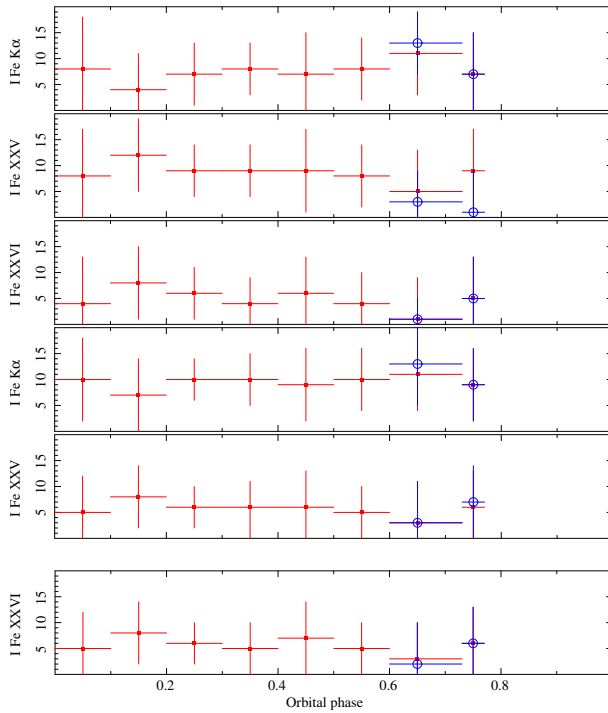


Fig. 16. Evolution of the Gaussian intensity of the Fe emission lines with orbital phase. *Top, second and third panels:* model described by equation (2). *Fourth, fifth and bottom panels:* model described by equation (5). The unit of the line flux I is 10^{-4} photons s^{-1} cm^{-2} . Filled red squares: initial values. Open blue circles: values obtained by constraining the range of values of the photon index (pre-ingress, ingress, eclipse and egress). The color figure can be viewed online.

phase-resolved spectra (Ebisawa et al. 1996), where the energies and line widths were fixed and the line intensities were left as free parameters in the fit.

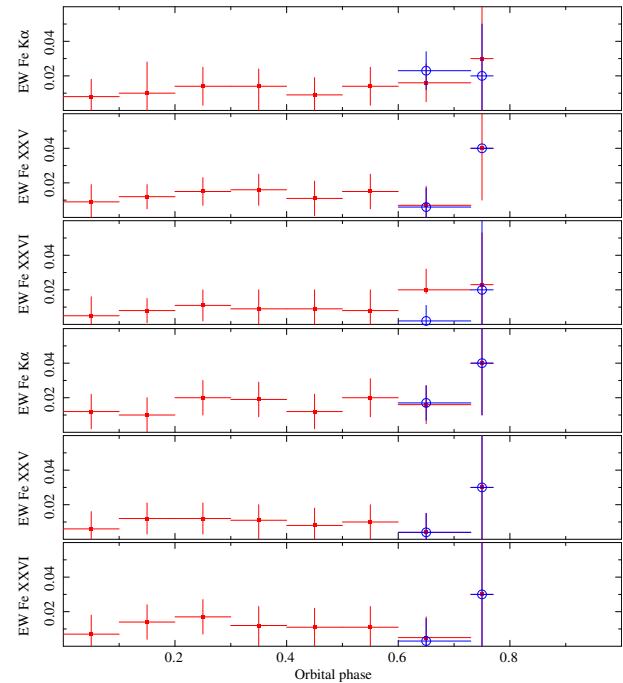


Fig. 17. Evolution of the equivalent width (EW) of the Fe emission lines with orbital phase. *Top, second and third panels:* model described by equation (2). *Fourth, fifth and bottom panels:* model described by equation (5). EW is in units of keV. Filled red squares: initial values. Open blue circles: values obtained by constraining the range of values of the photon index (pre-ingress, ingress, eclipse and egress). The color figure can be viewed online.

Unfortunately, none of the iron emission lines could be detected by *MAXI/GSC*, neither in the eclipse nor in the egress phases (Figure 16).

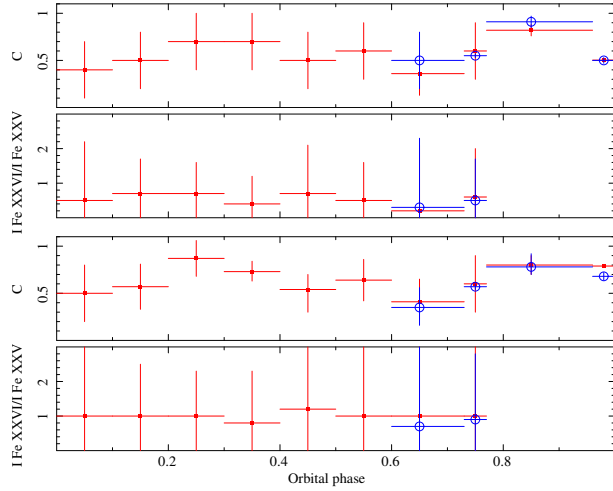


Fig. 18. Evolution of the partial covering fraction C and line intensity ratio Fe XXVI/Fe XXV. *Top and second panels*: model described by equation (2). *Third and bottom panels*: model described by equation (5). Filled red squares: initial values. Open blue circles: values obtained by constraining the range of values of the photon index (pre-ingress, ingress, eclipse and egress). The color figure can be viewed online.

All free parameters, line intensities, equivalent widths and line intensity ratio Fe XXVI/Fe XXV (Figures 16, 17 and 18, respectively) were found consistent with constant values within errors out-of-eclipse.

4.5. The Stellar Wind in Cen X-3

Thanks to our orbital phase-resolved spectroscopy, we can study the properties of the stellar wind in Cen X-3 by analysing the variation of the hydrogen column N_H^1 along the orbit. As a first step, we have applied a simple spherically stellar wind model to describe our observational data. This simple model reproduced the observed shape of the absorption curve along the entire orbit in the wind-fed HMXB 4U 1538-52 (Rodes et al. 2008) and it is consistent with the stellar wind description of Cen X-3 reported by Wojdowski et al. (2001).

The radial flow velocity takes the form (Castor et al. 1975; Abbott 1982):

$$v_w(r) = v_\infty \left(1 - \frac{R_c}{r}\right)^\alpha, \quad (6)$$

where v_∞ is the terminal velocity of the wind, R_c is the radius of the companion star, r is the distance from the centre of the companion star and α is the velocity gradient.

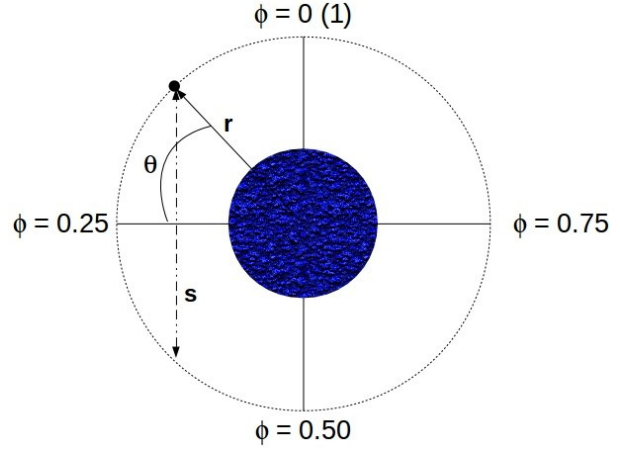


Fig. 19. Schematic view of the binary system. For simplicity we have assumed a circular orbit whose parameters r , s and θ are shown. We note that in this sketch the orbital phase 0 (1) is centred on the mid-time of eclipse. The color figure can be viewed online.

Conservation of mass requires:

$$n_H = \frac{\dot{M}_c}{4 \pi r^2 v_w}, \quad (7)$$

where \dot{M}_c is the mass loss rate from the primary and n_H is the wind density. Combining equations (6) and (7) and integrating the wind density along the line of sight to the X-ray source, it is possible to find a model which properly describes the variation in N_H with orbital phase. Defining s as the distance through the stellar wind along the line from the compact object toward the observer (see Figure 19), we have:

$$N_H = \int_0^s n_H ds = n_H s = n_H 2 r \sin \theta. \quad (8)$$

The angle θ is related to the orbital phase and equation (8) can be rewritten as:

$$N_H = \frac{\dot{M}_c}{4 \pi r^2 v_\infty \left(1 - \frac{R_c}{r}\right)^\alpha} 2 r \sin \left(\frac{\pi}{2} - 2 \pi \phi\right). \quad (9)$$

As we have mentioned before, N_H^1 represents the ISM plus the environment that surrounds the star. The stellar wind model is described by means of the following equation:

$$N_H = \frac{X_H \dot{M}_c}{m_H 2 \pi r v_\infty \left(1 - \frac{R_c}{r}\right)^\alpha} \sin \left(\frac{\pi}{2} - 2 \pi \phi\right), \quad (10)$$

where X_H , the hydrogen mass fraction which is equal to 0.76, m_H is the hydrogen atom mass, \dot{M}_c the

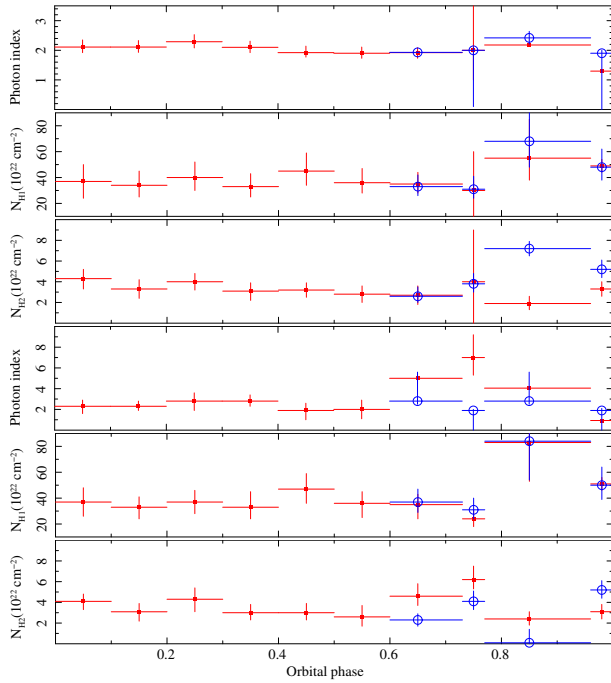


Fig. 20. Evolution of the photon index Γ and absorption columns N_H^1 and N_H^2 . *Top, second and third panels:* from equation (2). *Fourth, fifth and bottom panels:* from equation (5). Filled red squares: initial values. Open blue circles: values obtained by constraining the range of values of the photon index (pre-ingress, ingress, eclipse and egress). The color figure can be viewed online.

mass-loss rate, v_∞ is the terminal velocity of the wind in the range [1 000–3 000] km s⁻¹ (Falanga et al. 2015) and r represents the binary separation. Attempts were made to fit the local absorption N_H^1 using equation (10). A smooth wind model could possibly describe the behaviour of our data, although the large uncertainties prevent us from drawing strong conclusions from this result.

The evolution of the absorption column for both models is shown in Figure 20, and it is consistent with a constant value. The variation of the N_H^1 columns have been plotted together against the orbital phase in Figure 21. As can be seen from the graph, both values are consistent within errors and the fit has been represented by a dotted line. Suchy et al. (2008) studied Cen X-3 over two consecutive orbits with observations taken by the RXTE observatory. They found that N_H increased near eclipse-ingress and egress during both orbits. However, during the second orbit, N_H was relatively constant prior to mid-orbit and rose continuously afterward. They also interpreted the small increase in N_H seen in the orbital phase [0.3–0.4] as a bow shock in front of the accretion stream. The

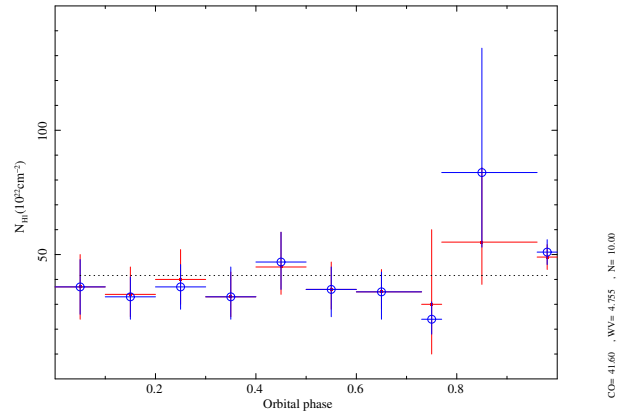


Fig. 21. Evolution of the absorption column N_H^1 (ISM plus local absorption). Red filled squares: from equation (2). Blue open circles: from equation (5). The dotted line represents the fit to a constant. A better fit could be obtained by applying equation (10), but the large uncertainties prevent us from draw by firm conclusions. The color figure can be viewed online.

two-dimensional numerical simulations performed by Blondin et al. (1991) provided the variation of the absorbing column of material, N_H , as a function of orbital phase. The dependence on binary separation showed a double-peaked structure, with one peak occurring slightly before orbital phase 0.5 and the second somewhat after (see their Figure 2). On the other hand, the orbital phase dependence of N_H taking the tidal stream and accretion wake into account showed small peaks associated with clumps in the wind and a strong jump at orbital phase 0.6 (see their Figure 8). They also plotted the column density of the undisturbed wind model showing a concave shape below the full simulated models. Blondin et al. (1990) also showed in their simulations that the column density throughout the orbit changes between consecutive orbits due to variability in the accretion flow. We have not found this behaviour in our long-term *MAXI/GSC* observations, although a small enhanced in N_H^1 could be present in the orbital phase [0.4–0.5] (see Figure 20). However, it cannot be directly probed within the context of our *MAXI/GSC* analysis, which only allows inferring the long-term properties of the source averaged over several orbital phase bins. To sum up, the models carried out by Blondin et al. (1991) do not describe well the observed behaviour for Cen X-3.

5. SUMMARY AND CONCLUSIONS

We have investigated the long-term variation of spectral parameters exploiting the continuous monitoring of Cen X-3 with *MAXI/GSC* and its out-

standing spectral capabilities. From the analysis of the MAXI/GSC light curve, we estimated the orbital period of the binary system, $P_{\text{orb}} = 2.0870 \pm 0.0005$ days, which agrees with the value given by Nagase et al. (1992) and Rodes et al. (2017), and we also noticed the presence of a superorbital period of $P_{\text{superorb}} = 220 \pm 5$ days which is included in the interval [93.3-435.1] days reported by Sugimoto et al. (2014), who detected it by using a power spectrum density technique.

We have described the X-ray spectra of Cen X-3 by two models consisting of a blackbody plus a power law and a Comptonisation of cool photons on hot electrons plus a power law, both modified by an absorption covering fraction factor and Gaussian functions, and have performed detailed spectral analysis (orbital phase-averaged and phase-resolved, in the 2.0–20.0 keV range). Our results can be summarised as follows:

- The blackbody emitting area has an averaged radius of $0.71_{-0.16}^{+0.19}$ km and its size varies from 1 or 3 km out-of-eclipse, which is consistent with a hot spot on the NS surface, to 9 ± 3 km in eclipse, covering a much larger area.

- From the unabsorbed flux, the total X-ray luminosities in the 2.0–20.0 keV were found to be $(1.9_{-0.8}^{+1.0}) \times 10^{37}$ erg s⁻¹ (equation 2) and $(2_{-1}^{+3}) \times 10^{37}$ erg s⁻¹ (equation 5) on average. This high luminosity in the long term, one order of magnitude larger than that for wind-fed X-ray binaries, indicates that accretion must be enhanced by other mechanisms. In the case of Cen X-3, this should be due to an accretion disc, matter co-rotating with the compact object and/or soft X-ray reflection from the inner accretion disc region. In addition, the out-of-eclipse X-ray luminosity was 10-30 times higher than in eclipse.

- From the comparison of the high-state, low-state and averaged spectra, it has been deduced that the emission region is compatible in size and consistent with thermal emission produced at the NS polar cap. The values obtained for the high and low state luminosities suggest that the difference can be attributed to a drop in the accretion rate rather than an overall enhancement of absorption.

- The column density of absorbing matter has two components: $N_H^2 \approx (2 - 7) \times 10^{22}$ cm⁻² which represents the ISM towards the system and $N_H^1 \approx (2 - 8) \times 10^{23}$ cm⁻², and both models yield similar column densities estimates within errors.

- The spectra show the iron fluorescence line at ≈ 6.4 keV which is detected by MAXI/GSC but it cannot resolve recombination iron lines. The de-

scription of the iron line complex adopted in this work suggests the presence of both near neutral iron line (Fe K α) and highly ionised species (Fe XXV and Fe XXVI) except in the eclipse and egress spectra, where none of the emission lines are detected. No modulation along the orbit is seen in the line intensities.

- The orbital dependence of the column density was compatible with a constant value within errors. The large value of the column density $N_H^1 \approx 4 \times 10^{23}$ cm⁻² strongly favours a highly inhomogeneous surrounding environment. To better constrain the Cen X-3 stellar wind properties it is necessary to improve uncertainties of the parameters, especially the column density and EW of iron emission lines, for probing the geometry and distribution of circumstellar matter around the compact object. Numerical simulations performed by Blondin et al. (1991) were not able to well describe the observed behaviour for Cen X-3.

We thank the referee for the useful and constructive review which helped us to improve the content of this paper. This work was supported by the Spanish Ministry of Education and Science project number ESP2017-85691-P. This research made use of MAXI data provided by RIKEN, JAXA and MAXI team. JJRR acknowledges the support by the Matsuura International Foundation Research Fellowship No14G04, and also thanks the entire MAXI team for the collaboration and hospitality in RIKEN. We would like to thank particularly T. Mihara and S. Nakahira for invaluable assistance in analysing MAXI data. This work has made use of data from the European Space Agency (ESA) mission Gaia (<https://www.cosmos.esa.int/gaia>), processed by the Gaia Data Processing and Analysis Consortium (DPAC, <https://www.cosmos.esa.int/web/gaia/dpac>). Funding for the DPAC has been provided by national institutions, in particular the institutions participating in the Gaia Multilateral Agreement.

REFERENCES

- Abbott, D. C. 1982, ApJ, 259, 282, <https://doi.org/10.1086/160166>
- Aftab, N., Paul, B., & Kretschmar, P. 2019, ApJS, 243, 29, <https://doi.org/10.3847/1538-4365/ab2a77>
- Audley, M. D., Kelley, R. L., Boldt, E. A., et al. 1996, ApJ, 457, 397, <https://doi.org/10.1086/176939>

- Bailer-Jones, C. A. L., Rybizki, J., Fouesneau, M., Demleitner, M., & Andrae, R. 2021, *AJ*, 161, 147, <https://doi.org/10.3847/1538-3881/abd806>
- Bildsten, L., Chakrabarty, D., Chiu, J., et al. 1997, *ApJS*, 113, 367, <https://doi.org/10.1086/313060>
- Blondin, J. M., Kallman, T. R., Fryxell, B. A., & Taam, R. E. 1990, *ApJ*, 356, 591, <https://doi.org/10.1086/168865>
- Blondin, J. M., Stevens, I. R., & Kallman, T. R. 1991, *ApJ*, 371, 684, <https://doi.org/10.1086/169934>
- Castor, J. I., Abbott, D. C., & Klein, R. I. 1975, *ApJ*, 195, 157, <https://doi.org/10.1086/153315>
- Chodil, G., Mark, H., Rodrigues, R., et al. 1967, *Phys. Rev. Lett.*, 19, 681, <https://doi.org/10.1183/PhysRevLett.19.681>
- Day, C. S. R. & Stevens, I. R. 1993, *ApJ*, 403, 322, <https://doi.org/10.1086/172205>
- Doroshenko, V., Santangelo, A., Nakahira, S., et al. 2013, *A&A*, 554, 37, <https://doi.org/10.1051/0004-6361/201321305>
- Ebisawa, K., Day, C. S. R., Kallman, T. R., et al. 1996, *PASJ*, 48, 425, <https://doi.org/10.1093/pasj/48.3.425>
- Falanga, M., Bozzo, E., Lutovinov, A., et al. 2015, *A&A*, 577, 130, <https://doi.org/10.1051/0004-6361/201425191>
- Fürst, F., Suchy, S., Kreykenbohm, I., et al. 2011, *A&A*, 535, 9, <https://doi.org/10.1051/0004-6361/201117665>
- Hutchings, J. B., Cowley, A. P., Crampton, D., van Paradijs, J., & White, N. E. 1979, *ApJ*, 229, 1079, <https://doi.org/10.1086/157042>
- Iaria, R., Di Salvo, T., Robba, N. R., et al. 2005, *ApJ*, 634, 161, <https://doi.org/10.1086/499040>
- Islam, N. & Paul, B. 2014, *MNRAS*, 441, 2539, <https://doi.org/10.1093/mnras/stu756>
- Kretschmar, P., Fürst, F., Sidoli, L., et al. 2019, *NewAR*, 860, 101546, <https://doi.org/10.1016/j.newar.2020.101546>
- Krzeminski, W. 1974, *ApJ*, 192, 135, <https://doi.org/10.1086/181609>
- Malacaria, C., Mihara, T., Santangelo, A., et al. 2016, *A&A*, 588, 100, <https://doi.org/10.1051/0004-6361/201527009>
- Martínez-Núñez, S., Kretschmar, P., Bozzo, E., et al. 2017, *Space Sci. Rev.*, 212, 59, <https://doi.org/10.1007/s11214-017-0340-1>
- Martínez-Núñez, S., Torrejón, J. M., Kühnel, M., et al. 2014, *A&A*, 563, 70, <https://doi.org/10.1051/0004-6361/201322404>
- Matsuoka, M., Kawasaki, K., Ueno, S., et al. 2009, *PASJ*, 61, 999, <https://doi.org/10.1093/pasj/61.5.999>
- Mihara, T., Nakajima, M., Sugizaki, M., et al. 2011, *PASJ*, 63, 623, <https://doi.org/10.1093/pasj/63.sp3.s623>
- Nagase, F., Corbet, R. H. D., Day, C. S. R., et al. 1992, *ApJ*, 396, 147, <https://doi.org/10.1086/171705>
- Naik, S. & Paul, B. 2012, *BASI*, 40, 503, [arXiv:1212.0949](https://arxiv.org/abs/1212.0949)
- Naik, S., Paul, B., & Ali, Z. 2011, *ApJ*, 737, 79, <https://doi.org/10.1088/0004-637x/737/2/79>
- Prat, L., Rodriguez, J., Hannikainen, D. C., & Shaw, S. E. 2008, *MNRAS*, 389, 301, <https://doi.org/10.1111/j.1365-2966.2008.13558.x>
- Press, W. H. & Rybicki, G. B. 1989, *ApJ*, 338, 277, <https://doi.org/10.1086/167197>
- Priedhorsky, W. C. & Terrell, J. 1983, *ApJ*, 273, 709, <https://doi.org/10.1086/161406>
- Raichur, H. & Paul, B. 2008a, *MNRAS*, 387, 439, <https://doi.org/10.1011/j.1365-2966.2008.13251.x>
- _____. 2008b, *ApJ*, 685, 1109, <https://doi.org/10.1086/591037>
- _____. 2010, *MNRAS*, 401, 1532, <https://doi.org/10.1111/j.1365-2966.2009.15778.x>
- Rawls, M. L., Orosz, J. A., McClintock, J. E., et al. 2011, *ApJ*, 730, 25, <https://doi.org/10.1088/0004-637x/730/1/25>
- Rodes, J. J., Mihara, T., Torrejón, J. M., et al. 2017, 7 years of MAXI: monitoring X-ray Transients (<https://indico2.riken.jp/indico/conferenceDisplay.py?confid=2537>), 159
- Rodes, J. J., Torrejón, J. M., & Bernabéu, G. 2008, *The X-ray Universe 2008* (<https://www.cosmos.esa.int/web/xmm-newton/2008-symposium>), 56
- Rodes-Roca, J. J., Mihara, T., Nakahira, S., et al. 2015, *A&A*, 580, 140, <https://doi.org/10.1051/0004-6361/201425323>
- Rodes-Roca, J. J., Page, K. L., Torrejón, J. M., Osborne, J. P., & Bernabéu, G. 2011, *A&A*, 526, 64, <https://doi.org/10.1051/0004-6361/201014324>
- Sanjurjo-Ferrín, G., Torrejón, J. M., Postnov, K., et al. 2021, *MNRAS*, 501, 5892, <https://doi.org/10.1093/mnras/staa3953>
- Schreier, E., Levinson, R., Gursky, H., et al. 1972, *ApJ*, 172, 79, <https://doi.org/10.1086/180896>
- Stevens, I. R. 1988, *MNRAS*, 232, 199, <https://doi.org/10.1093/mnras/232.1.199>
- Suchy, S., Pottschmidt, K., Wilms, J., et al. 2008, *ApJ*, 675, 1487, <https://doi.org/10.1086/527042>
- Sugimoto, J., Mihara, T., Sugizaki, M., et al. 2014, *JPSCP*, 2, 013104, <https://doi.org/10.7566/JPSCP.1.013104>
- Sugizaki, M., Mihara, T., Serino, M., et al. 2011, *PASJ*, 63, S635, <https://doi.org/10.1093/pasj/63.sp3.s635>
- Sunyaev, R. A. & Titarchuk, L. G. 1980, *A&A*, 86, 121
- Takeshima, T., Dotani, T., Mitsuda, K., & Nagase, F. 1991, *PASJ*, 43, 43
- Titarchuk, L. 1994, *ApJ*, 434, 570, <https://doi.org/10.1086/174760>
- Tjemkes, S. A., Zuiderwijk, E. J., & van Paradijs, J. 1986, *A&A*, 154, 77
- Tomida, H., Tsunemi, H., Kimura, M., et al. 2011, *PASJ*, 63, 397, <https://doi.org/10.1093/pasj/63.2.397>
- Tsunemi, H., Kitamoto, S., & Tamura, K. 1996, *ApJ*, 456, 316, <https://doi.org/10.1086/176652>

- Tsunemi, H., Tomida, H., Katayama, H., et al. , <https://doi.org/10.1093/pasj/62.6.1371>
- Valencic, L. A. & Smith, R. K. 2015, *ApJ*, 809, 66, <https://doi.org/10.1088/0004-637x/809/1/66>
- van der Meer, A., Kaper, L., van Kerkwijk, M. H., Heemskerk, M. H. M., & van den Heuvel, E. P. J. 2007, *A&A*, 473, 523, <https://doi.org/10.1051/0004-6361:20066025>
- Verner, D. A. & Yakovlev, D. G. 1995, *A&AS*, 109, 125
- Willingale, R., Starling, R. L. C., Beardmore, A. P., Tanvir, N. R., & O'Brien, P. T. 2013, *MNRAS*, 431, 394, <https://doi.org/10.1093/mnras/stt175>
- Wilms, J., Allen, A., & McCray, R. 2000, *ApJ*, 542, 914, <https://doi.org/10.1086/317016>
- Wojdowski, P. S., Liedahl, D. A., & Sako, M. 2001, *ApJ*, 547, 973, <https://doi.org/10.1086/318425>

G. Bernabéu, J. J. Rodes-Roca, and J. M. Torrejón: Department of Physics, Systems Engineering and Signal Theory, University of Alicante, 03080 Alicante, Spain.

G. Bernabéu, J. J. Rodes-Roca, G. Sanjurjo-Ferrín, Á. Torregrosa, and J. M. Torrejón: University Institute of Physics Applied to Sciences and Technologies, University of Alicante, 03080 Alicante, Spain (aat34@alu.ua.es).

AN ASTROPHYSICAL PERSPECTIVE OF LIFE. THE GROWTH OF COMPLEXITY

F. Sánchez^{1,2} and E. Battaner³

Received April 7 2022; accepted July 26 2022

ABSTRACT

The existence of life is one of the most fundamental problems of astrophysics. The intriguing existence of progressively complex and apparently improbable living beings should be a general tendency of life in the Universe. We are looking for general physical laws governing the growth of complexity in any astrophysical environment. We posit the existence of a vital scalar field. This scalar is sensitive to the gradient of the inverse of specific entropy, such that its distribution tends to very high values in the interior of living beings. Besides the classical mutations, vital field driven mutations only produce decrements of entropy. The field equations give rise to the existence of vital waves. This theory is able to deal with both the origin of life and the evolution of life. We show that the growth of complexity is accelerated by the vital field.

RESUMEN

La existencia de vida es uno de los problemas fundamentales de la astrofísica. La existencia intrigante de vivientes progresivamente complejos y aparentemente improbables debería ser una tendencia general de la vida en el Universo. Buscamos leyes físicas generales que gobiernen la emergencia de complejidad en cualquier sistema astrofísico. Proponemos la existencia de un campo vital escalar. Este escalar es sensible al gradiente del inverso de entropía específica, de forma que su distribución tiende a adquirir valores muy altos en el interior de los vivientes. Además de las mutaciones clásicas, hay otras mutaciones inducidas por el campo vital que sólo producen decrementos de entropía. Las ecuaciones del campo dan lugar a ondas vitales. Mostramos cómo el campo vital acelera el crecimiento de complejidad. Esta teoría puede aplicarse tanto el origen de la vida como a su evolución.

Key Words: astrobiology — cosmology: miscellaneous — hydrodynamics

1. INTRODUCTION

It is a fact that our Universe contains life, even if observations are still limited to only one planet. The origin and evolution of life in the Universe requires a general insight much beyond the precise knowledge that biology has reached in the particular case of living beings on Earth.

On the other hand, it is well known that, in the particular case of terrestrial life, a large impulse pushes living beings to perpetuate and benefit from any favourable circumstance that arises, and to progress. They tenaciously adapt themselves to the

medium, evolving and even modifying this medium to improve their own evolution. Life efficiently uses any resource and any kind of energy independently of its origin. This well-known and fascinating behaviour makes it logical and necessary to undertake the general problem of life in the evolution of the Universe as a fundamental astrophysical problem.

In his celebrated book *What is life?* Schrodinger (1944) wrote, “from all that we have learnt about the structure of living matter, we must be prepared to find it working in a manner that cannot be reduced to the ordinary laws of physics”. This opinion of Schrödinger’s inspired the present work, which aims to tackle essentially biological problems from a different viewpoint based on new physical laws. The

¹Instituto de Astrofísica de Canarias, Spain.

²Department of Astrophysics, ULL, Spain.

³Instituto Carlos I de Física Teórica y Computacional, Spain.

complexity inherent in life and its evolution beckon us to try out new emergent models built from hitherto untried perspectives.

We are not proposing an alternative to classical genetics but to reinforce it with new physical laws. This theory is neither teleological nor is based on the anthropic principle.

Many works have dealt with the physical interpretation of life, entropy, complexity and evolution (some representative classic examples could be: Prigogine 1981; Prigogine & Stengers 1984; Maturana & Varela 1981; McShea & Brandon 2010; Kauffman 2000; Margulis & Sagan 1997; Schneider & Sagan 2005; Krakauer 2011; Grassberger 1986; Day 2012; Gould 1996; Davies 2019; Adamsky et al. 2020; Zervovic & Brenner 2014) but their basic principles and scopes are very different from the one presented here. There are many genetic and astrobiological topics dealing with the evolution of life in the Universe, but here we restrict ourselves to the entropic problem. This paper aims to provide a fresh insight from a purely physics-based point of view.

We propose general physical laws for any kind of life in the Universe, terrestrial life just being a particular case. We need, however, to make a small number of general assumptions that are evident in terrestrial genetics; namely, that the existence of a molecular code similar or dissimilar to our DNA, that this code must be highly stable to subsist against replication and thermal noise, and that this stability is not completely perfect, so that it can be on rare occasions violated, thereby permitting mutations. The mechanism of natural selection should also be at work.

We introduce a vital field characterized by vital density and velocity. The vital field permeates the Universe and flows in space and time. We first define what this vital field *is* and later consider what this vital field *does*.

The properties of the vital field are defined by two proposed equations bearing formal similarity with the basic equations of the Eulerian fluid mechanics. From these equations, we deduce the existence of vital waves. We then propose that vital density has at least two effects on the evolution of species. First, it induces another type of mutation characterized by decrements of specific entropy (called VID mutations, Vital Intensity Driven mutations). Second, vital waves enable a mechanism that speeds up the dissemination of mutations.

The novel hypothesis proposed here may render some evolution processes more effective. With both VID mutations and standard mutations, natural se-

lection continues to be the mechanism that decides the progress of evolution. We could even suggest that the new hypothesis provides support to the traditional theory of evolution and can therefore be considered as complementary to it. We are not at all proposing an alternative to the standard theory of evolution. We do not exclude standard genetic concepts; instead we simply add new ones, albeit based on new physics.

2. MATHEMATICAL DERIVATIONS

2.1. Vital Field Equations

The physical magnitude characterizing the complexity referred to here is specific entropy (entropy per unit mass, or entropy per baryon), s . For living beings we also use the thermodynamic concept of entropy, S , or rather its statistical mechanical formulation according to the interpretation of Boltzmann. We shall also speak of the entropy of DNA, or any other equivalent code, on the basis of the relation between entropy and information by taking into account the information contained microscopically in the genome. This entropy is based on the thermodynamic weight (number of microstates of a macrostate). Since the two should be intimately interrelated, there is no risk of misinterpretation.

The scalar physical magnitude that defines the vital field is vital density, $\rho(x, y, z, t)$, defined for all space and time. The characteristics of the vital field are determined by two relations: the equation of vital flux and the continuity equation.

We define the vital flux by the product $\rho\vec{v}$, where \vec{v} is the characteristic fluid velocity of the spatial variations of vital density (not the velocity of propagation of the vitons, as we shall see later).

We write the equation of vital flux, i.e. using a hydrodynamic approach, as follows:

$$\frac{\partial}{\partial t}(\rho\vec{v}) + k_1\nabla\rho - k_2\nabla\frac{1}{s} = 0, \quad (1)$$

where k_1 and k_2 are constants.

In order to interpret this equation, let us first suppose the simple case of a stationary state:

$$\nabla\left(k_1\rho - \frac{k_2}{s}\right) = 0. \quad (2)$$

The simplest way to integrate this equation is by ignoring the sign of the gradient. We then obtain an equation that we can work with:

$$\rho \propto \frac{1}{s}. \quad (3)$$

In other words, only for stationary states, those points corresponding to the interior of a living being with very low entropy will have high vital density; outside, the density will be very low. The density will not be homogeneous inside because the constituent organs will not possess the same complexity, i.e. the same entropy.

In the general case around and within a living being, without considering steady state conditions, equation 1 tells us that the vital flux varies, owing to two gradients of opposing tendencies. The gradient of the inverse of the specific entropy points from the exterior to the interior and will tend to generate a vital flux towards the interior of the living being. The gradient of density also points inwards, but because of its negative sign, generates a vital flux outwards.

If the density distribution tends to have very high values inside, such values cannot be attained instantaneously. If, for example, the living being is displaced, the density distribution ‘follows’, although with a slight delay that is inappreciable if the velocity of the living being is very much less than the speed of light. For that to occur it is necessary that the constants k_1 and k_2 be very high (close to c^2). In the case of the displacement of a living being, both gradients act jointly to make the distribution of vital density and the inverse of the specific entropy coincide. This implies that, in practice, the density distribution seems to be in step with, or frozen into, the body of the living being.

Vital density does not represent life complexity, complexity being represented by low specific entropy. But low entropy attracts the density as shown by equation 1 and this effect takes place over very short characteristic times. Steady state conditions can be quickly reached and then the distribution of both the density and the inverse of specific entropy may coincide.

The causes of variability in vital flux correspond to rapid processes with very short characteristic times, in contradistinction to long-duration processes (i.e. those that operate on evolutionary time scales), which we shall discuss further on.

We call the second of the vital field equations the equation of continuity. In fluid mechanics the equation of continuity establishes the conservation of mass; here, in a similar way, the integrated density, is conserved throughout space from $-\infty$ to $+\infty$. We therefore have:

$$\iiint_{-\infty}^{+\infty} \rho d\tau = constant, \quad (4)$$

where $d\tau$ is the element of volume. The triple integral in this formula means that the total integrated density of the vital field in the whole Universe remains constant in time.

The equation of continuity tells us that if, in an element of volume, the divergence of the flux is positive (i.e. if more flux enters than leaves the volume element), the density will diminish:

$$\frac{\partial \rho}{\partial t} = -\nabla \cdot (\rho \vec{v}). \quad (5)$$

This equation establishes the conservation of integrated density. Interpretation of the equation of continuity of density brings us to the physics that we wish to highlight. During its lifetime a living being is a stable system. The only great changes occur at the foetal stage, infancy, and death. Throughout the rest of its life the organism remains extraordinarily constant. If its alimentation is of a chemical nature, the process of ingestion introduces entropy. As the system is in equilibrium, this increase of entropy must be eliminated through the expulsion of mass in the form of faeces and urine, in the case of terrestrial warm-blooded animals the process of perspiration results in heat exchange with the environment through the latent heat of vaporization, and so on. A living organism may be thought of as a stable heat engine (or a cyclic engine with a period of the order of one day). A stable living organism is a great ejector of entropy into its immediate surroundings. The ejection of entropy to the surroundings should even be inherent to the very concept and definition of life.

For any given instant of time in the Universe the density distribution associated with a living entity will be very high (even though non-uniformly distributed in the interior of the organized living entity) and very low in its immediate surroundings, asymptotically approaching the value associated with lifelessness towards infinity. The mean value would correspond to the lifeless value; the high value of density in the interior of the organism would compensate for the minimum value in its immediate surroundings through the ejection of entropy.

That is to say, a living being is not simply a highly dissipative system that consumes large quantities of energy in order to preserve its complexity, but also, and this must be emphasized, it ejects a great quantity of entropy below the lifeless density into its immediate surroundings. The density distribution is illustrated in Figure 1. A living organism absorbs energy from and *entropizes* its surroundings.

To measure the density, we can benefit from equation 3 only when steady state conditions are

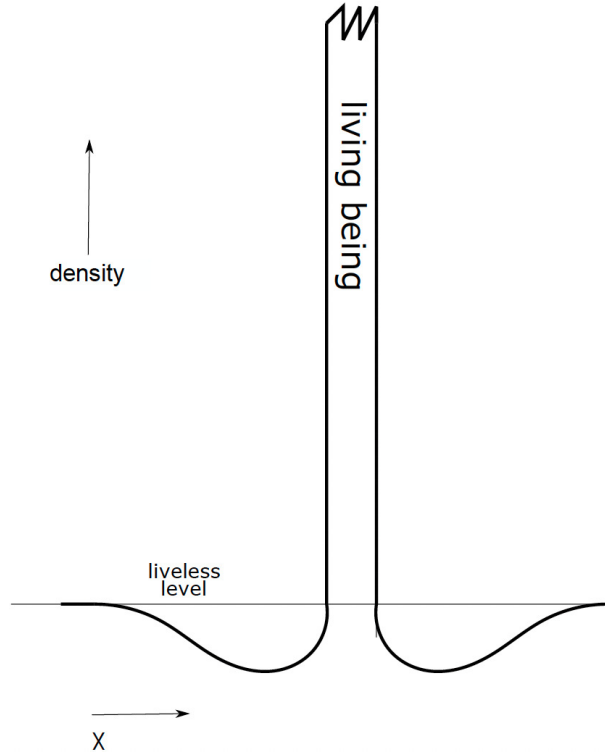


Fig. 1. Vital density field distribution for a living being and its environment.

satisfied. This can be achieved inside a living being or in an inhospitable medium, being nearly zero in an infertile medium. Inside a living being, the value of the densities would be as difficult to estimate as the specific entropy. The units of density would be the inverse of specific entropy, or entropy per baryon (i.e. K/erg, for example), or would be non-dimensional when the so-called system of geometrized units, with c , G and Boltzmann's constant equal to unity, is adopted, as is usual in cosmology and other astrophysical studies. We consider life to be an astrophysical issue.

2.2. Vital Field Waves and Vitons

We define vitons as particles associated with vital waves in accordance with the interpretation of the wave-particle duality. We demonstrate, with the two basic vital field equations, the existence of waves in the vital density field. We now consider the external medium surrounding living organisms. Using the method of linear perturbations and introducing small changes, magnitudes susceptible to variation when traversed by the wave are transformed in the following way:

$$\begin{aligned}\rho &\rightarrow \rho + \rho', \\ \vec{v} &\rightarrow \vec{v} + \vec{v}'.\end{aligned}$$

Unprimed magnitudes correspond to the unperturbed medium, and primed magnitudes are the perturbed magnitudes when traversed by the waves.

We introduce the following simplifications: (a) ρ has no gradients and no temporal variations; (b) the perturbationless velocity is zero; (c) the perturbations are very small, so that terms implying a product of two perturbed terms are negligible; and (d) there are no specific entropy variations far removed from living beings, so that the term involving s does not give rise to further complications. The waves would exist even without these simplifying assumptions, but their mathematical treatment and physical behaviour would be less simple. In particular, the propagation of vitons inside living beings would be not so simple, where gradients of specific entropy due to different organs would render the wave equation more realistic.

From the equation of continuity we get

$$\frac{\partial \rho'}{\partial t} + \rho \nabla \cdot \vec{v}' = 0, \quad (6)$$

and the equation of motion gives

$$\rho \frac{\partial \vec{v}'}{\partial t} + k_1 \nabla \rho' = 0. \quad (7)$$

We differentiated the first with respect to time and find the divergence in the second, and, since the spatial and temporal derivatives are independent and therefore commute, we obtain directly:

$$\frac{\partial^2 \rho'}{\partial t^2} = k_1 \nabla^2 \rho', \quad (8)$$

which is the wave equation. Now, k_1 is the wave velocity squared; that is to say, the velocity of the vitons. We may suppose that $k_1 = c^2$, where c is the speed of light, since these waves can propagate in vacuo. The wave velocity (or the velocity of the vitons) could be equal to the velocity of light or close to it. In the geometrized units, that are the custom in cosmology, with $c = 1$, $k_1 = 1$ also.

We could likewise derive a wave equation in terms of velocity. The propagation of the waves is accompanied by small fluctuations in velocity, \vec{v}' . It is to be noticed that this velocity is not the wave velocity, equal to $k_1^{1/2}$. In a fluid also, the velocities perturbed by the passage of the wave are not equal to the sound speed.

Inside a living being, this wave equation can be produced in the following way. A mutation can be produced at any given moment, giving rise to an abrupt variation in entropy, which is equivalent to a

sharp change in vital density. A density jump in a medium with the capacity to support waves generates the wave. In other words, mutations can create a wave and the emission of vitons. The amplitude of this wave, being a purely geometric factor, diminishes as the inverse square of distance. Vitons always travel at the speed of light or at least at a very high speed. There is some similarity between (energy-photons) and (entropy-vitons).

As in the case of normal mutations, VID mutations can be produced by auto-replication or induced by external agents, X-rays, and other means. We cannot provide examples of VID mutations, as their effects are noticeable only over long time scales (consider, for example, the huge range of complexity of mammals).

3. CHEMISTRY OF LIFE

The origin, evolution and fate of living beings are the result of the interrelation of both physical and chemical processes. In this paper we focus on the physical ones but it is clear that chemistry, more precisely, biochemistry, is of the greatest importance to understand life, both terrestrial and extraterrestrial. The knowledge of biochemistry is at present incomplete, but this is due to the great complexity of the problem rather than to the chemistry fundamentals themselves requiring to be revised. Biochemistry of cosmic life has been reviewed in several papers. The reader is addressed to two excellent books by Schulze-Makuch & Irwin (2018) and Trigo-Rodríguez (2010), with references therein. These authors not only examine the life chemistry in the Earth, but also speculate on alternative cosmic niches and study biochemistry under a cosmic perspective.

It is evident that life can develop at least when physical-chemical conditions are available. A suitable habitat requires chemical heterogeneity. In Earth, life macronutrients are C, H, O, N, K, Ca, P, Mg and S to form prebiotic monomeric inorganic compounds such as H_2 , N_2 , CO_2 , NH_3 , HCN . . . Of great importance was the emergence of photosynthesis, but this is a complicated mechanism that could not be at work in the primitive forms of life. Early chemolithotrophic life was important using redox metabolic reactions, in particular the oxidation of hydrogen to water, with 2.6 eV per reaction, coupled with the reduction of CO_2 (metanogenesis, 1.4 eV per reaction), which is as energetic as light (about 2 eV per photon depending on wavelength). Early cometary and meteoritic bombardment also delivered water and organic compounds thus enrich-

ing primordial chemistry, as first proposed by Oró (1961). Carbonaceous chondrites are rich in organic molecules, as witnesses of the protoplanetary disk chemistry.

Cyanobacteria and other chemoautotrophic organisms dramatically produced oxygen changing the atmosphere, rendering oxidation conditions. Life went from anaerobic to aerobic. This fact favoured the carbon chemistry with its ability to form complex stable molecules, starting with methane and other alkanes, reaching amino acids leading to proteins through connections by peptide bonds. Also, cycloalkane and polycyclic aromatic hydrocarbons (already present in the interstellar medium, in particular in molecular clouds) produced rings and later three-dimensional macromolecules with a non-racemic left-handed chirality. The carbon polymeric chemistry is able to build an almost unlimited range of molecules with strong covalent bonds, providing a very rich repertoire of metabolic reactions. This change of chemistry illustrates that not only life is adapted to the atmosphere but also that the atmosphere is adapted to life.

Life on Earth began with microscopic anaerobic prokaryotic cells, starting with LUCA (Last Universal Common Ancestor). Two billion years later the emergence of eukaryotic cells took place as a fusion of two or more prokariotes (Margulis & Sagan 1995), with sizes greater by an order of magnitude. The emergence of multi-cellular life is a poorly understood step. About 541 million year ago the Cambrian explosion was the origin of bilateral and homeothermic phyla. This homeothermia was an important step as metabolic reactions adapted to narrow to optimal temperature ranges. On the other hand, homeothermia provided an efficient way to heat the environment thus expelling entropy for keeping its disequilibrium state.

We cannot present a brief overview of the very wide branch of cosmochemistry. We limit ourselves to brief comments on biochemistry topics closer to the physics proposed in this paper: (a) the necessity of a solvent, (b) the required boundary and (c) the replication mechanism.

(a) The necessity of a solvent. Life is fundamentally a liquid based process. Terrestrial life uses water as a solvent especially efficient due to its high dipole moment. Atoms and molecules can move around nearly free to undergo chemical reactions. There is a perfect compatibility between carbon polymeric chemistry and water as a solvent. However, life was perhaps not originated in oceans or seas but in interfaces liquid-solid like in puddles alternating desiccation and re-

hydration, or porous media like pumice or even ice in contact with liquid water. A solid phase could preserve initial and later decreases of entropy.

(b) The required boundary. The existence of boundaries of living beings is of great importance to isolate the regions of disequilibrium inside from the environment closer to thermodynamic equilibrium, to isolate a region with very low entropy and a medium with very large entropy. Biomembranes preserve the high free energy state of the system from dissipation, encapsulating and confining a high concentration of interacting solutes and macromolecules. But isolation cannot be absolute. The semi-permeable boundaries must provide a selective transport of nutrients and waste. For this difficult task amphiphilic lipids (fatty acids, phospholipids) are essential as are hydrophilic toward the aqueous environment and hydrophobic toward the cell interior. The emergence of lipid protomembrane boundaries was a great jump in the early evolution of life.

(c) The replication mechanism. At present, in Earth's life, the information is stored in the one-dimensional form of a linear code (DNA) translated into the three-dimensional structure of proteins; but to reach this complex, precise, high fidelity mechanism, many previous insufficiently known steps were to be surmounted. There is at present a great difficulty to identify the first replicators. Kauffman (1995, 2000) proposed that the origin of life and the transmission of hereditary information was not due to a single molecule but to a network of interacting catalytic molecules. Probably there was a pre-RNA world followed by an RNA world before reaching the DNA-RNA world in which RNA is now an intermediate in the flow of information and responsible of the production of catalytic and auto-catalytic enzymes. There must be a transmission of information from parental to descendants or offsprings to assure an autonomous maintenance of phyla, a great biochemical challenge at early epochs. These molecular codes permit the evaluation of the entropic content of living individuals.

Much work must still be done to understand the establishment of terrestrial life chemistry, and still much more work to speculate about extraterrestrial life adapted to other energy sources and other habitats, but we do not suggest that new chemistry fundamentals are needed. On the other hand, it is here suggested that complementary physics as introduced in this paper, should favour the evolution to reach the chemical complexity of life, rendering some difficult steps more plausible.

4. RESULTS

4.1. Mutations Driven by Vital Density

Standard mutations, which occur completely at random, may give rise to both positive and negative variations in entropy in the molecular code. We add another kind of mutation driven by the vital density field and characterized solely by a diminution in entropy. We call these *VID mutations* (Vital Driven mutations). The existence of VID mutations is one of our fundamental hypotheses. Both types are random, coexist, are subject to natural selection, and drive the evolution of a given species. Although standard mutations might well dominate, the introduced kind are also essential because they enable us to better understand the progressive appearance of complexity through time, a problem that we are using to test our model.

The simplest mathematical way to express the effect of a VID mutation is to suppose that

$$ds = -k_3 \rho dt. \quad (9)$$

In other words, the temporal diminution in specific entropy is proportional to the vital density. Although the mutations are quantized in nature, after long periods of time a continuous description may be permitted, as expressed in equation 9.

The real evolution of species is the result of the joint action of standard and VID mutations, together with multiple interruptions, bifurcations, etc. The graph of specific entropy as a function of time is extremely complex, as testified by the history of evolution. In order to analyse the isolated effect of VID mutations we plot the curve of the variation of entropy against time by considering the ideal effect where VID mutations are alone responsible for this variation. By isolating the tendency of VID mutations in this way we may insert the result into a global interpretation involving all evolutionary effects.

If we combine equations 9 and 3,

$$ds = -k_3 \frac{k_1}{k_2} \frac{1}{s} dt = -k_4 \frac{1}{s} dt. \quad (10)$$

This differential equation integrates easily to produce:

$$\frac{s}{s_0} = \sqrt{1 - \frac{2k_4}{s_0^2} t}. \quad (11)$$

We avoid a constant of integration by choosing a suitable time origin. The constant s_0 represents the value of specific entropy at infinity, approaching the lifeless level. The value of k_4 must be very small for

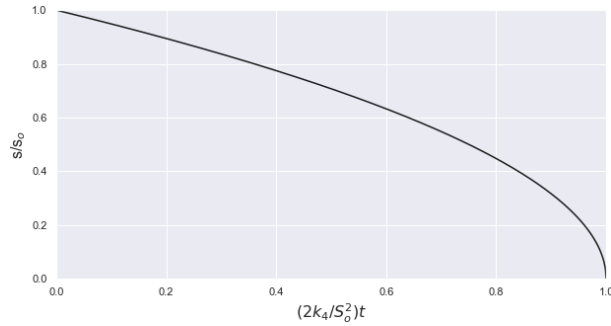


Fig. 2. Variation of specific entropy with time due to the isolated effect of VID mutations.

the effects of VID mutations to be applicable on evolutionary time scales. After a time interval of, say, 10^6 yr, k_4 would be of the order of $3 \times 10^{-14} \text{ s}^{-1}$. We calculate the value of the lifeless specific entropy per baryon to be of the order of $s_0 = 5 \times 10^{-15} \text{ erg K}^{-1}$. The estimation of this value is given in an appendix. Figure 2 shows the variation curve.

We see from equation 11 that for short times the specific entropy decreases slowly until approximately the characteristic time $s_0^2 k_4^{-1}$. At longer times the decrease becomes faster until reaching its minimum value, which is zero as the entropy is positive. The value of zero corresponds to DNA as a pure crystal, equivalent to zero temperature. It is therefore an ideal limit.

On small time scales the action of VID mutations will not be very great; when, however, it has attained a significant level of complexity, it could predominate. The specific entropy would eventually correspond to what we may term the *zero-entropy species*, beyond which there could be neither greater complexity nor further evolution. This ideal state would not, however, be unchangeable, depending on ecological or environmental conditions, on the action of normal mutation, etc. It is to be emphasized that this plot considers only the isolated effect of VID mutations.

The zero-entropy species is not the end of evolution, because normal mutations are always at work and can reverse the trend. Other evolution paths can then be explored. This ideal end will be reached only if only VID mutations were present, which is by no means assumed. In the real world other effects such as bifurcations and extinctions could take place. On the other hand, there are many paths to reducing entropy; there would be many end points. There would be not just one zero-entropy species, but many, and there is no way of telling which one of them would reach the final state chosen by natural selection. The most complex species need not be the

best adapted ones, so that almost perfect, but fragile and ailing species might result that are doomed to extinction from the start.

If we put $s = 0$ in equation 11, we get:

$$s_0^2 = 2k_4\tau, \quad (12)$$

where τ is the characteristic time for VID mutations to reach the condition of zero-entropy species. Bearing in mind the estimated values of s_0 (see Appendix) and assuming τ to be of order 10^9 yr, somewhat less than, but of the order of, a Hubble time, we have an estimation of the value of k_4 of the order of 10^{-14} s^{-1} .

It is tempting to identify the zero-entropy species as some kind of *superior* species, even to the point of imagining *superior humans*, but such a notion is untenable, given that a zero-entropy species would be the result of its evolutionary path, which cannot be determined beforehand, so a zero-entropy shark would be just as conceivable as a zero-entropy human or a zero-entropy extraterrestrial, for example. It is possible that the shark species has already reached a state close to zero entropy, further evolutionary progress being difficult, given its phylogenesis. There is, then, no anthropic principle at work in our hypothesis.

4.2. Spreading of Mutations

The great stability of many molecules, particularly DNA or any other equivalent code, implies that they are in a state of relative minimum energy. For a mutation to occur and a different state to be reached, a high potential energy barrier, ΔE , must be surmounted, and that barrier must be much higher than the thermal energy, kT (k being Boltzmann's constant and T the temperature), so the molecule does not easily change its state. This condition, equivalent to a very low temperature, was used by Schrödinger, who considered the gene to be an aperiodic solid, ideally at a temperature of absolute zero. Aside from a leap in entropy, ΔS , the mutation would undergo, independently of ΔE , a change in energy, E , from its initial to its final state, corresponding to a photon emitted in the mutation (see Figure 3).

The existence of vitons may clarify the manner in which a mutation (whether or not favourable, with ΔS either positive or negative) originating in an individual of a species can spread to other individuals of the same species to the point of mutating the entire species. Mutation is an entropic leap in a DNA molecule that creates a sharp increase in vital density, giving rise to the emission of a viton. When a viton meets a DNA molecule of the same individual,

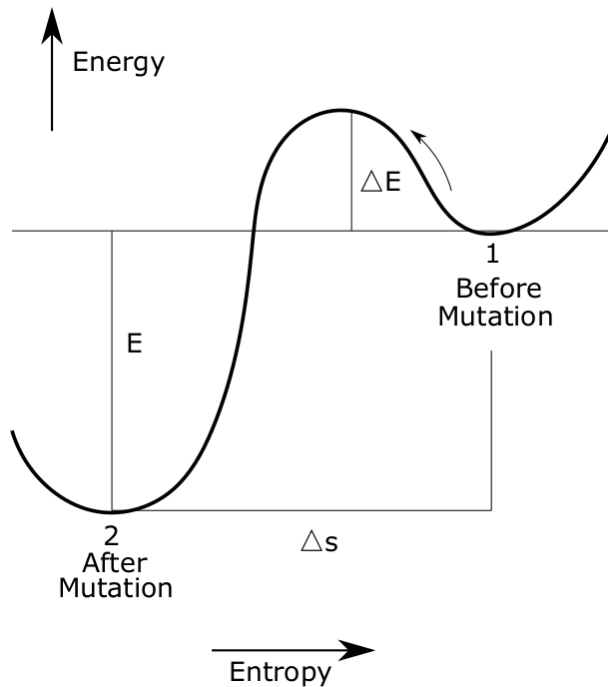


Fig. 3. Energy-entropy diagram showing states before and after a VID mutation.

or of other individuals of the same species, it will provoke the same entropic leap, ΔS , that gave rise to it, so that the viton will have propagated the mutation of the emitting DNA molecule to the receptor DNA molecule. In its turn, the receptor will emit another viton of exactly the same entropic leap, ΔS , thereby producing a scattering effect in the density waves. An analogy may be drawn with the processes of emission and absorption of photons. This mechanism would be at work in DNA molecules as well as in any other molecule used as information code.

For transmission to be effective the viton must carry information on both ΔS and ΔE , the energetic leap required for the mutation to take place. The viton would not only announce that a mutation is about to be produced but also would supply the energy to make it happen. No problem arises if the mutational leap gains more energy than it loses, i.e. if E is greater than ΔE (see Figure 3).

When the receptor organism in turn becomes an emitter, the mutation will be transmitted to neighbouring beings belonging to the species. In this way a mutation originating in an individual may become a mutation of the entire species.

A quantum leap in entropy could correspond numerically to more than one mutation. The receptor organism might undergo a different mutation from that of the emitting organism. This error in

transmission does not imply any evolutionary disadvantage since, for progressive mutation to occur, diminution in entropy is more important than precisely where the dislocation in the initial DNA takes place.

Standard mutations and VID mutations are not excluding each other. However, they are independent as they are produced by different mechanisms. Standard mutations are the results of random changes in the DNA molecule (excluding those produced by X-rays...) VID mutations are induced by vital waves. Let us clarify this point by finding other similar effects in classical systems. In a hot metal, for instance, electrons may escape the metal as a result of thermal noise. In addition, if the metal is exposed to UV radiation the electrons also escape due to the photoelectric effect. The two mechanisms co-exist, both contribute to the escape of electrons and are independent. The UV photons induce another way of ejecting electrons.

5. DISCUSSION

With regard to the problem of the origin and evolution of life there are three types of contributions: an astrophysical phase concerning the production of rather complex biomolecules and the provision of habitable environments, the contribution of genetics to identifying how evolution proceeds, and the contribution of astrophysics in dealing with entropy and the probabilities involved in evolution. Our paper only deals with the third aspect. How biomolecules are formed in space, in the proto-solar system and in atmospheres is, of course, crucial but beyond the scope of our paper. Here we restrict ourselves to the entropic problem of life.

When and how the vital field is originated in the Universe? Our vital field is present in all parts of the Universe, even with, in general, very low values of density, and its integrated value is a constant in time. The origin itself should be a cosmological problem that is far from the present preliminary state of the theory.

The existence of a vital field in the Universe provides an effective scenario for other forms of life in the Universe and sheds new light on a number of phenomena that are still controversial in the physics of life and its evolution. With this model we have been able to explain two of these phenomena: the appearance of species of growing complexity in Earth's history. This growing complexity should be a basic property also in other environments in the Universe. We have also explained the rapid dissemination of a mutation in an individual of the species that culminates in the mutation of the entire species.

This theory could be generalized to incorporate relativistic and quantum aspects, but given the exploratory and novel focus of this study, we have preferred to introduce it in a simple mathematical way.

We have considered the special case of living beings, but the vital field can be present in any place in the Universe, even in lifeless points far from living entities. Similarly, vital waves and vitons may be present anywhere.

The theory proposed here makes reference to the genome, but is quite independent of the specific mutation mechanism. When considering physical laws, which are in principle applicable to the entire Universe, these ideas could have general implications concerning the emergence and evolution of life as a cosmological fact.

Mutations, both standard and those driven by the vital field, must accept the verdict of natural selection. For standard mutations S may be positive or negative; for VID mutations S will be negative. The $[s, t]$ curve for VID mutations has a gentle slope for short times, but the slope becomes more pronounced for long periods of time and low specific entropy. This implies that, if the evolution reaches a very low level of entropy, VID mutations could become of greater importance. To put it succinctly, complexity breeds complexity.

Isolated VID mutations would lead to ideal zero-entropy species, but VID mutations, still with the restriction that $\Delta S < 0$, are also aleatory. Furthermore, such species are the result of their evolutionary path. For that reason we say that our theory is not teleological. Neither do humans possess any special privilege in our model, since it is not based in any way on the anthropic principle.

The concept of *zero-entropy species* is an idealization and would correspond to a minimum of entropy depending on the evolution path. A rabbit can be close to a *zero-entropy rabbit*, for example. In this model, there is no end point or point toward which evolution converges; on the contrary, there are as many end points as there are ways of reducing entropy at every step. As stated in § 3, the final end point will be the result of natural selection. Randomness here is limited but not eliminated. We just reduce the possibilities for VID mutations and preserve standard mutations. The adaption to changing environmental and ecological conditions is here considered as fundamental, too.

The density of the vital field tends to reach a distribution with very high values inside a system of very low specific entropy. A living being is conceived here as a system of very low entropy animated by

very high values of the density of the vital fluid at the same place occupied by the system. However, we have not focused this study on the concept of life itself, but rather on its evolution.

We have not considered sexual reproduction because the theory could be applicable to any form of life in the Universe for which we do not know the reproduction mechanism. In any case we do not at all exclude the advantages of sex to the rise of new species and biodiversity.

The densities in the living being contribute to an evolution that favours a decrease of entropy and, consequently, an increase of density. There is an intrinsic instability: low entropy produces increase of density (equation 1) and density reduces the entropy (equation 9). The first process is fast and the second slow. Although this instability takes place on evolutionary time scales, it is present in every phase.

It is even present at the origin of life. In effect, inert matter can undergo natural fluctuations from thermodynamic equilibrium; these lead to fluctuations in the distribution of specific entropy, which imply vital density fluctuations, which in turn produce a prezoic type of heterogeneity that, because of this instability, leads to the first prokaryotes. In terms of this model, the generation of life would not need to be stimulated by mechanisms different from those of evolution, although the generative process itself would require one of its most significant leaps.

One could argue that entropy is a magnitude that was introduced with other purposes in mind, and that the notion of a quantum of entropy does not fit into the original conception of entropy. However, Schrödinger has already spoken of a quantum theory of life. In physics it has often been the case that magnitudes have successfully been given a much broader interpretation than when they were first introduced. Also, the concept of energy, although both familiar and abstract, only began to be appreciated in the nineteenth and twentieth centuries, more or less at the same time at which the concept of entropy was established. On the other hand, we only consider quanta of entropy when dealing with mutational transitions.

6. CONCLUSIONS

The ideas presented here are not an alternative to the standard evolution paradigm, but rather introduce novel physical concepts that speed up the evolution of life, thus rendering more probable the growth of complexity.

There is an intrinsic instability: low entropy produces an increase of vital density; vital density produces a decrease of entropy. The first mechanism

is very fast and the second very slow, with typical characteristic evolution times. As a result of this instability, the distribution of both low entropy and vital density tends to reach very high values in small places, i.e. in living beings.

The higher the degree of complexity the faster becomes the decrement in entropy; therefore the faster the increase of vital density, the faster the increase of complexity. The net effect of the VID mutations introduced here is that complexity breeds complexity.

The similarity between the Eulerian fluid and the vital fluid considered here enables the existence of vital waves and their corresponding particles (vitons). The speed of vitons should be very high, as great as the light speed or slightly lower. This provides another way of accelerating evolution in terms of the faster dissemination of mutations among individuals of the same species. Energy-photons and entropy-vitons are another parallel that could be emphasized.

When we view the complexity of life from a new perspective, specific properties and laws emerge that we have tried here to identify. We have seen how simple physical propositions, together with straightforward and simple mathematics, have sufficed to clarify some of the most controversial questions in the evolution of life on Earth and may even be used to establish general guidelines for understanding life in the Universe. The growth of complexity could be an intrinsic characteristic of any kind of life in diverse astrophysical environments.

Acknowledgements: We are very grateful to an anonymous referee for his/her valuable comments. We are also very grateful to Estrella Florido and Terry Mahoney. Helpful discussions with our colleagues José I. Illana, Antonio Mampaso, Manuel Masip, Evencio Mediavilla, Fernando Moreno, Enrique Pérez, Ramón Román and Ignacio Trujillo have improved the paper.

APPENDIX

A. ESTIMATION OF THE VALUE OF THE MAXIMUM SPECIFIC ENTROPY, s_0

Let us consider Boltzmann's equation relating to entropy and thermodynamic weight (the number of microstates compatible with a macrostate):

$$S = k \ln W. \quad (\text{A13})$$

We assume that the inert matter is hydrogen. In one gram there are N_a hydrogen atoms, N_a being

Avogadro's number (approximately 6×10^{23}). We can exchange each atom by each atom and always obtain the same macroscopic result. The value of W in the inanimate universe will then be $(6 \times 10^{23})!$, where the symbol '!' means factorial. This seems difficult to calculate but we can use Stirling's formula for very large numbers:

$$\ln n! = n \ln n - n. \quad (\text{A14})$$

In our case

$$\ln 6 \times 10^{23}! = 54.7 \times 6 \times 10^{23} - 6 \times 10^{23} \simeq 3 \times 10^{25}. \quad (\text{A15})$$

The entropy of one gram in the inanimate universe will be of the order of

$$1.38 \times 10^{-16} \times 3 \times 10^{25} = 4 \times 10^9 \text{ erg/K}, \quad (\text{A16})$$

and the entropy per baryon:

$$s_0 = 5 \times 10^{-15} \text{ erg/K}. \quad (\text{A17})$$

In cosmological calculations 'geometrical units' are often used with c , G , $k = 1$; the specific entropy then becomes non-dimension and has the value $s_0 = 30$. With this value in equation 12 and assuming a characteristic time of evolution of 10^9 years we obtain k_4 to be of the order of 10^{-14} s^{-1} .

REFERENCES

- Adamsky, P., Eleveld, M., Sood, A. et al. 2020, *Nature Rev. Chemistry*, 4, 386, <https://doi.org/10.1038/s41570-020-0196-x>
- Davies, P. 2019, *The Demon in the Machine (How Hidden Webs of Information Are Solving the Mystery of Life)*, (Chicago, IL: UCP)
- Day, T. 2012, *J. R. Soc. Interface*, 9, 624, <https://doi.org/10.1098/rsif.3011.0479>
- England, J. 2013, *J. Chem. Phys.*, 139, 121923, <https://doi.org/10.1063/1.4818538>
- Gould, S. J. 1996, *Full House: the spread of excellence from Plato to Darwin* (New York, NY: Harmony Books)
- Grassberger, P. 1986, *IJTP*, 25, 907, <https://doi.org/10.1007/BF00668821>
- Kauffman, S. 1995, *At Home in the Universe: The Search for Laws of Self-Organization and Complexity* (OUP)
- _____. 2000, *Investigations* (OUP)
- Krakauer, D. C. 2011, *CHAOS*, 21, 037110, <https://doi.org/10.1063/1.3643064>
- Margulis, L. & Sagan, D. 1995, *What is life?* (Simon & Schuster)
- _____. 1997, *Microcosmos. Four billions years of microbial evolution* (UCP)

- Maturana, H. R. & Varela F. J. 1981, *Autopoiesis and Cognition. The Realization of the Living*. Boston Studies in the Philosophy and History of Science 42 (Dordrecht, Holland: D. Reidel Publishing Company), <https://doi.org/10.1007/978-94-009-8947-4>
- McShea, D. W. & Brandon, R. N. 2010, *Biology's First Law. The Tendency for Diversity and Complexity to Increase in Evolutionary Systems* (Chicago, IL: CUP)
- Oró, J. 1961, *Natur*, 190, 389, <https://doi.org/10.1038/190389a0>
- Prigogine, I. 1981, *From Being to Becoming: Time and Complexity in the Physical Sciences* (W. H. Freeman & Co)
- Prigogine, I. & Stengers, I. 1984, *Order Out of Chaos: Man's Dialogue with Nature*, (New York, NY: Bantam New Age Books)
- Schneider, E. D. & Sagan, D. 2005, *Into the Cool: Energy Flow, Thermodynamics and Life* (Chicago, IL: CUP)
- Schrödinger, E. 1944, *What is life: The Physical Aspect of the Living Cell* (Cambridge, MA: CUP)
- Schulze-Makuch, D. & Irwin, L. N. 2008, *Life in the Universe: Expectations and Constraints in Astrobiology and Biogeophysics* (Berlin, Heidelberg: Springer Verlag)
- Trigo-Rodríguez, J. M. 2010, *Las raíces cósmicas de la vida* (Ediciones UAB)
- Zeravcic, Z. & Brenner, M. P. 2014, *PNAS*, 111, 1748, <https://doi.org/10.1073/pnas.1313601111>

Eduardo Battaner: Instituto Carlos I de Física Teórica y Computacional, Universidad de Granada, Spain (battaner@ugr.es).

Francisco Sánchez: Instituto de Astrofísica de Canarias, Vía Láctea s/n, 38205 La Laguna, Tenerife, Spain & Department of Astrophysics, University of La Laguna, Avda. Astrofísico Francisco Sánchez s/n, 38206 Tenerife, Spain (fsm@iac.es).

THE PRINCIPAL ASTROPHYSICAL PARAMETERS OF THE OPEN CLUSTERS *GULLIVER 18* AND *GULLIVER 58* DETERMINED USING GAIA EDR3 DATA

A. L. Tadross and E. G. Elhosseiny

National Research Institute of Astronomy and Geophysics, Cairo, Egypt.

Received May 19 2022; accepted August 3 2022

ABSTRACT

A photometric and astrometric study of the two open star clusters *Gulliver18* and *Gulliver58* was carried out for the first time using the early third data release of the Gaia space observatory (Gaia-EDR3). By studying the proper motions, parallaxes, and color-magnitude diagrams of the two clusters, we determined their actual cluster membership. Therefore, ages, color excesses, and heliocentric distances of the clusters could be determined. The luminosity function, mass function, total mass, mass segregation, and relaxation time of *Gulliver18* and *Gulliver58* were estimated as well.

RESUMEN

Se realizó por primera vez un estudio fotométrico y astrométrico de dos cúmulos abiertos, *Gulliver18* y *Gulliver58*, con los datos preliminares de la tercera entrega del observatorio espacial Gaia (Gaia-EDR3). Estudiando los movimientos propios, las paralajes y los diagramas color-magnitud de ambos cúmulos determinamos la pertenencia de estrellas a ellos. Con estos resultados pudimos encontrar las edades, excesos de color y distancias heliocéntricas de los cúmulos. También estimamos la función de luminosidad, la función de masa, la masa total y la segregación de masas, así como el tiempo de relajamiento para *Gulliver18* y *Gulliver58*.

Key Words: astronomical data bases: miscellaneous — galaxies: photometry — Hertzsprung-Russell and colour-magnitude — open clusters and associations: individual: Gulliver 18, Gulliver 58

1. INTRODUCTION

This article is part of our series whose goal is to use ideal contemporary datasets to obtain the basic astrophysical properties of poorly studied and/or unstudied open star clusters. Open star clusters (OCs) are important astronomical objects to study the Milky Way structure and evolution. OCs supply useful information about star formation mechanisms, where their main parameters, i.e., age, distance, and reddening can be derived directly from their color-magnitude diagrams (CMDs). This can be accurately achieved when we first determine the actual membership of the clusters under study (Barnes 2007; Perren et al. 2015; Sariya et al. 2017; Marino et al. 2018).

From SIMBAD (<http://simbad.cds.unistra.fr/simbad/sim-fbasic>), we obtained the cluster centers in equatorial and Galactic coordinates.

Gulliver 18 (hereafter G18) is located at ($\alpha = 20^{\text{h}}11^{\text{m}}37^{\text{s}}$, $\delta = +26^{\circ}31'55''$, $l = 65.526^{\circ}$, $b = -3.97045^{\circ}$, $J2000$) in the Vulpecula constellation, whereas Gulliver 58 (hereafter G58) is located at ($\alpha = 12^{\text{h}}46^{\text{m}}4^{\text{s}}$, $\delta = -61^{\circ}57'54''$, $l = 302.3^{\circ}$, $b = 0.9^{\circ}$, $J2000$) in the Centaurus constellation. Figure 1 shows the negative images of G18 and G58 as taken from ALADIN at DSS-colored optical wavelengths. Cantat-Gaudin et al. (2018) studied the main astrometric parameters of those two clusters, i.e., coordinates, proper motions, parallaxes, and distances as newly discovered clusters in the Milky-Way Galaxy. They used the second data release of the Gaia DR2 database, Gaia Collaboration et al. (2018).

Here, we estimate the fundamental parameters of the two clusters G18 and G58 for the first time using the early third release of the Gaia database (Gaia EDR3) - Gaia Collaboration et al. (2021), which was

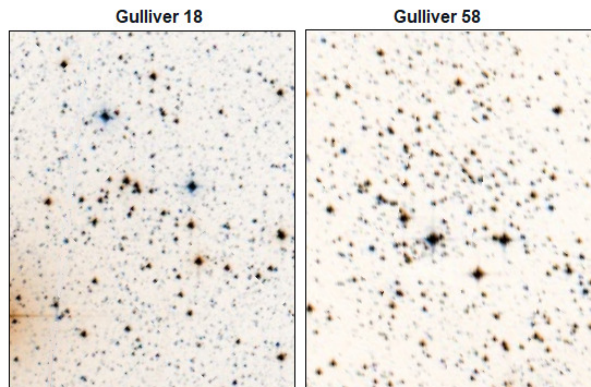


Fig. 1. Inverse colored (negative) images of the clusters *G18* and *G58* as taken from ALADIN at DSS colored optical wavelength. These two clusters lie in the Vulpecula and Centaurus constellations, respectively. North is up and East to the left. The color figure can be viewed online.

published on December 3, 2020. Gaia EDR3 offers improved astrometry and photometry for 1.8 billion sources brighter than $G \approx 21$ mag. Compared to Gaia DR2, the parallax enhancement is 20% and the proper motions are twice more accurate. The most important part of using the Gaia EDR3 involves five astrometric parameters: equatorial positions (α, δ), proper motions ($\mu\alpha \cos \delta, \mu\delta$), and parallaxes ($\bar{\omega}$). In addition, the magnitudes in three photometric filters (G, G_{BP}, G_{RP}) were obtained with better homogeneity due to the significant advance in several aspects (Gaia Collaboration et al. 2021; Torra et al. 2021; Riello et al. 2021). Of course, all of these improvements affect the astrophysical estimated parameters of the clusters under study.

The paper is organized as follows: the Gaia EDR3 dataset and membership determination are presented in § 2. § 3 shows the angular size according to the radial density profiles (RDPs). § 4 contains the photometry of the color-magnitude diagrams (CMDs). § 5 describes the clusters' dynamic states, i.e., luminosity functions (LFs), mass functions (MFs), mass segregation and relaxation times. § 6 summarizes the results and presents the conclusions.

2. GAIA EDR3 DATASET AND MEMBERSHIP

The standard dataset of *G18* and *G58* was downloaded from the Gaia EDR3 I/350 VizieR catalog website. A circular region of 20 arcmin radius centered in the celestial position was applied to each cluster. The error ranges of the parallaxes are up to 0.03 mas for $G < 15$ mag, 0.07 mas for $G \approx 17$ mag, 0.5 mas for $G \approx 20$ mag, and 1.3 mas for

$G \approx 21$ mag. The error ranges of the proper motions (PMs) are up to 0.03 mas/yr for $G < 15$ mag, 0.07 mas/yr for $G \approx 17$ mag, 0.5 mas/yr for $G \approx 20$ mag, and 1.4 mas/yr for $G \approx 21$ mag.

Using high-precision Gaia EDR3 parallaxes and proper motions, we can easily remove the background field stars from the cluster's main sequence (Bellini et al. 2009; Yadav et al. 2013; Sariya & Yadav 2015; Tadross 2018). The vector point diagrams (VPDs), $\mu\alpha \cos \delta$ vs $\mu\delta$ of *G18* and *G58* are shown in Figure 2. The greatest density area (the darkest spot) is taken as the subset of the cluster's most likely members (Tadross 2018; Tadross & Hendy 2021, 2022).

In our analysis, we used the software named TOPCAT. This is a tool that can handle huge and sparse datasets. It was initially created for astronomy to support virtual observatories. The acronym TOPCAT derives from Tool for OPERations on Catalogues And Tables. It can support several digital file formats, including FITS, which is widely used in astronomy (<http://www.star.bris.ac.uk/~mbt/topcat/>).

Within the subset of the cluster's most likely members, only those stars with magnitudes $G \leq 20.5$, located inside the cluster's estimated size (see § 3) were taken into account. Mean values and standard deviations of the parallax and the two components of the proper motions were calculated for all these stars (excluding negative values of the parallax, see the lower right-hand panel of Figure 4). Stars are then considered to be cluster members only if their 3σ parallax and proper motion errors lie within the cluster's mean values with respect to the background field ones. According to Lindegren et al. (2018), all the parallax values should be shifted by adding 0.029 mas to their values. In addition, the value of the renormalized unit weight error, RUWE, indicates how well the source matches the single-star model - it should be less than 1.4.

Using TopCat, we can identify comoving stars, i.e., those stars that move at the same speed and direction in the sky, as shown in Figure 3. It is worth noting that the selected subset of VPDs influences the CMDs and field star separation. The CMDs of the clusters appear cleaner when those conditions are applied (Anderson et al. 2006; Sariya et al. 2017).

3. ANGULAR SIZE

The boundary and core radii of *G18* and *G58* were calculated using King (1966) radial density profile (RDP). To do so, we built a series of concentric circles centered on the clusters' central coordinates.

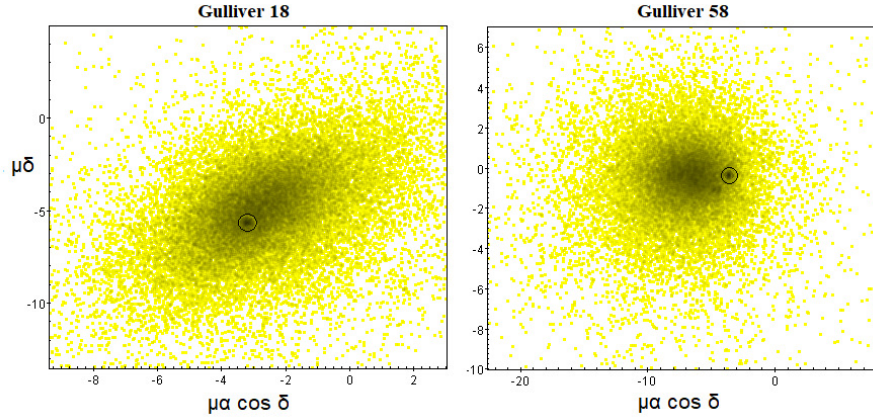


Fig. 2. The vector point diagrams of the clusters G18 and G58. The circles denote the darkest areas, in which the subsets of the most likely members lie. The color figure can be viewed online.

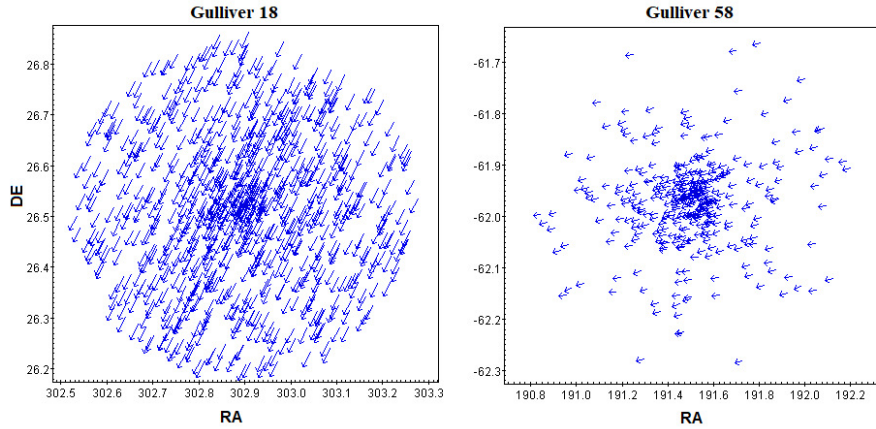


Fig. 3. Comoving stars of clusters G18 and G58. They are the stars included in the subsets we selected in the VPDs, i.e., the stars that move at the same speed and direction in the sky. The color figure can be viewed online.

The number of stars found in each ring was divided by the ring area to obtain the stellar density $f(R)$. The upper right-hand panel of Figure 4 shows the measured star density vs. the distance to the cluster center. The King model fit can be given by the equation:

$$f(R) = f_{bg} + \frac{f_0}{1 + (\frac{R}{R_c})^2}, \quad (1)$$

where R is the radius from the cluster center, f_0 the central density, R_c the core radius and f_{bg} the background density. We can find these parameters from the King model as follows:

	R_c	f_{bg}	f_0
G18	0.35	50	233
G58	0.27	33	305

When the stars approach the boundary radius, they begin to dissolve within the background density. Knowing the previous parameters, we can get the boundary radius by applying the equation of Bukowiecki et al. (2011) as follows:

$$R = R_c \sqrt{\frac{f_0}{3\sigma_{bg}} - 1}, \quad (2)$$

where σ_{bg} is the uncertainty of f_{bg} . Consequently, the estimated boundary radii of G18 and G58 are found to be 7.5 ± 0.5 arcmin (3.0 pc) and 4.5 ± 0.3 arcmin (1.9 pc), respectively.

On the other hand, the tidal radius of a cluster is defined as the distance from the cluster core at which the Galaxy's gravitational influence equals that of the cluster core. Estimating the total masses of G18 and G58 (see § 5), the tidal radius can be calculated

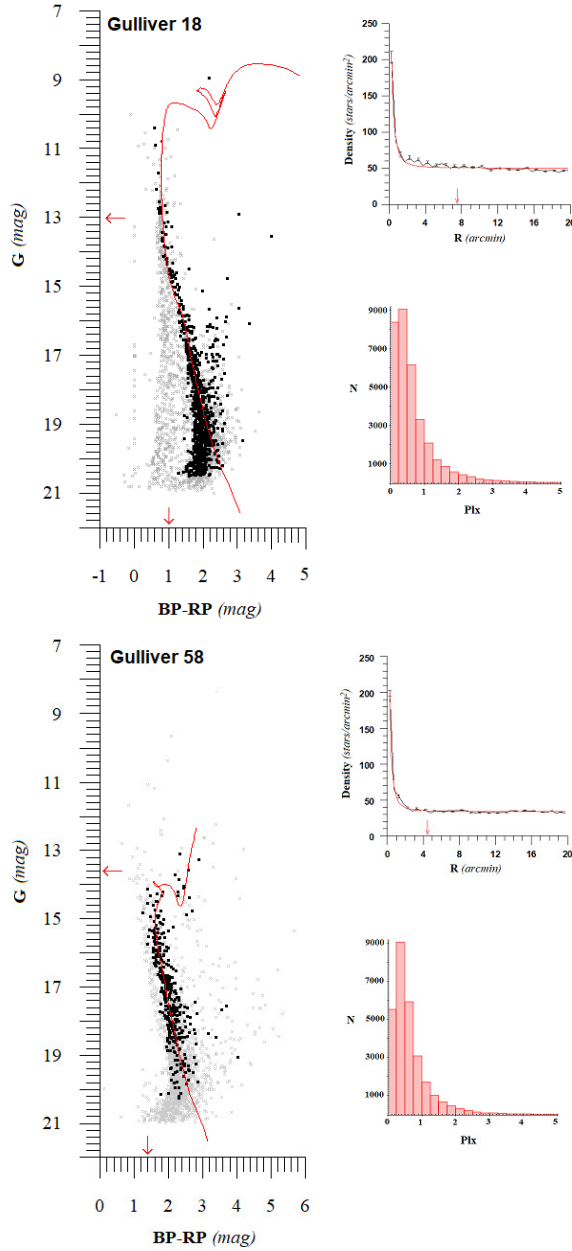


Fig. 4. The left-hand panels show the main sequence curves of *G18* and *G58* fitted to the solar metallicity theoretical isochrones of Padova. The ages are found to be 100 ± 10 Myr and 1.0 ± 0.1 Gyr, respectively. The distance moduli and color excesses are found to be 12.3, 13.6 (± 0.25) mag, 0.8 and 1.4 (± 0.10) mag, respectively. The right-hand panels show the radial density profiles fitted to the King (1966) model and the histograms of parallaxes of the selected stars ($\bar{\omega} > 0$). The estimated radii of *G18* and *G58* are found to be 7.5 and 4.5 (± 0.50) arcmin and the mean values of the parallaxes are found to be 0.50 and 0.45 (± 0.05) mas, respectively. The color figure can be viewed online.

using the form of Jeffries et al. (2001) as follows:

$$R_t = 1.46 \times M_c^{\frac{1}{3}}, \quad (3)$$

where R_t is the tidal radius (in parsec) and M_c the total mass of the cluster (in solar masses). The tidal radii of *G18* and *G58* are found to be 17.8 and 11.0 (± 0.2) pc, respectively. The concentration parameter of Peterson & King (1975), $C = \log(\frac{R}{R_c})$, shows us whether the cluster is prominent or condensed with respect to the background field stars. We found that both clusters are insufficiently condensed objects.

4. CMD PHOTOMETRY

The study of CMD is a widely used technique to characterize the observed main sequence of the cluster. This is achieved by finding the best fit of one of the Padova PARSEC databases of stellar evolutionary isochrones (<http://stev.oapd.inaf.it/cgi-bin/cmd>) of Bressan et al. (2012) to the observed main-sequence curve of the cluster. To decrease the effect of field stars contamination, only the most likely cluster members are taken into account. Since the cluster members have a common origin, they share the same speed and direction in the sky. This fact makes proper motions a valuable tool for removing nonmember stars from each cluster's main sequence (Yadav et al. 2013; Bisht et al. 2020).

Based on the CMDs of *G18* and *G58*, as shown in the left-hand panel of Figure 4, only the stars within the cluster's boundary size and parallaxes ranges are represented. The mean values of the parallaxes are found to be 0.50 and 0.45 (± 0.05) mas, respectively. Clusters fittings were quite good by shifting the isochrones of ages 100 ± 10 Myr and 1.0 ± 0.1 Gyr with apparent distance moduli ($m - M$) of 12.3 and 13.6 (± 0.25) mag, respectively. In addition, the color excesses $E(BP - RP)$ are found to be 0.8 and 1.4 (± 0.10) mag, respectively. Note that *G18* and *G58* are close to areas with a lot of dust with high differential extinction in their fields along their lines of sight, as displayed in the 3D extinction map (<http://argonaut.skymaps.info>).

Reddening is a critical parameter affecting the total absorption value that must be subtracted from the apparent distance modulus to obtain the true distance to the cluster. We used the Padova PARSEC database of stellar evolutionary tracks and isochrones, which is scaled to the solar metallicity of 0.0152. The Gaia filter passbands are taken from Riello et al. (2021), where $A_G/A_V = 0.836$, $A_{GBP}/A_V = 1.083$, and $A_{GRP}/A_V = 0.634$. These

TABLE 1
THE PRINCIPAL ASTROPHYSICAL PARAMETERS OF *G18* AND *G58**

Parameter	Gulliver 18	Gulliver 58
RA (h: m: s)	20:11:37	12:46:04
DE (°: ': ")	+26:31:55	-61:57:54
G. long. (°)	65.526	302.30
G. lat. (°)	-3.97	0.90
Age (Myr)	100 ± 10	1000 ± 100
Radius (arcmin)	7.5 ± 0.5	4.5 ± 0.3
Core Radius (arcmin)	0.35 ± 0.07	0.27 ± 0.04
Tidal Radius (pc)	17.8 ± 0.5	11.0 ± 0.5
m-M (mag)	12.3 ± 0.25	13.6 ± 0.25
E(BP-RP) (mag)	0.8 ± 0.1	1.4 ± 0.1
E(B-V) (mag)	0.61 ± 0.1	1.06 ± 0.1
Dist. (pc)	1370 ± 65 (1558.6)	1425 ± 65 (2344.2)
Relax. Time (Myr)	31.5 ± 5	9.5 ± 5
P.M. (mas/sec)	6.515 ± 0.45 (6.488)	3.652 ± 0.35 (3.609)
Plx. (mas)	0.50 ± 0.07 (0.613)	0.45 ± 0.07 (0.398)
Rgc (kpc)	6.75 ± 0.2	6.55 ± 0.2
X_{\odot} (pc)	-565 ± 40	-760 ± 60
Y_{\odot} (pc)	1241 ± 55	-1201 ± 50
Z_{\odot} (pc)	-95 ± 5	22 ± 5

*The values in brackets are the corresponding astrometric measurements obtained by Cantat-Gaudin et al. (2018).

ratios have been used for correction of the magnitudes for the interstellar reddening and for converting the color excess to $E(B - V)$, where $R_v = A_v/E(B - V) = 3.1$. Therefore, we can estimate the true distance moduli $(m - M)_0$ of *G18* and *G58*, from which we infer heliocentric distances of 1370 and 1425 (± 65) pc, respectively. Correspondingly, the Cartesian Galactocentric coordinates ($X_{\odot}; Y_{\odot}; Z_{\odot}$) and the distances from the Galactic center (R_g) are estimated for the two clusters as listed in Table 1. According to our calculations mentioned in Tadross (2011), the Y -axis connects the Sun to the Galactic center, being positive to the Galactic anticenter, while the X -axis is perpendicular to Y -axis, being positive in the first and second Galactic quadrants (Lynga 1982). We adopted a Galactocentric distance (R_g) of 7.2 kpc (Bica et al. 2006).

5. THE DYNAMIC STATE OF THE CLUSTERS

5.1. Luminosity and Mass Functions

We used the photometric dataset of Gaia EDR3 to derive the clusters' luminosity functions (LFs) and mass functions (MFs). The LF represents the distribution of the absolute magnitudes of the cluster's members. Using the distance moduli obtained from

the isochrone fittings, we transformed the apparent G magnitudes of the cluster members into absolute magnitudes. Then, the LF diagrams can be constructed as shown in the upper panel of Figure 5. Note that the LFs increase up to $M_G \approx 8.15$ and 4.20 mag for *G18* and *G58*, respectively.

The initial mass function (IMF) provides the main bond between the bright massive members and less massive fainter ones. It is a historic record of the star formation process and plays the main role in understanding the early dynamic development of star clusters. The IMF was estimated for the bright massive stars ($\geq 1M_{\odot}$) by Salpeter's (1955) power law, where the number of stars in each mass range decreases as the mass increases. It can be written as follows:

$$\log \frac{dN}{dM} = -(1 + x) \log(M) + const., \quad (4)$$

where dN is the number of stars in a mass bin dM with a central mass M and x is the MF slope. To convert LF into MF, we used the last version of the theoretical isochrones of Padova's stellar evolutionary tracks and isochrones. The resulting mass functions of *G18* and *G58* are shown in the lower panel of Figure 5. The derived values of the MF slope are

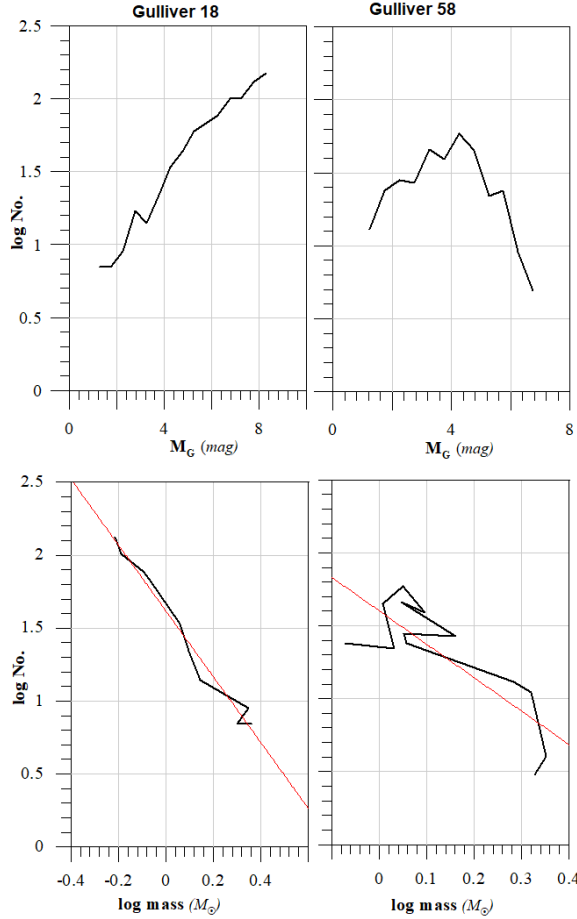


Fig. 5. The upper panel represents the luminosity functions of *G18* and *G58*. Note that the LFs increase up to $M_G \sim 8.15$ and 4.20 mag for *G18* and *G58*, respectively. The lower panel represents the mass distribution of the two clusters. The red lines show the linear fittings of the mass functions' slopes, which are found to be 2.25 and $2.29 (\pm 0.15)$ for *G18* and *G58*, respectively. The color figure can be viewed online.

found to be $x = 2.25$ and $2.29 (\pm 0.15)$ for *G18* and *G58*, respectively, which agree with Salpeter's mean value.

5.2. Mass Segregation

Mass segregation in a real cluster implies that the massive stars are more concentrated toward the cluster center than less massive stars. Mass segregation is a result of the dynamic evolution of the cluster and/or an impression of star construction processes themselves, or both (Sagar 2002). To explore if there is actual mass segregation, we divided the clusters' stars into four bands, $G < 17$; $17 \leq G \leq 18$; $18 \leq G \leq 19$ and $G \geq 19$ mag. Drawing these bands as a function

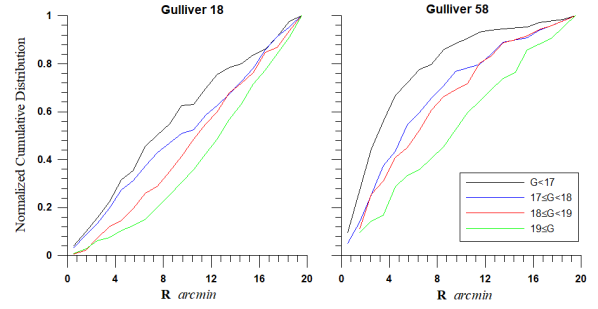


Fig. 6. The cumulative frequency distributions of *G18* and *G58* represent the radial distance and magnitude distributions of the clusters' member bands (mass segregation). The bright, massive stars are more likely to settle toward the clusters' centers than the fainter, less massive, ones. The color figure can be viewed online.

of the distances from the cluster's center as shown in Figure 6, we found that the bright massive stars are more likely to settle toward the cluster center than the less massive fainter ones.

5.3. Relaxation Time

Once the distribution of the cluster members' velocities becomes almost Maxwellian, a metric for understanding the dynamical evolution is considered. This period is known as "relaxation time" (T_R) and can be defined by the equation of Spitzer & Hart (1971) as follows:

$$T_R = \frac{8.9 \times 10^5 \sqrt{N} \times R_h^{1.5}}{\sqrt{\langle m \rangle} \times \log(0.4N)}, \quad (5)$$

where N is the number of cluster members, R_h is the cluster's radius that contains half of the cluster's total mass (in pc) and $\langle m \rangle$ is the average mass of a member star (in solar masses). Thus, the dynamic relaxation times are found to be 31.5 and $9.5 (\pm 5.0)$ Myr for *G18* and *G58*, respectively. The clusters under investigation are thus found to be older than their estimated relaxation times. We conclude that *G18* and *G58* are dynamically relaxed clusters.

6. RESULTS AND CONCLUSIONS

The principal properties of the two open clusters Gulliver 18 and Gulliver 58 were looked into in this paper for the first time using the Gaia EDR3 database. Both clusters are located in the Vulpecula and Centaurus constellations, respectively; they are not sufficiently condensed objects in the sky. The MF slopes of *G18* and *G58* are found to agree with

Salpeter's (1955) mean value. The two clusters are dynamically relaxed as their estimated relaxation times are much smaller than their ages. Table 1 summarizes the main results of our study.

This work is a part of the project named (IMHOTEP) No. 42088ZK between Egypt and France. It was begun in 2019 and finished in 2021. Many thanks to Prof. David Valls-Gabaud (Paris Observatory) for being a companion in that project. This work has made use of data from the European Space Agency (ESA) mission Gaia processed by the Gaia Data Processing and Analysis Consortium (DPAC), (<https://www.cosmos.esa.int/web/gaia/dpac/consortium>). Funding for the DPAC has been provided by national institutions, in particular, the institutions participating in the Gaia Multilateral Agreement (MLA). The Gaia mission website is <https://www.cosmos.esa.int/gaia>. The Gaia archive website is <https://archives.esac.esa.int/gaia>.

REFERENCES

- Anderson, J., Bedin, L. R., Piotto, G., et al. 2006, *A&A*, 454, 1029, <https://doi.org/10.1051/0004-6361/20065004>
- Barnes, S. A. 2007, *ApJ*, 669, 1167, <https://doi.org/10.1086/519295>
- Bellini, A., Piotto, G., Bedin, L. R., et al. 2009, *A&A*, 493, 959, <https://doi.org/10.1051/0004-6361/200810880>
- Bica, E., Bonatto, C., Barbuy, B., & Ortolani, S. 2006, *A&A*, 450, 105, <https://doi.org/10.1051/0004-6361/20054351>
- Bisht, D., Zhu, Q., Yadav, R. K. S., Durgapal, A., & Rangwal, G. 2020, *MNRAS*, 494, 607, <https://doi.org/10.1093/mnras/staa656>
- Bressan, A., Marigo, P., Girardi, L., et al. 2012, *MNRAS*, 427, 127, <https://doi.org/10.1111/j.1365-2966.2012.21948.x>
- Bukowiecki, L., Maciejewski, G., Konorski, P., & Strobel, A. 2011, *AcA*, 61, 231
- Cantat-Gaudin, T., Jordi, C., Vallenari, A., et al. 2018, *A&A*, 618, 93, <https://doi.org/10.1051/0004-6361/201833476>
- Gaia Collaboration, Brown, A. G. A., Vallenari, A., et al. 2018, *A&A*, 616, 1, <https://doi.org/10.1051/0004-6361/201833051>
- Gaia Collaboration, Brown, A. G. A., Vallenari, A., et al. 2021, *A&A*, 649, 1, <https://doi.org/10.1051/0004-6361/202039657>
- Jeffries, R. D., Thurston, M. R., & Hambly, N. C. 2001, *A&A*, 375, 863, <https://doi.org/10.1051/0004-6361:20010918>
- King, I. R. 1966, *AJ*, 71, 64, <https://doi.org/10.1086/109857>
- Lindegren, L., Hernández, J., Bombrun, A., et al. 2018, *A&A*, 616, 2, <https://doi.org/10.1051/0004-6361/201832727>
- Lynga, G. 1982, *A&A*, 109, 213
- Marino, A. F., Milone, A. P., Casagrande, L., et al. 2018, *ApJ*, 863, 33, <https://doi.org/10.3847/2041-8213/aad868>
- Perren, G. I., Vázquez, R. A., & Piatti, A. E. 2015, *A&A*, 576, 6, <https://doi.org/10.1051/0004-6361/201424946>
- Peterson, C. J. & King, I. R. 1975, *AJ*, 80, 427, <https://doi.org/10.1086/111759>
- Riello, M., De Angeli, F., Evans, D. W., et al. 2021, *A&A*, 649, 3, <https://doi.org/10.1051/0004-6361/202039587>
- Sagar, R. 2002, *IAUS 207*, Extragalactic Star Clusters, ed. D. Geisler, E. K. Grebel, & D. Minniti (San Francisco, CA: ASP), 515
- Salpeter, E. E. 1955, *ApJ*, 121, 161, <https://doi.org/10.1086/145971>
- Sariya, D. P., Jiang, I.-G., & Yadav, R. K. S. 2017, *AJ*, 153, 134, <https://doi.org/10.3847/1538-3881/aa5be6>
- Sariya, D. P. & Yadav, R. K. S. 2015, *A&A*, 584, 59, <https://doi.org/10.1051/0004-6361/201526688>
- Spitzer, L. Jr. & Hart, M. H. 1971, *ApJ*, 166, 483, <https://doi.org/10.1086/150977>
- Tadross, A. L. 2011, *JKAS*, 44, 1, <https://doi.org/10.5303/JKAS.2011.44.1.1>
- _____. 2018, *RAA*, 18, 158, <https://doi.org/10.1088/1674-4527/18/12/158>
- Tadross, A. L. & HENDY, Y. H. 2021, *ApJ*, 42, 6, <https://doi.org/10.1007/s12036-020-09648-5>
- _____. 2022, *AdSpR*, 69, 467, <https://doi.org/10.1016/j.asr.2021.09.014>
- Torra, F., Castañeda, J., Fabricius, C., et al. 2021, *A&A*, 649, 10, <https://doi.org/10.1051/0004-6361/202039637>
- Yadav, R. K. S., Sariya, D. P., & Sagar, R. 2013, *MNRAS*, 430, 3350, <https://doi.org/10.1093/mnras/stt136>

Ashraf L. Tadross and Eslam G. Elhosseiny: National Research Institute of Astronomy and Geophysics, Cairo, Egypt, EL Marsad Street 1, Helwan, Cairo, Egypt (altadross@nriag.sci.eg), (eslam.elhosseiny@nriag.sci.eg).

THE HII REGIONS AND BOW SHOCKS AROUND RUNAWAY O STARS

A. C. Raga¹, J. Cantó², and A. Noriega-Crespo³

Received May 19 2022; accepted August 3 2022

ABSTRACT

We present a model for the HII region and stellar wind bow shock formed by runaway O stars passing through the Galactic disk. We develop a quasi-analytic approach in which the absorption of stellar ionizing photons by the bow shock is considered. With these models we study the transition between a detached ionization front (leading the bow shock) and an ionization front trapped by the stellar wind bow shock. We find that for an O7 star one needs to have a stellar velocity of only a few km/s and an environmental density $> 10^5 \text{ cm}^{-3}$.

RESUMEN

Presentamos un modelo para la región HII y para el choque de proa del viento estelar producidas por estrellas O fugadas pasando a través del plano galáctico. Desarrollamos un modelo cuasi-analítico que incluye la absorción de los fotones ionizantes estelares por el choque de proa. Con estos modelos estudiamos la transición entre un frente de ionización libre (que precede al choque de proa) y un frente de ionización atrapado por el choque de proa. Encontramos que para una estrella O7 se necesita una velocidad estelar de unos pocos km/s y una densidad ambiental $> 10^5 \text{ cm}^{-3}$.

Key Words: HII regions — hydrodynamics — stars: winds, outflows

1. INTRODUCTION

Runaway O stars pass through the Galactic disk at velocities of $\approx 100 \text{ km s}^{-1}$ (see, e.g., Cruz-González et al. 1974). These stars interact with the interstellar medium of the disk, forming an inner stellar wind bow shock, and an outer “cometary” HII region. Observations of these structures are presented, e.g., by Van Buren et al. (1995) and Noriega-Crespo et al. (1997). We note that these HII regions have a somewhat elongated “tear-drop” shape, and that the “cometary” label that is applied to them is somewhat misleading.

The problem of the cometary HII region for a star in hypersonic motion was solved analytically by Rasiwala (1969) and numerically by Thuan (1975). Axisymmetric gasdynamic simulations of this flow were presented by Raga et al. (1997).

The standard, ram-pressure balance stellar wind bow shock has the well used analytic solution of Dyson (1975). Also, at a somewhat surprisingly later time, an analytic solution to the full, thin shell stellar wind bow shock problem (including the “centrifugal pressure”) was found (Wilkin 1996; Cantó et al. 1996). The stellar wind bow shock problem has been studied extensively with gasdynamic numerical simulations (see, e.g., Stevens et al. 1992).

Stellar wind bow shock models have been used to model compact/ultracompact HII regions formed by young O stars within molecular clouds (e.g., Van Buren 1990; Mac Low 1991), moving at velocities of a few km/s through the surrounding cloud. The models for these objects generally assume that the ionization front is trapped within the stellar wind bow shock, so that the flow differs from the detached bow shock/HII region found in runaway O stars. Gasdynamic simulations of bow shock compact HII regions have been presented by Arthur & Hoare (2006).

Simulations of bow shocks around runaway stars have been computed including thermal conduction (Meyer et al. 2014) and magnetic fields (Meyer et al. 2017). The cometary HII regions surrounding these bow shocks have been modeled in detail (in axisymmetry and 3D, including an environmental magnetic field) by Mackey et al. (2013). Interestingly, even in the work of Raga et al. (1997), which modeled both the bow shock and the cometary HII region of runaway O stars, these two structures of the flow have

¹Instituto de Ciencias Nucleares, UNAM, México.

²Instituto de Astronomía, UNAM, México.

³STScI.

been considered separately. In the present paper we explore the regime in which the bow shock, while not trapping the ionization front, produces a substantial absorption of the stellar ionizing photons, therefore modifying the surrounding HII region.

We describe the flow by considering the thin shell analytic solution (of Wilkin 1996; Cantó et al. 1996 and Cantó et al. 2005) for the stellar wind bow shock. A review of this solution is presented in §2. We then write a modified form for the equation of Rasiwala (1969) and Raga et al. (1997), including the absorption of ionizing photons by the bow shock (§3) and integrate it numerically to obtain the self-consistent HII region+bow shock solution for a set of parameters (§4). Finally, in the summary (§5) we discuss the possible application of the new model for the case of compact/ultracompact HII regions, and the further steps that will be necessary to study the full parameter space of these objects.

2. THE BOW SHOCK

A star with an isotropic wind of mass loss rate \dot{M}_w and (terminal) wind velocity v_w moving hyper-sonically at a velocity v_a through a uniform medium of density ρ_a produces a double bow shock (with one shock stopping the wind and the second shock pushing the environment). This is shown schematically in Figure 1, as seen in a reference system moving with the star.

Wilkin (1996) and Cantó et al. (1996) found an analytic solution for the steady, thin shell stellar bow shock problem:

$$R_b(\theta) = R_0 \csc \theta \sqrt{3(1 - \theta \cot \theta)}, \quad (1)$$

with

$$R_0 \equiv \sqrt{\frac{\dot{M}_w v_w}{4\pi \rho_a v_a^2}}, \quad (2)$$

and where the polar angle θ and the spherical radius R_b are shown in Figure 1.

Interestingly, the axisymmetric gasdynamic simulations of Raga et al. (1997) show that even though the bow shock driven by a runaway O star has a complex, time-dependent structure and a separation of $\approx 0.3R_0$ between the two bow shocks, it still approximately follows the thin shell solution of equation (1). We therefore adopt this thin shell solution as a valid description of the stellar wind bow shock.

We also use the emission measure:

$$EM = \int_0^h n^2 dl, \quad (3)$$

i.e., the square of the ion number density ($n = \rho/\bar{m}$ for fully ionized H and singly ionized He) integrated

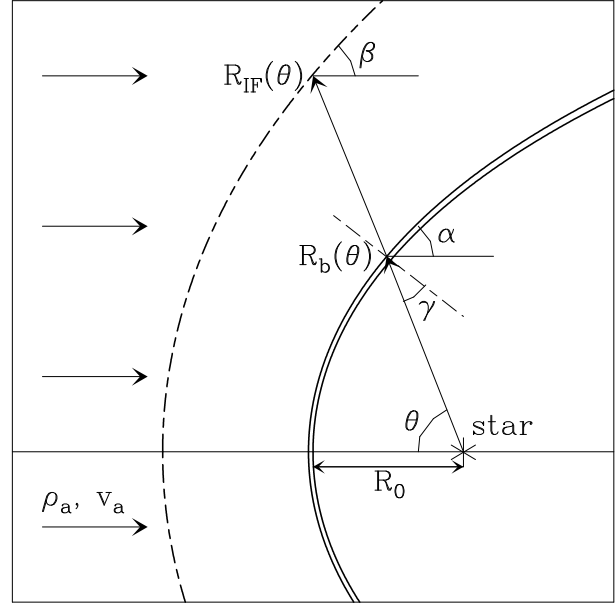


Fig. 1. Schematic diagram showing a star with an isotropic wind interacting with a uniform, streaming environment (of density ρ_a and velocity v_a). A two-shock stellar wind bow shock with a locus $R_b(\theta)$ (two thick, solid curves) and a detached ionization front of locus $R_{IF}(\theta)$ (thick, dashed curve) are formed. The angles θ , α and γ (used in the derivation of the model equations) are shown.

across the width h of the thin shell. This integral was calculated by Cantó et al. (2005) for a bow shock travelling into an environment with a density gradient, and their results can be used (by setting the density gradient to zero) to obtain the emission measure for a bow shock in a uniform environment:

$$EM = EM_0 [f_a(\theta) + f_w(\theta)] g_\sigma(\theta), \quad (4)$$

with

$$EM_0 = \frac{\rho_a v_a v_w}{2\bar{m}^2 c_0^2} \left(\frac{\dot{M}_w \rho_a}{4\pi v_w} \right)^{1/2}, \quad (5)$$

where $\bar{m} = 1.3 m_H$ for gas with 0.9 H and 0.1 He number abundance, $c_0 \approx 10 \text{ km s}^{-1}$ is the sound speed of the photoionized gas, and $f_a(\theta)$, $f_w(\theta)$ and $g_\sigma(\theta)$ are given in Appendix A.

3. THE EQUATION FOR THE HII REGION

For a star that emits S_* ionizing photons per unit time, if the bow shock shell does not trap the ionization front, we will have a cometary HII region surrounding the stellar wind bow shock (see the schematic diagram of Figure 1). For a hypersonic flow, the ionization front limiting this HII region will not produce a hydrodynamic perturbation, and the

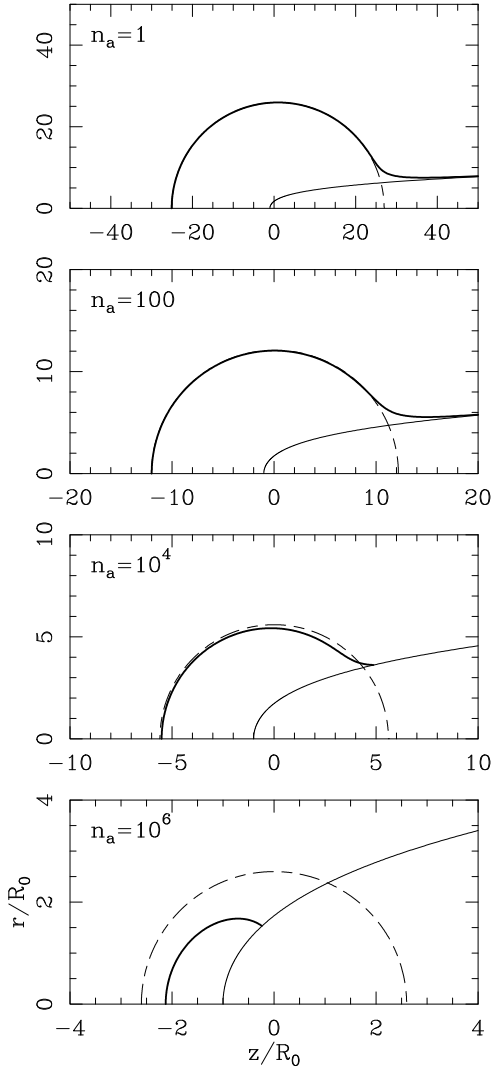


Fig. 2. The ionization front (thick, solid outer curve) and the stellar wind bow shock (thin, solid inner curve) obtained for models with $v_a = 20 \text{ km s}^{-1}$ and $n_a = 1$ (top frame), 100, 10^4 and 10^6 cm^{-3} (bottom). The dashed curves show the ionization front that would be obtained for a star with no wind. The (z, r) axes are given in units of R_0 .

environmental material will therefore flow with density ρ_a and velocity v_a until it intercepts the bow shock (see Figure 1).

The equation determining the locus $R_{IF}(\theta)$ of the ionization front is:

$$\frac{2\pi}{3} \sin \theta (R_{IF}^3 - R_b^3) n_a^2 \alpha_H + n_a v_a 2\pi r_{IF} \frac{dr_{IF}}{d\theta} = 2\pi \sin \theta \left(\frac{S_*}{4\pi} - \frac{R_b^2 EM \alpha_H}{\cos \gamma} \right), \quad (6)$$

where the terms in the equation represent:

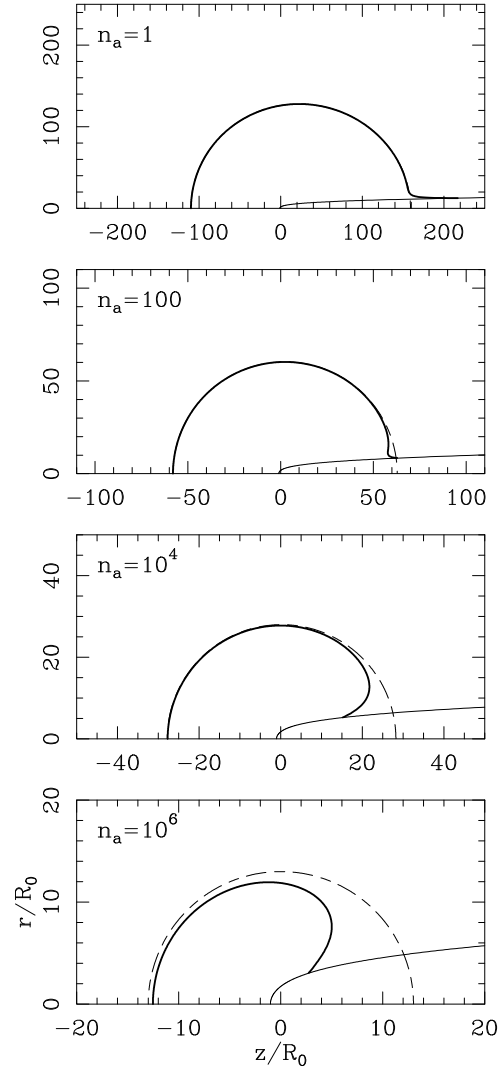


Fig. 3. The same as Figure 2, but for the $v_a = 100 \text{ km s}^{-1}$ models (see Table 1).

- first term on the left: recombination in the region with radii $R_b < R < R_{IF}$,
- second left term: flux of neutrals entering the ionization front,
- first term on the right: ionizing photon rate,
- second right term: recombinations within the bow shock shell,

per unit time within the solid angle between θ and $\theta + d\theta$. In this equation, $r_{IF} = R_{IF} \sin \theta$ is the cylindrical radius of the ionization front and α_H is the H recombination coefficient (we set $\alpha_H = 2.56 \times 10^{-13} \text{ cm}^3 \text{ s}^{-1}$).

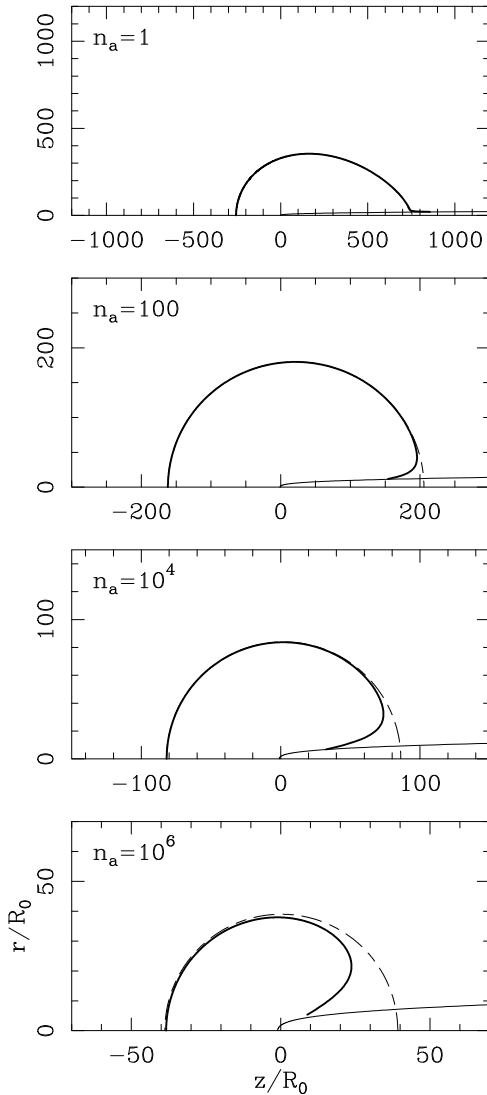


Fig. 4. The same as Figure 2, but for the $v_a = 200 \text{ km s}^{-1}$ models (see Table 1).

Combining equations (3-6) we obtain the dimensionless equation:

$$\left(\frac{R_{IF}}{R_0}\right)^3 - \left[\frac{R_b(\theta)}{R_0}\right]^3 + \chi \left(\frac{R_{IF}}{R_0}\right) \left[\frac{d(R_{IF}/R_0)}{d\theta} \sin \theta + \frac{R_{IF}}{R_0} \cos \theta \right] = \left(\frac{R_S}{R_0}\right)^3 - \frac{3M_a^2}{2} G(\theta), \tag{7}$$

where R_b/R_0 is given by equation (1),

$$M_a = \frac{v_a}{c_0} \tag{8}$$

is the Mach number of the impinging environment with respect to the isothermal sound speed of the photoionized gas,

$$R_S = \left(\frac{3S_*}{4\pi n_a^2 \alpha_H}\right)^{1/3} \tag{9}$$

is the Strömngren radius and

$$\chi = \frac{3v_a}{n_a R_0 \alpha_H}, \tag{10}$$

where $n_a = \rho_a/\bar{m}$ is ion+atom environmental number density. The $G(\theta)$ function (describing the absorption of the bow shock shell as a function of θ) is given in Appendix A.

Our equation (7) is a generalization of equation (12) of Raga et al. (1997) (which has a dimensionless parameter $\xi = \chi R_0/R_s$) to the case of a cometary HII region with an inner stellar wind bow shock producing an appreciable absorption of the stellar ionizing photons.

For $\theta = 0$ from equation (7) we have:

$$\left(\frac{R_{IF,0}}{R_0}\right)^3 - 1 + \chi \left(\frac{R_{IF,0}}{R_0}\right)^2 = \left(\frac{R_S}{R_0}\right)^3 - \frac{9M_a^2}{4}, \tag{11}$$

where we have used the fact that $G(0) = 3/2$ (see equation A17). This is a cubic equation which can be inverted (analytically or numerically) to obtain the on-axis radius $R_{IF,0}$ of the ionization front. This value can be used to start a numerical integration of the ordinary differential equation (7) which then gives the shape $R_{IF}(\theta)$ of the ionization front.

Depending on the values of the parameters χ , R_S/R_0 and M_a , we find that equation (11) has either:

- one real root with $R_{IF,0}/R_0 > 1$, or
- no root satisfying this condition

This latter situation corresponds to the case in which the head of the bow shock traps the ionization front,

4. NUMERICAL RESULTS

As there is a considerable number of free parameters, a general exploration of the possible parameter space is lengthy (and also not very enlightening). We therefore choose to explore a limited range of parameters, which is appropriate for the case of a runaway O star passing through the plane of the Galaxy.

TABLE 1
 MODELS FOR AN O7 STAR PASSING THROUGH THE GALACTIC PLANE

v_a [km/s]	n_a [cm $^{-3}$]	R_0 [pc]	R_S/R_0	χ	$R_{IF,0}/R_0$
20	1	2.61	26.0	2.90	25.1
20	100	0.261	12.1	0.290	12.0
20	10^4	2.61e-2	5.60	2.90e-2	7.45
20	10^6	2.61e-3	2.60	2.90e-3	3.25
100	1	0.522	130.0	72.4	109.8
100	100	5.22e-2	60.35	7.24	58.0
100	10^4	5.22e-3	28.01	0.724	27.7
100	10^6	3.22e-4	13.00	7.24e-2	12.5
300	1	0.174	390.1	651.8	255.8
300	100	1.74e-2	181.1	65.18	161.8
300	10^4	1.74e-3	84.0	6.518	81.8
300	10^6	1.74e-4	39.0	0.6518	38.3

For the runaway O star, we choose a O7V star with wind velocity $v_w = 2500 \text{ km s}^{-1}$, mass loss rate $\dot{M}_w = 4.5 \times 10^{-7} M_\odot \text{ yr}^{-1}$ and ionizing photon rate $S_* = 10^{49} \text{ s}^{-1}$. For the streaming environment we choose three possible velocities ($v_a = 20, 100$ and 300 km s^{-1}) and four possible number densities ($n_a = 1, 100, 10^4$ and 10^6 cm^{-3}). The values of R_0 , R_S/R_0 and χ corresponding to the chosen models are given in Table 1 (we do not list $M_a = v_a/10 \text{ km s}^{-1}$).

For the combinations of these environmental velocities and densities we first calculate the axial standoff distance $R_{IF,0}$ of the ionization front from equation (11). The results of this exercise are given in Table 1. It is clear that for all of the chosen parameters the bow shock does not trap the ionization front, and that an external HII region is produced. The smaller HII region (relative to the size of the bow shock) is found for the $v_a = 20 \text{ km s}^{-1}$, $n_a = 10^6 \text{ cm}^{-3}$ model, in which the on-axis radius of the ionization front is ≈ 3 times the bow shock radius (see Table 1).

With the $R_{IF}(\theta = 0) = R_{IF,0}$ initial condition, we integrate equation (7) to obtain the shape of the ionization front. The results for the $v_a = 20 \text{ km s}^{-1}$ models are shown in Figure 2, the ones for the $v_a = 100 \text{ km s}^{-1}$ models in Figure 3, and the results for the $v_a = 300 \text{ km s}^{-1}$ models in Figure 4,

Figures 2-4 show the stellar wind bow shock (equation 1), the ionization front R_{IF} obtained from equation (7), and the ionization front R_I obtained from equation (12) of Raga et al, (1997). R_I is the ionization front that would be obtained for a star producing a S_* ionizing photon rate, but with no wind (and therefore no stellar wind bow shock). In-

terestingly, in all but the $v_a = 20$ and 100 km s^{-1} , $n_a = 10^6 \text{ cm}^{-3}$ model, no difference can be seen in the leading hemisphere of the HII region (i.e., for $z < 0$).

Substantial differences between R_{IF} and R_I can be seen in the trailing hemisphere. The absorption of ionizing photons by the bow shock wings and the lack of absorption within the stellar wind region lead to the formation of either:

- a thin downstream “horn” of ionized gas (in the $v_a = 20 \text{ km s}^{-1}$, $n_a = 1 \rightarrow 10^4 \text{ cm}^{-3}$ models, see Figure 2, and in the other two $n_a = 1$ models, see Figures 3 and 4),
- or a neutral, conical structure surrounding the extended bow shock wings (in all of the other models),

Except for the trailing region close to the bow shock wings, and except for the $v_a = 300 \text{ km s}^{-1}$, $n_a = 1 \text{ cm}^{-3}$ model (top frame of Figure 4, which has a clearly non-spherical HII region), the ionization front always has an almost spherical shape, with a radius close to the Strömgren radius R_S for a star with S_* in a stationary medium of density n_a (given in the fourth column of Table 1). The sphere, however, is not centered on the position of the star, but on a position downstream of the star. This effect is described by the “ $\chi \ll 1$ solution” of equation (13) of Raga et al. (1997), which to first order in χ corresponds to a sphere of radius R_S centered on a point with a downstream offset of $\chi R_0/3$ with respect to the position of the star.

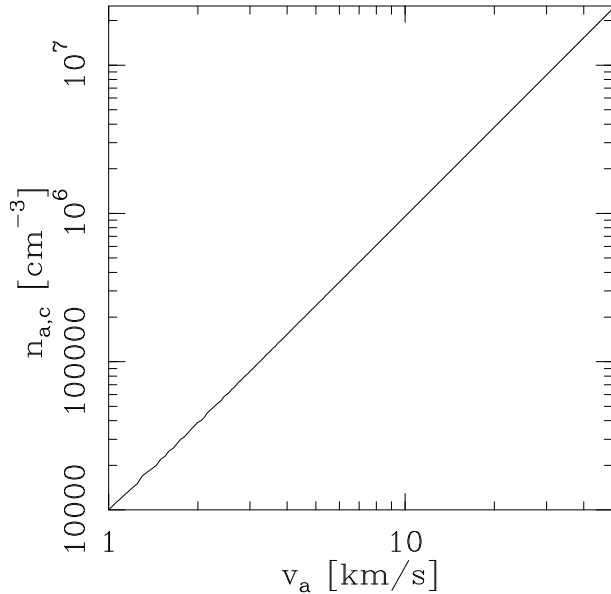


Fig. 5. Minimum environmental density $n_{a,c}$ (for capturing the ionization front) as a function of velocity v_a for the parameters of an O7V star (see the text).

5. DISCUSSION

Our exploration of the parameter space for the interaction of a runaway O7 star with the surrounding ISM shows that there is:

- a low density, high velocity regime (illustrated by our $v_a = 300 \text{ km s}^{-1}$, $n_a = 1 \text{ cm}^{-3}$ model, see the top frame of Figure 4) in which an elongated HII region with a tear-drop shape is formed, with a characteristic size of several hundred times the on-axis radius of the the stellar wind bow shock,
- a high density, low velocity regime (illustrated by our $v_w = 20 \text{ km s}^{-1}$, $n_a = 10^6 \text{ cm}^{-3}$ model, see the bottom frame of Figure 2) in which the photoionized environment is confined to a limited region around the head of the stellar wind bow shock,
- an “intermediate” regime (shown by all of the other models, see Figures 2-4), in which the HII region is approximately spherical, with a radius $\approx R_S$ and a small offset downstream from the stellar position, which intersects the stellar wind bow shock wings downstream of the star.

It is clear that we have not explored parameters for which the ionization front is trapped by the head of the stellar wind bow shock. Which parameters would be necessary for doing this? The condition for

ionization front capture at the head of the bow shock can be obtained by setting $R_{IF,0} = R_0$ in equation (11), which gives:

$$\left(\frac{R_S}{R_0}\right)^3 = \chi + \frac{9M_a^2}{4}, \quad (12)$$

where R_S is given by equation (9), R_0 by equation (2), M_a by equation (8) and χ by equation (10) as functions of the physical parameters of the flow. If we fix the stellar parameters for an O7V star, the remaining free parameters are the density and velocity of the streaming environment. Equation (12) then gives us the minimum environmental density $n_{a,c}$ as a function of velocity v_a necessary for the ionization front to be captured by the head of the bow shock. The results of this exercise are shown in Figure 5.

We see that for the $v_a = 1 \rightarrow 40 \text{ km s}^{-1}$ range shown in Figure 5, the critical density is in the $n_{a,c} \propto v_a^{1/2}$ regime obtained from equation (12) for $\chi \ll 1$. It is clear that for $v_a \geq 1 \text{ km s}^{-1}$, large environmental densities are required in order for the bow shock to capture the ionization front!

For $v_a > 10 \text{ km s}^{-1}$ stellar motions, $n_{a,c} > 10^7 \text{ cm}^{-3}$ environmental densities are required, so that it is unlikely that one will ever find such objects with ionization fronts captured by the stellar wind bow shocks. For lower values of v_a , one could have captured ionization fronts provided that the objects travel within a dense molecular cloud (of densities $\approx 10^5 \rightarrow 10^7 \text{ cm}^{-3}$, see Figure 5).

We are, of course, now talking about compact/ultracompact HII regions within dense molecular clouds, produced by massive stars with velocities of a few km/s with respect to the surrounding cloud. Interestingly, as we see in Figure 5, we could also have O stars with $v_a = 1 \rightarrow 10 \text{ km s}^{-1}$ with bow shocks that do not capture the ionization fronts. This parameter regime is interesting because it is not correctly described by our present model.

For $v_a < 10 \text{ km s}^{-1}$, the steady bow shock+HII region configuration (for a case in which the IF is not captured by the bow shock) will have a motion through the neutral environment that is subsonic with respect to the $c_0 \approx 10 \text{ km s}^{-1}$ isothermal sound speed of the ionized gas. Such an ionization front will have a strong hydrodynamical effect, driving a shock wave ahead of it into the neutral environment. The post-shock material will be almost at rest with respect to the star, and therefore will not shock again before reaching the contact discontinuity against the stellar wind.

The flow configuration will then have an inner shock involving the stellar wind, and an outer shock

surrounding an extended HII region. This outer bow shock will be somewhat peculiar, since all of the post-shock flow (even far along the bow shock wings) will be subsonic (because the pre-shock flow is subsonic with respect to c_0). Therefore, the post-bow shock flow will not have the typical division between a compact axial subsonic region and an extended super-sonic region farther away from the flow axis.

In a future paper we will continue with a study of this interesting regime (already explored by Arthur & Hoare 2006) with axisymmetric gasdynamic+radiative transfer simulations. Clearly, the codes needed to do this have already been fully developed (see, e.g., Mackey et al. 2021).

This work was supported by the DGAPA (UNAM) grant IG100422. We thank Dr. S. Kulka-rni for a very interesting discussion which gave rise to the work presented in this paper.

APPENDIX

A. ANGULAR DEPENDENCE OF THE EMISSION MEASURE

In this appendix we give the functions determining the angular dependence of the emission measure of the thin shell solution of equation (1). The functions that we give here correspond to the results of Cantó et al. (2005) evaluated for the case of a uniform environment,

We first give the functions used in equation (4):

$$f_a(\theta) = \frac{[R' \cos \theta + (dR'/d\theta) \sin \theta]^2}{R'^2 + (dR'/d\theta)^2}, \quad (A13)$$

$$f_w(\theta) = \frac{R'^2}{R'^2 + (dR'/d\theta)^2}, \quad (A14)$$

$$g_\sigma(\theta) = \frac{2 [(v_a/v_w)(1 - \cos \theta) + R'^2 \sin^2 \theta/2]^2}{R' \sin \theta \sqrt{(\theta - \sin \theta \cos \theta)^2 + (1 - R'^2)^2 \sin^4 \theta}}, \quad (A15)$$

where $R' = R_b/R_0$ is given by equation (1) and

$$\frac{dR'}{d\theta} = \frac{\sqrt{3} \csc \theta [(3 \csc^2 \theta - 2)\theta - 3 \operatorname{ctg} \theta]}{2\sqrt{1 - \theta \operatorname{ctg} \theta}}. \quad (A16)$$

We should note that $g_v(\theta)$ has a dependence on the v_a/v_w velocity ratio. For the case of a runaway O star, $v_a/v_w \ll 1$, and we can therefore put $v_a/v_w \approx 0$ in equation (A15) and eliminate this dependence.

Finally, the $G(\theta)$ function of equation (7) is:

$$G(\theta) = \left(\frac{R_b}{R_0}\right)^2 [f_a(\theta) + f_w(\theta)] g_\sigma(\theta) \sec \gamma, \quad (A17)$$

where γ is the angle between the normal to the bow shock and the direction towards the star (see Figure 1). This angle can be calculated through:

$$\cos \gamma = \sin(\theta + \alpha), \quad (A18)$$

where the slope of the bow shock shape is given by

$$\tan \alpha = \frac{2 \sin \theta (\sin 2\theta - 2\theta)}{12\theta \cos \theta - 9 \sin \theta - \sin 3\theta}. \quad (A19)$$

REFERENCES

Arthur, S. J. & Hoare, M. G. 2006, *ApJS*, 165, 283, <https://doi.org/10.1086/503899>
 Cantó, J., Raga, A. C., & Wilkin, F. P. 1996, *ApJ*, 469, 729, <https://doi.org/10.1086/177820>
 Cantó, J., Raga, A. C., & González, R. 2005, *RMxAA*, 41, 101
 Cruz-González, C., Recillas-Cruz, E., & Costero, R. 1974, *RMxAA*, 1, 211
 Dyson, J. E. 1975, *Ap&SS*, 35, 299, <https://doi.org/10.1007/BF00636999>
 Mac Low, M. M., Van Buren, D., Wood, D. O. S., & Churchwell, E. 1991, *ApJ*, 369, 395, <https://doi.org/10.1086/169769>
 Mackey, J., Green, S., Moutzouri, M., et al. 2021, *MNRAS*, 504, 983, <https://doi.org/10.1093/mnras/stab781>
 Mackey, J., Langer, N., & Gvaramadze, V. V. 2013, *MNRAS*, 436, 859, <https://doi.org/10.1093/mnras/stt1621>
 Meyer, D. M. -A., Mignone, A., Kuiper, R., Raga, A. C., & Kley, W. 2017, *MNRAS*, 464, 3229, <https://doi.org/10.1093/mnras/stw2537>
 Meyer, D. M.-A., Mackey, J., Langer, N., et al. 2014, *MNRAS*, 444, 2754, <https://doi.org/10.1093/mnras/stu1629>
 Noriega-Crespo, A., Van Buren, D., & Dgani, R. 1997, *AJ*, 113, 780, <https://doi.org/10.1086/118298>
 Raga, A. C., Noriega-Crespo, A., Cantó, J., et al. 1997, *RMxAA*, 33, 73
 Rasiwala, M. 1969, *A&A*, 1, 431
 Stevens, I. R., Blondin, J. M., & Pollock, A. M. T. 1992, *ApJ*, 386, 265, <https://doi.org/10.1086/171013>
 Thuan, T. X. 1975, *ApJ*, 198, 307, <https://doi.org/10.1086/153607>
 Van Buren, D., Noriega-Crespo, A., & Dgani, R. 1995, *AJ*, 110, 2914, <https://doi.org/10.1086/117739>
 Van Buren, D., Mac Low, M.-M., Wood, D. O. S., & Churchwell, E. 1990, *ApJ*, 353, 570, <https://doi.org/10.1086/168645>
 Wilkin, F. P. 1996, *ApJ*, 459, 31, <https://doi.org/10.1086/309939>

- J. Cantó: Instituto de Astronomía, Universidad Nacional Autónoma de México, Ap. 70-468, 04510 CDMX, México.
- A. Noriega-Crespo: Space Telescope Science Institute, 3700 San Martin Dr., Baltimore, MD 21211, USA.
- A. C. Raga: Instituto de Ciencias Nucleares, Universidad Nacional Autónoma de México, Ap. 70-543, 04510 CDMX, México (raga@nucleares.unam.mx).

OBSERVATIONAL CONSTRAINTS ON THE HD 5980 WIND-WIND COLLISION

Gloria Koenigsberger¹, Nidia Morrell², D. John Hillier³, Werner Schmutz⁴, Roberto Gamén⁵,
Julia Inés Arias⁶, Rodolfo Barbá⁷, and Gabriel Ferrero⁵

Received May 5 2022; accepted August 18 2022

ABSTRACT

Analysis of spectral line profile variations observed over 6 decades in the Wolf-Rayet system HD 5980 lead to the conclusion that *Star A*, the variable member of the system, has always dominated the wind collision zone (WCZ), contrary to suggestions that before 1994 the stronger wind belonged to its close companion, *Star B*. The observed variations are caused by a combination of physical occultations, wind eclipses and emission and absorption originating in the WCZ. The effects caused by the leading WCZ branch, which folds around *Star B*, are clearly seen as it crosses our line of sight to *Star A* during the secondary eclipse. These effects can inform on the WCZ velocity and density structures. We speculate that differences in line profiles at the same orbital phase but at different epochs may be linked to changes in the WCZ radiative properties. The 2017–2020 spectra indicate that HD 5980 was in a higher activity state than during 2010–2015.

RESUMEN

Se presentan observaciones recientes del sistema múltiple HD 5980 ubicado en la Nube Menor de Magallanes que se complementan con los resultados de observaciones efectuadas desde los años 1950s. Encontramos que la componente *Star A*, que actualmente posee el espectro dominante tipo Wolf-Rayet, siempre ha sido la estrella con el viento más intenso. Las variaciones en los perfiles de líneas en emisión se explican con una combinación de los siguientes procesos: eclipses atmosféricos, emisión y absorción proveniente de la zona de interacción de los vientos, y ocultamiento de regiones de esta misma zona. Las observaciones de 2017–2020 indican un incremento en el nivel de actividad comparado con los años 2010–2015.

Key Words: binaries: eclipsing — stars: evolution — stars: mass-loss — stars: winds, outflows — stars: Wolf-Rayet

1. INTRODUCTION

The current understanding of the structure and evolution of massive stars is based on extensive the-

oretical models (Brott et al. 2011; Ekström et al. 2012; Heger et al. 2000; Maeder & Meynet 2000; Paxton et al. 2019), which, however, have many tunable parameters (e.g., mass loss rate, mixing length, among others). Constraints on these calculations and additional insights into the stellar structure are gleaned from theoretical atmosphere models from which synthetic spectra are produced and can then be compared with observations (Hillier & Miller 1998; Hillier & Lanz 2001; Puls et al. 2005; Hubeny & Lanz 1995). Through this comparison, fundamental stellar parameters are derived.

An underlying assumption in nearly all theoretical models is that the observed spectrum arises in a spherically symmetric atmosphere and wind. Thus, the spectra of binary systems are generally modeled

¹Instituto de Ciencias Físicas, Universidad Nacional Autónoma de México, México.

²Las Campanas Observatory, The Carnegie Observatories, Chile.

³Department of Physics and Astronomy, & Pittsburgh Particle Physics, Astrophysics and Cosmology Center, University of Pittsburgh, USA.

⁴Physikalisch-Meteorologisches Observatorium Davos and World Radiation Center, Switzerland.

⁵Facultad de Ciencias Astronómicas y Geofísicas, Universidad Nacional de La Plata, and Instituto de Astrofísica de La Plata, CONICET–UNLP, Argentina.

⁶Departamento de Física, Universidad de La Serena, Chile.

⁷We mourn the loss of Rodolfo Barbá who passed away during the final preparation phases of this paper.

as the sum of the individual spectra arising in each of the two stars. However, massive stars emit intense ultraviolet radiation that drives a fast and dense stellar wind. If a binary system is composed of two massive stars, their mutual irradiation and wind interactions produce localized emission and absorption. Because an observer's line of sight to these localized line-emitting regions changes over the orbital cycle, their contribution to the observed spectrum produces orbital phase-dependent variations in the shape of spectral lines. This is referred to as line profile variability which, if significant, introduces uncertainties in the fundamental stellar parameters as derived from fitting spectra of single stars. Particularly noteworthy are the challenges involved in determining the contribution to the spectrum from a wind collision zone (WCZ).

The first observational evidence pointing to the presence of a WCZ in WN binary systems was obtained for V444 Cyg, HD 211853 and HD 90657 by Koenigsberger & Auer (1985). These authors detected orbital phase-dependent variations in the shape of the C IV $\lambda 1540$ P Cygni, consistent with a WCZ dominated by the WR component of the system. Shore & Brown (1988) used higher spectral resolution UV data of V444 Cyg to reach a similar conclusion. Auer & Koenigsberger (1994) modeled the line profile variability in the N IV $\lambda 1718$ line in V444 Cyg assuming it was due to wind eclipses, and found discrepancies between the model and the observations attributable to a WCZ. A similar analysis of the P V $\lambda 1117$ line observed in the FUV spectrum of HD 5980 led to the conclusion that the WR wind velocity structure is truncated on the hemisphere facing the companion due to the WCZ (Koenigsberger et al. 2006). These studies did not attempt to model the actual emission arising in the WCZ, an issue partially addressed by Luehrs (1997), who assumed that emission line sub-peaks in C III $\lambda 5696$ observed in the WC7+O5-8 binary HD 152270 could be modeled as two separate emission lines originating in the outflowing WCZ streams. The same geometrical model has been applied to several other binary systems (Hill et al. 2000; Hill 2020; Hill et al. 2018) leading to the conclusion that the excess emission produced in the WCZ is responsible for between 10%-100% of the observed line emission, depending on the spectral line and the binary system. A somewhat different approach was employed by Flores et al. (2001) who analyzed the excess emission over that expected from an unperturbed, spherical wind in the V444 Cyg binary, concluding that the WCZ contributed no more than 12% of the total

He II $\lambda 4686$ line emission. The major deficiency in the simple models is that they rely on the assumption that superposed peaks on a line profile can be attributed uniquely to excess emission. This neglects the possible presence of superposed absorption that can cut into the broad underlying emission, resulting in an appearance that mimics the presence of emission peaks. In addition, in many cases there is no certainty that the underlying stellar wind line profile can be approximated with a stellar wind model line profile unless this profile is computed self-consistently with the perturbations introduced by the collision process.

The collision of two supersonic winds produces a double shock structure between them where radiation is emitted in wavelengths ranging from X-rays to the radio spectral regions (Corcoran 2003; Nazé & Rauw 2017; Pittard 2009; Pittard & Dawson 2018; Russell et al. 2016; Richardson et al. 2017; Lamberts et al. 2012). The shape of the collision region is determined primarily by the mass-loss rates and the wind velocities, and in its simplest representation, the shock region can be thought of as conical, and folded towards the star having the weaker wind momentum (Prilutskii & Usov 1976; Cantó et al. 1996). In reality, however, the geometry and physical conditions within the WCZ are significantly more complex, and require 3D numerical simulations to be understood. Complicating factors include the Coriolis effect which breaks the symmetry of the shock cone with respect to the line connecting the two stars, the UV radiation field from the stellar continua and from the WCZ itself which can alter the pre-shock wind structure, and the cooling efficiency of the shocked gas which determines the thickness and radiating properties of the shocked region. Simulations taking these factors into account show that binary systems having different combinations of wind, stellar and orbital parameters can result in a WCZ that is either a dominant contributor or a relatively minor perturbation (Pittard 2009; Russell et al. 2016; Richardson et al. 2017; Pittard & Dawson 2018). Thus, in a sample of massive binary systems, each binary may have a unique set of parameters, and these result in a WCZ whose emitting properties differ from those of any other binary. This makes it challenging to determine general properties that characterize the impact of a WCZ on the observed spectrum. It is equally challenging to ascertain the relevance of the WCZ on the emission line profiles and their variability.

The close binary system in HD 5980 provides what could be described as nearly laboratory conditions for studying wind-wind collision physics.

Specifically, it is a system in which the masses and orbital elements have remained constant during the more than 60 years over which it has been observed but in which one of the components has suffered significant luminosity and wind structure changes. HD 5980 is located in the periphery of the young stellar cluster NGC 346 in the Small Magellanic Cloud, and consists of two binary systems. The first of these displays a nitrogen sequence Wolf-Rayet (WN) type spectrum, indicative of chemical abundances corresponding to an advanced evolutionary state (Koenigsberger et al. 2014; Shenar et al. 2016; Hillier et al. 2019). Its two stars are massive ($\approx 60 M_{\odot}$), luminous ($\approx 10^6 L_{\odot}$), and in a relatively close and eccentric orbit ($P=19.3$ d, $e = 0.3$). They are named *Star A* and *Star B*. The second binary system displays a late Of-type supergiant spectrum and is in a highly eccentric 97 d orbit with an unseen companion. This system, named *Star C*, contributed in 1978 approximately 40% of the light to the HD 5980 system (Perrier et al. 2009). There is at present no evidence indicating that both binary systems are gravitationally bound to each other. Hence, we focus hereafter on the *Star A* + *Star B* system.

Prior to its confirmation as a binary system, Smith (1968) and Walborn (1977) classified the observed WR spectrum as WN3, with the latter author remarking on the absence of N IV $\lambda 4058$ in spectra of 1973 and 1977. Curiously, about a decade later Niemela (1988) detected this line, prompting her to propose WN3 and WN4 for *Star A* and *Star B*, respectively. Unknown at the time was that the system had initiated in ≈ 1980 a slow brightness increase and that all the WR emission lines, including $\lambda 4058$, were becoming stronger. In 1993-1994, HD 5980 suffered two sudden and strong eruptive events, expelling $\approx 10^{-3} M_{\odot}$ (Barbá et al. 1995; 1995ApJ...452L.107K). The absence of $\lambda 4058$ in 1973 and 1977, its presence after that, and the appearance and strengthening of numerous UV Fe V and Fe VI lines leading up to the eruptions prompted Koenigsberger et al. (1995) to propose that the erupting component was the object responsible for the WR-type spectrum. At that time, however, it was believed that the dominant spectrum arose in *Star B*. However, subsequent RV measurements of these same Fe V/IV features showed them to instead follow the orbital motion of *Star A*, and Barbá et al. (1995) found indications of a large hydrogen abundance in the post-eruption spectra, not expected to be present in a *bona fide* WNE type star, as *Star B* was believed to be. Hence, the eruptive events were associated with an LBV-like process originating in *Star A*

which, at the time, was believed to be an Of-type supergiant.

At the peak of the eruption, the dominant spectral type was WN11, as determined from spectra in the optical range (Heydari-Malayeri et al. 1997) or B1.5Ia⁺ from UV spectra (Koenigsberger et al. 1996). After that, the brightness declined rapidly until ≈ 1996 , remaining at an apparent plateau until ≈ 2002 , after which it declined gradually. Currently, the N IV $\lambda 4058$ emission is still significantly stronger than N V $\lambda \lambda 4603-21$, indicating a WN6 spectral type. All strong lines follow the orbital motion of *Star A*.

Moffat et al. (1998) reviewed the behavior of HD 5980 prior to, during, and following the eruption and concluded that *Star A* must have been an O-type supergiant that through the eruptive process had transitioned to a WN star. They also proposed that the spectrum of this assumed O-type star and of *Star B* had been drowned out by wind collision emission, and proposed that the WCZ spectrum imitated that of a WN star. Applying the Luehrs method to spectra obtained in 1991/1992, they concluded that the WCZ extended perpendicular to the semimajor orbital axis and that the emission-line RVs could not be interpreted as representing in any way the orbital motion. This conclusion is in stark contrast with the CMFGEN radiative transfer model fit obtained to HD 5980's $\lambda \lambda 1200 - 10000$ spectral energy distribution and emission line intensities observed in 1999 and in 2014 (Koenigsberger et al. 2014; Shenar et al. 2016; Hillier et al. 2019). Thus, the bulk of the emission must arise in the stellar winds which, however, does not exclude the presence of additional emission and absorption arising in the WCZ.

The current scenario for HD 5980 is one in which *Star A* is a highly unstable hydrogen rich WN star and *Star B* is a hydrogen poor *bona fide* WN4 star, and that both objects have evolved quasi-homogeneously from $\approx 100 M_{\odot}$ stars (Koenigsberger et al. 2014; Shenar et al. 2016; Hillier et al. 2019). This scenario, however, leaves open the important question as to why *Star A* is so unstable, a question that is highly relevant to understanding the late stages of the evolution of very massive stars. It also begs an explanation for the peculiar behavior of the N IV $\lambda 4058$ line in 1973-1983 which would indicate that *Star B* was also somehow involved in the instability process.

In § 2 we describe the new data, summarize the historic data used in our analysis, and describe the measurements. In § 3 we present an overview of the system, including its known parameters, assumed ge-

ometry, and a definition of the orbital phases. In § 4 we present and discuss the radial velocity curves, the full width at half maximum variations in the emission lines and the hydrogen to helium line strength ratios. In § 5 we describe and discuss the line profile variability. The nature of *Star B* is discussed in § 6. § 7 contains a summary of the observational results and the conclusions.

2. OBSERVATIONAL MATERIAL

The new data presented in this paper were obtained at the Las Campanas observatories (LCO) with the Magellan Clay and Baade telescopes in 2007-2020 and with the DuPont telescope in 2015-2020. We also revisited all the previously analyzed spectroscopic data. The summary of spectra is listed in Table 1 where Column 1 gives the epoch in years of the observations, Column 2 the telescope or instrument, Column 3 the number of spectra available, Column 4 the type of dispersion (Low, Medium, High), Column 5 the approximate wavelength range covered, and Column 6 the reference where the spectra were first reported.

On the du Pont telescope, the standard setup was using the echelle spectrograph and a 1" slit. The spectral resolution of these data ranges from 0.15 to 0.22 Å ($R \approx 25000$) and the wavelength coverage goes from 3500 to 8800 Å. Spectra were reduced with *IRAF*. The high resolution Clay (Magellan-II) spectra were obtained with the Magellan Inamori Kyocera Echelle spectrograph (MIKE) using a 0.7" slit and applying a 2×2 binning to both blue and red detectors. This configuration results in a spectral resolution of ≈ 34000 (FWHM ranging from 0.10 to 0.25 Å).

Reductions were carried out with a combination of specially designed *IRAF* scripts contained in the ‘mtools’ package developed by Jack Baldwin and available at Las Campanas website, and the usual ‘echelle’ tasks in *IRAF*.

The instrumental response in the echelle orders needs to be corrected in order to analyze line profile variability. In the case of very weak and narrow lines that lie in orders that are not densely packed with spectral lines, rectification of the echelle orders can be accomplished by fitting a function to the line-free continuum regions in the order. This method was applied to the echelle order containing N V $\lambda 4944$, using a three to nine order spline function. This method, however, is useless for lines such as He II $\lambda 5411$ which occupy at least $\approx 64\%$ of the echelle order, leaving available only very narrow continuum regions near the edge of the order for locating the continuum level. In addition, there is no

guarantee that a function fit to the edges of an order will properly represent the continuum near the center. Although several of the LCO spectra were flux-calibrated using nearby standard stars, the continuum level near the edges of the orders generally departs significantly from the straight line expected over the ≈ 100 Å covered by the order.

The technique we have applied is to choose spectral lines for which adjoining orders are free from major line features and use these as representative of the response function. The best line to apply this technique is He II $\lambda 5411$, which generally lies on order #35 in our LCO spectra, and for which the two adjoining orders (34 and 36) are feature-free. We thus normalized this He II line on all our du Pontechelle spectra by dividing the counts registered in order #35 by the average counts of orders #34 and #36 for each pixel along the wavelength dispersion direction. This procedure yields a uniformly normalized set of line profiles. An additional advantage of using He II $\lambda 5411$ is that there are no overlapping transitions from other abundant atomic species that contaminate it in the hot star spectra. Thus, it is a reliable line for probing the processes responsible for the line profile variability and for obtaining automated radial velocity and intensity measurements.

Foellmi et al. (2008) showed that the majority of the He II and He II+H emission lines in the HD 5980 spectrum undergo similar orbital-phase dependent variability. Inspection of our current spectra indicates that this is still the case, so the conclusions derived from the variability of He II $\lambda 5411$ profiles are applicable to most other lines with the exception of N IV $\lambda 4058$. This line is in general narrower and the line profile variability is not as strong. Unfortunately, the echelle order on which it is found and the neighboring orders contain several other strong emission lines, making a reliable normalization in this region very uncertain.

Radial velocity and line strength measurements were performed using two methods. An automated procedure was used on the echelle orders that were uniformly normalized using neighboring orders. This procedure integrates over the emission line intensity above the normalized continuum level to obtain the total line strength and the intensity-weighted line centroid as defined in Koenigsberger & Schmutz (2020). This technique was applied to the He II $\lambda 5411$ line. Spectra for which a consistent continuum normalization from spectrum to spectrum is not straightforward were measured individually using the *IRAF* function that fits one or more Gaussians to a line profile, a method that provided the

TABLE 1
AVAILABLE SPECTROSCOPIC DATA

Epoch	Observatory/Instrument	Number	Disp	$\approx \Delta\lambda \text{ \AA}$	Reference
1955-1965	SAO Radcliff	22	L	4000-4900	Koenigsberger et al. (2010)
1973	CTIO	1	L	3300-4800	N. Walborn (Priv. Comm.)
1977	CTIO	1	L	3400-4900	N. Walborn (Priv. Comm.)
1978	IUE	1	L	1150-2000	Moffat et al. (1989)
1979-1981	IUE	7	H	1150-2000	Moffat et al. (1989)
1979-1981	IUE	7	H L	1800-3250	Koenigsberger et al. (2010)
1986	IUE	12	L	1150-2000	Moffat et al. (1989)
1991-1992	IUE	10	H	1150-2000	Koenigsberger et al. (1994)
1993	BEFS ORFEUS	1	H	920-1180	Koenigsberger et al. (2006)
1994	CTIO IUE	1	L	1170-8000	Koenigsberger et al. (1998b)
1994-1995	IUE	18	H	1150-2000	Koenigsberger (2004)
1998-1999	ESO 2.1m FEROS	28	H	3900-8500	Schweickhardt (2000)
1999-2000	FUSE	2	H	920-1180	Koenigsberger et al. (2006)
1999-2000	HST STIS	6	H L	1200-10000	Koenigsberger et al. (2000)
2002	FUSE	8	H	920-1180	Koenigsberger et al. (2006)
2005-2006	ESO 2.1m FEROS	13	H	3700-9000	Foellmi et al. (2008)
2009-2010	LCO IMACS B&C MagE	6	L	optical	This paper
2009	HST STIS	1	H	1200-1700	Georgiev et al. (2011)
2006-2020	LCO du Pont echelle	52	H	3480-9500	This paper
2007-2019	LCO MIKE	8	H	3330-9150	This paper
2014, 2016	HST STIS	1	H L	1200-10000	Hillier et al. (2019)
2018-2020	LCO MagE	10	M	3000-9000	This paper

radial velocity measurements of N V $\lambda 4944$ listed in Table 10. This line clearly splits into two components at orbital phases of maximum velocity and, because of its small transition probability, must be formed in high density regions such as near the continuum optical depth unity zone of the stellar wind. Hence, it is considered to be possibly the only emission in the optical spectral range that can be used to describe the binary orbital motion. Koenigsberger et al. (2014) measured it mostly on the non-echelle spectra to determine the orbital elements of *Star A* and *Star B*. Because this N V line is so narrow (GFWHM \approx 250 km/s in each star), there are available continuum segments on the echelle order on which it is located that can be used to normalize the spectrum. We have employed a spline function of 5th to 11th order (depending on the spectrum) which has produced a relatively flat continuum in the vicinity of this N V line, which was then measured by using two Gaussians to de-blend the velocity components. We also re-measured consistently the spectra reported in Koenigsberger et al. (2014), all of which were obtained prior to 2013.

The He II $\lambda 4686$ and He II+H β (Table 11), and the N IV $\lambda 3483$ and N IV $\lambda 4058$ (Table 12) lines

in the FEROS, HST/STIS, and low-dispersion LCO spectra were also measured, but here using a single Gaussian fit. The corresponding tables list radial velocity (RV), equivalent width (EW), and full width at half maximum intensity (FWHM), and previously determined values listed in Koenigsberger et al. (2010).

A useful matrix of the observed spectra per orbital phase and epoch is given in Table 9, where one can see that a very good orbital phase coverage exists for Epochs 1998-1999 (FEROS) and 2010-2012 (du Pont echelle). In addition, several of the orbital phases obtained at LCO in 2017-2018 overlap with the earlier data allowing a same-phase, epoch-to-epoch comparison.

Unless noted otherwise, all of the line profiles and radial velocities that are discussed in the text of this paper are corrected for the +150 km/s SMC systemic velocity. This choice of systemic velocity is based on the heliocentric radial velocity +150 km/s that was obtained by Niemela et al. (1986) from the He II photospheric absorption lines of a sample of massive stars in NGC 346.

TABLE 2
HD 5980 PARAMETERS

Parameter	Value	Comment	Reference
P_{AB} [d]	19.2654	Orbital period <i>Star A</i> + <i>Star B</i>	Sterken & Breysacher (1997)
T_0 [HJD]	2443158.71	Initial epoch (periastron)	Sterken & Breysahcer (1997)
i [deg]	86(1)	Orbital inclination	Perrier et al. (2009)
e	0.314(5)	Orbital eccentricity (photometry)	Perrier et al. (2009)
e	0.297(35)	Orbital eccentricity (RV curves)	Kaufer et al. (2002)
e	0.27(2)	Orbital eccentricity (RV curves)	Koenigsberger et al. (2014)
ω_{per} [deg]	132.5(1.5)	Longitude of periastron (photometry)	Perrier et al. (2009)
ω_{per} [deg]	134(4)	Longitude of periastron (RV curves)	Koenigsberger et al. (2014)
$a_A \sin i$ [R_\odot]	78(3)	<i>Star A</i> semimajor axis	Koenigsberger et al. (2014)
$a_B \sin i$ [R_\odot]	73(3)	<i>Star B</i> semimajor axis	Koenigsberger et al. (2014)
$a \sin i$ [R_\odot]	151(4)	Orbital semimajor axis	Koenigsberger et al. (2014)
$M_A \sin^3 i$ [M_\odot]	61(10)	<i>Star A</i> mass	Koenigsberger et al. (2014)
$M_B \sin^3 i$ [M_\odot]	66(10)	<i>Star B</i> mass	Koenigsberger et al. (2014)
r_{per} [R_\odot]	104	Periastron separation	Adopting $e=0.314$, $a=151$
r_{ap} [R_\odot]	199	Periastron separation	Adopting $e=0.314$, $a=151$
ρ_1	0.158(5)	Optically thick <i>Star A</i> relative radius	Perrier et al. (2009)
ρ_3	0.108(3)	Optically thick <i>Star B</i> " "	Perrier et al. (2009)
ρ_2	0.269(14)	Optically thick envelope " "	Perrier et al. (2009)
R_A [R_\odot]	24	<i>Star A</i> radius	From ρ_1 and $a=151$
R_B [R_\odot]	16	<i>Star B</i> radius	From ρ_2 and $a=151$
R_{env} [R_\odot]	41	<i>Star B</i> envelope radius	From ρ_3 and $a=151$
ℓ_A	0.398	Relative light contribution <i>Star A</i>	Perrier et al. (2009)
ℓ_B	0.300	Relative light contribution <i>Star B</i>	Perrier et al. (2009)
ℓ_C	0.302	Relative light contribution <i>Star C</i>	Perrier et al. (2009)
P_C [d]	96.56(1)	Orbital period <i>Star C</i>	Koenigsberger et al. (2014)
T_C [HJD]	2451183.40	Initial epoch <i>Star C</i> (periastron)	Koenigsberger et al. (2014)
e_C	0.815(20)	Orbital eccentricity <i>Star C</i>	Koenigsberger et al. (2014)
ω_{per} [deg]	252(3)	Longitude of periastron <i>Star C</i>	Koenigsberger et al. (2014)

3. OVERVIEW OF THE SYSTEM

Table 2 provides a summary of the HD 5980 parameters, with values that have been compiled from the references listed in the last column. Appendix A provides a detailed historical overview and describes the methods used to determine these parameters.

The eruptive variable in the system was named *Star A* by Barbá et al. (1996) and its close companion is *Star B*. This nomenclature has been retained ever since. *Star A* and *Star B* form an eclipsing system (Breysacher & Perrier 1980, 1991). The orbital phases throughout this paper are determined using the ephemerides of Sterken & Breysacher (1997): $T_0=2443158.705$, $P=19.2654$ d, where T_0 cor-

responds to primary eclipse (*Star A* between the observer and *Star B*).⁸

Star A and *Star B* are in an eccentric orbit, and our adopted orbital configuration is illustrated in Figure 1 in a frame of reference with origin in *Star B*. Orbital phase $\phi=0$ corresponds to the eclipse of *Star B* by *Star A*. The second eclipse occurs at $\phi=0.36$ and periastron passage occurs at $\phi=0.061$. The reason for choosing a frame of reference centered on *Star B* is that all the radial velocity (RV) measurements

⁸We have determined a possible revised ephemeris $P_{Gamen}=19.2658$ d, $T_{Gamen}=2443158.872$, with the latter value being similar to that obtained by Foellmi et al. (2008), $T_{Foellmi}=2443158.865$. The difference in the phases as determined with the Sterken & Breysacher (1997) ephemerides and the revised one is <0.025 , which has only a minor effect on the results of our current study. Hence, for consistency with our previous investigations, all our phases are calculated with the Sterken & Breysacher (1997) ephemeris.

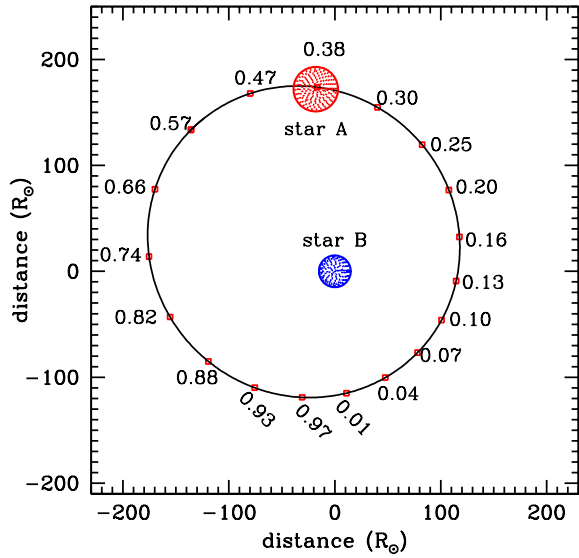


Fig. 1. *Star A + Star B* orbital phases in a coordinate system that is centered on *Star B* and an observer located at the bottom of the plot. Eclipses occur at $\phi=0$ and 0.36, and periastron at $\phi=0.061$, corresponding to $\omega_{per}=133^\circ$ (Perrier et al. 2009). The relative radii are drawn to scale, using the values that were obtained by Perrier et al. (2009) and a semi-major axis of the elliptic orbit $a=151 R_\odot$ as derived by Koenigsberger et al. (2014). The color figure can be viewed online.

of the strong emission lines follow the expected orbital motion of *Star A*, except for a brief phase interval centered around orbital phase 0.36, which will be discussed below. The observer is located at the bottom so that the maximum approaching velocity of *Star A* occurs in the phase interval $\approx 0.66-0.82$ and maximum receding velocity in the phase range $\approx 0.05-0.25$. The relative sizes of *Star A* and *Star B* that are depicted correspond to the continuum emitting disk, R_A and R_B based on the results of Perrier et al. (2009) and Koenigsberger et al. (2014).

The spectral energy distribution (SED) of HD 5980 is extremely blue, as is evident in Figure 2, which illustrates the SED at both eclipses and at two different observation epochs separated by 15 years. The observed HD 5980 spectral energy distribution includes the continuum and the photospheric absorption lines from a “third light source”, named *Star C*. This source was first discovered by Breysacher & Perrier (1980) and currently contributes approximately 30% of the total flux in the visual spectral region. Niemela (1988) showed that the photospheric absorptions remained static over the 19.3 d orbital

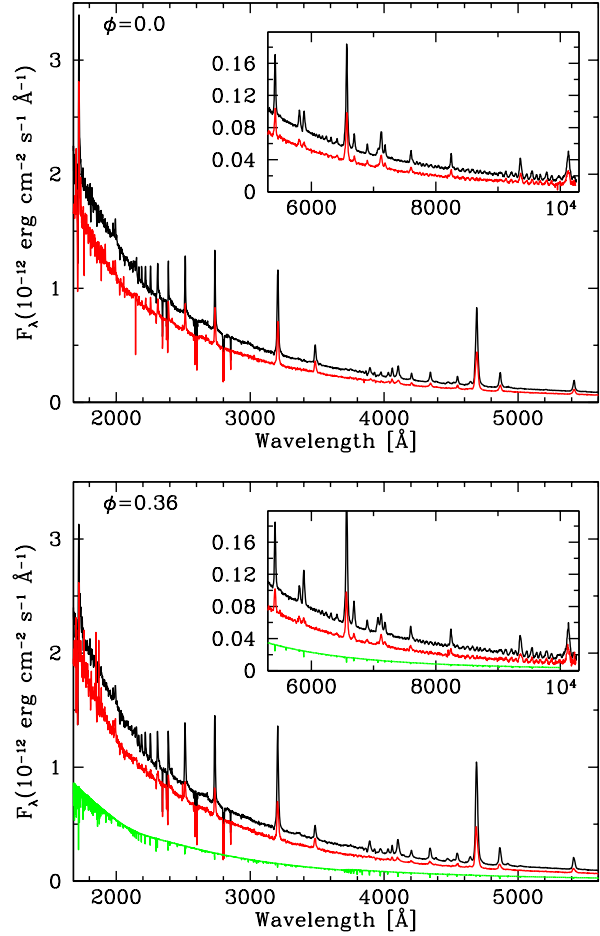


Fig. 2. Spectral energy distribution in epochs 1999-2000 (black) and 2014-2016 (red) obtained with *HST/STIS* showing the changes between the high (black) and low states (red) states. The top panel shows spectra at orbital phase $\phi=0$ and the bottom panel at $\phi=0.36$. The green spectrum in the bottom panel is a CMFGEN model of *Star C*. The color figure can be viewed online.

period. Kaufer et al. (2002) discovered that these absorptions follow a highly eccentric ($e \approx 0.8$) orbit with a period $P_C=97$ d. This result was confirmed and refined by Koenigsberger et al. (2014), who also discussed the possible relation between the *Star A + Star B* system and the *Star C* system. It is as yet not clear whether the two binary systems are bound and in a very long-period orbit, or whether it is a line-of-sight coincidence.

The photospheric absorption spectrum of *Star C* was analyzed by Georgiev et al. (2011) and Koenigsberger et al. (2002), and was shown to have a spectral type similar to that of an O5-7 supergiant. The CMFGEN model that was used in Hillier et al. (2019) to

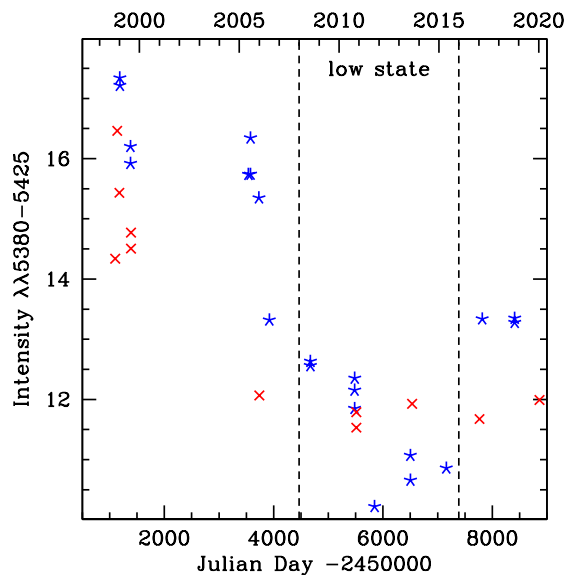


Fig. 3. Integrated intensity in the wavelength band $\lambda\lambda 5380-5440$ in spectra obtained at elongation phases plotted as a function of Julian day. The corresponding epoch in years is listed in the top scale. Orbital phases $\phi=[0.15, 0.26]$ are plotted in red and $[0.57, 0.80]$ are plotted in blue. The vertical lines mark the years 2008-2016 which enclose the time interval in which the system was in a low state. The color figure can be viewed online.

model its SED is illustrated in the bottom panel of Figure 2. The full width at half maximum (FWHM) of *Star C*'s absorption lines is ≈ 75 km/s and thus easily identified when superposed on the WR emission lines. The secondary component that orbits the supergiant star has remained undetected, thus sparking the speculation that it may be a very rapidly rotating star whose photospheric absorptions are too broad and weak to be detected.

3.1. The High and the Low Activity States

The stellar wind properties of *Star A* changed significantly between the late 1990s and the current epoch. The most evident change is the diminution in emission line strength, as illustrated in Figure 3 where we plot the integrated intensity of He II $\lambda 5411$ in the wavelength range $\lambda\lambda 5400-5425$ in epochs 1998-2020. Plotted are only data at elongation phases, when eclipse effects are minimized. The “high” state following the 1994 outburst persists in 1998 and 1999, followed by a relatively rapid transition during $\approx 2005-2007$ to a “low” state which persisted through $\approx 2010-2017$. Light curves obtained during the transition and during the low state are illustrated in the appendix (Figure 24).

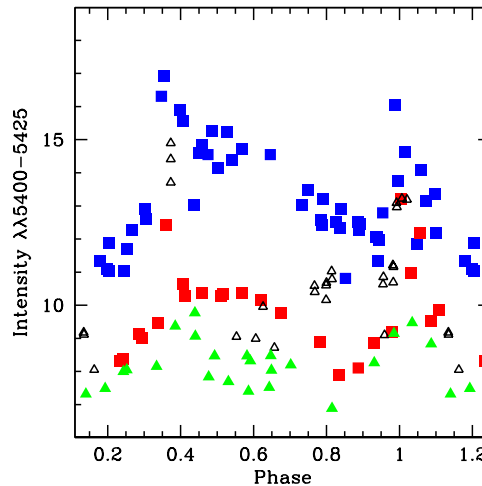


Fig. 4. Integrated intensity in the wavelength bands $\lambda\lambda 5400-5425$ as a function of orbital phase. The epochs are: 1998-1999 (blue squares), 2005-2009 (black triangles), 2010-2015 (green triangles), 2017-2020 (red squares). The color figure can be viewed online.

Also evident in Figure 3 is an increase in line intensity during 2017-2020, which suggests that the system was in a more active state. The orbital phase-dependent view of the same data is given in Figure 4, which indicates that in 2017-2020 maximum intensity is centered around orbital phase 0.5, very similar to the maximum observed during the high state. Conversely, Figure 4 also shows that during the low state of $\approx 2010-2015$, there is a reduced line intensity after orbital phase ≈ 0.5 , compared to other epochs. In this orbital phase interval the system is near apastron, and *Star A* is approaching the observer.

The high and low states can also be clearly identified in the HST/STIS spectra which provide the absolute-flux calibrated spectral energy distribution (SED) in the wavelength range $\lambda\lambda 1200-10000$. Six orbital phases were obtained during the 1999-2000 high state. Unfortunately, only one spectrum at each eclipse during the low state could be acquired. Thus, we can only compare the SEDs for different epochs at eclipse phases. In the low state, both the continuum and the lines are weaker (Figure 2). The diminution in continuum flux at $\lambda 5470$ is $\approx 27\%$ and is approximately equal at both eclipses. The diminution in emission line flux (above the continuum level) is 20%-68% depending on the line, and differs considerably at primary eclipse compared to secondary eclipse (see Table 3).

TABLE 3

FLUXES AND VELOCITIES (IUE AND HST)

Epoch	Phase	$\langle F_c \rangle$	F_{5411}	F_{3483}	F_{4058}	V_{wind}
1999	0.83	1.26	2.20	2.39	1.35	1770:
1999	0.05	1.06	1.53	1.19	1.20	1380
1999	0.15	1.30	2.14	2.85	1.22	1350
1999	0.36	1.04	2.08	1.81	1.06	2500
1999	0.40	1.14	1.91	1.97	1.05	2100
2000	0.00	0.95	1.68	2.39	1.03	1500
2002	0.99	1860
2009	0.99	2260
2014	0.00	0.70	0.94	1.46	0.54	2110
2016	0.36	0.74	0.89	1.45	0.34	2800:

Notes: $\langle F_c \rangle$ is the average flux in the continuum in the wavelength band 5460-5480 Å given in units of 10^{-13} ergs/(cm² s Å). F_λ is the integrated flux over the emission line above the continuum level, given in units of 10^{-12} ergs/(cm² s). V_{wind} is an estimate of the wind velocity obtained from the edge of the He II $\lambda 1640$ P Cygni profile given in km/s; values of 1999-2009 taken from Georgiev et al. (2011); the value of 1993 was measured on the PV 1117 Å line in the ORFEUS BEF spectrum that is reported in Koenigsberger et al. (2006).

4. RV CURVES, FWHM VARIATIONS AND H/HE LINE STRENGTHS

4.1. RV Curves

Figure 5 displays the RV measurements of N V $\lambda 4944$ in the 2008-2020 spectra and the RV curves that correspond to the orbital solution given by Koenigsberger et al. (2014). This line arises from a transition between two excited states and requires a high density region, such as the base of a WR wind, in order to become visible in the spectrum. In a system with an orbital separation such as that of HD 5980, the inner wind region is unlikely to be subjected to perturbations caused by the radiation field of the companion or the wind-collision. Thus, Figure 5 clearly shows that there are two sources of N V $\lambda 4944$ emission and leaves little doubt that the *Star A* + *Star B* system contains two very massive stars in an eccentric orbit, each of which has a wind dense enough to produce this emission.

Figure 5 includes the N IV $\lambda 4058$ RVs that were measured on spectra of 1994-2020. Its phase-dependent behavior is very similar to that of the *Star A* RV measurements of N V $\lambda 4944$, but with a smaller amplitude and larger scatter. N IV $\lambda 4058$ is plotted once again in Figure 6 (top left) together with N IV $\lambda 3483$, the latter showing a similar trend despite the scarcity of spectra containing this line.

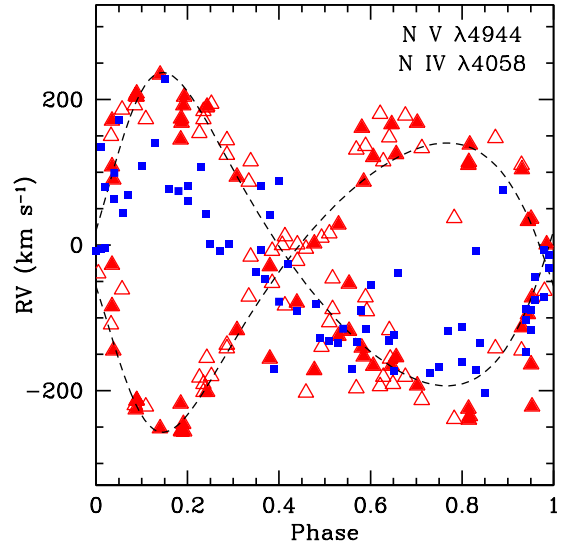


Fig. 5. Radial velocity of N V $\lambda 4944$ as a function of orbital phase for epochs 2008-2012 (filled triangles) and 2013-2020 (open triangles), and N IV $\lambda 4058$ (filled squares). The dash curves indicate the orbital solution given in Koenigsberger et al. (2014). The velocities are corrected for the SMC velocity. The color figure can be viewed online.

Figure 6 also shows the RV measurements of H β (top right) and He II $\lambda 4686$ (bottom left) which have an even smaller variability amplitude than N IV $\lambda 4058$.

The intensity-weighted RVs of He II $\lambda 5411$ in the FEROS and du Pont echelle spectra are plotted in Figure 6 (bottom right). This type of measurement differs from that performed on the other lines (Gaussian fits) in that it is automated, does not depend on a chosen continuum level, and the wavelength range over which the centroid is computed remains fixed. Despite the different measuring method, the He II $\lambda 5411$ RVs have a very similar behavior to those of H β and He II $\lambda 4686$. Noteworthy in the He II lines as plotted in Figure 6 is the lack of negative RVs. The amplitudes and systemic velocities of the RV curves of WR stars can often depend on the line being measured. The differences are related to optical depth effects and the wind ionization and velocity structure. However, the RV curve amplitude of an emission line profile produced in a spherically symmetric, constant, wind should remain constant. In fact, even in the close WN6+O6 binary V444 Cyg ($P_{orb}=4.2$ d) the He II $\lambda 4686$, $\lambda 5411$, N IV $\lambda 4058$ and N V $\lambda\lambda 4603-19$ RV curves have very similar shapes and amplitudes (Münch 1950; Marchenko et al. 1994). Thus, the lack of nega-

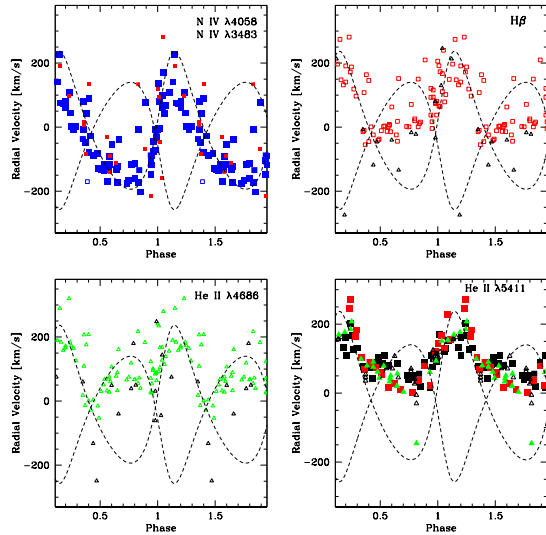


Fig. 6. Radial velocities of N IV $\lambda 4058$ (top left, blue squares, Table 12), N IV $\lambda\lambda 3478$ -3484 (top left, red squares, Table 12, shifted by -80 km/s), H β (top right, red squares, Table 11), and He II $\lambda 4686$ (bottom left, green triangles, Table 11). Black symbols correspond to historic values (Epochs 1955-1995). The bottom right panel shows the intensity weighted radial velocities of the He II $\lambda 5411$ emission contained within the wavelength band $\lambda\lambda 5380$ -5440. The symbols correspond to: 1998-1999 (black squares), 2005-2009 (black triangles), 2010-2015 (green triangles), 2017-2020 (red squares). All RVs are corrected for the adopted $+150$ km/s SMC systemic velocity. The color figure can be viewed online.

tive RVs in the HD 5980 He II lines is a significant piece of information, and it leads to the conclusion that these lines arise in both stellar components, although *Star A* is in general the dominant contributor. This, of course, is not unexpected given the fact that the N V $\lambda 4944$ line indicates that both stars possess WR-type winds.

Foellmi et al. (2008) actually observed a resolved blue-shifted emission in N V $\lambda 4603-21$, He II $\lambda 4341$, H γ and other lines at orbital phase $\phi=0.13$. The excess blue emission in N IV $\lambda 4058$ could also be inferred at $\phi=0.13$, although it is not resolved. Hence, although *Star B* is clearly associated with WR-type emission lines, the dominant component is *Star A*. Furthermore, the fact that the He II RV curves have retained the same shape since the 1950s leads to the conclusion that *Star A* has been the dominant contributor to the emission line spectrum throughout all epochs at which it has been observed. Hence, it was a WR star when the 1993-1994 eruptions took place.

A second conclusion is that the intensity weighted centroids of He II $\lambda 5411$ in epoch 2017-2020 have a

larger positive velocity than other epochs at orbital phases when *Star A* is receding from the observer, indicating that something has recently changed in the system.

4.2. Full Width at Half-Maximum (FWHM) Variations

An outstanding feature of the HD 5980 emission lines is the high amplitude variation in the full width at half maximum which has been observed since the 1970s (for references, see the historic review in the Appendix). We measured the FWHM in He II $\lambda 4686$ and H β in the majority of our new spectra and complemented these data with measurements of previous observations listed in Koenigsberger et al. (2010). The results, listed in Table 11 and summarized in Figure 7, can be described as follows. First, the variations are qualitatively the same in all epochs between 1955-2020, and they consist of two dips over the orbital cycle. The dips are centered ≈ 0.05 after eclipse minima, with the dip around primary minimum being significantly narrower than that at secondary minimum. Second, the descent in FWHM at primary minimum occurs very abruptly and is nearly identical in all observation epochs. The ascent after minimum appears to be similarly abrupt, but the data covering this part of the curve are insufficient to confirm this. Third, the maximum amplitude in 1955-1963 is very similar to that in 2005-2020 with $\max(\text{FWHM}) \approx 2000$ km/s, contrasting with the 1998-2000 epoch in which $\max(\text{FWHM}) \approx 1650$ km/s. This latter velocity is consistent with the derived wind velocity from UV P Cyg profiles in 1999-2000 at all orbital phases, except when *Star B* is in front (see Table 3). The downward shift of the FWHM curve of 1990-2000 reflects the fact that the lines were generally narrower during this post-outburst epoch, and it is consistent with the slower maximum wind speeds measured during those years.

The broader dip in the FWHM plot around the secondary eclipse is consistent with the presence of an extended envelope surrounding *Star B*, as has previously been found by Breysacher & Perrier (1980) and Perrier et al. (2009) from continuum light curves. Inspection of the Perrier et al. (2009) Figure 4 shows that the eclipse starts at $\phi \approx 0.30$ and ends at $\phi \approx 0.42$. As this is a continuum eclipse, the primary source of absorption/scattering of *Star A*'s continuum photons as they pass through *Star B*'s wind is electron scattering, which has a relatively small opacity. At spectral line frequencies, however, the opacity is much larger because the bound-bound transitions have cross-sections that are orders

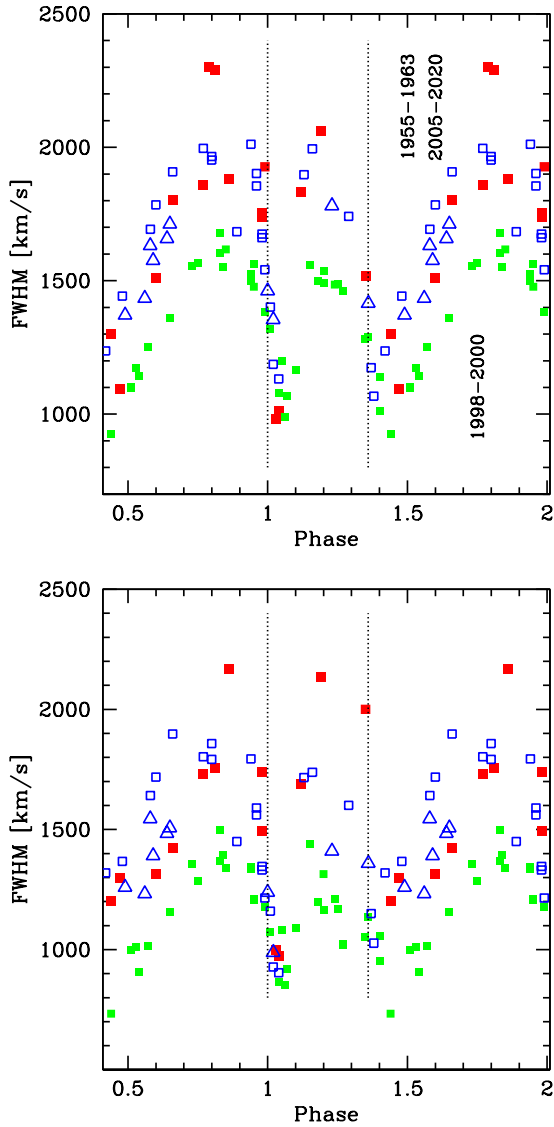


Fig. 7. Full-width at half maximum intensity of He II $\lambda 4686$ (top) and H β (bottom) in epochs 1955-1965 (red), 1990-2000 (green), 2005-2013 (blue rectangles) and 2014-2020 (blue triangles). The color figure can be viewed online.

of magnitude larger than electron scattering. Hence, an occultation caused by wind material at spectral line frequencies takes up a larger fraction of the orbital cycle than the eclipse at continuum frequencies.

The continuum photons from a source that is passing on the far side of a spherically expanding wind are absorbed/scattered in the wind, and the projected velocity field is such that the resulting emission line profile is absorbed at all wavelengths, but given the opacity distribution, the effect is most prominent in the line wings (Auer & Koenigsberger

1994). This leads to a narrower emission line profile during the wind eclipse phases compared to the out-of eclipse phases.

Focusing now on the secondary dip in the FWHM plot, one can see that its descent initiates at $\phi \approx 0.3$ (similar to the continuum light curves) but the ascent does not end until $\phi \approx 0.6$. This leads to the conclusion that the envelope around *Star B* is more extended post-eclipse than pre-eclipse.⁹ Hence, we interpret this asymmetry to be due to the trailing flow of the wind collision region which, as it passes in front of *Star A*, has a range of velocity components that provide added absorption to that of the intrinsic P Cyg absorption produced in *Star B*'s wind. An additional effect could be that *Star B*'s wind velocity is truncated by the collision with *Star A*'s wind, which would reduce the emission extent on the red side of the line center. Both effects taken together would naturally lead to a narrower emission feature.

We also measured the N IV $\lambda 4058$ line (Table 12) and we find $\text{FWHM} \approx 750 \pm 100$ km/s in epoch 1998-2000 and $\text{FWHM} \approx 850 \pm 100$ km/s in 2005-2020 with no apparent orbital-phase variations. Koenigsberger et al. (2010) noted that this line underwent a factor ≈ 2 variations in the few spectra in which it was visible during 1955-1965. Given its sporadic appearance during the early epochs, the width variations in this line may have been associated with the WCZ alone.

4.3. Hydrogen to Helium Line Strengths

Foellmi et al. (2003) suggested that most of the WN stars in the SMC were likely to be WNha stars; i.e., a massive stars with a substantial amount of hydrogen in their outer layers and having wind properties intermediate between the Of stars and classical WN stars. The fact that CMFGEN models of *Star A* indicate that its wind contains large amounts of hydrogen is consistent with this idea.

We measured the flux and equivalent width in all the He II and He II+H lines in the HST/STIS spectra at three orbital phases in 1999, and in the HST/STIS observations of 2000, 2014 and 2016. These spectra were chosen for this purpose because they are uniformly flux-calibrated and they contain all He II and H I lines within the $\lambda\lambda 1200-10000$ wavelength range. Each line equivalent width (EW) was normalized by the continuum flux at $\lambda 5000$, as in Koenigsberger et al. (1998b). The results are illustrated in Figure 8. Lines containing H are systematically more intense than those without H, consistent with the

⁹Perrier et al. (2009) found evidence for a similar conclusion, though they considered the result marginal given the uncertainties in the light curve solution.

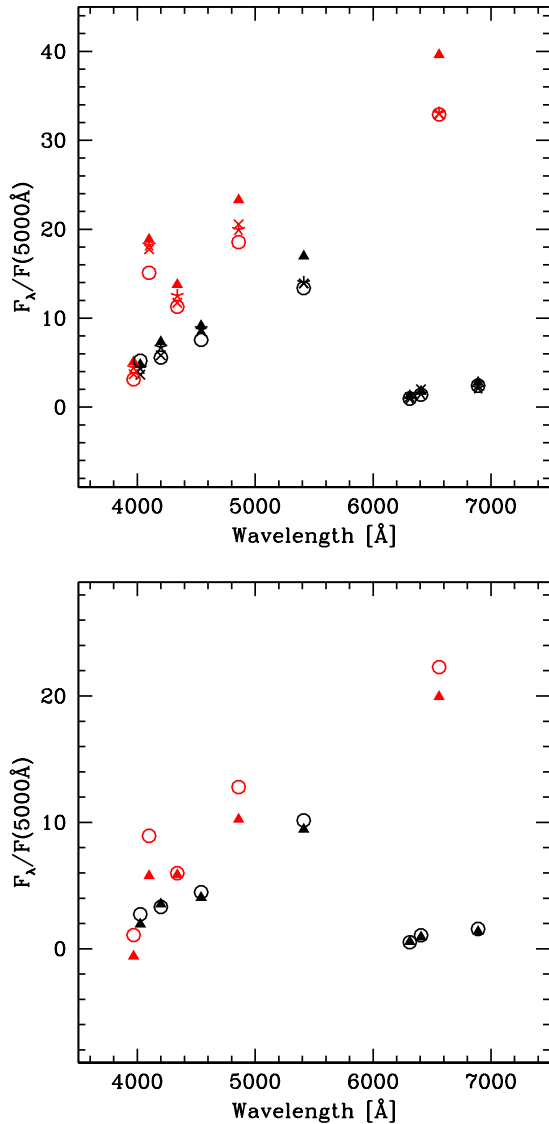


Fig. 8. Flux contained above the continuum level in lines of He II (black) and He II+HI (red) in the STIS spectra normalized to the continuum flux at $\lambda 5000\text{\AA}$. *Top*: Spectra of 1999/2000 at orbital phases 0.15 (crosses), 0.83 (stars), 0.36 (triangles), 0.00 (circles). *Bottom*: Spectra of 2014 (circles), 2016 (triangles). The color figure can be viewed online.

finding that a significant amount of H is still present in the system. This is similar to the result found by Koenigsberger et al. (1998b) based on observations at a single orbital phase. Here, we can compare the results for several orbital phases. In particular, we find that in 1999-2000 the lines containing H at $\phi=0.36$ (*Star B* in front) are stronger compared to $\phi=0$ (*Star A* in front) while the reverse seems to occur in 2014-2016. One interpretation of this result

is that the two components have different hydrogen mass fractions, which are reflected as they (partly) eclipse each other. However, the H/He ratios can also be affected by the conditions in the winds and the possible contribution coming from the WCZ, so at this stage we can only point out the phenomenon and await detailed modeling to arrive at an interpretation.

5. LINE PROFILE VARIATIONS AND WCZ SIGNATURES

The line profiles in HD 5980 are seldom found with the paraboloid shape predicted for a spherical wind. Its orbital phase-dependent line profile variability was amply discussed by Foellmi et al. (2008) and references therein. Moffat et al. (1989) attributed the UV variability to wind eclipses, and Moffat et al. (1998) and Breysacher & François (2000) discussed the optical lines from a qualitative standpoint, concluding that the line profile variations were dominated by the WCZ emission. However, the variations have never been systematized in the context of the epoch-to-epoch variability of *Star A*'s wind.

The emission produced in the WCZ is only one of the factors governing the line profile variability. The other factors are wind eclipses, physical occultation of wind and WCZ emission, lack of emission due to the “hole” in *Star A*'s wind which is filled with *Star B*'s wind, and absorption along the line of sight arising in the WCZ. The wind eclipses cause an emission line to become narrower and weaker due to absorption by the wind that is flowing both toward and away from the observer (Koenigsberger & Auer 1985; Auer & Koenigsberger 1994). The absorption along the line of sight arising in the WCZ acts in a similar manner, but its velocity field is very different. The asymmetrical configuration of the WCZ and the possibility that it is radiative, added to the other processes that affect the line profiles, require at least a 2D radiative transfer calculation in order to fully understand the line profiles and extract the information which they encode. A first step, however, is to constrain the importance of the non-spherically symmetric contribution in shaping the emission lines.

The focus of this paper is to identify the contribution from the WCZ, for which we will use Figure 9 in order to guide the ideas. This figure is an artistic representation of the WCZ and the assumed wind of *Star B* that is contained within it. It is based on the following considerations. The wind momentum ratio in HD 5980 is given by $\eta = \dot{M}_B V_B / \dot{M}_A V_A$, where \dot{M}_B and \dot{M}_A are the mass-loss rates of *Star B*

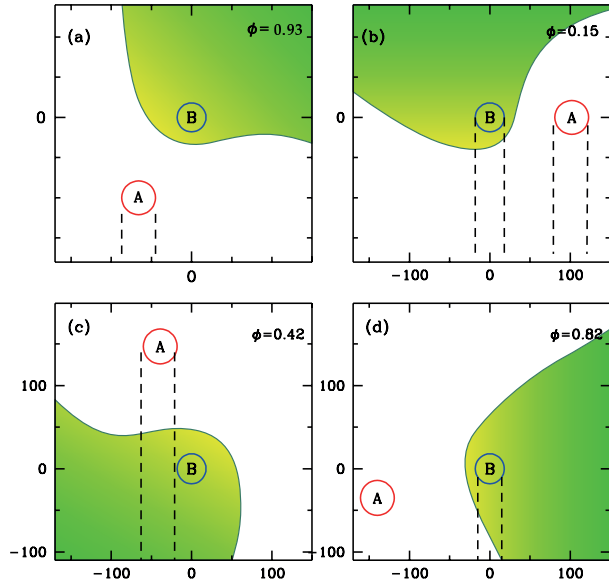


Fig. 9. Schematic illustration showing some of the sight-lines (dash lines) through the wind of *Star A* and the one crossing *Star B* + WCZ (green). The assumed hottest shocked regions are yellow-colored. The circles correspond to the continuum-emitting radii of both stars as determined by Perrier et al. (2009) and are drawn to scale with respect to the orbital separation, which is given in R_{\odot} in the axes. *Star B* is drawn at the origin of the coordinate system. Each panel represents a different orbital phase as indicated. The observer is at the bottom of the figure. The color figure can be viewed online.

and *Star A* respectively, and V_B and V_A are the corresponding wind velocities where the winds collide. The values of *Star A*'s velocities and of \dot{M}_A/\sqrt{f} are available for the years 2000, 2002 and 2009 from Georgiev et al. (2011) and for 2014 from Hillier et al. (2019). The parameter \sqrt{f} is the wind filling factor. The wind of *Star B* is assumed to correspond to that of a WNE star and to remain fairly stable from epoch to epoch. The derived values of η for epochs 2000-2014 are listed in Table 4, and lie in the range 0.13-0.16, confirming that the contact discontinuity of the shocks folds around *Star B*. Additionally, the WCZ is skewed with respect to the line connecting the centers of the two stars due to the Coriolis effect, which introduces an asymmetry between the leading and the trailing shocks (Gayley 2009; Lamberts et al. 2012).

A more precise shape of the WCZ requires calculations that are beyond the scope of this paper. For example, the shock-heated gas is contained between two shocks located on either side of the CD. Pittard & Dawson (2018) find that adiabatic shocks

TABLE 4
WIND MOMENTUM RATIO^a

Epoch	\dot{M}_A/\sqrt{f}	V_A	f	η
Year	$10^{-4}M_{\odot}\text{yr}^{-1}$	km s^{-1}
2000	3.5	2000	0.025	0.13
2002	2.5	2200	0.025	0.16
2009	2.3	2440	0.025	0.16
2014	1.4	2100	0.010	0.15

^aAssuming *Star B* has a constant wind, $\dot{M}_B = 2 \times 10^{-5} M_{\odot} \text{yr}^{-1}$, $V_B = 2200 \text{ km/s}$, $f = 0.1$.

flare beyond the CD in both the primary and secondary winds by ≈ 20 deg. The CD opening angle of an adiabatic collision can be estimated using the expression given by Gayley (2009) with the modification of Pittard & Dawson (2018): $\theta = 2 \tan^{-1}(\eta^{1/3})$. This yields $\theta_{CD} \approx 54$ deg and it then follows that $\theta_2 \approx 34$ deg (*Star B*'s shocked wind) and $\theta_1 \approx 74$ deg (*Star A*'s shocked wind). However, Pittard & Dawson (2018) note that the shocks in HD 5980 are most likely to be highly radiative and thus the above approximations may not be valid. Also, the skew angle depends on the orbital motion which, in an eccentric binary such as HD 5980, varies over the orbital cycle, and the wind speed which may be affected in the vicinity of the shock by radiative braking (Gayley et al. 1997). Finally, the wind properties of *Star B* have only been inferred from the notion that it is a WN4 type star but are not known for certain, and this introduces a major uncertainty into any WCZ calculation.

5.1. The Same Profiles are Observed at the Same Phase in Different Epochs

Given the unstable properties of HD 5980, it is somewhat surprising to find that emission-line profiles obtained at the same orbital phase in different epochs are nearly identical. This is illustrated in Figure 10 where we plot He II $\lambda 5411$ in the phase bins centered on $\phi \approx 0.24$ and 0.60 . The left panels show that for $\phi \approx 0.24$ the spectra of 2010 and 2013 are nearly identical and they are very similar to the ones observed in 2017 - 2020. The right panels show that for $\phi \approx 0.6$, the profiles of 2010 and 2013 are also nearly identical. The more recent spectra (2017-2020), however, differ considerably from those of the earlier epochs in the same phase bin. Specifically, the broad blue-shifted absorption located near line center that is present in the earlier epochs is now replaced by emission, and the line intensity relative to the continuum is stronger. This is consistent with

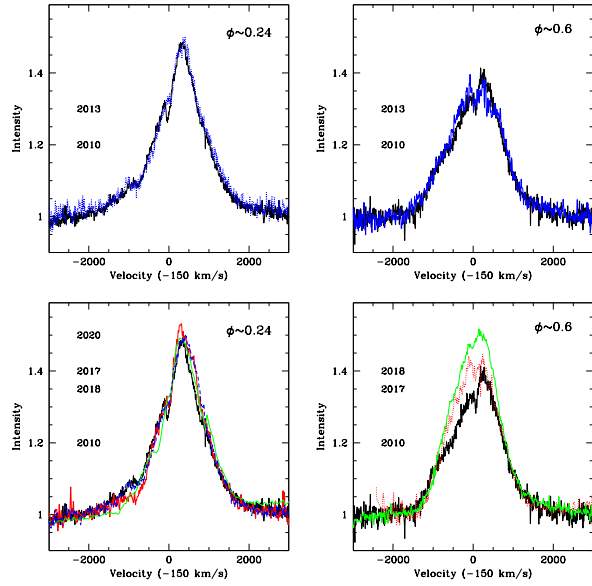


Fig. 10. Left: Line profiles of He II $\lambda 5411$ in the orbital phase bin 0.24-0.25 in spectra of 2010 (black, top and bottom), 2013 (blue, top), 2017 (red, bottom), 2018 (green, bottom), 2020 (blue dashes, bottom) showing a nearly identical shape. Right: The same line in the phase bin 0.58-0.64 in spectra of 2010 (black, top and bottom), 2013 (blue, top), 2017 (red, bottom) and 2018 (green, bottom) showing a significant change in the 2017 and 2018 profiles compared to 2010-2013. The narrow absorption near line center belongs to the photospheric spectrum of *Star C*. The color figure can be viewed online.

the differences already noted for this orbital phase in Figure 4.

Inspection of Figure 9 and Figure 1 suggests that the culprit for the absorption during the low state (2010 and 2013) is likely to be the trailing WCZ wake which at the $\phi \approx 0.6$ orbital phase is in the foreground of both *Star A* and *Star B*. The absence of this absorption in 2017-2018 may be due to significantly stronger emission in the trailing wake which drowns out the absorption, or a reduced optical depth along the line of sight to the background continuum sources. A similar inspection applied to the $\phi \approx 0.24$ bin discloses that the only material in the sightline to *Star A* is its own wind. The change in the line profile between 2010 and 2020 is minimal. It is surprising that such a minimal difference in line profiles at $\phi=0.24$ (which imply only a small change in wind structure) could have such a large effect on what is observed at $\phi \approx 0.6$. Thus, if our interpretation is correct, it seems like only a small change in *Star A*'s wind is necessary to noticeably alter the WCZ emitting properties.

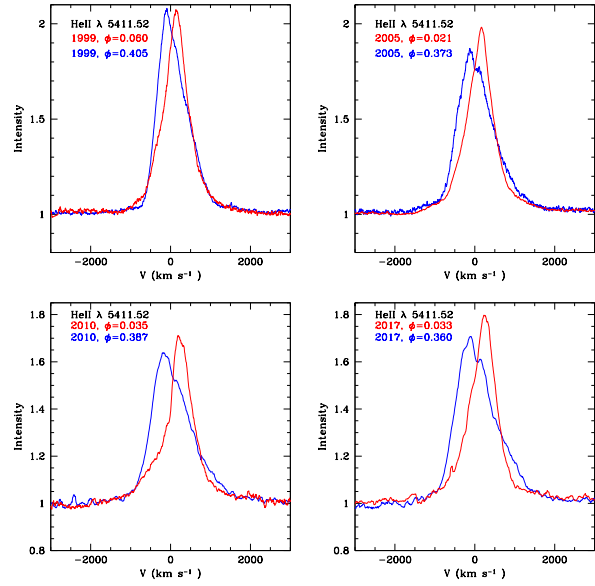


Fig. 11. Line profiles of He II $\lambda 5411$ at post-primary eclipse (red, $\phi > 0$, *Star A* in front) and post-secondary eclipse (blue, $\phi > 0.36$, *Star B* in front). Each panel corresponds to a different epoch. The general behavior has remained the same over the time frame 1999-2017. The color figure can be viewed online.

A broad blue shifted absorption that is superposed on HD 5980's emission lines near line center is a feature that frequently appears. An example can be seen Figure 10. Often, a similar feature is observed on the red side of line center. In both cases, its total width is of the order of 500 km/s and its centroid can be displaced by as much as 1000 km/s from line center which precludes it from being a photospheric absorption. One possible explanation is that it originates at the base of one of the winds, where the initial acceleration takes place. However, this would not explain it when it is red-shifted. Thus, another possible explanation is an eclipse effect, when emitting material that is flowing away from us is occulted (that is, there is missing light within a particular velocity range). Inspection of Figure 9 shows in the top left panel an orbital phase at which *Star A* would block a fraction of the emission from the receding WCZ, and the bottom right panel shows a phase at which *Star B* would block a fraction of this light.

5.2. Asymmetric Outflow at Conjunctions

We now turn our attention to the line profiles around the conjunction phases. Figure 11 shows the line profiles obtained within 0.05 in phase after the $\phi=0.36$ eclipse in four epochs between 1998 and 2017. These profiles are compared to those obtained

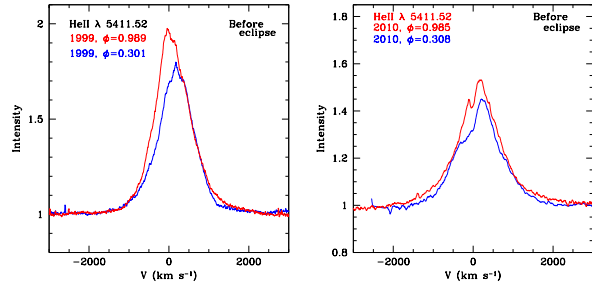


Fig. 12. Line profiles of He II $\lambda 5411$ at phases just before each eclipse ($\phi=0.99$, red, and $\phi=0.30$, blue) in epoch 1999 (left) and epoch 2010 (right). The color figure can be viewed online.

right after the opposite eclipse ($\phi=0$) and clearly indicate that a significant fraction of the He II $\lambda 5411$ emission arises in material that is flowing toward us when *Star B* is in front. The profiles when *Star A* is in front are redshifted, but this is likely due to a combination of the above-mentioned outflow, which at this phase is moving away from us, and the wind eclipse due to *Star A*'s wind which lies along the sightline to *Star B*. The relative shift between the maxima in each pair of orbital phases is 229 km/s in 1999, 281 km/s in 2005, 385 km/s in 2010, and 377 km/s in 2017. These epoch-to-epoch variations correlate with the increasing wind speed recorded for *Star A* based on the UV P Cyg absorption components. They also correlate with the relative intensity of the two maxima at each epoch. Thus, the qualitative nature of the profile variations is the same in all epochs: the line profile is always blue-shifted at $\phi \approx 0.36$.

Figure 12 compares the line profiles obtained at orbital phases just before eclipses, $\phi=0.301-0.305$ (*Star B* in front) and $\phi=0.985-0.989$ (*Star A* in front) for Epochs 1998-1999 and 2010-2012, the only two epochs for which we have such similar orbital phases. Once again, the most important point to note is that, despite the significant difference in line strengths between the high and the low states, the qualitative nature of the variation is the same. Also noteworthy is that the profiles just prior to $\phi \approx 0.36$ do not show the prominent blue-shifted emission seen after $\phi=0.36$ but instead have a strong absorption. This now brings us to the role of the leading branch of the WCZ.

5.3. The WCZ Leading Branch

The properties of the WCZ are determined by the velocity of the winds when they collide. The skewed WCZ orientation with respect to the line connecting the centers of the two stars introduces an asymme-

try between the leading and the trailing shocks. In the case of an unequal wind momentum ratio, as in HD 5980, Pittard (2009) finds that the emission measure of the WCZ is dominated by the shocked gas of the weaker wind, most of which is in the leading arm. Hence, the relative location of the leading WCZ arm with respect to our sightline to *Star A* and *Star B* will determine whether this shocked gas signals its presence as an absorption in the line profile or as an emission. Upon inspection of Figures 9 and 10 we see that right before $\phi=0.36$ the leading arm lies directly between us and *Star A* and it is flowing almost directly toward us¹⁰. Hence, its presence should be evident as blue-shifted absorption. After the $\phi=0.36$ conjunction, the leading branch is still flowing toward us but it is no longer projected onto *Star A* and hence we should observe it in emission. This behavior is precisely what is observed.

A detailed look at the transition that occurs as the leading WCZ arm passes in front of *Star A* around $\phi=0.36$ is shown in Figure 13, which illustrates two pairs of profiles obtained in the same orbital cycle. These pairs of profiles show that just prior to eclipse ($\phi=0.31-0.33$) there is a prominent blue absorption that “eats into” the underlying emission, while just after eclipse ($\phi=0.39$) this absorption is replaced by emission. The two pairs of profiles correspond to the two epochs, 2010 and 2013. The absorption in 2010 extends from near line center to approximately -800 km/s, which provides a constraint on the flow velocity of the leading arm in that portion projected onto *Star A*.

A similar result is found when comparing the pre- and post-eclipse line profiles of 1999, 2017 and 2018 shown in Figure 14. However, in this case the only available post-eclipse spectra are at phases ≈ 0.41 and pre-eclipse phases $\approx 0.22-0.30$. The latter display a different behavior near the base of the line. Specifically, they show the presence of emitting material flowing toward us with projected velocities > 1000 km/s, compared to the post-eclipse profiles which appear more absorbed. This fast emission (compared to the profiles closer to eclipse) is also seen in the earlier epochs as illustrated in Figure 15 where we compare the profiles shown in Figure 13 with profiles obtained further from central eclipse.

5.4. Line Profiles at Elongations

At elongation phases, the sightline to the close vicinity of *Star A* intersects only *Star A* wind, while the sightline to *Star B* intersects its wind and the

¹⁰See also the geometry in Figure 2 in Lamberts et al. (2012) and Figure 9 of Parking & Pittard (2008).

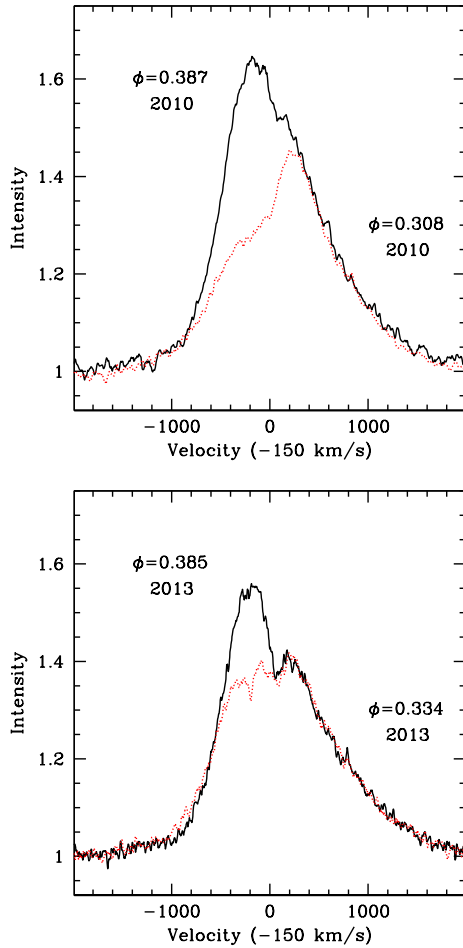


Fig. 13. Spectra pre- and post-secondary eclipse for epochs 2010 (left) and 2013 (right) illustrating the absorption caused by the WCZ leading branch as it first passes in front of *Star A* (red profiles) and the emission that appears shortly thereafter when it is no longer projected onto the *Star A* bright background continuum. The color figure can be viewed online.

WCZ (which includes shock-heated *Star A* and *Star B* wind). Depending on the aberration angle, some of the WCZ material may be flowing away from the observer, while some is flowing perpendicular to the sightline and other portions have velocity components toward the observer. Of all this material, that which lies along the sightline to the *Star A* and *Star B* cores can produce absorption.

Illustrated in Figure 16 is the profile of He II $\lambda 1640$ at the two elongation phases observed in 1999, $\phi \approx 0.8$ (*Star A* approaching the observer) and $\phi \approx 0.1-0.2$ (*Star A* receding). These profiles are shifted in velocity space to correct for *Star A*'s orbital motion, so any excess in the line profile can

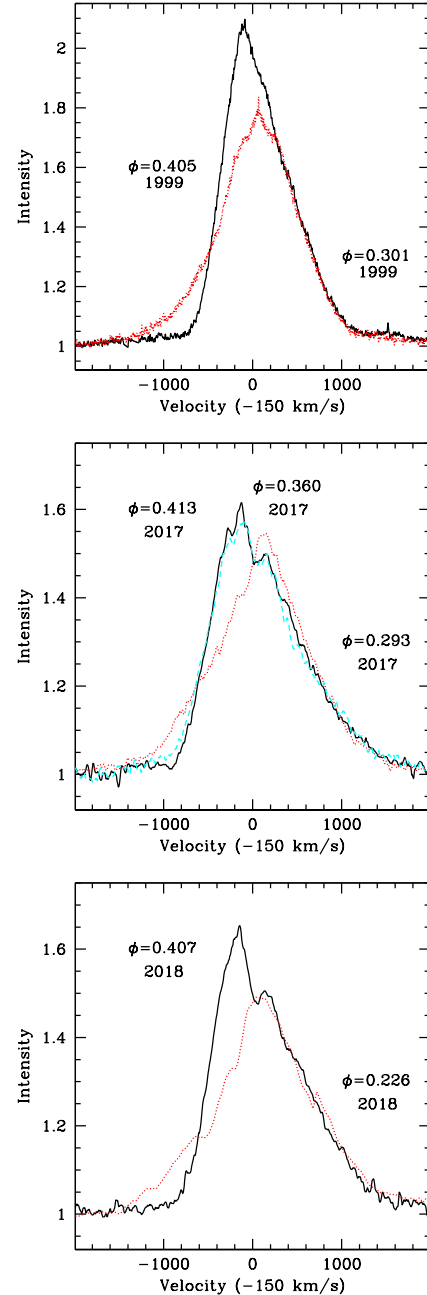


Fig. 14. Spectra pre- and post-secondary eclipse for epochs 1999 (top), 2017 (middle) and 2018 (bottom) illustrating the absorption caused by the WCZ leading branch as it first passes in front of *Star A* (red profiles) and the emission that appears shortly thereafter when it is no longer projected onto the *Star A* bright background continuum. The middle panel shows the line profile during eclipse (magenta) which is nearly identical to the post-eclipse profile. Spectra are shifted in the velocity scale to correct for the orbital motion of *Star A*. The color figure can be viewed online.

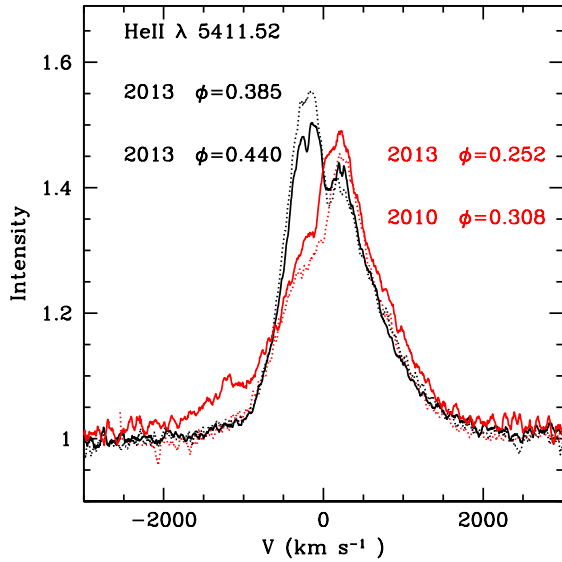


Fig. 15. Spectra pre- and post-secondary eclipse showing that the physical eclipse of the two stars plays little or no role in producing the variability around $\phi=0.36$, but rather it is associated with the WCZ geometry. Epochs 2010 and 2013 are both in the low state. The color figure can be viewed online.

be associated with emission arising in *Star B* and/or the WCZ. There is indeed such an excess redward of line center at $\phi \approx 0.7$, which is consistent with an origin in or near *Star B*. This excess emission shows up blueward of line center and around line center at the opposite elongation, when *Star B* is approaching the observer, and it fills in a part of the intrinsic *Star A* P Cygni absorption.

Analogous pairs of profiles for He II $\lambda 5411$ are shown in Figure 17 for epochs 1999, 2005, 2010 and 2018. The same excess red emission at $\phi \approx 0.7$ is evident in each epoch, but the blue excess at the opposite phase is concentrated at higher expansion speeds, i.e., closer to the base of the broad emission. This is probably only a consequence of the smaller optical depth in He II $\lambda 5411$ compared to He II $\lambda 1640$. Interestingly, the pairs of He II $\lambda 5411$ profiles show that the amount of excess red-shifted emission scales with the overall line intensity. The smallest amount of excess emission is seen in the 2010 spectra, when line intensities were near their minimum and the system was in the low state.

Georgiev et al. (2011) showed that increasing line emission correlates with increasing visual magnitude and, at the same time, correlates with decreasing wind velocity. If we assume that a smaller *Star A* wind speed implies that its density is higher, this

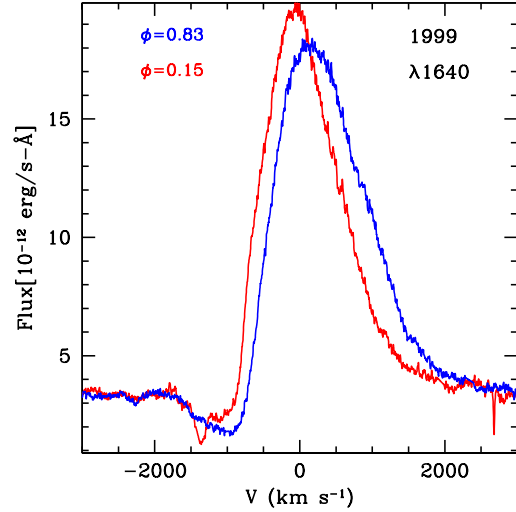


Fig. 16. Line profiles of He II $\lambda 1640$ obtained in 1999 at elongations in the rest frame of *Star A*. The color figure can be viewed online.

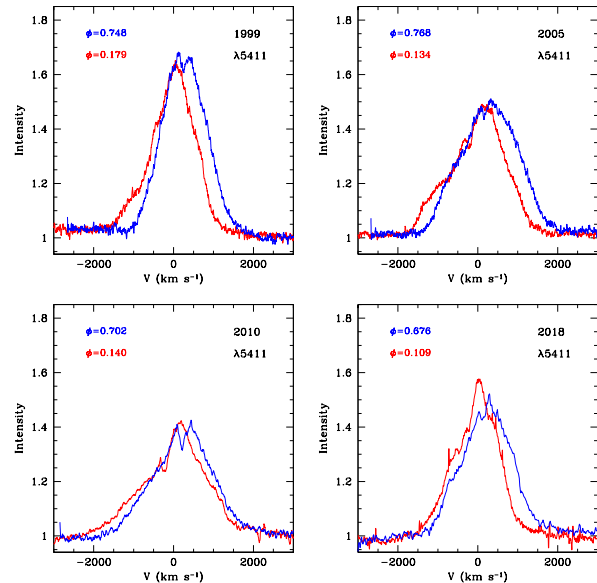


Fig. 17. Line profiles of He II $\lambda 5411$ at elongations in the rest frame of *Star A*. Top: Epochs 1999 (left) and 2005 (right). Bottom: 2010 (left) and 2018 (right). The color figure can be viewed online.

would mean that the WCZ is being fed with a higher density wind at epochs other than 2010, which would result in a larger emission measure. Following this line of reasoning leads to the conclusion that the excess emission along the line wings of the He II lines originates in the WCZ, and that this shocked region lies in the close vicinity of *Star B*.

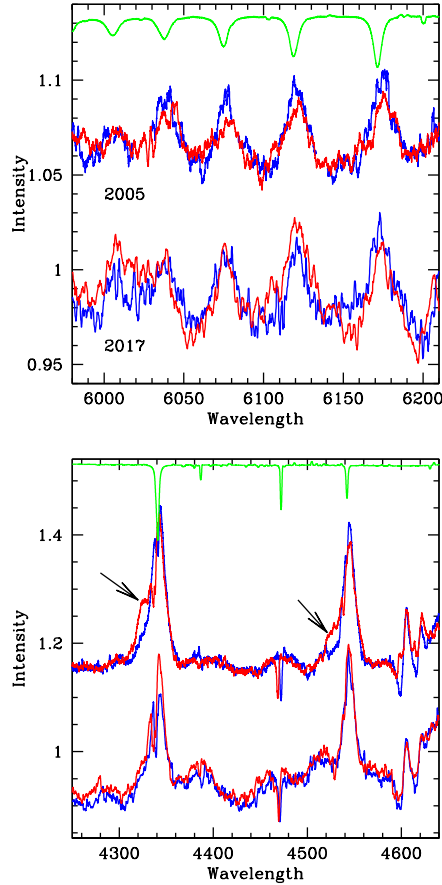


Fig. 18. Line profiles of He II and other lines obtained in 2005 at $\phi=0.98$ (blue) and 0.13 (red) compared to those of 2017 at $\phi=0.98$ (blue) and 0.08 (red). Spectra are shifted in wavelength to correct for *Star A* orbital motion. The 2005 spectra are shifted vertically for clarity. The arrows point to the blue-shifted excess emission at $\phi=0.08$ in 2005 and absent in 2017. The green curve shows the predicted *Star C* photospheric absorption spectrum. The color figure can be viewed online.

The *HST/STIS* 2016 observation of HD 5980 ($\phi=0.36$) revealed a very peculiar shape of the C IV $\lambda 1550$ P Cygni profile: there was notable excess emission blueward of line center extending out to approximately -900 km/s with respect to the HD 5980 rest frame. Because this C IV doublet is a resonance line, any outflowing material lying along the line of sight to either *Star A* or *Star B* would appear in absorption, not emission. Given the above discussion and our conclusions from the optical observations, the C IV excess emission must also arise in the uneclipsed WCZ outflow. There is at least one other UV spectrum that shows some C IV $\lambda 1550$ excess blue emission. It was obtained by *IUE* in 1981 (SWP15072) at orbital phase 0.80. There are unfor-

tunately no UV spectra obtained during that epoch around $\phi=0.36$ and no recent UV spectra obtained at other orbital phases.

6. ON THE NATURE OF *Star B*

Early studies of HD 5980 introduced the idea that *Star B* was the WR star in the system. This idea, however, was derived from a noisy RV curve of He II $\lambda 4686$ obtained from relatively low resolution photographic spectra. Subsequently, Niemela (1988) obtained RV curves of N IV $\lambda 4058$ indicating that this line was emitted by *Star B*. Noteworthy is its absence in the 1973-1977 time frame, a time when HD 5980's visual magnitude was at a minimum. The appearance of this line in the early 1980s coincides with a declining *Star A* wind speed. Thus, it appears that the changes in *Star A*'s properties led to changes in the WCZ that allowed N IV $\lambda 4058$ to become visible in the spectrum, as we already noted in the previous section.

The P Cygni absorption profiles of resonance lines at orbital phases when *Star B* is in front always indicate the presence of very fast outflows (≥ 3000 km/s) (Koenigsberger et al. 1998a; Georgiev et al. 2011; Hillier et al. 2019). At other orbital phases, the velocities have generally been slower (≤ 2000 km/s) since the mid-1980s. The very fast wind would be consistent with a WN3/4 or O3 type classification for *Star B*, and the fact that such a fast wind is not observed at phases other than near $\phi=0.36$ could be explained by a WCZ that truncates the wind long before terminal speeds are attained. However, it is not easy at this time to discard alternative scenarios. For example, *Star A*'s wind could be non-spherically symmetric such that it is faster in the direction of its companion, or that there is a small population of extremely fast particles produced in the wind-collision process, as found in the hydrodynamic simulations (Pittard 2009) and which would be observable only in the resonance lines.

We currently favor the first scenario because it is simplest and because the N V $\lambda 4944$ emission clearly splits into two well-defined components during elongations, indicative of orbital motion. This implies an origin in a relatively spherical distribution of gas around *Star B*. However, if the shocked gas can sustain the conditions to produce emission from this N V line, then *Star B* could well be an O-type star rather than a WN, and the very fast wind observed around $\phi=0.36$ could be due to one of the other mentioned scenarios.

The radii of the *Star A* and *Star B* occulting disks that were deduced from data of the late 1970s indicate that $R_A > R_B$. Thus, the $\phi=0.36$ (*Star B*

in front) eclipse is not total. Hillier et al. (2019) demonstrated that assuming the *Star B* wind can be neglected, the predicted spectrum at $\phi=0.36$ is still that of *Star A*, including P Cygni absorptions (see Figures 3 and 4 of Hillier et al. 2019). This provides an explanation for why the spectrum at $\phi=0.36$ is, in general terms, so similar to that observed at all other orbital phases, and shows that one cannot adopt the spectrum at this phase as representative of *Star B*'s spectrum. This again opens the possibility that *Star B* may not be a WN star.

It is also interesting to note the high degree of rapid polarimetric variability that was observed around $\phi=0.36$ by Villar-Sbaffi et al. (2003). These authors suggested that a very fast rotator model for *Star B* could at least qualitatively explain the observations, although we speculate that a clumpy WCZ might also lead to variable polarization.

Finally, the presence of a second set of photospheric-like absorptions in the 2018 spectrum opens the possibility of an absorption line spectrum associated with *Star B*. The spectrum in question was obtained at orbital phase 0.226 and the second set of absorptions has a velocity of -300 km/s (Figure 19), which however is faster than the expected *Star B* orbital motion at this phase, as deduced from the N V $\lambda 4944$ emission. If actually associated with *Star B*'s photosphere, the absorptions would imply that the N V $\lambda 4944$ emission arises mainly near the WCZ vertex that is lifted above *Star B*'s surface. However, an alternative explanation is that the blue-shifted absorption lines that mimic photospheric absorptions come from a shell of material surrounding the binary, product of an earlier instability that resulted in the ejection of this material (Barbá et al. 1995).

7. DISCUSSION AND CONCLUSIONS

7.1. Summary of Observational Results

In the previous sections we presented the analysis of high resolution spectroscopic observations obtained since 1998, complemented with historic spectra obtained since the 1950s. The summary of the results is as follows:

1. The integrated emission line intensity in observation epochs 1998-2006 were significantly stronger than in 2009-2016. We define a high state and a low state, corresponding to these two epochs. In the third set of epochs, 2017-2020, the system appears to have been in an intermediate state between low and high.

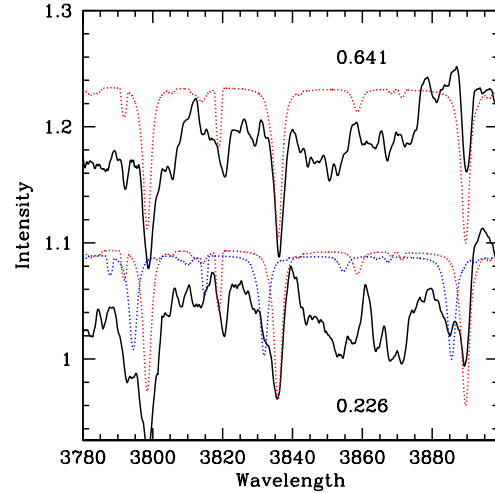


Fig. 19. MagE spectra at orbital phases 0.641 and 0.226 obtained in 2018 showing what appears to be a second set (blue dashes) of photospheric absorption at 0.226 which is shifted by -316 km/s with respect to the absorptions of *Star C* (red dashes). The spectrum at $\phi=0.641$ is shifted vertically for clarity in the figure. The wavelength units are \AA . The color figure can be viewed online.

2. The entire $\lambda\lambda 1200 - 10000$ spectral energy distribution had larger intensities during the high state than during the low state.
3. In 1998-1999 and 2017-2020, the integrated emission line intensities vary smoothly over orbital phase with a broad maximum centered around $\phi=0.5-0.6$ (apastron). In 2009-2015, the intensities mimic those of 2017-2020 except in the $\phi \approx 0.41-0.90$ interval, in which they are weaker as a consequence of stronger absorption superposed on the emission, blueward of line center (see Figure 10).
4. The RV curve of N IV $\lambda 4058$ from data of 1998-2020 is consistent with that of N V $\lambda 4944$, the latter currently believed to truly represent *Star A*'s orbit. The most significant difference occurs in the phase interval 0.1-0.3 which coincides with maximum approaching velocity of *Star B*. This implies that unresolved N IV *Star B* emission distorts *Star A*'s RV curve. However, the strength of this additional emission changes from epoch to epoch, being stronger during the high state.
5. The H β + He II RV curve (data obtained in 1955-2020) display a maximum around the same orbital phase as N IV $\lambda 4058$, but the peak-to-peak amplitude is a factor of ≈ 2 smaller. This

implies that there is a significant $H\beta + He II$ contribution arising in *Star B* and the WCZ. This extra emission is mostly evident around the time of periastron during the high state (see Figure 18). The $He II \lambda 4686$ line behaves similarly to $H\beta + He II$, but its RVs show significantly more scatter.

6. The phase-dependent FWHM variations in $He II \lambda 4686$ and $H\beta + He II$ in all epochs (1955-2020) display a nearly identical descent in the phase interval 0.95-0.05. This phase interval corresponds to the physical eclipse of *Star B* by *Star A*. The available data indicate that the ascent is equally steep. A second minimum in FWHM occurs in the phase interval 0.3-0.6. The descent here appears to be similar in all epochs but the ascent is epoch-dependent (see Figure 7). The most gradual ascent occurred in 1990-2000, when the system was in the high state pre- and post- eruption.
7. The emission line profiles of $He II \lambda 5411$ in spectra obtained in 2010-2020 in the orbital phase bin $\phi \approx 0.24$ are nearly identical (see Figure 10). This is an unexpected result given the strong variability that has characterized HD 5980.
8. The differences between the line profiles of $He II \lambda 5411$ observed at $\phi=0.02-0.06$ (*Star A* in front) and at $\phi=0.36-0.40$ (*Star B* in front) are qualitatively the same in all epochs. In the first of these phases, the line profile is skewed blueward, while in the second of these phases it is skewed redward (see Figure 11). Our recent observations showing this effect (and for which we have spectra at the required orbital phases) were obtained in 1999, 2005, 2010 and 2017. A similar, blueward-skewed profile at $\phi \approx 0.4$ was observed also in 1962 (Koenigsberger et al. 2010). The only possible explanation for the blue-shifted emission is the presence of material that flows in the direction of the observer at orbital phases when *Star B* is in front but that, at the same time, is not projected onto either *Star A*'s or *Star B*'s continuum emitting core.
9. Using spectra obtained within the same orbital cycle, we show that the $He II$ line profiles have a strong absorption blueward of line center just before the $\phi=0.36$, and that this absorption is replaced by emission just after this phase (see Figure 13 and 14). We attribute this behavior to absorption in the leading WCZ branch as it

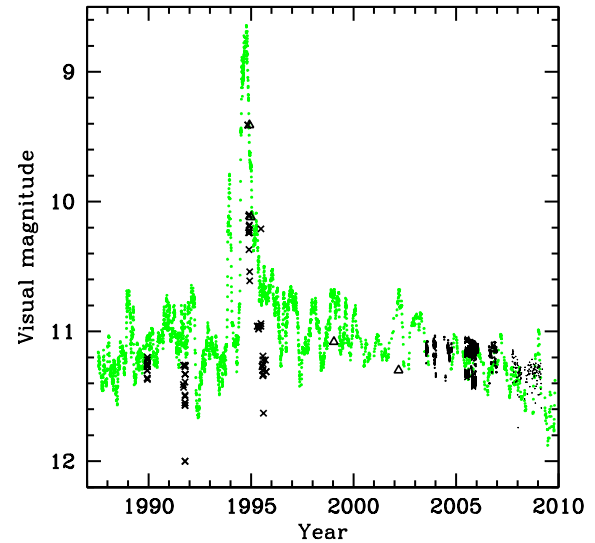


Fig. 20. Historic light curve of HD 5980 in epochs 1987-2010 illustrating the underlying plateau around the time of maximum. Green dots: visual magnitudes obtained by A. Jones shifted by +0.3 mag, after applying a 9-point boxcar average smoothing. Triangles: m_v data listed in Table 6. Black crosses: *International Ultraviolet Explorer* FES magnitudes (Georgiev et al. 2011). Black dots: Swope, SMARTS, ESO, ASAS-SN and LCOGT photometry listed in Table 5. The color figure can be viewed online.

passes in front of *Star A* just prior to conjunction, and emission from this same region once it is no longer along our line of sight to *Star A*. The velocity range over which the changes occur is approximately -800 to $+200$ km/s, consistent with the line-of-sight velocities along the wind-collision contact discontinuity that were estimated by Koenigsberger (2004, Figure 20) for the case of a large wind momentum ratio in favor of *Star A*.

10. A significant amount of hydrogen is evident in the spectra of 1999-2000 and 2014-2016 (Figure 8). In 1999-2000, the lines containing H are stronger at $\phi=0.36$ than at $\phi=0.0, 0.15$ and 0.83 , while in 2014-2016 they are weaker at $\phi=0.36$ than at other phases.

7.2. *Star A* has Dominated the Emission-Line Spectrum Since 1955

The evidence leading to this conclusion is the following. First, there has been a persistent presence in all epochs since 1955 of excess blue-shifted emission in $He II$ lines at secondary eclipse ($\phi=0.36$). At

this phase, *Star B* is in front and the excess blue emission can only be interpreted as originating in material flowing toward the observer and which lies outside the line of sight to either *Star A* or *Star B*. A wind collision zone that folds around *Star B* and constrains its wind within it is the most feasible scenario to explain the blue-shifted excess. Second, all strong emission lines have displayed RV variations since 1955 that are consistent with their origin in *Star A*. This includes N IV $\lambda 4058$ which is now strong, but in the past was often absent or too weak to be detected (for example, in 1962-1965, 1973, and 1977). N IV $\lambda 4058$ became prominent in the 1980s at the same time that the UV lines of Fe V, Fe VI and N IV] $\lambda 1486$ also emerged. These changes coincided with a reduction in the extent of the UV P Cygni absorptions, indicating a slower wind speed.

The fact that the He II $\lambda 4686$ and H β lines approximately followed the orbit of *Star A* even when N IV $\lambda 4058$ was weak/absent suggests that the state of *Star A* during the mid-1970s and before was similar to that of a H-rich WN3 star but which intermittently oscillated between WN3 and WN4 before transitioning through the later sub-types as it brightened and headed for the eruption.

Hillier et al. (2019) noted the similarity in the UV P Cyg line profiles that were observed in the early 1980s and early 1990s with those of 2014-2016 (see their Figure 19). Furthermore, Koenigsberger et al. (2010) showed that the line profile variation in He II $\lambda 4686$ were qualitatively the same in 1962 and 1999 (see their Figures 8 and 9). Specifically, they have a very narrow and blue-shifted shape when *Star B* is in front, compared to elongations, just as is currently observed. Finally, the RV curve of He II $\lambda 4686$ in the early 1980s displayed a systematic blue-shift precisely around the time of secondary eclipse, indicating that the blue-shifted emission was also prominent in $\approx 1981-1983$ and $1991-1992$. This leads to the conclusion that the wind collision region has folded around *Star B* since the 1960s, if not earlier. Thus, *Star A*'s wind has always been the dominant wind in the system.

7.3. *The Emission Line Profile Variations and the Distorted RV Curves are Consistent with a Skewed WCZ that Folds Around Star B and Provides a Source of Excess Emission and Absorption*

The general scenario that emerges is that *Star A*'s wind produces the majority of the emission at line frequencies, and the region where its wind interacts with *Star B* produces a secondary set of emission

lines. The strength and location in velocity space of these secondary lines depend on *Star A*'s wind. Thus, the epoch-dependent changes in the WCZ line emission echo the *Star A* wind variations. This explains the varying amplitude of the RV curves obtained at different epochs, the prime example being the N IV $\lambda 4058$ RV curve. Weak lines that arise from excited transitions are much less affected, as appears to be the case for the He II $\lambda\lambda 6000-6200$ lines shown in Figure 18.

We are able to identify the effects caused by the leading WCZ branch when it occults *Star A* at phases just prior to the $\phi=0.36$ eclipse and produces absorption superposed on the He II $\lambda 5411$ emission line. We then see how it produces excess blue-shifted emission shortly thereafter in the same velocity range as observed previously in the absorption. Around the time of the opposite eclipse, the WCZ emission outflow is directed mostly away from the observer, but is largely eclipsed by *Star A*'s opaque disk, and radiation transfer effects through *Star A*'s wind reduce its visibility.

The effects due to the more extended WCZ trailing branch are mostly evident in the photometric eclipse light curves, in the secondary eclipse egress, and in the $\phi \approx 0.6$ line profiles (see Figure 10).

7.4. *The Brightness Increase Around Periastron*

The *Star A* + *Star B* system is eccentric and the tidal interaction model predicts larger energy dissipation rates around the time of periastron (Moreno et al. 2011). The flux-calibrated HST/STIS spectrum of 1999 at orbital phase 0.15 is $\approx 5\%$ brighter than at orbital phase 0.83. Table 5 shows that the average visual magnitude is often brighter in the $\phi=0.1-0.2$ phase interval, and a brightening at orbital phases after $\phi \approx 0.04$ was already noted by Sterken & Breysacher (1997).

An alternative interpretation for the continuum brightness increase around periastron is that the wind collision energy is believed to be higher at periastron, which would also lead to a larger brightness at this phase. However, contrary to this expectation, Nazé et al. (2018) found that X-ray maximum occurs close to apastron instead of periastron. This inconsistency between expectations and X-ray observations and the increased brightness around periastron require further investigation.

7.5. *The 1993-1994 Sudden Eruptions*

The long term brightening of the system that started in ≈ 1980 reached a plateau around the year 2000 where it remained until approximately 2004.

TABLE 5
RECENT PHOTOMETRIC DATA

Epoch	JD start	JD end		$\phi=0.6-0.8$		$\phi=0.1-0.2$		Source	
Year	-2400000	-2400000	N	$\langle m_v \rangle$	s.d.	N	$\langle m_v \rangle$	s.d.	
2003-04	52838.8	53288.8	33	11.130	0.025	4	11.049	0.010	Swope
2005-07	53561.9	53693.8	138	11.134	0.011	12	11.069	0.006	Foellmi
2005-06	53591.9	54092.7	44	11.132	0.032	36	11.102	0.026	SMARTS
2014/06	56809.9	57080.5	58	11.454	0.028	24	11.433	0.020	ASAS-SN
2015/05	57152.9	57207.8	13	11.409	0.027	5	11.403	0.020	ASAS-SN
2015/07	57222.8	57357.6	19	11.389	0.022	4	11.414	0.052	ASAS-SN
2017/08	57982.7	57985.9	2	11.424	0.008	0	—	—	ASAS-SN
2017/10	58054.5	58073.6	158	11.469	0.029	12	11.472	0.020	LCOGT
2017/11	58074.0	58087.5	190	11.527	0.015	0	—	—	LCOGT
2017-2022	58029.5	59626.5	290	11.37 ^a	0.04	109	11.35 ^a	0.04	ASAS-SN

^aThese are the average uneclipsed magnitudes obtained in the Sloan g-band between 2017-10-03 and 2022-02-16, and a zero-point shift of +0.14 mag was added to make them consistent with the Johnson V-band magnitudes that were obtained during the same epochs with other instruments.

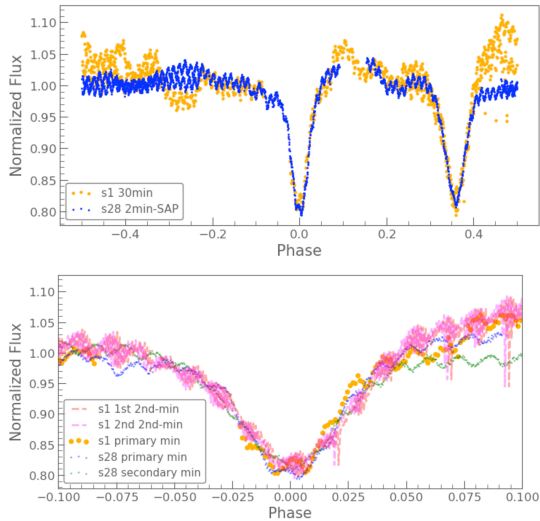


Fig. 21. Normalized TESS photometric data for Sectors 1 and 28 (s1, s28) showing the primary eclipse at phase= 0 and on top of the light curve folded with the period $P = 19.2654$ d. Clearly seen are the oscillations with a period of $P_{\text{osc}} = 0.25$ d, observed at both eclipses of the *Star A* + *Star B* system. Upper panel: Two secondary and one primary eclipse were observed in Sector 1 and one primary and one secondary were observed in Sector 28. Lower panel: As above, but the abscissa gives the distance in orbital phase from mid-eclipse of the five eclipses. The color figure can be viewed online.

Then the brightness and emission line intensities declined reaching an apparent minimum in 2010-2013. The sudden outburst occurred in 1994, with a “precursor” in 1993, both prior to the maximum in the

long term trend. We illustrate in Figure 20 the visual magnitude evolution of HD 5980 during the time frame 1987-2010. The complete light curve covering epochs 1950-2018 is presented in Figure 22.

One of the possible scenarios that might explain the long-term behavior is that *Star A* was undergoing an evolutionary transition making it brighter and more extended until it reached a critical radius at which the sudden outburst was triggered. If this were the case, however, it is not clear whether the loss of $\approx 10^{-3} M_{\odot}$ would have been sufficient to slow the expansion and then allow the star to contract once again to its current state. However, luminous blue variables (LBVs) are known to undergo cyclical changes that impact their photospheric and wind properties. If this were the case, then *Star A* would be the only known LBV with WR spectral characteristics (except possibly the erupting variable in η Carinae).

An alternative interpretation is that the tidal shear energy dissipation in sub-surface *Star A* layers caused it to slowly expand until it reached a critical condition at which an external layer was ejected, thus liberating the accumulated energy. Tidal shear energy dissipation was shown to be a viable mechanism for bloating a star in the case of the red nova V1309 Sco (Koenigsberger & Moreno 2016). In the case of HD 5980, Toledano et al. (2007) outlined the manner in which an increasing stellar radius would lead to increasing tidal shear, eventually causing the eruption.

A more speculative possibility for the outbursts is that they could have been triggered by unstable ac-

cretion of *Star A* material onto *Star B*, as it has been proposed for the case of η Carinae (Soker & Behar 2006). Our observational results leave open the possibility that *Star B* may not be a typical WNE star. The observations indicate that, as *Star A*'s mass-loss rate increased, the WCZ emission also increased, implying a denser collision region. Hydrodynamical wind-wind collision studies show that when the wind momentum of one of the stars is significantly larger than that of its companion, a fraction of the shocked wind is accreted (Matsuda et al. 1992; Ruffert & Arnett 1994; Nagae et al. 2004). Under stationary conditions, the accretion rate is (probably) not sufficient to affect the secondary, but if the incoming stellar wind evolves over time becoming denser and slower, then the numerical simulations find that high density clumps produced by the instabilities in the shocks will fall onto the secondary star (Kashi 2020), potentially leading to non-negligible accretion rates. If such a phenomenon occurred in 1992-1994, the violent expulsion of the material accreted onto *Star B* could have been responsible for the transitory B1.5Ia⁺ spectrum observed in 1994 and the rapid spectral evolution of the system over the following two years. The persistent underlying WN spectrum at that time (Koenigsberger 2004) would in this case have been that of *Star A*.

7.6. Future Work

A treasure trove of information is encoded in the line profile variations. Future investigations could make use of the detailed variability of just a single line such as HeII 5411 to constrain the geometrical extent, general physical conditions, and velocity fields in the WCZ, but to do so requires the use of 3D radiative-hydrodynamic simulations and a densely packed (in orbital phase) set of observations over an entire orbital cycle. Though costly in observing time and computational resources, the expected outcome would include very valuable information on the structure of highly radiative shocks, and would yield a deeper understanding of the *Star A* + *Star B* interacting system.

Our new RV curves are consistent with those analyzed in Koenigsberger et al. (2014), and thus the derived masses are not expected to change with respect to those obtained previously. Also, the relative continuum luminosities are unaffected by our new results, so the conclusion that both objects are extremely massive and luminous still holds. A possible change lies in what is assumed for the evolutionary state of *Star B*. Its high luminosity suggests a chemically homogeneous evolutionary path

(Koenigsberger et al. 2014). However, if it is not a WN star, then a potentially interesting (speculative) scenario is one in which mass transferred from *Star A* to *Star B* via unstable wind accretion has led to sequential violent ejections from *Star B*'s surface reducing its mass and prolonging its main sequence lifetime. Clearly, this conjecture requires the identification of an instability violent enough to eject the material from *Star B*'s surface and leave the system. The alternative conjecture, that *Star A* is the source of the 1993-1994 eruption, also requires further investigation, as no other WNh type star is known to have presented such a violent instability.

The properties of the “third light” source, *Star C* also merit further studies. Although a well-defined photospheric line spectrum is associated with one of the components in this highly eccentric ($e \approx 0.8$, $P_C = 96$ d) system, there is no information as yet regarding the nature of its companion, nor whether it is gravitationally bound to the *Star A* + *Star B* system. *Star C*'s high eccentricity, line of sight coincidence to the *Star A* + *Star B* system, and brightness make it tempting to suggest that both binaries may be in a very wide orbit around each other.

Finally, it is also interesting to ponder the question of HD 5980's apparent uniqueness. It may be so only because it is a massive eclipsing system that we have been lucky enough to catch in a very short-lived evolutionary state that many other systems already have or will experience. Given its location in the low-metallicity SMC environment, HD 5980 could be typical of many massive objects yet to be identified in distant extragalactic sources.

This investigation is based on observations obtained at the Las Campanas Observatory, one of the Carnegie Institution for Science Observatories, which we gratefully acknowledge. We thank Abraham Villaseñor for Figure 9. GK thanks the Department of Astronomy at the University of Indiana for hosting a visit during which a large portion of this paper was written, and B. Lazotte for guidance and help in the use of computing facilities. GK acknowledges funding from CONACYT Grant 252499 and UNAM/PAPIIT IN103619. We thank Ricardo Covarrubias and Konstantina Boutsia for obtaining the MIKE observations of 2007 and 2019.

APPENDIX

A. HISTORIC OVERVIEW 1955-2016

Hillier et al. (2019) provided a general historical overview of HD 5980. In this section we incorporate

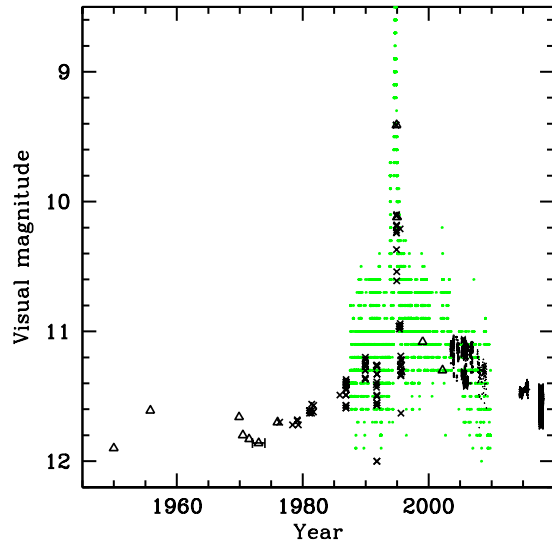


Fig. 22. Same as Figure 20, but here containing all the historic photometric data available. The color figure can be viewed online.

additional information relevant to the problems addressed in this paper.

A.1. Epoch I: <1981

The earliest photometric measurements obtained in the early 20th century were summarized by Breysacher (1997). We reproduce these data in Table 6 and in Figure 22. HD 5980 was first observed photometrically by Gascoigne (1954) and subsequently by Feast et al. (1960) who reported it to be variable. Its eclipses were discovered by Hoffmann et al. (1978) and the correct orbital period of 19.3d determined by Breysacher & Perrier (1980). The photometric light curve described in Breysacher & Perrier (1991) (consisting of 705 Strömgren v filter measurements, obtained in 1979-1981 according to Breysacher (1997)) were analyzed by Perrier et al. (2009), from which the relative continuum emitting radii of *Star A* and *Star B* were deduced, $R_A/a=0.158$ and $R_B/a=0.108$, where a is the semimajor axis. The analysis method took into account the presence of an extended semi-transparent envelope around *Star B*, interpreted to be the WR stellar wind, allowing its extent to be estimated, $R_{env}/a=0.269$. Using the orbital solution of Koenigsberger et al. (2014), who derived $a = 151 R_\odot$, the relative dimensions were found as $R_A/R_\odot = 24$, $R_B/R_\odot = 16$, $R_{env}/R_\odot = 40$.

Koenigsberger et al. (2010) noted the presence of N IV $\lambda 4058$ in addition to the typical WNE He II $\lambda 5411$ lines in the spectra of 1955-1962

TABLE 6

HISTORIC VISUAL MAGNITUDES

Epoch	m_v	Reference
1950	11.66	(a)
1955.8	11.61	Feast et al. (1960)
1964-65	11.75	Smith (1968)
1966	11.66	Butler (1972)
1969.9	11.66	Mendoza (1970)
1970-71	11.80	Osmer (1973)
1971-72	11.83	Ardeberg & Maurice (1977)
1972-74	11.86	Azzopardi & Vigneanu (1975)
1976	11.7	(d) van den Bergh (1976)
1978-79	11.7	(b) Koenigsberger et al. (2010)
1981	11.6	(b) FES Koenigsberger et al. (2010)
1986	11.4	(b) Moffat et al. (1989)
1989-91	11.25	(b) Koenigsberger et al. (2010)
1994.92	9.41	Barbá et al. (1995)
1994.99	10.12	Koenigsberger et al. (1998b)
1995	11.3:	(b) Koenigsberger et al. (2010)
1999.04	11.08	(e) Massey & Duffy (2001)
2002.2	11.3	(f)

^aHarvard plates, Barbá Priv.Comm. 2009.

^bFES magnitudes from IUE.

^cJD 2440543.604, $\phi \approx 0.26$

^dJD 2443053.76 ($\phi \approx 0.55$).

^eOrbital phase unknown.

^fS. Dufau, Private communication, 2009.

that were obtained at the South African Radcliff observatory, but its absence in a few of the spectra between 1962 and 1965. For example, this line appears to be absent in the spectrum 5581 (1962, $\phi=0.19$, Table 11). Walborn (1977) also noted its absence in spectra of 1973 and 1977. These spectra were not published at the time but kindly provided by N. Walborn in the late 1990's and a digitized version¹¹ is shown in Figure 23. These spectra show strong N IV 3483 but no N IV 4058 above the noise level.

Another interesting feature of spectrum number 5581 is that the He II $\lambda 4686$ line is clearly blue-shifted with respect to the other spectra. If this shift is real, it would have been one of the few times that a spectral feature associated with *Star B* was seen.

Barbá et al. (1997) also provided an example of a spectrum obtained in 1980 Feb. 2 in which the N IV $\lambda 4058$ emission line is not evident. In this case, the neighboring H I $\lambda 4100$ line and other lines, in-

¹¹Kindly provided by Orsola De Marco in 1999 who together with Paul Crowther obtained an estimated wavelength calibration.

cluding the N V $\lambda 4603 - 21$ doublet, are significantly weaker. Two days earlier, on 1980 Jan 31, all these lines were strong and sharp, but significantly narrower than on Feb. 2. This latter spectrum was obtained at $\phi \approx 0.8$, when the lines are generally broader.

Feast et al. (1960) noted the very large variations in the full width at half maximum (FWHM) in He II $\lambda 4686$. These were also seen by Westerlund (1978) who remarked on the sharp minima occurring near the eclipses. The FWHM ranged from 1000 km s^{-1} to 2200 km s^{-1} in spectra of the 1950's. In the few Radcliff spectra with good enough S/N at N IV 4058 and in which this line is visible, it behaved similarly. For example, in spectrum 5212 it had $FWHM \approx 500 \text{ km s}^{-1}$ while in 3074 it had $\approx 900 \text{ km s}^{-1}$ (Koenigsberger et al. 2010).

Ultraviolet observations by *IUE* obtained in 1978-1981 displayed the P Cygni profiles in the lines of N V 1240, OV 1370, C IV 1550, He II $\lambda 1640$ and N IV 1718 Å typically seen in WNE star. The N V 1240 and C IV 1550 P Cyg absorptions appeared to have two components with the faster one indicating wind speed $\geq 3000 \text{ km s}^{-1}$ (see Figure 2 in Hillier et al. (2019)). The semi-forbidden line NIV]1486 was either very weak or absent. In the $\approx 1800\text{-}3200 \text{ \AA}$ region, no strong emission features were evident.

A.2. Epoch II: 1981 - 1992

The first determination of radial velocities as a function of orbital phase was published by Breysacher, Moffat & Niemela (1982 henceforth BMN82), based on data acquired in 1981-1983. These determinations were then complemented with data of 1991-1992 (Moffat et al. 1998). Inspection of the RV curve published in the latter paper shows an apparent maximum around orbital phase 0.1 and an apparent minimum around $\phi \approx 0.3\text{-}0.4$. However, the scatter in the data points is too large to say much else.

Niemela (1988) measured the RV variations of the N IV 4058 and N V 4603-21 lines on the same photographic spectra of 1981-1983 discussed in BMN82 and concluded that the NIV line arose mostly from the star which is “behind during primary eclipse”. Based on her Figure 1, primary eclipse is at light curve phase $\phi \approx 0$, and the star she concludes is responsible for the N IV emission is approaching at $\phi \approx 0.2$. This would have been *Star B* in our current naming convention.

BMN82 also measured the radial velocities of upper Balmer absorption lines and found a correlation

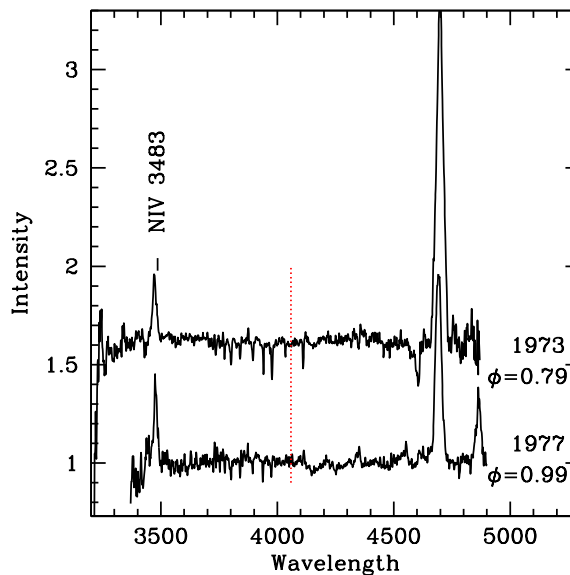


Fig. 23. Spectra obtained by N. Walborn in 1973 and 1977 (unpublished, digitized and calibrated by O. de Marco and P. Crowther). The vertical dotted line indicates the location of the N IV 4058 Å emission line that is notably absent during this epoch. The color figure can be viewed online.

with the upper level of the transition; i.e., optically thicker lines had more negative speeds, and they interpreted this in terms of the lines being formed in an accelerating atmosphere. Given that these lines did not follow the 19.3 d orbit (Niemela 1988), these results must be taken to refer to *Star C*.

Three *IUE* observing campaigns were carried out during this epoch, starting in 1986 with a series of low-resolution spectra covering an orbital cycle (Moffat et al. 1989). These spectra revealed prominent spectral variations that were interpreted in terms of wind eclipses. Specifically, the flux in the NIV 1718 Å emission line and the Fe V-VI pseudo-continuum region become significantly weaker during the phases when *Star B* was in front of *Star A*, compared to the opposite conjunction and to the elongations. The 1989 and 1991 *IUE* campaigns provided a limited number of high resolution spectra over an orbital cycle and showed significantly stronger emission line intensities compared to the spectra that had been obtained in 1979-1981. Particularly relevant was the emergence of strong N IV] 1486 and Fe V/VI emission lines, all of which displayed RV variations consistent with *Star A*'s orbital motion. The P Cyg absorption components were also less extended, suggesting a slower wind speed. A surprising result was that the slower wind speed was also evident during

elongations, which contradicted the notion that the fast ≈ 3000 km/s wind arose in *Star B*. The changes prompted the suggestion that HD 5980 was undergoing an outburst (Koenigsberger et al. 1994).

A.3. *Epoch III: 1993-1995*

During this epoch HD 5980 underwent two sudden outbursts superposed on what appears to be a plateau in the average visual magnitude. Both events were observed by Albert Jones, who had been recording visual magnitudes (henceforth, V_J) since the mid 1980's (Bateson & Jones 1994; Bateson et al. 1994). These data¹² showed a “precursor” outburst lasting approximately 90 days (\approx JD2449290-2449380 1993 to Oct 29-1994 Jan 27), with a peak brightness $V_J \approx 9.2$. The “base level” before and after this first eruption was $V_J \approx 10.5$. Shortly thereafter, V_J jumped from ≈ 10.5 on 1994 May 25 to ≈ 8.2 on 1994 Jul 17 (53 days). The descent started on approximately 1994 Nov 24 and V_J leveled off to ≈ 10.2 by 1995 August 30.

Koenigsberger et al. (1994) had reported unprecedented changes that were observed in HD 5980's UV spectrum between 1981 and 1992, including a visual magnitude brightening, and suggested that it could be a luminous blue variable (LBV). The spectroscopic discovery of the outburst was reported by Barbá et al. (1994) RV curves of N III 4634-40, N IV 4058 and He II $\lambda 5411$ constructed with spectra obtained between 1994 December and 1995 August were consistent with the lines originating in *Star A* (Barbá et al. 1996). They classified the 1994 June 18-19 spectrum as WN7.

Photometric monitoring during 1995 November-December by Sterken & Breysacher (1997) yielded an orbital phase-dependent light curve that differed from the one obtained in 1979-1981 (BP91) in that the primary eclipse minimum was much broader and asymmetrical and the secondary eclipse showed more extended “wings”. In addition, the light curve had a rounded form between the primary and secondary eclipses, and coherent variability on a timescale of 0.25 d was discovered. These “microvariations” were still detected 24 years later in *TESS* observations (Kołaczek-Szymański et al. 2021).

Monitoring of the outburst with *IUE* started in 1994 November, and the changes in spectral properties between this first UV spectrum and the end of the *IUE* operations in late 1995 are fully documented in Koenigsberger (2004) and Georgiev et al. (2011). Here we simply note that the *IUE* spectrum of 1994 November is very similar to that of a B1.5Ia+

star (Koenigsberger et al. 1996) except for the presence of Si IV $\lambda 1400$ P Cyg features which, however, were interpreted to arise in the “fossil” wind that left the system just prior to the outburst. Because this wind was traveling faster than the outburst ejecta, the “fossil” wind would have been unperturbed by the latter. The maximum speed gleaned from the Si IV P Cyg absorption component is ≈ 1700 km/s, similar to that derived from an FUV spectrum obtained by ORFEUS on 1993 September 17 (orbital phase 0.075), just ≈ 42 days prior to the start of the precursor outburst (Koenigsberger et al. 2006). The Si IV P Cyg absorptions are not saturated on the early post-eruption *IUE* spectra and show substructure that could be interpreted as several pulses having occurred prior to the major outburst.

The reported optical spectra of 1994 September 10-13 (Heydari-Malayeri et al. 1997) are similar to that of the well-known LBV star P Cygni (B1Ia) except for the broad He II $\lambda 4686$ emission whose strength increased by 50% over a two day time interval. Hillier et al. (2019) remarked on the puzzling presence of this line in these spectra and also in the 1994 December 30 spectrum published in Koenigsberger et al. (1998b), which in addition showed other WNE-type lines (including N IV $\lambda 4058$). It had been assumed that *Star B* is a H-poor WN star whose wind dominated the spectrum during the late 1970s (Breysacher et al. 1982; Moffat et al. 1998) and that the eruption consisted in a rapid expansion and cooling of the *Star A* outer layers. However, Hillier et al. (2019) noted that according to spectral fits of the *Star A* spectrum, its optically thick wind in 1994 and early 1995 extended out to ≈ 130 -280 R_\odot and would have completely engulfed *Star B*.

The results published by Heydari-Malayeri et al. (1997) include observations of 1993 September 21-23 (a few days after the ORFEUS spectrum mentioned above). These spectra displayed mostly WN6-type lines, although they noted that the relative strength of the N III and He I lines were more typical of WN8.

A.4. *Epoch IV: 1998-2002*

In 1999 HST/STIS observed the system at 5 orbital phases with a sixth phase being obtained in early 2000. A densely spaced set of optical spectra was obtained by FEROS on the ESO 1.5m telescope in 1998-1999 and reported in Schweickhardt et al. (2000) and Kaufer et al. (2002), who analyzed the optical photospheric absorption lines and discovered that the unblended and isolated O III 5592 Å line undergoes RV variations with $P \approx 97$ d and suggesting a highly eccentric $e \approx 0.8$ orbit. This result provided

¹²Kindly provided to us during 2002-2008 by A. Jones.

spectroscopic confirmation of the “third light source” in the eclipse light curve solution of Breysacher & Perrier (1981) and later once again confirmed by Perrier et al. (2009).

Koenigsberger et al. (2002) analyzed the HST/STIS spectra of 1999 and showed that the photospheric lines superposed on the Fe V and Fe VI emissions were stationary on the 19.3 d orbital cycle and that they were similar to those of the O3V(F^*) star MPG 355, thus providing a strong constraint on the nature of the third light source.

Koenigsberger et al. (2002) obtained an RV curve for the Fe VI 1296 Å emission line based on IUE and HST observations showing a maximum around orbital phase 0.15 and a minimum around 0.5, with a peak-to-peak amplitude ≈ 270 km/s, confirming that the Fe-lines that first appeared in the mid-1980s still followed the orbital motion of *Star A*.

FUSE observations obtained in 2002 provided FUV continuum and line profiles at 10 orbital phases (Koenigsberger et al. 2006). Most relevant for our current study is that the FUV flux at $\lambda 1060$ Å in the ORFEUS spectrum that was obtained just prior to the 1993 precursor outburst was very similar to that of the FUSE 2002 spectrum at nearly the same orbital phase. Similarly, the P V 1117 line profiles in both spectra were very similar, except for a small difference in the absorption minimum which in the ORFEUS spectrum reached -1530 km/s and -1760 km/s in the FUSE spectrum. In addition, the line profiles of PV 1117 Å showed wind eclipse effects at orbital phases $\phi=0.92-0.12$, indicative of the dense *Star A* wind. The wind-eclipse model led to the conclusion that *Star A*'s accelerating wind was truncated in the direction of the companion.

A.5. Epoch V: >2003

A second set of FEROS observations was obtained in 2005-2006. The emission line strength had decreased significantly compared to the set obtained in 1998-1999 (Foellmi et al. 2008). Contemporaneous photometric observations provided a full phase coverage of the secondary eclipse minimum, yielding a minimum $m_v \approx 11.4$. The average value outside eclipses $m_v \approx 11.1$ is listed in Table 5.

Koenigsberger et al. (2014) identified two sets of moving emission lines associated with the NV 4944 Å transition. This transition is significantly less optically thick than the other NV lines visible in the spectrum and is formed very close to the base of the stellar wind. Hence, its radial velocity variations were attributed to orbital motion allowing an estimate of the system's masses ($61 \pm 10 M_\odot$, $66 \pm 10 M_\odot$) and orbital separation.

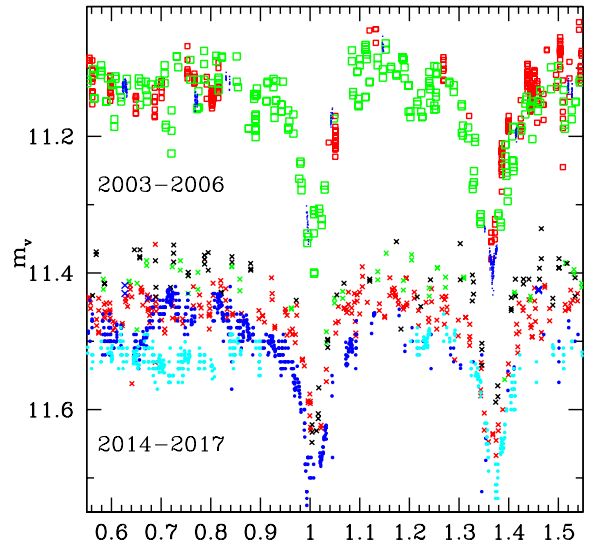


Fig. 24. Photometric light curves for observations obtained in 2003-2006 and in 2014-2017. The abscissa is orbital phase and the ordinate is visual magnitude as determined from the observations with each telescope. No relative shifts have been introduced in this figure. Epochs 2003-2006: SWOPE (red); (Foellmi et al. 2008) (blue), SMARTS (green); Epochs 2014-2017: 2014, ASAS-SN (red), 2015 May, ASAS-SN (green), 2015 July, ASAS-SN (black); 2017 August, ASAS-SN (blue); 2017 Oct, LCOGT (blue dots); 2017 Nov, LCOGT (cyan dots). The color figure can be viewed online.

The more recent data shown in Figure 24 are summarized in Table 5 and consist of ESO Danish photometer data (Foellmi et al. 2008), Swope and SMARTS (Morrell & Massey, unpublished), and ASAS-SN and Las Cumbres Observatory data that were retrieved from the public data bases. Note that the apparent visual magnitudes may not correspond to the same filter system, but they provide a measure of the general brightness at each epoch.

The light curves of this epoch (Figure 24) show a decline by ≈ 0.35 mag between the years 2003-2006 and 2014-2017. A change in the orbital-phase dependence is also notable: Although both epochs show deep eclipses, the “bump” that is present in the earlier epoch around the time of elongation ($\phi \approx 0.6-0.85$) seems to have vanished by 2017.

We quantify the average value of the visual magnitude over the phase intervals 0.6-0.8 and 0.1-0.2 in Table 5, showing that $\langle m_v \rangle$ is systematically brighter in the phase interval $\phi=0.1-0.2$ in the years 2003-2005 while no significant difference is evident in the

remainder of the epochs listed. Perrier et al. (2009) reported a similar post-periastron brightening.

HST/STIS observations were obtained in 2014 and 2016 and analyzed in Hillier et al. (2019). The most outstanding result concerns the line profile of C IV $\lambda 1550$ on the two spectra, obtained at eclipse phases. Although the $\lambda\lambda 1200\text{-}10000$ SED was successfully fit with the CFMGEN model, the observed data showed excess emission shortward of line-center, impossible to account for in the model, in addition to an extent of the P Cyg absorption components far in excess of the wind velocities predicted by the model.

B. LISTS OF OBSERVATIONS

TABLE 7

HIGH DISPERSION LCO SPECTRA

Year	Telescope	Instrument	HJD	Phase
...	-2400000	19.2654d
2006	DuPont	echelle	53920.861	0.626
2007	Clay Mag 2	MIKE	54342.731	0.524
2008	DuPont	echelle	54670.799	0.553
2008	DuPont	echelle	54671.823	0.606
2008	DuPont	echelle	54672.799	0.656
2008	Clay Mag 2	MIKE	54774.800	0.951
2009	Clay Mag 2	MIKE	55161.687	0.033
2010	Clay Mag 2	MIKE	55205.520	0.308
2010	DuPont	echelle	55341.902	0.387
2010	DuPont	echelle	55342.889	0.439
2010	DuPont	echelle	55480.501	0.581
2010	DuPont	echelle	55481.756	0.646
2010	DuPont	echelle	55482.811	0.702
2010	DuPont	echelle	55506.500	0.931
2010	DuPont	echelle	55507.542	0.985
2010	DuPont	echelle	55508.508	0.035
2010	DuPont	echelle	55509.500	0.087
2010	DuPont	echelle	55510.521	0.140
2010	DuPont	echelle	55511.546	0.193
2010	DuPont	echelle	55512.502	0.243
2011	Clay Mag 2	MIKE	55761.866	0.186
2011	DuPont	echelle	55844.530	0.477
2011	DuPont	echelle	55845.564	0.530
2011	DuPont	echelle	55846.620	0.585

TABLE 7 (CONTINUED)
HIGH DISPERSION LCO SPECTRA

Year	Telescope	Instrument	HJD	Phase
...	-2400000	19.2654d
2012	Clay Mag 2	MIKE	56084.887	0.953
2012	DuPont	echelle	56120.766	0.815
2013	DuPont	echelle	56496.804	0.334
2013	DuPont	echelle	56497.804	0.385
2013	DuPont	echelle	56498.833	0.440
2013	DuPont	echelle	56501.750	0.592
2013	DuPont	echelle	56502.754	0.643
2013	DuPont	echelle	56533.737	0.252
2015	DuPont	echelle	57154.896	0.493
2015	DuPont	echelle	57157.896	0.649
2017	DuPont	echelle	57766.535	0.242
2017	DuPont	echelle	57767.523	0.293
2017	Magellan II	MIKE	57775.602	0.712
2017	DuPont	echelle	57815.498	0.783
2017	DuPont	echelle	57816.494	0.835
2017	DuPont	echelle	57817.493	0.887
2017	DuPont	echelle	57933.918	0.930
2017	DuPont	echelle	57934.875	0.980
2017	DuPont	echelle	57935.895	0.033
2017	DuPont	echelle	57936.906	0.085
2017	DuPont	echelle	57980.732	0.360
2017	DuPont	echelle	57981.763	0.413
2017	DuPont	echelle	57983.760	0.517
2017	Magellan II	MIKE	57985.895	0.628
2018	Magellan I	MagE	58119.527	0.564
2018	DuPont	echelle	58166.540	0.005
2018	DuPont	echelle	58167.554	0.057
2018	DuPont	echelle	58168.540	0.109
2018	DuPont	echelle	58408.609	0.569
2018	DuPont	echelle	58409.609	0.621
2018	DuPont	echelle	58410.667	0.676
2018	DuPont	echelle	58482.543	0.407
2018	DuPont	echelle	58483.543	0.459
2019	DuPont	echelle	58484.527	0.510
2020	DuPont	echelle	58864.530	0.235
2020	DuPont	echelle	58865.520	0.286
2020	DuPont	echelle	58866.520	0.338

TABLE 8
SUMMARY LOWER DISPERSION LCO SPECTRA

Telescope	Instrument	Year	HJD -2400000	ϕ_{AB} 19.26d	ϕ_C km/s	V_{Helio}
Baade Mag 1	IMACS	2009	54900.496	0.476	0.495	+7.06
Baade Mag 1	IMACS	2009	54902.494	0.579	0.516	+7.41
DuPont	B&C	2009	55031.832	0.293	0.855	...
DuPont	B&C	2009	55037.833	0.604	0.917	...
DuPont	B&C	2009	55038.833	0.656	0.928	...
Baade Mag 1	IMACS	2009	55072.798	0.419	0.280	-4.78
Clay Mag 2	MagE	2009	55140.702	0.944	0.983	-12.88
Clay Mag 2	MagE	2009	55142.508	0.038	0.001	-12.74
Clay Mag 2	MagE	2009	55143.504	0.089	0.012	-12.74
Clay Mag 2	MagE	2010	55527.770	0.035	0.991	-12.15
Baade Mag 1	MagE	2018	58119.527	0.564	0.832	...
Baade Mag 1	MagE	2018	58436.512	0.018	0.160	-14.3
Baade Mag 1	MagE	2018	58440.526	0.226	0.201	-14.1
Baade Mag 1	MagE	2018	58447.511	0.589	0.274	-13.5
Baade Mag 1	MagE	2018	58448.516	0.641	0.284	-13.4
Baade Mag 1	MagE	2020	59179.512	0.584	0.906	...

TABLE 9
MATRIX OF ORBITAL PHASES PER EPOCH

Oct 1998	1998- 1999	2005	2006- 2009	2010- 2012	2013	2015	2017	2018	2019- 2020
...	0.989	0.982	...	0.985	0.979
...	...	0.992
...	...	0.007	0.005	...
...	0.060	0.021	0.033	0.035	0.033	0.018L	...
...	0.073	0.087	0.085	0.057	...
...	0.097	0.109	...
...	...	0.135	...	0.140
...	0.179	0.163
0.204	0.198	0.193	0.235
0.245	0.252	0.243	0.252	...	0.242	0.226L	...
...	0.268	0.293	...	0.286
...	0.301	0.308	0.334	...	0.360	...	0.338
...	...	0.373	...	0.387	0.385	0.407	...
...	0.405	0.413
...	0.436	0.439	0.440
...	0.459	0.477	0.459	...
...	0.475	0.493	0.517	0.510	...
...	0.527	...	0.524	0.531
...	0.541	0.539
0.569	0.553	0.569	...
...	0.582
...	0.606	0.586	0.591	0.589L	...
...	0.626	0.628	0.621
...	0.656	...	0.647	...	0.643	0.649	...	0.641L	...
...	0.732	0.702	0.712L	0.676	...
...	0.748	0.767
...	...	0.800
0.827	...	0.815	...	0.815	0.783
...	0.838	0.835
...	0.887	0.887
0.935	0.939	0.931	0.930
0.954	...	0.955	0.953

TABLE 10

N λ 4944 MEASUREMENTS

HJD	ϕ	RV ¹	RV ²	RV(NaD) ³
54670.799	0.553	-78.0	-13.0	-140.0
54671.823	0.606	-126.0	161.0	-140.0
54672.799	0.656	-114.0	165.0	-140.0
54774.800	0.951	-124.0	76.0	-124.0
55140.702	0.944	-55.0	73.0	-127.0
55142.508	0.038	-105.0	130.0	-130.0
55143.504	0.089	-173.0	248.0	-125.0
55143.504	0.089	-174.0	244.0	-127.0
55205.520	0.308	-77.0	134.0	-132.0
55341.897	0.380	-116.0	11.0	-145.0
55342.889	0.439	...	-39.0	-148.0
55480.501	0.581	-101.0	201.0	-127.0
55481.756	0.646	-126.0	206.0	-126.0
55482.811	0.702	-153.0	208.0	-125.0
55506.500	0.931	-73.0	144.0	-125.0
55507.542	0.985	...	41.0	-125.0
55508.508	0.035	13.0	211.0	-125.0
55509.500	0.087	-186.0	245.0	-125.0
55510.521	0.140	-212.0	274.0	-125.0
55511.546	0.193	-216.0	244.0	-125.0
55512.502	0.243	-162.0	230.0	-125.0
55527.770	0.035	-44.0	148.0	-130.0
55761.841	0.185	-178.0	185.0	-142.0
55761.856	0.186	-215.0	214.0	-143.0
55761.874	0.187	-216.0	208.0	-142.0
55761.893	0.191	-206.0	232.0	-142.0
55844.530	0.477	-132.0	42.0	-126.0
55845.564	0.530	-85.0	68.0	-126.0
55846.620	0.585	-113.0	127.0	-126.0
56084.887	0.953	-182.0	-32.0	-147.0
56120.744	0.814	-185.0	150.0	-141.0
56120.765	0.815	-200.0	154.0	-141.0
56120.790	0.817	-195.0	178.0	-141.0
56496.804	0.334	-31.0	127.0	-140.0
56497.804	0.385	-12.0	32.0	-140.0
56498.833	0.440	18.0	41.0	-139.0
56501.750	0.592	-51.0	...	-139.0
56502.754	0.643	-116.0	...	-139.0
56533.737	0.252	-140.0	234.0	-130.0
57154.896	0.493	-100.0	50.0	-149.0
57157.896	0.649	-151.0	...	-150.0
57766.535	0.242	-115.0	229.0	-133.0
57815.498	0.783	-199.0	77.0	-138.0
57817.493	0.873	-102.0	187.0	-138.0
57933.918	0.930	-105.0	150.0	-150.0
57934.875	0.980	...	-23.0	-148.0
57935.893	0.033	-69.0	190.0	-151.0
57936.908	0.085	-180.0	232.0	-158.0
57934.875	0.980	...	-23.0	-148.0
57981.763	0.413	-43.0	52.0	-134.0

TABLE 10 (CONTINUED)

N λ 4944 MEASUREMENTS

HJD	ϕ	RV ¹	RV ²	RV(NaD) ³
57935.893	0.033	-69.0	190.0	-151.0
57936.908	0.085	-180.0	232.0	-158.0
57981.763	0.413	-43.0	52.0	-134.0
57983.760	0.517	-48.0	-6.0	-135.0
57985.895	0.628	-141.0	155.0	-132.0
58166.540	0.005	...	1.0	-138.0
58167.554	0.057	-21.0	226.0	-138.0
58168.540	0.109	-182.0	213.0	-139.0
58408.609	0.569	-157.0	171.0	-124.0
58409.609	0.621	-154.0	220.0	-124.0
58410.667	0.676	-141.0	218.0	-124.0
58440.526	0.226	-142.0	194.0	-124.0
58447.511	0.589	-32.0	176.0	-122.0
58448.516	0.641	-77.0	188.0	-127.0
58482.543	0.407	...	40.0	-128.0
58483.543	0.459	-163.0	35.0	-128.0
58484.527	0.510	-66.0	56.0	-129.0
58864.530	0.235	-151.0	224.0	-133.0
58865.520	0.286	-97.0	184.0	-133.0
58866.520	0.338	24.0	155.0	-134.0
58864.530	0.235	-162.0	213.0	-133.0
58865.520	0.286	-102.0	164.0	-133.0
58866.520	0.338	9.0	176.0	-134.0
55844.530	0.477	-132.0	42.0	-126.0
55845.564	0.530	-85.0	68.0	-126.0
55846.620	0.585	-113.0	127.0	-126.0
56084.887	0.953	-182.0	-32.0	-147.0
56120.744	0.814	-185.0	150.0	-141.0
56120.765	0.815	-200.0	154.0	-141.0
56120.790	0.817	-195.0	178.0	-141.0
56496.804	0.334	-31.0	127.0	-140.0
56497.804	0.385	-12.0	32.0	-140.0
56498.833	0.440	18.0	41.0	-139.0
56501.750	0.592	-51.0	...	-139.0
56502.754	0.643	-116.0	...	-139.0
56533.737	0.252	-140.0	234.0	-130.0
57154.896	0.493	-100.0	50.0	-149.0
57157.896	0.649	-151.0	...	-150.0
57766.535	0.242	-115.0	229.0	-133.0
57815.498	0.783	-199.0	77.0	-138.0
57817.493	0.873	-102.0	187.0	-138.0
57933.918	0.930	-105.0	150.0	-150.0
57934.875	0.980	...	-23.0	-148.0
57935.893	0.033	-69.0	190.0	-151.0
57936.908	0.085	-180.0	232.0	-158.0
57981.763	0.413	-43.0	52.0	-134.0

TABLE 10 (CONTINUED)
N λ 4944 MEASUREMENTS

HJD	ϕ	RV ¹	RV ²	RV(NaD) ³
57983.760	0.517	-48.0	-6.0	-135.0
57985.895	0.628	-141.0	155.0	-132.0
58167.554	0.057	-21.0	226.0	-138.0
58168.540	0.109	-182.0	213.0	-139.0
58408.609	0.569	-157.0	171.0	-124.0
58409.609	0.621	-154.0	220.0	-124.0
58410.667	0.676	-141.0	218.0	-124.0
58440.526	0.226	-142.0	194.0	-124.0
58447.511	0.589	-32.0	176.0	-122.0
58448.516	0.641	-77.0	188.0	-127.0
58482.543	0.407	...	40.0	-128.0
58483.543	0.459	-163.0	35.0	-128.0
58484.527	0.510	-66.0	56.0	-129.0
58864.530	0.235	-151.0	224.0	-133.0
58865.520	0.286	-97.0	184.0	-133.0

TABLE 10 (CONTINUED)
N λ 4944 MEASUREMENTS

HJD	ϕ	RV ¹	RV ²	RV(NaD) ³
58866.520	0.338	24.0	155.0	-134.0
58864.530	0.235	-162.0	213.0	-133.0
58865.520	0.286	-102.0	164.0	-133.0
58866.520	0.338	9.0	176.0	-134.0

Laboratory wavelength used to measure the RVs: N λ 4944.37, and Na λ 5889.9509

¹Radial velocity of the de-blended component on the left, in units of km s^{-1} , as measured in the observed spectrum and corrected for the SMC velocity. Heliocentric velocity and zero-point shifts in the data by using the NaD measurement listed in Column 5.

²Same as in Column 3 but for the de-blended component on the right.

³In units of km s^{-1} . This is the centroid of the SMC component of NaD as measured on the observed spectrum.

TABLE 11
 COMPENDIUM HE II $\lambda 4686$ AND $H\beta$ +HE II MEASUREMENTS

Num	Year	HJD	ϕ	RV ¹	FWHM ¹	EW ²	RV ¹	FWHM ¹	EW ²	Notes
...	...	-2400000	...	HeII 4686			H β +He II			...
2597	1955	35333.3	0.81	200.	2290.	35.0	128.	1754.	7.7	R
2645	1955	35388.3	0.66	110.	1802.	98.0	16.	1422.	8.7	R
3074	1956	35742.3	0.04	294.	1013.	96.0	396.	973.	11.7	R
3793	1957	116.	2070.	73.0	265.	1625.	14.0	R
3872	1958	443.	1217.	79.0	283.	1000.	9.8	R
3882	1958	258.	1900.	63.0	258.	1000.	8.3	R
4613	1959	36916.3	0.98	181.	1740.	69.0	117.	1740.	18.0	R
4963	1960	174.	1431.	83.0	74.	1227.	10.7	R
5182	1961	37542.3	0.47	-99.	1095.	107.0	104.	1300.	13.5	R
5212	1961	37572.3	0.03	105.	982.	80.0	280.	1000.	15.3	R
5543	1962	429.	1973.	54.0	482.	2115.	12.2	R
5571	1962	388.	1176.	74.0	392.	1249.	14.4	R
5581	1962	37922.3	0.19	-220.	2062.	67.0	-124.	2134.	12.7	R
5586	1962	37925.3	0.35	210.	1517.	68.0	143.	2000.	14.0	R
5594	1962	...	0.60	199.	1511.	71.0	110.	1315.	13.9	R
5601	1962	37933.3	0.77	189.	1858.	69.0	133.	1731.	18.1	R
5602	1962	37946.3	0.44	18.	1300.	77.0	32.	1201.	14.8	R
5603	1962	37954.3	0.86	1730.	1880.	82.0	1410.	2170.	13.2	R
5605	1962	...	0.98	89.	1754.	72.0	230.	1494.	17.5	R
5611	1962	37959.3	0.12	225.	1831.	73.0	363.	1690.	12.4	R
6078	1963	13.	1713.	67.0	6.	1455.	11.6	R
7127	1965	200.	2200.	52.0	282.	2390.	11.0	R
...	1973	...	0.79	330::	2300	69	...	W
...	1977	...	0.99	398::	1927	178::	1541	31	8.8	W
...	1975	42684.6	0.39	34.3	4.5	BW
...	1976	42973.6	0.39	26.5	2.2	BW
...	1976	43083.6	0.10	44.0	5.7	BW
...	1976	43084.6	0.15	44.5	6.2	BW
...	1977	43194.6	0.86	43.6	7.3	BW
...	81-84	82.0	PM
...	1989	47784.4	0.11	67.0	H-M
...	1991	48618.4	0.39	87.0	H-M
...	1993	49259.5	0.36	78.0	11.8	H-M
...	1994	49605.5	0.73	1.4	18.5	H-M
...	1994	49716.8	0.39	156	1400.	81.0	275	900.	41.5	K98
3571	1998	51094.8	0.94	178.	1527.	76.0	243.	1343.	14.3	F
6981	1998	51100.8	0.24	334.	1485.	78.0	322.	1212.	14.1	F
8851	1998	51133.7	0.95	175.	1477.	66.0	146.	1207.	15.6	F
11811	1998	51138.5	0.20	316.	1537.	66.0	291.	1167.	14.9	F
14981	1998	51145.5	0.57	219.	1251.	88.0	152.	1014.	16.4	F
17081	1998	51150.5	0.83	205.	1605.	72.0	151.	1368.	16.1	F
23711	1998	51174.5	0.07	289.	1066.	71.0	252.	920.	15.0	F
24471	1998	51176.5	0.18	309.	1500.	72.0	282.	1197.	14.5	F
25781	1999	51181.5	0.44	154.	927.	67.0	126.	733.	13.0	F
26441	1999	51183.5	0.54	218.	1143.	83.0	154.	909.	16.4	F
27241	1999	51185.5	0.65	239.	1360.	92.0	168.	1158.	17.7	F

TABLE 11 (CONTINUED)
 COMPENDIUM He II λ 4686 AND H β +He II MEASUREMENTS

Num	Year	HJD	ϕ	RV ¹	FWHM ¹	EW ²	RV ¹	FWHM ¹	EW ²	Notes
...	...	-2400000	...	HeII 4686			H β +He II			...
27941	1999	51187.5	0.75	225.	1565.	86.0	151.	1286.	17.7	F
28681	1999	51189.5	0.85	190.	1617.	68.0	166.	1340.	11.7	F
29441	1999	51191.5	0.95	204.	1564.	64.0	167.	1211.	11.3	F
30311	1999	51193.5	0.06	265.	988.	74.0	229.	851.	15.5	F
31461	1999	51197.5	0.27	315.	1463.	73.0	269.	1021.	15.2	F
1020	1999	51305.3	0.83	367.	1680.	101.0	300.	1500.	25.4	HST
3020	1999	51308.9	0.05	430.	1200.	94.0	390.	1080.	19.0	HST
4020	1999	51310.8	0.15	440.	1560.	103.0	424.	1440.	24.0	HST
5020	1999	51314.9	0.36	357.	1290.	120.0	258.	1135.	20.0	HST
6020	1999	51315.8	0.40	358.	1140.	105.0	296.	1055.	18.0	HST
79411	1999	51375.9	0.53	201.	1173.	102.0	152.	1012.	17.7	F
80871	1999	51379.9	0.73	216.	1554.	111.0	152.	1356.	18.1	F
82121	1999	51381.9	0.84	222.	1552.	96.0	161.	1393.	19.0	F
83811	1999	51383.9	0.94	221.	1497.	93.0	188.	1334.	17.6	F
84511	1999	51384.8	0.99	214.	1382.	105.0	188.	1179.	19.5	F
85181	1999	51385.8	0.04	278.	1080.	91.0	261.	865.	17.0	F
85771	1999	51386.9	0.10	306.	1167.	90.0	299.	1090.	17.8	F
86321	1999	51388.8	0.20	322.	1490.	92.0	341.	1314.	16.7	F
86701	1999	51389.9	0.25	323.	1487.	91.0	338.	1168.	14.9	F
87751	1999	51391.8	0.35	168.	1281.	119.0	136.	1052.	19.6	F
88931	1999	51392.8	0.40	151.	1012.	95.0	105.	953.	18.1	F
90131	1999	51394.9	0.51	180.	1100.	102.0	139.	997.	17.6	F
...	2000	51830.5	0.20	85.0	MD01
o2020	2000	51655.1	0.01	385.	1320.	94.0	342.	1074.	18.0	HST
617801	2005	53538.9	0.80	217.	1952.	98.0	170.	1792.	17.2	F
620221	2005	53541.9	0.96	251.	1855.	84.0	244.	1590.	13.4	F
710740	2005	53561.9	0.99	239.	1541.	94.0	231.	1215.	15.8	F
725630	2005	53576.8	0.77	269.	1996.	96.0	221.	1803.	15.8	F
925220	2005	53638.7	0.98	235.	1675.	84.0	226.	1346.	13.6	F
928161	2005	53641.7	0.13	340.	1897.	86.0	347.	1716.	14.4	F
1022731	2005	53665.5	0.37	136.	1174.	103.0	95.	1150.	16.7	F
f12	2006	53715.8	0.98	236.	1661.	84.0	224.	1331.	13.7	F
f34	2006	53716.5	0.02	255.	1187.	92.0	214.	928.	14.8	F
f56	2006	53731.5	0.80	218.	1966.	90.0	176.	1858.	15.0	F
f8	2006	53734.6	0.96	245.	1902.	73.0	266.	1561.	13.2	F
f9	2006	53735.5	0.01	243.	1401.	93.0	216.	1160.	16.9	F
f1112	2006	53738.5	0.16	334.	1994.	82.0	298.	1738.	13.0	F
phi476L	2009	54900.4	0.48	135	1442	68	109	1367	10.1	LCO
phi579L	2009	54902.5	0.58	178	1693	71	159	1641	11.3	LCO
phi293L	2009	55031.8	0.29	276	1741	64	247	1601	10.0	LCO
phi604L	2009	55037.8	0.60	257	1784	73	213	1718	11.1	LCO
phi656L	2009	55038.8	0.66	311	1908	73	302	1898	11.8	LCO
phi419L	2009	55072.8	0.42	122.	1237.	58.0	151.	1320.	8.7	LCO
phi944L	2009	55140.7	0.94	273	2011	72	271	1794	11.8	LCO
phi038L	2009	55142.5	0.38	326	1067	61	314	1027	10.6	LCO

TABLE 11 (CONTINUED)
 COMPENDIUM He II $\lambda 4686$ AND H β +He II MEASUREMENTS

Num	Year	HJD	ϕ	RV ¹	FWHM ¹	EW ²	RV ¹	FWHM ¹	EW ²	Notes
...	...	-2400000	...	HeII 4686			H β +He II			...
phi089L	2009	55143.5	0.89	333	1684	63	360	1450	10.5	LCO
phi035L	2010	55527.8	0.04	318	1132	55	317	904	8.0	LCO
o9020	2014	56741	0.0	391	1462	67	356	1239	21.0	HST
phi0.49	2015	57154.9	0.49	97	1371	59	113	1260	10.1	LCO
phi0.65	2015	57157.9	0.65	183	1712	79	106	1507	9.9	LCO
o1140	2016	57653	0.36	259	1415	68	140	1359	23.0	HST
phi564L	2018	58119.5	0.56	182	1434	75	137	1233	12.4	LCO
phi018L	2018	58436.5	0.02	317	1354	76	323	988	12.9	LCO
phi226L	2018	58440.5	0.23	470	1781	62	431	1410	10.5	LCO
phi589L	2018	58447.5	0.59	211	1576	68	136	1391	10.8	LCO
phi641L	2018	58448.5	0.64	228	1658	72	126	1484	10.7	LCO
phi584L	2020	59179.5	0.58	225	1632	69	156	1545	10.5	LCO

Notes: R=Radcliff; BW=Breysacher & West-erlund (1978); H-M=Heydari-Malayeri et al. (1997); K98=Koenigsberger et al. (1998b); F=FEROS; HST=Hubble Space Telescope; MD01= Massey & Duffy (2001); LCO=Las Campanas Observatory; Laboratory wavelength used to measure the radial velocities: $\lambda 4685.70$ and $\lambda 4861.32$ from the CMFGEN model spectrum.

¹In units of km s⁻¹, not corrected for SMC motion.

²In units of Å.

³The density-to-intensity calibration of this spectrum is uncertain.

TABLE 12
 N IV $\lambda 3483$ AND $\lambda 4058$

Num	Year	HJD	ϕ	RV ¹	FWHM ¹	EW ²	RV ¹	FWHM ¹	EW ²	Notes
...	...	-2400000	...	N IV $\lambda 3483$			N IV $\lambda 4058$...
...	1994	49716.8	0.39	bl	bl	1.6	-20	702	0.50	New
3571	1998	51094.8	0.94	3	672	4.1	F
6981	1998	51100.8	0.24	193	505	3.7	F
8851	1998	51133.7	0.95	61	752	4.2	F
11811	1998	51138.5	0.20	231	840	4.8	F
14981	1998	51145.5	0.57	17	744	4.4	F
17081	1998	51150.5	0.83	-22	775	3.9	F
23711	1998	51174.5	0.07	219	786	4.1	F
24471	1998	51176.5	0.18	224	839	4.2	F
25781	1999	51181.5	0.44	60	573	2.4	F
26441	1999	51183.5	0.54	35	639	3.3	F
27241	1999	51185.5	0.65	26	770	3.8	F
27941	1999	51187.5	0.75	281	800	4.1	F
28681	1999	51189.5	0.85	-53	624	2.9:	F
29441	1999	51191.5	0.95	33	578	3.0	F
30311	1999	51193.5	0.06	194	712	5.1	F
31461	1999	51197.5	0.27	142	773	4.3	F
1020	1999	51305.3	0.83	364	1136	5.2	142	1001	4.6	HST
3020	1999	51308.9	0.05	513	1081	3.0	322	926	4.8	HST
4020	1999	51310.8	0.15	422	1300	6.1	378	900	4.0	HST
5020	1999	51314.9	0.36	247	1181	4.9	231	985	4.5	HST

TABLE 12 (CONTINUED)
N IV λ 3483 AND λ 4058

Num	Year	HJD	ϕ	RV ¹	FWHM ¹	EW ²	RV ¹	FWHM ¹	EW ²	Notes
...	...	-2400000	...	N IV λ 3483			N IV λ 4058			...
f8	2006	53734.6	0.96	74	870	3.5	F
f910	2006	53735.5	0.01	145	838	3.1	F
f1112	2006	53738.5	0.16	227	856	2.7	F
phi476L	2009	54900.4	0.48	69	836	1.9	LCO
phi579L	2009	54902.5	0.58	61	966	2.3	LCO
phi293L	2009	55031.8	0.29	151	987	2.2	LCO
phi604L	2009	55037.8	0.60	95	850	2.0	LCO
phi656L	2009	55038.8	0.66	112	952	1.9	LCO
phi419L	2009	55072.8	0.42	124	613	1.7	LCO
phi944L	2009	55140.7	0.94	14	1004	6.1	47	770	2.0	LCO
phi038L	2009	55142.5	0.38	146	1205	6.2	192	896	2.4	LCO
phi089L	2009	55143.5	0.89	161	1163	5.8	236	906	2.4	LCO
phi035L	2010	55527.8	0.04	70	1013	4.2	249	882	1.6	LCO
o9020	2014	56741	0.0	349	1243	5.5	142	941	2.6	HST
phi0.49	2015	57154.9	0.49	22	749	2.0	LCO
phi0.65	2015	57157.9	0.65	-23	825	2.2	LCO
o1140	2016	57653	0.36	236	1273	5.0	144	753	1.9	HST
phi564L	2018	58119.5	0.56	199	1109	4.6:	-21	800	2.8	LCO
phi018L	2018	58436.5	0.02	185	1040	7.8	229	932	3.2	LCO
phi226L	2018	58440.5	0.23	326	997	4.8	257	680	2.5	LCO
phi589L	2018	58447.5	0.59	141	1039	4.6:	35	698	2.4	LCO
phi641L	2018	58448.5	0.64	117	991	4.8	19	711	2.4	LCO
phi584L	2020	59179.5	0.58	90	1117	5.8	59	851	2.0	LCO
f8	2006	53734.6	0.96	74	870	3.5	F
f910	2006	53735.5	0.01	145	838	3.1	F
f1112	2006	53738.5	0.16	227	856	2.7	F
phi476L	2009	54900.4	0.48	69	836	1.9	LCO
phi579L	2009	54902.5	0.58	61	966	2.3	LCO
phi293L	2009	55031.8	0.29	151	987	2.2	LCO
phi604L	2009	55037.8	0.60	95	850	2.0	LCO
phi656L	2009	55038.8	0.66	112	952	1.9	LCO
phi419L	2009	55072.8	0.42	124	613	1.7	LCO
phi944L	2009	55140.7	0.94	14	1004	6.1	47	770	2.0	LCO
phi038L	2009	55142.5	0.38	146	1205	6.2	192	896	2.4	LCO
phi089L	2009	55143.5	0.89	161	1163	5.8	236	906	2.4	LCO
phi035L	2010	55527.8	0.04	70	1013	4.2	249	882	1.6	LCO
o9020	2014	56741	0.0	349	1243	5.5	142	941	2.6	HST
phi0.49	2015	57154.9	0.49	22	749	2.0	LCO
phi0.65	2015	57157.9	0.65	-23	825	2.2	LCO
o1140	2016	57653	0.36	236	1273	5.0	144	753	1.9	HST
phi564L	2018	58119.5	0.56	199	1109	4.6:	-21	800	2.8	LCO
phi018L	2018	58436.5	0.02	185	1040	7.8	229	932	3.2	LCO
phi226L	2018	58440.5	0.23	326	997	4.8	257	680	2.5	LCO
phi589L	2018	58447.5	0.59	141	1039	4.6:	35	698	2.4	LCO
phi641L	2018	58448.5	0.64	117	991	4.8	19	711	2.4	LCO
phi584L	2020	59179.5	0.58	90	1117	5.8	59	851	2.0	LCO

Notes: Same as in Table 11.

N IV reference wavelengths are (3478.7+3483.00+3484.93)/3.= λ 3482.21 and λ 4057.76.

¹In units of km s⁻¹, not corrected for SMC motion.

²In units of Å.

C. POSSIBLE *Star B* SPECTRUM

In an attempt to extract the *Star B* spectrum, we use the HST/STIS observation obtained in 1999. We shift the $\phi=0.83$ and 0.15 spectra in velocity to the *Star A* reference frame (add 180 km/s and subtract 236 km/s, respectively). Then under the assumption that *Star B* is mostly hidden from view at $\phi=0.0$, we subtract this eclipse spectrum from the shifted ones. Finally, we shift both residuals in velocity to the rest frame of *Star B*. This is accomplished once again using the RV curve of Koenigsberger et al. (2014). The shifts are, respectively, $+320$ km/s ($\phi=0.83$) and -490 km/s ($\phi=0.15$). The result is shown in Figure 25 which suggests that *Star B* emits a relatively narrow (FWHM ~ 600 km/s) line at He II $\lambda 1640$, with no obvious P Cyg absorption. Both N V $\lambda 1240$ and C IV $\lambda 1550$ show similarly narrow emission but in this case include an extended P Cyg absorption component extending to -2200 km/s. In the visual range, the He II $\lambda 4686$ line appears as a relatively weak emission with FWHM ~ 2300 km/s, as well as many of the other transitions with varying intensities and widths.

The residual spectrum, assumed to correspond to *Star B*, is not the same at both elongations. This is not unexpected given that the emission line profiles differ somewhat between these two phases, as shown in Figure 16. The average continuum flux between 1575 - 1600 Å is 6.32×10^{-13} ($\phi=0.83$) and 7.91×10^{-13} ($\phi=0.15$) erg/cm²s in the *Star B* spectrum alone. However, we have already established that the continuum brightness in general is larger around periastron. Because only one *Star A* spectrum was used to obtain the residuals, it is impossible to determine which of the two stars is responsible for the periastron brightening. (The average continuum flux for A+B+C in the $\phi=0.83$ and the $\phi=0.15$ spectra is, respectively, 3.04×10^{-12} , 3.20×10^{-12}).

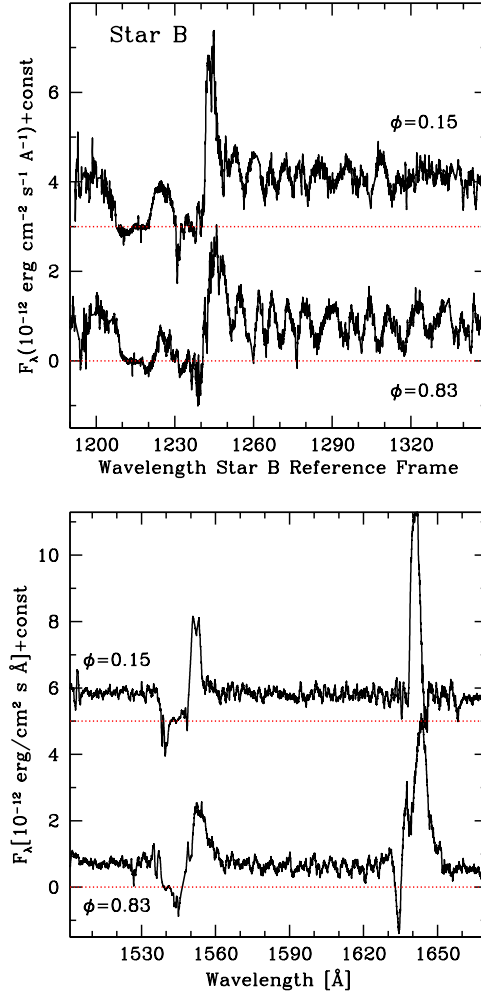


Fig. 25. Difference between the HST/STIS spectrum obtained at elongations in 1999 and the spectrum obtained during primary eclipse ($\phi=0$) in 2000. The spectrum at $\phi=0.15$ is shifted vertically by $5. \times 10^{-12}$ ergs/(s Å). The horizontal dash line indicates the zero flux level. The color figure can be viewed online.

D. EXAMPLE OF THE ECHELLE ORDERS THAT WERE USED TO NORMALIZE ORDER 35

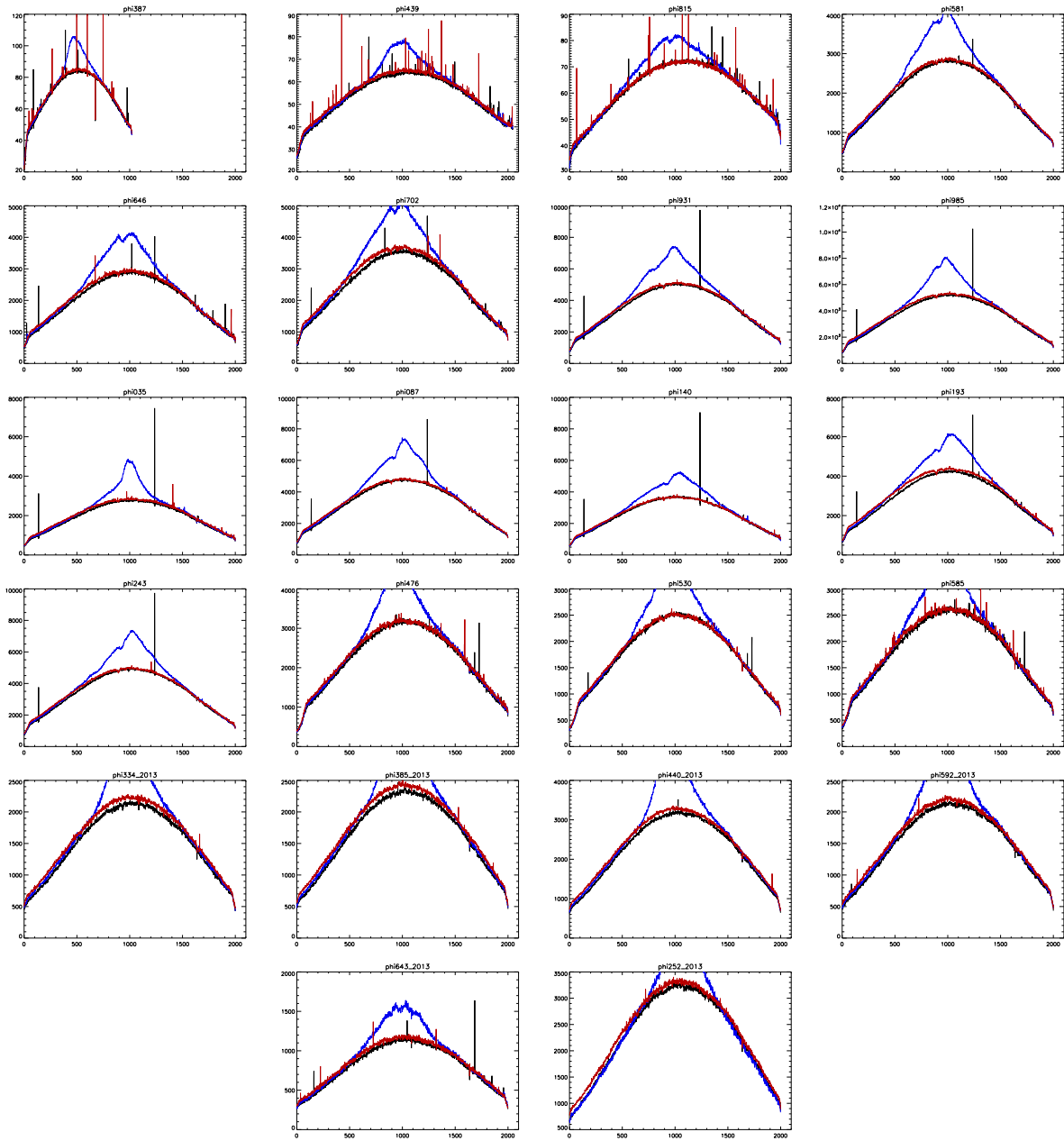


Fig. 26. Echelle orders 34, 36 (red) and 35 (blue), the latter containing the He II $\lambda 5411$ line. The abscissa shows pixel number on the echelle image. The ordinate shows counts. The normalized profiles were constructed by dividing the counts of order35 by the average counts $(\text{order34} + \text{order36})/2$, after which the spectrum was cleaned of cosmic rays. Each panel is labeled by the orbital phase (2010-2012) and the spectra of 2013 are so labeled. The color figure can be viewed online.

REFERENCES

- Ardeberg, A. & Maurice, E. 1977, *A&AS*, 30, 261
- Auer, L. H. & Koenigsberger, G. 1994, *ApJ*, 436, 859, <https://doi.org/10.1086/174963>
- Azzopardi, M. & Vigneanu, J. 1975, *A&AS*, 19, 271
- Barbá, R. H., Morrell, N. I., Niemela, V. S., et al. 1996, *RMxAC*, 5, 85
- Bateson, F. M., Gilmore, A., & Jones, A. F. 1994, *IAUC*, 6102, 3
- Bateson, F. M. & Jones, A. F. 1994, *PVSS*, 19, 50
- Breysacher, J. 1997, *ASPC* 120, *Luminous Blue Variables: Massive Stars in Transition*, ed. A. Nota & H. Lamers, 227
- Breysacher, J. & François, P. 2000, *A&A*, 361, 231
- Breysacher, J., Moffat, A. F. J., & Niemela, V. S. 1982, *ApJ*, 257, 116, <https://doi.org/10.1086/159969>
- Breysacher, J. & Perrier, C. 1980, *A&A*, 90, 207
- . 1991, *IAUS* 143, *Wolf-Rayet Stars and Interrelations with Other Massive Stars in Galaxies*, ed. K. van der Hucht & B. Hidayat (Dordrecht, Kluwer Academic Publisher), 229
- Breysacher, J. & Westerlund, B. E. 1978, *A&A*, 67, 261
- Brott, I., Evans, C. J., Hunter, I., et al. 2011, *A&A*, 530, 116, <https://doi.org/10.1051/0004-6361/201016114>
- Butler, C. J. 1972, *DunOP*, 1, 133
- Cantó, J., Raga, A. C., & Wilkin, F. P. 1996, *ApJ*, 469, 729, <https://doi.org/10.1086/177820>
- Corcoran, M. F. 2003, *IAUS* 212, *A Massive Star Odyssey: From Main Sequence to Supernova*, ed. K. van der Hucht, A. Herrero & E. Céspedes (San Francisco, CA: ASP), 130
- Ekström, S., Georgy, C., Eggenberger, P., et al. 2012, *A&A*, 537, 146, <https://doi.org/10.1051/0004-6361/201117751>
- Feast, M. W., Thackeray, A. D., & Wesselink, A. J. 1960, *MNRAS*, 121, 337, <https://doi.org/10.1093/mnras/121.4.337>
- Foellmi, C., Koenigsberger, G., Georgiev, L., et al. 2008, *RMxAA*, 44, 3
- Foellmi, C., Moffat, A. F. J., & Guerrero, M. A. 2003, *MNRAS*, 338, 360, <https://doi.org/10.1093/j.1365-8711.2003.06052.x>
- Gayley, K. G. 2009, *ApJ*, 703, 89, <https://doi.org/10.1088/0004-637x/703/1/89>
- Gayley, K. G., Owocki, S. P., & Cranmer, S. R. 1997, *ApJ*, 475, 786, <https://doi.org/10.1086/303573>
- Georgiev, L., Koenigsberger, G., Hillier, D. J., et al. 2011, *AJ*, 142, 191, <https://doi.org/10.1088/0004-6256/142/6/191>
- Heger, A., Langer, N., & Woosley, S. E. 2000, *ApJ*, 528, 368, <https://doi.org/10.1086/308158>
- Heydari-Malayeri, M., Rauw, G., Esslinger, O., & Beuzit, J.-L. 1997, *A&A*, 322, 554
- Hill, G. M. 2020, *Stellar Magnetism: A Workshop in Honour of the Career and Contributions of John D. Landstreet*, ed. G. Wade, E. Alecian, D. Bohlender, & A. Sigut, 11, 164
- Hill, G. M., Moffat, A. F. J., & St-Louis, N. 2018, *MNRAS*, 474, 2987, <https://doi.org/10.1093/mnras/stx2943>
- Hill, G. M., Moffat, A. F. J., St-Louis, N., & Bartzakos, P. 2000, *MNRAS*, 318, 402, <https://doi.org/10.1046/j.1365-8711.2000.03705.x>
- Hillier, D. J., Koenigsberger, G., Nazé, Y., et al. 2019, *MNRAS*, 486, 725, <https://doi.org/10.1093/mnras/stz808>
- Hillier, D. J. & Lanz, T. 2001, *ASPC* 247, *Spectroscopic Challenges of Photoionized Plasmas*, ed. G. Ferland & D. W. Savin (San Francisco, CA: ASPC), 343
- Hillier, D. J. & Miller, D. L. 1998, *ApJ*, 496, 407, <https://doi.org/10.1086/305350>
- Hubeny, I. & Lanz, T. 1995, *ApJ*, 439, 875, <https://doi.org/10.1086/175226>
- Kashi, A. 2020, *MNRAS*, 492, 5261, <https://doi.org/10.1093/mnras/staa203>
- Kaufer, A., Schmid, H. M., Schweickhardt, J., & Tubbesing, S. 2002, *ASPC* 260, *Interacting Winds from Massive Stars*, ed. A. F. J. Moffat & N. St-Louis (San Francisco, CA: ASPC), 489
- Koenigsberger, G. 2004, *RMxAA*, 40, 107
- Koenigsberger, G. & Auer, L. H. 1985, *ApJ*, 297, 255, <https://doi.org/10.1086/163523>
- Koenigsberger, G., Auer, L. H., Georgiev, L., & Guinan, E. 1998a, *ApJ*, 496, 934, <https://doi.org/10.1086/305398>
- Koenigsberger, G., Peña, M., Schmutz, W., & Ayala, S. 1998b, *ApJ*, 499, 889, <https://doi.org/10.1086/305659>
- Koenigsberger, G., Fullerton, A. W., Massa, D., & Auer, L. H. 2006, *AJ*, 132, 1527, <https://doi.org/10.1086/506956>
- Koenigsberger, G., Georgiev, L., Barbá, R., et al. 2000, *ApJ*, 542, 428, <https://doi.org/10.1086/305529>
- Koenigsberger, G., Georgiev, L., Hillier, D. J., et al. 2010, *AJ*, 139, 2600, <https://doi.org/10.1088/0004-6256/139/6/2600>
- Koenigsberger, G., Guinan, E., Auer, L., & Georgiev, L. 1995, *ApJ*, 452, 107, <https://doi.org/10.1086/309719>
- Koenigsberger, G., Kurucz, R. L., & Georgiev, L. 2002, *ApJ*, 581, 598, <https://doi.org/10.1086/344215>
- Koenigsberger, G., Moffat, A. F. J., St-Louis, N., et al. 1994, *ApJ*, 436, 301, <https://doi.org/10.1086/174905>
- Koenigsberger, G., Morrell, N., Hillier, D. J., et al. 2014, *AJ*, 148, 62, <https://doi.org/10.1088/0004-6256/148/4/62>
- Koenigsberger, G. & Schmutz, W. 2020, *A&A*, 639, 18, <https://doi.org/10.1051/0004-6361/201937305>
- Koenigsberger, G., Shore, S., Guinan, E., & Auer, L. 1996, *RMxAC*, 5, 92
- Kołaczek-Szymański, P. A., Pigulski, A., Michalska, G., Moździerski, D., & Różański, T. 2021, *A&A*, 647, 12, <https://doi.org/10.1051/0004-6361/202039553>

- Lamberts, A., Dubus, G., Lesur, G., & Fromang, S. 2012, *A&A*, 546, 60, <https://doi.org/10.1051/0004-6361/201219006>
- Luehrs, S. 1997, *PASP*, 109, 504
- Maeder, A. & Meynet, G. 2000, *ARA&A*, 38, 143, <https://doi.org/10.1146/annurev.astro.38.1.143>
- Marchenko, S. V., Moffat, A. F. J., & Koenigsberger, G. 1994, *ApJ*, 422, 810, <https://doi.org/10.1086/173773>
- Massey, P. & Duffy, A. S. 2001, *ApJ*, 550, 713, <https://doi.org/10.1086/319818>
- Matsuda, T., Ishii, T., Sekino, N., et al. 1992, *MNRAS*, 255, 183, <https://doi.org/10.1093/mnras/255.2.183>
- Mendoza, E. E. 1970, *BOTT*, 5, 269
- Moffat, A. F. J., Koenigsberger, G., & Auer, L. H. 1989, *ApJ*, 344, 734, <https://doi.org/10.1086/167838>
- Moffat, A. F. J., Marchenko, S. V., Bartzakos, P., et al. 1998, *ApJ*, 497, 896, <https://doi.org/10.1086/305475>
- Moreno, E., Koenigsberger, G., & Harrington, D. M. 2011, *A&A*, 528, 48, <https://doi.org/10.1051/0004-6361/201015874>
- Münch, G. 1950, *ApJ*, 112, 266, <https://doi.org/10.1086/145341>
- Nagae, T., Oka, K., Matsuda, T., et al. 2004, *A&A*, 419, 335, <https://doi.org/10.1051/0004-6361:200040070>
- Nazé, Y., Koenigsberger, G., Pittard, J. M., et al. 2018, *ApJ*, 853, 164, <https://doi.org/10.3847/1538-4357/aaa29c>
- Nazé, Y. & Rauw, G. 2017, *IAUS* 239, The Lives and Death-Throes of Massive Stars, 359
- Niemela, V. S., Marraco, H. G., & Cabanne, M. L. 1986, *PASP*, 98, 1133, <https://doi.org/10.1086/131910>
- Osmer, P. S. 1973, *ApJ*, 181, 327, <https://doi.org/10.1086/152051>
- Paxton, B., Smolec, R., Schwab, J., et al. 2019, *ApJS*, 243, 10, <https://doi.org/10.3847/1538-4365/ab2241>
- Perrier, C., Breysacher, J., & Rauw, G. 2009, *A&A*, 503, 963, <https://doi.org/10.1051/0004-6361/200911707>
- Pittard, J. M. 2009, *MNRAS*, 396, 1743, <https://doi.org/10.1111/j.1365-2966.2009.14857.x>
- Pittard, J. M. & Dawson, B. 2018, *MNRAS*, 477, 5640, <https://doi.org/10.1093/mnras/sty1025>
- Prilutskii, O. F. & Usov, V. V. 1976, *AZh*, 53, 6
- Puls, J., Urbaneja, M. A., Venero, R., et al. 2005, *A&A*, 435, 669, <https://doi.org/10.1051/0004-6361:20042365>
- Richardson, N. D., Russell, C. M. P., St-Jean, L., et al. 2017, *MNRAS*, 471, 2715, <https://doi.org/10.1093/mnras/stx1731>
- Ruffert, M. & Arnett, D. 1994, *ApJ*, 427, 351, <https://doi.org/10.1086/174145>
- Russell, C. M. P., Corcoran, M. F., Hamaguchi, K., et al. 2016, *MNRAS*, 458, 2275, <https://doi.org/10.1093/mnras/stw339>
- Schweickhardt, J. 2000, PhD Thesis, Landessternwarte, Heidelberg/Königstuhl
- Schweickhardt, J., Wolf, B., Schmid, H. M., et al. 2000, *ASPC* 204, Thermal and Ionization Aspects of Flows from Hot Stars, ed. H. Lamers & A. Sapar, 113
- Shenar, T., Hainich, R., Todt, H., et al. 2016, *A&A*, 591, 22, <https://doi.org/10.1051/0004-6361/201527916>
- Smith, L. F. 1968, *MNRAS*, 140, 409, <https://doi.org/10.1093/mnras/140.4.409>
- Soker, N. & Behar, E. 2006, *ApJ*, 652, 1563, <https://doi.org/10.1086/508336>
- Sterken, C. & Breysacher, J. 1997, *A&A*, 328, 269
- Toledano, O., Koenigsberger, G., & Moreno, E. 2007, *ASPC* 367, Massive Stars in Interactive Binaries, ed. N. St. -Louis & A. F. J. Moffat, 437
- van den Bergh, S. 1976, *IAUC* 2993, ed. B. G. Marsden, 2
- Villar-Sbaffi, A., Moffat, A. F. J., & St-Louis, N. 2003, *ApJ*, 590, 483, <https://doi.org/10.1086/374970>

Julia I. Arias and R. Barbá: Departamento de Física, Universidad de La Serena, Av. Juan Cisternas 1200 Norte, La Serena, Chile (jarias@userena.cl).

G. Ferrero and R. Gamen: Facultad de Ciencias Astronómicas y Geofísicas, Universidad Nacional de La Plata, and Instituto de Astrofísica de La Plata (CCT La Plata-CONICET), Paseo del Bosque S/N, B1900FWA, La Plata, Argentina (gferrero@fcaglp.unlp.edu.ar, rgamen@fcaglp.unlp.edu.ar).

D. J. Hillier: Department of Physics and Astronomy, & Pittsburg Particle Physics, Astrophysics and Cosmology Center (PITT PACC), 3941 O'Hara Street, University of Pittsburgh, Pittsburgh, PA 15260, USA (hillier@pitt.edu).

G. Koenigsberger: Instituto de Ciencias Físicas, Universidad Nacional Autónoma de México, Ave. Universidad S/N, Cuernavaca, Morelos, 62210, México (gloria@icf.unam.mx).

N. Morrell: Las Campanas Observatory, Carnegie Observatories, Casilla 601, La Serena, Chile (nmorrell@lco.edu).

W. Schmutz: Physikalisch-Meteorologisches Observatorium Davos and World Radiation Center, Dorfstrasse 33, CH-7260 Davos Dorf, Switzerland (werner.schmutz@pmodwrc.ch).

OBITUARY



Renan Arcadio Poveda Ricalde
1930–2022

Arcadio Poveda passed away in Mexico City on March 24th, 2022. He was a Professor at the Instituto de Astronomía of the Universidad Nacional Autónoma de México (UNAM). He also held a Chair of Excellence, and was an Emeritus Professor of both UNAM and the Sistema Nacional de Investigadores of Consejo Nacional de Ciencia y Tecnología (Conacyt).

He was born in Mérida, Yucatán on July 15th, 1930. From an early age he showed great interest in science and research. He moved from Mérida to Mexico City to study Physics at the Facultad de Ciencias,

UNAM. At the same time, he attended astronomy lectures delivered by Paris Pishmish at the Observatorio Astronómico Nacional. He continued his studies at the University of California at Berkeley, where he obtained his PhD in 1956. Upon his return to Mexico City he was appointed Associate Researcher at the Instituto de Astronomía of UNAM, where he continued for the rest of his career. Early on, he showed great interest in lecturing and incorporating young students into research projects. He was intensely dedicated and productive, and soon several students were excited by his enthusiasm for astrophysics. In 1962, he directed my BSc thesis on Stromgren Spheres. Since the beginning of the operation of the first computer in Mexico, the IBM 650 at UNAM Computing Center, he encouraged his students to become familiar with this instrument for the development of their future research.

The astrophysical topics he studied were very diverse, I will mention briefly some of his main subjects of interest.

Poveda realized that the masses of elliptical galaxies could be derived from their observable photometric and kinematic properties, specifically from the dispersion of their star velocities with the help of the Virial Theorem. Masses play an important role in correlations of galaxian properties, as unified in the Fundamental Plane. This work formed a foundation for many subsequent studies.

In 1965, from just a handful of observational data related to star formation then available, he proposed a scenario with several predictions that were well ahead of that time. Originally motivated by two puzzling facts then known, the existence of young stars below the main sequence and the so-called Faulkner-Griffiths-Hoyle paradox, Poveda went on to predict the existence of infrared excesses in young stars, to speculate on the ubiquity of planetary systems, and to present a modern view that described several key characteristics of the Herbig-Haro objects. These predictions were later confirmed observationally and constitute an important part of our present knowledge of stellar and planetary formation.

Poveda was also interested in supernova explosions and their remnants. His collaboration with Ludowijk Woltjer led to an empirical relation linking the surface brightness at radio wavelengths with the diameter of supernova remnants: the sigma-D Relation. While the theoretical explanation of this relation is not fully satisfactory, its practical utility in the estimation of distances to supernova remnants made it very appealing in the study of their galactic distribution.

In 1967 Poveda and Christine Allen proposed a new mechanism that drives runaway stars as the result of the gravitational collapse of proto-stellar clusters. Over the years, this mechanism has proved to be viable, and it is now recognized as one of the two most accepted mechanisms that give rise to runaway stars in our Galaxy. In their research they wondered about the formation of double and multiple stars. They concluded that there were three processes involved: multiple condensations, capture, and fission. They and others made much progress on multiple condensations and cluster disintegration. In later work, they pointed out that young double stars can be found at large separations (up to 100,000 AU) while the maximum separations found became smaller the older the systems are. The work on runaway stars triggered interest to catch escaping stars “in flagranti” among the Orion Trapezium members, and their close neighbors. This problem has encouraged some colleagues to obtain data to improve our knowledge on the kinematics of that very young and relatively nearby stellar system. Recent observations of components A, B and E in the Orion Trapezium, favor very recent, and probably ongoing, violent dynamical activity among the Trapezium members which are, in turn, multiple systems themselves. As part of their work on trapezia, they found that they can eject members either early on in their evolution (1000 yr) or much later (a million yr). Depending on their configuration, trapezia can completely disintegrate in times as short as several thousand years, or they can last up to a million years.

Poveda extended his scientific interests to planetary sciences, namely to comets, asteroids, meteorites, and impact craters. In particular, the Chicxulub impact crater caught his attention. Chicxulub is the best preserved of the large multi-ring craters in the terrestrial record and its impact has been related to the global environmental climatic effects and the mass extinction that marks the Cretaceous-Tertiary boundary. In addition to studying the crater, he investigated asteroid and cometary impacts in the inner solar system, impact chronologies, and near-Earth objects, thus bringing a planetary perspective to crater studies.

In addition to his astronomical work, Poveda was active in academic-administrative tasks that led to the development of several research institutions. In 1968 he was appointed Director of the Instituto de Astronomía, UNAM. Around 1973, and full of enthusiasm, he started the construction of the Observatorio Astronómico Nacional in the Sierra de San Pedro Mártir, in Baja California. This site had been identified by Guillermo Haro as suitable for this purpose a few years earlier. Much of Poveda’s effort was the development and construction

of this observatory. Three telescopes that are still in operation were installed (84 cm, 1.5 m and 2.1 m in diameter). The observatory was inaugurated in September 1979. From the beginning of this development, the need to establish an operations station, as well as an astronomical research center in the nearby city of Ensenada, was recognized. This center was inaugurated in 1980. A few years later, Poveda became a leading administrator at UNAM. He was appointed as member of the Governing Board of this university, and later as Dean of Science, in addition to participating in various planning committees.

Apart from his activities at UNAM, he promoted the foundation of the Centro de Investigación Científica y Educación Superior de Ensenada, Baja California (CISESE); and also the foundation of the Centro de Investigación en Óptica (CIO) in León Guanajuato, among other projects. He also held various advisory positions in other academic institutions.

He was a member of the Mexican Academy of Sciences, the American Astronomical Society, and the International Astronomical Union.

His work was widely recognized through the many distinctions he received: the Prize for Young Scientist from the Academia Mexicana de Ciencias (1966), the National Prize for Sciences and Arts (1975), the Eligio Ancona Medal from the Government of Yucatan (1977), and honorary doctorates from the Universidad de Yucatán (1977), from the Centro de Investigación en Óptica (2000), and from the University Council of UNAM (2001). He was appointed as member of El Colegio Nacional in 1989. The public planetarium in his native Mérida, Yucatán, bears his name in recognition of his academic merits.

He is survived by his son Renan, his daughter Laila, and several grandchildren.

Manuel Peimbert

OBITUARY



María Estela de Lara Andrade

On April 25, B.S María Estela de Lara Andrade passed away in the city of Ensenada, Baja California. She worked for more than forty years as an Academic Technician at the Institute of Astronomy (IA) of the National Autonomous University of Mexico (UNAM), where she carried out various tasks in support of astronomical research, but where she also made her own original contributions. While still a student, Estela joined the IA

staff in 1973 to write her Bachelor thesis in Physics. Under the direction of Dr. Carlos Chavarría Kleinhenn, she developed a research topic suggested by Dr. Harold L. Johnson. She concluded this work in 1976, and successfully defended it at the Faculty of Sciences of the UNAM. The title of her thesis was “Photoelectric Photometry with a Silicon Detector”. Since her first staff appointment she became an assiduous user of the two telescopes installed at the then nascent National Astronomical Observatory, developed by UNAM on the top of the Sierra de San Pedro Mártir, Baja California. She thus became a pioneer at this new observatory. Due to the frequency and number of observations required for her work, in 1975 she decided to settle down in Ensenada, where she also formed a solid family.

The photoelectric photometry of young stars was her main astronomical research subject. More than twenty research papers published in specialized international journals reflect her contribution. She also participated with presentations at various scientific congresses.

Her interest in disseminating astronomical knowledge was enduring, which is why she dedicated an important part of her time to outreach work, especially aimed at children. Her work enabled many children to safely enjoy the total solar eclipse of 1991 and the passage of Venus in front of the solar disk in 2012. In addition to giving a large number of talks, she organized conference cycles, which over time have become institutional. She was also a co-author of a couple of books. Starting in 2008, and until her retirement in 2014, she was co-editor of the *Gaceta Ensenada*, a periodic journal that UNAM publishes for that city.

In 2011, her work was deservedly valued, when UNAM awarded her the “Sor Juana Inés de la Cruz” recognition.

Marco Arturo Moreno Corral

AUTHOR INDEX

- Abdel-Salam, E. A-B** ANN and Analytical Solutions to Relativistic Isothermal Gas Spheres . *Mohamed I. Nouh, Yosry A. Azzam, Emad A-B Abdel-Salam, Farag I. Elnagahy, & Tarek M. Kamel*, 321
- Acerbi, F.** Photometric Analysis of Two K Spectral Type Contact Binary Systems. *C. Barani, M. Martignoni, F. Acerbi, R. Michel, H. Aceves & V. Popov*, 237
- Aceves, H.** Photometric Analysis of Two K Spectral Type Contact Binary Systems. *C. Barani, M. Martignoni, F. Acerbi, R. Michel, H. Aceves & V. Popov*, 237
- Aguilar-Argüello, G.** Assessing the Hierarchical Hamiltonian Splitting Integrator for Collisionless N -body Simulations. *G. Aguilar-Argüello, O. Valenzuela, H. Velázquez, J. C. Clemente, & J. A. Trelles*, 197
- Ahmed, N.** A Non-Singular Closed Bouncing Universe Without Violation of Null Energy Condition. *Nasr Ahmed, Tarek M. Kamel, & Mohamed I. Nouh*, 245
- Alarie, A.** Temperature Discrepancy with Photoionization Models of the Narrow-Line Region. *L. Binette, M. Villar Martín, G. Magris C., M. Martínez-Paredes, A. Alarie, A. Rodríguez Ardila, & I. Villacaña-Pedraza*, 133
- Alton, K. B.** CCD Photometry and Evolutionary Status of the HADS Variable PT Com. *Kevin B. Alton* , 109
- Arellano Ferro, A.** A New Visit to the Variable Stars in M56 and its Colour-Magnitude Diagram Structure. *D. Deras, A. Arellano Ferro, I. Bustos Fierro, & M. A. Yepez*, 121
- Arellano Ferro, A.** A Vindication of the RR Lyrae Fourier Light Curve Decomposition for the Calculation of Metallicity and Distance in Globular Clusters . *A. Arellano Ferro*, 257
- Arias, J.I.** Observational Constraints on the HD 5980 Wind-Wind Collision. *G. Koenigsberger, N. Morrell, D. J. Hillier, W. Schmutz, R. Gamen, J. I. Arias, R. Barbá, & G. Ferrero*, 403
- Arreaga-García, G.** Simulations of Unequal Binary Collisions Embedded in a Turbulent Gas Cloud far from a Massive Gravitational Center. *G. Arreaga-García*, 273
- Azzam, Y. A.** ANN and Analytical Solutions to Relativistic Isothermal Gas Spheres . *Mohamed I. Nouh, Yosry A. Azzam, Emad A-B Abdel-Salam, Farag I. Elnagahy, & Tarek M. Kamel*, 321
- Banks, T.** A Study of the NGC 1193 and NGC 1798 Open Clusters Using CCD UBV Photometric and Gaia EDR3 Data. *Talar Yontan, Hikmet Çakmak, Selçuk Bilir, Timothy Banks, Michel Raúl, Remziye Canbay, Seliz Koç, Seval Taşdemir, Hülya Erçay, Burçin Tanık Öztürk, & Deniz Cennet Dursun*, 333
- Barani, C.** Photometric Analysis of Two K Spectral Type Contact Binary Systems. *C. Barani, M. Martignoni, F. Acerbi, R. Michel, H. Aceves & V. Popov*, 237
- Barbá, R.** Observational Constraints on the HD 5980 Wind-Wind Collision. *G. Koenigsberger, N. Morrell, D. J. Hillier, W. Schmutz, R. Gamen, J. I. Arias, R. Barbá, & G. Ferrero*, 403
- Battaner, E.** An Astrophysical Perspective of Life. The Growth of Complexity. *F. Sánchez & E. Battaner*, 375
- Bernabéu, G.** Cen X–3 as Seen by MAXI During Six Years. *Á. Torregrosa, J. J. Rodes-Roca, J. M. Torrejón, G. Sanjurjo-Ferrín, & G. Bernabéu*, 355
- Bilir, S.** A Study of the NGC 1193 and NGC 1798 Open Clusters Using CCD UBV Photometric and Gaia EDR3 Data. *Talar Yontan, Hikmet Çakmak, Selçuk Bilir, Timothy Banks, Michel Raúl, Remziye Canbay, Seliz Koç, Seval Taşdemir, Hülya Erçay, Burçin Tanık Öztürk, & Deniz Cennet Dursun*, 333
- Binette, L.** Temperature Discrepancy with Photoionization Models of the Narrow-Line Region. *L. Binette, M. Villar Martín, G. Magris C., M. Martínez-Paredes, A. Alarie, A. Rodríguez Ardila, & I. Villacaña-Pedraza*, 133
- Branham Jr., Richard L.** A New Orbit for Comet C/1830 F1 (Great March comet). *Richard L. Branham Jr.*, 309
- Bulut, S.** Precise Measurement of Orbital and Physical Parameters of Bright Detached Solar Analog Eclipsing Binaries. *Ö. Çakırlı, B. Hoyman, S. Bulut, A. Dervişoğlu, & C. Kayhan* , 3
- Bustos Fierro, I.** A New Visit to the Variable Stars in M56 and its Colour-Magnitude Diagram Structure. *D. Deras, A. Arellano Ferro, I. Bustos Fierro, & M. A. Yepez*, 121
- Çakırlı, Ö.** Precise Measurement of Orbital and Physical Parameters of Bright Detached Solar Analog Eclipsing Binaries. *Ö. Çakırlı, B. Hoyman, S. Bulut, A. Dervişoğlu, & C. Kayhan* , 3

- Çakmak, T.** A Study of the NGC 1193 and NGC 1798 Open Clusters Using CCD UBV Photometric and Gaia EDR3 Data. *Talar Yontan, Hikmet Çakmak, Selçuk Bilir, Timothy Banks, Michel Raúl, Remziye Canbay, Seliz Koç, Seval Taşdemir, Hülya Erçay, Burçin Tanık Öztürk, & Deniz Cennet Dursun*, 333
- Canbay, R.** A Study of the NGC 1193 and NGC 1798 Open Clusters Using CCD UBV Photometric and Gaia EDR3 Data. *Talar Yontan, Hikmet Çakmak, Selçuk Bilir, Timothy Banks, Michel Raúl, Remziye Canbay, Seliz Koç, Seval Taşdemir, Hülya Erçay, Burçin Tanık Öztürk, & Deniz Cennet Dursun*, 333
- Cantó, J.** Mildly Relativistic, Ballistic Corkscrew Jets as Rotated Spirals. *A. C. Raga, J. Cantó, A. Castellanos-Ramírez, A. Rodríguez-González, & P. R. Rivera-Ortiz*, 301
- Cantó, J.** The Bondi-Hoyle Accretion Tail of Point Sources Travelling Hypersonically Through a Dense Environment. *A. C. Raga, J. Cantó, A. Castellanos-Ramírez, A. Rodríguez-González, & P. R. Rivera-Ortiz*, 215
- Cantó, J.** The HII Regions and Bow Shocks Around Runaway O Stars. *A. C. Raga, J. Cantó, & A. Noriega-Crespo*, 395
- Castellanos-Ramírez, A.** Mildly Relativistic, Ballistic Corkscrew Jets as Rotated Spirals. *A. C. Raga, J. Cantó, A. Castellanos-Ramírez, A. Rodríguez-González, & P. R. Rivera-Ortiz*, 301
- Castellanos-Ramírez, A.** The Bondi-Hoyle Accretion Tail of Point Sources Travelling Hypersonically Through a Dense Environment. *A. C. Raga, J. Cantó, A. Castellanos-Ramírez, A. Rodríguez-González, & P. R. Rivera-Ortiz*, 215
- Clemente, J. C.** Assessing the Hierarchical Hamiltonian Splitting Integrator for Collisionless N -body Simulations. *G. Aguilar-Argüello, O. Valenzuela, H. Velázquez, J. C. Clemente, & J. A. Trelles*, 197
- de Melo, C. F.** A Study on Different Attitude Strategies and Mission Parameters Based on LightSail-2. *L. G. Meireles, A. F. B. A. Prado, C. F. de Melo, & M. C. Pereira*, 23
- Deras, D.** A New Visit to the Variable Stars in M56 and its Colour-Magnitude Diagram Structure. *D. Deras, A. Arellano Ferro, I. Bustos Fierro, & M. A. Yepez*, 121
- Dervişoğlu, A.** Precise Measurement of Orbital and Physical Parameters of Bright Detached Solar Analog Eclipsing Binaries. *Ö. Çakırlı, B. Hoyman, S. Bulut, A. Dervişoğlu, & C. Kayhan*, 3
- Dursun, D.C.** A Study of the NGC 1193 and NGC 1798 Open Clusters Using CCD UBV Photometric and Gaia EDR3 Data. *Talar Yontan, Hikmet Çakmak, Selçuk Bilir, Timothy Banks, Michel Raúl, Remziye Canbay, Seliz Koç, Seval Taşdemir, Hülya Erçay, Burçin Tanık Öztürk, & Deniz Cennet Dursun*, 333
- Echevarría, J.** New Photometry and Spectroscopy of DW Cancri. *S. H. Ramírez, O. Segura Montero, R. Michel, & J. Echevarría*, 47
- Eftekhar, M.** Comprehensive Analysis of the Full TESS Orbital Phase Curve of WASP-121b. *M. Eftekhar*, 99
- Elhosseiny, E. G.** The Principal Astrophysical Parameters of the Open Clusters *Gulliver* 18 and *Gulliver* 58 Determined Using Gaia EDR3 Data. *A. L. Tadross & E. G. Elhosseiny*, 387
- Elnagahy, F. I.** ANN and Analytical Solutions to Relativistic Isothermal Gas Spheres. *Mohamed I. Nouh, Yosry A. Azzam, Emad A-B Abdel-Salam, Farag I. Elnagahy, & Tarek M. Kamel*, 321
- Erçay, H.** A Study of the NGC 1193 and NGC 1798 Open Clusters Using CCD UBV Photometric and Gaia EDR3 Data. *Talar Yontan, Hikmet Çakmak, Selçuk Bilir, Timothy Banks, Michel Raúl, Remziye Canbay, Seliz Koç, Seval Taşdemir, Hülya Erçay, Burçin Tanık Öztürk, & Deniz Cennet Dursun*, 333
- Ferrero, G.** Observational Constraints on the HD 5980 Wind-Wind Collision. *G. Koenigsberger, N. Morrell, D. J. Hillier, W. Schmutz, R. Gamen, J. I. Arias, R. Barbá, & G. Ferrero*, 403
- Frelíj, H.** C, T_1, T_2 : A Complementary Method to Detect Multiple Populations with the Washington Filter System. *H. Frelíj, D. Geisler, S. Villanova, & C. Munoz*, 181
- Gamen, R.** Observational Constraints on the HD 5980 Wind-Wind Collision. *G. Koenigsberger, N. Morrell, D. J. Hillier, W. Schmutz, R. Gamen, J. I. Arias, R. Barbá, & G. Ferrero*, 403
- García, L. A.** The Properties of High Redshift Galaxies. *L. A. García*, 83
- Geisler, D.** C, T_1, T_2 : A Complementary Method to Detect Multiple Populations with the Washington Filter System. *H. Frelíj, D. Geisler, S. Villanova, & C. Munoz*, 181
- Guerrero, C. A.** Off-axis Exact Ray Tracing Algorithm for Zero Coma Point Determination in Classical and Non-Classical Reflective Telescopes. *J. Herrera, M. N. Najera, & C. A. Guerrero*, 37
- Herrera, J.** Off-axis Exact Ray Tracing Algorithm for Zero Coma Point Determination in Classical and Non-Classical Reflective Telescopes. *J. Herrera, M. N. Najera, & C. A. Guerrero*, 37
- Hidalgo-Gómez, A.M.** Morphological Study of a Sample of Dwarf Tidal Galaxies Using the C - A Plane. *I. Vega-Acevedo & A. M. Hidalgo-Gómez*, 61
- Hillier, D.J.** Observational Constraints on the HD 5980 Wind-Wind Collision. *G. Koenigsberger, N. Morrell, D. J. Hillier, W. Schmutz, R. Gamen, J. I. Arias, R. Barbá, & G. Ferrero*, 403

- Hoyman, B.** Precise Measurement of Orbital and Physical Parameters of Bright Detached Solar Analog Eclipsing Binaries. *Ö. Çakırh, B. Hoyman, S. Bulut, A. Dervişoğlu, & C. Kayhan*, 3
- Hudec, R.** CzeV502 – an M Dwarf Near the Leo Triplet with Very Strong Flares. *J. Liška, R. Hudec, Z. Mikulášek, M. Zejda, J. Janík, & J. Štrobl*, 155
- Janík, J.** CzeV502 – an M Dwarf Near the Leo Triplet with Very Strong Flares. *J. Liška, R. Hudec, Z. Mikulášek, M. Zejda, J. Janík, & J. Štrobl*, 155
- Kamel, T. M.** A Non-Singular Closed Bouncing Universe Without Violation of Null Energy Condition. *Nasr Ahmed, Tarek M. Kamel, & Mohamed I. Nouh*, 245
- Kamel, T. M.** ANN and Analytical Solutions to Relativistic Isothermal Gas Spheres. *Mohamed I. Nouh, Yosry A. Azzam, Emad A-B Abdel-Salam, Farag I. Elnagahy, & Tarek M. Kamel*, 321
- Kayhan, C.** Precise Measurement of Orbital and Physical Parameters of Bright Detached Solar Analog Eclipsing Binaries. *Ö. Çakırh, B. Hoyman, S. Bulut, A. Dervişoğlu, & C. Kayhan*, 3
- Koenigsberger, G.** Observational Constraints on the HD 5980 Wind-Wind Collision. *G. Koenigsberger, N. Morrell, D. J. Hillier, W. Schmutz, R. Gamen, J. I. Arias, R. Barbá, & G. Ferrero*, 403
- Koç, S.** A Study of the NGC 1193 and NGC 1798 Open Clusters Using CCD UBV Photometric and Gaia EDR3 Data. *Talar Yontan, Hikmet Çakmak, Selçuk Bilir, Timothy Banks, Michel Raül, Remziye Canbay, Seliz Koç, Seval Taşdemir, Hülya Erçay, Burçin Tanık Öztürk, & Deniz Cennet Dursun*, 333
- Liška, J.** CzeV502 – an M Dwarf Near the Leo Triplet with Very Strong Flares. *J. Liška, R. Hudec, Z. Mikulášek, M. Zejda, J. Janík, & J. Štrobl*, 155
- Magris C., G.** Temperature Discrepancy with Photoionization Models of the Narrow-Line Region. *L. Binette, M. Villar Martín, G. Magris C., M. Martínez-Paredes, A. Alarie, A. Rodríguez Ardila, & I. Villicaña-Pedraza*, 133
- Makarov, V. V.** The Hipparcos Pleiades Parallax Error is Also a Proper Motion Error. *Valeri V. Makarov*, 315
- Martignoni, M.** Photometric Analysis of Two K Spectral Type Contact Binary Systems. *C. Barani, M. Martignoni, F. Acerbi, R. Michel, H. Aceves & V. Popov*, 237
- Martínez-Paredes, M.** Temperature Discrepancy with Photoionization Models of the Narrow-Line Region. *L. Binette, M. Villar Martín, G. Magris C., M. Martínez-Paredes, A. Alarie, A. Rodríguez Ardila, & I. Villicaña-Pedraza*, 133
- Meireles, L. G.** A Study on Different Attitude Strategies and Mission Parameters Based on LightSail-2. *L. G. Meireles, A. F. B. A. Prado, C. F. de Melo, & M. C. Pereira*, 23
- Michel, R.** New Photometry and Spectroscopy of DW Cancri. *S. H. Ramírez, O. Segura Montero, R. Michel, & J. Echevarría*, 47
- Michel, R.** Photometric Analysis of Two K Spectral Type Contact Binary Systems. *C. Barani, M. Martignoni, F. Acerbi, R. Michel, H. Aceves & V. Popov*, 237
- Mikulášek, Z.** CzeV502 – an M Dwarf Near the Leo Triplet with Very Strong Flares. *J. Liška, R. Hudec, Z. Mikulášek, M. Zejda, J. Janík, & J. Štrobl*, 155
- Moreno Corral, Marco Arturo** Obituary – María Estela de Lara Andrade. *M. A. Moreno Corral*, 447
- Morrell, N.** Observational Constraints on the HD 5980 Wind-Wind Collision. *G. Koenigsberger, N. Morrell, D. J. Hillier, W. Schmutz, R. Gamen, J. I. Arias, R. Barbá, & G. Ferrero*, 403
- Munoz, C.** C, T_1, T_2 : A Complementary Method to Detect Multiple Populations with the Washington Filter System. *H. Frelíj, D. Geisler, S. Villanova, & C. Munoz*, 181
- Najera, M. R.** Off-axis Exact Ray Tracing Algorithm for Zero Coma Point Determination in Classical and Non-Classical Reflective Telescopes. *J. Herrera, M. N. Najera, & C. A. Guerrero*, 37
- Nelson, R. H.** The Overcontact Binary V563 Lyrae. *R. H. Nelson*, 223
- Noriega-Crespo, A.** The HII Regions and Bow Shocks Around Runaway O Stars. *A. C. Raga, J. Cantó, & A. Noriega-Crespo*, 395
- Nouh, M. I.** A Non-Singular Closed Bouncing Universe Without Violation of Null Energy Condition. *Nasr Ahmed, Tarek M. Kamel, & Mohamed I. Nouh*, 245
- Nouh, M. I.** ANN and Analytical Solutions to Relativistic Isothermal Gas Spheres. *Mohamed I. Nouh, Yosry A. Azzam, Emad A-B Abdel-Salam, Farag I. Elnagahy, & Tarek M. Kamel*, 321
- Oostra, B.** The Differential Redshift of Titanium Lines in K Stars. *B. Oostra & P. Vargas*, 173
- Peimbert, Manuel** Obituary – Renan Arcadio Poveda Ricalde. *M. Peimbert*, 443
- Pereira, M. C.** A Study on Different Attitude Strategies and Mission Parameters Based on LightSail-2. *L. G. Meireles, A. F. B. A. Prado, C. F. de Melo, & M. C. Pereira*, 23
- Popov, V.** Photometric Analysis of Two K Spectral Type Contact Binary Systems. *C. Barani, M. Martignoni, F. Acerbi, R. Michel, H. Aceves & V. Popov*, 237
- Prado, A. F. B. A.** A Study on Different Attitude Strategies and Mission Parameters Based on LightSail-2. *L. G. Meireles, A. F. B. A. Prado, C. F. de Melo, & M. C. Pereira*, 23

- Raga, A. C.** Mildly Relativistic, Ballistic Corkscrew Jets as Rotated Spirals. *A. C. Raga, J. Cantó, A. Castellanos-Ramírez, A. Rodríguez-González, & P. R. Rivera-Ortiz*, 301
- Raga, A. C.** The Bondi-Hoyle Accretion Tail of Point Sources Travelling Hypersonically Through a Dense Environment. *A. C. Raga, J. Cantó, A. Castellanos-Ramírez, A. Rodríguez-González, & P. R. Rivera-Ortiz*, 215
- Raga, A. C.** The HII Regions and Bow Shocks Around Runaway O Stars. *A. C. Raga, J. Cantó, & A. Noriega-Crespo*, 395
- Ramírez, S. H.** New Photometry and Spectroscopy of DW Cancri. *S. H. Ramírez, O. Segura Montero, R. Michel, & J. Echevarría*, 47
- Raúl, M.** A Study of the NGC 1193 and NGC 1798 Open Clusters Using CCD UBV Photometric and Gaia EDR3 Data. *Talar Yontan, Hikmet Çakmak, Selçuk Bilir, Timothy Banks, Michel Raúl, Remziye Canbay, Seliz Koç, Seval Taşdemir, Hülya Erçay, Burçin Tanık Öztürk, & Deniz Cennet Dursun*, 333
- Rivera-Ortiz, P. R.** Mildly Relativistic, Ballistic Corkscrew Jets as Rotated Spirals. *A. C. Raga, J. Cantó, A. Castellanos-Ramírez, A. Rodríguez-González, & P. R. Rivera-Ortiz*, 301
- Rivera-Ortiz, P. R.** The Bondi-Hoyle Accretion Tail of Point Sources Travelling Hypersonically Through a Dense Environment. *A. C. Raga, J. Cantó, A. Castellanos-Ramírez, A. Rodríguez-González, & P. R. Rivera-Ortiz*, 215
- Rodes-Roca, J. J.** Cen X-3 as Seen by MAXI During Six Years. *Á. Torregrosa, J. J. Rodes-Roca, J. M. Torrejón, G. Sanjurjo-Ferrín, & G. Bernabéu*, 355
- Rodríguez Ardila, A.** Temperature Discrepancy with Photoionization Models of the Narrow-Line Region. *L. Binette, M. Villar Martín, G. Magris C., M. Martínez-Paredes, A. Alarie, A. Rodríguez Ardila, & I. Villacaña-Pedraza*, 133
- Rodríguez-González, A.** Mildly Relativistic, Ballistic Corkscrew Jets as Rotated Spirals. *A. C. Raga, J. Cantó, A. Castellanos-Ramírez, A. Rodríguez-González, & P. R. Rivera-Ortiz*, 301
- Rodríguez-González, A.** The Bondi-Hoyle Accretion Tail of Point Sources Travelling Hypersonically Through a Dense Environment. *A. C. Raga, J. Cantó, A. Castellanos-Ramírez, A. Rodríguez-González, & P. R. Rivera-Ortiz*, 215
- Sánchez, F.** An Astrophysical Perspective of Life. The Growth of Complexity. *F. Sánchez & E. Battaner*, 375
- Sanjurjo-Ferrín, G.** Cen X-3 as Seen by MAXI During Six Years. *Á. Torregrosa, J. J. Rodes-Roca, J. M. Torrejón, G. Sanjurjo-Ferrín, & G. Bernabéu*, 355
- Schmutz, W.** Observational Constraints on the HD 5980 Wind-Wind Collision. *G. Koenigsberger, N. Morrell, D. J. Hillier, W. Schmutz, R. Gamen, J. I. Arias, R. Barbá, & G. Ferrero*, 403
- Segura Montero, O.** New Photometry and Spectroscopy of DW Cancri. *S. H. Ramírez, O. Segura Montero, R. Michel, & J. Echevarría*, 47
- Štrobl, J.** CzeV502 – an M Dwarf Near the Leo Triplet with Very Strong Flares. *J. Liška, R. Hudec, Z. Mikulášek, M. Zejda, J. Janík, & J. Štrobl*, 155
- Tadross, A. L.** The Principal Astrophysical Parameters of the Open Clusters *Gulliver 18* and *Gulliver 58* Determined Using Gaia EDR3 Data. *A. L. Tadross & E. G. Elhosseiny*, 387
- Tanık Öztürk, B.** A Study of the NGC 1193 and NGC 1798 Open Clusters Using CCD UBV Photometric and Gaia EDR3 Data. *Talar Yontan, Hikmet Çakmak, Selçuk Bilir, Timothy Banks, Michel Raúl, Remziye Canbay, Seliz Koç, Seval Taşdemir, Hülya Erçay, Burçin Tanık Öztürk, & Deniz Cennet Dursun*, 333
- Taşdemir, S.** A Study of the NGC 1193 and NGC 1798 Open Clusters Using CCD UBV Photometric and Gaia EDR3 Data. *Talar Yontan, Hikmet Çakmak, Selçuk Bilir, Timothy Banks, Michel Raúl, Remziye Canbay, Seliz Koç, Seval Taşdemir, Hülya Erçay, Burçin Tanık Öztürk, & Deniz Cennet Dursun*, 333
- Torregrosa, Á.** Cen X-3 as Seen by MAXI During Six Years. *Á. Torregrosa, J. J. Rodes-Roca, J. M. Torrejón, G. Sanjurjo-Ferrín, & G. Bernabéu*, 355
- Torrejón, J. M.** Cen X-3 as Seen by MAXI During Six Years. *Á. Torregrosa, J. J. Rodes-Roca, J. M. Torrejón, G. Sanjurjo-Ferrín, & G. Bernabéu*, 355
- Trelles, J. A.** Assessing the Hierarchical Hamiltonian Splitting Integrator for Collisionless N -body Simulations. *G. Aguilar-Argüello, O. Valenzuela, H. Velázquez, J. C. Clemente, & J. A. Trelles*, 197
- Valenzuela, O.** Assessing the Hierarchical Hamiltonian Splitting Integrator for Collisionless N -body Simulations. *G. Aguilar-Argüello, O. Valenzuela, H. Velázquez, J. C. Clemente, & J. A. Trelles*, 197
- Vargas, P.** The Differential Redshift of Titanium Lines in K Stars. *B. Oostra & P. Vargas*, 173
- Vega-Acevedo, I.** Morphological Study of a Sample of Dwarf Tidal Galaxies Using the C - A Plane. *I. Vega-Acevedo & A. M. Hidalgo-Gómez*, 61
- Velázquez, H.** Assessing the Hierarchical Hamiltonian Splitting Integrator for Collisionless N -body Simulations. *G. Aguilar-Argüello, O. Valenzuela, H. Velázquez, J. C. Clemente, & J. A. Trelles*, 197
- Villanova, S.** C, T_1, T_2 : A Complementary Method to Detect Multiple Populations with the Washington Filter System. *H. Freilijj, D. Geisler, S. Villanova, & C. Munoz*, 181

- Villar Martín, M.** Temperature Discrepancy with Photoionization Models of the Narrow-Line Region. *L. Binette, M. Villar Martín, G. Magris C., M. Martínez-Paredes, A. Alarie, A. Rodríguez Ardila, & I. Villicaña-Pedraza*, 133
- Villicaña-Pedraza, I.** Temperature Discrepancy with Photoionization Models of the Narrow-Line Region. *L. Binette, M. Villar Martín, G. Magris C., M. Martínez-Paredes, A. Alarie, A. Rodríguez Ardila, & I. Villicaña-Pedraza*, 133
- Yepez, M. A.** A New Visit to the Variable Stars in M56 and its Colour-Magnitude Diagram Structure. *D. Deras, A. Arellano Ferro, I. Bustos Fierro, & M. A. Yepez*, 121
- Yontan, T.** A Study of the NGC 1193 and NGC 1798 Open Clusters Using CCD UBV Photometric and Gaia EDR3 Data. *Talar Yontan, Hikmet Çakmak, Selçuk Bilir, Timothy Banks, Michel Raúl, Remziye Canbay, Seliz Koç, Seval Taşdemir, Hülya Erçay, Burçin Tanık Öztürk, & Deniz Cennet Dursun*, 333
- Zejda, M.** CzeV502 – an M Dwarf Near the Leo Triplet with Very Strong Flares. *J. Liška, R. Hudec, Z. Mikulášek, M. Zejda, J. Janík, & J. Štrobl*, 155

La *Revista Mexicana de Astronomía y Astrofísica*, fundada en 1974, publica trabajos originales de investigación en todas las ramas de la astronomía, astrofísica y temas vinculados a éstas. Se editan dos números por año y su distribución es gratuita a todas las instituciones relacionadas con los campos cubiertos por esta revista.

La política editorial de la *RMxAA* consiste en enviar a arbitrar los artículos recibidos a especialistas en el campo. Los interesados en publicar en nuestra revista deberán enviar por correo electrónico, a la dirección rmaa@astro.unam.mx, la versión completa de su artículo en formato PostScript o PDF y el archivo LaTeX. Estos archivos deberán ir acompañados de una carta de presentación. Todos los trabajos deben ser preparados en inglés usando la versión más reciente del macro en LaTeX de la *RMxAA* “*rmaa.cls*” (disponible en <https://www.itya.unam.mx/rmaa/>). Se requiere un “Abstract” no mayor que 12 líneas, y un “Resumen” en español (este último podrá ser provisto por los editores de ser necesario); también se incluirán de 1 a 6 palabras clave (“Keywords”) de la lista de las revistas astronómicas internacionales. Se requiere que cada tabla incluida en el texto esté numerada y con título; las figuras deberán estar en formato PostScript (.ps) o PostScript encapsulado (.eps), estar numeradas y con leyenda explicativa. Se requiere que cada tabla y figura estén mencionadas en el texto. El estilo de las referencias sigue las normas astronómicas internacionales recientes. Para mayor información sobre el estilo de la *RMxAA* se puede consultar el archivo de ejemplo que viene incluido en los macros. La publicación es gratuita para los autores.

En 1995 se inició la Serie de Conferencias de la *Revista Mexicana de Astronomía y Astrofísica*, dedicada a la publicación de las memorias de reuniones astronómicas efectuadas en México y en otros países del continente. Hasta 1994 las memorias de reuniones astronómicas de la región se publicaron como volúmenes especiales de la *RMxAA*.

Las condiciones de publicación de cada volumen de las memorias de conferencias serán el resultado de un convenio establecido entre la *RMxAC* y los organizadores de cada evento. Los detalles de la publicación, que incluyen fechas y extensión de los textos, serán anunciados por los editores de cada conferencia. Las contribuciones extensas estarán en inglés con un resumen en español (o portugués en caso de las Reuniones regionales). Los resúmenes de las reuniones que no son temáticas tendrán una extensión máxima de 300 palabras incluyendo título, autores y afiliación; serán exclusivamente en inglés. Los macros LaTeX para las memorias se encuentran en <http://www.astroscu.unam.mx/~rmaa>. Todas las contribuciones y resúmenes deberán estar en estos formatos.

Se concede permiso a los autores de artículos y libros científicos para citar trabajos publicados en la *RMxAA* y en la *RMxAC* siempre y cuando se dé la referencia completa. También se permite la reproducción de figuras y tablas bajo las mismas condiciones.

La *RMxAA* aparece indexada en Current Contents, Science Citation Index, Astronomy and Astrophysics Abstracts, Physics Briefs, Publicaciones Científicas en América Latina, Astronomy and Astrophysics Monthly Index, PERIODICA, RedALyC, Latindex y SciELO.

The *Revista Mexicana de Astronomía y Astrofísica*, founded in 1974, publishes original research papers in all branches of astronomy, astrophysics and closely related fields. Two numbers per year are issued and are distributed free of charge to all institutions engaged in the fields covered by the *RMxAA*.

All papers received by the *RMxAA* are sent to a specialist in the field for refereeing. Authors interested in publishing in the *RMxAA* should send their papers to the e-mail address rmaa@astro.unam.mx, in PostScript or PDF format, along with the LaTeX file. A submission letter should also be sent. Papers should be prepared in English, using the most recent version of the *RMxAA* LaTeX document class “*rmaa.cls*” (available from <https://www.itya.unam.mx/rmaa/>). An “Abstract” of at most 12 lines is required, as well as a “Resumen” in Spanish. The latter can be provided by the Editors, if necessary. A total of six or fewer “Keywords”, taken from the lists of international astronomical journals should be included. Tables should be numbered and include a title. Figures should be submitted in PostScript (.ps) or Encapsulated PostScript (.eps) format, should be numbered, and should include a caption. Both tables and figures should be mentioned in the text. The style of the references follows recent international astronomical usage. For more information about the style norms of *RMxAA* please consult the example included in the LaTeX package. Publication in *RMxAA* is free of charge to authors.

The Conference Series of *Revista Mexicana de Astronomía y Astrofísica* was founded in 1995 to publish the proceedings of astronomical meetings held in Mexico and other countries throughout the continent. Until 1994 such proceedings had been published as special issues of *Revista Mexicana de Astronomía y Astrofísica*.

Conditions of publication of proceedings of each conference will be the result of a mutual agreement between the *RMxAC* and the organizing committee. Details of publication, including length of papers, will be announced by the editors of each event. The extensive contributions should be in English, and should include an abstract in Spanish (or Portuguese for regional meetings). The abstracts of non-thematic meetings should not exceed 300 words including title, authors, and affiliation; they should be exclusively in English. The LaTeX templates specially prepared for proceedings can be obtained at <http://www.astroscu.unam.mx/~rmaa>; all papers should be submitted in this format.

Authors of scientific papers and books may quote articles published both in *RMxAA* and *RMxAC* provided that a complete reference to the source is given. Reproduction of figures and tables is also permitted on the same basis.

The *RMxAA* is indexed in Current Contents, Science Citation Index, Astronomy and Astrophysics Abstracts, Physics Briefs, Publicaciones Científicas en América Latina, Astronomy and Astrophysics Monthly Index, PERIODICA, RedALyC, Latindex, and SciELO.